DETERMINATION OF NASCENT H_2 ROVIBRATIONAL DISTRIBUTIONS BY LASER INDUCED FLUORESCENCE: APPLICATIONS TO FORMALDEHYDE PHOTODISSOCIATION AND HYDROGEN EXCHANGE REACTIONS

Thesis by

Garth Rockwood Parker, Jr.

In Partial Fulfillment of the Requirements

for the Degree of

Doctor of Philosophy

Division of Chemistry and Chemical Engineering

California Institute of Technology

Pasadena, California

1988

(Submitted April 25, 1988)

ACKNOWLEDGEMENTS

The work in this dissertation could not have been accomplished without the assistance of many fine people. I would like to thank the personnel of the Divisional support staff, especially Tom Dunn of the Electronics Support Group who built the LASER TIMING CONTROLLER, Ray Garcia of the Instrument Shop who built the three compartment cell used in all the VUV and LIF experiments, and Dan Zirin who helped me erradicate many bugs on the Divisional VAX-11/780. I would also like to thank the group secretaries over the years, Adria, Heidi, Laurie, and Lena, for their friendliness and superb assistance with all our problems.

I would also like to thank the many members of the group with whom I have worked these past seven years: Dave, Jerry, Jim, Charlie, Dorothy, Kerry, Diane, Tim, Paul, Steve, Mark, Peng, Isaac, Ashraf, and Mary. I would especially like to thank Maria Arnazzi for all of her assistance over the past several months in helping with the experiments in this thesis. I wish her all the best as she takes over the resources of 013 Noyes.

My advisor, Aron Kuppermann, has shown remarkable patience with all aspects of this project, especially the hydrogen exchange reaction. I know how much he wanted that experiment to work. He has provided a great deal of support and encouragement over the years, both scientifically and emotionally.

Most importantly, I must acknowledge the support and love from my wife, Karen, who has stood by my side, from dawn to midnight (and then some), over these many years.

Many, many thanks!!!

ABSTRACT

Individual quantum states of H_2 have been detected using the technique of Laser Induced Fluorescence. This technique is extremely sensitive, with a detection sensitivity of 6×10^8 states cm^{-3} in a probed volume of 0.029 cm^3 with a signal-to-noise ratio of 3. This technique is also accurate. A spectrum of room temperature H_2 had a rotational temperature of 305.8 ± 3.0 K. LIF detection of H_2 was used to study the H_2CO photodissociation reaction under essentially collision-free conditions. Following excitation of the ${}^rR_3$ bandhead of the $2_0^1 4_0^3$ transition at 30388.5 cm^{-1}, the principal product was *ortho*-H_2. States as high as $v = 4$, $J = 5$ were seen. Within the $v = 1$ channel, the rotational distribution peaked at $J = 3$. Following excitation of the ${}^rR_4$ bandhead of the $2_0^1 4_0^3$ transition at 30396.7 cm^{-1}, the principal product was *para*-H_2. This is the first report of the *para*-H_2 distribution following H_2CO dissociation. The rotational distribution is similar to that for *ortho*-H_2 and peaks at $J = 4$ within $v = 1$ channel. This result contradicts a recent theoretical calculation that predicted that the *para*-H_2 distribution would be bimodal with a minimum at $J = 6$. Quantitative analysis of higher vibrational levels was hampered by a lack of spectroscopic knowledge (both transition energies and intensities) when the the $\tilde{B}$ and $\tilde{C}$ states perturb each other. Attempts to use LIF to study the hydrogen exchange reaction have been unsuccessful.

TABLE OF CONTENTS

CHAPTER 1.

INTRODUCTION

Three laser techniques have recently been developed to detect individual quantum states of molecular hydrogen. These techniques are Coherent Anti-Stokes Raman Scattering (CARS), Resonantly Enhanced Multi-Photon Inonization (REMPI), and Laser Induced Fluorescence (LIF).

The first technique, CARS,[1,2] is a third-order nonlinear process which utilizes two high power lasers, one of fixed frequency, ω_P, and a second of variable frequency, ω_S. When ω_S is tuned so that $\omega_P - \omega_S$ is resonant with a Raman active vibrational transition in the medium, a coherent beam of radiation at the anti-Stokes frequency, $\omega_{AS} = 2\omega_P - \omega_S$, is generated. The CARS spectra of gases, including H_2, was first obtained by Rado[3] in 1967. Regnier and Taran[4] in 1973 observed CARS spectra of H_2 at the 10–100 ppm level in 1 atm of N_2 (10^{13} states cm^{-3}). They were able to map the concentration and rotational temperature of H_2 within a Bunsen burner flame. Nibler *et al.*[5] obtained the rotational and vibrational temperature of D_2 within an electric discharge. Other workers have studied H_2 plasmas[6] (10^{12} states cm^{-3}), the hydrogen exchange reaction[7,8,9], and formaldehyde photodissociation.[10,11]

The second technique used to detect H_2 in a quantum state specific manner is REMPI.[12] This is a second or higher order process in which the molecule is ionized following the absorption of several photons. The photon frequencies are chosen such that a combination of these frequencies will be resonant with an excited electronic state of the molecule. Three such processes have been developed for the detection of H_2. The first, developed by Marinero *et al.*[13] in 1982, involves a two photon excitation to the $\tilde{E}, \tilde{F}\ ^1\Sigma_g^+$ state at 98000 cm^{-1}, followed by absorption of a third photon to the ionization continuum. They were able to detect millitorr levels of H_2. The second process, developed by Rottke and Welge[14] in 1983, involves a single photon absorption to the $\tilde{B}\ ^1\Sigma_u^+$ state at 91000 cm^{-1}, followed by absorption of a second photon to the ionization continuum. Using a quadrupole mass spectrometer

to detect the H_2^+ ions they obtained a detection limit of 10^{10} states cm^{-3}. The third process, developed by Pratt *et al.*[15] in 1983, involves a three photon excitation to the $\tilde{B}$ followed by absorption of a fourth photon to the ionization continuum. The only chemical dynamics study using the REMPI technique to detect individual quantum states of H_2 was by Marinero *et al.*[16] who studied the hydrogen exchange reaction.

The third technique, LIF,[17] is a first order technique in which the molecule absorbs a single photon to populate an excited electronic state, which then radiates the energy as fluorescence. The principal difficulty of this technique when applied to H_2 is that the lowest energy electronic transitions are at wavelengths deep in the vacuum ultraviolet (VUV).[18] Such wavelengths are not accessible using tunable dye lasers directly or their second harmonics. The first LIF experiments on H_2 were by Marinero *et al.*[19] in 1983. They excited the $\tilde{B}$ and $\tilde{C}$ $^1\Pi_u$ states using laser radiation at 97.3–102.3 nm. This radiation was generated by frequency tripling the second harmonic of a Nd:YAG pumped dye laser in a pulsed Ar source. Their detection sensitivity was $\approx 2 \times 10^8$ states cm^{-3}. Northrup *et al.*[20] also obtained LIF spectra of H_2. They excited the $\tilde{B}$ state using radiation at 105.8–106.8 nm generated by frequency tripling the second harmonic of a Nd:YAG pumped dye laser in a static Xe cell. Their detection sensitivity was $\approx 10^9$ states cm^{-3}. Meier *et al.*[21] have used LIF to study the rotational relaxation rates for the $v = 1$ levels of H_2 and D_2. LIF detection of H_2 has not yet been used to study the products of a chemical reaction.

This dissertation describes two applications of the LIF detection of individual quantum states of H_2 to problems of interest to chemical physicists. The first is the determination of the rovibrational distributions for H_2 produced by the photolysis of H_2CO. The second is a preliminary experiment investigating the

rovibrational distributions of the H_2 produced by the hydrogen exchange reaction, $H + H_2 \rightarrow H_2 + H$.

This dissertation is organized as follows. Chapter 2 presents background material on the H_2CO photodecomposition process and on the hydrogen exchange reaction. Chapter 3 presents background material on the theory of four-wave mixing processes which are used to generate the necessary VUV laser radiation. Chapter 4 presents experiments on the generation of VUV laser radiation at wavelengths from 109.6–112.0 nm, discussing conditions for four-wave mixing processes in this wavelength region. Chapter 5 presents background material on the spectroscopy of H_2, H_2CO, and the potential H precursors HI and H_2S. Chapter 6 presents results on the detection of H_2 by LIF, showing the sensitivity and accuracy of the technique. Chapters 7 and 8 present results of the H_2CO photodissociation experiments and the hydrogen exchange reaction, respectively. Chapter 9 is a summary of the results and includes an analysis of the applicability of LIF of H_2 to studies of these kinds of processes.

Several appendices follow. Appendix 1 is a summary of the laser systems used for the work described in this dissertation, while Appendix 2 describes the electronics used in the data collection. Included are schematics for all homebuilt equipment.

REFERENCES

1. W. M. Tolles, J. W. Nibler, J. R. McDonald, and A. B. Harvey, *Appl. Spectrosc.* **31**, 253 (1977).
2. J. W. Nibler and G. V. Knighten, in *Raman Spectroscopy of Gases and Liquids*, edited by A. Weber, (Springer-Verlag, Berlin, 1979).
3. W. G. Rado, *Appl. Phys. Lett.* **11**, 123 (1967).
4. P. Regnier and J.-P. E. Taran, *Appl. Phys. Lett.* **23**, 240 (1973).
5. J. W. Nibler, J. R. McDonald, and A. B. Harvey, *Opt. Commun.* **18**, 371 (1976).
6. M. Peálat, J.-P. E. Taran, J. Taillet, M. Bacal, and A. M. Bruneteau, *J. Appl. Phys.* 52, 2687 (1981).
7. D. P. Gerrity and J. J. Valentini, *J. Chem. Phys.* **79**, 5202 (1983).
8. D. P. Gerrity and J. J. Valentini, *J. Chem. Phys.* **81**, 1298 (1984).
9. D. P. Gerrity and J. J. Valentini, *J. Chem. Phys.* **82**, 1323 (1985).
10. M. Peálat, D. Debarre, J. M. Marie, J.-P. E. Taran, A. Tramer, and C. B. Moore,*Chem. Phys. Lett.* **98**, 299 (1983).
11. D. Debarre, M. Lefebvre, M .Peálat, J.-P. E. Taran, D. J. Bamford, and C. B. Moore,*J. Chem. Phys.* **83**, 4476 (1985).
12. D. H. Parker in *Ultrasensitive Laser Spectroscopy*, edited by D. S. Kliger, (Academic Press, NY, 1983) Chapter 4.
13. E. E. Marinero, C. T. Rettner, and R. N. Zare, *Phys. Rev. Lett.* **48**, 1323 (1982).
14. H. Rottke and K. H. Welge, *Chem. Phys. Lett.* **99**, 456 (1983).
15. S. T. Pratt, P. M. Dehmer, and J. L. Dehmer, *J. Chem. Phys.* **78**, 4315 (1983).
16. E. E. Marinero, C. T. Rettner, and R. N. Zare, *J. Chem. Phys.* **80**, 4142 (1984).

17. J. L. Kinsey, *Ann. Rev. Phys. Chem.* **28**, 349 (1977).

18. K. P. Huber and G. Herzberg, *Molecular Spectra and Molecular Structure. IV. Constants of Diatomic Molecules*, (Van Nostrand Reinhold, NY, 1979).

19. E. E. Marinero, C. T. Rettner, R. N. Zare, and A. H. Kung, *Chem. Phys. Lett.* **95**, 486 (1983).

20. F. J. Northrup, J. C. Polanyi, S. C. Wallace, and J. M. Williamson, *Chem. Phys. Lett.* **105**, 34 (1984).

21. W. Meier, G. Ahlers, and H. Zacharias, *J. Chem. Phys.* **85**, 2599 (1986).

CHAPTER 2

BACKGROUND

I. THE PHOTODECOMPOSITION OF FORMALDEHYDE

A. INTRODUCTION

Formaldehyde, H_2CO, is the smallest stable molecule containing only C, H, and O. In spite of its simplicity, H_2CO has an extremely complex photochemistry.[1-3] Following excitation into the lowest excited singlet state, the principal processes are fluorescence and dissociation into molecular ($H_2CO \rightarrow H_2 + CO$) or radical ($H_2CO \rightarrow H + HCO$) fragments. These processes are extremely sensitive to the exact energy of the system. In one study, single rotational level lifetimes varied from 66 ns to 4.2 μs within a single vibronic level; in the most extreme case an energy variation of 8×10^{-4} cm^{-1} caused a factor of three variation in lifetime.

Formaldehyde is an important species in several areas. It is an intermediate of hydrocarbon combustion.[4-6] It has been observed in interstellar space.[7-11] It is a component of smog and indoor air pollution.[12-15] The presence of H_2CO in the air has become a source of public debate ever since it was determined to be airborne carcinogen in several species of animals.[16-18] It has been used for laser isotope separations.[19-23] It is also important to chemical physicists studying photochemical processes.[3]

Within the past decade there have been several major review aricles concerned with H_2CO. In 1981 Sodeau and Lee[1] discussed many of the chemical reactions involving H_2CO, Clouthier and Ramsay[2] in 1983 reviewed the spectroscopy, and in the same year Moore and Weisshaar[3] reviewed the photophysical aspects of the dissociation reactions.

In this chapter the state of knowledge about H_2CO photochemistry is reviewed. First will be a discussion of the energy levels and potential energy surfaces for H_2CO and its reaction intermediates and products. Second will be a discussion of early experimental work, most of which was concerned with identifying the product channels, determining quantum yields, and measuring fluorescence lifetimes. Third

will be a review of theoretical calculations concerning the dissociative process. Fourth, the recent experimental work will be reviewed. This latter section will concentrate on the recent determination of nascent internal state distributions. Finally, the proposed experiment is discussed.

B. ENERGY LEVELS AND POTENTIAL SURFACES

Two dissociation reactons[3] have been observed in H_2CO following excitation from the ground electronic state ($\tilde{X}\ ^1A_1, S_0$) to the first excited electronic state[2] ($\tilde{A}\ ^1A_2, S_1$) which has its origin at 28188.22 cm^{-1}. The lowest triplet state[2] ($\tilde{a}\ ^3A_2, T_1$) has its origin at 25194.34 cm^{-1}. H_2CO spectroscopy will be discussed in Chapter 5. In the first reaction, known as the molecular channel, the products are the stable molecules H_2 and CO. In the second reaction, known as the radical channel, the products are the free radicals H and HCO.

The molecular channel is known to be nearly isoenergetic, with recent determinations[24,25] giving $\Delta H^0_{298.15} = -0.47 \pm 0.12$ kcal mole^{-1}. The dissociation reaction, however, has a large barrier. Bachler and Halevi[26] studied the symmetry of the reaction and showed that if C_{2v} symmetry were maintained during the reaction, all but one of the occupied orbitals of H_2CO correlated with orbitals that are occupied in the products. The lone exception was the $2b_2$ orbital which starts as a n lone pair on the O and is correlated with a π^* orbital of CO. Thus, the dissociation from the ground electronic state is "forbidden." If the molecule is distorted so that the plane of symmetry containing the nuclei is maintained but that one of the C–H bond lengths increases (a b_2 distortion giving C_s symmetry), then the barrier to reaction is greatly reduced.

Bachler and Halevi[26] also studied the symmetry of the molecular dissociation from the first excited state. If the C_{2v} symmetry is maintained, the singly occupied H_2CO $2b_1$ π^* orbital also correlates with a π^* orbital of CO. Thus, the dissociation from the lowest excited state is also "forbidden."

Many theoretical calculations have been performed in an attempt to locate the precise location of the reaction barriers. (The reported energies are classical activation energies including zero-point effects). Jaffe *et al.*[27] using a minimal Slater basis set calculation with CI and thorough geometry optimization, calculated ground state activation energies of 7.75 eV (62500 cm^{-1}) in C_{2v} symmetry and 4.85 eV (39000 cm^{-1}) in C_s symmetry. In 1981 Frisch *et al.*[28] calculated a ground state activation energy of 3.45 eV (27800 cm^{-1}) using Møller-Plesse perturbation calculations to fourth order with a triple zeta basis set. That same year Goddard *et al.*[29] calculated a ground state activation energy of 3.56–3.77 eV (28700–30400 cm^{-1}) using a double zeta plus polarization basis set and configuration interacton (CI) including single and double shell excitations. More recently, in 1983 Dupuis *et al.*[30] reported an activation energy of 3.51 ± 0.13 eV (28300 ± 1000 cm^{-1}) using a multiconfiguration self-consistent field calculation with CI. Their error limits include basis set errors, correlation error, incorrect transition state structure and uncertainty in the zero-point energy correction.

The radical channel has a high endoergicity of 3.73 ± 0.05 eV (30000 ± 400 cm^{-1}) because it is a homolytic bond cleavage.[31] The radical channel was also studied by Bachler and Halevi.[26] In C_s symmetry the dissociation is an allowed reaction since all of the occupied ground state orbitals correlate with the ground state product orbitals. It is therefore expected that there is little if any barrier to reaction beyond the endoergicity. The S_1 state correlates without a barrier with the first excited state of HCO, 9294 cm^{-1} above the HCO ground state.[32] The T_1 state correlates with ground state HCO, but it exhibits a small barrier.[33,34] The presence of rotational structure and singlet triplet interactions at energies of 30600 cm^{-1} implies that the barrier is above this energy.[35]

Many of the interesting features of formaldehyde photochemistry arise because the origin of the $\tilde{A}$ and $\tilde{a}$ states, the molecular channel barrier and the radical

channel endoergicity are so close together, all within 2000 cm. Figure 1 shows a schematic of the energy levels.

C. EARLY EXPERIMENTS

While it has been known for some time that there are two reaction channels in formaldehyde, early work[36–40] disagreed on the relative quantum yields for the two channels and the wavelength at which the radical channel opened up. Early work was extremely inconsistent, with the relative quantum yields of the molecular channel to the radical channel at 365 nm varying from 0.2 to 2.0 and at 313 nm varying from 0.2 to 0.01. In 1969 McQuigg and Calvert[41] studied H_2CO decomposition following Xe lamp flash photolysis using mass spectrometric product yield determinations. Sample pressures were on the order of 40 torr. They showed that the total quantum yield for dissociation was ≈ 1.0 for twenty different vibrational bands between 365 and 280 nm. The radical channel quantum yield was 0.00 at 365 nm and increased with decreasing wavelength, reaching ≈ 0.21 at 339 nm, ≈ 0.29 at 329 nm, and ≈ 0.41 at 313 nm. From this they concluded that the C–H bond energy in H_2CO was less than 85 kcal mol^{-1} (3.69 eV).

In 1978 Clark *et al.*[42] studied H_2CO decomposition following flashlamp pumped dye laser photolysis using gas chromatographic product yield determinations. Sample pressures were on the order of 5–10 torr. Because of the much narrower linewidth of the excitation source, they had much better resolution with respect to the opening of the radical channel. For H_2CO, total dissociation quantum yields were $\approx 0.68 \pm 0.10$ at 353 nm and rose to essentially unity by 339 nm; however, for D_2CO, total dissociation quantum yields were 0.05 at 352.8 nm and weren't near unity until 332 nm. For H_2CO, the radical dissociation quantum yields were near 0.0 for wavelengths at or above 339.2 nm, 0.32 ± 0.10 at 329.8 nm, and then near 0.45 at all shorter wavelengths studied. These results place the opening of the radical channel at 3.73 ± 0.05 eV.

Later that same year Reilly *et al.*[31] studied H_2CO decomposition following flashlamp pumped dye laser photolysis using intracavity dye laser absorption spectra of the HCO product, the first experiment to actually look for the HCO radical and not its molecular decay products. Sample pressures were on the order of 2–10 torr. They were not able to measure an absolute radical channel quantum yield, but they did show that the relative quantum yield was 1.00 at 294.145 nm, 0.74 at 329.74 nm, and < 0.02 at 339.208 nm. Thus, the threshold for the radical channel is definitely between 329.7 and 339.2 nm; however, the lack of strong absorption bands between these two wavelengths make it difficult to narrow the uncertainty further.

Most of the previous work was carried out at pressures on the order of 10 torr at room temperature. Moortgat *et al.*[43] carried out studies under more normal atmospheric conditions of 100 ppm H_2CO in 200–800 torr of synthetic air at temperatures of 220 and 300 K. Their results are generally consistent with the low pressure work: the radical quantum yield is 0 for wavelengths at or above 339 nm, rises to 0.8 at 320 nm, and then slowly decays to 0.35 at wavelengths below 265 nm. The quantum yield at 327 nm was sensitive to temperature whereas that at 316 nm was not. From an extrapolation of the quantum yields to 0 K, they concluded that the threshold wavelength is 328.4 ± 2.3 nm, corresponding to a dissociation energy of 3.78 ± 0.03 eV (30450 ± 200 eV), very close to the previous results taken under much different conditions.

On the basis of the integrated absorption spectrum,[44] the total oscillator strength for the $S_1 \leftarrow S_0$ band in H_2CO is $(2.40 \pm 0.05) \times 10^{-4}$, implying radiative lifetimes on the order of 5 μs. Single vibronic level fluorescence lifetimes have been measured for many vibrational levels of H_2CO, HDCO, D_2CO.[45–49] In most cases, the observed lifetimes are much shorter than the radiative lifetimes. One of the first studies was by Yeung and Moore.[45] They used a UV laser with a 1 Å bandwidth

and sample pressures on the order of 0.05–5.0 torr. In H_2CO the extrapolated zero pressure lifetime for the 4^1 band (124 cm^{-1} of vibrational excitation) was 282 ns while that for the 2^14^3 band (2152 cm^{-1} of vibrational excitation) was 29 ns. HDCO gave similar results, 290 and 42 ns for the same two bands. The situation is different in D_2CO where the 4^1 lifetime of ≈ 4.5 μs is close to the expected radiative lifetime. Overall, the decay rates increase rapidly with increasing vibraional energy, though the trend is not uniform.

Baronavski *et al.*[50] studied H_2CO in the region of 7000–9000 cm^{-1} of vibrational excitation and observed lifetimes on the order of 2–14 ps based on line-broadening measurements.

Miller and Lee[47] obtained fluorescence quantum yields and lifetimes for single vibronic levels of H_2CO, HDCO, and D_2CO. They used a D_2 or Xe lamp with a monochromater with a bandpass of either 0.05 or 2.5 nm. Their zero pressure fluorescence quantum yields were 0.035, 0.049, and 1.02 for the 4^1 bands of H_2CO, HDCO, and D_2CO, respectively, while for the 2^14^3 band they were 0.0015, 0.0063, and 0.191 for the same three species. They observed the general trend of decreasing quantum yields with increasing energy. However, in many cases they observed lifetimes significantly shorter than those found by Yeung and Moore, sometimes by as much as a factor of three, *i.e.*, for the 4^1 and 2^14^3 bands of H_2CO they observed 82 and 10.8 ns as opposed to the previously reported 282 and 29 ns.

The discrepancy was explained when advances in lasers made it possible to determine the fluorescence lifetimes and quantum yields for individual rotational states of a given vibrational level. Shibuya and Lee[51] examined the 4^1 band of H_2CO and D_2CO using a laser with a linewidth of 0.2 cm^{-1}. Unexpectedly, they found that fluorescence quantum yields were strongly dependent on rotational level. As an example, the quantum yields varied by a factor of 5 for various J' lines in the $K' = 4$ level, with no systematic variations. Thus, different workers

measuring single vibronic level fluorescence lifetimes and yields will get different results depending on the rotational levels they excite.

This work was confirmed by Weisshaar and Moore.[52] They studied 104 rotational lines in the 4_1^0 hot band of H_2CO and D_2CO at pressures as low as 0.5 mtorr. Stern-Volmer plots were non-linear until pressures less than 10 mtorr were reached, at which point the quenching rate was $\approx 10^8$ s^{-1} $torr^{-1}$. In H_2CO, collision free lifetimes varied from 66 ns to 4.2 μs. Individual lifetimes showed no systematic variation with J', K', and E_{rot}. K' doublet levels split by as litle as 8×10^{-4} cm^{-1} had different lifetimes. Such studies have been extended to other vibrational bands using collision free conditions in bulbs[53] and supersonic jets.[54–56] The magnitude of rotational fluctuations diminish with increasing energy but still exceed a factor of two in the 5^1 band which has 2997 cm^{-1} of vibrational excitation.[57]

Recently, this work was extended by measuring the change in lifetimes as a function of an applied voltage (Stark effect tuning of energy levels) for J, K, M resolved states.[53,59,60] Lifetimes of individual rotational states vary by more than an order of magnitude for an energy shift of 0.2 cm^{-1}.

The experimental data has led to the following conclusions about the H_2CO decomposition following excitation into the S_1 state.[3] As can be seen from Figure 1, dissociation is only possible from the S_0 state. The density of S_0 vibrational levels at these energies (approximately 10 vibrational states per cm^{-1}, of which only 1/4 will have the correct symmetry) is too small for discrete, bound S_0 levels to provide the final states for irreversible decay. However, if these S_0 levels are broadened by predissociation, then they form a "lumpy continuum" for irreversible nonradiative

transitions. Thus, the photodissociation of H_2CO has the following mechanism:

$$S_0 + h\nu \rightarrow S_1$$

$$S_1 \rightarrow S_0^*$$

$$S_0^* \rightarrow H_2 + CO$$

$$S_0^* \rightarrow H + HCO$$

D. THEORY

Several types of theoretical calculations have been performed. The earliest calculations were concerned with the energy levels and transition state structure. Later came calculations on the $S_1 \rightarrow S_0^*$ coupling elements. The third type of calculations involved studies of the S_0^* dissociation. Recently calculations of the energy disposal in the fragments have been performed.

The principal calculations involving determinations of the activation energies have already been mentioned.[26-30] Table 1 summarizes the calculated transition state geometries and compares them with the experimental geometries of the H_2CO ground state and first excited state, H_2, and CO. The transition state is planer (plane of symmetry is perpendicular to the plane of symmetry in S_1), but is strongly bent so that both H's are on the same side of the CO bond. The torque on separation would give rotationally excited CO. The CO bond length in the transition state is only 0.05 Å longer than in free CO,[61] so one would not expect large amounts of CO fragment vibration based on the Franck-Condon principle. The most notable feature of the transition state is the long H–H bond length of $\approx$ 1.28 Å, almost 75% greater than the equilibrium H_2 bond length of 0.741 Å.[61] A simple Franck-Condon analysis would predict that the H_2 would be vibrationally excited. The 1.28 Å bond length is between the outer classical turning points for $v = 3$ (1.22 Å) and $v = 4$ (1.32 Å) of H_2.[62]

Several groups have calculated the rate of $S_1 \rightarrow S_0^*$ radiationless transfer. Heller *et al.*[63] performed these calculations in 1978 using a Herzberg-Teller expansion. When the S_1 energy is several thousand cm^{-1} above the barrier, nonradiative decay occurs on a 100 ns time-scale for H_2CO and a little slower for D_2CO. For energies below the barrier there is no nonradiative decay on an observable time-scale. van Dijk *et al.*[64] presented *ab initio* CI calculation of radiationless decay at energies below the barrier. They determined that the total anharmonic vibrational state density in S_0 of H_2CO was 10 per cm^{-1} for the 4^1 band rising to 18 per cm^{-1} for the $2^1 5^1$ band. The coupling matrix elements were all very small, the largest only being 5×10^{-6} a.u. (1 cm^{-1}) with most being below 10^{-7} a.u. (0.02 cm^{-1}). They concluded that the density of states was so low that any interaction between S_1 and S_0^* depends on a fortuitous overlap of the two levels. In D_2CO the level density is about two times greater than H_2CO at the same S_1 level; however, the couplings were an order of magnitude smaller. The addition of rotational coupling did not alter their conclusions.

The result of these calculations showed that if S_0^* was to provide a role in the H_2CO dissociation mechanism, the energy levels would need to be significantly broadened.

Miller[65] calculated RRKM rate constants with tunnelling corrections (Eckart potential) for the dissociation of S_0^*. At the energy of the S_1 ground vibrational level, the calculated rate constants are 5.8×10^6, 9.5×10^5, and 1.4×10^5 s^{-1} for $J = 0$ of H_2CO, HDCO, and D_2CO. The rate constant for $J = 10$ was an order of magnitude slower. At the energy of the $2^1 4^3$ band, the dissociation rate of S_0^* exceeds 10^9 s^{-1}. Miller and coworkers[66] later extended this work using a more accurate potential and a reaction path Hamiltonian model for the tunnelling. In this case for $J = 0$ they calculated a rate constant at the energy of the S_1 origin of 5.9×10^6 s^{-1} assuming a 87 kcal $mole^{-1}$ activation energy. This result is extremely

sensitive to the barrier height, changing by a factor of 2.75 for every ± 1 kcal mole^{-1}. Troe[67] later performed RRKM calculations including J and K dependencies with tunnelling corrections, getting results similar to those of Miller. Troe's results are usually about 30% lower then Miller's because of the inclusion of anharmonicity. Troe also calculated RRKM rate constants for the radical channel. As expected, the radical channel rate constant dominates the molecular channel rate constant soon after the radical channel opens up.

These RRKM calculations show that S_0^* dissociates rapidly, causing a broadening of energy levels sufficient to provide a path for radiationless decay from S_1.

Miller[68] later examined the effects of symmetry along the reaction path. Specifically, he showed that if a symmetry is conserved along a reaction path, C_s for formaldehyde, then states corresponding to different irreducible representations do not interact, and a separate rate constant should be calculated for each irreducible representation. In formaldehyde, one gets different rate constants depending on if the out-of-plane bending mode, ν_4, is even or odd, at least for $J = 0$. The states with even ν_4 quanta have increased rate constants relative to the no symmetry case, while those with odd ν_4 have decreased rate constants. This decrease occurs mostly because the energy tied up in ν_4 can not couple to the reaction coordinate, raising the effective barrier height. In the regions where tunnelling is important, the difference in rate constants is approximately a factor of 20. This work was confirmed by Schatzberger *et al.*[69] in an analysis of static SCF solutions.

All of the previous theoretical studies concentrated on the processes occurring before or at the time the transition state is reached. Recently, Schinke[70] calculated the rotational state distributions of both the H_2 and CO fragments. For his ultra-simple model of photofragmentation he extended the formalism of the infinite order sudden (IOS) photodissociation amplitude of a triatomic molecule to the tetratomic

molecule case. The ingredients of the model are the potential energy surface in the exit channel and the geometry of the transition state, both of which are known from *ab initio* calculations.

The vibrational degrees of freedom were frozen, the total angular momentum of the system was frozen at $J = 0$, and the energy was fixed at 29500 cm^{-1}. The calculated distribution for *ortho*-H_2 is sharply peaked around $J = 5$, with both $J = 1$ and $J = 9$ having probabilities a factor of 5 smaller. The distribution for *para*-H_2 is extremely different. It is predicted that the distribution peaks at $J = 0$, reaches a minimum at $J = 6$, and reaches a second maximum at $J = 10$ with 35% of the $J = 0$ probability. The predicted HD distribution from HDCO photodissociation is also predicted to be bimodal, with maxima for $J \approx 5$ and $J \approx 16$. The distributions are controlled by a projection integral of the transition state wavefunction onto a rotational quantum number axis. A sensitivity analysis clearly showed that "the H_2 rotational distributions are completely determined by the Franck-Condon principle and that final state interaction between translation and H_2 rotation is negligible."

The CO rotational distributions were also calculated. The distribution is Gaussian in appearance, with a maximum at $J = 42$ and a full-width at half-maximum of ≈ 15. The CO distribution is mainly determined by the CO potential anisotropy while the transition state geometry had a very weak influence.

The CO and *ortho*-H_2 distributions are both very close to the experimental results discussed in the next section.

E. RECENT EXPERIMENTS

Recently, the energy distribution among the various degrees of freedom of the recoiling fragments have been determined. This information has greatly increased the understanding of the formaldehyde photodissociation process.

The first such experiments were by Houston and Moore[71] in 1976. They used a CO laser to probe for the presence of CO in rotational levels near $J = 10$. They found that the appearance rate of CO was pressure dependent and was some two orders of magnitude less than the fluorescence rate in the low pressure regime. These results were extremely unexpected. The proposed mechanism requires that S_0^* have a rapid decay in order for the lines to be broadened sufficiently to account for the rapid collision free internal conversion rate from the initially prepared S_1 state, yet the CO appearance rate was much too slow and was dependent on collisions.

These contradicting results caused much effort as alternative hypotheses were advanced, many involving the presence of long lived intermediate or intersystem crossing to the T_1 state.[3] However, all of these hypotheses had the same difficulty: the density of states is order of magnitudes too low for there to be efficient coupling to S_1 unless the states were broadened by dissociation.

In 1982 Ho *et al.*[72] published results of crossed molecular beam laser beam experiments. Such experiments are definitely in the collision free pressure regime. The H_2CO was dissociated througth the $2_0^1 4_0^1$ band near 339 nm, specifically, the ${}^rQ_1(3,4)$ lines at 29515.2 cm^{-1}. They found that the CO angular distribution in the center of mass reference frame is isotropic. The translational energy distribution peaked near 55 kcal/mole, approximately 65% of the available energy. Dissociation of the 4^1 band gave similar results. The detector viewing angle allowed the detection of dissociation events that occurred within $\approx$ 3 μs of the dissociation pulse. Since they saw a signal level corresponding to the detection of all the expected dissociation products, they concluded that the dissociation was completed within 3 μs. This result contradicted the long lived intermediate required from the CO experiment.

They also studied the dissociation of 283.9 nm. Only HCO was detected, placing an upper limit on the molecular product of 10% of the radical product. This is more HCO than found by the earlier quantum yield experiments. This discrepancy was attributed to collisional effects in the earlier higher pressure experiments.

The identity of the long lived intermediate was resolved in 1982. In that year Ho and Smith[73] observed the CO fragment by VUV laser induced fluorescence using the CO $\tilde{A}\ ^1\Pi(v=1) \leftarrow \tilde{X}\ ^1\Sigma^+(v=0)$ band near 150 nm following dissociation at 355 nm. They found that the CO rotational distribution was extremely hot, with $J = 25$–63 observed. Studies of the time evolution of the $J = 36$ state showed that the rotationally hot CO molecules were indeed the missing intermediate. The $J = 36$ state population increased on a timescale comparable to the H_2CO fluorescence rate, and the $J = 36$ state decay rate at longer times was comparable to the appearance rate of $J = 12$.

Their results were amplified by Bamford *et al.*[74] in 1985. The CO fragments were detected by LIF, with an estimated detection sensitivity of $\approx 10^8$ state cm^{-3} They photolyzed individual rotational lines of the $2_0^1 4_0^1$ band near 339 nm, specifically the ${}^rQ_1(3,4)$ lines near 29515.2 cm^{-1}. Sample pressures were 0.05 to 0.10 torr and the time delay between the photolysis and probe lasers was 150 ns. They found that the CO $v = 0$ rotational distribution is peaked at $J = 42$ with a FWHM of ≈ 20 J units. Increasing the initial angular momentum did not change the peak of the rotational distribution, but it did broaden it by a couple of J units. The CO $v = 1$ rotational distribution was nearly unchanged. Approximately 13% of the available energy was in the CO rotational degrees of freedom. The CO $v = 1$ population was $14\% \pm 5\%$ of the CO $v = 0$ population. Approximately 1% of the available energy was in CO vibration. From the rotational distribution it was possible to estimate the range of product impact parameters. Ignoring H_2

internal state energy and angular momentum, they estimated that the product impact parameter is 0.8 Å. This implies that the point of impact is outside of the carbon atom.

The last distribution to be measured was the H_2 rovibrational distribution, which was first measured by Peálat *et al.*[75] The formaldehyde was dissociated using 338.928 nm radiation, a wavelength which overlaps several lines of the ${}^rQ_1$, ${}^rP_1$, ${}^rR_1$, and ${}^pR_1$ subands of the $2_0^1 4_0^1$ vibronic band. The H_2 was detected by CARS. Because of the poor detection sensitivity for H_2 on the order of 10^{13} states cm^{-3}, they decided to measure the vibrational distribution with the rotational distributions relaxed. To that end, the sample pressures were 1 torr of H_2CO and 150 mbar He. The time delay between the photolysis and probe laser beams was 150 ns. They used a background cancellation procedure which reduced the background but this process supresses the line asymmetry and they were unable to determine the sign of the population differences. They observed only odd J's for the product H_2.

The presence of two identical fermions in H_2CO (the two H's) requires that the total wavefunction of the molecule must be antisymmetric with respect to the interchange off the two H's. Thus, H_2CO exhibits nuclear spin weighting factors[76] similar to those for H_2. Consequently, there are two forms of H_2CO, *ortho*-H_2CO which has only odd K_A's and *para*-H_2CO(not to be confused with the polymer paraformaldehyde) which has only even K_A's, in the ground electronic state. If the nuclear spin configuration is conserved during the photodissociation process, then states originating from odd K_A states of H_2CO must give odd J states of H_2.

The observation of only odd J's by Peálat *et al.* confirm that the nuclear spin configuration is conserved. More detailed experiments on the spin conservation were performed by Schramm *et al.*[77] They photodissociated H_2CO using either an *ortho* or a *para* rotational line in the $2_0^1 4_0^1$ band near 339 nm. After photolysis,

the formaldehyde was frozen out and the rotational levels of the product H_2 were determined using Raman spectroscopy. When *ortho*-H_2CO was dissociated, the *para*-H_2 impurity was less than 5% of the natural abundance. When *para*-H_2CO was dissociated, the *ortho*-H_2 impurity was 3% of the natural abundance. *ortho–para* interconversion of formaldehyde occurs rapidly on the few minutes timescale of their experiments.

The most detailed H_2 distributions were obtained by Debarre *et al.*[78] CARS was used to monitor the rovibrational distributions of H_2 produced from the photodissociation of H_2CO at 29496.5 cm^{-1}. This wavelength is in the center of a group of ${}^rR_1$, ${}^pR_1$, ${}^rP_1$, and ${}^rQ_1$ lines in the $2^1_0 4^1_0$ band. Their detection sensitivity is 10^{12} state cm^{-3}. This sensitivity is insufficient for the nascent H_2CO distributions to be obtained. Instead, He buffer is added to cool the translational energy to thermal levels. The sample pressures were 3.5 mbar of H_2CO and 9 mbar of He. The time delay between the photolysis and probe laser pulses was 150 ns.

Nuclear spin was conserved during the dissociation, so only odd rotational states were studied. The rotational distributions were peaked at $J = 5$, 5, 5, 3, and 3 for $v = 0$ to 4, respectively. The rotational distributions were nearly Boltzmann, with rotational temperatures on the order of 2400 K. Their observed distribution is very similar to that calculated by Schinke, with the exception of an excess of $J = 1$. This could be the result of a slight rotational cooling during the time delay. They found that 5% of the available energy is in the H_2 rotational degrees of freedom. The vibrational distribution is highly nonthermal, with the distribution peaking for $v = 1$. They found that 16% of the available energy is in the H_2 vibrational degree of freedom. The vibrational excitation is expected from a Franck-Condon analysis of the transition state.

The results just presented are remarkedly consistent. Three different laboratories performed three different experiments to determine 5 energy distributions

(translational, CO rotational and vibrational, and H_2 rotational and vibrational). The average energy contained in each of these distributions when added together gave 100%. These results are shown in Table 2.

F. PROPOSED EXPERIMENTS

The consistency between the three sets of experiments investigating the energy disposal in formaldehyde is very good. There are, however, several questions which still must be answered.

First, what is the distribution of even H_2 rotational states following the photodissociation of even K_A states of H_2CO? Will the distribution be similar to that previously seen for odd K_A states, or will the distribution be bimodal and peak at $J = 0$ as Schinke[70] has predicted? Second, what is the distribution of H_2 rotational states if $K_A > 1$ states of H_2CO are dissociated? Will the H_2 distribution remain unchanged, or will it broaden as the CO rotational distribution did? Third, what happens when the radical and molecular channels are competing? Fourth, were the H_2 rotational distributions affected by the long time delay between the pump and probe laser pulses?

In order to provide an answer to these questions, it is proposed that the photodissociation of formaldehyde be studied using LIF detection of the molecular H_2 fragment. The increased sensitivity of this technique would allow the detection of H_2 at lower H_2CO pressures after shorter time delays without the need for He buffer to slow the molecules down to thermal energies. The H_2CO will be dissociated from both odd and even K_A states, specifically using rotational lines in the ${}^rR_3$ and ${}^rR_4$ subbands. In addition, a different vibrational band will be used, specifically the $2_0^1 4_0^3$ band at 329 nm. This state will have the same symmetry as the $2_0^1 4_0^1$ band at 339 nm used by the previous work, but the additional energy will allow the radical channel to open up, allowing for competition between the two processes.

II. THE HYDROGEN EXCHANGE REACTION

A. INTRODUCTION

The $H + H_2 \rightarrow H_2 + H$ exchange reaction and its isotopic variants is of great importance in the study of gas phase chemical reactions. It is the simplest reaction involving neutral atoms and molecules and is a prototype reaction for both experimentalists and theoreticians. Because of the extreme lightness of the reagents, quantum mechanical effects such as tunnelling at low energies near threshold and resonances at higher energies are expected to have major contributions to the dynamics. Each of the 3 H atoms can be replaced by Mu (μ^+e^-), D, or T. Excluding the Mu, there are 15 possible reagent isotope combinations leading to 21 distinct reactions with initial and final reduced masses varying from 0.6719 to 2.0107 amu. The reaction of Mu with H_2 has initial and final reduced masses of 0.1124 and 0.5321, respectively. Isotope effects could be significant because of the wide range of masses. In addition, there is the possibility that breakdowns in the Born-Oppenheimer approximation could have dynamically important consequences, especially for the reactions involving Mu.

Because of its importance, the hydrogen exchange reaction has been extensively reviewed several times in the past decade. In 1976 and 1977 Truhlar and Wyatt published a pair of review articles:[79,80] the latter concentrated on the potential energy surface while the former concentrated on the reaction itself. In 1986 Schatz[81] published a review of the major advances in the past decade, concentrating mostly on theoretical treatments of the reaction.

This chapter will summarize the experimental and theoretical results. In addition, the recent hot atom/single collision experiments of Gerrity and Valentini[82–84] and those of Marinero, Rettner, and Zare,[85,86] which are very similiar to the experiments in this thesis, are described in some detail.

B. THEORETICAL STUDIES

1. Potential Energy Surface

The hydrogen exchange reaction is characterized by a single potential energy hypersurface in the Born-Oppenheimer approximation. After accounting for the motion of the center of mass of the reactants (3 degrees of freedom) and the overall rotation of the reactants (3 degrees of freedom), there are 3 degrees of freedom left with which to describe the H_3 potential energy surface. There are several coordinate systems which can be used: in one system the three coordinates are 2 H–H distances and the included H–H–H angle; alternatively, the three coordinates are the interatomic separation of the diatom, the separation of the atom from the center of mass of the diatom, and the angle between the atom and the diatom axis at the diatom center of mass.

The earliest treatment of the H_3 hypersurface was by London[87] in 1929. He presented a formula for the energy of the lowest adiabatic electronic state of H_3 as a function of Coulomb and exchange integrals for each pair of atoms. Eyring and Polanyi[88] developed a semiempirical method to evaluate the integrals in the London formulation in terms of properties of the diatoms. This methodology gives the LEP potential. One of the terms in the calculation is the fraction ρ which equals the Coulomb integral divided by the sum of the Coulomb and exchange integrals. While $\rho \approx 0.14$ at large distances, it is often treated as an adjustable parameter, values from 0.00 to 0.20 having been used.[80] For any ρ the method predicts that the lowest energy reaction path is linear. For low values of ρ the barrier to reaction is symmetric but much too high; for larger ρ's the symmetric configuration is a local minimum flanked by twin nonsymmetric barriers. For example, for $\rho = 0.0035$ the barrier is 0.91 eV while for $\rho = 0.10$ the local minimum is 0.49 eV and the barriers are 0.56 eV.

The LEP method was modified by Sato[89-91] in 1955 to give the LEPS method. This method introduces a new parameter, δ. This parameter is also varied in an attempt to obtain agreement between theory and experiment.[80] When applied to H_3, the LEPS surface has a symmetric saddle point for all values of δ examined. For $\delta = 0.1475$ the barrier height is 0.358 eV at an internuclear separation of 1.76 a_0.

A different semiempirical method was used by Porter and Karplus[92] which also predicts a symmetric saddle point. They came up with 4 different surfaces, one of which, (PK2), has been extensively used for dynamics calculations. The barrier height on this surface is 0.398 eV at an internuclear separation of 1.70 a_0.

In addition to the semiempirical methods, there have been many attempts to calculate the H_3 hypersurface by *ab initio* calculations. The first such calculation was the minimal basis set calculation by Coolidge and James[93] in 1934. A flurry of similiar calculations showed that the saddle point for the collinear reaction is symmetric and that the potential energy rose upon bending. The results of Hirschfelder *et al.*[94] showed that the H_3 binding energy of -2.94 eV was 1.08 eV above that for H_2 calculated at the same level of theory.

The next level of theory used an extended basis set of s orbitals on each H. The first such calculation was by Boys *et al.*[95,96] in 1956. They found a binding energy of -3.48 eV and an estimated barrier height of 0.66 eV.

Later calculations included p and d orbitals, multiple ζ's, pseudo-natural orbitals, and configuration interactions.[80] The published "state-of-the-art" for such calculations is the results of Liu[97] in 1973. He studied the potential energy surface for linear H_3 using a contracted basis set consisting of 4 s-type , 3 p-type, and 2 d-type Slater orbitals for each H and included an almost complete CI calculation. He determined that the symmetric saddle point occurred at an internuclear separation of 1.757 a_0 with a binding energy of -4.302 eV. This represents an absolute upper bound on the barrier height of 0.446 eV by comparison with the exact H_2 binding

energy of -4.748 eV determined by Kolos and Wolniewicz.[98] After comparison of his H_2 results (-4.727 eV) with the exact results, he concluded that the actual binding energy was $-4.323^{+0.021}_{-0.013}$ eV with a barrier of $0.425^{+0.021}_{-0.013}$ eV with "best" values of -4.327 ± 0.005 eV and 0.420 ± 0.005 eV (9.69 ± 0.12 kcal/mole), respectively.

This work was later extended to nonlinear geometries by Siegbahn and Liu.[99] To simplify the calculation they used a contracted basis set consisting of 4 *s*-type, 3 *p*-type, and 1 *d*-type Gaussian orbitals. This calculation yielded a barrier of 0.429 eV; however, the collinear surface of the new calculation was parallel to the previous one within 0.001 eV for all points examined with a separation between 1.4 and 3.5 a_0.

Truhlar and Horowitz[100] parametrized the results of the Liu and the Siegbahn and Liu calculations. They fit all 267 *ab initio* points to an analytic expresion using 8 nonlinear parameters and 15 linear parameters with a global root-mean-square (rms) error of 0.007 eV and a maximum deviation of 0.024 eV. The rms error of the fit is only 0.004 eV for the collinear geometry. This surface, known as LSTH, is believed to be the first potential energy hypersurface to achieve a "chemical" accuracy of 1.0 kcal/mole. The barrier height of this surface is 0.425 eV.

The LSTH surface includes a small van de Waals' well. The spherical average of the potential has a shallow well with a depth of 1.6 meV at an atom-diatom separation of 6.59 a_0. This is consistent with various experimental determinations; for example, Welz[101] determined a well depth of 2.6 meV at 6.56 a_0 from measurements of the integral cross section at energies down to $E_{rel} \approx 1$ meV.

More recent *ab initio* calculations suggest that the LSTH barrier is slightly too large and should be decreased. Liu[102] recently performed a new calculation on a few geometries in the vicinity of the saddle point which used a contracted basis set consisting of 3 *s*-type, 3 *p*-type, 2 *d*-type, and one *f*-type Slater orbitals on each H. The symmetric saddle point occurred at an internuclear separation of 1.759 a_0

with a binding energy of -4.320 eV. This represents an absolute upper bound on the barrier height of 0.428 eV. After corrections for errors in the H_2 calculation, the barrier height is believed to be 0.418 eV with a "best" value of 0.416 ± 0.003 eV.

Recently, Varandas *et al.*[103,104] determined a new parameterization of the H_3 hypersurface based on a double many-body expansion, known as the the DMBE surface. This potential is designed to be valid at higher energies than the LSTH surface. In addition, long-range forces are treated more accurately so it is believed that the base of the barrier and the van de Waals' well are more accurate. This potential has a barrier height of 0.418 eV.

The DMBE potential, like the LSTH potential, is based primarily on the 267 *ab initio* points from Liu[97] and from Siegbahn and Liu.[99] An additional 31 points from Blomberg and Liu[105] were included. These 298 points were corrected by a semiempirical formula in order to reduce the barrier height by 0.007 eV. Varandas *et al.* calculated the potential at 18 new geometries, giving a total of 316 *ab initio* points. The final fit had a global rms error of 0.010 eV with an rms error of only 0.008 eV for collinear geometries.

2. Quasiclassical Trajectories

Given the potential energy surface, it is possible to solve for the motion of the 3 H atoms classically using either the Newtonian, Lagrangian, or Hamiltonian equations of motions.[106] Such calculations are known as classical trajectory calculations. If the initial motion of the reagents is quantized to fulfill quantum mechanical rotational and vibrational quantization, then the calculation involves quasiclassical trajectories (QCT).

The first classical trajectories were calculated by Hirschfelder *et al.*[107] in 1936. The first detailed QCT calculation was by Karplus *et al.*[108–110] in the mid 1960's using the PK2 surface. The observed threshold energy for $v = j = 0$ was at $E_{rel} = 0.25$ eV. The reaction cross section increases slowly to 0.01 a_0^2 at

E_{rel} = 0.30 eV, then increases approximately linearly with energy until a plateau of 4.5 a_0^2 is reached at E_{rel} = 1.1 eV. Later workers carried the calculations to higher energy and to other isotopes on this surface.[79]

Mayne and coworkers[111-114] later carried out a detailed QCT study of the hydrogen exchange reaction using the LSTH surface. The reaction threshold for H + H_2 was $E_{rel} = 0.31 \pm 0.01$ eV on this surface. The first paper examined isotope effects, the second and fourth papers examined the effects of vibrational and rotational excitation on reactivity, and the third paper compared the calculated rate constants and angular distributions with experiment.

Their major results are as follows: 1) in the reaction series H, D, T + H_2, T is more reactive than D which is more reactive than H while in the reaction series H + H_2, D_2, T_2, H_2 is more reactive than D_2 which is more reactive than T_2; 2) initial vibration of the diatom increases reactivity at a given translational energy and broadens the final rotational and angular distributions while small amounts of initial rotation of the diatom reduces reactivity near threshold and broadens the final rotational, but not angular, distributions while larger amounts of initial rotation increase reactivity; 3) the agreement in theoretical rate constants and angular distributions with the experimental results is quite good considering that quantum mechanical effects such as tunnelling have obviously been neglected.

Other QCT calculations have been performed at particular energies of interest. Blais and Truhlar[115,116] calculated state-to-state reactive cross sections for the H + D_2 system at relative translational energies of 0.55, 0.98, 1.1, and 1.3 eV. These are the energies sampled by Gerrity and Valentini[82-84] and by Marinero, Rettner, and Zare[85,86] in their recent hot atom/single collision condition experiments. Mayne and Prasad[117] extended the earlier work of Mayne *et al.* to much higher energies (10 eV) for comparison with D + H_2 crossed molecular beam experiments.

Table 3 gives a comparison of thermal rate constants calculated by QCT with experimental results. The calculations by Mayne *et al.* on the LSTH surface agree with experiment to better than 30% for all but the lowest temperatures where tunnelling is expected to be a significant fraction of the total reaction. Table 4 gives a comparison between the hot atom/single collison condition experiments and the QCT trajectories of the total reactive cross section while Table 5 gives a comparison of the energy distribution within the products.

3. Quantum Mechanical Scattering

In the quantum mechanical treatment of reactive scattering, the motion of the particles subject to a given potential surface is determined by solving the Schrödinger equation.[81] The complete problem in 3-dimensional space requires 6 mathematical degrees of freedom for the solution. Many levels of approximation can be made to reduce the computational effort. One of these is to reduce the 3-D problem to 2-D or 1-D by restricting the reagents to a plane or line which is fixed in space, reducing the mathematical degrees of freedom to 4 or 2, respectively.

The most accurate method is the coupled channel (CC) method which involves solving the Schrödinger equation exactly.[81] This method involves choosing a reaction coordinate; the remaining degrees of freedom then constitute the internal coordinates. The complete wavefunction is expanded in a basis set consisting of wavefunctions in the internal coordinates. Inserting this expansion into the Schrödinger equation gives a set of coupled ordinary differential equations in the reaction coordinate which can be solved by standard methods. Analysis of the resulting solution provides a scattering matrix, from which all observable quantities can be derived. Various CC methods differ in choice of the reaction coordinate and in the choice of basis set.

The best approximation to this is the "coupled states" (CS) method which neglects the kinematic coupling between different projection quantum states.[81]

Further simplifications involve approximations to the rotational motion, either the "infinite-order sudden approximation" (IOSA) in which the atom-diatom angle is fixed in the reagent and product channels and the "reduced dimensionality exact quantum" (RDEQ) method in which the coupled rotational and bending motion is treated adiabatically. Another approach is the "distorted wave Born approximation" (DWBA) in which the reaction is considered to be a small perturbation on the nonreactive collision. The nonreactive wavefunction can be constructed by either the CC, CS, or RDEQ methods.

The first three-dimensional CC calculation was in 1975 by Schatz and Kuppermann.[118,119] Their calculation was for H + H_2 on the PK2 surface for energies of E_{rel} = 0.03 to 0.43 eV. Elkowitz and Wyatt also presented results for the PK2 surface.[120,121] Walker *et al.*[122] performed the only converged calculations on the LSTH surface. In going from the PK2 to the LSTH surface, the "reaction threshold" is shifted up by approximately 0.05 eV while the location of the first resonance is shifted by only 0.015 eV. For all energies in the range E_{rel} = 0.33–0.73 eV, the reaction cross section from the LSTH calculation is approximately 20–30% less than the corresponding results from the PK2 surface.

Coltan and Schatz[123] have recently performed CS calculations for the H + H_2 reaction on the LSTH surface for translational energies below 1.4 eV. The H + D_2 reaction was studied by Schatz[124] at E_{rel} = 0.55 eV using the CS method on the LSTH surface. Schatz[125] has also studied the Mu + H_2 reaction on the LSTH surface. Schatz *et al.*[126] performed a CS calculation on the PK2 surface for $E_{rel} < 0.25$ eV for D + H_2, H + DH, and H + HD.

Within the past year several groups have presented new CC results. Webster and Light[127] presented reaction probabilities for total angular momentum $J = 0$ for H + H_2, D + H_2, and H + D_2 for $0.50 < E_{tot} < 1.50$ eV on the LSTH surface. Hipes and Kuppermann[128,129] presented reaction probabilities and lifetimes for $J = 0$ for

$H + H_2$ for $0.40 < E_{tot} < 1.60$ on the PK2 surface. They observed 6 resonances at 0.61, 0.847, 0.971, 1.170, 1.382, and 1.56 eV. These calculations have recently been repeated on the LSTH surface.[130] The resonance energies on this surface are 0.65, 0.880, 0.981, 1.193, 1.363, and 1.55 eV. These resonances have been identified with progressions in the symmetric stretching and bending motions of the H_3 transition state. Parker *et al.*[131] reported reaction probabilities for $J = 0, 1$ for $H + H_2$ and for $J = 0$ for $D + H_2$ for energies up to 1.0 eV, also on the PK2 surface.

Table 3 compares the thermal rate constants calculated by quantum mechanical methods with those calculated by QCT and the experimental results. The agreement between the QCT and CS results on the PK2 surface is only fair. The CS results exceed the QCT results by a factor of 1.4 and 2.0 at 600 and 400 K, respectively. At lower temperatures the agreement is much poorer, almost surely because the QCT calculations ignore tunnelling. The agreement between the CS and CC results is much better, the largest deviation being a factor of 1.45 at 200 K.

The agreement between the QCT and CS results on the LSTH surface is much better, with almost perfect agreement at temperatures above 300 K where tunnelling is not expected to be significant. The reason why the QCT calculations are in better agreement with the CS calculations on the LSTH surface than on the PK2 surface is not fully understood;[81] however, it is believed to be a result of the QCT calculations ignoring tunnelling and vibrational adiabaticity. Fully converged CC calculations on the LSTH surface are not yet available.

C. EXPERIMENTAL STUDIES

There have been essentially three classes of experiments performed on the hydrogen exchange reaction: bulk rate constant experiments, crossed molecular beam experiments, and hot atom experiments. Each class of experiments provides different information about the reaction: the first provides overall thermal rate constants, the second provides differential and integral reactive cross sections, while

the third provides either integral or state resolved reactive cross sections. The first class of experiments involves Boltzmann distributions of the internal states and initial collision velocities while in the second and third classes of experiments non-Boltzmann distributions are involved.

1. Thermal Rate Constant Experiments

Thermal rate constants are the most general information on reaction rates. They are proportional to the rate of the reaction under thermal equilibrium conditions, from which it is possible to determine such parameters as the "entropy of activation" and the "enthalpy of activation." They do not provide information as to the reaction rate under non-thermal equilibrium conditions, nor do they provide information about the detailed dynamics of the reaction, *i.e.*, mechanism and energy disposal.

The earliest measurements of the thermal rate constants were by Farkas[132–133] in the 1930's. The definitive measurements were made by Le Roy and coworkers[134–137] and by Westenberg and de Haas[138.139] in the late 1960's. Le Roy and coworkers studied the $H + H_2$, $H + D_2$, $D + D_2$, and $D + H_2$ reactions at temperatures from room temperature to 450 K by in a flow system using a hot tungsten filament to produce the reagent atoms and an isothermal calorimetric probe to determine the atom concentration. The Arrhenius plots for two of the reactions showed appreciable curvature which they attributed to tunnelling effects.

Westenberg and de Haas studied the $H + D_2$ and $D + H_2$ reactions at temperatures from near room temperature to 750 K in a flow system using a microwave discharge to produce the reagent atoms and ESR to determine the atom concentration. They observed less curvature in their Arrhenius plots than did Le Roy *et al.*

Mitchell and Le Roy[140] later reported that some of their results for $D+H_2$ were in error because of back diffusion problems within their apparatus. They repeated

the experiment using the same detection scheme as Westenberg and de Haas, extending the measurements to 167 K. The corrected results from their previous experiments and the results of Westenberg and de Haas smoothly overlapped with the new results.

In 1985 Garner *et al.*[141] studied the Mu + H_2 and Mu + D_2 reactions over the temperature range 610 to 850 K using the technique of muon spin rotation. More recently, Reid *et al.*[142] repeated these experiments with significantly greater precision over the temperature range 473 to 843 K. These reactions have large endothermicities and activation barriers because of large increases in zero-point energy in the products and in the activated complex compared with the appropriate H analog reaction; consequently, the rate constants are one to two orders of magnitude lower.

Table 3 compares the experimental rate constants with those calculated using various techniques. It is seen that at elevated temperatures both the QCT and CS calculations on the LSTH surface agree well with the experimental results.

2. Crossed Molecular Beam Experiments

Crossed molecular beam experiments yield much more specific information about the details of a chemical reaction than do thermal rate constants.[143] The primary result of a crossed molecular beam experiment is the differential cross section, which can be used to determine the potential energy function for the interaction, the time-scale of the reaction (fast or slow compared with rotation) and the mechanism. If the velocity distribution of the reagents is sufficiently narrow and the velocity distribution of the products is measured, it is also possible to determine the product internal energy distribution. In some cases it possible to accurately measure the integral reactive cross section.

Most of the crossed molecular beam experiments on the hydrogen exchange reaction have involved similiar experimental protocols. All the experiments except

one studied the $D + H_2 \rightarrow HD + H$ reaction. A low temperature effusive beam of H_2 is crossed at right-angles by a beam of D atoms produced by a high temperature source, either a tungsten oven or an arc discharge. The product HD is detected by a mass spectrometer which can rotate around the intersection point of the two beams. The mass spectrometer is tuned to mass 3 to detect the HD product; however, there is a severe background from the HD produced in wall reactions, from the HD impurities in the D atom source and to a much smaller extent in the H_2 beam, and from H_3^+ ions formed from ion-molecule reactions within the ionizer.

The first work using this method was by Datz and Taylor[144] in 1963. They had severe trouble with HD background, but were able to conclude that in the center of mass reference frame the molecular products are scattered backwards with respect to the atomic reagent.

Geddes *et al.*[145,146] repeated the experiments in 1970. The most probable initial relative energy was 0.48 eV with an energy spread (FWHM) of 0.32 eV. They measured the HD product velocity using a phase modulation technique. They concluded that the reaction products were scattered backwards and that the observed velocity distributions were consistent with the assumption of little internal excitation of the products.

Götting, *et al.*[147–149] recently completed a detailed study of the D + H_2 reaction. Using a pseudo-random chopper and a time-of-flight mass spectrometer they were able to determine the product HD velocities. They used an arc-discharge for their D atom source. This provided an intense, but variable, beam of D atoms. The most probable collision energy was 1.5 eV, with an energy spread (FWHM) slightly less than 3 eV. The differential cross section was not backwards peaked, but instead showed a maximum at an angle of 125°. The absolute reactive cross section was determined to be 1.7 ± 0.8 Å^2. They did not directly determine the dynamic parameters of interest by deconvoluting their data, but instead used QCT

results convoluted with the appropriate system response functions to simulate the experiments. The calculated differential cross section was in reasonable agreement with the experimental differential cross section, the agreement in the angular distribution being better than that for the velocity distribution. The calculated final state distributions had very little vibrational excitation (less than 10%) and significant rotational excitation (peaked at $J = 12$). A sensitivity analysis lead them to conclude that they could determine J_{max} to within 1 quanta (it should be noted that an HD rotational quanta is approximately 0.14 eV at these levels of excitation). They therefore concluded that only 52% of the available energy went into product translation, with most of the remaining energy being in product rotation.

The above experiments were all hampered by the HD background signal. Kwei and Lo[150] used a different detection scheme in their studies on the $H + T_2$ reaction. They used MoO_3 coated buttons located at 10° intervals as a getter surface for H or T atoms, then used liquid scintillation counting to determine the number of T atoms on each button. The most probable center of mass collision energy was 0.60 eV with a width of 0.51 eV (FWHM). Their analysis showed that the T atoms were scattered forward in the center of mass system, consequently, the molecular product was scattered backwards.

A major difficulty to the complete analysis of these experiments is the very broad translational energy distribution of the atomic beam which leads to a large uncertainty in the collision energy and to large amounts of smearing of the differential cross section. Buntin *et al.*[151] developed a novel crossed molecular beam technique to reduce the uncertainty in the atomic beam velocity. Instead of using a thermal D atom source, they used a photolytic source in which D_2S was photolyzed under nearly collisionless conditions by an ArF excimer laser operating at 193 nm. After collimation by skimmers, the pulse of D atoms had an pulsewidth

of $\Delta t = 0.9$ μsec and a velocity resolution of $\Delta v/v = 11\%$. The collision energy is varied by changing the intersection angle between the D atom source and the H_2 beam. The time-of-flight distribution of the product HD was measured by a mass spectrometer. At a center of mass collision energy of 0.95 eV the energy uncertainty was only 0.24 eV, approximately a factor of 4 better than that obtained using a thermal D atom source. The complete analysis of their experiments has not yet been published; however, preliminary results at one laboratory scattering angle show that they are able to clearly resolve vibrational distributions. Preliminary analysis by computer simulation yielded a $v = 0$ to $v = 1$ population ratio of 5.1, while the rotational distribution peaked at $J = 5$ or $J = 6$, depending on the model chosen. If these results are confirmed then they are seeing greater vibrational and less rotational excitation than Götting *et al.*[149]

3. Hot Atom Experiments

Experimental studies of the hydrogen exchange reaction which involve hot atoms have two major advantages over the previous classes of reactions. First, it is possible to generate H atoms with an extremely narrow spread in laboratory velocities by the photolysis of an appropriate precursor. Therefore, it is possible to study the reaction within a narrow initial transational energy range, unlike the case for bulk rate constants or crossed molecular beams in which the uncertainty in the initial relative translational energy can exceed the most probable energy. Second, it is possible to directly determine the product nascent internal state distributions by using pulsed lasers to spectroscopically detect the product molecules.

All hot atom reactions use one of two techniques to generate the reagent atomic species:[80] photolysis or nuclear recoil. In the photolysis method a H containing molecule is photodissociated. Given the incident photon wavelength along with knowledge of the dissociation energy and the internal energy distribution of each fragment and the constraint of energy conservation, it is possible to predict the

energy released into fragment recoil. The constraint of momentum conservation allows for a determination of the partition of the released energy between the two fragments. When a bond between a H atom and the rest of the molecule is cleaved, most of the released energy is carried off by the H fragment because it is much lighter than the other fragment. In the nuclear recoil method, an energetic T ion is formed by the nuclear reaction $^3He + n \rightarrow T^- + p^+$. The T^- ion is neutralized as it thermalizes, at which point the T atom can undergo chemical reactions. The nuclear recoil method will not be discussed further.

Several molecules have successfully been used as H atom precursors. The most commonly used precursors are the hydrogen halides and H_2S. The hydrogen halides have several advantages. First, it is impossible for the fragments to have vibrational or rotational excitation because the precursor is a diatomic molecule; consequently the translational energy of the recoiling fragments is precisely known. Second, transitions to the dissociative states of the heavier hydrogen halides are in wavelength ranges which are easily accessible to lasers and spectral lamps, which make them convienient to use.[152]

The experiments involving photolytically generated hot H atoms can be convienently broken into two classes: the early experiments undertaken before the widespread introduction of lasers into the laboratory, and the recent experiments using lasers. The early experiments determined integrated reaction yields as a function of translational energy under non-Boltzmann, many collision conditions. The recent experiments determined total and state-to-state reactive cross sections as a function of translational energy under single collision conditions.

When a hydrogen halide is continuosly photodissociated, the steady-state velocity distribution of the H atom should show two peaks: one peak corresponding to the nascent energy of the recoiling H atom fragment, and a second peak corresponding to thermalized H atoms.[80] It is assumed that the two different

H atom "species" (hot and thermal) will have different reactivity. By varying the relative concentrations of reactant species, moderators, and thermal H atom scavengers it is possible to determine the integrated reaction yield, *i.e.*, the fraction of hot H atoms which react when they collide with the target molecule. By varying the photolysis wavelength it is possible to "scan" the hot atom translational energy.

The first use of this approach on the hydrogen exchange reaction was by Carter *et al.*[153] in 1955. They photolyzed mixtures of DI/H_2 using 253.7 nm radiation. Martin and Willard[154] performed a similiar experiment in 1964 in which HBr/D_2 mixtures were photolyzed using 184.9 nm radiation.

The classic experiments using the above approach were performed by White,[155] Betts,[156] and Kuppermann[157] in the late 1960's. White photolyzed DI/H_2 mixtures at 5 wavelengths and DBr/H_2 mixtures at a single wavelength. The initially prepared hot D atoms had E_{rel} in the range 0.15 to 0.90 eV. He observed a threshold of $E_{rel} = 0.33 \pm 0.02$ eV. Betts studied DBr/H_2 and DI/H_2 mixtures photolyzed at 13 different wavelengths with E_{rel} in the range 0.311 to 1.43 eV. Further analysis of both data sets led to a revised threshold of 0.25 eV. This is actually a minimum value since the high energy tail of the H_2 thermal velocity distribution spreads out E_{rel}. In addition, this is a phenomenological threshold which does not have a precise definition in terms of the reactive cross section. For comparison, the threshold energy from QCT calculations[111] for the D + H_2 reaction on the LSTH surface is $E_{rel} = 0.28 \pm 0.01$ eV.

Several groups have recently used lasers to study the hydrogen exchange reaction under single collision conditions. One set of experiments involves the determination of the total reactive cross section.[158,159] A mixture of an H atom precursor and D_2 is photolyzed to produce hot H atoms. The number density of reagent H atoms and product D atoms is monitored at a slightly later time by laser induced fluorescence at the Lyman-α lines at 82259 and 82281 cm^{-1}, respectively.

The UV photolysis laser pulse is provided by an excimer laser while the detection laser radiation at the appropriate VUV wavelength is generated by third harmonic generation of the second harmonic of a tunable dye laser.

Tsukiyama *et al.*[158] used H_2S as their precursor. The photolysis wavelengths were 248 and 193 nm, corresponding to E_{rel} = 0.84 and 1.95 eV, respectively. Total pressures did not exceed 153 mTorr. The time delay between the laser pulses was 87 ± 3 ns. Gerlach-Meyer *et al.*[159] used HBr and HCl as their precursor. The photolysis wavelength for both precursors was 193 nm, corresponding to E_{rel} = 2.11 and 1.54 eV for HBr and HCl, respectively. Total pressures did not exceed 110 mTorr. They used a time delay of 40 ± 3 ns.

The results from these two experiments, along with QCT results,[111,115,116,160] are given in Table 4. Of the four experimental total reactive cross sections, three exceed the QCT cross sections, sometimes by a wide margin. For example, Tsukiyama *et al.*[158] report a cross section of 1.68 Å^2 at a relative energy of 1.95 eV with an rms deviation of 0.12 Å^2 for five measurements. The 95% confidence level of the mean is 0.17 Å^2. The QCT cross section[160] at this energy is only 1.30±0.05 Å^2. The deviation between the experimental and calculated results is significant at the 95% confidence level.

The second set of hot atom experiments using lasers involve a determination of the nascent internal quantum state distribution of the product hydrogen molecule.[82–86] In these experiments a mixture of an H atom precursor and H_2 is photolyzed by a UV laser. After a short time delay the number density of the product molecules in each quantum state is measured. The time delay is chosen short enough that the H atom has time for only one collision with the H_2 molecule.

Three laser based methods for detecting molecular hydrogen have been developed: CARS, REMPI, and LIF. Of these, both CARS and REMPI have been used to measure the product state distribution of the hydrogen exchange

reaction. The reaction that was studied was $H + D_2 \rightarrow HD(v'', J'') + D$. Gerrity and Valentini[82–84] studied this reaction at center of mass collision energies of 1.3, 1.1, and 0.98 eV using CARS, while Marinero, Rettner, and Zare[85,86] studied the reaction at only 1.3 eV using REMPI.

In the Gerrity and Valentini[82–84] experiments, HI was photolyzed by the Nd:YAG fourth harmonic at 266 nm or by the second harmonic of a Nd:YAG pumped dye laser at 280 or 291 nm. The fixed frequency in the CARS detection scheme is the Nd:YAG second harmonic at 532 nm while the variable frequency is provided by a Nd:YAG pumped dye laser operated at 637–660 nm. The three laser beams are combined together with dichroic mirrors and focused into a 2 m long, differentially pumped cell through which an approximately equimolar mixture of HI and D_2 is flowed at $\approx$ 4 torr total pressure. The collinearly produced anti-Stokes beam is separated from the three incident laser beams by a series of prisms and monochromaters before being imaged onto the photocathode of a photomultiplier. The time delay between the photolysis and CARS laser pulses was 5, 15, or 28 ns, with a jitter of $\approx$ 3 ns. Most of their results were obtained at a delay of $\approx$ 5 ns. At the 1.3 eV collision energy, they observed the product in the following HD quantum states: $v = 0$, $J = 1$–10,12, $v = 1$, $J = 1$–9, and $v = 2$, $J = 2$–5.

In the Marinero *et al.*[85,86] experiments, HI was photolyzed by the Nd:YAG fourth harmonic at 266 nm. The $\approx$ 195 nm laser radiation needed for the REMPI detection scheme was produced by Raman shifting the second harmonic of a Nd:YAG pumped dye laser. The two laser beams traversed the reaction region in opposite directions. The ions produced from the REMPI detection scheme were detected by a time-of-flight mass spectrometer. Because the efficient detection of ions requires low pressures, the reagents were introduced into the differentially pumped reaction chamber through a glass capillary. The reagent pressures within the reaction zone were estimated at $\approx$ 30 and $\approx$ 5 mtorr for H_2 and HI, respectively.

The time delay between the photolysis and REMPI laser pulses varied between -25 to 425 ns. Most of their results were obtained at a delay of $\approx$ 60 ns. At the 1.3 eV collision energy, they observed the HD product in the following quantum levels: $v = 1$, $J = 0$–6 and $v = 2$, $J = 0$–6. The HD $v = 0$ product was observed, but the large contribution from the HD impurity made it impossible to determine the amount from the reaction.

The rotational distributions obtained from the two sets of experiments can be compared with those from the QCT calculations of Blais and Truhlar.[115,116] The qualitative agreement is reasonably good. For example, at a collision energy of 1.3 eV, Blais and Truhlar predict that the rotational distributions will peak at $J = 8$, 4, and 5 for $v = 0$, 1, and 2, respectively. The experimental distributions of Gerrity and Valentini peak at $J = 3$, 3, and 3, respectively for the same vibrational levels. The experimental distributions of Marinero *et al.* at the same energy peak at $J = 4$ and 2 for $v = 1$ and 2, respectively. Thus, in terms of the peak of the rotational distributions, the two experiments seem to agree while the calculations seem to predict slightly more rotational excitation than was observed. A further examination of the three sets of data shows less agreement. The rotational distributions of Marinero *et al.* are more sharply peaked than that of the other two data sets while the distributions of Blais and Truhlar seem to extend to higher J

A quantitative analysis of the three sets of data show some significant disagreements. Using an information theoretic approach,[177] the rotational and vibrational distributions can often be fit to a linear suprisal function,

$$P(v,J) = P^0(v,J)e^{-\lambda_0 - \lambda_V f_v - \theta_R(v) g_{vJ}}$$

where $f_v = \frac{E_{vib}(v)}{E_{tot}}$ is the fraction of energy in vibration, $g_{vJ} = \frac{E_{rot}(J)}{E_{tot} - E_{vib}(v)}$ is the fraction of energy in rotation, λ_V is the vibrational linear suprisal parameter and

$\theta_R(v)$ is rotational linear suprisal parameter for state v, and the prior distribution is

$$P^0(v,J) = \frac{(2J+1)\sqrt{E_{tot} - E_{vib}(v) - E_{rot}(J)}}{\sum_{v'=0}^{v^*} \sum_{J'=0}^{J^*(v')} (2J'+1)\sqrt{E_{tot} - E_{vib}(v') - E_{rot}(J')}}$$

where $J^*(v')$ is the largest energetically allowed rotational state for the given vibrational level and E_{tot} while v^* is the largest energetically allowed vibrational state.

Gerrity and Valentini[83] calculated rotational and vibrational suprisals for both sets of experiments and the QCT calculations at 1.3 eV. For their own experiment, they obtained $\theta_R(0) = 3.0$ and $\theta_R(1) = 3.5$, from the Marinero *et al.* experiments they obtained $\theta_R(1) = 5.3$ and $\theta_R(2) = 5.0$, and from the QCT calculations they obtained $\theta_R(0) = 3.4$, $\theta_R(1) = 3.0$, and $\theta_R(2) = 2.3$. They found that their own data could be adequately represented by the single rotational suprisal parameter $\theta_R = 3.0$ and the vibrational suprisal parameter $\lambda_V = 2.6$. Thus, the rotational suprisal parameters from the Marinero *et al.* experiment are significantly larger than that from the other data sets, implying that their distribution is "colder" than the others. The reason for the discrepancy is unknown.

A similiar analysis can be carried out for the other two collision energies examined by Gerrity and Valentini.[84] In each case they find that their experimental results and the QCT calculations give linear suprisal parameters. In addition, the calculated rotational distributions were slightly broader and extended to slightly higher J's.

Table 5 is a summary of the results from the Blais and Truhlar QCT calculations and the Gerrity and Valentini hot atom/single collision condition experiments with CARS detection of HD. In each case the fraction of the available energy going into rotation, vibration, and product translation is given. The overall agreement is quite good; however, the QCT calculations consistently give a slightly

greater degree of rotational and vibrational excitation than the experimental results. In view of the large uncertainties in both the calculations and the experiments, the significance of these deviations is unknown.

C. PROPOSED EXPERIMENTS

In view of the importance of the hydrogen exchange reaction, it is gratifying that the agreement between the theoretical and experimental work is as good as it is. However, one would hope for even better quantitative agreement than there seems to be, especially for the hot atom/single collision condition experiments. Specifically, the rotational distributions predicted on the basis of QCT calculations on the LSTH potential energy surface seem to be slightly "hotter" than those found experimentally. In addition, the total reactive cross sections predicted on the basis of QCT calculations are significantly lower than those found experimentally at center of mass collision energies near 2.0 eV

There are three potential sources for the quantitative disagreement between theory and experiment. First, the only theory which has been used at the energies of the experiments is QCT calculations. It is possible that the disagreements will resolve themselves when full, converged, CC quantum mechanical results are available. Second, the calculations have all been performed on the LSTH potential energy surface. Newer surfaces, such as the DMBE, have lower barriers and other subtle differences compared with the LSTH surface. The use of a newer, more accurate surface, might resolve the disagreements.

In addition, there could be an error in the experiments. It is disheartening that the two hot atom/single-collision/state-resolved experiments gave such significantly different product rotational distributions, especially since the only major difference was in the H_2 detection scheme used. The two schemes, CARS and REMPI, each involve a nonlinear optical process. Such processes are difficult to calibrate as they

depend critically on the instantaneous power density and are sensitive to temporal, spatial and phase fluctuations within the incident laser beams.

It is proposed that the hydrogen exchange reaction be studied by a hot atom/single-collision/state-resolved experiment using LIF as the H_2 detection scheme. It is hoped that the use of a linear optical process in the detection scheme will resolve the disagreements between the two previous experiments. It is further hoped that the product rovibrational distribution will resolve some of the disagreements between experiment and theory on this very important reaction.

TABLE 1. Formaldehyde Geometries

	S_0 (expt)[2]	S_1 (expt)[2]	(calc)[27]	$S_0^{\ddagger}$ (calc)[29]	(calc)[30]	CO,H_2 (expt)[61]
r_{CO}	1.203	1.323	1.18	1.18	1.18	1.128
$r_{CH'}$	1.101	1.098	1.73	1.57	1.88	
$r_{CH''}$	1.101	1.098	1.11	1.10	1.10	
r_{HH}	1.872		1.34	1.21	1.30	0.714
$\angle_{OCH'}$	121.8		108.	111.	120.	
$\angle_{H'CH''}$	116.3	118.4	50.	50.	42.	
$\angle_{OCH''}$	121.8		202.	199.	198.	
ρ	0.0	34.0	0.0	0.0	0.0	
Symmetry	C_{2v}	C_s	C_s	C_s	C_s	

1. All distances in Å, all angles in degrees.

TABLE 2. Formaldehyde Photodissociation Product Energy Distributions

FRAGMENT	$\frac{E_t}{E_{avail}}$	$\frac{E_v}{E_{avail}}$	$\frac{E_r}{E_{avail}}$
CO	0.04	0.01	0.13
H_2	0.61	0.16	0.05

TABLE 3. Calculated and Experimental Thermal Rate Constants[a]

REACTION	T(K)	$-\log(k)$					
			QCT		CS	CC	EXPT
		PK2	LSTH	PK2	LSTH	PK2	
$H+H_2$[b]	200	18.08	18.62	16.96	18.00	16.80	
	300	15.51	15.92	15.02	15.77	15.00	15.57
	400	14.23	14.51	13.92	14.47	13.96	14.53
	500	13.43	13.66	13.23	13.64	13.30	13.66
	600	12.89	13.08	12.74	13.06	12.85	
$H+D_2$	200		19.92				
	300	16.14	16.92				16.58
	400	14.74	15.37				15.20
	500	13.92	14.34				14.20
	600	13.31					13.51
$D+H_2$	200		17.85				17.71
	300	15.28	15.44				15.52
	400	14.10	14.21				14.29
	500	13.32	13.43				13.49
	600	12.80	12.89				12.92
$Mu+H_2$	300				19.14		
	400				16.86		
	500				15.45		15.41
	600				14.50		14.45
	700				13.82		13.75
	800				13.31		13.24

a) Rate constants in cm^3 $molecule^{-1}$ sec^{-1}.

b) Distinguishable atom rate constants for $H + H_2$.

TABLE 4. Calculated and Experimental Total Reactive Cross Sections

REACTION	E_{rel} (eV)	Calculated Cross section (Å^2)	Experimental Cross section (Å^2)
$H+D_2$	0.40	0.04 ± 0.01	
	0.48	0.14 ± 0.01	
	0.55	0.31 ± 0.01	
	0.65	0.41 ± 0.02	
	0.84	0.71 ± 0.04	0.99 ± 0.13
	0.98	0.86 ± 0.02	
	1.10	0.96 ± 0.02	
	1.30	1.13 ± 0.02	
	1.54		1.10 ± 0.23
	1.95	1.30 ± 0.05	1.68 ± 0.13
	2.11		1.95 ± 0.49

a) Error limits are $\pm$ one standard deviation.

TABLE 5. Hydrogen Exchange Reaction Product Energy Distributions

REACTION	METHOD	E_{rel}	$\frac{E_t}{E_{avail}}$	$\frac{E_v}{E_{avail}}$	$\frac{E_r}{E_{avail}}$
$H+D_2$	QCT	0.55	0.89	0.02	0.10
		0.98	0.73	0.07	0.21
		1.10	0.70	0.08	0.23
		1.30	0.67	0.09	0.24
$H+D_2$	Hot-atom	0.98	0.73	0.06	0.21
		1.10	0.73	0.04	0.22
		1.30	0.70	0.08	0.22
$D+H_2$	Crossed-beam	0.95	0.67	0.07	0.25
		1.50	0.52	< 0.1	≈ 0.4

a) Results are calculated from linear suprisal results if known, otherwise, directly from the experimental results. Results are rounded to nearest 0.01.

b) $E_{avail} = E_{rel} - \Delta E_{reaction}$.

REFERENCES

1. J. R. Sodeau and E. K. C. Lee, *Rev. Chem. Inter.* **4**, 259 (1981).
2. D. J. Clouthier and D. A. Ramsay, *Ann. Rev. Phys. Chem.* **34**, 31 (1983).
3. C. B. Moore and J. C. Weisshaar, *Ann. Rev. Phys. Chem* **34**, 525 (1983).
4. B. J. Finlayson, J. N. Pitts, and R. Atkinson, *J. Am. Chem. Soc.* **96**, 5356 (1974).
5. R. S. Sheinson and F. W. Williams, *Combust. and Flames* **21**, 221 (1973).
6. D. J. Bogan, R. S. Sheinson, and F. W. Williams, *J. Am. Chem. Soc.* **98**, 1034 (1976).
7. D. M. Rank, C. H. Towns, and W. J. Welsh, *Science* **174**, 1083 (1971).
8. W. Boland and T. deJong, *Astron. Astrophys.* **98**, 149 (1981).
9. S. Green, B. J. Garrison, W. A. Lester, Jr., and W. H. Mille, *Astrophys. J. Suppl. Ser.* **37**, 321 (1978).
10. K. Henning, *Astro Astrophys. Suppl. Ser.* **44**, 405 (1981).
11. A. Wootten, R. Snell, and N. J. Evans, *Astrophys. J.* **240**, 532 (1980).
12. J. G. Calvert, J. A. Kerr, K. L. Demerjian, and R. D. McQuigg, *Science* **175**, 751 (1971).
13. K. L. Demerjian, J. A. Kerr, J. G. Calvert, *Adv. Environ. Sci. Technol.* 4, 1 (1974).
14. R. S. Berry and P. A. Lehman, *Ann. Rev. Phys. Chem.* **22**, 47 (1971).
15. J. A. Logan, M. J. Prather, S. C. Wofsy, and M. B. McElroy, *J. Geophys. Res.* **86**, 7210 (1981).
16. J. A. Swenberg, R. E. Kerns, R. E. Mitchell, E. J. Gralla, and K. L. Pavlow, *Cancer Research* **40**, 3908 (1980).
17. *Formaldehyde, Analytical Chemistry and Toxicology*, edited by V. Turoski, (American Chemical Society, Washington, 1985).

18. *Formaldehyde Release From Wood Products*, edited by B. Meyer, B. A. K. Andrews, and R. M. Runhardt, (American Chemical Society, Washington, 1986).

19. E. S. Yeung and C. B. Moore, *Appl. Phys. Lett.* **21**, 109 (1972).

20. R. E. M. Hedges, P. Ho, and C. B. Moore, *Appl. Phys.* **23**, 25 (1980).

21. J. Marling, *J. Chem. Phys.* **66**, 4200 (1977).

22. C. B. Moore, *Accouns Chem. Res.* **6**, 322 (1973).

23. V. S. Letokhov, *Ann. Rev. Phys. Chem.* **28**, 133 (1977).

24. R. A. Fletcher and G. Pilcher, *Trans. Far. Soc.* **66**, 794 (1970).

25. D. D. Wagman, W. H. Evans, V. B. Parker, R. H. Schumm, T. Halow, S. M. Bailey, K. L. Churney, and R. L. Nuttall, *The NBS Tables of Chemical Thermodynamic Properties*, *J. Phys. Chem. Ref. Data.* **11 Sup 2** 107,382 (1982).

26. V. Bachler and E. A. Halevi, *Theoret. Chim. Acta. (Berl)* **59**, 595 (1981).

27. R. L. Jaffe and K. Morokuma, *J. Chem. Phys.* **64**, 4881 (1976).

28. M. J. Frisch, R. Krishnan, and J. A. Pople, *J. Phys. Chem.* **85**, 1467 (1981).

29. J. D. Goddard, Y. Yamaguchi, and H. F. Schaefer, III, *J. Chem. Phys.* **75**, 3459 (1981).

30. M. Dupuis, W. A. Lester, Jr., B. H. Lengsfield, III, and B. Liu, *J. Chem. Phys.* **79**, 6167 (1981).

31. J. P. Reilly, J. H. Clark, C. B. Moore, and G. C. Pimentel, *J. Chem. Phys.* **69**, 4381 (1978).

32. J. W. C. Johns, S. H. Priddle, and D. A. Ramsay, *Disc. Far. Soc.* **35**, 90 (1963).

33. W. H. Fink, *J. Am. Chem. Soc.* **94**, 1073 (1972).

34. D. M. Hayes and K. Morokuma, *Chem. Phys. Lett.* **12**, 539 (1972).

35. J. C. D. Brand and C. G. Stevens, *J. Chem. Phys.* **58**, 3331 (1973).

36. E. Gorin *J. Chem. Phys.* **7**, 256 (1939).

37. L. J. Schoen, *Fifth Int. Symp. on Combustion*, (Reinhold Publishing Corp, NY, 1955) p. 786.

38. R. Klein and L. J. Schoen, *J. Chem. Phys.* **24**, 1094 (1956).

39. A. G. Harrison and F. P. Lossing. *Can. J. Chem.* **38**, 544 (1960).

40. B. A. DeGraff and J. G. Calvert, *J. Am. Chem. Soc.* **89**, 2247 (1967).

41. R. D. McQuigg and J. G. Calvert, *J. Am. Chem. Soc.* **91**, 1590 (1969).

42. J. H. Clark, C. B. Moore, and N. S. Nogar, *J. Chem. Phys.* **68**, 1264 (1978).

43. G. K. Moortgat, W. Seiler, P. Warneck, *J. Chem. Phys.* **78**, 1185 (1983).

44. S. J. Strickler and R. J. Barnhart *J. Phys. Chem.* **86**, 448 (1982).

45. E. S. Yeung and C. B. Moore, *J. Chem. Phys.* **58**, 3988 (1973).

46. V. S. Antonov, I. N. Knyazev, V. S. Letokhov, and V. G. Movshev, *Sov. Phys. JETP* 46, 697 (1977).

47. R. G. Miller and E. K. C. Lee, *J. Chem. Phys.* **68**, 4448 (1978).

48. E. W. Schlag, W. E. Henke, and S. H. Lin, *Int. Rev. Phys. Chem* **2**, 43 (1982).

49. J. C. Weisshaar, A. P. Baronavski, A. Cabello, and C. B. Moore, *J. Chem. Phys.* **69**, 4720 (1978).

50. A. P. Baronavski, A. Hartford, Jr., and C. B. Moore, *J. Mol. Spectrosc.* **60**, 111 (1976).

51. K. Shibuya and E. K. C. Lee, *J. Chem. Phys.* **69**, 6912 (1978).

52. J. C. Weisshaar and C. B. Moore, *J. Chem. Phys.* **70**, 5135 (1979).

53. J. C. Weisshaar and C. B. Moore, *J. Chem. Phys.* **72**, 5415 (1980).

54. W. E. Henke, H. L. Selzle, T. R. Hays, E. W. Schlag, and S. H. Lin, *J. Chem. Phys.* **76**, 1327 (1982).

55. H. L. Selzle and E. W. Schlag, *Chem. Phys.* **43**, 111 (1979).

56. E. C. Apel and E. K. C. Lee, *J. Phys. Chem.* **89**, 1391 (1985).

57. K. Y. Tang, P. W. Fairchild, and E. K. C. Lee, *J. Chem. Phys.* **66**, 3303 (1977).

58. K. Shibuya, P. W. Fairchild, and E. K. C. Lee, *J. Chem. Phys.* **75**, 3397 (1981).

59. J. C. Weisshaar and C. B. Moore, *J. Chem. Phys.* **72**, 2875 (1980).

60. D. R. Guyer, W. F. Polik, and C. B. Moore, *J. Chem. Phys.* **84**, 6519 (1986).

61. K. P. Huber and G. Herzberg, *Molecular Spectra and Molecular Structure IV. Constants of Diatomic Molecules*, (Van Nostrand Reinhold, NY, 1979).

62. R. J. Spindler, Jr., *J. Quant. Spectrosc. Radiat. Transfer* **9**, 597 (1969).

63. D. F. Heller, M. L. Elert, and W. M. Gelbart, *J. Chem. Phys.* **69**, 4061 (1978).

64. J. M. F. van Dijk, M. J. H. Kemper, J. H. M. Kerp, and H. M. Buck, *J. Chem. Phys.* **69**, 2462 (1978).

65. W. H. Miller, *J. Am. Chem. Soc.* **101**, 6810 (1979).

66. S. K. Gray, W. H. Miller, Y. Yamaguchi, and H. F. Schaefer III, *J. Am. Chem. Soc.* **103**, 1900 (1981).

67. J. Troe, *J. Phys. Chem.* **88**, 4375 (1984).

68. W. H. Miller, *J. Am. Chem. Soc.* **105**, 216 (1983).

69. R. Schatzberger, E. A. Halevi, and N. Moiseyev, *J. Phys. Chem.* **89**, 4691 (1985).

70. R. Schinke, *J. Chem. Phys.* **84**, 1487 (1986).

71. P. L. Houston and C. B. Moore, *J. Chem. Phys.* **65**, 757 (1976).

72. P. Ho, D. J. Bamford, R. J. Buss, Y. T. Lee, and C. B. Moore, *J. Chem. Phys.* **76**, 3630 (1982).

73. P. Ho, A. V. Smith, *Chem. Phys. Lett.* **90**, 407 (1982).

74. D. J. Bamford, S. V. Filseth, M. F. Foltz, J. W. Hepburn, and C. B. Moore, *J. Chem. Phys.* **82**, 3032 (1985).

75. M. Peálat, D. Debarre, J.-M. Marie, J.-P.E. Taran, A. Tramer, and C. B. Moore, *Chem. Phys. Lett.* **98**, 299 (1983).

76. H. C. Allen and P. C. Cross, *Molecular Vib-Rotors* (Wiley, NY, 1963).

77. B. Schramm, D. J. Bamford, and C. B. Moore, *Chem. Phys. Lett.* **98**, 305 (1983).

78. D. Debarre, M. Lefebvre, M. Peálat, J.-P. E. Taran, D. J. Bamford, and C. B. Moore, *J. Chem. Phys.* **83**, 4476 (1985).

79. D. G. Truhlar and R. E. Wyatt, *Ann. Rev. Phys. Chem.* **27** 1 (1976).

80. D. G. Truhlar and R. E. Wyatt, *Adv. Chem. Phys.*, **36** 141 (1977).

81. G. C. Schatz, in *The Theory of Chemical Reaction Dynamics*, edited by D. C. Clary, (D. Reidel Publishing, Boston, 1986) p. 1–26.

82. D. P. Gerrity and J. J. Valentini, *J. Chem. Phys.* **79**, 5202 (1983).

83. D. P. Gerrity and J. J. Valentini, *J. Chem. Phys.* **81**, 1298 (1984).

84. D. P. Gerrity and J. J. Valentini, *J. Chem. Phys.* **82**, 1323 (1985).

85. C. T. Rettner, E. E. Marinero, and R. N. Zare, in *Physics of Electronic and Molecular Collisions*, edited by J. Eichler, I. V. Hertel, and N. Stolterfoht (North Holland, Amsterdam, 1984), p. 51.

86. E. E. Marinero, C. T. Rettner, and R. N. Zare, *J. Chem. Phys.* **80**, 4142 (1984).

87. F. London, *Z. Electrochem.* **35**, 552 (1929).

88. H. Eyring and M. Polanyi, *Naturwiss* **18**, 914 (1930).

89. S. Sato, *Bull. Chem. Soc. Jpn.* **28**, 450 (1955).

90. S. Sato, *J. Chem. Phys.* **23**, 592 (1955).

91. S. Sato, *J. Chem. Phys.* **23**, 2465 (1955).

92. R. N. Porter and M. Karplus, *J. Chem. Phys.* **40**, 1105 (1964).

93. A. S. Coolidge and H. M. James, *J. Chem. Phys.* **2**, 811 (1934).

94. J. O. Hirschfelder, H. Diamond, and H. Eyring, *J. Chem. Phys.* **5**, 695 (1937).

95. S. F. Boys, G. B. Cook, C. M. Reeves, and I. Shavitt, *Nature* **178**, 1207 (1956).

96. S. F. Boys and I. Shavitt, *Univ. of Wis. NRL Tech. Rep. WIS-AF-13*, 1959.

97. B. Liu, *J. Chem. Phys.* **58**, 1925 (1973).

98. W. Kolos and L. Wolniewicz, *J. Chem. Phys.* **43**, 2429 (1965).

99. D. Siegbahn and B. Liu, *J. Chem. Phys.* **68**, 2457 (1978).

100. D. G. Truhlar and C. J. Horowitz, *J. Chem. Phys.* **68**, 2466 (1978).

101. W. Welz, Ph.D. Thesis, Bonn, 1976.

102. B. Liu, *J. Chem. Phys.* **80**, 581 (1984.).

103. A. J. C. Varandas, F. B. Brown, C. A. Mead, D. G. Truhlar, and N. C. Blais, to be published.

104. B. C. Garrett, D. G. Truhlar, A. J. C. Varandas, and N. C. Blais, *Int. J. Chem. Kinet.* **18**, 1065 (1986).

105. M. R. A. Blomberg and B. Liu, *J. Chem. Phys.* **82**, 1050 (1985).

106. L. M. Raff and D. L. Thompson, in *Theory of Chemical Reaction Dynamics, Vol. III*, edited by M. Baer (CRC Press, Boca Raton, FL xxxx) pp. 1–121.

107. J. O. Hirschfelder, H. Eyring, and B. Topley, *J. Chem. Phys.* **4**, 170 (1936).

108. M. Karplus, R. N. Porter, and R. D. Sharma, *J. Chem. Phys.* **40**, 2033 (1964).

109. M. Karplus, R. N. Porter, and R. D. Sharma, *J. Chem. Phys.* **43**, 3259 (1965).

110. M. Karplus, R. N. Porter, and R. D. Sharma, *J. Chem. Phys.* **45**, 3871 (1966).

111. H. R. Mayne, *J. Chem. Phys.* **73**, 217 (1980).

112. G.-D. Barg, H. R. Mayne, and J. P. Toennies, *J. Chem. Phys.* **74**, 1017 (1981).

113. H. R. Mayne and J. P. Toennies, *J. Chem. Phys.* **75**, 1794 (1981).

114. C. A. Boonenberg and H. R. Mayne, *Chem. Phys. Lett.* **108**, 67 (1984).

115. N. Blais and D. G. Truhlar, *Chem. Phys. Lett.* **102**, 120 (1983).

116. N. Blais and D. G. Truhlar, *J. Chem. Phys.* **83**, 2201 (1985).

117. H. R. Mayne and S. S. Prasad, *Int. J. Chem. Kinet.* **18**, 977 (1986).

118. A. Kuppermann and G. C. Schatz, *J. Chem. Phys.* **62**, 2502 (1975).

119. G. C. Schatz and A. Kuppermann, *J. Chem. Phys.* **65**, 4668 (1976).

120. A. B. Elkowitz and R. E. Wyatt, *J. Chem. Phys.* **62**, 2504 (1975).

121. A. B. Elkowitz and R. E. Wyatt, *J. Chem. Phys.* **63**, 702 (1975).

122. R. B. Walker, E. B. Stechel, and J. C. Light, *J. Chem. Phys.* **69**, 2922 (1978).

123. M. C. Coltan and G. C. Schatz, *Int. J. Chem. Kinet.* **18**, 961 (1986).

124. G. C. Schatz, *Chem. Phys. Lett.* **108**, 532 (1984).

125. G. C. Schatz, *J. Chem. Phys.* **83**, 3441 (1985).

126. G. C. Schatz, N. M. Harvey, and A. Kuppermann, to be published.

127. F. Webster and J. C. Light, *J. Chem. Phys.* **85**, 4744 (1986).

128. A. Kuppermann and P. G. Hipes, *J. Chem. Phys.* **84**, 3962 (1986).

129. P. G. Hipes and A. Kuppermann, *Chem. Phys. Lett.* **131**, 1 (1987).

130. P. G. Hipes, private communication.

131. G. A. Parker, R. T. Pack, B. J. Archer, and R. B. Walker, submitted for publication.

132. A. Farkas, *Z. Electrochem* **36**, 782 (1930).

133. A. Farkas, *Z. Physik Chem.* **B10**, 419 (1930).

134. W. R. Schulz and D. J. Le Roy, *Can. J. Chem.* **42**, 2480 (1964).

135. W. R. Schulz and D. J. Le Roy, *J. Chem. Phys.* **42**, 3869 (1965).

136. B. A. Ridley, W. R. Schulz, and D. J. Le Roy, *J. Chem. Phys.* **44**, 3344 (1966).

137. D. J. Le Roy, B. A. Ridley, and K. A. Quickert, *Disc. Far. Soc.* **44**, 92 (1967).

138. A. A. Westenberg, *Disc. Far. Soc.* **44**, 169 (1967).

139. A. A. Westenberg and N. de Haas, *J. Chem. Phys.* **47**, 1393 (1967).

140. D. N. Mitchell and D. J. Le Roy, *J. Chem. Phys.* **58**, 3449 (1973).

141. D. M. Garner, D. G. Fleming, and R. J. Mikula, *Chem. Phys. Lett.* **121**, 80 (1985).

142. I. D. Reid, D. M. Garner, L. Y. Lee, M. Senba, D. J. Arseneau, and D. G. Fleming, *J. Chem. Phys.* **86**, 5578 (1987).

143. R. B. Bernstein, *Chemical Dynamics via Molecular Beam and Laser Techniques*, (Oxford University Press, NY, 1982) Chap. 3.

144. S. Datz and E. H. Taylor, *J. Chem. Phys.* **39**, 1896 (1963).

145. J. Geddes, H. F. Krause, and W. L. Fite, *J. Chem. Phys.* **52**, 3297 (1970).

146. J. Geddes, H. F. Krause, and W. L. Fite, *J. Chem. Phys.* **56**, 3298 (1972).

147. R. Götting, H. R. Mayne, and J. P. Toennies, *J. Chem. Phys.* **80**, 2230 (1984).

148. R. Götting, J. P. Toennies, and M. Vodegal *Int. J. Chem. Kinet.* **18**, 949 (1986).

149. R. Götting, H. R. Mayne, and J. P. Toennies, *J. Chem. Phys.* **85**, 6396 (1986).

150. G. H. Kwei and V. W. S. Lo, *J. Chem. Phys.* **72**, 6265 (1980).

151. S. A. Buntin, C. F. Giese, and W. R. Gentry, submitted for publication

152. K. P. Huber and G. Herzberg, *Molecular Spectra and Molecular Structure. IV. Constants of Diatomic Molecules* (Van Nostrand Reinhold, NY, 1979).

153. R. J. Carter , W. H. Hamill, and R. R. Williams, *J. Am. Chem. Soc.* **77**, 6457 (1955).

154. R. M. Martin and J. E. Willard, *J. Chem. Phys.* **40**, 3007 (1964).

155. J. M. White, Ph.D. Thesis, University of Illinois, Urbana, 1966.

156. J. A. Betts, Ph.D. Thesis, California Institute of Technology, 1971.

157. A. Kuppermann and J. M. White, *J. Chem. Phys.* **44**, 4352 (1966).

158. K. Tsukiyama, B. Katz, and R. Bersohn, *J. Chem. Phys.* **84**, 1934 (1986).

159. U. Gerlach-Meyer, K. Kleinermanns, E. Linnebach, and J. Wolfrum, *J. Chem. Phys.* **86**, 3047 (1987).

160. J. R. Green and D. Margerison, *Statistical Treatment of Experimental Data*, (Elsevier Scientific, NY 1978).

161. Ref. 143, Chap. 9.

FIGURE CAPTIONS

Figure 1. Energy level and correlation diagram for formaldehyde dissociation processes.

FIGURE 1.

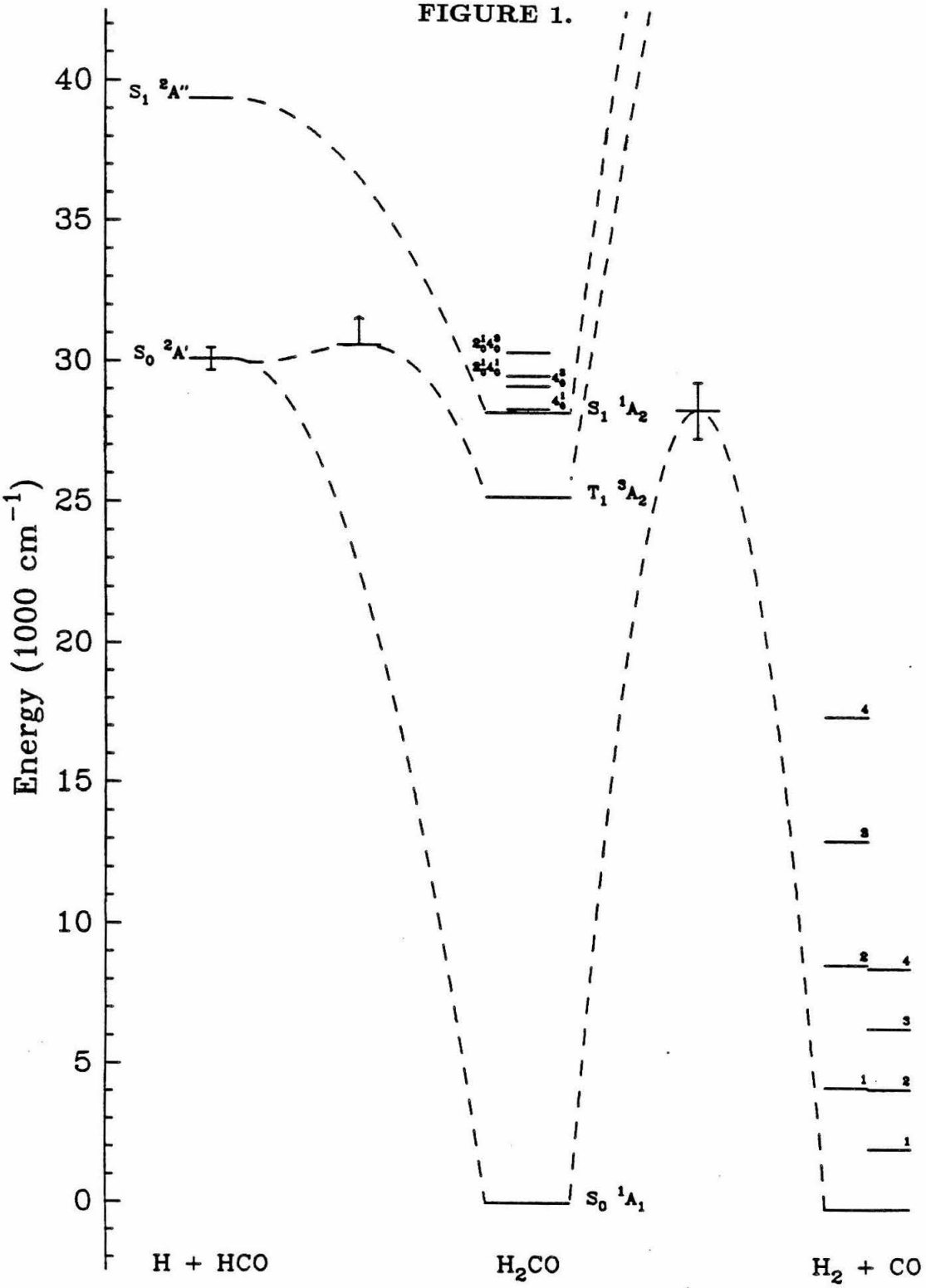
Energy (1000 cm^{-1})
40
35
30
25
20
15
10
5
0
$S_1\ ^2A''$
$S_0\ ^2A'$
$S_1\ ^1A_2$
$T_1\ ^3A_2$
$S_0\ ^1A_1$
H + HCO
H_2CO
H_2 + CO

CHAPTER 3.

THEORY OF FOUR-WAVE MIXING PROCESSES

I. INTRODUCTION

With the advent of high power lasers, multiwave mixing processes within nonlinear media have been extensively used to convert laser radiation from one wavelength to another. The lowest order process, three-wave mixing (TWM), involves the interaction of two photons to create a third photon with frequency given by $\omega_3 = \omega_1 \pm \omega_2$. The degenerate case in which $\omega_3 = 2\omega_1$, second harmonic generation (SHG), is the most common form of TWM. Second harmonic generation of laser radiation was first demonstrated by Franken *et al.*[1] in 1961 when a quartz crystal was used to convert ruby laser radiation at 694.3 nm to the second harmonic at 347.15 nm.

The next highest order, four-wave mixing (FWM), involves the interaction of three photons to create a fourth photon with frequency given by $\omega_4 = \omega_1 \pm \omega_2 \pm \omega_3$. The degenerate case in which $\omega_4 = 3\omega_1$, third harmonic generation (THG), is the most common form of FWM. Third harmonic generation of laser radiation was first observed by Maker *et al.*,[2,3] in 1963 using various crystals, glasses, and liquids as the nonlinear media. Later experiments by Ward and New[4,5] in 1967 demonstrated THG in a number of gases.

Higher order processes are also possible. Radiation at 38.0 nm was generated in He as the seventh harmonic of the 266.1 nm Nd:YAG fourth harmonic,[6] a process which is 28-th order overall. In addition, the ninth harmonic of a Nd:glass laser has been observed at 118 nm using Na vapor as the nonlinear medium.[7]

Along with the experimental advances in multiwave mixing processes there has been a great deal of theoretical work. Most of this work has been semiclassical: the radiation field is treated classically while quantum mechanics is used to describe the atomic systems. The first studies using high order perturbation theory on the interaction of electromagnetic radiation with matter were carried out in the late 1920's and early 1930's.[8,9] Interest was revived with the discovery of the laser.

The theory of TWM was developed by Armstrong *et al.*[10] and later extended by Kleinmann and coworkers.[11,12] This theory is now well developed and can be found in texts on quantum electronics.[13,14] The theory of FWM was also developed by Armstrong *et al.*[10] and has been extended by numerous groups.[4,15–18] Nayak has given a quantum mechanical treatment of THG:[19] both the atomic field and the radiation field were described quantum mechanically.

In this chapter the semiclassical description of four-wave mixing is developed. First, properties of Gaussian laser beams are reviewed. Second, the theory of nonlinear optical processes is reviewed. Third an expression describing the radiation field generated by a FWM process is derived. Fourth, properties of the third order nonlinear susceptibility are reviewed. And fifth, properties of the phase matching factor Φ are reviewed.

II. GAUSSIAN LASER BEAMS

The electromagnetic field described by the electric field vector $\mathcal{E}$ and the magnetic field vector $\mathcal{H}$ satisfies Maxwell's equations, which in the absence of currents and free charges are[20]

$$\nabla \times \mathcal{H} = \frac{1}{c}\frac{\partial \mathcal{D}}{\partial t}, \tag{3.1}$$

$$\nabla \times \mathcal{E} = -\frac{1}{c}\frac{\partial \mathcal{B}}{\partial t}, \tag{3.2}$$

$$\nabla \cdot \mathcal{B} = 0, \tag{3.3}$$

$$\nabla \cdot \mathcal{D} = 0, \tag{3.4}$$

where $\mathcal{D}$ and $\mathcal{B}$ are the electric displacement and magnetic induction vectors, respectively. These are given by

$$\mathcal{D} = \mathcal{E} + 4\pi\mathcal{P}, \tag{3.5}$$

$$\mathcal{H} = \mathcal{B} - 4\pi\mathcal{M}, \tag{3.6}$$

where $\mathcal{P}$ and $\mathcal{M}$ are the electric and magnetic polarizations vectors, respectively.

In diamagnetic and paramagnetic materials, the magnitude of the magnetic polarization vector is approximately three orders of magnitude smaller than that of the electric polarization vector.[20] Therefore, $\mathcal{M}$ will be ignored for the rest of this chapter.

If one subsitutes Eq. 3.5 and 3.6 into Eq. 3.1 and 3.2, takes the curl of both sides of Eq. 3.2, substitutes Eq. 3.1 into Eq. 3.2, and uses the vector identity $\nabla \times \nabla \times \mathcal{A} = \nabla(\nabla \cdot \mathcal{A}) - \nabla^2\mathcal{A}$,[21] the following wave equation is obtained

$$\left[\nabla^2 - \frac{1}{c^2}\frac{\partial^2}{\partial t^2}\right]\mathcal{E} = \frac{4\pi}{c^2}\frac{\partial^2 \mathcal{P}}{\partial t^2}. \tag{3.7}$$

In a linear medium, the polarization depends only on the electric field

$$\mathcal{P} = \chi^{(1)}\mathcal{E}. \tag{3.8}$$

Substituting into Eq. 3.7 leads to

$$\left[\nabla^2 - \frac{1+4\pi\chi^{(1)}}{c^2}\frac{\partial^2}{\partial t^2}\right]\mathcal{E} = 0. \tag{3.9}$$

Assuming that $\mathcal{E}$ is separable into time and spatial coordinates

$$\mathcal{E} = \sum_j \Theta_j(t)\Psi_j(x,y,z), \tag{3.10}$$

substituting in Eq. 3.9, and requiring that each term of the sum separately be equal to 0 leads to the wave equation

$$\frac{\nabla^2\Psi_j}{\Psi_j} - \frac{1+4\pi\chi^{(1)}}{c^2\Theta_j}\frac{\partial^2\Theta_j}{\partial t^2} = 0. \tag{3.11}$$

The left-hand term depends only on spatial coordinates while the right-hand term depends only on time. Thus, Eq. 3.11 can be satisfied if and only if each term is equal to a constant, $-k_j^2 = -(1+4\pi\chi^{(1)})\omega_j^2/c^2 = -n_j^2\omega_j^2/c^2$ where n_j is the index of refraction. With this choice of the separation constants, k_j will be the wave-vector of the beam and ω_j will be the optical frequency of the radiation. Eq. 3.11 can then be separated to yield the two wave equations

$$\left[\frac{d^2}{dt^2} + \omega_j^2\right]\Theta_j(t) = 0, \tag{3.12}$$

$$\left[\nabla^2 + k_j^2\right]\Psi_j(x,y,z) = 0. \tag{3.13}$$

Eq. 3.12 can be solved by inspection to yield

$$\Theta_j(t) = e^{\pm i\omega_j t}. \tag{3.14}$$

The solution of Eq 3.13 is non-trivial. The derivation of the appropriate Ψ_j will not be given here but can be found in Ref. 22. Instead, just the important results will be summarized.

It is assumed that the laser beam propagates along the z-axis with a focal position at $z = f$. At the focus the beam has its smallest radius, denoted by ω_0

(note: this is a different ω than the one found in Eqs. 3.12 and 3.14). It is assumed that the imaginary part of $\chi^{(1)}$ is equal to 0 so that there is no gain or loss within the medium. Thus, k_j is real. The confocal parameter is defined by

$$b = k\omega_0^2 \tag{3.15}$$

It is convienent to measure distances along the z-axis by the dimensionless coordinate

$$\xi = 2(z - f)/b. \tag{3.16}$$

The simplest solution is obtained when the transverse dependence is only a function of $r = \sqrt{x^2 + y^2}$. In this case the electric field amplitude is given by[13,22]

$$\Psi(r, z) = \frac{\mathrm{E}_0}{1 + i\xi} \exp\left[ikz - \frac{kr^2}{b(1 + i\xi)}\right] \tag{3.17}$$

or equivalently

$$\Psi(r, z) = \mathrm{E}_0 \frac{\omega_0}{\omega(\xi)} \exp\left[-\frac{r^2}{\omega^2(\xi)} - i\left(\frac{r^2\xi}{\omega^2(\xi)} - kz + \tan^{-1}(\xi)\right)\right] \tag{3.18}$$

where $\omega(\xi) = \omega_0\sqrt{1 + \xi^2}$.

The first term within the exponential gives the Gaussian variation in field amplitude with distance r from the z-axis. At a distance of $\omega(\xi)$ from the beam axis the field amplitude is $1/e$ times that on axis. The second term within the exponential contains the radius of curvature, R, of the nearly spherical wave fronts on the z-axis. R is defined by

$$R = \frac{k\omega^2(\xi)}{2\xi}. \tag{3.19}$$

The third term within the exponential gives the phase shift along the axis for a plane wave while the fourth term gives the additional phase shift resulting from the focus. The total phase shift along the axis is therefore

$$\psi = kz - \tan^{-1}(\xi). \tag{3.20}$$

The pre-exponential factor gives the electric field amplitude at the beam center as a function of position along the z-axis.

The behaviour of $\omega(\xi)$ shows that the beam expands hyperbolically from its minimum size at the focus. The confocal parameter is important since it gives the length of the focal region. At a distance of $b/2$ from the focus the beam size has increased by a factor of $\sqrt{2}$ and the beam area has doubled. The far field diffraction half angle is given by

$$\delta = \frac{2\omega_0}{b} = \frac{\lambda}{n\pi\omega_0} = \frac{2}{\sqrt{bk}} \tag{3.21}$$

If the solution to Eq. 3.13 is expressed in cylindrical coordinates, r, ϕ, and z, the electric field amplitude is given by[18,22]

$$\Psi(r,\phi,z) = \mathrm{E}_0 \frac{\omega_0}{\omega(\xi)} \eta^{l/2} \mathrm{L}_p^l(\eta) \times \exp\left[-\frac{r^2}{\omega^2(\xi)} - i\left(\frac{r^2\xi}{\omega^2(\xi)} + l\phi - kz + (2p+l+1)\tan^{-1}(\xi)\right)\right] \tag{3.22}$$

where the variable η is defined by $\eta = 2r^2/\omega^2(\xi)$, $\mathrm{L}_p^l(x)$ is the generalized Laguerre polynomial of order p and l, and the other symbols are the same as before. The overall shape of the beam is the same as before since the beam waist, $\omega(\xi)$, wavefront radii of curvature, R, and diffraction half-angle, δ, are the same. However, the beam is now described by the additional quantum numbers p and l. The terms associated with these quantum numbers have the effect of spreading the beam out and introducing p radial and l angular nodes in the field amplitude. In addition, the phase shift along the axis is now given by

$$\psi = kz - (2p+l+1)\tan^{-1}(\xi). \tag{3.23}$$

The solutions represented by Eq. 3.22 are known as the "modes of propagation." They form a complete and orthogonal set of functions in the transverse coordinates r and ϕ; therefore, every distribution of monochromatic

light propagating along the z-axis can be expanded in terms of these modes. The simplest Gaussian laser beam described by Eq. 3.17 or 3.18 is the mode with $l = p = 0$.

If the solution to Eq. 3.13 is instead expressed in cartestian coordinates, the electric field amplitude is given by[13,22]

$$\Psi(x,y,z) = \mathrm{E}_0 \frac{\omega_0}{\omega(\xi)} \mathrm{H}_l\left(\sqrt{2}\frac{x}{\omega(\xi)}\right) \mathrm{H}_m\left(\sqrt{2}\frac{y}{\omega(\xi)}\right) \times \exp\left[-\frac{x^2+y^2}{\omega^2(\xi)} - i\left(\frac{(x^2+y^2)\xi}{\omega^2(\xi)} - kz + (l+m+1)\tan^{-1}(\xi)\right)\right] \tag{3.24}$$

where $\mathrm{H}_l(x)$ is the Hermite polynomial of order l and the other symbols are defined as before. The overall shape of the beam is the same as before; however, additional quantum numbers l and m are needed to describe it. Terms associated with these quantum numbers have the effect of spreading the beam out and introducing l nodes in the x-direction and m nodes in the y-direction. In addition, the total phase shift along the axis is now given by

$$\psi = kz - (l+m+1)\tan^{-1}(\xi). \tag{3.25}$$

The solutions represented by Eq. 3.24 are also called the "modes of propagation" and are symbolized by TEM_{lm}. They form a complete and orthogonal set of functions in the transverse coordinates x and y; therefore, every arbitrary distribution of monochromatic light propagating along the z-axis can be expanded in terms of these modes. The simplest Gaussian laser beam, described by Eq. 3.17 or 3.18, is the TEM_{00} mode.

III. NONLINEAR OPTICAL PROCESSES

In understanding nonlinear optical processes, one starts with Eq. 3.7 which relates the electric field vector to the polarization vector. If the polarization is a nonlinear function of the applied electric field, the polarization vector will have components at frequencies differing from the incident frequencies. These new frequencies in the polarization vector create electric fields at the additional frequencies. In this section, general principles of nonlinear optical processes are reviewed. For a more complete review than provided here, see the recent books by Reintjes[23] and Shen.[24]

Several approximations will be made in order to simplify the derivations in this section. First, it is assumed that variations in the field amplitudes are small in one optical period, allowing the slowly varying envelope approximation to be made. Second, it is assumed that the wavelengths of light involved in the nonlinear process are large compared to the size of atoms, allowing a multipole expansion–dipole approximation to be made. Third, it is assumed that changes in the laser pulse intensity occur on a timescale long compared to the response time of the medium, allowing for the time-independent polarization approximation. Fourth, it is assumed that the optical fields are sufficiently weak that the polarization can be represented as a sum of linear and nonlinear terms, the latter given by an expansion in powers of the optical field.

These assumptions are valid for most experiments. The period of oscillation of visible light is approximately 10^{-15} sec, while most common laboratory lasers have a picosecond to nanosecond pulsewidth. The wavelength of the shortest radiation generated by a nonlinear process is 38.0 nm,[6] while most atoms have radii less than 2 Å. The last two assumptions are usually valid unless a resonant or near resonant process or high power laser is used.[23]

The slowly varying envelope approximation is used to represent the electric field as a product of a slowly varying component and a component oscillating at the optical frequency. For a wave propagating along the z-axis, The electric field is represented by

$$\mathcal{E}(\mathbf{r},t) = \frac{1}{2}\left[\mathbf{E}(\mathbf{r},t)e^{-i(\omega t - kz)} + c.c.\right]. \tag{3.26}$$

where $\mathbf{E}$ is the peak amplitude of the electric field, k is the wave-vector, and ω is the optical frequency.

It is anticipated that as a result of the nonlinear process, the radiation field will contain components at more than one frequency. If these frequencies are not too close together, the electric field can be represented as a sum of terms of the form of Eq. 3.26, specifically

$$\mathcal{E}(\mathbf{r},t) = \frac{1}{2}\sum_i \left[\mathbf{E}_i(\mathbf{r},t)e^{-i(\omega_i t - k_i z)} + c.c.\right]. \tag{3.27}$$

A similar expression can be written down for the induced polarization

$$\mathcal{P}(\mathbf{r},t) = \frac{1}{2}\sum_j \left[\mathbf{P}_j(\mathbf{r},t)e^{-i(\omega_j t - k_j^P z)} + c.c.\right]. \tag{3.28}$$

The wave vector of the polarization is labeled by k_j^P to specifically designate that this wave vector can differ from the wave vector of an optical field at the same frequency.

If the incident fields are sufficiently weak, the polarization of the nonlinear medium can be separated into a linear and nonlinear term, with the former given by Eq. 3.8, resulting in

$$\mathcal{P} = \chi^{(1)}\mathcal{E} + \mathcal{P}^{NL}. \tag{3.29}$$

If Eq. 3.27, 3.28, and 3.29 are substituted into Eq. 3.7, the following set of coupled differential equations for the electric field amplitudes in terms of the nonlinear polarizations are obtained

$$\begin{aligned}
&\left[\nabla_\perp + 2ik_1\frac{\partial}{\partial z} + \frac{2in_1^2\omega_1}{c^2}\frac{\partial}{\partial t}\right]\mathbf{E}_1 = -\frac{4\pi\omega_1^2}{c^2}\mathbf{P}_1^{NL}e^{-i\Delta k_1 z},\\
&\qquad\vdots\\
&\left[\nabla_\perp + 2ik_j\frac{\partial}{\partial z} + \frac{2in_j^2\omega_j}{c^2}\frac{\partial}{\partial t}\right]\mathbf{E}_j = -\frac{4\pi\omega_j^2}{c^2}\mathbf{P}_j^{NL}e^{-i\Delta k_j z},\\
&\qquad\vdots
\end{aligned} \tag{3.30}$$

where $\nabla_\perp$ is for the transverse coordinates and $\Delta k_j = k_j - k_j^P$ is the wave vector mismatch for the j'th wave. As a result of the slowly varying envelope approximation, the following approximations were used

$$\frac{\partial^2\mathbf{E}_j}{\partial z^2} \ll k_j\frac{\partial\mathbf{E}_j}{\partial z}, \qquad \frac{\partial^2\mathbf{E}_j}{\partial t^2} \ll \omega_j\frac{\partial\mathbf{E}_j}{\partial t}. \tag{3.31}$$

In most situations, it is assumed that the group velocities of the various waves are equal. In that case, transformation to a coordinate system which propagates at the common group velocity eliminates the explicit time derivative in Eq. 3.30. The resulting equations are the same as those that describe interactions with steady-state fields,

$$\begin{aligned}
&\left[\nabla_\perp + 2ik_1\frac{\partial}{\partial z}\right]\mathbf{E}_1 = -\frac{4\pi\omega_1^2}{c^2}\mathbf{P}_1^{NL}e^{-i\Delta k_1 z},\\
&\qquad\vdots\\
&\left[\nabla_\perp + 2ik_j\frac{\partial}{\partial z}\right]\mathbf{E}_j = -\frac{4\pi\omega_j^2}{c^2}\mathbf{P}_j^{NL}e^{-i\Delta k_j z},\\
&\qquad\vdots
\end{aligned} \tag{3.32}$$

The index j covers all frequencies, including those in the incident radiation fields and those generated in the medium as a result of the nonlinear interaction. Eq. 3.32 is an infinite set of equations representing all of the possible fields

resulting from arbitrary combinations of all of the radiation fields. Fortunately, the physical situation will often provide constraints such that only a few equations are important. One such situation is when the incident fields are sufficiently weak that their amplitudes are not significantly changed during the interaction. As a result the equations for the incident field amplitudes may be dropped. Another situation occurrs when one nonlinear process dominates the overall interaction. As a result, only those equations involving the dominant process are needed. A third situation occurs when the generated radiation is so weak that it has no effect on the nonlinear polarization. In this case, only terms in the nonlinear polarization arising from the incident fields need to be kept, greatly reducing the number of equations.

In order to evaluate Eq. 3.32, the nature of the nonlinear polarization needs to be determined. The complete derivation of the nonlinear polarization will not be given here, but can be found in Reintjes[23] and Shen.[24] For most situations not involving saturation, dielectric breakdown, or resonant interactions, the nonlinear dipole polarization is given by a power series in the total incident field,

$$\mathcal{P}^{NL} = \sum_{j=2}^{\infty} \chi^{(j)} \mathcal{E}_t^j. \tag{3.33}$$

There are also nonlinear polarization terms which arise from the electric quadrupole and other higher order multi-poles. These terms are usually much weaker and will be ignored.

A Fourier analysis of Eq. 3.33 shows that $\mathcal{P}^{NL}$ has components with frequencies not present in the incident fields. For the process $\omega_q = \omega_1 + \omega_2 + \omega_3 + \cdots + \omega_n$, the amplitude of the nonlinear polarization at frequency ω_q in terms of the various field amplitudes is given by

$$\mathbf{P}^{NL}(\omega_q) = \frac{g}{2^{n-1}} \chi^{(n)}(-\omega_q, \omega_1, \omega_2, \omega_3, \cdots, \omega_n) \mathbf{E}_1 \mathbf{E}_2 \mathbf{E}_3 \cdots \mathbf{E}_n \tag{3.34}$$

where g corresponds to the number of distinct permutations of the incident fields and the factor of $1/2^{n-1}$ comes from the definitions in Eq. 3.27 and 3.28. If a frequency-difference process is used and ω_j is subtracted instead of added, the complex conjugate of the electric field $\mathbf{E}_j^*$ is used instead of $\mathbf{E}_j$.

Even though Eq. 3.34 has been written as a scalar, the electric fields are vectors and the n-th order susceptibility is an $(n+1)$-rank tensor with in general 3^{n+1} components. The tensor nature of the third order susceptibility will be discussed further in Sec. V.

There are two kinds of susceptibilities being considered: one being the microscopic χ_{micro} of an individual atom, and the second being the macroscopic χ_{macro} of the bulk medium. In a dilute material where local field corrections can be ignored, such as in a gas, $\chi_{\text{macro}} = N \times \chi_{\text{micro}}$ where N is the number density of the medium.[23,24] The correct χ being used in any given formula can always be inferred by context: if N appears than χ_{micro} is being used, otherwise, χ_{macro} is used.

Specific optical processes can often be associated with specific terms in the nonlinear susceptibilities. For example, the following are the four terms associated with three wave mixing:

second harmonic generation

$$\mathbf{P}_i(\omega_3 = 2\omega_1) = \frac{1}{2}\chi^{(2)}_{ijk}(-\omega_3, \omega_1, \omega_1)\mathbf{E}^{\omega_1}_j \mathbf{E}^{\omega_1}_k, \tag{3.35a}$$

sum- and difference-frequency mixing

$$\mathbf{P}_i(\omega_3 = \omega_1 + \omega_2) = \chi^{(2)}_{ijk}(-\omega_3, \omega_1, \omega_2)\mathbf{E}^{\omega_1}_j \mathbf{E}^{\omega_2}_k, \tag{3.35b}$$

$$\mathbf{P}_i(\omega_3 = \omega_1 - \omega_2) = \chi^{(2)}_{ijk}(-\omega_3, \omega_1, -\omega_2)\mathbf{E}^{\omega_1}_j (\mathbf{E}^{\omega_2}_k)^*, \tag{3.35c}$$

optical rectification

$$\mathbf{P}_i(\omega_3 = 0) = \chi^{(2)}_{ijk}(0, \omega_1, -\omega_1)\mathbf{E}^{\omega_1}_j (\mathbf{E}^{\omega_1}_k)^*. \tag{3.35d}$$

Similar identification can be made for four-wave mixing interactions: third-harmonic generation

$$\mathbf{P}_i(\omega_4 = 3\omega_1) = \frac{1}{4}\chi^{(3)}_{ijkl}(-\omega_3, \omega_1, \omega_1, \omega_1)\mathbf{E}^{\omega_1}_j \mathbf{E}^{\omega_1}_k \mathbf{E}^{\omega_1}_l, \tag{3.36a}$$

sum- and difference-frequency mixing

$$\mathbf{P}_i(\omega_4 = 2\omega_1 + \omega_2) = \frac{3}{4}\chi^{(3)}_{ijkl}(-\omega_3, \omega_1, \omega_1, \omega_2)\mathbf{E}^{\omega_1}_j \mathbf{E}^{\omega_1}_k \mathbf{E}^{\omega_2}_l, \tag{3.36b}$$

$$\mathbf{P}_i(\omega_4 = 2\omega_1 - \omega_2) = \frac{3}{4}\chi^{(3)}_{ijkl}(-\omega_3, \omega_1, \omega_1, -\omega_2)\mathbf{E}^{\omega_1}_j \mathbf{E}^{\omega_1}_k (\mathbf{E}^{\omega_2}_l)^*, \tag{3.36c}$$

$$\mathbf{P}_i(\omega_4 = \omega_1 + \omega_2 + \omega_3) = \frac{6}{4}\chi^{(3)}_{ijkl}(-\omega_3, \omega_1, \omega_2, \omega_3)\mathbf{E}^{\omega_1}_j \mathbf{E}^{\omega_2}_k \mathbf{E}^{\omega_3}_l, \tag{3.36d}$$

$$\mathbf{P}_i(\omega_4 = \omega_1 + \omega_2 - \omega_3) = \frac{6}{4}\chi^{(3)}_{ijkl}(-\omega_3, \omega_1, \omega_2, -\omega_3)\mathbf{E}^{\omega_1}_j \mathbf{E}^{\omega_2}_k (\mathbf{E}^{\omega_3}_l)^*, \tag{3.36e}$$

$$\mathbf{P}_i(\omega_4 = \omega_1 - \omega_2 - \omega_3) = \frac{6}{4}\chi^{(3)}_{ijkl}(-\omega_3, \omega_1, -\omega_2, -\omega_3)\mathbf{E}^{\omega_1}_j (\mathbf{E}^{\omega_2}_k)^* (\mathbf{E}^{\omega_3}_l)^*. \tag{3.36f}$$

There are many other terms which are responsible for self-focusing or defocusing, two-photon absorption, degenerate four-wave mixing, and several kinds of Raman effects.

Using the coupled differential equations 3.30 and the nonlinear polarization given by Eq. 3.34, it is possible to describe almost any nonlinear optical process. In the next section, the four-wave mixing of Gaussian beams is examined in some detail.

IV. FOUR-WAVE MIXING OF GAUSSIAN BEAMS

The first theoretical analysis of FWM was by Armstrong *et al.*[10] Ward and New[4] extended their work to cover the simple case of THG with an incident TEM_{00} laser beam. Bjorklund[15] studied arbitrary FWM processes assuming that each of the incident TEM_{00} laser beams had identical confocal parameters and focal spot positions. Tomov and Richardson[16] also studied arbitrary FWM of TEM_{00} laser beams, but they did not assume identical confocal parameters and focal spot positions. Unfortunately, some of their published equations are in error. Yiu *et al.*,[18] studied THG with incident laser beams having a cylindrical spatial-mode structure, as defined by Eq. 3.22. Unlike all of the other studies which assumed low incident power and low conversion efficiencies, Puell and Vidal[17] studied THG of TEM_{00} laser beams under high power conditions including effects due to pump beam depletion and intensity dependent refractive indices.

In this section, expressions describing the generated electric field, the final power levels, and the total energy converted are derived for an arbitrary FWM process. It is assumed that each of the three incident beams is in a TEM_{00} mode propagating along the z-axis with arbitrary confocal parameters and focal spot positions.

Instead of using the approach of Tomov and Richardson[16] and attempting to solve the coupled differential Eqs. 3.32 using Green's functions, a second approach is taken similar to that used by Bjorklund[15] which uses a Fourier decomposition. In summary, the spatial variation of the driving polarization is specified, the plane wave components of the driving polarization are obtained by a Fourier decomposition, the generated radiation field arising from each component is determined, and the total generated radiation field is determined by summing the contributions of each component. In the absence of pump depletion, the two techniques give identical results.[12]

For the process $\omega_4 = \omega_1 + \omega_2 + \omega_3$, the incident electric field is given by

$$\mathcal{E}(\mathbf{r},t) = \frac{1}{2}\left[\mathbf{E}_1(\mathbf{r})e^{-i\omega_1 t} + \mathbf{E}_2(\mathbf{r})e^{-i\omega_2 t} + \mathbf{E}_3(\mathbf{r})e^{-i\omega_3 t} + c.c.\right], \tag{3.37}$$

with

$$\mathbf{E}_j(x,y,z) = \frac{\mathbf{E}_{0j}}{1+i\xi_j}\exp\left[ik_j z - \frac{k_j(x^2+y^2)}{b_j(1+i\xi_j)}\right]. \tag{3.38}$$

$\mathbf{E}_{0j}$ is the electric field amplitude of the j-th beam, k_j is the wave vector of the j-th beam, b_j is the confocal parameter of the j-th beam, and ξ_j is the the scaled z-coordinate for the j-th beam as defined by Eq. 3.16.

The driving polarization at ω_4 is given by

$$\mathcal{P}_4(\mathbf{r},t) = \frac{1}{2}\left[\mathbf{P}_4(\mathbf{r})e^{-i\omega_4 t} + c.c\right] \tag{3.39}$$

where

$$\left(\mathbf{P}_4(\mathbf{r})\right)_i = \sigma N \chi^{(3)}_{ijkl}(-\omega_4,\omega_1,\omega_2,\omega_3)\left(\mathbf{E}_1(\mathbf{r})\right)_j\left(\mathbf{E}_2(\mathbf{r})\right)_k\left(\mathbf{E}_3(\mathbf{r})\right)_l. \tag{3.40}$$

where σ is the degeneracy factor ($1/4, 3/4, 6/4$ for three, two, or no degenerate incident frequencies), $\chi^{(3)}_{ijkl}$ is the atomic third-order nonlinear susceptibility tensor, and N is number density of the nonlinear medium.

It is assumed that the fundamental and generated beams are linearly polarized in the same direction, allowing the vector nature of the electric fields and the tensor nature of the third order nonlinear susceptibility to be ignored.

The nonlinear medium is considered to occupy the region from $z = 0$ to $z = L$. Combining Eqs 3.38 and 3.40, the driving polarization is given by

$$\mathbf{P}_4(\mathbf{r}) = \frac{\sigma N \chi^{(3)}\mathbf{E}_{01}\mathbf{E}_{02}\mathbf{E}_{03}e^{ik'z}}{(1+i\xi_1)(1+i\xi_2)(1+i\xi_3)} \times \exp\left[\left(\frac{k_1}{b_1(1+i\xi_1)} + \frac{k_2}{b_2(1+i\xi_2)} + \frac{k_3}{b_3(1+i\xi_3)}\right)(x^2+y^2)\right]\mathrm{B}(z). \tag{3.41}$$

where the wavevector of the driving polarization is

$$k' = k_1 + k_2 + k_3, \tag{3.42}$$

and the occupancy of the medium is

$$\mathrm{B}(z) = \begin{cases} 0, & z < 0; \\ 1, & 0 \leq z \leq L; \\ 0, & L < z. \end{cases} \tag{3.43}$$

Next, a Fourier decomposition of $\mathbf{P}_4(\mathbf{r})$ is performed to determine the plane-wave components of the driving polarization. $\mathbf{P}_{4(\mathbf{K})}$, the amplitude of the plane-wave component with wave vector $\mathbf{K}$, is defined by

$$\mathbf{P}_{4(\mathbf{K})} = (2\pi)^{-3} \int_{-\infty}^{\infty} \int_{-\infty}^{\infty} \int_{-\infty}^{\infty} \mathbf{P}_4(\mathbf{r}'') \exp(-i\mathbf{K} \cdot \mathbf{r}'')\, dx''\, dy''\, dz''. \tag{3.44}$$

Next, $\mathbf{E}_{4(\mathbf{K})}(\mathbf{r})$, the generated radiation field arising from $\mathbf{P}_{4(\mathbf{K})}$ is determined. Using Maxwell's equations and the appropriate boundary conditions, Kleinmann[11] has shown that if $K_x, K_y \ll K_z$ and $|\mathbf{K}| - k_4 \ll |\mathbf{K}|, k_4$, then

$$\mathbf{E}_{4(\mathbf{K})}(\mathbf{r}) = \frac{i\ 2\pi k_0^2}{k_4} g(U_{\mathbf{K}}) \exp(i\mathbf{K} \cdot \mathbf{r}) \mathbf{P}_{4(\mathbf{K})} \tag{3.45}$$

where k_4 and k_0 are the wave vectors of the generated radiation in the nonlinear medium and in vacuum, respectively, while

$$g(x) = \int_0^1 \exp(-xp)\, dp \tag{3.46}$$

and

$$U_{\mathbf{K}} = iz \left(K_z - k_4 + \frac{K_x^2 + K_y^2}{2k_4} \right). \tag{3.47}$$

The wave vector mismatch is defined by

$$\Delta k = k_4 - k'. \tag{3.48}$$

Letting $p = -(\xi_1' - \xi_1)/2z$ and substituting into equations Eqs. 3.46 and 3.47 yields (assuming $\Delta k \ll k_4, k'$)

$$g(U_{\mathbf{K}}) = \frac{b_1}{2z} \int_{\xi_1 - 2z/b_1}^{\xi_1} \exp\left[\frac{ib_1}{2}(\xi_1' - \xi_1)\left(K_z - k' + \frac{K_x^2 + K_y^2}{2k'} - \Delta k\right)\right] d\xi_1'. \tag{3.49}$$

Finally, the total generated field $\mathbf{E}_4(\mathbf{r})$ is found by combining the $\mathbf{E}_{4(\mathbf{K})}(\mathbf{r})$,

$$\mathbf{E}_4(\mathbf{r}) = \int_{-\infty}^{\infty}\int_{-\infty}^{\infty}\int_{-\infty}^{\infty} \mathbf{E}_{4(\mathbf{K})}(\mathbf{r})\, dK_x\, dK_y\, dK_z. \tag{3.50}$$

Substituting in the appropriate equations, one gets

$$\begin{aligned}\mathbf{E}_4(\mathbf{r}) = \int_{-\infty}^{\infty}\int_{-\infty}^{\infty}\int_{-\infty}^{\infty}\int_{-\infty}^{\infty}\int_{-\infty}^{\infty}\int_{\xi_1 - 2z/b_1}^{\xi_1} & \exp(ik'z'')\frac{i\sigma N\chi^{(3)}k_0^2 b_1 \mathbf{E}_{01}\mathbf{E}_{02}\mathbf{E}_{03}}{k_4 8\pi^2} \\ & \times (1 + i\xi_1'')^{-1}(1 + i\xi_2'')^{-1}(1 + i\xi_3'')^{-1} \\ & \times \exp\left[\frac{ib_1}{2}(\xi_1' - \xi_1)\left(K_z - k' + (K_x^2 + K_y^2)/2k' - \Delta k\right)\right] \\ & \times \exp\left[-\left(\frac{k_1}{b_1(1 + i\xi_1'')} + \frac{k_2}{b_2(1 + i\xi_2'')} + \frac{k_3}{b_3(1 + i\xi_3'')}\right)(x''^2 + y''^2)\right] \\ & \times \exp\left[i\mathbf{K}\cdot(\mathbf{r} - \mathbf{r}'')\right] B(z'') \\ & d\xi_1'\, dx''\, dy''\, dz''\, dK_x\, dK_y\, dK_z,\end{aligned} \tag{3.51}$$

where the notation ξ_i' or ξ_i'' signifies that in the definition of ξ given by Eq. 3.16 either z' or z'' is to be used, respectively.

First, the integral over dK_z is performed, yielding a factor of $2\pi\delta(z' - z'')$. Next the integral over dz'' is evaluated. Then, the integrals over dx'', dy'', dK_x, and dK_y are evaluated in any order using the definite integral[21]

$$\int_{-\infty}^{\infty} \exp(-iqx - isx^2)\, dx = \left(\frac{\pi}{is}\right)^{1/2} \exp\left(\frac{iq^2}{4s}\right), \qquad \mathrm{Im}(s) < 0, \tag{3.52}$$

to give

$$\mathbf{E}_4(\mathbf{r}) = \frac{i\sigma N\chi^{(3)}b_1\pi}{k_4} \times \mathbf{E}_{01}\mathbf{E}_{02}\mathbf{E}_{03} \times \exp(ik'z) \times \int_{\xi_1-2z/b_1}^{\xi_1} \frac{\exp\left[-\frac{x^2+y^2}{\beta(z')} - \frac{ib_1\Delta k}{2}(\xi_1' - \xi_1)\right] d\xi_1'}{\alpha(z')\beta(z')(1+i\xi_1)(1+i\xi_2)(1+i\xi_3)} \tag{3.53}$$

with

$$\alpha(z') = \frac{k_1}{b_1(1+i\xi_1')} + \frac{k_2}{b_2(1+i\xi_2')} + \frac{k_3}{b_3(1+i\xi_3')} \tag{3.54}$$

and

$$\beta(z') = \frac{k'}{\alpha(z')} - \frac{ib_1(\xi_1' - \xi_1)}{k'} \tag{3.55}$$

Eq. 3.53 gives the electric field amplitude at every point within the nonlinear medium. The generated power is related to the electric field amplitude by

$$P_4(z) = \frac{cn_4}{8\pi}\int_{-\infty}^{\infty}\int_{-\infty}^{\infty} \mathbf{E}_4(\mathbf{r})\mathbf{E}_4^*(\mathbf{r})\,dx\,dy. \tag{3.56}$$

The total power at ω_4 at the output of the nonlinear medium is given by

$$P_4(z=L) = \frac{4096\pi^6\sigma^2\left|N\chi^{(3)}\right|^2 P_{01}P_{02}P_{03}k_0}{\lambda_1\lambda_2\lambda_3\lambda_4 n_4 c^2 k'} \times \Phi \tag{3.57}$$

where P_{0i} is the incident power of the i-th beam and the dimensionless phase matching factor, Φ, is given by

$$\Phi = 2k'^2 q_1 q_2 q_3 \int_{-2f_1/L}^{2(1-f_1/L)}\int_{-2f_1/L}^{2(1-f_1/L)} \frac{\exp[-iL\,\Delta k(\zeta-\zeta')/2]}{\left(m_1(\zeta)+m_1^*(\zeta')\right)m_2(\zeta)m_2^*(\zeta')}\,d\zeta\,d\zeta' \tag{3.58}$$

with

$$m_1(\zeta) = \frac{k'}{\frac{k_1q_1}{1+iq_1\zeta} + \frac{k_2q_2}{1+iq_2\zeta} + \frac{k_3q_3}{1+iq_3\zeta}} - i\zeta \tag{3.59}$$

and

$$\begin{aligned} m_2(\zeta) =& k_1q_1\left(1+iq_2(\zeta+\delta_2)\right)\left(1+iq_3(\zeta+\delta_3)\right) \\ &+ k_2q_2\left(1+iq_1\zeta\right)\left(1+iq_3(\zeta+\delta_3)\right) \\ &+ k_3q_3\left(1+iq_1\zeta\right)\left(1+iq_2(\zeta+\delta_2)\right). \end{aligned} \tag{3.60}$$

The parameters $q_i = L/b_i$ and $\delta_i = 2(f_1 - f_i)/L$ give the relative tightness of focusing and difference in focal positions of the i-th beams.

If the temporal distribution of the laser pulses is known, then it is possible to use Eq. 3.57 to estimate the total energy generated at ω_4. It is assumed that each incident pulse has a Gaussian temporal profile centered at time $t = 0$ given by

$$P_i = \frac{E_i\, 2\sqrt{\ln 2}}{\tau_i\sqrt{\pi}} \exp\left[-4\ln 2(t/\tau_i)^2\right] \tag{3.61}$$

where E_i is the total pulse energy and τ_i is the full-width at half-maximum pulse width of the i-th laser beam.

The total energy at ω_4, E_4, is then given by

$$E_4 = \frac{16384\pi^5\, \ln 2\, \sigma^2 \left|N\chi^{(3)}\right|^2 k_0}{\lambda_1\lambda_2\lambda_3\lambda_4 n_4 c^2 k'} \times \frac{E_1E_2E_3\tau_4}{\tau_1\tau_2\tau_3} \times \Phi, \tag{3.62}$$

where the resulting laser beam a ω_4 has a Gaussian temporal profile cenered at $t = 0$ with a pulse width $\tau_4 = (\tau_1^{-2} + \tau_2^{-2} + \tau_3^{-2})^{-1/2}$.

It is helpful to express Eq 3.62 in the common units for work in this field. If N is expressed as a pressure of p torr at temperature of T, $\chi^{(3)}$ is given in ESU/atom ($\mathrm{cm^6 erg^{-1} atom^{-1}}$), E in mJ, τ in nsec, and λ in nm, one gets

$$E_4 = 3.61 \times 10^{77} \times \frac{\sigma^2 \left|p\chi^{(3)}\right|^2}{T^2\lambda_1\lambda_2\lambda_3\lambda_4} \times \frac{E_1E_2E_3\tau_4}{\tau_1\tau_2\tau_3} \times \Phi. \tag{3.63}$$

It is seen that the expressions derived for the output power/energy (Eqs. 3.57 and 3.62) of a four wave mixing process can be separated into three terms. The first term contains variables which depend on the process, the nonlinear medium chosen, and on the pressure of the nonlinear medium. Except for the pressure, all of the other variables within this term are subject to outside constraints (most importantly, what λ_4 is desired and what lasers are available) and are not easily altered. Some properties of the nonlinear susceptibility and its role on conversion efficiency are discussed in the next section of this chapter.

The second term contains parameters which depend on the lasers available as pump sources. For any given laser, the pulse width is essentially constant while the laser power/energy can be adjusted only up to the maximum output. Notice that the output power/energy goes as the product of the three incident laser power/energies, as expected for a third-order nonlinear process before saturation effects become important.

The third term, the phase matching factor Φ, contains all of the parameters describing the experimental geometry: the length of the nonlinear medium, the location of the foci, and the confocal parameters. It also contains the wavevector mismatch, Δk. It is this term which is most under the control of the experimenter. A discussion of Φ is given in Sec. VI.

The results in this section were derived for the frequency summing process $\omega_4 = \omega_1 + \omega_2 + \omega_3$. Similar results can be obtained for the frequency difference processes $\omega_4 = \omega_1 \pm \omega_2 - \omega_3$ by taking the complex conjugate of the appropriate terms in Eq. 3.51, defining $k' = k_1 \pm k_2 - k_3$, and performing the same set of mathematical manipulations. The only difference in the results will be a change in the exact form of Φ.

V. THIRD ORDER NONLINEAR SUSCEPTIBILITY

A. Tensor Properties

The n-th order nonlinear susceptibility is a $(n+1)$ rank tensor with $3^{(n+1)}$ components. Thus, the second, third, and fourth order nonlinear susceptibilities have 27, 81, and 243 components, respectively, which need to be determined. Symmetry properties can be used to reduce the amount of calculations.

In a medium with inversion symmetry, even-order dipole susceptibilities are identically equal to zero. This situation holds for all gases, liquids, and centrosymmetric crystals. This can easily be shown by writing the even-order polarization as

$$\mathcal{P}_T^{(2n)} = \chi^{(2n)}(\mathcal{E}_T)^{(2n)} \tag{3.64}$$

and

$$\mathcal{P}_T'^{(2n)} = \chi'^{(2n)}(\mathcal{E}_T')^{(2n)} \tag{3.65}$$

in a normal and inverted coordinate system, respectively. When inverted, both $\mathcal{P}_T$ and $\mathcal{E}_T$ must change sign while $\chi^{(2n)}$, which has the symmetry of the medium, does not change sign. Thus, $\mathcal{P}' = -\mathcal{P}$, $\mathcal{E}_T' = -\mathcal{E}_T$, and $\chi'^{(2n)} = \chi^{(2n)}$. Substituting into Eq. 3.65 leads to

$$\mathcal{P}_T^{(2n)} = -\chi^{(2n)}(\mathcal{E}_T)^{(2n)}. \tag{3.66}$$

Equations 3.64 and 3.66 are consistent if and only if $\chi^{(2n)}$ is identically equal to zero.

In isotropic media the third order nonlinear susceptibility tensor is the first nonzero term in the $\mathcal{P}^{NL}$ expansion given by Eq. 3.33; therefore, effects due to this term should dominate effects due to other terms under most circumstances. This tensor contains 81 separate components, but only 21 of these are nonzero

because of inversion symmetry. Additionally, only 3 of these 21 components are independent:[26]

$$\begin{array}{lllllllllll}
\chi^{(3)}_{xxxx} & = & \chi^{(3)}_{yyyy} & = & \chi^{(3)}_{zzzz}. & & & & & & \\
\chi^{(3)}_{xxyy} & = & \chi^{(3)}_{xxzz} & = & \chi^{(3)}_{yyxx} & = & \chi^{(3)}_{yyzz} & = & \chi^{(3)}_{zzxx} & = & \chi^{(3)}_{zzyy}, \\
\chi^{(3)}_{xyxy} & = & \chi^{(3)}_{xzxz} & = & \chi^{(3)}_{yxyx} & = & \chi^{(3)}_{yzyz} & = & \chi^{(3)}_{zxzx} & = & \chi^{(3)}_{zyzy}, \\
\chi^{(3)}_{xyyx} & = & \chi^{(3)}_{xzzx} & = & \chi^{(3)}_{yxxy} & = & \chi^{(3)}_{yzzy} & = & \chi^{(3)}_{zxxz} & = & \chi^{(3)}_{zyyz}, \\
\chi^{(3)}_{xxxx} & = & \chi^{(3)}_{xxyy} & + & \chi^{(3)}_{xyxy} & + & \chi^{(3)}_{xyyx}. & & & &
\end{array} \tag{3.67}$$

Several properties of the output polarization can be determined by examination of Eq. 3.67. First, if all three incident beams are linearly polarized in the same direction then the output beam will also be linearly polarized in that direction. Second, if two of the incident beams are linearly polarized in one direction and the third incident beam is linearly polarized perpendicularly to the first two, then the output beam will be linearly polarized in the same direction as the third beam. Third, if the incident beams are circularly polarized in the same direction then third harmonic generation and sum- or difference-frequency mixing cannot occur. Fourth, if two of the incident beams are circularly polarized in one direction and the third is circularly polarized in the opposite direction, then sum- or difference-frequency mixing can occur. These polarization restrictions can be used to supress unwanted processes.

B. Determination of $\chi^{(3)}$

Each component of the nonlinear susceptibility can be calculated from a perturbation expansion of the density matrix of the system.[26] A completely general expression for $\chi^{(3)}_{ijkl}(-\omega_4, \omega_1, \omega_2, \omega_3)$ was given by Bloembergen *et al.*[26] For any given arrangement of frequencies, each component of the tensor is a 48 term summation which is further summed over all intermediate states of appropriate

parity within the atom. The steady-state susceptibility per atom in the dipole approximation for third harmonic generation is[23]

$$\chi^{(3)}_{ijkl}(-3\omega,\omega,\omega,\omega) = \frac{(ea_0)^4}{(\hbar c)^3} \sum_{\alpha,\beta,\gamma} (\mathbf{r}_{0\alpha})_l (\mathbf{r}_{\alpha\beta})_k (\mathbf{r}_{\beta\gamma})_j (\mathbf{r}_{\gamma 0})_i \times \left[\frac{1}{(\omega_{\alpha 0} - \omega)(\omega_{\beta 0} - 2\omega)} \left(\frac{1}{\omega_{\gamma 0} - 3\omega} + \frac{1}{\omega^*_{\gamma 0} + \omega} \right) + \frac{1}{(\omega^*_{\alpha 0} + \omega)(\omega^*_{\beta 0} + 2\omega)} \left(\frac{1}{\omega^*_{\gamma 0} + 3\omega} + \frac{1}{\omega_{\gamma 0} - \omega} \right) \right] \tag{3.68}$$

where the transition frequencies, $\omega_{ab} = (E_b - E_a)/\hbar - i\Gamma_{ba}$, are in cm^{-1} and the distance operator matrix elements between states a and b, $\mathbf{r}_{ab} = \langle a \mid \mathbf{r} \mid b \rangle$, are in units of the bohr radius. E_a is the energy of the quantum state a and Γ_{ba} is the damping rate for the transition between b and a. The symbols i, j, k,and l can stand for any one of the three cartesian components x, y, and z while the summation over the intermediate states α, β, and γ is to include all discrete or continuum states of appropriate parity within the atom.

A similar expression can be derived for the process $\omega_4 = 2\omega_1 \pm \omega_2$ and can be found in Reintjes.[23] It contains 12 terms in the summation, but since it does not provide additional insight into the behavior of $\chi^{(3)}$, it will not be repeated here.

Several important properties of $\chi^{(3)}$ can be elucidated by examination of Eq. 3.68. First, $\chi^{(3)}$ is largest in atoms or molecules which have large distance operator matrix elements connecting the various states. Second, $\chi^{(3)}$ is a slowly varying function of ω except in the vicinity of a one-, two-, or three-photon resonance. In this case the real part of the denominator of one term in the summation approaches zero and $\chi^{(3)}$ becomes large and imaginary. This is known as resonance enhancement of the nonlinear susceptibility.

One-photon resonances are undesirable since it means that the incident beam can be strongly absorbed, leading to depletion and loss of output power. In fact,

the theoretical treatment of FWM in this chapter has ignored pump absorption and will be invalid if there is such a one photon resonance. A three-photon resonance is also undesirable since it means that the third harmonic output can be strongly attenuated by a one photon absorption. The absorption due to a two-photon resonance is generally much weaker than the absorption that accompanies one- or three-photon resonances. Thus, only two-photon resonances are expected to be useful for significantly increasing the magnitude of $\chi^{(3)}$.

Detailed calculations of $\chi^{(3)}$ are difficult.[23] First, direct calculation of the appropriate matrix elements requires very accurate wavefunctions for many levels of the atom. Experimentally determined oscillator strengths can provide the magnitude, but not the sign, of the matrix elements. Second, the sum over states becomes an integral over continuum states for photon energies above the ionization potential. This integral is important at photon energies below the IP if the continuum contains most of the oscillator strength. Third, accurate calculation of $\chi^{(3)}$ near resonances is extremely difficult. Knowledge of the damping constants Γ_{ab} is needed, but collisional damping depends on the sample pressure. More importantly, at resonace many of the approximations used to develop Eq. 3.68 fail and a time-dependent polarization needs to be determined.

In spite of these difficulties, the magnitude of $\chi^{(3)}$ has been calculated for some of the rare gases, alkaline earths, and alkali metals. At very low frequencies, $\chi^{(3)}$ is independent of wavelength. Relative to a $\chi^{(3)}$ of 4×10^{-39} ESU/atom for He,[5] $\chi^{(3)}$ for Ar, Be, Ca, Li, and K is estimated to be 2×10^{-37}, 6×10^{-36}, 1×10^{-34}, 6×10^{-35}, and 2×10^{-34} ESU/atom, respectively. These results illustrate the importance of strong distance operator matrix elements to the magnitude of $\chi^{(3)}$. Resonance enhancements by several orders of magnitude are possible; $\chi^{(3)}$ can exceed 10^{-30} ESU/atom for Rb[28] and Cs[29] near resonances.

The large variations in $\chi^{(3)}$ can lead to large variations in the power generated at ω_4. All other parameters being equal, it is expected that the power generated by a FWM process will be nine orders of magnitude greater in K than in He. Two-photon resonance enhancement can increase the generated power by many more orders of magnitude.

C. Summary

In summary, there are two major means by which $\chi^{(3)}$ influences the output of a FWM process. First, the tensor properties of $\chi^{(3)}$ in isotropic media place restrictions on what processes are possible given the polarizations of the incident beams. It is possible to completely supress an undesired process while having almost no effect on the desired process. Second, the magnitude of $\chi^{(3)}$ places limits on the power generated by the FWM process. Some of the alkali metals are expected to be nine orders of magnitude more efficient than He, everything else being equal.

VI. PROPERTIES OF THE PHASE MATCHING FACTOR, Φ

The phase matching factor for frequency summing by FWM, Φ, was defined by Eq. 3.58. This factor is very important in understanding FWM processes as it contains all of the parameters which are easily adjustable by the experimenter. It contains the wave vector mismatch, Δk, along with parameters relating to the experimental geometry: length of cell, L, confocal parameters, b, and location of foci, f.

In this section, several properties of Φ are investigated. First, the behaviour of Φ in the limiting cases of very loose, ($b \gg L$), or very tight, ($b \ll L$), focusing. Second, means of adjusting Δk, and hence Φ, are discussed. And third, means of calculating Δk are reviewed.

A. Limiting behaviour of Φ

In studying Φ, the work is greatly simplified if it is assumed that all of the incident beams have the same confocal parameters and foci. As mentioned by Bjorklund,[15] in this case the generated radiation will be a lowest order Gaussian beam with the same confocal parameter as the incident beams. It will be further assumed that the focal spot is at the center of the nonlinear medium ($f = L/2$). With these assumptions, Φ can be given more simply as

$$\Phi = \left| \int_{-L/b}^{L/b} \frac{\exp\left[\frac{-ib\,\Delta k}{2}\zeta\right]}{(1+i\zeta)^2} d\zeta \right|^2 . \tag{3.69}$$

1) Collimated beams

In many experiments, the confocal parameter is much larger than the length of the nonlinear medium. In this case, the beam remains effectively collimated throughout the nonlinear medium. If the following identities[21] are substituted into

Eq. 3.69, $(1+ix)^{-1} = (1+x^2)^{-1/2}\exp[-i\tan^{-1}x]$ and $\tan^{-1}x = x - x^3/3 + x^5/5\cdots$, one finds that

$$\Phi = \left| \int_{-L/b}^{L/b} \frac{\exp\left[-i\left(\frac{b\Delta k}{2} + 2 - \frac{2\zeta^2}{3} + \cdots\right)\zeta\right]}{1+\zeta^2} d\zeta \right|^2 . \tag{3.70}$$

In the collimated beam limit of $L \ll b$, the limits of integration are small compared to unity and hence ζ always remains very small. Therefore, the ζ^2 term in the denominator and the $2\zeta^2/3$ and higher order terms in the exponential can be safely ignored. Φ can then be found by performing the integral in Eq. 3.70, yielding

$$\Phi_{cb} \approx \frac{4L^2}{b^2} \frac{\sin^2(L\,\Delta k/2 + 2L/b)}{(L\,\Delta k/2 + 2L/b)^2}. \tag{3.71}$$

Of the factors which influence Φ_{cb}, L and b are parameters of the experimental geometry while Δk is a property of the medium which is usually adjustable. Sec. IV.B. will discuss methods of adjusting Δk.

The function Φ_{cb} is symmetrical about its optimal point,

$$\Delta k_{cb,opt} = -4/b. \tag{3.72}$$

The full-width at half-maximum (FWHM) of Φ_{cb} is given by

$$\Delta k_{cb,1/2} = 5.56/L. \tag{3.73}$$

Combining the above two equations, one sees that the optimum Δk is a function of the FWHM,

$$\Delta k_{cb,opt} = -.719(L/b)\Delta k_{cb,1/2}. \tag{3.74}$$

These results show that the maximum of Φ_{cb} is offset from $\Delta k = 0$ by an amount $\Delta k_{cb,opt} = -4/b$; however, this offset is much less than the width of Φ_{cb}. This last result is important since it means that Φ_{cb} is essentially symmetric with respect to $\Delta k = 0$ and is nonzero for $\Delta k > 0$ and for $\Delta k < 0$.

Perfect phase matching occurs when the wave vector of the generated radiation equals that of the driving polarization; however, for collimated Gaussian laser beams the optimum Δk is not the 0 of perfect phase matching but is instead $-4/b$. This offset of the optimum Δk from 0 is a characteristic of frequency summing with Gaussian laser beams.

As noted in Sec. II., the phase shift of a lowest order Gaussian beam along the axis is given by

$$\psi = kz - \tan^{-1}\xi \tag{3.20}$$

which is approximately

$$\psi \approx kz - 2z/b \tag{3.75}$$

near the focal position. Therefore, the effective wave vector of the generated radiation near the focus is

$$k_{\text{eff,gen}} = k_4 - 2/b \tag{3.76}$$

while that of the driving polarization is given by the sum of the incident k_{eff}'s,

$$k_{\text{eff,pol}} = k' - 6/b. \tag{3.77}$$

The difference in effective wave vectors is then given by

$$\Delta k_{\text{eff}} = k_4 - 2/b - (k' - 6/b) = \Delta k + 4/b. \tag{3.78}$$

When there is perfect phase matching of the effective wave vectors, one finds that $\Delta k_{cb,opt} = -4/b$, the same result found from the exact solution.

2) Tight Focusing

Another common experimental geometry involves tight focusing in which case the confocal parameter is much less than the length of the nonlinear medium, $L \gg b$. Under these circumstances, the region of interaction is only a small fraction of the total length of the nonlinear medium. In this case, the limits of

the integration in Eq. 3.69 can be replaced by ∞'s, allowing the integral to be solved exactly[21], yielding

$$\Phi_{tf} = \begin{cases} (\pi b \Delta k)^2 \exp(b \Delta k) & \Delta k < 0; \\ 0 & \Delta k \geq 0. \end{cases} \tag{3.79}$$

Φ_{tf} behaves much differently than Φ_{cb}. First, Φ_{tf} is nonzero only for $\Delta k < 0$ as compared with Φ_{cb} which can be nonzero for $\Delta k \geq 0$ or $\Delta k < 0$. Second, the optimum wave vector mismatch is given by

$$\Delta k_{tf,opt} = -2/b. \tag{3.80}$$

Third, Φ_{tf} is unsymmetrical about $\Delta k_{tf,opt}$, being above the half-maximum level for $-4.156/b \leq \Delta k \leq -0.7612/b$.

The offset of the optimum Δk from 0 once again results from the phase shift that Gaussian beams undergo as a result of the focus.[15] In the absence of dispersion, the relative phase shift between the generated radiation and the driving polarization is 0 at $\xi = -\infty$, π at $\xi = 0$, and 2π at $\xi = +\infty$. Thus the electric field generated in the second half of the cell is exactly out of phase with that generated in the first half, leading to a complete return of energy to the incident beam. A negative Δk offsets part of this cancellation, allowing for there to be a net conversion of energy to the new frequency.

The requirement that $\Delta k < 0$ for Φ_{tf} be nonzero places restrictions on the possible nonlinear media. In the next subsection, means of adjusting Δk will be discussed.

B. Adjusting Δk

As shown in the previous subsections, the sign and magnitude of Δk is critical to the optimization of any FWM process, where Δk is given by

$$\begin{aligned} \Delta k &= k_4 - k' \\ &= 2\pi \left(\frac{n_{\lambda_4} - n_{\lambda_1}}{\lambda_1} + \frac{n_{\lambda_4} - n_{\lambda_2}}{\lambda_2} + \frac{n_{\lambda_4} - n_{\lambda_3}}{\lambda_3} \right). \end{aligned} \tag{3.81}$$

For example, under tight focusing conditions, $\Phi_{tf} = 0$ if $\Delta k \geq 0$. It is therefore important that means of adjusting Δk be known and understood. In this subsection, several techniques will be reviewed: 1) adjusting wavelengths, 2) using a multicomponent mixture of gases, 3) adjusting the pressure of a single gas. In the next subsection, methods of calculating Δk will be reviewed.

1) Adjusting Wavelength

The refractive index of atoms in the gas phase is generally a monotonically increasing function of the radiation frequency. This behaviour is known as normal dispersion. In the vicinity of a one-photon resonant absorption, a different behavior, anomalous dispersion, can occur. As the frequency increases across some absorption lines, the refractive index becomes quite large, decreases to quite small levels ($n < 1$ is possible), and then begins to increase again.[20]

It is obvious that by the correct choice of wavelengths and by using anomalous dispersion, almost any Δk can be obtained, thus optimizing Φ. This technique can be used to get high conversion efficiencies. It is possible to pick the wavelengths in order to get a resonant enhanced nonlinear susceptibility while maintaining the correct Δk. Unfortunately, the best use of this method may require 3 separate dye lasers in order to optimize both $\chi^{(3)}$ and Φ simultaneously.

2) Multicomponent Gas Mixtures

A second method of adjusting Δk is the use of multicomponent gas mixtures. In the normal application of this method, a gas with a positive Δk is mixed with a second gas with a negative Δk. By varying the ratio of the gases, essentially any Δk intermediate to that of the pure gases can be obtained.

To illustrate this method, it will be assumed that the refractive index of a gas is related to the number density by

$$n_{ij} - 1 = N_i \alpha_{ij} \tag{3.82}$$

where i identifies the species and j identifies the wavelength. The proportionality constant α_{ij} will be discussed later.

For a two component mixture, Δk is then given by

$$\Delta k = 2\pi N_1 \left[\left(\frac{\alpha_{14} - \alpha_{11}}{\lambda_1} + \frac{\alpha_{14} - \alpha_{12}}{\lambda_2} + \frac{\alpha_{14} - \alpha_{13}}{\lambda_3} \right) + \frac{N_2}{N_1} \left(\frac{\alpha_{24} - \alpha_{21}}{\lambda_1} + \frac{\alpha_{24} - \alpha_{22}}{\lambda_2} + \frac{\alpha_{24} - \alpha_{23}}{\lambda_3} \right) \right]. \tag{3.83}$$

Normally, only one of the components has a significant third order nonlinear susceptibility. An example of this is when a negatively dispersive alkali metal is used as the nonlinear medium while a positively dispersive rare gas is used for phase matching. The pressure of the significant component is held constant, giving a constant $\left|N\chi^{(3)}\right|^2$ term in Eq. 3.57, while the pressure of the second component is adjusted to give the optimum Δk for the experimental geometry.

However, in some cases, both components have a similar third-order nonlinear susceptibility, such as when two rare gases are used. In these cases the $\left|N\chi^{(3)}\right|$ term in Eq. 3.57 is more correctly given by $\left|N_1\chi_1^{(3)} + N_2\chi_2^{(3)}\right|$. Correct optimization of the FWM process is slightly more difficult under these circumstances because changes in N_2 to adjust Δk and Φ also adjusts the $\left|N_1\chi_1^{(3)} + N_2\chi_2^{(3)}\right|$ term. It is even possible that the nonlinear susceptibilities of the two components have opposite signs, leading to a decrease in signal even at perfect phase-matching.

The use of multi-component gas mixtures also allows for high conversion efficiencies. Any amount of the nonlinear component can be correctly phase matched using the appropriate amount of the second component. It is therefore possible in principle to increase N_1 in order to get the necessary power output since the conversion efficiency goes as N^2. However, the total pressure cannot be raised infinitely high because other processes start to become a factor limiting the overall efficiency. The principal difficulty of this method is in the maintenance

of an accurate homogenous multicomponent gas mixture, especially if dissimilar materials are used such as a metal vapor and a rare gas.

3. Pressure of a Single Component

The simplest method of adjusting Δk is to vary the pressure of a single nonlinear medium. This has the advantage of not requiring many lasers and not needing to make accurate gas mixtures. The big difficulty is that for any given set of incident wavelengths, a gas is going to be either positively or negatively dispersive. Thus, by adjusting the pressure of a gas, it is possible to adjust the magnitude, but not the sign, of Δk.

When the pressure is varied the optimum Δk's determined earlier are no longer valid. This is because Δk is proportional to N, and N occurs in Eq. 3.57 outside of Φ. Assume that

$$\Delta k = N\beta. \tag{3.84}$$

where β is the wave vector mismatch per atom. Then Eq. 3.57 can be rewritten as

$$P_4(z=L) = \frac{4096\pi^6\sigma^2 \left|\frac{\chi^{(3)}}{b\beta}\right|^2 P_{01}P_{01}P_{03}k_0}{\lambda_1\lambda_2\lambda_3\lambda_4 n_4 c^2 k'} \times \Phi' \tag{3.85}$$

where $\Phi' = (b\,\Delta k)^2 \times \Phi$.

The limiting behaviour of Φ' is

$$\Phi'_{cb} = 16\sin^2(L\,\Delta k/2) \tag{3.86}$$

for loose focusing and

$$\Phi'_{tf} = \begin{cases} \pi^2(b\,\Delta k)^4 \exp(b\,\Delta k), & \Delta k < 0, \\ 0, & \Delta k \geq 0 \end{cases} \tag{3.87}$$

for tight focusing. The optimum Δk's are now given by

$$\Delta k_{cb,opt} = n\pi/L \qquad n = \pm 1, \pm 3, \pm 5, \cdots \tag{3.88}$$

and

$$\Delta k_{tf,opt} = -4/b. \tag{3.89}$$

These optimum conditions are much different from those derived earlier. The ratio of optimized conversion efficiencies in the two limiting cases is seen to be

$$\frac{\Phi'_{tf}(opt)}{\Phi'_{cb}(opt)} = \begin{cases} 2.892, & \Delta k < 0, \\ 0, & \Delta k \geq 0, \end{cases} \tag{3.90}$$

if all other parameters are the same. Thus, for a fixed b there is only a slight advantage in going to the tight focusing limit if $\Delta k < 0$, while loose focusing is infinitely more advantageous for $\Delta k \geq 0$. For either kind of dispersion or in either focusing limit, the output power increases as b gets smaller if limiting processes can be ignored.

C. Determination of Δk

As mentioned earlier, Δk is given by

$$\Delta k = 2\pi \left(\frac{n_{\lambda_4} - n_{\lambda_1}}{\lambda_1} + \frac{n_{\lambda_4} - n_{\lambda_2}}{\lambda_2} + \frac{n_{\lambda_4} - n_{\lambda_3}}{\lambda_3} \right). \tag{3.81}$$

Thus, a calculation of Δk is essentially a calculation of linear refractive indices. In dilute media, the refractive index is related to the atomic linear susceptibility $\chi^{(1)}$ by[23,24,30]

$$\frac{n^2 - 1}{n^2 + 2} = \frac{4\pi}{3} N \chi^{(1)}. \tag{3.91}$$

The linear susceptibility is found in a manner similiar to that used previously for the third-order nonlinear susceptibilty, yielding[24]

$$\begin{aligned} \chi^{(1)}_{ij} &= \frac{e^2 a_0^2}{\hbar c} \sum_{\alpha} \frac{(\mathbf{r}_{0\alpha})_i (\mathbf{r}_{\alpha 0})_j}{\omega_{\alpha 0} + \omega} + \frac{(\mathbf{r}_{0\alpha})_j (\mathbf{r}_{\alpha 0})_i}{\omega^*_{\alpha 0} - \omega} \\ &= \frac{e^2 a_0^2}{\hbar c} \sum_{\alpha} \frac{(\mathbf{r}_{0\alpha})_i (\mathbf{r}_{\alpha 0})_j (\omega_{\alpha 0} + \omega^*_{\alpha 0})}{(\omega + \omega_{\alpha 0})(\omega - \omega^*_{\alpha 0})} \end{aligned} \tag{3.92}$$

The oscillator strength of an atomic transition is proportional to the square of the distance operator matrix element times the transition energy.[23] Making the

appropriate substitutions, converting to wavelengths, and using an integral for the sum over continuum states, one gets[31]

$$\chi^{(1)} = \frac{\lambda^2}{4\pi^2}\left[\alpha^2 a_0 \sum_{i=1}^{n_d} \frac{\lambda_i^2 f_i}{\lambda^2 - \lambda_i^2} + \frac{1}{\pi}\int_0^{\lambda_{IP}} \frac{\sigma(\lambda_i)\, d\lambda_i}{\lambda^2 - \lambda_i^2}\right] \tag{3.93}$$

where α is the fine structure constant, a_0 is the bohr radius, f_i is the oscillator strength of the i'th transition, σ is the absorption cross section in cm^2, and N is the number density in cm^{-3}. The summation is over the n_d discrete transitions while the integration is over the entire continuum.

Further substitution into Eq. 3.91 yields

$$\frac{n^2-1}{n^2+2} = \frac{N\lambda^2}{3\pi}\left[\alpha^2 a_0 \sum_{i=1}^{n_d} \frac{\lambda_i^2 f_i}{\lambda^2 - \lambda_i^2} + \frac{1}{\pi}\int_0^{\lambda_{IP}} \frac{\sigma(\lambda_i)\, d\lambda_i}{\lambda^2 - \lambda_i^2}\right] \tag{3.94}$$

For most gases, $n \approx 1$. This allows Eq. 3.94 to be simplified to

$$n - 1 = 2\pi N\chi^{(1)} = \frac{N\lambda^2}{2\pi}\left[\alpha^2 a_0 \sum_{i=1}^{n_d} \frac{\lambda_i^2 f_i}{\lambda^2 - \lambda_i^2} + \frac{1}{\pi}\int_0^{\lambda_{IP}} \frac{\sigma(\lambda_i)\, d\lambda_i}{\lambda^2 - \lambda_i^2}\right] \tag{3.95}$$

By inspection, one sees that the constant in Eq. 3.83 is given by $\alpha_{ij} = 2\pi\chi^{(1)}$.

Eq. 3.95 can be very accurate. Mahon, *et al*,[32] used this equation to calculate the refractive indices for Ar, Kr, and Xe from the near infared down to the first ionization limit. Using literature values for all of the oscillator strengths and ionization cross sections, they found that their calculations were 1% higher, 5% lower, and 2% higher than the experimental values for Ar, Kr, and Xe, respectively.

D. Summary

In this section the properties of the phase matching factor Φ have been reviewed. Analytic expressions for Φ were determined, which led to the concept of an optimum Δk. Next, methods of experimentally adjusting Δk, and hence Φ were discussed. And third, the methods of calculating Δk, and hence regions where FWM is possible, were discussed

VII. SUMMARY

This chapter has provided a theoretical background to the understanding of four-wave mixing processes. The principal results are as follows:

1) A gaussian laser traveling along the z-axis is described by

$$\Psi(r,z) = \mathrm{E}_0 \frac{\omega_0}{\omega(\xi)} \exp\left[-\frac{r^2}{\omega^2(\xi)} - i\left(\frac{r^2\xi}{\omega^2(\xi)} - kz + \tan^{-1}(\xi)\right)\right]. \tag{3.18}$$

2) The electric field amplitude is related to the nonlinear polarization by the coupled differential equations

$$\begin{aligned}
&\left[\nabla_\perp + 2ik_1\frac{\partial}{\partial z}\right]\mathbf{E}_1 = -\frac{4\pi\omega_1^2}{c^2}\mathbf{P}_1^{NL}e^{-i\Delta k_1 z},\\
&\vdots\\
&\left[\nabla_\perp + 2ik_j\frac{\partial}{\partial z}\right]\mathbf{E}_j = -\frac{4\pi\omega_j^2}{c^2}\mathbf{P}_j^{NL}e^{-i\Delta k_j z},\\
&\vdots
\end{aligned} \tag{3.32}$$

3) The n-th order nonlinear polarization for the process $\omega_q = \omega_1 + \omega_2 + \omega_3 + \cdots + \omega_n$ is given by

$$\mathbf{P}^{NL}(\omega_q) = \frac{g}{2^{n-1}}\chi^{(n)}(-\omega_q,\omega_1,\omega_2,\omega_3,\cdots,\omega_n)\mathbf{E}_1\mathbf{E}_2\mathbf{E}_3\cdots\mathbf{E}_n. \tag{3.34}$$

4) The output power from the interaction $\omega_4 = \omega_1 + \omega_2 + \omega_3$ is given by

$$P_4(z=L) = \frac{4096\pi^6\sigma^2\left|N\chi^{(3)}\right|^2 P_{01}P_{02}P_{03}k_0}{\lambda_1\lambda_2\lambda_3\lambda_4 n_4 c^2 k'} \times \Phi \tag{3.57}$$

where Φ is the phase matching factor.

5) In the limits of loose focusing (collimated beams) or tight focusing, Φ is given by

$$\Phi_{cb} \approx \frac{4L^2}{b^2}\frac{\sin^2(L\,\Delta k/2 + 2L/b)}{(L\,\Delta k/2 + 2L/b)^2} \tag{3.71}$$

and

$$\Phi_{tf} = \begin{cases} (\pi b\,\Delta k)^2\exp(b\,\Delta k) & \Delta k < 0; \\ 0 & \Delta k \geq 0. \end{cases} \tag{3.79}$$

6) There are three principal methods of adjusting Δk: adjusting the wavelengths of the incident beams, using a multicomponent gas mixture, or adjusting the pressure of a single gas. In general, the first process will give the highest conversion efficiencies and will be the most difficult, while the third is the simplest and will give the lowest conversion efficiencies.

This chapter was a review of the basic material needed to understand four-wave mixing processes. There are many effects that were not covered, chiefly the processes such as MPI, nonlinear refractive index, Kerr effect, saturation, and pump depletion which limit the conversion efficiency. The interested reader is urged to read the books by Reintjes[23] and Shen[24] for a more comprehensive treatment.

REFERENCES

1. P. A. Franken, A. E. Hill, C. W. Peters, and G. Weinreich, *Phys. Rev. Lett.* **7**, 118 (1961).
2. P. D. Maker, R. W. Terhune, and C. M. Savage, in *Proccedings of th Third International Conference on Quantum Electronics, Paris, 1963*, edited by P. Grivet and N. Bloembergen, (Columbia University Press, New York, 1964), p. 1559.
3. P. D. Maker and R. W. Terhune, *Phys. Rev.* **137**, 801 (1965).
4. G. H. C. New and J. F. Ward, *Phys. Rev. Lett.* **19**, 556 (1967).
5. J. F. Ward and G. H. C. New, *Phys. Rev.* **185**, 57 (1969).
6. J. Reintjes, C. Y. She, and R. C. Eckardt, *IEEE J. Quantum Electron.* **QE-14**, 581 (1978).
7. M. G. Grozeva, D. I. Metchkov, V. M. Mitev, L. I. Pavlov, and K. V. Stamenov, *Opt. Commun.* **23**, 77 (1977).
8. P. A. M. Dirac, *Proc. Roy. Soc.* **A-114**, 143,710 (1927).
9. M. Goeppert-Mayer, *Ann. Physik* **9**, 273 (1931).
10. J. A. Armstrong, N. Bloembergen, J. Ducuing, and P. S. Pershan, *Phys. Rev.* **127**, 1918 (1962).
11. D. A. Kleinmann, *Phys. Rev.* **128**, 1761 (1962).
12. D. A. Kleinmann, A. Ashkin, and G. D. Boyd, *Phys. Rev.* **145**, 338 (1966).
13. A. Yariv, *Quantum Electronics, 2nd ed.*, (John Wiley & Sons, New York, 1975).
14. D. Marcuse, *Principles of Quantum Electronics*, (Academic Press, New York, 1980).
15. G. C. Bjorklund, *IEEE J. Quantum Electron.* **QE-11**, , ().287 (1975).
16. I. V. Tomov and M. C. Richardson, *IEEE J. Quantum Electron.* **QE-12**, 521 (1976).

17. H. B. Puell and C. R. Vidal, *IEEE J. Quantum Electron.* **QE-14**, 364 (1978).

18. Y. M. Yiu, T. J. McIlrath, and R. Mahon, *Phys. Rev.* **A-20**, 2470 (1979).

19. N. Nayak, *IEEE J. Quantum Electron.* **QE-16**, 843 (1980).

20. J. D. Jackson, *Classical Electrodynamics, 2nd ed.*, (John Wiley, New York, 1975).

21. I. S. Gradshteyn and I. M. Ryzhik, *Tables of Integrals, Series, and Products*, (Academic Press, New York, 1980).

22. H. Kogelink and T. Li, *Appl. Opt.* **5**, 1550 (1966).

23. J. F. Reintjes, *Nonlinear Optical Parametric Processes in Liquids and Gases*, (Academic Press, New York, 1984).

24. Y. R. Shen, *The Principles of Nonlinear Optics*, (John Wiley, New York, 1984).

25. C. Flytzanis, in *Quantum Electronics, Vol. 1, Part A*, edited by H. Rabin and C. L. Tang, (Academic Press, New York, 1975), p. 30.

26. N. Bloembergen, H. Lotem, and R. T. Lynch, Jr., *Indian J. Pure Appl. Phys.* **16**, 151 (1978).

27. P. W. Langhoff, J. D. Lyons, and R. P. Hurst, *Phys. Rev.* **148**, 18 (1966).

28. R. B. Miles and S, E. Harris, *IEEE J. Quantum Electron.* **QE-9**, 470 (1973).

29. K. M. Leung, J. F. Ward, and B. J. Orr, *Phys. Rev.* **A-9**, 2440 (1974).

30. M. Born and E. Wolf, *Principles of Optics, 6th ed.*, (Pergamon Press, New York, 1980).

31. P. L. Smith, M. C. E. Huber, and W. H Parkinson, *Phys. Rev.* **A-13**, 1422 (1976).

32. R. Mahon, T. J. McIlrath, V. P. Myerscough, and D. W. Koopman, *IEEE J. Quantum Electron.* **QE-15**, 444 (1979).

CHAPTER 4

EXPERIMENTS ON VUV GENERATION

I. INTRODUCTION

In order to detect molecular hydrogen using the technique of laser induced fluorescence, it is necessary that laser radiation at an appropriate wavelength be generated. As discussed in a later chapter, the first discrete H_2 absorption band is the $\tilde{B}\ ^1\Sigma_u^+ \leftrightarrow \tilde{X}\ ^1\Sigma_g^+$ band in the vacuum ultraviolet (VUV) at wavelengths near 111 nm.[1] Tunable laser radiation at this wavelength cannot be generated directly, nor can it be generated using the frequency conversion techniques of second harmonic generation or other 3-wave mixing processes ($\omega_3 = \omega_1 \pm \omega_2$). Instead, the frequency conversion technique of third harmonic generation or other 4-wave mixing processes ($\omega_4 = \omega_1 \pm \omega_2 \pm \omega_3$) must be used.[2]

The preceding chapter discussed the theoretical background for 4-wave mixing processes. In this chapter experiments generating VUV radiation near 111 nm are discussed. First, the behaviour of the important parameters Δk and $\chi^{(3)}$ is examined for several gases which conceivably could be used for the nonlinear medium. These parameters place restrictions on the materials used for the experiments. Second, the apparatus used for the experiments is described in detail. Third, results for third harmonic generation (THG) are presented while the fourth section presents results for the process $\omega_4 = 2\omega_2 + \omega_1; \omega_2 = 2\omega_1$, abbreviated $(2(2)+1)\omega$.

II. Δk AND $\chi^{(3)}$

Before one can generate VUV radiation by a 4-wave mixing process, one needs to know what gases can be used for the nonlinear medium. Two properties of the gas are important: the wave vector mismatch, Δk, and the third order nonlinear susceptibility, $\chi^{(3)}$. The wavevector mismatch determines the phase matching properties of the system. As discussed in Chapter 3, THG is impossible in the tight focusing limit if $\Delta k > 0$; therefore, knowledge of Δk for a given gas gives the wavelength regions in which it can be used as a nonlinear medium. The third order nonlinear susceptibility determines the overall efficiency of the nonlinear process.

A. Δk

The wave vector mismatch for the process $\omega_4 = \omega_1 + \omega_2 + \omega_3$ is given by

$$\Delta k = 2\pi \left(\frac{n_{\lambda_4} - n_{\lambda_1}}{\lambda_1} + \frac{n_{\lambda_4} - n_{\lambda_2}}{\lambda_2} + \frac{n_{\lambda_4} - n_{\lambda_3}}{\lambda_3} \right) \tag{3.81}$$

which equals

$$\Delta k = 6\pi \left(\frac{n_{\lambda_4} - n_{\lambda_1}}{\lambda_1} \right) \tag{4.1}$$

for THG. The refractive index, n_λ, at wavelength λ is given by

$$\frac{n_\lambda^2 - 1}{n_\lambda^2 + 2} = \frac{4}{3}\pi N \left[\frac{\alpha^2 \alpha_0}{4\pi^2} \sum_{i=1}^{n_d} \frac{f_i}{\lambda_i^{-2} - \lambda^{-2}} + \frac{1}{4\pi^3} \int_0^{\lambda_{IP}} \frac{\sigma_{\lambda_i}}{1 - \left(\frac{\lambda_i}{\lambda}\right)^2} d\lambda_i \right] \tag{3.94}$$

$$= N \left[2.9899 \times 10^{-28} \sum_{i=1}^{n_d} \frac{f_i}{\lambda_i^{-2} - \lambda^{-2}} + 3.3774 \times 10^{-27} \int_0^{\lambda_{IP}} \frac{\sigma_{\lambda_i}}{1 - \left(\frac{\lambda_i}{\lambda}\right)^2} d\lambda_i \right]$$

where α is the fine structure constant, α_0 is the bohr radius, N is the number density of the gas (cm^{-3}), f_i is the oscillator strength for the discrete transition at λ_i (nm), and σ_{λ_i} is the absorption cross section (Mb = 10^{-18} cm^2) for the ionization continuum at λ_i. The summation is over all the discrete states and the integration is over the entire continuum.

Mahon *et al.*[3] used similar equations to calculate Δk for THG in Ar, Kr, and Xe throughout the VUV region of the spectrum. It was decided to repeat the calculation using more recent oscillator strength and continuum cross section measurements. It is desired to confirm their results for THG and generate the first Δk data for the $(2(2)+1)\omega$ process. In addition, it is desired to have quantitative knowledge of Δk in the wavelength region of interest, 109–112 nm.

The same procedure was followed for Ar, Kr, and Xe. The oscillator strengths used in the calculations were the arithmetic mean of f_i's determined by electron energy loss spectrometry and optical techniques (lifetime, absorption) (Ar,[4–7] Kr,[4,8–11] Xe[4,9,11–16]). The positions of the discrete absorption lines were taken from high resolution absorption spectra (Ar,[17] Kr,[18] Xe[19]). Cross sections for the autoionization region of the continuum between the $^2P_{3/2}$ and $^2P_{1/2}$ ionization potentials (IP) were read off published photoionization spectra at a spacing of 0.05, 0.1, and 0.2 nm for Ar,[20] Kr,[21] and Xe,[20] respectively. The continuum absorption cross sections from the $^2P_{1/2}$ IP to the X-ray region were taken from recent critical compilations (Ar,[22] Kr,[22] Xe[23]). The compilations excluded significant amounts of oscillator strength in the X-ray region of the spectrum. The oscillator strengths compiled by Kumar and Meath[24] for this spectral region were added in as a discrete line.

The data used in the calculation is sparse in the vicinity of the ionization potential. The discrete absorption lines get closer together and are no longer resolvable using electron energy loss spectrometry; hence, f_i's for these transitions are unknown. In the continuum absorption spectrum between the $^2P_{3/2}$ and $^2P_{1/2}$ IP's there is intense structure due to autoionization which is finer than the grid used for the integration. It is therefore expected that this region of the spectrum will be underrepresented in the calculations. It was decided to add to the calculation an additional discrete line at a wavelength halfway between the $^2P_{3/2}$ and $^2P_{1/2}$ IP's

with sufficient oscillator strength for the calculated refractive index at 546.2258 nm to agree with the critical evaluation of Leonard.[25] The oscillator strengths for the discrete spectrum that were used in the final spectrum are given in Tables 1, 2, and 3 for Ar, Kr, and Xe, respectively.

It was decided to use second virial coefficients[26] when determining the number density of the rare gases. This correction is relatively small, on the order of 0.6% for Xe at STP conditions and even less for Kr and Ar.

The data used for the refractive index calculations can also be used to calculate the total oscillator strength:[27]

$$f_{tot} = \sum_{i=1}^{n_d} f_i + \frac{1}{\pi\alpha^2\alpha_0}\int_0^{\lambda_{IP}} \frac{\sigma_{\lambda_i}}{\lambda_i^2} d\lambda_i \qquad (4.2)$$

$$= \sum_{i=1}^{n_d} f_i + 11.2959 \int_0^{\lambda_{IP}} \frac{\sigma_{\lambda_i}}{\lambda_i^2} d\lambda_i$$

and the static dielectric polarizability:[27]

$$\alpha_N = \frac{\alpha^2\alpha_0}{4\pi^2}\sum_{i=1}^{n_d} f_i\lambda_i^2 + \frac{1}{4\pi^3}\int_0^{\lambda_{IP}} \sigma_{\lambda_i}\, d\lambda_i \qquad (4.3)$$

$$= 7.1379\times10^{-5}\sum_{i=1}^{n_d} f_i\lambda_i^2 + 8.0629\times10^{-4}\int_0^{\lambda_{IP}} \sigma_{\lambda_i}\, d\lambda_i$$

where α_N is the static dielectric polarizability in Å^3. According to the Thomas-Reiche-Kuhn sum rule,[27] the total oscillator strength of an atom or molecule is equal to the number of electrons in the atom or molecule. The calculated polarizability can be compared directly with experimental results. The largest contribution to the oscillator strength is from very short wavelengths while the largest contribution to the polarizability is from longer wavelengths. For example, in Xe 57% of the oscillator strength is at wavelengths below 2 nm while 45% of the polarizability is from the discrete spectrum above 102 nm.

The calculated refractive index and Δk for THG in Ar are shown in Figures 1 and 2. Without the correction term of $f_{IP} = 0.1273$, the visible refractive index was low by 3.40%. After making this correction the calculated oscillator strength of 17.73 is only 1.5% below the expected 18.00 while the calculated polarizability of 1.643 Å^3 is close to recent determinations of 1.641 and 1.642 Å^3.[28,25]

The calculated refractive index and Δk for THG in Kr are shown in Figures 3 and 4. Without the correction term of $f_{IP} = 0.3084$, the visible refractive index was low by 6.64%. After making this correction the calculated oscillator strength of 33.92 is 5.77% below the expected 36.00 while the calculated polarizability of 2.484 Å^3 falls between the recent determinations of 2.480 and 2.487 Å^3.[28,25]

The calculated refractive index and Δk for THG in Xe are shown in Figures 5 and 6. Without the correction term of $f_{IP} = 0.0386$, the visible refractive index was low by 0.64%. After making this correction the calculated oscillator strength of 49.39 is 8.54% below the expected 54.0 while the calculated polarizability of 4.017 Å^3 is close to the experimentally determined 4.044 and 4.016 Å^3.[28,25]

The refractive indices of Ar, Kr, and Xe have been well studied[25,29–33] at wavelengths above 140 nm and the calculated indices are in close agreement with experiment as can be seen in Figs. 1, 3, and 5; however, there have been few measurements at wavelengths near 111 nm. Bideau-Mehu *et al.*[32] measured the refractive index for Ar, Kr, and Xe at wavelengths between 250 and 140.4 nm. The deviation between the calculated and experimentally determined refractive indices, $n - 1$ at STP, at 140.4 nm is quite small for all three species: +0.37% for Ar, +0.35% for Kr, and +8.58% for Xe. It should be noted that for Xe this wavelength falls in a region of high dispersion just below the resonance line at 146.9612 nm and that the deviation is only -2.35% at 152.3 nm. Chaschina *et al.*[29,30] measured refractive indices down to 110 nm in Ar, 133 nm in Kr, and 155 nm in Xe. The deviation between the calculated and experimental refractive indices is +0.70%

for Ar at 121.567 nm and is +2.62% for Kr at 130 nm (Leonard[25] believes that the experimental refractive indices are low by a percent or two at these short wavelengths). Gladushchak *et al.*[33] measured the Kr refractive index at 121.567 nm by determining the amount of Ar needed to make a Kr/Ar mixture have a positive Δk. At an unspecified temperature they obtained $n - 1 = -9 \times 10^{-5}$ while the calculated value is $n - 1 = -1.362 \times 10^{-4}$ at STP. Kramer *et al.*[34] measured the Xe refractive index between 115.2 and 117 nm. Their results were not tabulated but were shown on a logarithmic plot. The calculated indices were slightly less negative than the experimental indices, the deviation being approximately $10^{-0.07}$. At 116.34 nm the calculated refractive index was $n - 1 = -1.528 \times 10^{-3}$ while the experimental result was $n - 1 \approx -1.8 \times 10^{-3}$. In summary, the calculated refractive indices are known to be of high quality for wavelengths above 140 nm. While there is no high quality experimental data in the VUV at 111 nm with which to judge the calculations, they are consistent with experimental data at nearby wavelengths.

It is believed that the calculated Δk's shown in figures 2, 4, and 6 are reasonably accurate. It can be seen in Fig. 2 that in Ar $\Delta k > 0$ for all wavelengths above 106.7 nm. Thus, Ar cannot be used as a nonlinear medium at 111 nm, but it can be used for phase matching purposes. Fig. 4 shows that in Kr $\Delta k < 0$ within the two wavelength regions 109.55–116.4867 nm and 120.34–123.5838 nm. The first of these includes the H_2 absorption band while the second region includes the H Lyman-α line at 121.567 nm. Thus, Kr can be used as a nonlinear medium for generating VUV radiation at the wavelengths where H and H_2 absorb. Fig. 6 shows that in Xe $\Delta k < 0$ in numerous wavelength intervals. However, each of these intervals is relatively narrow, so it is expected that THG in Xe would not have a wide tunability range. In addition, within the wavelength region where the H_2 absorption band is located there are several absorption lines which would absorb the generated VUV if Xe was used for phase matching. It is therefore expected

that Xe would neither be a suitable nonlinear medium nor would it be a suitable gas for phase matching in the wavelength region of interest.

Table 4 gives the regions where $\Delta k < 0$ for both THG and $(2(2) + 1)\omega$ processes, along with the results of the Mahon *et al.*[3] calculation and several experiments.[35–39] The overall agreement between the new calculations and the previous results is very good. The wavelength at which $\Delta k = 0$ provides a sensitive test of the VUV refractive indices. At that wavelength, the VUV refractive index equals that of the incident UV radiation. Since the calculated UV refractive indices are known to be highly accurate, agreement between experiment and theory as to the VUV wavelength at which $\Delta k = 0$ implies that the calculated VUV refractive index is also accurate. There have also been a few measurements of Δk in the VUV region of the spectrum. Cotter[41] measured a $\Delta k = -0.18$ cm^{-1} torr^{-1} at 112.4 nm at an unspecified temperature. The calculated mismatch at that wavelength at 298 K is $\Delta k = -0.195$ cm^{-1} torr^{-1}, an extremely close agreement. Mahon *et al.*[3] calculated a mismatch at 121.567 nm of $\Delta k = -0.394$ cm^{-1} torr^{-1} (when converted to 298.15 K) which agrees closely with the calculated value of $\Delta k = -0.361$ cm^{-1} torr^{-1}. They also measured[42] the mismatch at that wavelength to be $\Delta k = -0.4$ cm^{-1} torr^{-1}, also at an unspecified temperature. This close agreement between the calculated and measured wave vector mismatches shows that the calculated refractive indices are accurate not only in the visible, UV, and near VUV regions of the spectrum, but also in the deep VUV near 111 nm.

In summary, calculations of the wave vector mismatch for THG in Ar, Kr, and Xe show that only Kr can be used as a nonlinear medium in the vicinity of 111 nm. Additionally, only Ar would be a suitable material for phase matching purposes. Additional calculations of the wave vector mismatch for the $(2(2) + 1)\omega$ process had the same results.

B. $\chi^{(3)}$

The third order nonlinear susceptibility, $\chi^{(3)}$, is important in that it determines the overall efficiency of of any 4-wave mixing process. Three properties of $\chi^{(3)}$ are important: its magnitude, its phase, and its tensor components. The magnitude of $\chi^{(3)}$ determines the maximum overall conversion efficiency. No matter how good the phase matching, if $\chi^{(3)} = 0$ then no VUV generation can take place. Conversely, knowledge of $\chi^{(3)}$ can direct the experimenter to wavelength combinations which increase the conversion efficiency by many orders of magnitude through resonance enhancement. The phase of $\chi^{(3)}$ is unimportant if only one species is used as a nonlinear medium; however, if more than one species is used one must be careful that the $\chi^{(3)}$'s do not cancel each other. Third, the tensor nature of $\chi^{(3)}$ must be remembered. For normal THG with linearly polarized radiation the tensor properties can be safely ignored; however, if circularly polarized radiation or multiple wavelengths are used, the tensor properties can not be ignored. It is possible to use these properties to suppress undesired background processes. A more detailed description of $\chi^{(3)}$ and its properties is given in Section V of Chapter 3.

In the dipole approximation the susceptibility per atom for third harmonic generation is given by

$$\chi^{(3)}_{ijkl}(-3\omega,\omega,\omega,\omega) = \frac{(e\alpha_0)^4}{(\hbar c)^3} \sum_{\alpha,\beta,\gamma} (\mathbf{r}_{0\alpha})_l (\mathbf{r}_{\alpha\beta})_k (\mathbf{r}_{\beta\gamma})_j (\mathbf{r}_{\gamma 0})_i \times \left[\frac{1}{(\omega_{\alpha 0} - \omega)(\omega_{\beta 0} - 2\omega)} \left(\frac{1}{\omega_{\gamma 0} - 3\omega} + \frac{1}{\omega^*_{\gamma 0} + \omega} \right) + \frac{1}{(\omega^*_{\alpha 0} + \omega)(\omega^*_{\beta 0} + 2\omega)} \left(\frac{1}{\omega^*_{\gamma 0} + 3\omega} + \frac{1}{\omega_{\gamma 0} - \omega} \right) \right] \tag{3.68}$$

where the transition frequencies, $\omega_{ab} = (E_b - E_a)/\hbar - i\Gamma_{ba}$, are in cm^{-1} and the distance operator matrix elements between states a and b, $\mathbf{r}_{ab} = \langle b|\mathbf{r}|a\rangle$, are in

units of the bohr radius. E_a is the energy of quantum state a and Γ_{ba} is the damping rate for the transition between b and a. The symbols i, j, k, and l stand for any one of the three cartesian coordinates x, y, and z while the summation over intermediate states α, β, and γ is to include all discrete or continuum states of appropriate parity within the atom.

A calculation of $\chi^{(3)}$ is much more difficult than a calculation of n_λ. First, a refractive index calculation only requires the magnitude squared of the distance matrix elements while the susceptibility calculation requires the magnitude and phase of the distance matrix elements. Second, in the dipole approximation a refractive index calculation only involves states which are directly coupled by one photon to the ground state while a susceptibility calculation involves states which can be coupled by several photons to the ground state. In addition, the susceptibility calculation requires knowledge of matrix elements between excited states, not just between the ground state and excited states.

There are several approaches which can be used for determining the appropriate matrix elements. First, there is the "exact" computational method in which the Schrödinger equation is solved for the ground state and all excited states of interest by appropriate techniques and then the distance matrix element is determined numerically. This is a difficult method in that the wave functions of highly excited states must be known very accurately. Spin-orbit coupling and configuration interactions must be taken into account. Second, there is the approximate method of Bates and Damgaard[43] as corrected by Bebb.[44] In this quantum defect Coulomb function model the departure of the potential from its asymptotic Coulomb form is neglected. A short algorithm gives the distance matrix elements as a function of the effective principal quantum number and angular momentum quantum number for each state. The method was shown to be reasonably accurate for simple systems such as the alkalies, sometimes giving

results better than that obtained from Hartree-Fock calculations. However, the agreement is not as good for more complicated systems. In the third method the magnitude of the matrix element is obtained from the experimental oscillator strength and transition energy while the phase is obtained from the approximate method of Bates and Damgaard. This third method was used by Miles and Harris[45] when they calculated $\chi^{(3)}$ for third harmonic generation in Li, Na, K, Ru, and Cs. Spin-orbit coupling was ignored in their calculations.

The magnitude of the distance matrix element is given by:[46]

$$\left|(\mathbf{r}_{ab})_i\right| = \left|\langle b|\mathbf{r}|a\rangle\right|_i = \mathcal{Z}_{Jl}\sqrt{\frac{g_a f_{ab}}{E_b - E_a}} \tag{4.4}$$

where f_{ab} is the oscillator strength for transitions from a to b, g_a is the degeneracy of a, and $\mathcal{Z}_{Jl}$ is an angular momentum term. It should be noted that $g_a f_{ab} = -g_b f_{ba}$ with absorption oscillator strengths positive and emission oscillator strengths negative. The exact form of $\mathcal{Z}_{Jl}$ depends on the angular momentum coupling used to describe the states involved in the transition and on the polarization of the incident radiation.

The energies and configurations of Kr excited states are taken from the tables of Moore.[47] In the rare gases the angular momentum coupling is intermediate between LS and jj coupling and consequently a jl coupling notation is used: singly excited configurations of Kr are represented by $4p^5(^2P_{j_l})nl[K]_J$ where $4p^5(^2P_{j_l=3/2,1/2})$ is the ionic core, nl is the principal quantum number and angular momentum quantum number of the excited electron, K is a half-integer such that $|l - j_l| \leq K \leq l + l_j$, and $J = K \pm 1/2$. If the entire configuration has odd parity a superscript o is appended. To simplify notation, states built on a $j_l = 3/2$ core are represented by $nl[K]_J$ and those on a $j_l = 1/2$ core are represented by $nl'[K]_J$.

The ground state configuration of Kr has even parity and has $J = 0$. The states directly coupled to the ground state by dipole allowed transitions (α and γ

in Eq. 3.68) are odd with $J = 1$. These states include $ns[3/2]^o_1$, $ns'[1/2]^o_1$, $nd[1/2]^o_1$, $nd[3/2]^o_1$, and $nd'[3/2]^o_1$. States which are directly coupled to these excited states by dipole allowed transitions (β in Eq. 3.89) are even states with $J = 0, 1, 2$. These states include the ground state, $np[1/2]_0$, $np[1/2]_1$, $np[3/2]_1$, $np[3/2]_2$, $np[5/2]_2$, $np'[1/2]_0$, $np'[1/2]_1$, $np'[3/2]_1$ and $np'[3/2]_2$. If only intermediate states with principal quantum number less than 5 are used, then a total of 80 matrix elements are needed and the summation will have 640 terms; however, if quantum numbers up to 6 or 7 are used then there will be 247 or 486 matrix elements and 3241 or 8748 terms, respectively.

Aymar and Coulombe[48] calculated the magnitude of the Kr matrix elements in a central field model including intermediated coupling and configuration mixing. They reported the oscillator strength and the square of the matrix element for $4p^6$, $4p^5np(n = 5, 6, 7) \rightarrow 4p^5ns(n = 5, 6, 7)$, $4p^5nd(n = 4, 5, 6)$, a total of over 800 transitions. The four strongest transitions from the ground state are at 123.584, 116.487, 100.110, and 94.654 nm. The oscillator strengths of these four transitions as used in the refractive index calculation were 0.2048, 0.1863, 0.1470, and 0.1240, respectively, while Aymar and Coulombe calculated 0.185, 0.175, 0.248, and 0.540, respectively. The oscillator strength they obtained for 15 transitions from the ground state was 2.75, much greater than the 1.07 determined by Kumar and Meath[24] for the entire discrete spectrum. It should also be noted that they believe that the assignments by Kaufman and Humphreys,[49] by Moore,[47] and by Yoshino and Tanaka[18] are in error and that the $6s[3/2]^o_1$ state at 100.1060 nm should be interchanged with the $4d[3/2]^o_1$ state at 100.3550 nm.

There have also been a few experimental determinations of the oscillator strengths for transitions between excited states. Much of the work is by Fonesca and Campos[50–52] who measured the transition probabilities for six $5p$ to $5s$ and

thirteen $5p'$ to $5s$ and $5s'$ transitions. This represents only a small fraction of the needed experimental data.

Even without detailed knowledge about the matrix elements, it is possible to answer some questions about $\chi^{(3)}$ in Kr. First, for the wavelength regions of interest there will be little to no resonance enhancement of the susceptibility. To generate 111 nm radiation by THG, the incident radiation is 333 nm, or 30030 cm^{-1}. The virtual state populated by a single photon is 50887 cm^{-1} from the nearest excited state ($5s[3/2]_1^o$), the virtual state populated by a two photon process is 19912 cm^{-1} from the lowest allowed excited state ($5s[3/2]_2$), and the final virtual state is 4243 cm^{-1} above the $5s'[1/2]_1^o$ state. To generate the same VUV wavelength by the $(2(2)+1)\omega$ process, the incident radiation is 555 nm (18018 cm^{-1}) and 277.5 nm (36036 cm^{-1}). Under these circumstances, the two possible single photon virtual states will 62899 or 44881 cm^{-1} from the nearest allowed state while the two possible two photon virtual states are 25919 and 7901 cm^{-1} from the lowest allowed state. As noted in the previous chapter, the preferred method for increasing $\chi^{(3)}$ is through a two photon resonance; in both cases, the two photon virtual states are non-resonant with a real state of the molecule.

Second, it is possible to determine what are the important states. If $\chi^{(3)}$ was determined principally by only a few states then the triple summation in Eq. 3.68 could be greatly reduced. Unfortunately, that is not the case in Kr. The principal difficulty is that the oscillator strength of the atom is not confined to a few strong transitions, but is instead spread out over a large number of discrete states and the continuum. Therefore, the distance operator matrix elements will all be of comparable size. The one and two photon virtual states are not near real states of appropriate parity; consequently, there will be no or little resonance enhancement of $\chi^{(3)}$ and most of α and β terms in Eq. 3.68 will have to be retained. It is possible to slightly reduce the number of states responsible for

the coupling back to the ground state, *i.e.*, γ in Eq. 3.68. An approximate idea as to the relative importance of various states can be obtained using Eq. 4.4 and neglecting the $\mathcal{Z}_{Jl}$ angular momentum function. The four strongest transitions from the ground state mentioned earlier involve the $5s[3/2]_1^o$, $5s'[1/2]_1^o$, $6s[3/2]_1^o$, and $5d[3/2]_1^o$ excited states. In addition, there are weak states at 103.002 nm, $4d[1/2]_1^o$, and at 100.355 nm, $4d[3/2]_1^o$, with oscillator strengths of 0.0050 and 0.0733, respectively. Four of the $\mathcal{Z}_{JL}$'s are expected to be the same because they all involve a transition to a $[3/2]_1$ state while the other two $\mathcal{Z}_{Jl}$'s are likely to be different. The relative magnitude of these six matrix elements is approximately 1.00 : 0.93 : 0.14 : 0.54 : 0.76 : 0.68, in order of increasing transition energy. After being weighted by the appropriate denominator, the relative contribution at 111 nm of these states to $\chi^{(3)}$ is approximately 1.00 : 2.00 : 0.19 : 0.52 : 0.71 : 0.40. In fact, there are more than a dozen states with a relative contribution > 0.10. It is obvious why accurate knowledge of the phases is important: with no dominant term to $\chi^{(3)}$ the possibility exists for there to be almost equal contributions from several terms which could cancel each other.

It was decided to not pursue a calculation of $\chi^{(3)}$ any further. The number of discrete matrix elements needed greatly exceeds the number known or accurately calculated, and in addition, the published work only gives the magnitude, not the phase, of the matrix elements. Without accurate knowledge of the phase, it is not possible to determine if several equally important terms will cancel each other. It is expected that the continuum will provide a significant contribution. It is believed that the information gained would be incommensurate with the effort expended in trying to accurately determine the phase of the matrix elements.

III. APPARATUS

A. Laser Systems

Two dye laser systems were used for generating VUV laser radiation. The early work was done using dye laser system 1, while dye laser system 2 was used for the final experiments.

Dye laser system 1 consists of a Molectron MY-34 pulsed Nd:YAG laser and a Molectron DL-18 dye laser.[53] Dye laser system 2 consists of a Quanta Ray DCR-2A Nd:YAG laser, a Quanta Ray PDL-2 dye laser, and a Quanta Ray WEX-1 wavelength extension unit.[55] These two systems are described in more detail in Appendix 1.

333 nm radiation is needed to generate VUV radiation at 111 nm by third harmonic generation. This wavelength is easily provided by doubling the 666 nm output of the dye laser; thus, the overall process generates the sixth harmonic of the dye laser.

Several dyes are known to lase at wavelengths near 660 nm when pumped by the Nd:YAG second harmonic at 532 nm.[56,57] Oxazine 720 (Ox 720, Oxazine 170), 9-Ethylamino-5-ethylimino-10-methyl-5*H*-benzo(a)phenoxazonium perchlorate, has a lasing maximum in ethanol of 670 nm. DCM, 4-(dicyano-methylene)-2-methyl-6-(*p*-dimethylaminostyryl)-4*H*-pyran, has a lasing maximum in ethanol of 640 nm.

Original experiments used Ox 720 in ethanol. Later experiments showed that the efficiency was greatly increased when R590 was added. R590 has the additional property of shifting the lasing maximum to 660 nm. This dye mixture was 3× more efficient when the final amplifier was transversly pumped. Using laser system I without a preamplifier the maximum dye laser efficiency was 20.5%. In laser system II with the delay line but without a preamplifier the maximum dye laser efficiency was 20.2%.

Later experiments used DCM in methanol/DMSO (50:50 v:v). The DMSO shifted the lasing maximum to 650 nm. Because DCM is a much higher gain dye than Ox 720, it was possible to get sufficient output power using a longitudinally pumped final amplifier. The dye laser output beam is therefore of a higher quality and UV and VUV conversion efficiencies are expected to improve. In laser system II using the delay line without the preamplifier the dye laser efficiency was 7.0%, with the preamplifier the efficiency rose to 21%.

Some experiments used the $(2(2) + 1)\omega$ process. This process generates the fifth harmonic of the dye laser; therefore, laser radiation at 555 nm is needed. Rhodamine 590, Ethyl [6-(ethylamino)-3-(ethylimino)-2,7,-dimethyl-3*H*-xanthen-9-yl]benzoate chloride, perchlorate, or tetrafluoroborate, is the most logical choice of dye in this wavelength region. Because this dye has the highest lasing efficiency of any dye when pumped by the 532 nm Nd:YAG second harmonic, it is used in testing dye laser performance. Its lasing maximum is at 560 nm and conversion efficiencies of 30% are obtainable with either dye laser using a longitudinally pumped amplifier without a preamplifier. Quanta-Ray recommends the tetrafluoroborate counter-ion because it gives slightly superior performance.

B. Optics

The optical configuration is shown in Figure 7. The UV output from either dye laser system passes through a right angle prism and then is focused into the sample cell by a lens. A small fraction of the incident radiation, $\approx 8\%$, is diverted to a Laser Precision Corp RkP-735 or RjP-735 pyroelectric joulemeter[58] in order to measure the incident pulse energy. The pyroelectric joulemeters were calibrated against a Scientech 380101 volume absorbing power meter[59] to directly read the UV power incident incident on the sample cell. A slight amount of radiation exiting the cell can be diverted to a HP 5082-4220 photodiode[60] to monitor the temporal

profile of the laser. When operated with an -18 V reverse bias, this photodiode has an $\approx$ 1.5 ns rise- and fall-time.

Two lenses are used for these experiments. The first is a "best form" 100 mm Suprasil singlet lens (LLU-25-100 by Optics for Research[61]) with radii of curvature chosen to minimze spherical aberration at the design wavelength of 300 nm. The second is a 100 mm UV-visible achromatic doublet lens, also by Optics for Research. This is a custom lens and is designed so that the 280 nm and 560 nm focal lengths are identical as is required for the $(2(2)+1)\omega$ process. This lens has negligible spherical aberration and is considered to be diffraction limited. However, the optimized design was such that back reflections from the second and third surfaces were brought to a focus a fraction of a mm in front of the first surface. The high power densities at this back reflection focal point often damaged the lens. The lens was redesigned to eliminate this problem.

The properties of the lens can be used to estimate the radius of the laser beam at the focal point and hence the confocal parameter, b. There are two reasons why the focal region will have a finite size: diffraction and spherical aberration. Diffraction is a fundamental restriction on the size of the beam due to interference effects while spherical aberration is a function of the lens quality and design.

A Gaussian laser beam has a far field diffraction half angle δ given by

$$\delta = \frac{2\omega_0}{b} = \frac{\lambda}{\pi\omega_0} = \frac{2}{\sqrt{bk}} \tag{3.21}$$

where ω_0 is the beamwaist radius at the focal point. For a collimated laser beam incident on a positive lens the final convergence as given by geometrical optics is

$$\tan\delta = r_l/f \tag{4.5}$$

where r_l is the radius of the incident beam and f is the focal length of the lens. Consequently, to a very good approximation

$$(\omega_0)_d = \frac{\lambda f}{\pi r_l} = 0.318310\frac{\lambda f}{r_l} \tag{4.6}$$

where it has been assumed that $\tan\delta \approx \delta$, *i.e.*, $f \gg r_l$.

Diffraction is a purely interference effect. Spherical aberration is normally considered using geometrical optics. This aberration is caused by the fact that lenses and mirrors made from spherical surfaces cannot bring all rays incident on the optic which are parallel to the optical axis to a common focus.[62] For a positive lens the rays which go through the margins of the lens are over refracted and brought to a focus closer to the lens then those rays which go through the central regions. This change in focal position is known as longitudinal spherical aberration (Long.SA). Related to this is lateral spherical aberration (Lat.SA) which gives the distance from the axis the ray intersects the paraxial focal plane.

These errors occur because the approximation $\sin x = x$ is made in paraxial or first order geometrical optics. In third order theory, the approximation $\sin x = x - \frac{x^3}{3!}$ is used. It can be shown that at the paraxial focus the Lat.SA in exact third order theory is[62]

$$h_{pf} = \frac{4h_l^3}{f^2}C \tag{4.7}$$

and the Long.SA is

$$\Delta f = \frac{4h_l^2}{f}C \tag{4.8}$$

where f is the paraxial focal length, h_l is the height of the incident ray above the optical axis, h_{pf} is the height at which the ray strikes the paraxial focal plane, and

C is a constant for any given system. For a single thin lens in exact third-order theory, C is given by

$$C = \frac{-1}{32(n-1)^2}\left[n^2 + \frac{n+2}{n}q^2 + \frac{4(n^2-1)}{n}pq + \frac{(3n+2)(n-1)^2}{n}p^2\right] \tag{4.9}$$

where the lens shape factor, q, is a dimensionless function of the radii of curvature of the lens surfaces given by

$$q = \frac{R_2 + R_1}{R_2 - R_1} \tag{4.10}$$

and the position factor, p, is a dimensionless function of the position of the lens relative to the source and image given by

$$p = \frac{s_2 - s_1}{s_2 + s_1} = 1 - 2\frac{f}{s_2} \tag{4.11}$$

where s_1 is the lens to object distance and s_2 is the lens to image distance.

For any position factor there is an optimum lens shape that minimizes spherical aberration given by

$$q_{opt} = \frac{-2(n^2-1)}{n+2}p. \tag{4.12}$$

If the incident rays are parallel to each other then the object is considered to be at infinity, the image will be at the paraxial focal plane, and $p = -1$. This is approximately the case for a collimated laser beam. Thus, the optimum C when focusing a laser beam is given by

$$C_{opt} = -\frac{n(4n-1)}{32(n-1)^2(n+2)}. \tag{4.13}$$

The plane of best geometric focus is the plane where the image beam radius is minimized.[63] For pure third order aberration theory, this plane is located 3/4 of the way from the paraxial focus plane to the marginal ray focal plane and the beam radius is exactly 1/4 of the Lat.SA found at the paraxial focus.

The plane of best diffraction focus is the plane where the axial irradiance is maximized.[63] For pure third order aberration theory, this plane is located 1/2 of the way from the paraxial focus plane to the marginal ray focal plane and the beam radius is exactly 1/2 of the Lat.SA found at the paraxial focus.

The following formulas represent the optimum beam radius that can be obtained for focusing a collimated beam of radius r_l with a single lens subject only to spherical aberration:

paraxial focus:

$$f_{pf} = f \tag{4.14}$$

$$(\omega_0)_{opt,pf} = \frac{n(4n-1)}{8(n-1)^2(n+2)} \frac{r_l^3}{f^2} \tag{4.15}$$

diffraction focus:

$$f_{df} = f - \frac{n(4n-1)}{16(n-1)^2(n+2)} \frac{r_l^2}{f} \tag{4.16}$$

$$(\omega_0)_{opt,df} = \frac{n(4n-1)}{16(n-1)^2(n+2)} \frac{r_l^3}{f^2} \tag{4.17}$$

geometric focus:

$$f_{gf} = f - \frac{3n(4n-1)}{32(n-1)^2(n+2)} \frac{r_l^2}{f} \tag{4.18}$$

$$(\omega_0)_{opt,gf} = \frac{n(4n-1)}{32(n-1)^2(n+2)} \frac{r_l^3}{f^2} \tag{4.19}$$

A detailed description of the mutual effects of diffraction and spherical aberration is beyond this dissertation, but can be found in Born and Wolf's "Principles of Optics."[64] A conservative estimate of the final beam waist is to add the diffraction beam waist to the spherical aberration beam waist, giving

$$(\omega_0)_{d,gf} = (\omega_0)_d + (\omega_0)_{opt,gf} \tag{4.20a}$$

$$= \frac{\lambda}{\pi} \frac{f}{r_l} + \frac{n(4n-1)}{32(n-1)^2(n+2)} \frac{r_l^3}{f^2} \tag{4.20b}$$

for an optimized lens where it has been decided to use the geometric focus beam waist instead of the diffraction or paraxial focus beam waists.

The diffraction contribution to the focal spot size is an inverse function of the incident beam radius while the spherical aberration contribution increases as the cube of the beam radius. At some intermediate beam radius the focal spot size will be a minimum. If the focal length is held constant, this minimum spot size occurs for

$$r_l = \left(\frac{32(n-1)^2(n+2)}{3\pi n(4n-1)} \lambda f^3 \right)^{1/4} \tag{4.21}$$

The magnitude of these effects and an estimate of the focused beam spot size can be made. The single lens used was made from Suprasil, a high quality UV grade of fused silica. The lens was designed for minimal spherical aberration at 300 nm. At that wavelength the refractive index[63] is 1.48779 while the refractive index at 330 nm is 1.48059. This change in the refractive index of -0.48% will cause a -1.56% change in q_{opt}. Consequently, it is not suprising that the lens when operated at 330 nm will have more spherical aberration than when it is operated at its design wavelength of 300 nm: $\mathcal{C} = -0.28331$ as compared with $\mathcal{C} = -0.27739$. Inserting the appropriate constants, one can estimate that when a "best form" 100 mm Suprasil lens with a design wavelength of 300 nm is used at 330 nm the minimum beam waist will be

$$(\omega_0)_{d,gf} = \frac{1.066 \times 10^{-2}}{r_l} + 2.750 \times 10^{-5} r_l^3 \tag{4.22}$$

which will occur at a geometric focal point of

$$f_{gf} = 101.5 - 8.37 \times 10^{-3} r_l^2 \tag{4.23}$$

where all distances are in mm. Figure 8 shows the calculated beam waist radius for this lens and the contributions from diffraction and spherical aberration.

At the optimum r_l of 3.37 mm the beam waist will be $\approx 4.22 \times 10^{-3}$ mm. The actual incident beam radius of ≈ 2.4 mm will lead to a beam waist radius of 4.8×10^{-3} mm. It should be noted that only 8% of the beam spot size is a result of spherical aberration; consequently, the final result is not strongly dependent on the choice of using spherical abberation at the geometric focus instead of at the diffraction or paraxial focus.

The above analysis of beam spot size has assumed that the lens is a simple thin lens. A well designed achromatic lens is considered to be "diffraction limited" because spherical aberration is kept to a small fraction of a wavelength of light. Under these circumstances spherical aberration can be totally ignored and the beam waist at the focal point will be given entirely by Eq. 4.6. Therefore, the beam waist should be smaller if the achromatic lens is used instead of the simple lens, though the difference is small for the actual conditions employed in these experiments.

C. Experimental Cell

The experimental cell consists of three compartments. The first compartment is used to hold the Kr used as a nonlinear medium. The second compartment is where the reaction takes place and H_2 is detected by laser induced fluorescence. The third compartment is used to detect the generated VUV.

The first compartment, 4.25 in long by 1.5 in OD, is constructed of stainless steel. The entrance is a 1 in diameter, 1/16 in thick, Suprasil window with a clear aperture of 0.5 in. The window is mounted with O-rings for ease of removal for cleaning or replacement. The exit is a 1 in diameter, 1 mm thick, VUV grade LiF window with a clear aperture of 0.5 in. The short wavelength cutoff of LiF is lower than than that of any other material, with usable transparency to 104 nm.[65] This window is also mounted with O-rings. All interior surfaces are painted flat black to minimize scattered light.

The second compartment, 5.00 in long by 1.5 OD, is constructed of stainless steel and is bolted directly to the first compartment. This compartment holds the sample for spectroscopic (absorption and fluorescence) studies. Therefore, it contains a series of Al apertures to minimize scattered light. Mounted perpendicular to the cell axis is the PMT used for fluorescence experiments. The axis of the PMT is 2.0 in from the entrance window while the plane of the photocathode is 2.0 in from the optical axis. The exit from this compartment is a second LiF window mounted identically to the first. All interior steel surfaces are painted flat black to minimize scattered light, while Al surfaces are black anodized.

The third compartment, 7.75 in by 1.5 in OD, is also constructed of stainless steel and is mounted directly to the second compartment. The exit is a 1 in diameter, 1/16 in thick Suprasil window. It is mounted in a manner similiar to all the other windows except that the clear aperture is 0.65 in.

All three compartments have appropriate vacuum line connections. During experiments the cell is connected to a small glass vacuum line equipped with only a liquid nitrogen trap and a mechanical pump. This line is used to fill and evacuate the various compartments without disturbing the experimental arrangement, often while taking data. When not in use the experimental cell is connected to a glass vacuum line equipped with a 2 in oil diffusion pump. The ultimate vacuum is $\approx 3 \times 10^{-7}$ torr.

Figure 9 shows a cross section of the assembled cell. Also shown is the approximate path of the UV radiation through the cell for a 2.2 mm radius laser beam focused by a 100 mm lens located 0.75 in before the first window. This is the largest beam which can entirely clear all apertures and exit the cell.

As noted in the previous section, the estimated beam spot size is 4.8×10^{-4} cm. This implies a confocal parameter,

$$b = k\omega_0^2 \tag{3.15}$$

of approximately 4.2×10^{-2} cm. The calculations performed earlier predict a wave vector mismatch of approximately -0.0213 cm^{-1} torr^{-1} at 298 K at 110 nm. The optimum Kr pressure is then predicted to be 4500 torr at that wavelength, based on the analysis performed in the previous chapter which showed that the phase matching function is optimized for $b\Delta k = -4$.

It is possible to estimate the maximum acceptable pressure differential across the LiF windows. According to the manufacturer of the LiF,[65] the maximum pressure is

$$p_{\max} = \frac{4F_a}{K \times S}\left(\frac{t}{D}\right)^2 \tag{4.23}$$

where F_a is the flexural apparent elastic limit, t and D are the thickness and unsupported diameter of the window, K is constant depending on the method of mounting the window, and S is a safety factor. This maximum pressure is not the pressure that will cause the window to catastrophically fail but is rather the pressure at which the elastic deformation of the window could permanently alter the optical properties. For the LiF windows mounted in this cell, $F_a = 1580$ psi, $K = 1.125$ and $t/D = 0.0787$, the maximum pressure is

$$P_{\max} = \frac{1750}{S}\text{torr}. \tag{4.24}$$

Therefore, it would not be prudent to use pressures as high as 4500 torr, the estimated optimum pressure for generation of 110 nm. The Suprasil windows used on the first and third compartments are much stronger and thicker than the LiF, so it is believed that these windows will have no difficulty withstanding the pressures involved.

The third compartment is an ionization cell used to detect the generated VUV radiation. Several gasses could be used as the detection medium. Carver and Mitchell[66] investigated several gasses; NO, acetone, carbon disulphide, ethyl

bromide, and ethyle chloride. NO had the greatest sensitivity at wavelengths below 115 nm, although there was some structure on the response curve. Ethyl chloride had the most featureless response curve, but the absolute sensitivity was only 20% of that for NO.

Many ionization chambers consist of a central electrode surrounded by a second electrode. This configuration would be unacceptable for these experiments because the high intensity of UV radiation used to generate the VUV radiation would produce photoelectrons if any electrode were in the laser beam. Instead, a parallel plate electrode assembly is used. The electrodes are approximately 15.8 cm by 1.7 cm by 0.08 cm Ni plates. The side facing the laser beam is covered with 0.025 mm thick Pt foil to reduce the number of photoelectrons from the UV radiation. At each end the electrodes are mounted on a teflon spacer with a clear aperture of 1.9 cm. The total electrode separation is 2.5 cm. The electrode assembly is further wrapped in teflon to prevent the electrodes from contacting the grounded cell and to prevent any scattered laser radiation from reaching the stainless steel walls of the cell.

NO has been extensively studied. The ionization potential[67] is 74721.5 $\pm$ 0.5 cm^{-1}; therefore, only photons with a wavelength below 133.83 nm can lead to a single photon photoionization process while only photons below 267.7 nm can lead to a two photon photoionization process.

The photoabsorption cross section has been measured by Guest and Lee[68] in the wavelength interval 200.0–106.0 nm, by Watanabe *et al.*[69] in the interval 135.0–58.0 nm, and by Metzger[70] in the interval 95.0–60.0 nm. The electron energy loss spectrum has been studied by Vichon *et al.*,[71] Frueholz *et al.*,[72] and by Stubbs *et al.*[73]

The states above 12 eV are predominantly Rydberg states converging to excited electronic states of the NO^+ ion. These states have been classified by

Edqvist *et al.*[74] The region between 11 and 12 eV is especially complex, with many features which cannot be reconciled with Rydberg transitions. This is the region in which the VUV is to be generated in these experiments. There are features at 112.70, 110.97, 108.61, 108.16, 107.78, and 106.51 nm.

The expected response of the NO ionization cell is a function of the cell geometry and the properties of NO. Specifically, the charge collected per laser pulse is[75]

$$Q = \kappa e \phi \times \left(1 - \mathrm{e}^{-N\sigma z_2}\right) \times \mathrm{e}^{-N\sigma z_1} \tag{4.25}$$

where Q is the total charge, κ is the electron detection efficiency, e is the charge on an electron, ϕ is the ionization quantum yield, N is the NO number density, σ is the absorption cross section, and z_2 and z_1 are the electrode length and the distance from the entrance to the electrodes. This formula can be thought of as follows: the right-hand term gives the fraction by which the incident photon flux is reduced before reaching the electrodes, the central term gives the fraction of photons which are absorbed by NO within the electrode assembly, and the left-hand term gives the fraction of absorbed photons which lead to ionization to give a detectable charge. Because the electrodes do not start at the beginning of the cell, there is an optimum NO number density given by

$$N_{opt} = \frac{1}{\sigma z_2} \ln\left(\frac{z_2 + z_1}{z_1}\right). \tag{4.26}$$

At higher densities all the photons will be absorbed before the electrodes while at lower densities none of the photons will be absorbed.

The average absorption cross section is 4.811×10^{-18} cm^2 over the wavelength interval 112.0–109.0 nm using the data of Watanabe *et al.*[69] The electrodes are 15.8 cm long and the gap between the electrodes and the entrance is 2.0 cm. Appropriate substitution gives $N_{opt} = 2.88 \times 10^{16}$ cm^{-3} which is equivalent to a pressure of 0.889 torr at 298 K. Figure 10 shows the expected wavelength

response of the NO ionization cell in the interval 113–108 nm when it is operated with this optimum NO pressure, assuming that the collection efficiency is unity. Considering that the absorption cross section varies by a factor of 3.7 over this region the expected spectral response is quite flat. In the central regions of this wavelength interval the response is very flat, varying by less than 10%. The average response over the interval 109–112 nm is $(8.67 \pm 0.52) \times 10^{-8}$ pC/photon or $(1.15 \pm 0.08) \times 10^{7}$ photons/pC.

D. Reagents

The dyes DCM and Rhodamine 590 were purchased from Exciton Chemical. They were dissolved in reagent grade DMSO and/or spectroscopic grades of methanol or ethanol.

The nonlinear medium used is Kr. Research grade, 99.995%, Kr from Alpha Products is used. The Kr cylinder is connected directly to the small vacuum line mounted on the laser table. Kr is withdrawn from the cylinder as needed without further purification.

NO is used as the ionizing medium in the ionization cell. C.P. grade, 99.0%, NO from Matheson gas products is used. Before use it is purified by a series of vacuum distillations. First, there are a series of freeze/pump/thaw cycles using liquid nitrogen (77 K). This eliminates gases such as O_2, N_2, and other non-condensibles. The sample is then warmed to 90 K using a isopentane/liquid nitrogen slush, the vapors being collected in a second flask kept at 77 K. The heavier nitrogen oxides are trapped behind. The purified NO is stored in a blackened glass bulb at room temperature.

The pressure reading devices on both vacuum lines were designed for measuring differential pressures as high as 2 atm and are not well suited to reading pressures as low as 0.8 torr with a high degree of accuracy. A 10.0% NO in He mixture was prepared using high purity grade, 99.995%, He from Matheson. This mixture

was prepared infrequently from the purified NO and stored in a blackened glass flask. 8.8 torr of this mixture was used to fill the ionization cell on each day of experiments.

E. Electronics and Data Acquisition

This section describes the electronics used to process the raw signal and the data acquisition procedures. Fig. 11 is a diagram of the electronics. For the VUV generation experiments described in this chapter, two channels of data are collected: the output from the NO ionization chamber and the output from the pyroelectric joulemeter, PEJM. The former channel is the VUV signal channel, abbreviated as VUV, while the latter channel is the UV incident laser intensity channel, abbreviated as UV.

The NO ionization chamber is used to measure the VUV photon flux, the total charge detected during each laser pulse being directly proportional to the number of VUV photons as can be seen from Eq. 4.25. The electrons produced during the photoionization are collected by the parallel plate electrode assembly described earlier which is biased with 47 V, producing a current pulse. One of two charge sensitive preamplifiers is used to integrate the current pulse to give an output voltage pulse proportional to the total charge produced in the cell. The first of these preamplifiers was a Canberra model 2001A spectroscopy preamplifier. This device has a nominal sensitivity of either 2 V/pC or 10 V/pC with a maximum output of 10 V (implying a 5 pC limit). The second preamplifier was a homebuilt charge sensitive preamplifier based on a LeCroy TRA1000 monolithic circuit. With a 47 pF feedback capacitor, the design sensitivity is 21.3 mV/pC with a maximum output of 1 V (implying a 47 pC limit). Calibration with current pulses as short as 4 ns showed that the sensitivity (95% confidence levels, 33 pts) was 20.90 ± 0.33 mV/pC and 22.90 ± 0.31 mV/pC for the inverted and noninverted outputs, respectively. Both preamplifiers had an approximately 50 μs decay time on the output falling

edge. Most of the work reported in this chapter used the inverted output of homebuilt preamplifier. A more detailed discussion of this amplifier is contained in Appendix II.

The pyroelectric joulemeter is used to measure the incident UV laser pulse energy. The output of the probe is a voltage pulse, the maximum amplitude of which is proportional to the energy absorbed by the probe surface. The probes are connected to readout units which, besides supplying power, determine the maximum voltage amplitude following an external trigger and convert this reading into appropriate units for display, *i.e.*, J, mJ, or μJ per pulse. The displays are updated after each individual pulse or after 10 or 100 pulse averages. In addition, the readout units also buffer the pulse from the probe for a "direct output."

The signals from the charge sensitive preamplifier and the PEJM "direct output" are further amplified by either an inverting 10× homebuilt amplifier based on an AD528 op amp (DC–50 MHz bandwidth) or a Molectron model 131 Amplifier/Shaper (DC–1.6 MHz bandwidth). The signals from the amplifiers are then "integrated" by a pair of Molectron model 112 Differential Gated Integrator, one for each channel of data collection. This device consists of a matched pair of RC integrators which are active only during an externally supplied gate. Gate 1 is normally adjusted to measure the signal pulse while gate 2 is normally adjusted to measure the signal baseline. The output is the differential response between the outputs of the gate 1 integrator and the gate 2 integrator. A more detailed discussion is contained in Appendix II.

The data is collected by an Intel SBC 80/20 single board computer. An Analog Devices RTI-1200 real time interface equipped with a programmable gain amplifier, a sample and hold amplifier, and a 12 bit A/D converter is used to digitize the *VUV* and *UV* channel outputs from the gated integrators. The result of each data acquisition is displayed on an X-Y plotter. After each scan is complete the

data is transferred to 8 in floppy disk for later analysis on the divisional Digital VAX 11/780 minicomputer. A further discussion on the computer systems is contained within Appendix II.

IV. EXPERIMENTAL RESULTS FOR THG

In this section the experimental results for THG are presented. Three types of experiments were performed: VUV signal as a function of Kr pressure, VUV signal as a function of incident UV laser pulse energy, and VUV signal as a function of incident UV laser wavelength. All three experiments were originally performed with the Molectron dye laser system; however, after the acquisition of the Quanta Ray dye laser system they were repeated.

The factors which influence the THG conversion efficiency were determined in Ch. 3. The principal result for a general four-wave mixing process is Eq. 3.63. When specialized to THG in a single component gas, the result is

$$E_{VUV} = 4.82 \times 10^{74} \times \left| \frac{p\chi^{(3)}}{T} \right|^2 \times \frac{E_{UV}^3}{\tau_{UV}^2 \lambda_{VUV}^4} \times \Phi \qquad 4.27$$

which can be further reduced to

$$E_{VUV} = 4.76 \times 10^{75} \times \left| \frac{\chi^{(3)}}{Tb\alpha} \right|^2 \times \frac{E_{UV}^3}{\tau_{UV}^2 \lambda_{VUV}^4} \times (bp\alpha)^4 e^{bp\alpha} \qquad 4.28$$

if it is assumed that the incident laser beam is in a TEM_{00} mode and the tight focusing limit is reached. In these equations, E is the pulse energy in mJ, $\chi^{(3)}$ is the non-linear susceptibility in ESU/atom, T is the gas temperature in K, b is the incident confocal parameter in cm, α is the wave-vector mismatch in $cm^{-1}\,torr^{-1}$, τ is the temporal width of the incident laser beams in nsec, λ is a wavelength in nm, and p is the gas pressure in torr.

A. VUV Signal vs. Kr Pressure

The first experiments were concerned with measuring the VUV signal as a function of the Kr pressure at a fixed wavelength. The goal was to determine the optimum conditions for generating VUV radiation.

In these experiments data was collected at a rate of 100 pts/min. Every 2 min the Kr pressure in the first compartment was adjusted. In a typical 1 hr experiment the pressure would be varied from 0 to $\approx$ 2000 torr and back to 0 two times.

The data analysis proceeded through several steps. First, the effects of drifting UV laser intensity, $UV(t)$, were eliminated. This was accomplished by assuming that the observed time, t, and pressure, p, dependent signal from the NO ionization cell, $VUV(p,t)$, is composed of a VUV signal term cubic in $UV(t)$ and a pressure independent background term linear in $UV(t)$. The corrected signal, $VUV'(p,t)$, is given by

$$VUV'(p,t) = VUV(p,t)\frac{\langle UV\rangle^3}{UV(t)^3} + \alpha(t)\langle UV\rangle\left(1 - \frac{\langle UV\rangle^2}{UV(t)^2}\right) \tag{4.29}$$

where $\langle UV\rangle$ is the average UV pulse energy during the experiment and $\alpha(t)$ is the average background function determined by a linear least squares fitting procedure to $VUV(p=0,t)/UV(t)$ vs. t.

Second, the data from each 2 min time interval of constant pressure is averaged together, giving the average signal and its standard deviation, $VUV'(p,\bar{t})$ and $\sigma_{VUV'(p,\bar{t})}$.

Third, the pressure and time dependence of $VUV'(p,\bar{t})$ was determined. From Eq. 3.87, the phase matching factor, Φ'_{tf}, for a TEM_{00} incident laser beam when the pressure of a single gas is adjusted to provide phase matching is given by

$$\Phi'_{tf} = \begin{cases} \pi^2(b\Delta k)^4 e^{b\Delta k}, & \text{if } b\Delta k < 0, \\ 0, & \text{if } b\Delta k \geq 0, \end{cases} \tag{3.87}$$

where b is the confocal parameter and Δk is the wavevector mismatch. In most circumstances it can be assumed that Δk is a linear function of the pressure, *i.e.*, $\Delta k = \alpha p$. It is therefore assumed that the observed signal can be fit by the following equation:

$$VUV'(p,\bar{t}) = \left(a_1 + a_2 p^{a_3} e^{-a_4 p}\right)(1 - a_5\bar{t}). \tag{4.30}$$

The a_1 coefficient represents any pressure independent background, the a_2, a_3, and a_4 coefficients represent the VUV signal, and the $1 - a_5\bar{t}$ term corrects for the generally small drift in signal as a result of a decrease in window transmission. The coefficients are found by a weighted nonlinear least squares analysis using the Simplex or Marquardt algorithms. Each point is weighted in the usual manner by $1/\sigma^2$.

Figure 12 is a representative result from a VUV signal as a function of Kr pressure experiment. The displayed data has already been corrected for the changes in UV intensity (-7.7%) and window transparency (-0.44%) during the hour long experiment. The dye laser was operated at a wavelength of 660.00 nm in air, giving a VUV wavelength of 110.03 nm. The average UV pulse energy for this experiment was 7.59 mJ/pulse. The solid line is the least squares fit using Eq. 4.30. The fit is seen to be exceptionally good. The dashed line is that of Eq. 3.87 adjusted so that the background and maximum agrees with that found from the least squares analysis. It is seen that the two curves are almost identical. From the fit it is possible to determine that the maximum signal of 14.7 pC/ pulse ($\approx 1.69 \times 10^8$ photons/pulse or 0.305 nJ/pulse) occurs at a Kr pressure of 1120 torr. The background was 1.08 pC/pulse, only 6.8% of the total. From a set of 6 experiments it was possible to determine that the optimum pressure at this wavelength with this apparatus is 1115 ± 43 torr (95% confidence level).

This data can be used provide an estimate of the confocal parameter, b. For an incident laser beam consisting of a pure TEM_{00} mode, the VUV intensity maximizes for $b\Delta k = -4$. Using the observed optimum pressure and the previously calculated α, it is possible to determine b. α is not strictly independent of p since refractive indices are a nonlinear function of p (see Eq. 3.94); however, at 110.03 nm α varies by only 3% for pressures from 0 to 10,000 torr. Using the value

of $\alpha = 0.02370\,\mathrm{cm}^{-1}\,\mathrm{torr}^{-1}$ calculated at 110.03 nm for 1000 torr at 298 K, the final calculated result is $b = 0.151 \pm .006$ cm.

A major problem with using the above method for determining b is that it assumes a perfect TEM_{00} mode. Yiu *et al.* studied the phase matching for incident beams in a $\mathrm{TEM}_{\rho l}$ mode (cylindrical symmetry, see Eq. 3.22). If the incident radiation is in a pure azimuthal mode, TEM_{0l}, than the optimum still is at $b\Delta k = -4$; however, the efficiency decreases as l increases. If the incident radiation is in a pure radial mode, $\mathrm{TEM}_{\rho 0}$, then the optimum occurs for $b\Delta k = -4$, -13, and -22.7 for $\rho = 0$, 1, and 2; the efficiency increases as ρ increases for the cases they studied. If the incident radiation is either mixed mode or multi-mode then there is no simple analytical expression for the phase-matching factor and the optimum $b\Delta k$.

The confocal parameter can also estimated from knowledge of the incident laser beam. The beam profile is not circularly symmetric, but rather is elliptical with the region of maximum intensity offset from the center. A burn pattern showed that the semi-major axis was ≈ 2.8 mm and the semi-minor axis was ≈ 2.2 nm. A knife-edge test along the major axis gave $1/e$ semi-major axes of 1.9 and 2.9 mm, illustrating the side to side asymmetry of the intensity distribution. It is estimated that $b = 0.064$ cm using Eqs. 4.22 and 3.15 with the smaller knife edge "radius" of 1.9 mm.

These two calculations of b agree to within a factor of 2.5. This is a very good agreement under the circumstances. First, both calculations assume that the incident laser beam is adequately described as a Gaussian TEM_{00} mode. This is known to not be the case. Second, the value of b calculated from the VUV signal vs. Kr pressure data requires an external source for the wave-vector mismatch per unit pressure, α . The value of α at 110.03 nm is very small because of the near equality of the refractive index at 110 and 330 nm. Consequently, α is extremely

sensitive to the inputs to the refractive index calculation described earlier. For example, a 5% increase in the oscillator strength for the 116 nm line (well within the experimental errors) would cause a 43% increase in $|\Delta k|$ at 110.03 nm.

In summary, these experiments have examined the VUV intensity as a function of Kr pressure. The observed results have a functional form close to that predicted. The value of the confocal parameter, b, calculated from the optimum Kr pressure is within a factor of 2.5 of that calculated from measurements of the incident laser beam and geometrical optics.

B. VUV Intensity vs. UV Intensity

The second set of experiments was concerned with measuring the VUV intensity as a function of UV pulse energy at a fixed Kr pressure and a fixed laser wavelength. It is expected that there will be a cubic relationship in the absence of competing processes and saturation effects.

In these experiments the same laser wavelength was used as for the previously described VUV signal vs. Kr pressure experiments. Data was collected at a rate of 100 pts/min. The gated integrator time constants were chosen short enough that the recorded data has contributions from only the most recent one or two laser pulses in order to reduce the artifacts introduced by smoothing. By varying the number of Schott UG-11, Corning 7-54, and Corning 7-39 UV transmitting filters placed after the WEX, it was possible to vary the UV pulse energy by a factor of 16 without introducing major changes in the beam intensity distribution.

Figure 13 shows typical experimental results. The UV pulse energy was varied from 0.5 to 5 mJ/pulse, a factor of 10. The VUV signal varied from 1 fC/pulse to 10 pC/pulse, a factor of 1000.

The data was analyzed by several methods. First, it was assumed that the VUV signal was entirely the result of a single process with an unknown dependency

on the UV pulse energy, *i.e.*,

$$VUV(t) = a_1 UV(t)^{a_2}. \qquad 4.31$$

where $VUV(t)$ is the VUV signal in pC/pulse and $UV(t)$ is the UV pulse energy in mJ/pulse.

Assuming this functional form, two methods were used to obtain least squares fits to the data. The first involved an appropriately weighted linear least squares fit following a logarithmic transformation of the data, yielding $\ln a_2 = -2.552 \pm .065$ and $a_2 = 3.011 \pm .044$ (95% confidence levels). This curve gives the solid line line in the figure. The second involved a nonlinear least squares fit, yielding $a_1 = 0.0516 \pm .004$ and $a_2 = 3.233 \pm .056$. This curve gives the dashed line in the figure.

However, as good as these fits appear, it is known that there is a small background to the VUV signal, see Fig. 12 for example, which is assumed to be dependent on the UV pulse energy. It was decided to perform several other nonlinear least squares fits to slightly different functional forms which included background correction terms. The results are as follows:

$$VUV(t) = -(0.064 \pm .044) + (0.0570 \pm .0065)UV(t)^{3.166 \pm 0.073} \qquad 4.32a$$

$$= (0.31 \pm .15) - (0.45 \pm .19)UV(t)^1 + (0.148 \pm .052)UV(t)^{2.69 \pm .14} \qquad 4.32b$$

$$= (0.16 \pm .11) - (1.1 \pm 1.8)UV(t)^2 + (1.0 \pm 1.7)UV(t)^{2.26 \pm .32} \qquad 4.32c$$

$$= (0.23 \pm .44) - (0.3 \pm 1.4)UV(t)^1 - (0.2 \pm 2.7)UV(t)^2 + (0.3 \pm 1.8)UV(t)^{2.5 \pm 1.7} \qquad 4.32d$$

All of these fits contain background terms which are physically unrealistic, as they predict negative signal levels near the smallest $UV(t)$'s. In addition, in many cases the 95% confidence limits are larger than the parameter. Apparently, the scatter in the data precludes an accurate determination of the background.

The three fits with the smallest confidence limits gave values of $3.011 \pm .044$, $3.166 \pm .073$, and $3.233 \pm .056$, with a weighted average of 3.11, for the exponent on $UV(t)$. If all six fits were included, then the weighted average is 3.08. All of these fits are reasonably close to the expected exponent of 3. There are several explanations as to the source of the deviation from the expected value. First, if the time constant of the gated integrator was too long, then each data point would represent a weighted average of the previous laser pulses. Under these circumstances, it would not be possible to accurately determine the relationship because $\langle VUV/UV^n \rangle \neq \langle VUV \rangle / \langle UV \rangle^n$. The actual time constant was approximately equal to the time between laser pulses, so it is expected that there was very little smoothing. Second, there is a large amount of scatter in the data caused by fluctuations in the UV laser beam modes and phases which is not accounted for. This makes it difficult to correct for the slight amount of background which is important at lower UV pulse energies. Third, and most likely, there is the possibility that competing processes could become important at higher pulse energies. If the THG process was saturating, for example, then the VUV signal would no longer be cubic in the UV pulse energy, but would increase at a slower rate. Alternatively, if a process such dielectric breakdown became predominant, the signal would appear to increase at a faster rate because the NO ionization cell is sensitive to the radiation emmitted by the plasma recombination.

In summary, the VUV signal increases with the 3.08 power of the UV pulse energy. This is reasonably close to the value of 3 that was expected for THG.

B. VUV Signal vs. VUV Wavelength

The third set of experiments was concerned with measuring the VUV signal as a function of VUV wavelength at several fixed Kr pressures. The goal was to determine the optimum conditions for taking VUV spectra. The optimum conditions involve a trade-off between VUV intensity and tuning range.

Eq. 4.28 gives the expected VUV signal as a function of experimental conditions and properties of the nonlinear medium. Many of these factors are wavelength dependent; specifically, λ, E_{UV}, b, α, and $\chi^{(3)}$. For illustrative purposes, the magnitude of the variation of these factors in going from 110 to 112 nm will be considered. This is the interval of a typical scan and consists of a change of only 1.8% in wavelength. b will have the smallest wavelength dependence over this interval, changing by only -1.8%. The variation of E_{UV} with wavelength depends on several factors, most noticeably the tuning curve of the dye laser solutions, the efficiency of the autotracking on the WEX, and the transmission of all the optics. By careful manipulation of the composition of the dye solutions and by careful tuning of the WEX it is possible to get a UV laser beam in which the pulse energy varies by less than 10% over the wavelength interval 327 to 339 nm. Even so, this could still cause a 30% variation in VUV intensity. The optics between the WEX and the Kr cell are all made of UV grade fused silica (Suprasil) which has a short wavelength cutoff near 160 nm. It is highly unlikely that these optics will have a significant variation in transmission over the narrow wavelength region being considered. On the other hand, the LiF windows, which are located between the first and second and between the second and third compartments, have a short wavelength cutoff near 104 nm. Consequently, it is expected that the LiF windows would have an increase in transmission in going from 110 to 112 nm.

The factor with the largest uncertainty as to its wavelength dependence is $\chi^{(3)}$. As mentioned earlier, it was not possible to accurately calculate this quantity because of a lack of information on the relative phases of the matrix elements involved in the calculation. However, it is possible to show the direction of the wavelength dependency. It is safely assumable that the contribution of the one and two photon virtual states will be essentially unchanged over such a small wavelength interval since these virtual states are well removed from any actual

states with which they may couple. However, the three photon virtual states are in close proximity to the strong absorption line at 116.49 nm; consequently, it is expected that $\chi^{(3)}$ will be much larger at 112 nm than at 110 nm. Indeed, the contribution of the 116.49 nm term to the $\chi^{(3)}$ calculation increases by 47% in going from 110 to 112 nm. However, a more detailed analysis of the wavelength dependence of $\chi^{(3)}$ requires a knowledge of the phase of the various matrix elements, which are unknown.

The factor which apparently has the greatest variability with wavelength is α, the wave-vector mismatch per unit pressure. According to the calculations described earlier, α will vary from -0.0213 cm^{-1} torr^{-1} to -0.1582 cm^{-1} torr^{-1} in going from 110 to 112 nm, a change of 650%. As a consequence, the optimum pressure will drastically change between these two wavelengths, from 1240 torr to 170 torr (calculated with $b = 0.151$ cm), a decrease of 87%.

Including all of these factors, one finds that the ratio of maximum VUV intensity between these two wavelengths is expected to be:

$$\frac{E_{110}}{E_{112}} \approx 57 \times \frac{\left|\chi^{(3)}_{110}\right|^2}{\left|\chi^{(3)}_{112}\right|^2} \times \left(\frac{E_{330}}{E_{336}}\right)^3 . \qquad 4.33$$

Figure 14 shows the predicted VUV tuning curves for THG in Kr calculated for a confocal parameter $b = 0.151$ cm, under the assumption that $\chi^{(3)}$ and E_{UV} are constant, over the wavelength interval 109.5 to 112 nm for various Kr pressures. As expected, the maximum signal gets larger and shifts to shorter wavelengths as the Kr pressure increases. In addition, the tuning range decreases dramatically, with a FWHM of yy nm at 400 torr and only xxx nm at 2000 torr.

Figure 15 shows the experimental results after corrections for changes in UV laser pulse energy. Several features are immediately apparent. First, the short wavelength cutoff, *i.e.*, the point at which α=0, is $\approx$ 109.57 nm. This result

compares quite well with the predicted value of 109.63 nm. Second, the decrease in signal at increasing wavelength is not as great as had been predicted in Fig. 14, most likely because of an increase in $\chi^{(3)}$ as the 116.49 nm line is approached.

Third, the tuning curves are not smooth, but show some structure. The strong dips in intensity at 111.07 nm and at 109.97 nm are almost certainly the result of the Xe impurity in the Kr. Xe has absorption lines at 90032.65 $cm^{-1}(6d[3/2]_1^o, f \approx 0.097)$ and at 90932.94 $cm^{-1}(8s[3/2]_1^o, f \approx 0.026)$ which are at the same position as the dips. Xe will influence the VUV signal not only by absorbing VUV photons but by also changing α and $\chi^{(3)}$ because of resonance enhancement near the absorption lines. The observed width of these features becomes quite broad and asymmetric at high pressures. Since most of the effects of Xe are expected to be roughly symmetric around the line center, it is hypothesized that XeKr dimers are also present in the system, with transition energies located slightly below those of Xe. Such dimers are known to exist, but the observed spectra taken to date are at wavelengths above 115 nm. These dimer absorption lines are generally located at energies just below the Xe absorption lines.

The behaviour near 109.71 nm (91150 cm^{-1}) is unusual. It is not certain whether there is an absorption at energies slightly below this level or an increase in VUV intensity at energies slightly above this level, or a combination of both. This feature is not the result of a dipole allowed transition in Ar, Kr, Xe. The $5p[1/2]_1$ state of Kr at 91169.3 cm^{-1}or the $5d'[5/2\_2^o$ state of Xe at 91153.2 $cm^{-1}$are both nearby, so it is hypothesized that one of them is responsible for either a Kr_2 or XeKr molecule with an allowed transition in this vicinity. No attempt was made to differentiate between the two possible molecules.

In conclusion, the VUV signal as a function of wavelength generally follows the pattern expected, with the exception of a greater tuning range for any given Kr pressure. The features seen in the tuning curves are believed to be the result

of absorption by the Xe impurity and by Kr_2 and XeKr van de Waals complexes formed at the high pressures used.

V. EXPERIMENTAL RESULTS FOR $(2(2)+1)\omega$

In this section the experimental results for the $(2(2)+1)\omega$ process, *i.e.*, $\omega_{VUV} = 2\omega_{UV} + \omega_{VIS} : \omega_{UV} = 2\omega_{VIS}$. The expected VUV signal level is given by

$$E_{VUV} = 5.81 \times 10^{75} \times \frac{\left|p\chi^{(3)}\right|^2}{T^2\lambda_{VUV}^4} \times \frac{E_{VIS}E_{UV}^2}{\tau_{VIS}^2} \times \Phi \qquad (4.34)$$

where the symbols have all been previously defined.

The $(2(2)+1)\omega$ process is expected to be more efficient than THG for several reasons. First, one of the laser pulse energy terms is for the dye laser fundamental, which is more intense than the second harmonic. Second, the dye laser will be operated at $\approx$ 555 nm with the dye Rhodamine 590 which is a more efficient dye than DCM, which was used for THG. Since the increase in dye laser efficiency is $\approx$ 50%, and since the doubling crystals are approximately 20% efficient, it is expected that the $(2(2)+1)\omega$ process could generate approximately 16 times as much VUV laser radiation as the THG process, all other factors being equal.

The experiments in this section were performed with the Molectron dye laser system. The focusing lens used was the 100 mm UV-VIS achromatic lens that has been described earlier.

A. VUV Signal vs. Kr Pressure

The first experiments were concerned with measuring the VUV signal as a function of the Kr pressure at fixed wavelength. The goal was to determine the optimum conditions for generating VUV radiation by the $(2(2)+1)\omega$ process.

The procedure followed was similiar to that used previously to study the THG process. Because two different laser intensities are involved, and because it was not possible to measure both intensities simultaneously, no attempt was made to normalize the data for changes in laser intensity.

Figure 16 shows a typical experimental result, taken with the dye laser operated at 560.0 nm, implying a VUV wavelength of 112.03 nm. Several features

are immediately obvious. First, the background of 5 pC/pulse is a large fraction of the total observed signal, approximately 56% of the maximum signal. The source of this large background is not known, although it is believed to arise from the the photoelectric effect. The background is not entirely the result of multiphoton ionization of the NO within the ionization cell since the background more than doubles when the NO/He gas mixture is evacuated. However, the only materials within the ionization cell facing the laser radiation are Pt (work function of 5.6 eV), and the insulators Teflon, quartz, and LiF.

Second, the peak VUV signal of approximately 4 pC/pulse (4.60×10^7 photons/pulse or 83.1 pJ/pulse) occurred at 190 torr Kr. This signal level is significantly above that produced by THG at the same wavelength. This confirms the increased efficiency of the $(2(2)+1)\omega$ process compared with the THG process.

Third, at pressures above 300 torr the VUV signal starts to increase to levels above the optimum. This increase is the result of dielectric breakdown occurring within the Kr, as evidenced by wild swings in the output from the NO ionization cell accompanied by visible flashes of light and an audible pinging sound.

The phase matching factor, Φ, is in general a much more complicated function for the $(2(2)+1)\omega$ process then for the THG process. Only in the case of equal confocal parameters, b, for the visible and ultraviolet laser radiation is Φ given by Eq. 3.87. Otherwise, the much more complicated double integral given by Eq. 3.58 must be used. The data was fit to Eq. 4.29, giving the solid line in Fig. 16. The fit is seen to be adequate. The a_3 coefficient was found to be 1.98, which is significantly below the 3.54 seen for THG and the theoretical 4.0 in Eq. 3.87. This illustrates that the $(2(2)+1)\omega$ process definitely does not behave as if the two laser beams have equal confocal parameters.

B. VUV Signal vs. VUV Wavelength

The second set of experiments was concerned with measuring the VUV signal as a function of VUV wavelength at several fixed Kr pressures. The goal was to determine the optimum conditions for taking VUV spectra, which will involve a consideration of both VUV intensity and tuning range.

It was expected that the $(2(2)+1)\omega$ process would be superior to the THG process in terms of VUV intensity, as was found. Unfortunately, the VUV tuning range was greatly diminished for two reasons. First, the tuning curve for Rhodamine 590 dye solutions shows a sharp drop in power near 555 nm; consequently, it was not possible to generate VUV radiation below 111 nm with the $(2(2)+1)\omega$ process. Second, and more importantly, the VUV tuning curves had very broad and intense dips in intensity. This problem was eventually traced to a failure of the Molectron DL-18 doubling crystal to maintain accurate phase-matching. If the crystal angle is just a slight amount off from the optimum then the UV laser beam will exit the crystal with an slight angle relative to the visible radiation. This shift in angle causes the UV focal point to be shifted laterally with respect to the visible focal point, causing a large drop in VUV intensity.

Because of the difficulties in obtaining a usable VUV tuning range with the $(2(2)+1)\omega$ process and the Molectron dye laser system, this process was abandoned. No attempt has been made to repeat these experiments using the auto-locking feature of the Quanta-Ray WEX doubling system.

TABLE 1. Discrete Spectrum of Ar

State	λ	f
$4s[3/2]_1^o$	106.6660	0.0645
$4s'[1/2]_1^o$	104.8220	0.2503
$3d[1/2]_1^o$	89.4310	0.0010
$5s[3/2]_1^o$	87.9948	0.0280
$3d[3/2]_1^o$	87.6058	0.0930
$5s'[1/2]_1^o$	86.9754	0.0117
$3d'[3/2]_1^o$	86.6801	0.1000
$4d[1/2]_1^o$	84.2806	0.0040
$6s[3/2]_1^o$	83.5001	0.0094
$4d[3/2]_1^o$	83.4390	0.0480
$4d'[3/2]_1^o$	82.6364	0.0150
$6s'[1/2]_1^o$	82.5345	0.0224
$5d[1/2]_1^o$	82.0123	0.0030
$7s[3/2]_1^o$	81.6463	0.0140
$5d[3/2]_1^o$	81.6231	0.0230

TABLE 2. Discrete Spectrum of Kr

State	λ	f
$5s[3/2]_1^o$	123.5838	0.2048
$5s'[1/2]_1^o$	116.4867	0.1863
$4d[1/2]_1^o$	103.0022	0.0050
$4d[3/2]_1^o$	100.3550	0.0733
$6s[3/2]_1^o$	100.1060	0.1470
$5d[1/2]_1^o$	96.3374	0.0139
$4d'[3/2]_1^o$	95.3403	0.0430
$6s'[1/2]_1^o$	95.1055	0.0103
$5d[3/2]_1^o$	94.6536	0.1240
$7s[3/2]_1^o$	94.5441	0.0530
$6d[1/2]_1^o$	92.8710	0.0833
$6d[3/2]_1^o$	92.3712	0.0323
$8s[3/2]_1^o$	92.2738	0.0240
$7d[1/2]_1^o$	91.4554	0.0003
$7d[3/2]_1^o$	91.1670	0.0110
$9s[3/2]_1^o$	91.0918	0.0080
$8d[1/2]_1^o$	90.6697	0.0042
$8d[3/2]_1^o$	90.4862	0.0001
$10s[3/2]_1^o$	90.4004	0.0044
$5d'[3/2]_1^o$	90.3071	0.0289
$7s'[1/2]_1^o$	90.0876	0.0095
$9d[1/2]_1^o$	90.0313	0.0037
$9d[3/2]_1^o$	89.9651	0.0172
$11s[3/2]_1^o$	89.9515	0.0068
$10d[1/2]_1^o$	89.7435	0.0005
$10d[3/2]_1^o$	89.6698	0.0052
$12s[3/2]_1^o$	89.6568	0.0019
$11d[1/2]_1^o$	89.5108	0.0003

TABLE 3. Discrete Spectrum of Xe

State	λ	f
$6s[3/2]_1^o$	146.9612	0.2504
$6s'[1/2]_1^o$	129.5588	0.1958
$5d[1/2]_1^o$	125.0210	0.0135
$5d[3/2]_1^o$	119.2037	0.3903
$7s[3/2]_1^o$	117.0413	0.0989
$6d[1/2]_1^o$	112.0310	0.0023
$6d[3/2]_1^o$	111.0713	0.0971
$8s[3/2]_1^o$	109.9716	0.0255
$7d[1/2]_1^o$	108.5441	0.0232
$7d[3/2]_1^o$	107.8584	0.0022
$9s[3/2]_1^o$	107.0411	0.0035
$5d'[3/2]_1^o$	106.8168	0.1955
$8d[1/2]_1^o$	106.1256	0.0078
$8d[3/2]_1^o$	105.6128	0.1160
$10s[3/2]_1^o$	105.4996	0.0177
$9d[1/2]_1^o$	105.0107	0.0042
$9d[3/2]_1^o$	104.7136	0.0625
$11s[3/2]_1^o$	104.6123	0.0025
$7s'[1/2]_1^o$	104.3834	0.0290
$10d[1/2]_1^o$	104.2613	0.0035
$10d[3/2]_1^o$	104.1170	0.0386
$12s[3/2]_1^o$	104.0336	0.0050
$11d[1/2]_1^o$	103.8259	0.0005
$11d[3/2]_1^o$	103.7087	0.0250
$13s[3/2]_1^o$	103.6476	0.0023
$12d[1/2]_1^o$	103.5022	0.0005
$12d[3/2]_1^o$	103.4184	0.0160
$14s[3/2]_1^o$	103.3724	0.0014

TABLE 4. Wavelength Regions in Which $\Delta k < 0$[a,b]

Species	From	To			
		Current Results		Previous Results	
		THG	$(2(2)+1)\omega$	THG	$(2(2)+1)\omega$
Xe	146.961–	140.31	140.24	140.1[c]	
				140.3[e]	
	129.559–	126.73	126.70	126.7[c]	126.6[d]
	125.021–	124.74	124.74		
	119.204–	117.53	117.52	117.6[c]	117.2[d]
	117.041–	113.54	113.50	113.5[c]	113.4[d]
	112.931–	112.87	112.86		
	111.071–	110.33	110.33		
	109.972–	109.49	109.48		
	108.544–	108.37	108.37		
	107.858–	107.85	107.85		
	107.041–	107.04	107.04		
	106.817–	106.23	106.23	106.15[f]	
	106.126–	106.05	106.05	105.85[f]	
Kr	123.584–	120.28	120.26	120.2[c]	120.0[d]
				120.3[e,g]	
	116.487–	109.63	109.53	109.8-108.6[c]	110.0[d]
				109.58[j]	
	103.002–	102.96	102.96		
	100.355–	100.28	100.28		
	100.106–	98.07	98.05	97.8[c]	
Ar	106.666–	106.32	106.32		
	104.750–	96.41	96.30	96.9-95.1[c]	
				97.4[h,i]	

a) All wavelengths in nm.
b) THG is third harmonic generation, $(2(2)+1)\omega$ is $\omega_4 = 2\omega_2 + \omega_1; \omega_2 = 2\omega_1$.
c) Calculated results of Mahon *et al.*[3] In some cases $|\Delta k|$ was so small as to not be shown on their logarithmic plots for a wide wavelength interval, making it impossible to accurately measure where $\Delta k = 0$.
d) Experiments by Hilbig and Wallenstein.[35]
e) Experiments by Hilbig and Wallenstein.[36]
f) Experiments by Northrup *et al.*[37]
g) Experiments by Cotter.[38]
h) Experiments by Marinero *et al.*[39]
i) Experiments by Hilbig and Wallenstein.[40]

j) Experimental results in this dissertation.

REFERENCES

1. P. G. Wilkinson, *Can. J. Phys.* **46**, 1225 (1968).
2. J. F. Reintjes, *Nonlinear Optical Parametric Processes in Liquids and Gases,* (Academic Press, NY, 1984).
3. R. Mahon, T. J. McIlrath, V. P. Myerscough, and D. W. Koopman, *IEEE J. Quantum Electron.* **QE-15**, 444 (1979).
4. S. Natali, C. E. Kuyatt, and S. R. Mielczarek, unpublished results quoted in Ref. 27.
5. J. Geiger, unpublished results quoted in Ref. 7
6. G. M. Lawrence, *Phys. Rev.* **175**, 40 (1968).
7. W. B. Westerveld, Th. F. A. Mulder, and J. van Eck, *J. Quant. Spectrosc. Radiat. Transfer* **21**, 533 (1979).
8. A. Delâge and J.-D. Carette, *J. Phys.* **B-9**, 2399 (1976).
9. J. Geiger, *Z. Physik* **A-282**, 129 (1977).
10. J. M. Vaughan, *Phys. Rev.* **166**, 13 (1968).
11. E. Mathias, R. A. Rosenberg, E. D. Poliakoff, M. G. White, S.-T. Lee, and D. A. Shirley, *Chem. Phys. Lett.* **52**, 239 (1977).
12. A. Delâge and J.-D. Carette, *Phys. Rev.* **A-14**, 1345 (1976).
13. K. T. Lu, *Phys. Rev.* **A-4**, 579 (1971).
14. P. G. Wilkinson *J. Quant. Spectrosc. Radiat. Transfer* **6**, 823 (1966).
15. G. I. Chashchina and E. Ya. Shreider, *Opt. Spectrosc. (USSR)* **20**, 283 (1966).
16. W. Wieme and P. Mortier, *Physica* **65**, 198 (1973).
17. K. Yoshino, *J. Opt. Soc. Am.* **60**, 1220 (1970).
18. K. Yoshino and Y. Tanaka, *J. Opt. Soc. Am.* **69**, 159 (1979).
19. K. Yoshino and D. E. Freeman, *J. Opt. Soc. Am.* **B-2**, 1268 (1985).

20. R. E. Huffman, Y. Tanaka, and J. C. Larrabee, *J. Chem. Phys.* **39**, 902 (1963).

21. R. E. Huffman, T. Tanaka, and J. C. Larrabee, *Appl. Opt.* **2**, 947 (1963).

22. G. V. Marr and J. B. West, *Atom. Dat. Nucl. Dat. Tab.* **18**, 497 (1976).

23. J. B. West and J. Morton, *Atom. Dat. Nucl. Dat. Tab.* **22**, 103 (1978).

24. A. Kumar and W. J. Meath, *Can. J. Chem.* **63**, 1616 (1985).

25. P. J. Leonard, *Atom. Dat. Nucl. Dat. Tab.* **14**, 21 (1974).

26. J. A. Beattie in *Argon, Helium, and the Rare Gases, Vol. I*, G. A. Cook, ed., (Interscience Publishers, NY, 1961), Chapter VIII.

27. J. Berkowitz, *Photoabsorption, Photoionization, and Photoelectron Spectroscopy*, (Academic Press, NY, 1979).

28. R. R. Teachout and R. T. Pack, *Atom. Dat.* **3**, 195 (1971).

29. G. I. Chashchina, V. I. Gladushchak, and E. Ya. Shreider *Opt. Spectrosc. (USSR)* **24**, 542 (1968).

30. G. I. Chashchina and E. Ya. Shreider, *Opt. Spectrosc. (USSR)* **25**, 79 (1968).

31. P. L. Smith, W. H. Parkinson, and M. C. E. Huber, *Opt. Commun.* **14**, 374 (1975).

32. A. Bideau-Mehu, Y. Guern, R. Abjean, and A. Johannin-Gilles, *J. Quant. Spectrosc. Radiat. Transfer* **25**, 395 (1981).

33. V. P. Gladushchak, S. A. Moshkalev, G. I. Chashchina, and E. Ya. Shreider, *Opt. Spectrosc. (USSR)* **51**, 608 (1981).

34. S. D. Kramer, M. G. Payne, and C. H. Chen, *J. Opt. Soc. Am.* **B-2**, 1284 (1985).

35. R. Hilbig and R. Wallenstein, *Appl. Opt.* **21**, 913 (1982).

36. R. Hilbig and R. Wallenstein, *IEEE J. Quantum Electron.* **QE-17**, 1566 (1981).

37. F. J. Northrup, J. C. Polanyi, S. C. Wallace, and J. M. Williamson, *Chem. Phys. Lett.* **105**, 34 (1984).

38. D. Cotter, *Opt. Commun.* **31**, 397 (1979).

39. E. E. Marinero, C. T. Rettner, R. N. Zare, and A. H. Kung, *Chem. Phys. Lett.* **95**, 486 (1983).

40. R. Hilbig and R. Wallenstein, *Opt. Commun.* **44**, 283 (1983).

41. D. Cotter, *Opt. Lett.* **5**, 134 (1979).

42. R. Mahon, T. J. McIlrath, and D. W. Koopman, *Appl. Phys. Lett.* **33**, 305 (1978).

43. D. R. Bates and A. Damgaard, *Phil. Trans.* **A-242**, 101 (1949).

44. H. B. Bebb, *Phys. Rev.* **149**, 25 (1966).

45. R. B. Miles and S. E. Harris, *IEEE J. Quantum Electron.* **QE-9**, 470 (1973).

46. E. U. Condon and G. H. Shortly, *The Theory of Atomic Spectra*, (Cambridge University Press, Cambridge, 1970).

47. C. E. Moore, *Atomic Energy Levels, NSRDS-NBS 35*, (U.S. Government Printing Office, Washington, 1971).

48. M. Aymar and M. Coulombe, *Atom. Dat. Nucl. Dat. Tab.* **21**, 537 (1978).

49. V. Kaufman and C. J. Humphreys, *J. Opt. Soc. Am.* **59**, 1614 (1969).

50. M. V. Fonesca and J. Campos, *Phys. Rev.* **A-17**, 1080 (1978).

51. M. V. Fonesca and J. Campos, *Physica* **97C**, 312 (1979).

52. M. V. Fonesca and J. Campos, *J. Phys.* **B-13**, 3957 (1980).

53. Molectron Corp., Cooper Lasersonics, Santa Clara, CA 95051.

54. D. J. Moll, Ph.D. Thesis, California Institute of Technology, Pasadena, CA.

55. Quanta Ray., Spectra Physics, Mountain View, CA 94039.

56. Exciton Chemical Corp., Dayton, OH 45341.

57. Kodak Laser Products, Eastman Kodak Co., Rochester, NY 14650.

58. Laser Precision Corp., Utica, NY 13502.

59. Scientech, Inc., Boulder, CO 80303.

60. Hewlett-Packard, Palo Alto, CA 94303.

61. Optics for Research, Caldwell, NJ 07006.

62. M. V. Klein, *Optics*, (John Wiley & Sons, NY, 1970).

63. *Optics Guide 3*, (Melles Griot, Irvine, CA 1985).

64. M. Born and E. Wolf, *Principles of Optics, 6th. ed.*, (Pergamon Press, Oxford, 1980).

65. Harshaw Chemical Co., Solon, OH 44139

66. J. H. Carver and P. Mitchell, *J. Sci. Instrum.* **41**, 555 (1964).

67. E. Miescher, *Can. J. Phys.* **54**, 2074 (1976).

68. J. A. Guest and L. C. Lee, *J. Phys.* **B-14**, 3401 (1981).

69. K. Watanabe, F. M. Matsunaga, and H. Sakai, *Appl. Opt.* **6**, 391 (1967).

70. P. H. Metzger, G. R. Cook, and M. Ogawa, *Can. J. Phys.* **45**, 203 (1967).

71. D. Vichon, R. I. Hall, F. Gresteau, and J. Mazeau, *J. Mol. Spectrosc.* **69**, 341 (1978).

72. R. P. Frueholz, R. Rianda, and A. Kuppermann, *Chem. Phys.* **31**, 315 (1978).

73. R. J. Stubbs, T. A. York, andJ. Comer, *Chem. Phys.* **106**, 161 (1986).

74. O. Edqvist, E. Lindholm, L. E. Selin, H. Sjögren, and L. Åsbrink, *Arkiv Fysi* **40**, 439 (1070).

75. S. D. Kramer, C. H. Chen, M. G. Payne, G. S.Hurst, and B. E. Lehman, *Appl. Opt.* **22**, 3271 (1983).

76. Alfa Products, Inc., Danvers, MA 01923.

77. Matheson Gas Products, Inc.,

FIGURE CAPTIONS

Figure 1). The calculated refractive index for Ar at 1.00 atm pressure and a temperature of 273.15 K. The * represent the experimental points in Leonard[25] and Bideau-Mehu *et al.*[32]

Figure 2). The calculated wave vector mismatch for third harmonic generation in Ar at a pressure of 1 torr and a temperature of 298.15 K.

Figure 3). The calculated refractive index for Kr at 1.00 atm pressure and a temperature of 273.15 K. The * represent the experimental points in Leonard[25] and Bideau-Mehu *et al.*[32]

Figure 4). The calculated wave vector mismatch for third harmonic generation in Kr at a pressure of 1 torr and a temperature of 298.15 K. The ⊙ represent the experimental points of Cotter[41] at 112.4 nm and Mahon *et al.*[42] at 121.567 nm.

Figure 5). The calculated refractive index for Xe at 1.00 atm pressure and a temperature of 273.15 K. The * represent the experimental points in Leonard[25] and Bideau-Mehu *et al.*[32]

Figure 6). The calculated wave vector mismatch for third harmonic generation in Xe at a pressure of 1 torr and a temperature of 298.15 K.

Figure 7). Scale drawing of a typical experimental layout for VUV generation experiments. This drawing represents the situation when the Quanta Ray Nd:YAG pumped dye laser is used. The following abbreviations are used: A– aperture, BS– beam splitter, PEJM– pyroelectric joulemeter, P– right angle prism, PD– photodiode.

Figure 8). Calculated focal spot radius as a function of incident beam radius for a collimated 330 nm laser beam focused by a "best form" 100 mm Suprasil lens with a design wavelength of 300 nm. It is assumed that the beam is subject only to diffraction (– – –) and spherical aberration (·····).

Figure 9). Scale drawing of the assembled cell for VUV experiments consisting of three compartments: VUV generator, spectroscopic sample holder, VUV detector. The construction details have not been included in the figure. The material of each window is shown below the figure. The approximate location of the 100 mm focusing lens and ray traces showing the margin of the laser beam are also shown. The ⊗ represent the valves on the vacuum line connections.

Figure 10). Calculated response of NO ionization cell as a function of VUV wavelength.

Figure 11). Diagram of the electronics used for the experiments described in this chapter. The solid lines represent analog data signals, the — · — lines represent analog control signals, and the ··· represent digital control signals.

Figure 12). Experimental determination of the VUV signal as a function of Kr pressure for THG. The dye laser fundamental wavelength is 660.00 nm, the approximate wavelength of the generated radiation is 110.03 nm. The signal from the NO ionization chamber was collected and analyzed as described in the text. The solid line represents a weighted non-linear least squares fit to the experimental data while the dashed line is the theoretical phase matching function Φ' adjusted to give the same background and maximum as the experimental data.

Figure 13). Experimental determination of the VUV signal as a function of UV pulse energy THG. The dye laser fundamental wavelength is 660.00 nm, the approximate wavelength of the generated radiation is 110.03 nm. The signal from the NO ionization chamber was collected and analyzed as described in the text. The solid line is a weighted linear least squares fit to $\ln(VUV) = a + b \cdot \ln(UV)$, the — — line is a nonlinear least squares fit

to $VUV = a \cdot UV^b$, and the $- \cdot -$ line is a nonlinear least squares fit to $VUV = a + b \cdot UV^c$

Figure 14). Predicted VUV tuning curves for THG in Kr for VUV wavelengths near 110 nm at Kr pressures of 400, 800, 1200 and 1600 torr, using the wave-vector mismatch calculated previously. The calculations assumed a confocal parameter of 0.151 cm, and further assumed that $\chi^{(3)}$ and E_{UV} are constant.

Figure 15). Experimental VUV tuning curves for THG in Kr for VUV wavelengths near 110 nm. The Kr pressures were 400, 800, 1200, and 1600 torr.

Figure 16). Experimental determination of the VUV signal as a function of Kr pressure for the $(2(2) + 1)\omega$ process. The dye laser fundamental was 560.0 nm; the approximate wavelength of the generated VUV radiation is 112.03 nm.

FIGURE 1.

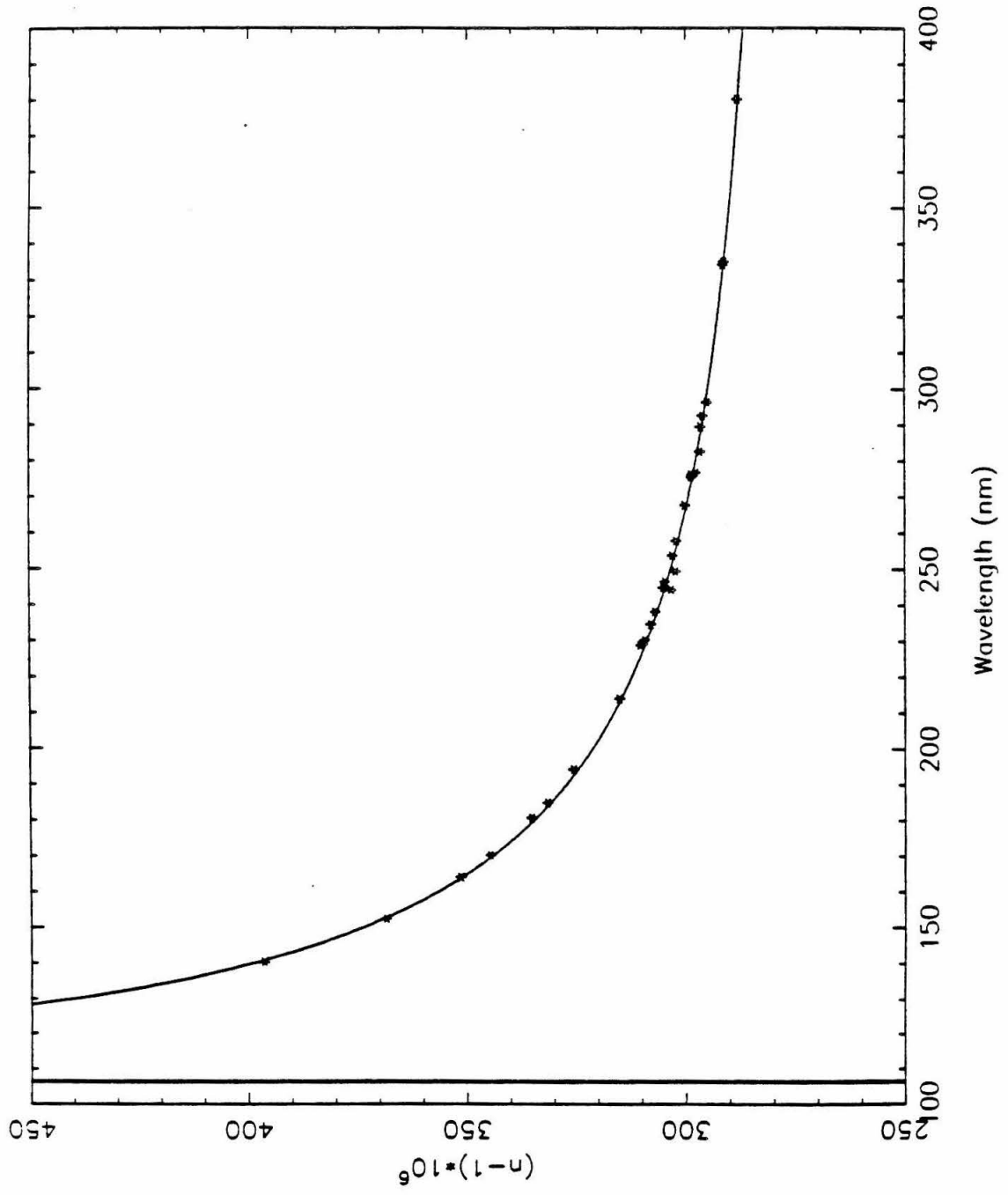
Wavelength (nm)
100
150
200
250
300
350
400
250
300
350
400
450
(n−1)*10^6

FIGURE 2.

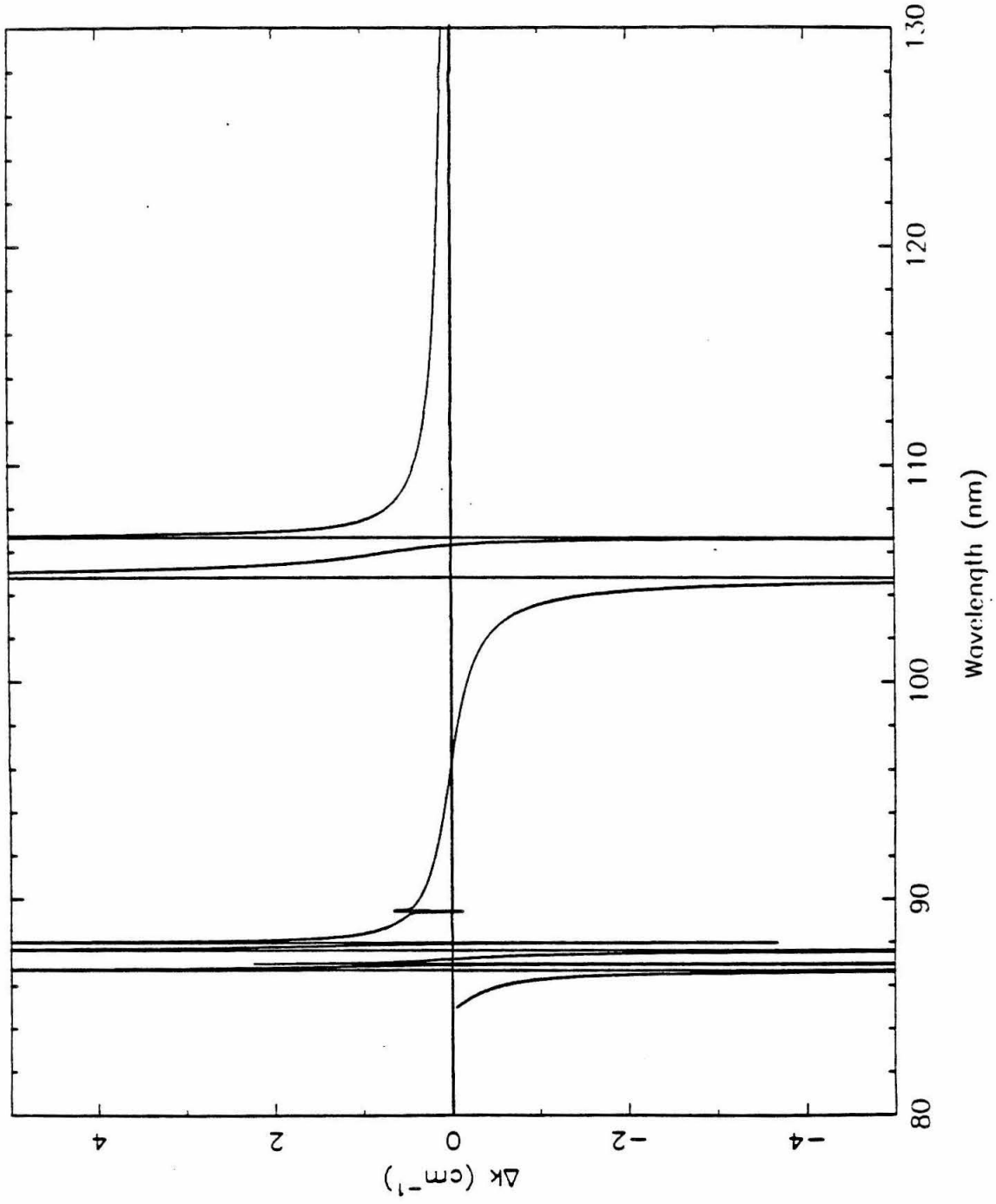

FIGURE 3.

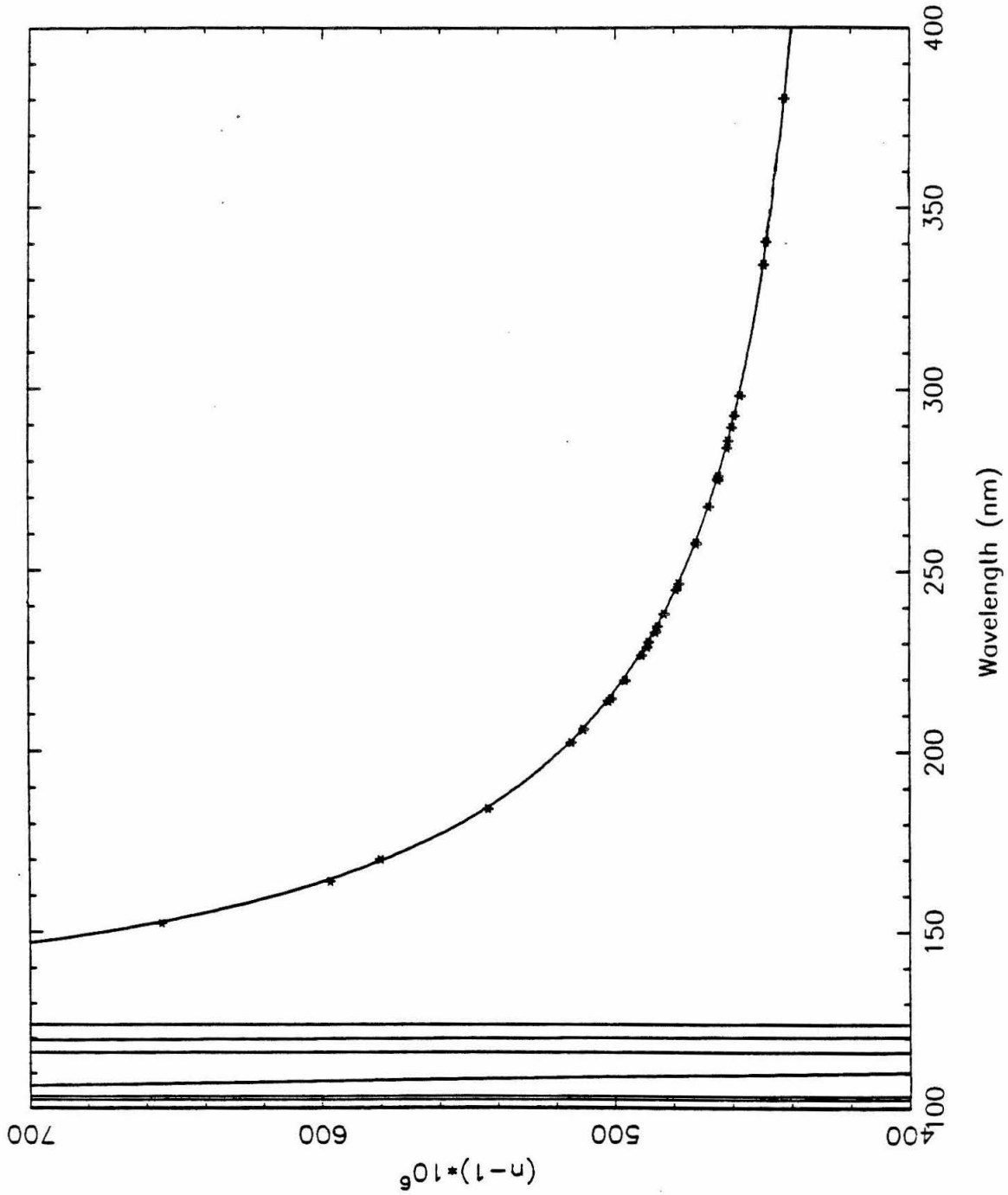

FIGURE 4.

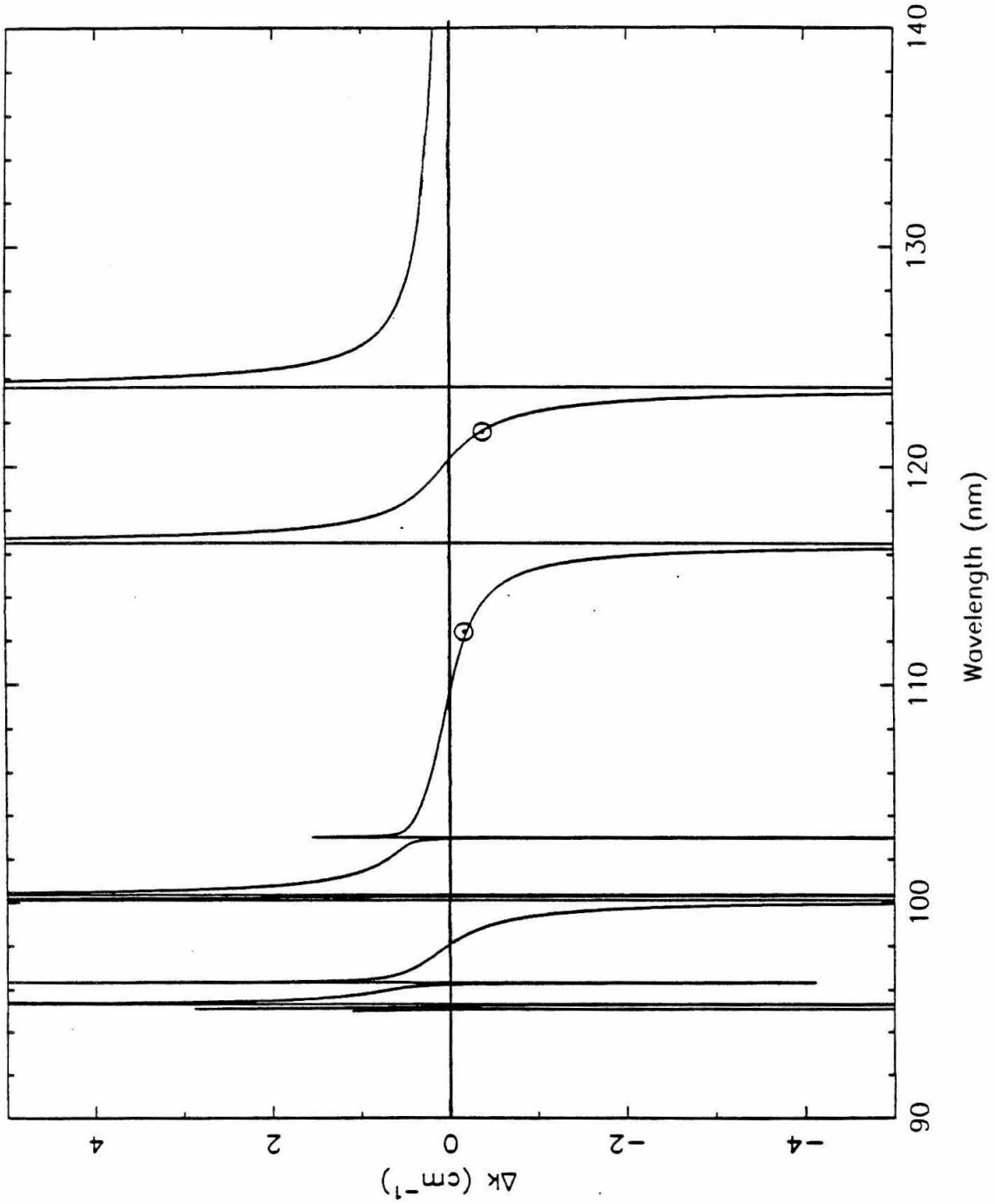

FIGURE 5.

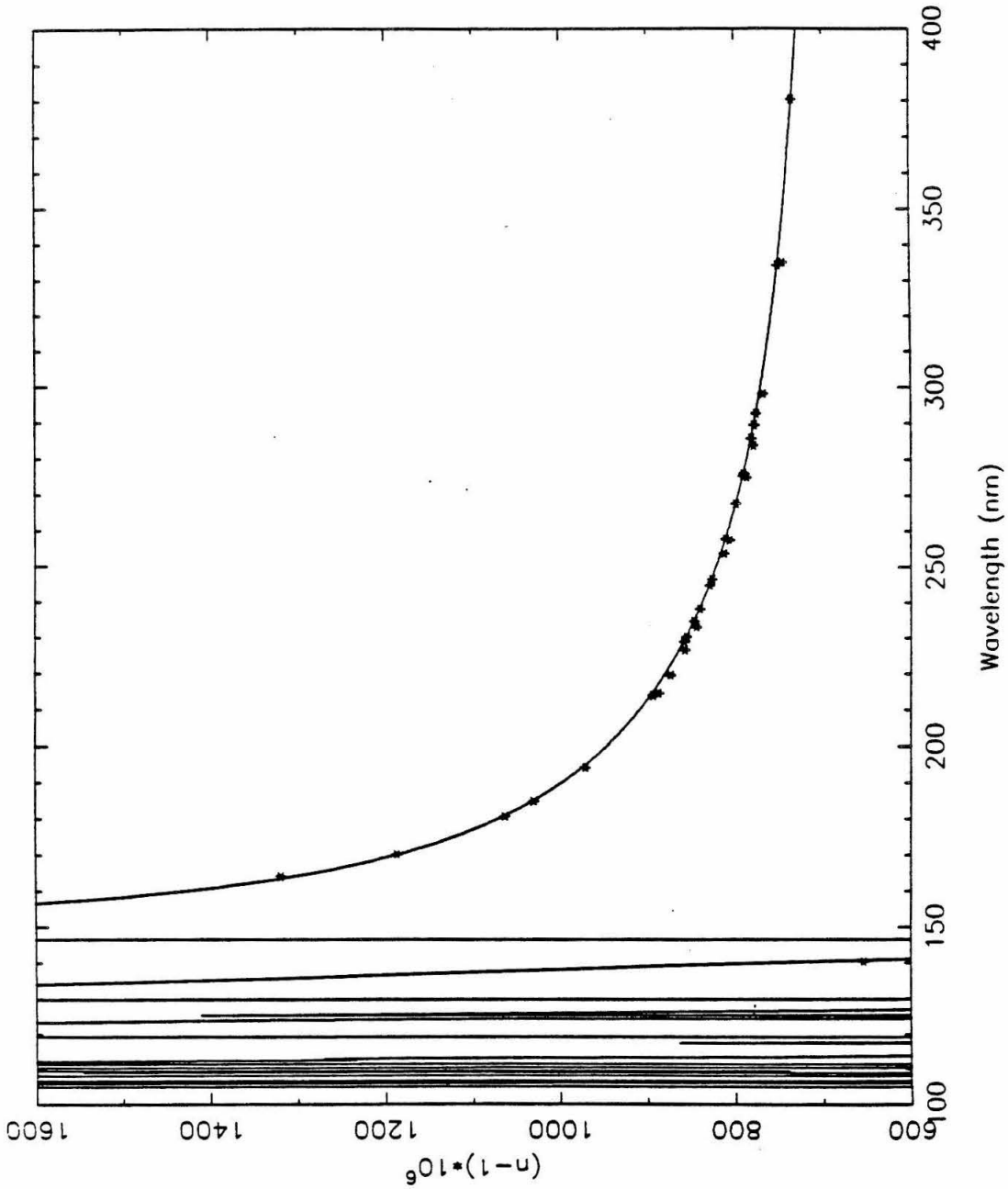
400
350
300
250
200
150
100
Wavelength (nm)
600
800
1000
1200
1400
1600
(n−1)*10^6

FIGURE 6.

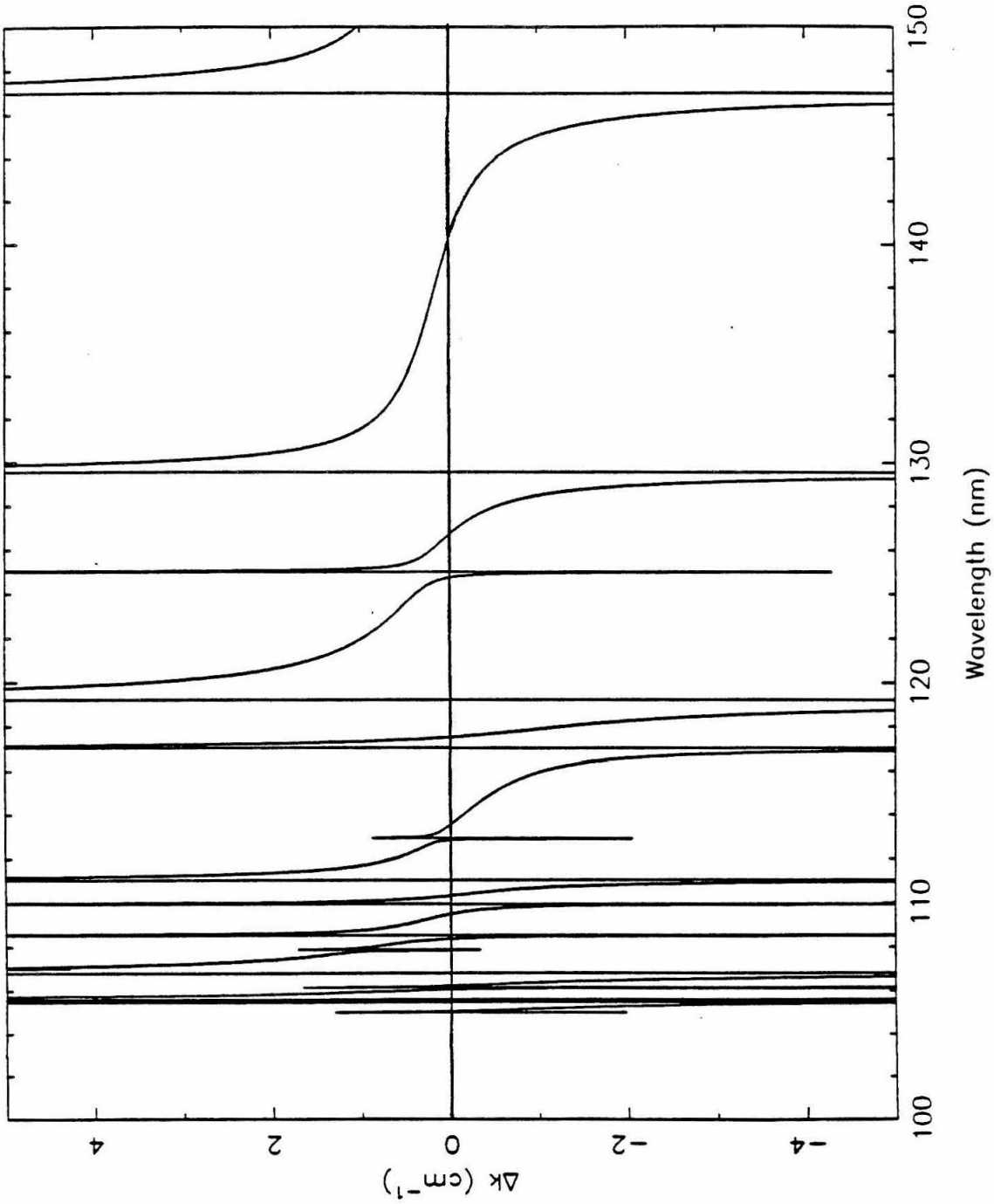

FIGURE 7.

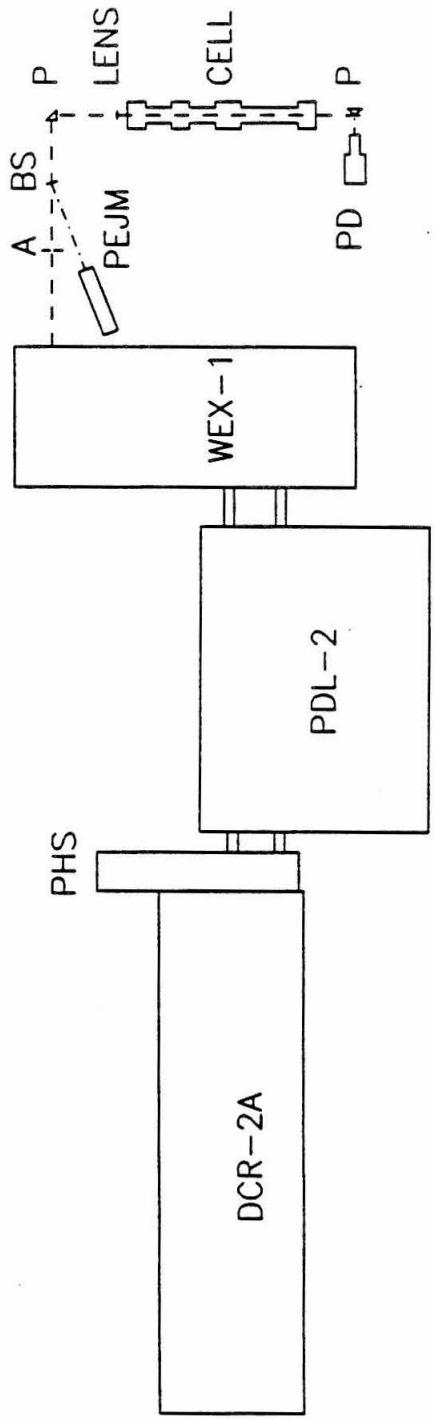

FIGURE 8.

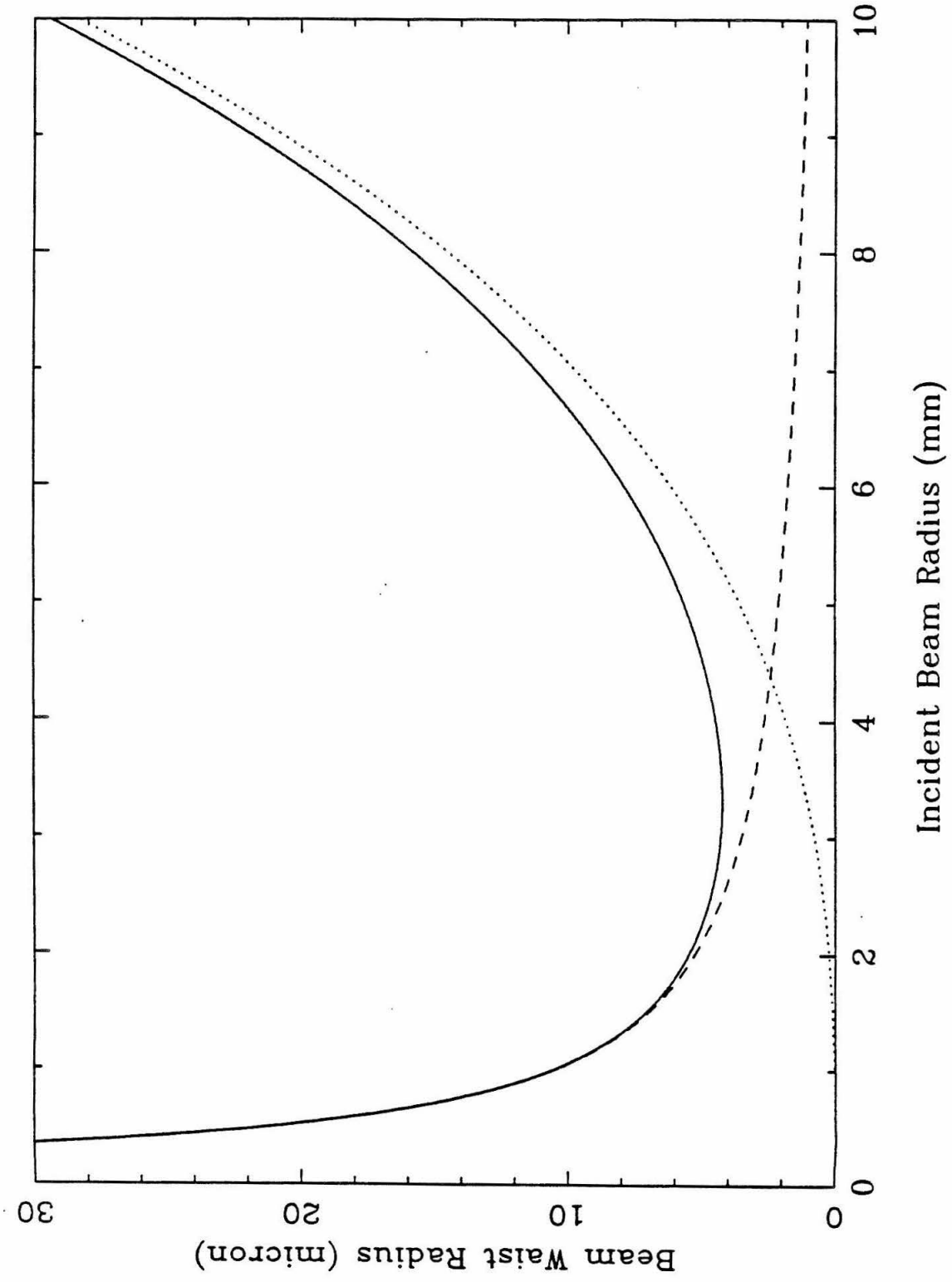
Beam Waist Radius (micron)
0
10
20
30
Incident Beam Radius (mm)
0
2
4
6
8
10

FIGURE 9.

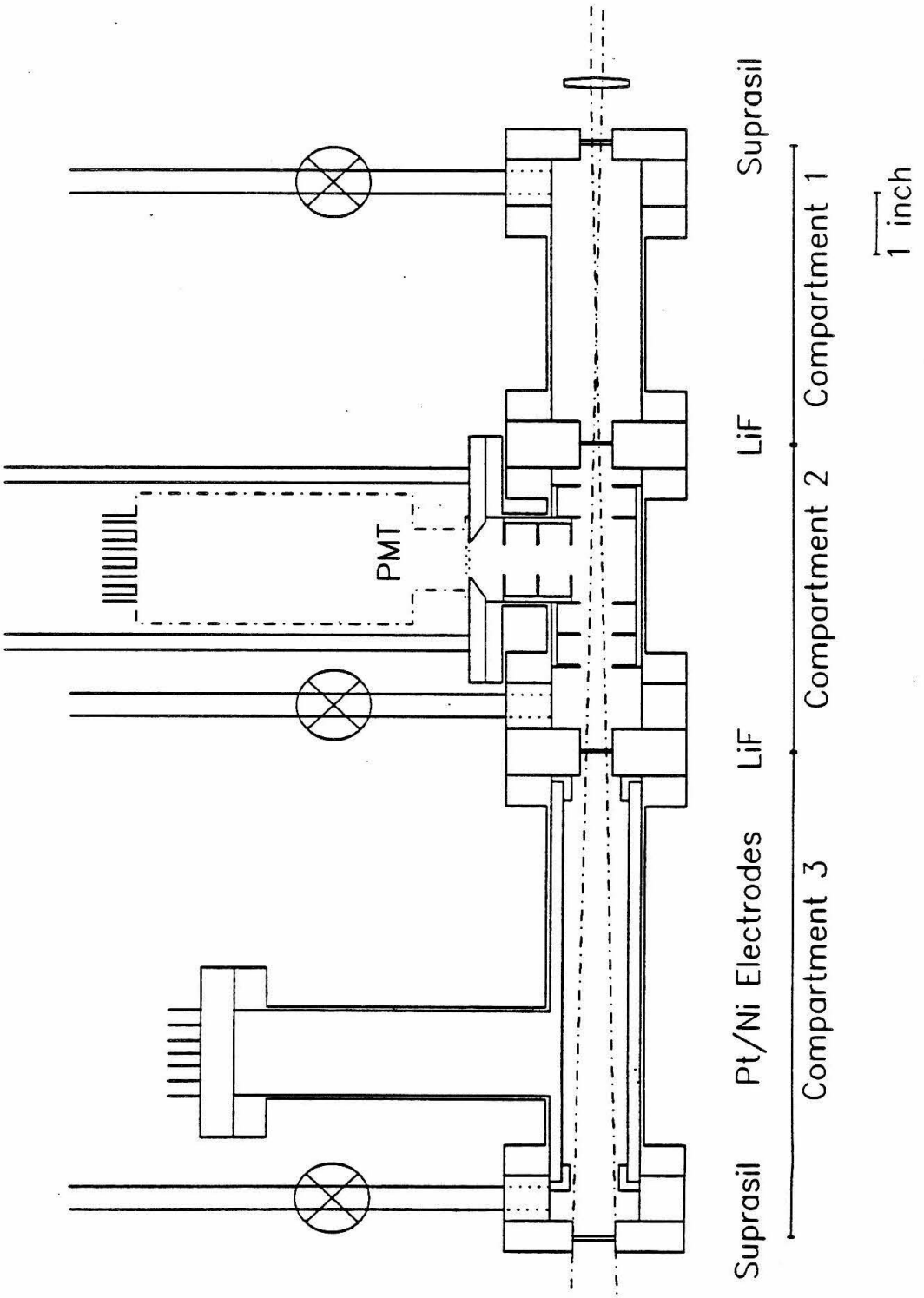
PMT
Suprasil
LiF
Compartment 1
Compartment 2
LiF
Pt/Ni Electrodes
Compartment 3
Suprasil
1 inch

FIGURE 10.

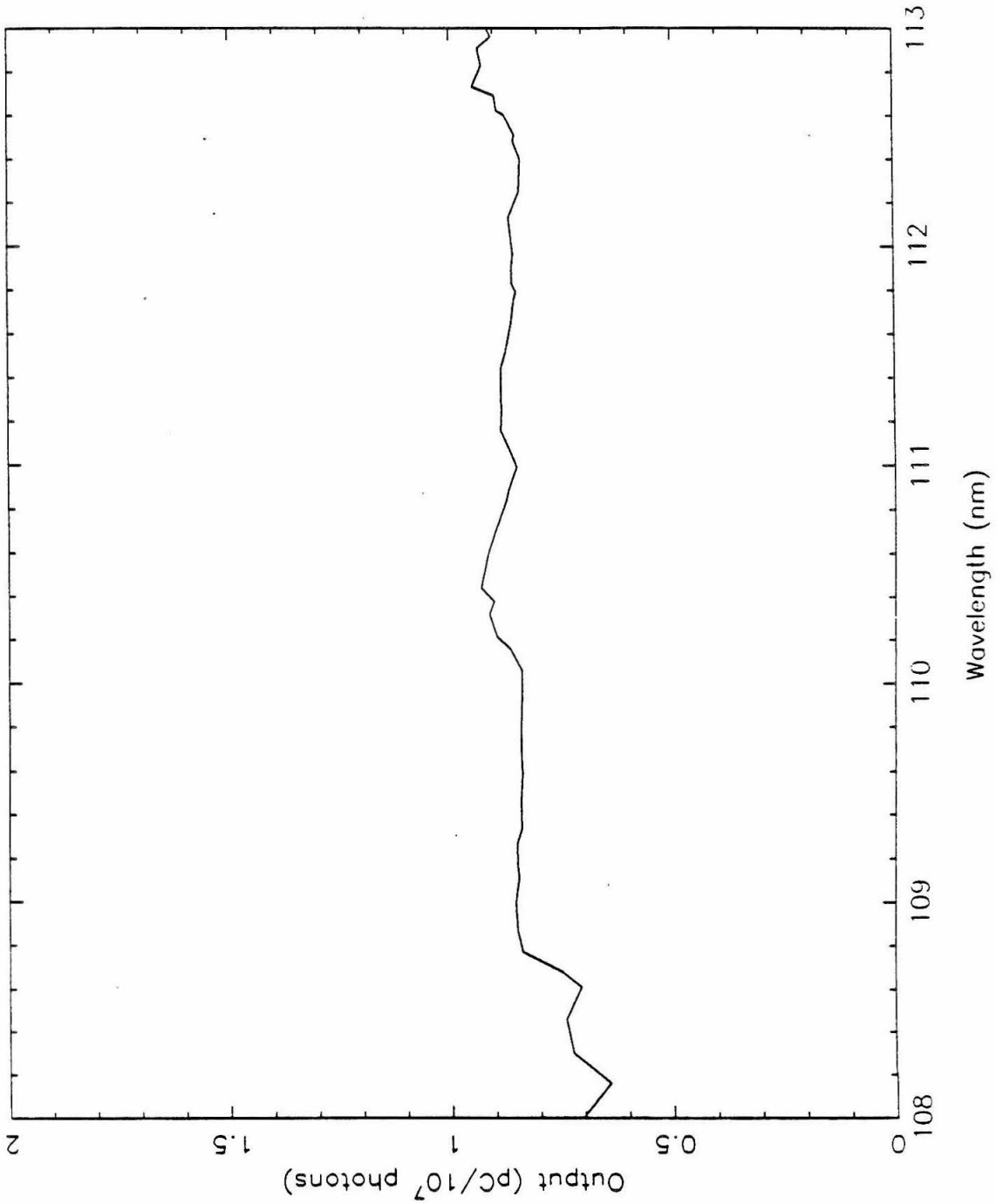
Output (pC/10⁷ photons)
0
0.5
1
1.5
2
108
109
110
111
112
113
Wavelength (nm)

FIGURE 11.

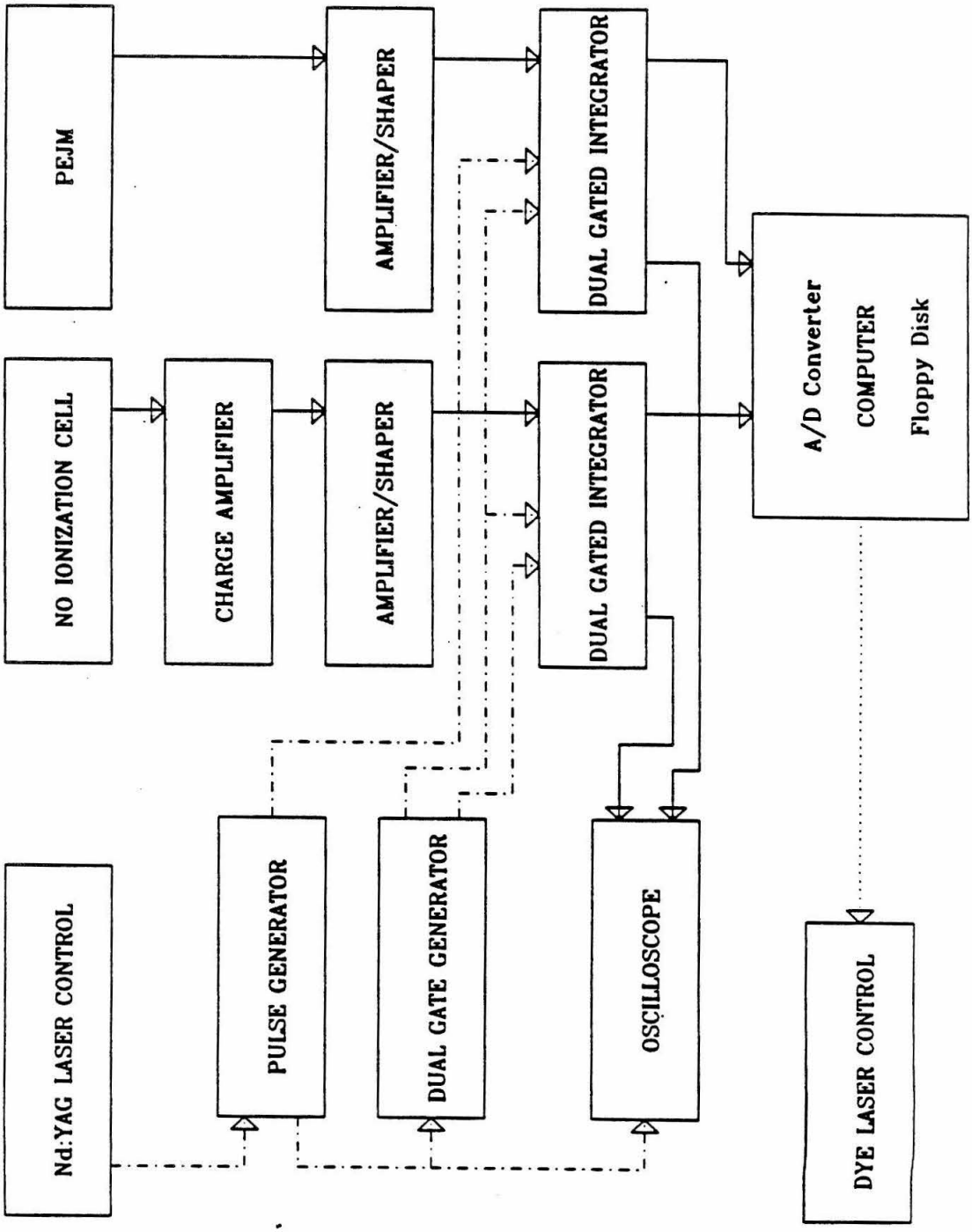
PEJM
AMPLIFIER/SHAPER
DUAL GATED INTEGRATOR
NO IONIZATION CELL
CHARGE AMPLIFIER
AMPLIFIER/SHAPER
DUAL GATED INTEGRATOR
A/D Converter
COMPUTER
Floppy Disk
Nd:YAG LASER CONTROL
PULSE GENERATOR
DUAL GATE GENERATOR
OSCILLOSCOPE
DYE LASER CONTROL

FIGURE 12.

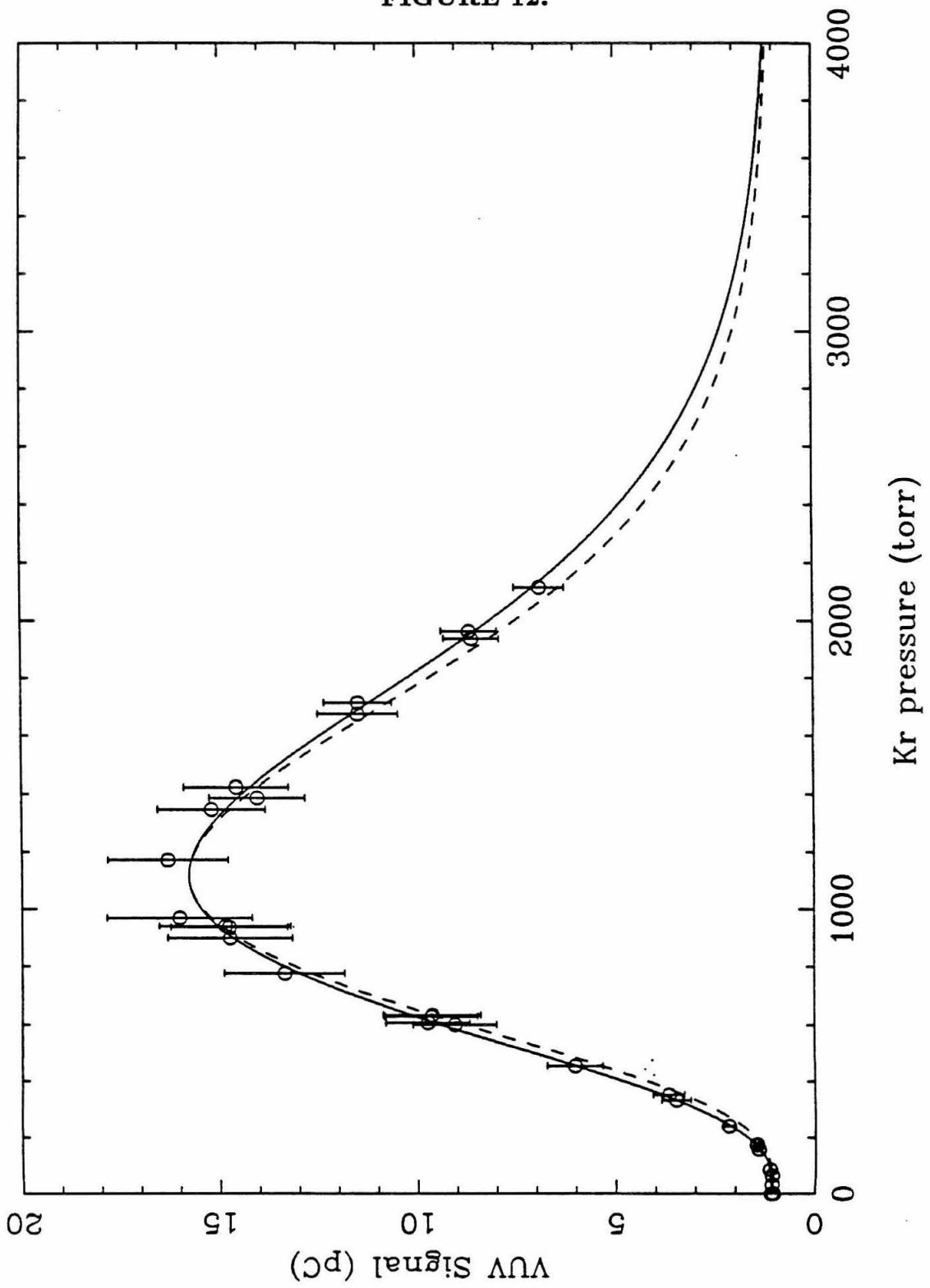
VUV Signal (pC)
0
5
10
15
20
Kr pressure (torr)
0
1000
2000
3000
4000

FIGURE 13.

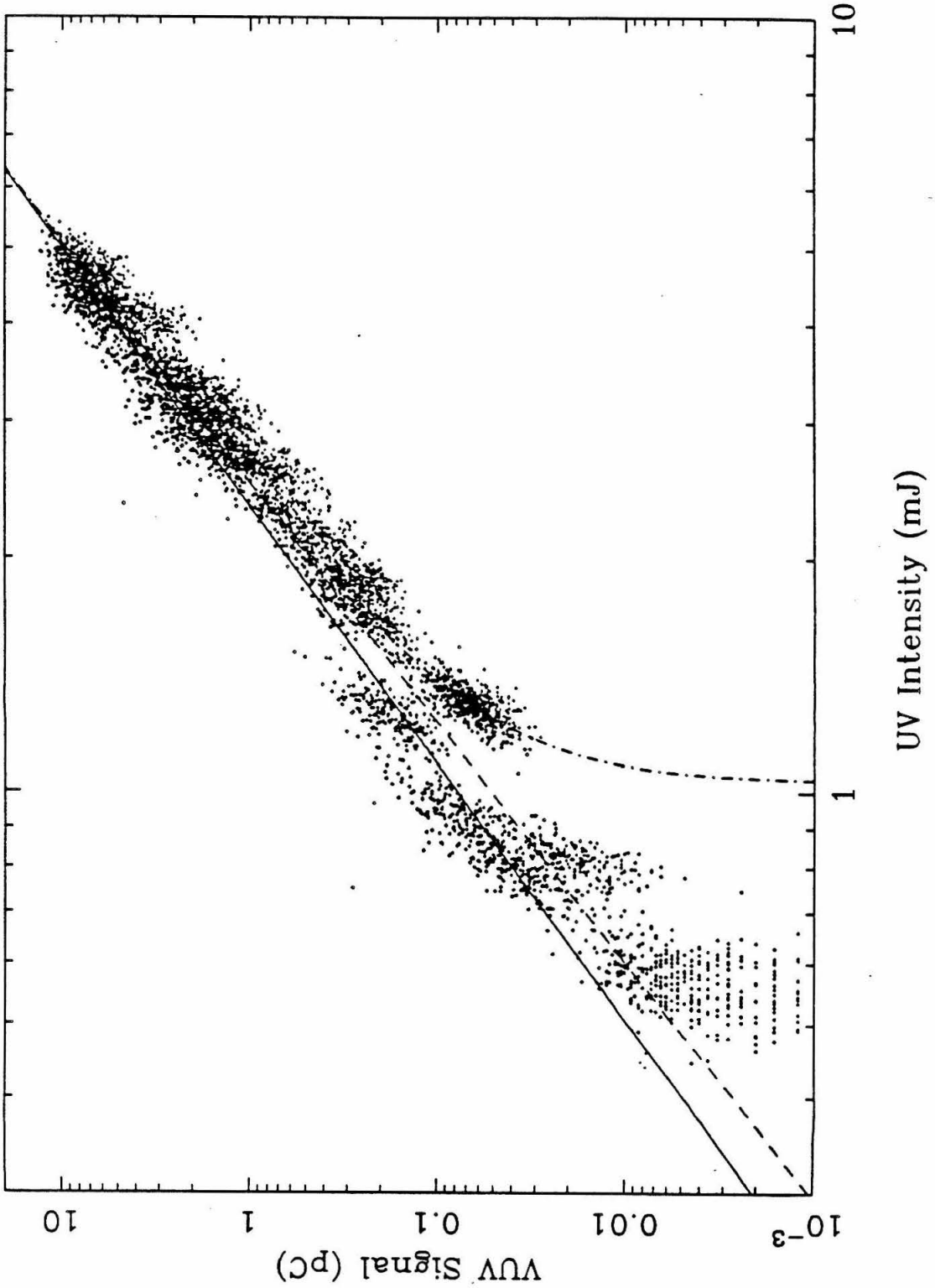

FIGURE 14.

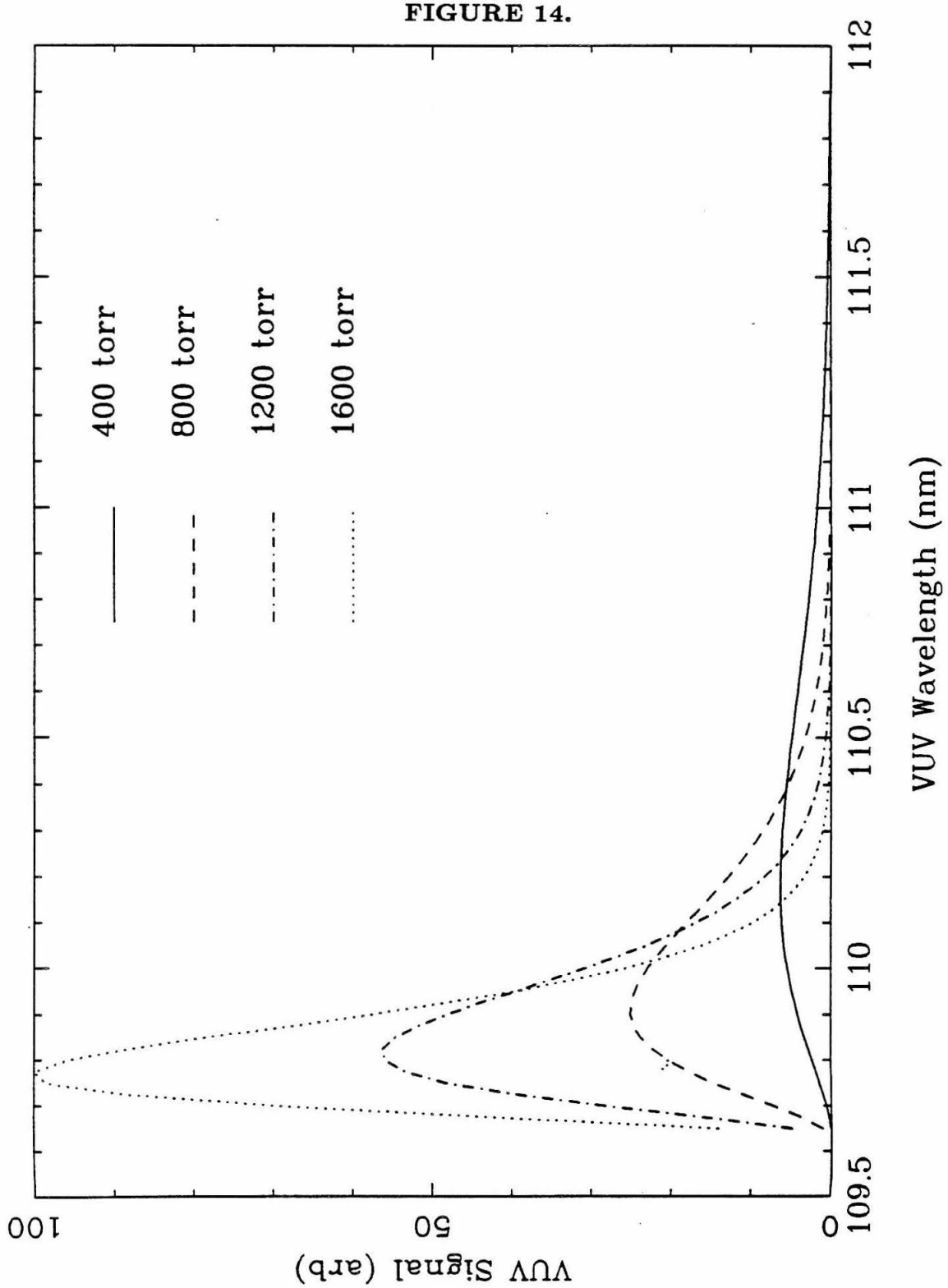
400 torr
800 torr
1200 torr
1600 torr
VUV Signal (arb)
0
50
100
VUV Wavelength (nm)
109.5
110
110.5
111
111.5
112

FIGURE 15.

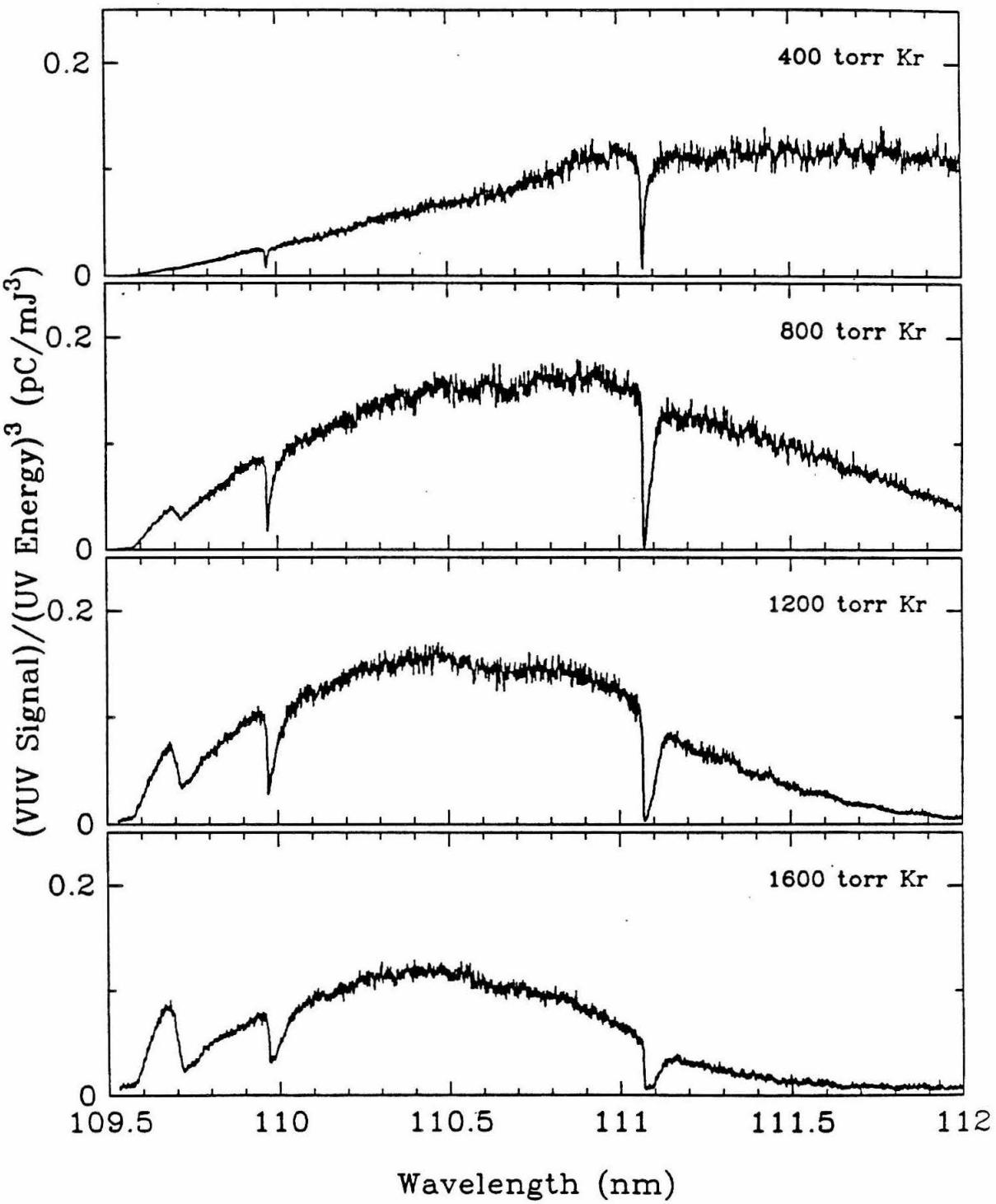
400 torr Kr
800 torr Kr
1200 torr Kr
1600 torr Kr
0.2
0
(VUV Signal)/(UV Energy)^3 (pC/mJ^3)
109.5
110
110.5
111
111.5
112
Wavelength (nm)

FIGURE 16.

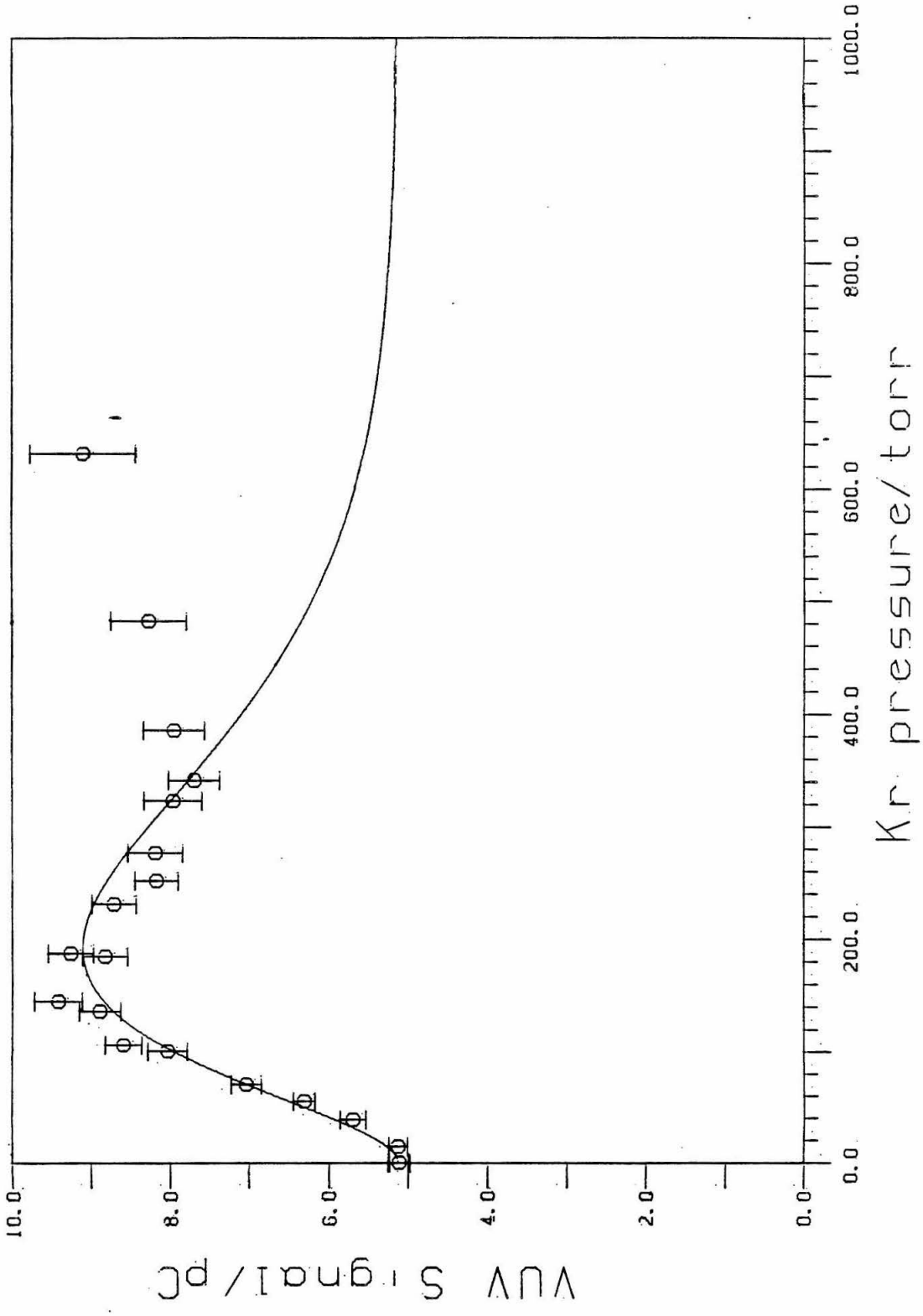
VUV Signal/pC
10.0
8.0
6.0
4.0
2.0
0.0
0.0
200.0
400.0
600.0
800.0
1000.0
Kr pressure/torr

CHAPTER 5.

SPECTROSCOPIC DATA

I. INTRODUCTION

The detection of H_2 produced by a chemical reaction using the technique of Laser Induced Fluorescence (LIF) requires accurate spectroscopic knowledge of several molecules. First, in order to use the technique of LIF to determine the population of individual H_2 quantum states, knowledge of the location and strength of H_2 absorption and emission lines is needed. Second, one needs spectroscopic data for the reagent molecules, not only to determine the appropriate wavelength for photoinitiation of the reaction, but also to evaluate any conflict with the detection of H_2.

In this chapter the spectroscopic data on H_2, H_2CO, and the potential H atom precursors HI and H_2S are reviewed. First, the locations of important electronic transitions are determined. Second, the contributions of ionization, fluorescence, and dissociation processes to the total absorption cross section are estimated at wavelengths of interest. And third, my own measurements are given and compared with the results of other workers.

II. H_2 SPECTROSCOPIC DATA

A. Background

The hydrogen molecule and its isotopic analogs have been extensively studied using theoretical and experimental techniques. An accurate potential energy surface for the ground state of H_2 was determined in 1964 by Kolos and Wolniewicz.[1] More recent calculations by them which included larger internuclear distances,[2] larger basis sets,[3,4] and nonadiabatic[5] corrections give vibrational-rotational energies which agree well with experiment. Their calculations have been extended to several excited states.[2,6-9] Experimental information about the ground state has principally been obtained from Raman,[10] quadrupole rotation-vibration,[11-16] and pure rotation[17-18] spectra. Additionally, HD has a weak dipole-allowed rotation-vibration spectrum.[19] Further information on the ground state and all the information about the electronically excited states is obtained from emission[20-32] and absorption[33-46] spectra.

The ground state electronic configuration is $(1s\,\sigma)^2\ \tilde{X}\ ^1\Sigma_g^+$ in the one electron molecular orbital approximation[47] in the united atom limit. The equilibrium internuclear separation[47] is 0.741 Å, the dissociation energy[5] is 36 118.3 cm^{-1}, and the ionization potential[48] is 124 418.4 cm^{-1}. The dissociation products are a pair of ground state atoms, $H(1s) + H(1s)$. From the Raman[10] and quadrupole[11-16] spectra the energy levels of the lowest rotational states of the first several vibrational levels have been determined with high accuracy (0.001 cm^{-1}). From analysis of emission spectra,[20-31] the first 7 to 9 rotational levels for all of the bound vibrational levels, (v''_{max}=14, 17, 21 in H_2, HD, and D_2, respectively) were determined at a slightly lower accuracy (0.01 cm^{-1}). Recently, Dabrowski changed the H_2 discharge conditions and saw significant rotational excitation.[32] Almost every bound rotational-vibrational state was observed, up to J''=29 for

some vibrations. Thus the experimental knowledge of the ground state rotational energy levels is much more complete for H_2 than for its isotopic analogs.

The electronic configuration of the first bound excited state[47] is $(1s\,\sigma)(2p\,\sigma)$ $\tilde{B}\,^1\Sigma_u^+$ in the one electron molecular orbital approximation in the united atom limit. This state has an equilibrium internuclear separation[47] of 1.29 Å and minimum and dissociation energies[47] of 89 404.7 and 118 375.6 cm^{-1}, respectively, above the v=0 level of the $\tilde{X}$ state. The dissociation products[47] are a ground state atom and an excited state atom, $H(1s) + H(2p)$, though a theoretical analysis of the wavefunction shows that at intermediate separations this state is mostly ionic in character.[9] From an analysis of the absorption[33-46] and emission[20-32] spectra the energy of almost all of the bound vibrational levels (v'_{max}=36, 43, 51 for H_2, HD, D_2, respectively) are known. As is the case for the ground state, many more $\tilde{B}$ state rotational energy levels are known for H_2 than in HD or in D_2.

The electronic configuration of the second bound excited state[47] is $(1s\,\sigma)(2p\,\pi)$ $\tilde{C}\,^1\Pi_u$ in the one electron molecular orbital approximation in the united atom limit. This state has an equilibrium internuclear separation[47] of 1.032 Å and minimum and dissociation energies[47] of 97 813.1 and 118 375.6 cm^{-1}, respectively, above the v=0 level of the $\tilde{X}$ state. The dissociation products are a ground state atom and an excited state atom, $H(1s) + H(2p)$. From analysis of the absorption[35-40,46] and emission[20-32] spectra the energy of almost all of the bound vibrational levels (v'_{max}=13, 15, and 19 for H_2, HD, and D_2, respectively) are known. Unlike the case for the $\tilde{X}$ or $\tilde{B}$ states, the number of observed rotational levels is comparable for all three species.

Figure 1 shows the potential energy curves and the position of the vibrational levels for $\tilde{X}$, $\tilde{B}$, and $\tilde{C}$.

The $\tilde{B} \leftrightarrow \tilde{X}$ transitions form the Lyman band system and the $\tilde{C} \leftrightarrow \tilde{X}$ transitions form the Werner band system of H_2. High resolution absorption spectra

of the first 5 vibrational bands of the Lyman system in H_2, HD, and D_2 were obtained by Wilkinson.[43] The $\tilde{B}\,(v'=0,J'=1) \leftrightarrow \tilde{X}\,(v''=0,J''=0)$ transition, *i.e.*, the 0–0 R(0) transition, occurs at 90 242.32, 90 429.23, and 90 653.40 cm^{-1} for H_2, HD, and D_2, respectively. Because this is a $^1\Sigma_u^+ \leftrightarrow {}^1\Sigma_g^+$ transition, there is no Q branch, just a P and an R branch.[49a] Both the P and the R branches are shaded to lower energy, hence, the highest energy transition within each vibrational band is the R(0) line. The band origins of the 0–0 band in the Werner system occur at[32,31,46] 99 089.90, 99 252.86, and 99 409.18 cm^{-1} in H_2, HD, and D_2, respectively. Because this is a $^1\Pi_u \leftrightarrow {}^1\Sigma_g^+$ transition, there are P, Q, and R branches.[49a] These bands are also shaded to lower energy.

Perturbations exist between $^1\Sigma_u^+$ and $^1\Pi^+$ states;[49b] consequently, there are perturbations between the $\tilde{B}$ and $\tilde{C}$ states of H_2. These perturbations are severe at times, shifting states by as much as 50 cm^{-1} from their expected positions. These perturbations have been studied in detail by Monfils.[35–39] In a first order approximation, the observed state energies ($E^*_{\tilde{B}}$ and $E^*_{\tilde{C}}$) are related to the expected energies in the absence of perturbations ($E_{\tilde{B}}$ and $E_{\tilde{C}}$) by

$$\left.\begin{matrix} E^*_{\tilde{B}} \\ E^*_{\tilde{C}} \end{matrix}\right\} = \frac{E_{\tilde{B}} + E_{\tilde{C}}}{2} \pm \sqrt{\frac{\left(E_{\tilde{B}} - E_{\tilde{C}}\right)^2}{4} + W^2_{\tilde{B}\tilde{C}} J(J+1)} \qquad (5.1)$$

where $W_{\tilde{B}\tilde{C}}$ is the perturbation parameter. The exact value of $W_{\tilde{B}\tilde{C}}$ varies with species and with the interacting vibrational levels, but average values are $\approx$ 8.5, $\approx$ 5.5, and $\approx$ 3.0 cm^{-1} for H_2, HD, and D_2, respectively.

The energy levels within an electronic state ignoring perturbations can be represented by the Dunham equation[50]

$$\mathrm{E}(v,J) = \sum_{i=1} \sum_{j=0} Y_{ij} (v+0.5)^i [J(J+1)]^j \qquad (5.2)$$

where the energy zero is the bottom of the potential energy function for the state. The Y_{ij}'s correspond (except for sign conventions and minor corrections) to the

normal spectroscopic constants: $Y_{10} = \omega_e$, $Y_{20} = -\omega_e x_e$, $Y_{30} = \omega_e y_e$, $Y_{01} = B_e$, $Y_{11} = -\alpha_e$, $\cdots$. Another term, Y_e, is included for the electronic excitation energy of excited states. The published Dunham constants[30-32,46] for the $\tilde{X}$ and $\tilde{B}$ states do a poor job of representing the experimental energy levels. The H_2 constants have several sign errors while the HD and D_2 expansions have no Y_{ij} for $j > 1$. Therefore, the Dunham coefficients needed to be redetermined.

Two different set of Dunham constants were determined. The first set was for all known rotational[32,40] levels with $J \leq 15$ of the $v \leq 14$, $v \leq 19$, and $v \leq 5$ levels of the $\tilde{X}$, $\tilde{B}$, and $\tilde{C}$ states, respectively, of H_2. These coefficients were found using the following algorithm. The rotational energy levels within each vibrational band were fit by least squares analysis to a polynomial in $[J(J+1)]$. The $j = 0$ terms from each vibrational level were then fit to a polynomial in $[v + 0.5]$, giving the Y_{i0} coefficients for the Dunham equation. Then the $j = 0$ term for each vibrational level was held constant at the value calculated using these coefficients while a new polynomial in $[J(J+1)]$ was evaluated. The process was repeated with the $j = 1$, $j = 2$, *etc.*, terms untill convergence was obtained. In order to reduce the effects of the perturbations on the coefficients, the following pairs of states were not included in the calculations: $\left(\tilde{B}(v,J) - \tilde{C}(v,J)\right)$, (8,6)–(0,6), (10,5)–(1,5), (12,4)–(2,4), and (14,1)–(3,1). The final coefficients are given in Table 1. The overall fit is reasonably good; the root-mean-square (rms) deviation for 503 states is 2.0 cm^{-1}. Most of the error comes from a few high J levels and the perturbed $\tilde{B}$ and $\tilde{C}$ states. For example, if the $v = 11$, $J = 14$ level of $\tilde{X}$ and the $v = 7$, $J = 12$ level of $\tilde{B}$ with errors of -22.8 and 21.0 cm^{-1}, respectively, are ignored, then the rms deviation is only 1.46 cm^{-1}. The rms deviation is less than 0.25 cm^{-1} for $v \leq 9$ in $\tilde{X}$.

A second method was used to calculate the Dunham coefficients for the low-lying levels of H_2, HD, D_2. The published rotational constants[30-32,46] B_v and D_v (also H_v and L_v where known) for $v \leq 8$ were fitted to a polynomial in $(v + 0.5)$.

The coefficients were determined by a least squares analysis, the appropriate polynomial order (≤ 5) being determined by the minimum standard deviation. These coefficients can be seen in Table 2. These constants fit the experimental energy levels very well: for v=0–7, J=0–7 (12 for H_2) of the $\tilde{X}$ ground state, the (rms) dispersion was 0.15, 0.12, and 0.17 cm^{-1} for H_2, HD, and D_2, respectively. The energy of the $\tilde{B} \leftrightarrow \tilde{X}$ transitions were also determined accurately, with an rms dispersion for the first 4 vibrational bands of only 0.11, 0.15, and 0.23 cm^{-1} for H_2, HD, and D_2, respectively. For transitions involving quantum numbers outside of the range used in the fitting procedure, the fit will obviously be much worse.

Because of the large change in equilibrium internuclear separation between the $\tilde{X}$ and the $\tilde{B}$ states, it is expected that the Franck-Condon factor will be very small for the 0–0 transition and will favor $|\Delta v| \gg 0$. The band oscillator strength, $f_{v''}^{v'}$, for H_2 has been measured experimentally by photoabsorption[51–54] and inelastic electron scattering[55–57] techniques. The band oscillator strength contains both the oscillator strength for the electronic transition and also the appropriate Franck-Condon factors for the vibrational transitions. Fabian and Lewis[53] determined the absorption oscillator strength to be $(1.75 \pm .16) \times 10^{-3}$ for $v' = 0$ and $(2.58 \pm .15) \times 10^{-2}$ for $v' = 5$. Using the Kolos and Wolniewicz surfaces, Allison and Dalgarno[58] have calculated band oscillator strengths and transition probabilities for all possible $\tilde{B} \leftrightarrow \tilde{X}$ and $\tilde{C} \leftrightarrow \tilde{X}$ transitions in H_2, HD, and D_2. Their values for the band oscillator strength of the Lyman band system of H_2 are 1.689×10^{-3} for $v' = 0$, 2.571×10^{-2} for $v' = 5$, and a maximum of 2.704×10^{-2} for $v' = 6$. The agreement with experiment is seen to be good. For emission from the $v' = 0$ level of the $\tilde{B}$ state, the total transition probability is 1.868×10^9 s^{-1}. They calculate that 66.3% of the transitions terminate in the $v'' = 3$–5 levels and 94.7% terminate in the $v'' = 2$–7 levels. The most intense emission is into the v''=4 level which has an R(0) line[32] at 74 992.06 cm^{-1}. It is obvious that the wavelength of

the fluorescent radiation is significantly offset from that of the incident radiation, especially for $v'=0$.

$\tilde{B} \rightarrow \tilde{X}$ transitions are not always into bound states of $\tilde{X}$. It is possible for a molecule to couple directly with the $\tilde{X}$ continuum and dissociate. Dalgarno and Stephens[59] have calculated for H_2 the fraction of $\tilde{B}$ molecules which dissociate. This fraction is less than 10^{-3} for $v' \leq 4$ and can approach unity for high v'.

The change in equilibrium internuclear separation between the $\tilde{C}$ and $\tilde{X}$ states is much less than that between the $\tilde{B}$ and $\tilde{X}$ states. It is therefore expected that the Frank-Condon factors will favor only small $|\Delta v|$'s. According to the theoretical calculations of Allison and Dalgarno,[58] the largest oscillator strength for H_2 absorption in the Werner band system is 7.28×10^{-2} for $v'=1$. For emission from the $v'=0$ level of the C state, the total transition probability is 1.18×10^9 s^{-1}. They further calculate that 66.3% of the transitions terminate in the v'' =1–2 levels and that 95.4% of the transitions terminate in the v'' =0–3 levels. The most intense transitions are into the $v''=1$ level with a band origin[32] of 94 928.76 cm^{-1}. In this case, the wavelength of the fluorescent radiation is only slightly offset from that of the incident radiation. The fraction of $\tilde{C}$ molecules which dissociate is less than 10^{-3} for $v' \leq 7$.

B. Absorption Experiments on H_2

Absorption spectra were taken using the apparatus described in the previous chapter. The ionization chamber was filled with an appropriate amount of the NO/He mixture while the VUV chamber was filled with an appropriate amount of Kr. During a series of experiments, the NO/He mixture was untouched while the Kr was replaced approximately once an hour.

Because the apparatus is a single beam instrument, it is impossible to obtain both the incident and transmitted VUV intensity simultaneously. Instead, a cycle of scans was used to obtain average values. Each cycle consisted of a scan of VUV

intensity as a function of dye laser wavelength taken with the center compartment evacuated, two such scans taken with the compartment filled, and a fourth scan taken with the compartment evacuated. Except for filling and evacuating the central compartment, no part of the apparatus was disturbed during a cycle. The appropriate scans from several cycles were averaged together to give the average incident and transmitted VUV intensity. The average transmitted VUV data was divided point by point by the average incident VUV data to give I_{trans}/I_{inc} for each wavelength, from which the absorption cross section can be obtained.

Figure 2 shows the absorption spectrum of H_2 obtained in such a manner. It is the result of 7 complete hour long data collection cycles at sample pressures of 4–6 torr. The H_2 was research grade (99.9999%) from Alfa Products and was used without further purification. The cross section was determined by dividing $\ln(I_{trans}/I_{inc})$ by the total H_2 number density and the pathlength. Thus, no attempt was made to correct for the different population of each rotational state. Because the determination of the absorbance involves the division of a large noisy signal by another large noisy signal, it is not suprising that the signal to noise ratio is poor. The background drift is caused by changes in the VUV tuning curve which did not completely cancel. The figure shows part of the 0–0 and 1–0 bands of the $\tilde{B} \leftarrow \tilde{X}$ transition. All observed lines were easily assignable and were found to be within a few wavenumbers of the literature values. The weakest line observed was the P(5) line of the 1–0 band. This implies a detection limit of $\approx 10^{14}$ states cm^{-3}, based on a room temperature population of 3×10^{13} states cm^{-3} $torr^{-1}$ for J''=5.

The expected line intensities are easily obtained and the formalism is developed in the next chapter. Figure 3 shows the absorption spectrum of H_2 calculated from Eq. 6.52, using the theoretical band oscillator strength and Hönl-London factors, a room temperature Boltzmann distribution of rotational state populations, a room temperature Doppler linewidth for the H_2 and a laser linewidth of $\Delta\nu_L =$

1.87 cm^{-1}. The agreement of the cross sections with the observed spectrum is poor for the strong transitions, but much better for the weak ones. It is believed that the discrepancy is the result of neglecting saturation and other such effects and also the difficulty of completely removing all of the H_2 from the cell during the blank runs.

The poor sensitivity and the low signal to noise ratio precludes the use of H_2 absorption as a technique to accurately measure product quantum state distributions arising from reactions. However, the presence of H_2 absorption bands proves that VUV radiation is being generated.

C. Summary

In summary, H_2 can be excited from the ground state to the first two electronic states ($\tilde{B}$ and $\tilde{C}$) by absorption of a photon with energy above $\approx$ 90 000 cm^{-1} (111.1 nm) and $\approx$ 100 000 cm^{-1} (100 nm), respectively. The $\tilde{B}$ state cannot ionize, has a negligibly small probability for dissociation, and fluoresces with a 5.4×10^{-10} s lifetime at a most probable photon energy of 75 000 cm^{-1} (133 nm). The $\tilde{C}$ state cannot ionize, has a negligibly small probability for dissociation, and fluoresces with a 7.6×10^{10} s lifetime at a most probable photon energy of 95 000 cm^{-1}. Therefore, it should be possible to detect individual quantum states of H_2 by exciting it with 111 nm VUV laser radiation and monitoring the resulting fluorescence, *i.e.*, by using the technique of laser induced fluorescence (LIF). The next chapter discusses LIF detection of H_2 in more detail.

III. H_2CO SPECTROSCOPIC DATA

A. Background

The UV absorption spectrum of formaldehyde was first recorded by Henri and Schou[60] in the late 1920's. Of principal interest was the absorption band near 300 nm which has resolvable vibrational and rotational structure. In 1934 Dieke and Kistiakowsky[61] analyzed the rotational structure of some of the bands, the first rotational analysis of an electronic transition of a polyatomic molecule. The vibrational analysis proceeded more slowly untill 1956 when Brand[62] realized that the upper state was not planar but instead was pyramidal. Even so, it wasn't until 1979 that the last fundamental frequency of the excited state was determined.[63]

Because of its simplicity, H_2CO has been studied by numerous experimental and theoretical techniques. The spectroscopic data has been reviewed in great detail by Moule and Walsh[64] in 1974 and Clouthier and Ramsay[65] in 1983. These two reviews include references to over 200 papers covering all aspects of H_2CO spectroscopy.

The ground state of H_2CO has C_{2v} symmetry. The ground state electronic configuration[66] of H_2CO in the one electron molecular orbital approximation is $(1a_1)^2(2a_1)^2(3a_1)^2(4a_1)^2(1b_2)^2(5a_1)^2(1b_1)^2(2b_2)^2\ \tilde{X}\ ^1A_1$. The $1b_1$ orbital is the CO π orbital and the $2b_2$ orbital is a nonbonding orbital located on the O perpendicular to the CO axis. The lowest excited electronic configurations are:

$(1b_1)^2(2b_2)^1(2b_1)^1$	$^3A_2$	$^1A_2$	(n,π^*)
$(1b_1)^2(2b_2)^1(6a_1)^1$	$^3B_2$	$^1B_2$	(n,σ^*)
$(1b_1)^1(2b_2)^2(2b_1)^1$	$^3A_1$	$^1A_1$	(π,π^*)

The H_2CO ground state has two dissociation channels,[67] as was discussed in Chapter 2. The first of these, the molecular channel, leads to the formation of H_2 and CO by a molecular rearrangement. This channel is nearly isoenergetic but has a barrier to reaction of 3.51 ± 0.13 eV. The second dissociation process, the

radical channel, leads to the formation of H and HCO by a simple bond fission. This reaction is endothermic by 3.73 ± 0.05 eV. The first ionization potential of the ground state is 10.87 ± 0.01 eV (114.1 nm), while the second and third ionization potentials are 14.09 and 15.85 eV, respectively.[64]

The low intensity absorption band near 300 nm is the $^1A_2 \leftrightarrow {}^1A_1$ ($\pi^* \leftrightarrow n$) band.[64] This transition is electric-dipole forbidden in C_{2v} symmetry. It is seen because of Herzberg-Teller vibronic interactions or because of magnetic dipole allowed transitions. The $^1A_2$ state is nonplanar, taking on a pyramidal configuration with the oxygen and hydrogen atoms forming the base. Inversion of the pyramid is along an extremely anharmonic double minimum potential, one of the reasons the vibrational structure of the excited state was so difficult to elucidate.[62]

Only a few of the expected higher energy intravalence transitions have been seen experimentally.[64] The $\pi^* \leftrightarrow \sigma$ transition is at 8.68 eV. The $\pi^* \leftrightarrow \pi$ transition has a calculated energy of $\approx$ 10 eV, but both Whitten[68] and Buenker and Peyerimhoff[69] find that the potential surface of this excited state is dissociative with respect to carbonyl bond stretching.

H_2CO has 6 normal modes of vibration.[65] They are ν_1 with a_1 symmetry which is the symmetric C–H stretching mode; ν_2, (a_1), C–0 stretch; ν_3, (a_1), symmetric H–C–H bending; ν_4, (b_1), out-of-plane bending; ν_5, (b_2), antisymmetric C–H stretching; and ν_6, (b_2), H–C–H rocking.

H_2CO is an asymmetric top molecule.[65] By convention, the a-axis is parallel to the z-axis which is parallel with the CO axis, the b-axis is parallel to the y-axis which is in the plane of the molecule, and the c-axis is parallel to the x-axis which is perpendicular to the plane of the molecule. The rotational constants for the ground state derived from both the microwave spectrum and the optical spectrum are given by Winnewisser *et al.*,[70] including all centrifugal distortion correction

terms to 6'th order. The principal rotational constants are $A = 281970.581$ MHz, $B = 38836.0455$ MHz, and $C = 34002.2131$ MHz. The asymmetry parameter[71] $\kappa = \frac{2B-A-C}{A-C}$, which varies from -1 for a prolate symmetric top to $+1$ for an oblate symmetric top, is -0.961 for the ground state of H_2CO, showing that H_2CO is very close to the prolate symmetric top limit. It is therefore expected that $K_a = K_{pro}$ will be a "good" quantum number in most cases.

The quantitative absorption spectrum in the vicinity of the H_2 absorption lines was obtained by Mentall *et al.*[72] in 1971. They found that the total absorption cross section at 110 nm is 15.1 Mb (1 Mb = 10^{-18} cm^2) with only weak diffuse structure. The ionization cross section at this same wavelength is 11.7 Mb. More recently, Suto *et al.*[73] measured a total cross section at this wavelength of 15.3 Mb, excellent agreement with the results of Mentall *et al.*[72] They also measured the fluorescence following excitation in the VUV. The fluorescence quantum yield peaks at 1.6% near 116 nm, then drops sharply for wavelengths below the ionization limit of 114 nm and is less than 0.1% by 110 nm. The fluorescence contains a VUV component due to CO fluorescence ($\tilde{A}\ ^1\Pi \rightarrow \tilde{X}\ ^1\Sigma^+$) and a UV-visible component due to HCO ($\tilde{B}\ ^2A' \rightarrow \tilde{X}\ ^2A'$)

The absorption cross section at 110 nm is less than that of HI and H_2S (see discussion in next two sections). Thus, H_2CO will attenuate the VUV less than those other molecules for the same sample pressure. It is estimated that a sample pressure of 0.1 torr will attenuate the VUV by only 45% over the entire 12.5 cm length of the central compartment. The VUV attenuation will be only 20% by the region of the PMT. Consequently, it is not expected that H_2CO will greatly interfere with the detection of H_2 by LIF.

B. $^1A_2 \leftrightarrow {}^1A_1$ Transition

The formaldehyde photodissociation reaction studied in this dissertation is initiated by a transition from the ground electronic state to the first excited

electronic state, the $^1A_2 \leftrightarrow {}^1A_1$ transition near 300 nm. Because of tne non-planarity of the excited state, the symmetry is C_s and this state should be labeled $^1A''$; however, it is derived from a $^1A_2$ state in C_{2v} symmetry and that is how it is usually referred to.

As mentioned earlier, this transition is electric dipole forbidden by symmetry, but is allowed by vibronic interactions.[49b] As a first approximation, the strength of the vibronic interaction between the states $\tilde{X}$ and $\tilde{Y}$ depends on the proximity of a third electronic state, $\tilde{Z}$. If the $\tilde{Z} \leftrightarrow \tilde{X}$ transition is allowed, and if $\tilde{Y}$ is near to $\tilde{Z}$, then the $\tilde{Y} \leftrightarrow \tilde{X}$ transition "borrows" intensity from $\tilde{Z} \leftrightarrow \tilde{X}$ because of a mixing of eigenfunctions. This mixing requires that the states have the same vibronic species. In a first approximation, this requires that $\tilde{Y}$ and $\tilde{Z}$ differ by no more than the species of a normal vibration.

Strickler and Barnhart[74] have taken a quantitative absorption spectrum of the entire $^1A_2 \leftrightarrow {}^1A_1$ transition. They determined that the oscillator strength for the entire band is $(2.40 \pm 0.05) \times 10^{-4}$. They derived approximate oscillator strengths for each vibronic band. van Dijk *et al.*[75] performed an *ab initio* calculation and derived an oscillator strength for every vibronic band that involved only a single mode with b_1 or b_2 symmetry.

The strongest vibronic bands[74,75] in the $^1A_2 \leftrightarrow {}^1A_1$ transition are those with B polarization, which is a "perpendicular" transition. These bands require that the changes in vibrational quanta in the b_1 modes are odd, changes in the b_2 modes are even, and changes in the a_1 modes are unrestricted.[76] Examples of these vibronic bands are 4_0^1 at 353.2 nm, 4_0^3 at 343.2 nm, $2_0^1 4_0^1$ at 339.0 nm, $2_0^1 4_0^3$ at 329.6 nm, and $2_0^2 4_0^1$ at 326.2 nm.

The rotational structure of these bands is complicated but straightforward. The rotational quantum number selection rules for the B polarized bands are $\Delta J = 0, \pm 1$ except $J' = 0 \not\leftrightarrow J'' = 0$, $\Delta K_a = \Delta K_{pro} = \pm 1$ and $\Delta K_c = \Delta K_{obl} = \pm 1$. A

detailed analysis of 11 rotational bands of H_2CO was made by Job *et al.*[76,77] More recently, Kerr *et al.*[78] obtained high resolution, 0.005 cm^{-1}, absorption spectra and magnetic rotation spectra for 4 B polarized bands.

The $2_0^1 4_0^3$ vibronic band at 30340.055 cm^{-1} is used for the photodissociation experiments in this dissertation. A rotational analysis of the $2^1 4^3$ state was performed by Sethuraman *et al.*[77] and Kerr *et al.*[78] This state is perturbed strongly for $K_a' > 4$ because of Coriolis interactions with the nearby $2^1 6^1$ (30252.2 cm^{-1}) and $2^1 4^1 6^1$ (30395.0 cm^{-1}) states. From the work of Strickler and Barnhart[74] the approximate ratio of absorption intensities for the $2_0^1 4_0^3 : 2_0^1 6_0^1 : 2_0^1 4_0^1 6_0^1$ vibronic bands is 1.00 : 0.13 : 0.01. This band and the perturbations have been studied recently by Apel and Lee.[79] The fluorescence lifetimes for individual rotational states of $2^1 4^3$ were too short to be measured, implying that they are < 15 ns. The lifetimes of the $2^1 6^1$ state vary from 20 ns to 90.5 ± 2.3 ns, a fourfold variation in fluorescence lifetime for a state more than 2000 cm^{-1} above the origin. This provides further evidence of the "lumpy" continuum. The lifetimes of the $2^1 4^1 6^1$ state are on the order of 20 ns. The $2^1 4^3$ $K_a' = 5$ stack of rotational levels is perturbed by a c-axis Coriolis resonance with the $2^1 4^1 6^1$ $K_a' = 4$ stack of levels which are within 1.25 cm^{-1} of each other. The perturbation for this particular interaction is $0.15 cm^{-1} \times \sqrt{J(J+1) - 20}$

C. Photoacoustic Spectrum

A photoacoustic spectrum of H_2CO was taken using the photoacoustic cell described in the dissertation of D. J. Moll.[80] This provides an overview of the spectrum in the region of interest. The H_2CO was obtained from the room temperature vaporization of the polymer, paraformaldehyde, obtained from J. T. Baker and was used without further purification. Sample pressures were on the order of 0.1 torr. In order to provide efficient collisional relaxation and a strong photoacoustic signal, several hundred torr of He were added. The He pressure was

extremely critical and had to be adjusted before every scan. Pressure changes of 25 torr would cause greater than an order of magnitude change in signal.

Figure 4 shows a photoacoustic spectrum taken from 317.5 to 335.0 nm using the Molectron laser system. Many vibronic bands are seen. The two vibronic bands with B polarization in this region, $2_0^1 4_0^3$ and $2_0^2 4_0^1$, are obviously the strongest two bands in the spectrum. According to the theoretical calculations[75] and absorption spectra,[74] the oscillator strength of the $2_0^1 4_0^3$ is about one-half that of the $2_0^2 4_0^1$ band. In Fig. 4 these bands have comparable areas. It is not known if this discrepancy is an experimental artifact caused by changing sensitivity or sample pressure during a scan, or if it reflects the change in dissociation mechanism which occurs in this region of the spectrum. As pointed out by Moll, the photoacoustic technique is sensitive to changes in quantum yield and energy released in translation.

Figure 5 is a closeup showing just the $2_0^1 4_0^3$ band. The top spectrum was obtained using the Molectron laser system while the middle spectrum was obtained using the Quanta Ray laser system. The two spectra are identical except for changes due to different linewidths of the UV laser radiation.

The bottom spectrum in Figure 5 is a theoretical spectrum. The ground state rotational constants of Winnewisser *et al.*[70] and the excited state rotational constants of Kerr *et al.*[78] were used to determine the energy levels up to 6'th order in the centrifugal distortion correction terms. This neglects the effects of the perturbations. The line strengths were calculated to second order using the procedure of Lide,[81] also neglecting the effects of perturbations. The ground state populations were calculated using a 298.15 K Boltzmann distribution and included the nuclear spin degeneracy. The assumed linewidth was 0.62 cm^{-1} which corresponds to the convolution of the room temperature Doppler linewidth of 0.16 cm^{-1} and a UV laser linewidth of 0.60 cm^{-1}, the linewidth expected if the dye laser linewidth in the visible is the specified 0.3 cm^{-1}.

The calculated spectrum is similar to the experimental spectra. The principal difference appears to be that the experimental linewidths are much greater than expected, especially for the spectrum taken with the Molectron dye laser system. It is believed that this is a result of a larger dye laser linewidth than specified, implying that the Molectron DL-18 dye laser oscillator cavity is out of adjustment. The linewidth of the Quanta Ray system is almost exactly 0.60 cm^{-1} in the UV from analysis of the H_2 LIF spectrum in the next chapter. The other possibility is that the several hundred torr of He is broadening the lines significantly. From the spectrum taken with the Quanta Ray laser system it appears that the linewidth is on the order 1 cm^{-1}. A linewidth of 1 cm^{-1} from the pressure broadening of 500 torr of He would require a He–H_2CO cross section of 150 $Å^2$. While rotational energy transfer processes of H_2CO with H_2CO can have cross sections as large as 300 $Å^2$,[82] it seems unlikely that the He–H_2CO interaction would be close to that. The H_2CO-H_2CO hard sphere collsion cross section is only 63 $Å^2$.[79]

Figure 6 is a closeup of a portion of the $2_0^1 4_0^3$ band. This spectrum shows the region of the ${}^rR_{K_a''}$ bandheads for $K_a'' = 2$–7 (the notation is ${}^{\Delta K_a}\Delta J_{K_a''}$). This figure shows the good agreement between the calculated and experimental spectra with respect to the position and intensity of absorption lines. The larger than expected linewidths in the experimental spectra are obvious. The ${}^rR_3$ and ${}^rR_4$ bandheads are labeled. These are the two transitions used in the photodissociation experiments discussed in a later chapter.

D. Summary

The H_2CO molecule has well resolved rotational structure, allowing for the excitation of specific K_a' states in the $2^1 4^3$ vibronic level of the $^1A_2$ excited electronic state. H_2CO is not expected to significantly interfere with the detection of H_2 by LIF.

IV. HI SPECTROSCOPIC DATA

One potential H atom precursor is HI. Because it is a diatomic molecule, there is only one neutral photodissociation pathway available: H + I. Since there is only one dissociative process and there can be no rotational or vibrational excitation of the atomic I fragment, it is expected that the H atom would have an extremely well defined recoil energy. Because of the simplicity of HI, it is not as likely as larger molecules to interfere with H_2 detection. In the first subsection, previous experimental work on HI is reviewed; in the second, my own experiments are reviewed.

A. Background

The UV and vacuum UV (VUV) absorption spectrum of HI was first studied by Price[83] in the 1930's using a moderate dispersion VUV spectrograph (2Å/mm). Some of the major peaks were fit into three Rydberg series converging to 89 130 cm^{-1} (11.05 eV). Other studies[84–87] concentrated on the broad continuum starting near 27 800 cm^{-1} with a maximum at 45 500 cm^{-1}. The maximum absorption cross section is $\approx 8.4 \times 10^{-19}$ cm^{-2}. Even under high resolution no structure has been seen. A theoretical analysis of this continuum by Mulliken[88,89] showed that it is caused by direct absorption to several intersecting repulsive states. More recently, Ginter and coworkers[90–93] have reexamined the absorption spectrum from 50 000–74 400 cm^{-1} with a high dispersion (0.31 Å/mm) 6.65 meter VUV spectrograph (resolution < 0.2 cm^{-1}). A complete rotational analysis and electronic assignment of each band was performed. The photoionization[94–97] spectrum has been obtained from 82 600 to 116 300 cm^{-1}. The highest resolution[97] of ≈ 7 cm^{-1} was obtained from 82 600 to 90 900 cm^{-1}. The photoelectron spectrum has also been obtained.[98–100] The spectroscopic results are summarized in Ref. 101.

The ground state electronic configuration of HI in the one electron molecular orbital approximation is $KLMN_{spd}(5s\sigma)^2(5p\sigma)^2(5p\pi)^4$ $\tilde{X}$ $^1\Sigma^+$ in the united

atom limit[94] and is $\cdots(9\sigma)^2(10\sigma)^2(5\pi)^4(2\delta)^4(11\sigma)^2(6\pi)^4$ $\tilde{X}\ ^1\Sigma^+$ in molecular orbital symmetry notation.[102] The lowest excited electronic configurations for the hydrogen halides are given by:[93,103]

$(\sigma^2\pi^3)\,a\sigma^*$	$a\ ^3\Pi_i$,	$A\ ^1\Pi$
$(\sigma\pi^4)\,a'\sigma^*$	$t\ ^3\Sigma^+$,	$V\ ^1\Sigma^+$
$(\sigma^2\pi^3)\,b\sigma$	$b\ ^3\Pi_i$,	$C\ ^1\Pi$
$(\sigma^2\pi^3)\,c\sigma$	$d\ ^3\Pi_i$,	$D\ ^1\Pi$
$(\sigma^2\pi^3)\,c\pi$	$e\ ^3\Sigma^+$,	$E\ ^1\Sigma^+$
	$f\ ^3\Delta_i$,	$F\ ^1\Delta$
	$g\ ^3\Sigma^-$,	$G\ ^1\Sigma^-$
$(\sigma^2\pi^3)\,d\pi$	$h\ ^3\Sigma^+$,	$H\ ^1\Sigma^+$
	$i\ ^3\Delta_i$,	$I\ ^1\Delta$
	$j\ ^3\Sigma^-$,	$J\ ^1\Sigma^-$
$(\sigma^2\pi^3)\,d\sigma$	$n\ ^3\Pi_i$,	$N\ ^1\Pi$
$(\sigma^2\pi^3)\,a\delta$	$k\ ^3\Pi_r$,	$K\ ^1\Pi$
	$l\ ^3\Phi$,	$L\ ^1\Phi$
$(\sigma^2\pi^3)\,e\sigma$	$m\ ^3\Pi_i$,	$M\ ^1\Pi$
$(\sigma^2\pi^3)\,f\sigma$	$r\ ^3\Pi_i$,	$R\ ^1\Pi$
$\vdots$	$\vdots$	$\vdots$

The term symbols were derived assuming (Λ, S) coupling. As discussed by Ginter *et al.*,[90–93,102] (Λ, S) coupling is descriptive of state ancestry while (Ω, ω) coupling is often a more accurate description of the observed angular momentum coupling. The r and i subscripts show whether the multiplet structure is regular or inverted. Of the above states, only the h, i, I, J, l, and L states have not yet been identified in HI or DI.

Those states with a $(\sigma^2\pi^3)\,n\lambda$ configuration are based on the $(\sigma^2\pi^3)$ $\tilde{X}\ ^2\Pi_i$ core of the HI^+ ion. The first three ionization potentials for HI are 10.386, 11.0495, and 14.1 eV which correspond to ionization to the $(\sigma^2\pi^3)$ $\tilde{X}\ ^2\Pi_{\frac{3}{2}}$, $(\sigma^2\pi^3)$ $\tilde{X}\ ^2\Pi_{\frac{1}{2}}$, and $(\sigma\pi^4)$ $\tilde{A}\ ^2\Sigma^+$ states of HI^+, respectively.[96–100] The observed spin-orbit splitting of the ground state ion is -5350 cm^{-1}, which compares with a splitting of -7603.15 cm^{-1} for neutral I.[104] Absorption to states between the $^2\Pi_{\frac{3}{2}}$ and $^2\Pi_{\frac{1}{2}}$ ionization potentials autoionize, leading to several well developed Rydberg series

converging to the $^2\Pi_{\frac{1}{2}}$ limit in the photoionization spectrum.[97] However, between the $^2\Pi_{\frac{1}{2}}$ and $^2\Sigma^+$ ionization potentials there is only some weak autoionization Rydberg series converging to the v=1 level of the $^2\Pi_{\frac{1}{2}}$ ion (11.31 eV) and one broad feature at 12.34 eV in the photoionization spectrum.[96]

According to Mulliken, of the states derived from the first two electronically excited configurations, only the V state is bound.[88] The dissociative states $\tilde{a}\ ^3\Pi_1$ and $\tilde{A}\ ^1\Pi$ correlate to H + I($^2P_{\frac{3}{2}}$) while the dissociative states $\tilde{a}\ ^3\Pi_{0+}$ and $t\ ^3\Sigma^+$ correlate to H + I*($^2P_{\frac{1}{2}}$). The transition dipole moment for diatomic molecules must be parallel or perpendicular to the internuclear axis, *i.e.*, the electric field vector of the incident photon must be parallel or perpendicular to the molecular axis.[105] From symmetry considerations, transitions from a Σ^+ state to Σ^+ or $^3\Pi_{0+}$ states will be parallel transitions while those to $^3\Pi_1$ or $^1\Pi$ states will be perpendicular transitions. Thus, Mulliken's analysis of the HI continuum predicts that ground state I($^2P_{\frac{3}{2}}$) is formed from perpendicular transitions while excited I*($^2P_{\frac{1}{2}}$) is formed from parallel transitions.

It is therefore possible that two dissociation processes can occur after photon absorption into the 45 500 cm^{-1} (5.64 eV) continuum, HI $\rightarrow$ H + I or HI $\rightarrow$ H + I*. From thermochemical data the dissociation energy[101] of HI is 3.054 eV to ground state I and 3.997 eV to excited state I*. Since the difference in energy between the two channels is a large fraction of the total excitation energy, it is important to measure the relative proportions of the two processes, *i.e.*, the branching ratio. Early direct measurements by Donovan and Husain using a broadband photolysis flashlamp showed that roughly one-fifth of the iodine atoms were electronically excited.[106] Later, the branching ratio was measured at the 266 nm Nd:YAG fourth harmonic by Clear, *et al.*[107] Using time-of-flight mass spectroscopy to measure the angular distribution and velocity of the recoiling H atoms, they found that $(36 \pm 5)\%$ of the I atoms were excited. Recently, Schmiedl *et al.*[108] used Lyman-α

laser induced fluorescence Doppler spectroscopy to determine the recoil velocity, angular distribution, and branching ratio at the 266 nm Nd:YAG fourth harmonic. Their measured recoil velocities agreed almost exactly with those predicted from knowing the photon energy, the literature dissociation energies, and the kinematics of a direct photodissociation process. They found that (40±5)% of the I atoms were excited, in good agreement with the previous measurements of Clear *et al.* Both groups found that I was formed from a perpendicular transition and that I* was formed from a parallel transition, in agreement with the prediction by Mulliken.

It is important to know whether HI would interfere with the detection of H_2 by a laser induced fluorescence scheme. The VUV radiation at ≈ 91 000 cm (110 nm) is generated by tripling ultraviolet radiation at ≈ 330 nm in Kr, as discussed in the previous chapter. The residual 330 nm radiation will be absorbed by the low energy tail of the HI dissociative continuum, leading to some H + I production. Previous measurements show that the absorption cross section at this wavelength[86] is $\approx 1 \times 10^{-21}\,cm^2$ which is negligibly small.

The total absorption cross section at 110 nm has not been reported in the literature. This spectral region has energies between the $^2\Pi_{\frac{1}{2}} v{=}0$ and $^2\Pi_{\frac{1}{2}} v{=}1$ ionization potentials and is expected to be part of the ionization continuum. It was recently estimated that the state specific ionization cross section at 110 nm is 8×10^{-18} cm^2 and 2×10^{-18} cm^2 for v=0 and 1, respectively. The nearby feature at 100.5 nm seen in photoionization experiments is extremely broad because of predissociation.[96] It is estimated for that state the predissociation rate exceeds the autoionization rate by a factor of 9. It can be estimated that if the total cross section is between 10^{-17} and 10^{-16} cm^2, then a 0.1 torr sample of HI will absorb 33–98% of the incident radiation with the current experimental apparatus, a significant amount. Since the VUV laser intensity is so low, it is expected that any dissociation or ionization products due to the VUV radiation would be insignificant

to the H_2 detection scheme. However, the strong attenuation of the incident VUV radiation is a potential problem which requires more accurate total absorption cross sections to properly evaluate.

The H_2 fluorescence will be over many discrete lines over a broad energy range centered at $\approx$ 75 000 cm^{-1}. The HI absorption spectrum in this general region consists of many discrete lines. A detailed listing of the observed spectral features has only extended to 74 400 cm^{-1}. However, it is considered unlikely that the H_2 emission lines would exactly coincide with the HI absorption lines.

It would appear that HI would not significantly interfere with H_2 detection by laser induced fluorescence. However, a report has recently appeared in the literature which claims that HI interferes with the detection of H atoms by Lyman-α (121.56 nm) laser induced fluorescence[109] by also fluorescing. No experimental details were provided, so it is unclear as to the intensity, wavelength, or temporal behaviour of this HI fluorescence. This is an extremely suprising result. The initially populated state can relax to the ground state, the dissociative continuum, or an excited electronic state by emission of a photon. Since the geometry of almost all the HI excited states is very similiar to that of the ground state, the Franck-Condon factors should not favor large $|\Delta v|$'s. Hence, any fluorescence to the ground state should have a wavelength almost identical to that of the excitation wavelength. In the HI photodissociation experiments of Schmiedl *et al.*,[108] a Lyman-α band-pass filter was placed between the reaction region and the photomultiplier. No HI fluorescence was reported. Thus, it does not appear likely that the final state after fluorescence is the ground state. If the final state was a continuum state, the maximum photon energy would be 7.14 eV (173 nm). Lorenz *et al.*[110] studied the $H + HI \rightarrow HH + I$ reaction using a Lyman-α resonance fluorescence detection scheme to follow the H atom concentration. In their experiments HI was present at an initial 6–40 fold excess, yet without filtering

or disperising the fluorescence they were able to obtain a H atom detection limit of 5×10^9 molecules cm^{-3} using a photomultiplier equipped with a CsI photocathode. They did not report any HI fluorescence. Thus, it seems unlikely that the final state after fluorescence is in the dissociative continuum. If the final state was an electronically excited state, the maximum photon energy would be 3.28 eV (378 nm) which would be undetectable with a solar blind photomultiplier. Another possibility is that the HI dissociates to form H atoms and electronically excited I atoms which then fluoresce, as has been suggested by Bersohn.[111] In this case, the maximum photon energy would be 7.14 eV (173 nm) which is within the detection range of a PMT with a CsI photocathode. I does have strong emission lines[112] at 183.0 nm and 184.4 nm, so these transitions are good candidates for the wavelength of the conflicting fluorescence if Bersohn's hypothesis is correct.

B. Experiments on HI

HI was obtained from Matheson and was purified by several liquid nitrogen freeze-pump-thaw cycles followed by a fractional distillation from a glass flask immersed in a dry ice/acetone slush bath to a glass flask immersed in liquid nitrogen. The purified HI was stored at room temperature in darkened glass bulbs untill needed.

1. Electron energy loss spectroscopy

Figure 7 shows an electron energy loss spectrum of HI taken under nearly optical conditions (50 eV, 10°) in the region of 4–12 eV. It provides an overview of the HI optical absorption spectrum. Table 3 shows the assignment of all peaks and shoulders seen in Fig. 7. The agreement with the optical spectrum is exceptionally good. All but a few lines were assigned, most of the unassigned lines lying in the region above the high resolution spectrum of Ginter *et al.*[90–93,102] and below the Rydberg series seen in photoionization.[97] All lines that should have been seen were observed.

The spectrum shows the strong continuum at energies above 11 eV. Unfortunately, it is impossible from this spectrum to obtain a quantitative estimate of the optical absorption cross section. The spectrum does suggest a possible excited state for the HI fluorescence to come from. At the Lyman-α energy of 10.1989 eV, there are several nearby Rydberg states, specifically at 10.15 and 10.20 eV. The rotational envelopes for these bands are likely to exceed 0.05 eV and could possibly overlap the Lyman-α line. The absorption cross section at 11.1 eV is approximately 70% less than that at 10.2 eV; thus it can be expected that the HI fluorescence at 11.1 ev will also be 70% less than that reported by Tsukiyama, *et al.*[109]

2. Absorption spectroscopy

The VUV absorption spectrum of HI was obtained in a manner similiar to that of H_2. A representative spectrum is shown in Fig. 8. It is the result of 5 complete data collection cycles taken with pure HI. The spectrum was extremely difficult to obtain for two reasons. First, the HI pressure was not constant but continually decreasing due to absorption onto the cell walls. Attempts to reduce this absorption were unsuccessful. In order to minimize the effect of of pressure changes, the scans were taken in both wavelength directions and averaged. Second, material was constantly being deposited on the LiF windows where the VUV laser beam entered the central compartment. It was necessary to continually shift the laser beam position through the cell.

It is believed that the curvature in the spectrum is the result of the HI pressure decreasing during each scan. Even so, there does not appear to be any significant structure to the absorption. The absorption cross section of 20 Mb at the ends of the scan are approximately what is expected based on the ionization cross section of 10 Mb in this region.

C. Summary

The HI dissociative continuum near 45 500 cm^{-1} provides H atoms with two well defined translational energies. The VUV absorption cross section is not known exactly, but it appears that it will be large enough that 0.1 torr samples of HI will strongly attenuate the VUV radiation used for the LIF detection of H_2. There are reports that when HI is excited with Lyman-α radiation there is strong fluorescence, but the effect of this on the LIF detection of H_2 is not yet known.

IV. H_2S SPECTROSCOPIC DATA

A second potential H atom precursor is H_2S. Because it is a triatomic molecule there are two neutral photodissociation pathways available: $H_2S \rightarrow H + HS$ or $H_2S \rightarrow H_2 + S$. It is expected that the simple bond scission would predominate, and since H_2S is a bent molecule, a further expectation is that the recoiling SH fragment would be rotationally, but not vibrationally, excited.

A. Background

The discrete UV and VUV absorption spectrum of H_2S was first studied by Price[113] in 1936. Several Rydberg series were found converging to an average value of 84 470 cm^{-1}. Other studies[114–121] examined not only the discrete transitions in more detail but also the continuum which starts near 37 000 cm^{-1} and reaches a maximum at $\approx$ 51 000 cm^{-1} with an absorption cross section[114] of 7.4×10^{-18} cm^2. Most of the VUV spectra were taken under moderate resolution and were not rotationally resolved. The photoelectron spectrum[122–126] has been obtained with a highest accuracy[126] of 16 cm^{-1}. This molecule has also been extensively studied theoretically.[127–129]

The ground state of the H_2S molecule has C_{2v} symmetry. The ground state electronic configuration in the one electron molecular orbital approximation[120] is $(1a_1)^2(2a_1)^2(1b_2)^2(3a_1)^2(1b_1)^2(4a_1)^2(2b_2)^2(5a_1)^2(2b_1)^2 \quad X\ ^1A_1$. The first 5 orbitals are essentially the $1s$, $2s$, and $2p$ orbitals of the sulphur atom while the $(2b_1)$ orbital is the nonbonding $3p$ orbital of the sulphur atom with electron density perpendicular to the molecular plane. The expected Rydberg orbitals are

$$n\,s: \quad a_1 \qquad n \geq 4$$

$$n\,p: \quad b_2, a_1, b_1 \qquad n \geq 4$$

$$n\,d: \quad a_1, a_2, b_2, a_1', b_1 \qquad n \geq 3.$$

Almost all of the transitions observed in the VUV have been assigned to Rydberg orbitals built on a $\cdots(2b_1)^1$ core.[120] However, the identity of the states

responsible for the broad continuum is still debated. The dominant process is photodissociation to give an H atom and an SH radical.[130] However, the continuum does show a weak vibrational progression in the ν_2 bending mode.[116] It is believed that the dissociation is a result of a predissociation process involving at least 2 electronic states, one Rydberg in character and the rest essentially valence-shell in nature. It is believed that the Rydberg state is the $\cdots(2b_1)^1(4s\,a_1)^1\ {}^1B_1$ state while the valence-shell state could be $\cdots(2b_1)^1(3b_2)^1\ {}^1A_2$, $\cdots(2b_1)(6a_1)^1\ {}^1B_1$, or $\cdots(2b_2)^1(3b_2)^1\ {}^1A_1$ according to different researchers.[117,127–129]

Not only is the assignment of the continuum state uncertain, but also the internal energy of the recoiling SH fragment is uncertain. The dissociation energy[131] is 3.91 eV. For example, after photodissociation at 193 nm one group using LIF to detect the SH fragment directly found no vibrationally excited product ($< 0.5\%$) and very little rotational excitation[132,133] while another group using time-of-flight spectroscopy to measure the translational energy of the recoiling H atom found evidence of significant SH vibrational excitation ($\approx 10\%$ of the molecules).[134] Even so, no more than 7% of the excess energy appeared as internal energy, the rest appearing as translational energy.

The first three ionization potentials[126] are at 10.466, 12.777, and 14.643 eV, corresponding to removal of a $(2b_1)$, $(5a_1)$, and $(2b_2)$ electron, respectively. The spin orbit splitting is negligibly small. The lowest state of the ion, $\cdots(2b_1)^1\ X\ {}^2B_1$, has a geometry very similiar to that of the neutral molecule, as expected for the removeal of an non-bonding electron. The absorption cross section[116] between the first two IP's has been studied at low resolution ($\approx$3Å). There are many diffuse bands superimposed upon a continuum. Photoionization accounts for only 30 to 60% of the total absorption cross section in this region, the rest presumably being due to photodissociation.

It is important to know whether H_2S would interfere with the detection of H_2 by laser induced fluorescence. The residual 330 nm radiation will not be absorbed by the H_2S dissociative continuum. The total absorption cross section[116] reaches a maximum in the region of the H_2 absorption lines of 5×10^{-17} cm^2 at 110 nm. Therfore, a 0.1 torr sample of H_2S would absorb approximately 87% of the incident VUV radiation. This is more than either H_2CO or HI would absorb.

B. Experiments on H_2S.

H_2S was obtained from Matheson. It was purified by repeated liquid nitrogen freeze-pump-thaw cycles followed by a fractional distillation from a glass flask immersed in a dry ice/acetone slush bath to a glask flask immersed in liquid nitrogen. Purified samples were stored at room temperature in darkened glass flasks.

1. Electron Energy Loss Spectroscopy

Figure 8 show an electron energy loss spectrum of H_2S taken under nearly optical conditions (50 eV, 10° in the region of 4–12 eV. It provides an overview of the H_2S optical absorption spectrum. Table 4 shows the assignment of all observed shoulders and peaks. The agreement with the optical spectrum is exceptionally good. All but a few shoulders were identified.

2. Absorption spectroscopy

The VUV absorption spectrum of H_2S was obtained in a manner similiar to that of H_2. A representative spectrum is shown in Fig. 9. It is the result of 3 complete data collection cycles taken with 100 torr of a 0.1% H_2S in He mixture. Unlike the HI spectrum, there was no difficulty with deposits on the LiF windows.

The agreement between the expected and observed cross section is reasonably good. At the sample pressures used, 85% of the incident light was absorbed instead of the predicted 90%. Thus, it is not suprising that the total cross sections differ

by $\approx$ 20%. In addition, a previously seen broad spectral feature at 110.3 nm was observed.

C. Summary

H_2S has a broad continuum near 50 000 cm^{-1} which yields high energy H atoms. There is some disagreement on the exact degree of internal excitation of the SH fragment, but more than 93% of the released energy appears as product translational energy. H_2S has a strong VUV absorption cross section in the vicinity of the H_2 absorption lines which will interfere with the LIF detection scheme by severely attenuating the VUV photon intensity.

TABLE 1. Dunham Equation Constants for H_2

	$\tilde{X}\ ^1\Sigma_g^+$	$\tilde{B}\ ^1\Sigma_u^+$	$\tilde{C}\ ^1\Pi^+$	$\tilde{C}\ ^1\Pi^-$
Y_e	0.00	91700.05	100055.01	100055.01
Y_{10}	4403.28	1358.56	2446.64	2446.64
Y_{20}	-123.48	-21.374	-70.247	-70.247
Y_{30}	1.6978	9.7657(-1)	8.6450(-1)	8.6450(-1)
Y_{40}	-1.5638(-1)	-1.2536(-1)	-4.9091(-2)	-4.9091(-2)
Y_{50}	1.3877(-2)	1.0683(-2)		
Y_{60}	-1.3623(-3)	-5.4522(-4)		
Y_{70}	6.5724(-5)	1.5317(-5)		
Y_{80}	-1.5840(-6)	-1.8183(-7)		
Y_{01}	60.896	19.985	32.073	31.402
Y_{11}	-3.2425	1.1220	-2.4138	-1.8264
Y_{21}	2.6169(-1)	8.9542(-2)	4.1365(-1)	2.0284(-1)
Y_{31}	-1.1319(-1)	-6.1262(-3)	-4.3431(-2)	-6.6271(-2)
Y_{41}	3.1433(-2)	1.5923(-4)		1.0446(-2)
Y_{51}	-5.3877(-3)			-6.1937(-4)
Y_{61}	5.6570(-4)			
Y_{71}	-3.5895(-5)			
Y_{81}	1.2660(-6)			
Y_{91}	-1.9252(-8)			
Y_{02}	-4.7288(-2)	-1.6350(-2)	-3.6739(-2)	-2.2647(-2)
Y_{12}	5.2485(-3)	1.5935(-3)	5.3626(-2)	8.4436(-3)
Y_{22}	-3.6031(-3)	3.2329(-4)	-3.7394(-2)	-7.1957(-3)
Y_{32}	1.6453(-3)	-1.3551(-4)	1.1891(-2)	2.7908(-3)
Y_{42}	-4.1272(-4)	1.4604(-5)	-1.9703(-2)	-4.7769(-4)
Y_{52}	5.9343(-5)	-4.4216(-7)	1.2516(-4)	2.9671(-5)
Y_{62}	-4.8800(-6)			
Y_{72}	2.1290(-7)			
Y_{82}	-3.8262(-9)			
Y_{03}	5.2539(-5)	1.3597(-5)		3.2961(-5)
Y_{13}	-2.5978(-5)	4.7385(-6)		-6.2997(-5)
Y_{23}	2.3509(-5)	-5.5909(-6)		5.9815(-5)
Y_{33}	-1.0432(-5)	1.7781(-6)		-2.3594(-5)
Y_{43}	2.4948(-6)	-2.9948(-7)		4.0671(-6)
Y_{53}	-3.3844(-7)	3.3926(-8)		-2.5280(-7)
Y_{63}	2.5819(-8)	-2.4081(-9)		
Y_{73}	-1.0210(-9)	6.463(-11)		
Y_{83}	1.608(-11)			

Y_{04}	-5.9126(-8)	-2.8406(-9)
Y_{14}	8.2740(-8)	-1.8231(-8)
Y_{24}	-8.2517(-8)	1.5253(-8)
Y_{34}	3.9448(-8)	-4.9336(-9)
Y_{44}	-1.0341(-8)	7.687(-10)
Y_{54}	1.5700(-9)	-3.467(-11)
Y_{64}	-1.378(-10)	-7.452(-12)
Y_{74}	6.514(-12)	1.087(-13)
Y_{84}	-1.290(-13)	-3.507(-14)

a) All constants in cm^{-1}.

b) The numbers in parentheses are the powers of ten by which the preceding decimal number should be multiplied.

TABLE 2. Dunham Equation Constants for H_2, HD, and D_2($v < 7$)

	$\tilde{X}\ ^1\Sigma_g^+$			$\tilde{B}\ ^1\Sigma_u^+$		
	H_2	HD	D_2	H_2	HD	D_2
Y_e	0.00	0.00	0.00	91700.44	91698.91	91679.40
Y_{10}	4402.32	3813.33	3114.88	1357.68	1177.22	962.36
Y_{20}	-122.482	-91.836	-61.193	-20.618	-15.645	-10.432
Y_{30}	1.2254	7.8559(-1)	3.7680(-1)	6.4482(-1)	4.4544(-1)	2.0660(-1)
Y_{40}	-3.8767(-2)	-2.1699(-2)	-1.1291(-3)	-5.0774(-2)	-3.1066(-2)	-7.2946(-3)
Y_{50}	-2.6755(-3)	-1.2606(-3)	-8.9631(-4)	1.7707(-3)	9.6065(-4)	
Y_{01}	60.841	45.651	30.461	20.036	15.058	10.045
Y_{11}	-3.0434	-1.9805	-1.1273	-1.2544	-7.7998(-1)	-3.5715(-1)
Y_{21}	4.6391(-2)	2.9814(-2)	5.0398(-2)	1.8529(-1)	8.2147(-2)	-1.7140(-2)
Y_{31}	-3.4778(-3)	-2.0817(-3)	-1.1913(-2)	-3.4245(-2)	-1.0295(-2)	1.2686(-2)
Y_{41}	1.2369(-4)		1.4056(-3)	3.7930(-3)	8.0343(-4)	-1.8910(-3)
Y_{51}	-1.7141(-5)		-6.2498(-5)	-1.7313(-4)	-2.7495(-5)	9.1761(-5)
Y_{02}	-4.6286(-2)	-2.6201(-2)	-1.2027(-2)	-1.6903(-2)	-9.5894(-3)	-3.8930(-3)
Y_{12}	1.7192(-3)	4.6956(-4)	1.7896(-3)	2.8264(-3)	1.2790(-3)	-2.5664(-4)
Y_{22}	-4.0280(-5)	5.7608(-5)	-1.0671(-3)	-4.0022(-4)	-1.7245(-4)	5.0559(-4)
Y_{32}	-2.6021(-6)	-5.5481(-6)	2.9643(-4)	2.6070(-5)	1.0553(-5)	-1.6887(-4)
Y_{42}			-3.5542(-5)			2.2687(-5)
Y_{52}			1.5305(-6)			-1.0733(-6)
Y_{03}	4.6047(-5)	2.2(-5)	3.3(-6)	1.6964(-5)	7.2(-6)	
Y_{13}	-2.7091(-6)			-3.4676(-6)		
Y_{23}	3.2569(-7)			2.3755(-7)		
Y_{33}	-2.3235(-8)					
Y_{04}	-3.6359(-8)			-1.0575(-8)		
Y_{14}	3.4440(-9)			1.9029(-9)		
Y_{24}	-5.131(-10)					
Y_{34}	2.165(-11)					

a) All constants in cm^{-1}.

b) The numbers in parentheses are the powers of ten by which the preceding decimal number should be multiplied.

TABLE 3. Electron Energy Loss Spectrum of HI

E_{obs} (eV)	Label	Assignment[a] e^{-1} Config.[b]	Term Sym.	v	E_{lit}[a] (ev)
4.5-6.5	a_1, a_0, A	$(\sigma^2\pi^3)\, a\sigma^*$	$^3\Pi_1, ^3\Pi_{0+}, ^1\Pi$		3.5-6.6
6.940	b_2	$(\sigma^2\pi^3)\, b\sigma$	$^3\Pi_2$	0	6.922
7.037	b_1	$(\sigma^2\pi^3)\, b\sigma$	$^3\Pi_1$	0	7.035
7.548	b_0	$(\sigma^2\pi^3)\, b\sigma$	$^3\Pi_0$	0	7.544
7.727	C	$(\sigma^2\pi^3)\, b\sigma$	$^1\Pi$	0	7.727
7.919	d_1	$(\sigma^2\pi^3)\, c\sigma$	$^3\Pi_1$	0	7.921
7.952	e	$(\sigma^2\pi^3)\, c\pi$	$^3\Sigma^+$	0	7.960
8.008	f_3	$(\sigma^2\pi^3)\, c\pi$	$^3\Delta_3$	0	8.006
8.028	f_2	$(\sigma^2\pi^3)\, c\pi$	$^3\Delta_2$	0	8.021
8.171	d_2	$(\sigma^2\pi^3)\, c\sigma$	$^3\Pi_2$	1	8.184
8.192	g_{0+}	$(\sigma^2\pi^3)\, c\pi$	$^3\Sigma^-$	0	8.186
8.243					
8.269					
8.361					
8.458	H	$(\sigma^2\pi^3)\, d\pi$	$^1\Sigma^+$	0	8.465
8.473	V	$(\sigma^1\pi^4)\, a'\sigma^*$	$^1\Sigma^+$	(m+1)	8.492
8.555	k_1	$(\sigma^2\pi^3)\, a\delta$	$^3\Pi_1$	0	8.554
8.616	V	$(\sigma^1\pi^4)\, a'\sigma^*$	$^1\Sigma^+$	(m+3)	8.607
8.652	f_1	$(\sigma^2\pi^3)\, c\pi$	$^3\Delta_1$	0	8.640
8.672	V	$(\sigma^1\pi^4)\, a'\sigma^*$	$^1\Sigma^+$	(m+4)	8.668
8.693	F	$(\sigma^2\pi^3)\, c\pi$	$^1\Delta$	0	8.707
8.713	H	$(\sigma^2\pi^3)\, d\pi$	$^1\Sigma^+$	1	8.709
8.739	V	$(\sigma^1\pi^4)\, a'\sigma^*$	$^1\Sigma^+$	(m+5)	8.742
8.790	m_2	$(\sigma^2\pi^3)\, e\sigma$	$^3\Pi_2$	0	8.783
8.846	m_1	$(\sigma^2\pi^3)\, c\sigma$	$^3\Pi_1$	0	8.839
8.945	H	$(\sigma^2\pi^3)\, d\pi$	$^1\Sigma^+$	2	8.954
9.000	E	$(\sigma^2\pi^3)\, c\pi$	$^1\Sigma^+$	1	9.008
9.035	m_1	$(\sigma^2\pi^3)\, e\sigma$	$^3\Pi_1$	1	9.042
9.094	j	$(\sigma^2\pi^3)\, d\pi$	$^3\Sigma^-$	0	9.083
9.122	V	$(\sigma^1\pi^4)\, a'\sigma^*$	$^1\Sigma^+$	(m+11)	9.108
9.204	K	$(\sigma^2\pi^3)\, a\delta, 6d\delta$	$^1\Pi$	0	9.210
9.224	r_1	$(\sigma^2\pi^3)\, f\sigma$	$^3\Pi_1$	0	9.215
9.373	N	$(\sigma^2\pi^3)\, d\sigma$	$^1\Pi$	1	9.378
9.465	M	$(\sigma^2\pi^3)\, e\sigma$	$^1\Pi$	0	9.456
9.536					
9.557		$(\sigma^2\pi^3)\, 7s\sigma$		0.	9.551
9.628					
9.659					
9.684					

9.705			
9.802			
9.879			
10.001			
10.042	$(\sigma^2\pi^3)\,7d\delta$	0	10.057
10.083			
10.104			
10.124			
10.150	$(\sigma^2\pi^3)\,7d\sigma$	0	10.149
10.201	$(\sigma^2\pi^3)\,8s\sigma$	0	10.205
10.231			
10.252			
10.288			
10.339			
10.395			
10.446	$(\sigma^2\pi^3)\,8d\delta$	0	10.443
10.482	$(\sigma^2\pi^3)\,8d\sigma$	0	10.492
10.502	$(\sigma^2\pi^3)\,9s\sigma$	0	10.504
10.543			
10.579	$(\sigma^2\pi^3)\,9p\pi$	0	10.577
10.625	$(\sigma^2\pi^3)\,9d\delta$	0	10.634
10.656	$(\sigma^2\pi^3)\,9d\sigma$	0	10.663
10.676	$(\sigma^2\pi^3)\,10s\sigma$	0	10.679
10.732			
10.758	$(\sigma^2\pi^3)\,10d\delta,\sigma$	0	10.749, 10.764
10.783			
10.829	$(\sigma^2\pi^3)\,11d\delta,\sigma$	0	10.821, 10.830
10.855			
10.906	$(\sigma^2\pi^3)\,12d\delta,\sigma$	0	10.906, 10.910
10.927			

a) Assignments and literature energy levels taken from the absorption spectra of Ginter *et al.*[90–93,102] for energies below 9.5 eV and from the photoionization spectra of Eland and Berkowitz[97] for the Rydberg states.

b) The ground state configuration in molecular orbital notation is given by $\cdots(9\sigma)^2(10\sigma)^2(5\pi)^4(2\delta)^4(11\sigma)^2(6\pi)^4 \quad \tilde{X}\ ^1\Sigma^+$.

TABLE 4. Electron Energy Loss Spectrum of H_2S

E_{obs} (eV)	e^{-1} configuration[b]	Assignment[a] Term Symbol	v	E_{lit}[a] (ev)
6.309	$(2b_1)^1\,(6a_1/4sa_1)$	$^1B_1$	(0,0,0)	6.326
7.889	$(2b_1)^1\,4p\,b_2$	$^1A_2$	(0,0,0)	7.851
8.027	$(2b_1)^1\,4p\,b_1$	$^1A_1$	(0,0,0)	8.026
8.184	$(2b_1)^1\,4p\,a_1$	$^1B_1 - 1$	(0,0,0)	8.181
8.226	$(2b_1)^1\,4p\,a_1$	$^1B_1 - 2$	(0,0,0)	8.217
8.287	$(2b_1)^1\,4p\,a_1$	$^1B_1 - 3$	(0,0,0)	8.272
8.329	$(2b_1)^1\,4p\,a_1$	$^1B_1 - 4$	(0,0,0)	8.324
8.407	$(2b_1)^1\,4p\,a_1$	$^1B_1 - 3$	(0,1,0)	8.409
8.437	$(2b_1)^1\,4p\,b_2$	$^1A_2$	(2,0,0)	8.430
8.480	$(2b_1)^1\,3d\,b_2$	$^1A_2$	(0,0,0)	8.464
8.510	$(2b_1)^1\,4p\,a_1$	$^1B_1 - 1$	(1,0,0)	8.512
8.582	$(2b_1)^1\,4p\,a_1$	$^1B_1 - 3$	(1,0,0)	8.572
8.667	$(2b_1)^1\,3d\,a_1$	$^1B_1$	(0,0,0)	8.661
8.799	$(2b_1)^1\,3d\,a_2, b_1$	$^1B_2, ^1A_1$	(0,0,0)	8.805
8.853	$(2b_1)^1\,5s\,a_1$	$^1B_1$	(0,0,0)	8.837
8.908	$(2b_1)^1\,3d\,a_1'$	$^1B_1$	(0,0,0)	8.914
9.088	$(2b_1)^1\,3d\,a_1'$	$^1B_1$	(0,1,0)	9.057
9.119	$(2b_1)^1\,3d\,a_2, b_1$	$^1B_2, ^1A_1$	(1,0,0)	9.110
9.161	$(2b_1)^1\,4p\,b_2$	$^1A_2$	(0,0,0)	9.170
9.221	$(2b_1)^1\,3d\,a_1'$	$^1B_1$	(1,0,0)	9.221
9.251	$(2b_1)^1\,3d\,b_1$	$^1A_1$	(1,1,0)	9.257
9.282	$(2b_1)^1\,5p\,b_1$	$^1A_1$	(0,0,0)	9.275
9.300	$(2b_1)^1\,5p\,a_1$	$^1B_1$	(0,0,0)	9.315
9.324				
9.420				
9.444	$(2b_1)^1\,4d\,a_1$	$^1B_1$	(0,0,0)	9.441
9.553	$(2b_1)^1\,4d\,a_2, b_1$	$^1B_2, ^1A_1$	(0,0,0)	9.542
9.583				
9.601	$(2b_1)^1\,4d\,a_1'$	$^1B_1$	(0,0,0)	9.602
9.686				
9.776	$(2b_1)^1\,6p\,a_1$	$^1B_1$	(0,0,0)	9.788
9.886	$(2b_1)^1\,5d\,a_2, b_1$	$^1B_2, ^1A_1$	(0,0,0)	9.889
9.903	$(2b_1)^1\,5d\,a_1'$	$^1B_1$	(0,0,0)	9.919
10.005	$(2b_1)^1\,7p\,a_1$	$^1B_1$	(0,0,0)	10.017
10.047				
10.083	$(2b_1)^1\,6d\,a_1'$	$^1B_1$	(0,0,0)	10.087
10.180	$(2b_1)^1\,7d\,a_1'$	$^1B_1$	(0,0,0)	10.184
10.240	$(2b_1)^1\,8d\,a_1'$	$^1B_1$	(0,0,0)	10.253
10.295	$(2b_1)^1\,9d\,a_1'$	$^1B_1$	(0,0,0)	10.300

10.325	$(2b_1)^1\ 10\,da_1'$	$^1B_1$	(0,0,0)	10.330
10.355	$(2b_1)^1\ 11\,da_1'$	$^1B_1$	(0,0,0)	10.354
10.379	$(2b_1)^1\ 12d\,a_1'$	$^1B_1$	(0,0,0)	10.371
10.500	$(2b_1)^1\ 7d\,a_1'$	$^1B_1$	(1,0,0)	10.489
10.578	$(2b_1)^1\ 8d\,a_1'$	$^1B_1$	(1,0,0)	10.557
10.626	$(2b_1)^1\ 9d\,a_1'$	$^1B_1$	(1,0,0)	10.606
10.729				
10.783				
10.831				
10.879				
10.964				

a) Assignments and literature energy levels taken from Masuko *et al.*[120]

b) Ground state electronic configuration is $\cdots(2b_2)^2(5a_1)^2(2b_1)^2 \quad \tilde{X}\ ^1A_1$ in the one electron molecular orbital approximation.

REFERENCES

1. W. Kolos and L. Wolniewicz, *J. Chem. Phys.* **41**, 3663 (1964).
2. W. Kolos and L. Wolniewicz, *J. Chem. Phys.* **43**, 2429 (1965).
3. W. Kolos and L. Wolniewicz, *J. Chem. Phys.* **49**, 404 (1968).
4. W. Kolos and L. Wolniewicz, *J. Mol. Spectrosc.* **54**, 303 (1975).
5. L. Wolniewicz, *J. Chem. Phys.* **78**, 6173 (1983).
6. W. Kolos and L. Wolniewicz, *J. Chem. Phys.* **45**, 509 (1966).
7. W. Kolos and L. Wolniewicz, *J. Chem. Phys.* **48**, 3672 (1968).
8. W. Kolos and L. Wolniewicz, *J. Chem. Phys.* **50**, 3228 (1969).
9. W. Kolos and L. Wolniewicz, *Can. J. Phys.* **53**, 2189 (1975).
10. B. P. Stoicheff, *Can. J. Phys.* **35**, 730 (1957).
11. G. Herzberg, *Nature* **166**, 563 (1950).
12. U. Fink, T. A. Wiggins, and D. H. Rank, *J. Mol. Spectrosc.* **18**, 384 (1965).
13. J. V. Foltz, D. H. Rank, and T. A. Wiggins, *J. Mol. Spectrosc.* **21**, 203 (1966).
14. P. J. Brannon, C. H. Church, and C. W. Peters, *J. Mol. Spectrosc.* **27**, 44 (1968).
15. H. L. Buijs and H. P. Gush, *Can. J. Phys.* **49**, 2366 (1971).
16. S. L. Bragg, J. W. Brault, and W. H. Smith, *Astrophys. J.* **263**, 999 (1982).
17. J. Reid and A. R. W. McKellar, *Phys. Rev.* **A-18**, 224 (1978).
18. D. E. Jennings and J. W. Brault, *Astrophys. J.* **256**, L29 (1982).
19. R. A. Durie and G. Herzberg, *Can. J. Phys.* **38**, 806 (1960).
20. G. H. Dieke and J. J. Hopfield, *Phys. Rev.* **30**, 400 (1927).
21. T. Hori, *Z. Physik* **44**, 834 (1927).
22. H. H. Hyman, *Phys. Rev.* **36**, 187 (1930).
23. C. R. Jeppeson, *Phys. Rev.* **44**, 165 (1933).
24. C. R. Jeppeson, *Phys. Rev.* **45**, 480 (1934).

25. K. Mie, *Z. Physik* **91**, 475 (1934).

26. Y. Fujioka and T. Wada, *Sci. Papers Inst. Phys. Chem. Res. (Tokyo)* **27**, 210 (1935).

27. C. R. Jeppeson, *Phys. Rev.* **49**, 797 (1936).

28. G. Herzberg and L. L. Howe, *Can. J. Phys.* **37**, 636 (1959).

29. S. Takezawa, F. K. Innes, and Y. Tanaka, *J. Chem. Phys.* **46**, 4555 (1967).

30. H. Bredohl and G. Herzberg, *Can. J. Phys.* **51**, 867 (1973).

31. I. Dabrowski and G. Herzberg, *Can. J. Phys.* **54**, 525 (1976).

32. I. Dabrowski, *J. Chem. Phys.* **62**, 1639 (1984).

33. Y. Tanaka, *Sci. Papers Inst. Phys. Chem. Res. (Tokyo)* **42** 49 (1944).

34. G. Herzberg and A. Monfils, *J. Mol. Spectrosc.* **5**, 482 (1960).

35. A. Monfils, *Bull. Acad. R. Belg. Cl. Sci.* **47** 585 (1961).

36. A. Monfils, *Bull. Acad. R. Belg. Cl. Sci.* **47** 599 (1961).

37. A. Monfils, *Bull. Acad. R. Belg. Cl. Sci.* **47** 816 (1961).

38. A. Monfils, *Bull. Acad. R. Belg. Cl. Sci.* **48** 460 (1962).

39. A. Monfils, *Bull. Acad. R. Belg. Cl. Sci.* **48** 482 (1962).

40. T. Namioka, *J. Chem. Phys.* **40**, 3154 (1964).

41. A. Monfils, *J. Mol. Spectrosc.* **15**, 265 (1965).

42. A. Monfils, *J. Mol. Spectrosc.* **25**, 513 (1968).

43. P. G. Wilkinson, *Can. J. Phys.* **46**, 1225 (1968).

44. G. Herzberg, *J. Mol. Spectrosc.* **33**, 147 (1970).

45. S. Takezawa and Y. Tanaka, *J. Chem. Phys.* **56**, 6125 (1972).

46. I. Dabrowski and G. Herzberg, *Can. J. Phys.* **52**, 1110 (1974).

47. T. E. Sharp, *Atom. Dat.* **2**, 119 (1971).

48. G. Herzberg, *Phys. Rev. Lett.* **23**, 1081 (1969).

49. G. Herzberg, *Molecular Spectra and Molecular Structure: I. Spectra of Diatomic Molecules, 2nd ed.*, (Van Nostrand Reinhold, New York, 1950) a) pp. 240–280. b) pp. 280–298.

50. J. L.Dunham, *Phys. Rev.* **41**, 721 (1932).

51. G. N. Haddad, K. H. Lokan, A. J. D. Farmer, and J. H. Carver, *J. Quant. Spectrosc. Radiat. Transfer* **8**, 1193 (1968).

52. J. E. Hesser, N. H. Brooks, and G. M. Lawrence, *J. Chem. Phys.* **49**, 388 (1968).

53. W. Fabian and B. R. Lewis, *J. Quant. Spectrosc. Radiat. Transfer* **14**, 523 (1974).

54. B. R. Lewis, *J. Quant. Spectrosc. Radiat. Transfer* **14**, 537 (1974).

55. J. Geiger, *Z. Physik* **181**, 413 (1964).

56. J. Geiger and M. Topschowsky, *Z. Naturforsch* **A21**, 626 (1966).

57. J. Geiger and H. Schmoranzer, *J. Mol. Spectrosc.* **32**, 39 (1969).

58. A. C. Allison and A. Dalgarno, *Atom. Dat.* **1**, 289 (1970).

59. A. Dalgarno and T. L. Stephens, *Astrophys. J.* **160**, L107 (1970).

60. V. Henri and S. A. Schou, *Z. Physik* **49**, 774 (1928).

61. G. H. Dieke and G. B. Kistiakowsky, *Phys. Rev.* **45**, 4 (1934).

62. J. C. D. Brand, *J. Chem. Soc.* 858 (1956).

63. J. L. Harwick and S. M. Till, *J. Chem. Phys.* **70**, 2340 (1979).

64. D. C. Moule and A. D. Walsh, *Chem. Rev.* **75**, 67 (1975).

65. D. J. Clouthier and D. A. Ramsay, *Ann. Rev. Phys. Chem.* **34**, 31 (1983).

66. V. Bachler and E. A. Halevi, *Theoret. Chim. Acta.* **59** 595, (1981).

67. C. B. Moore and J. C. Weisshaar, *Ann. Rev. Phys, Chem.* **34**, 525 (1983).

68. J. L. Whitten, *J. Chem. Phys.* **56**, 5458 (1972).

69. R. J. Buenker and S. D. Peyerimhoff, *J. Chem. Phys.* **53**, 1368 (1970).

70. G. Winnewisser, R. A. Cornet, F. W. Birss, R. M. Gordon, D. A. Ramsay, and S. M. Till, *J. Mol. Spectrosc.* **74**, 327 (1979).

71. H. C. Allen and P. C. Cross, *Molecular Vib-Rotors*, (Wiley, NY, 1963).

72. J. E. Mentall, E. P. Gentieu, M. Krauss, and D. Neumann, *J. Chem. Phys.* **55**, 5471 (1971).

73. M. Suto, X. Wang, and L. C. Lee, *J. Chem. Phys.* **85**, 4228 (1986).

74. S. J. Strickler and R. J. Barnhart, *J. Phys. Chem.* **86**, 448 (1982).

75. J. M. F. van Dijk, M. J. H. Kemper, J. H. M. Kerp, and H. M. Buck, *J. Chem. Phys.* **69**, 2453 (1978).

76. V. A. Job, V. Sethuraman, and K. K. Innes, *J. Mol. Spectrosc.* **30**, 365 (1969).

77. V. Sethuraman, V. A. Job, and K. K. Innes, *J. Mol. Spectrosc.* **33**, 189 (1970).

78. C. M. L. Kerr, D. A. Ramsay, *Can. J. Phys.* **61**, 6 (1983).

79. E. C. Apel and E. K. C. Lee, *J. Chem. Phys.* **85**, 1261 (1986).

80. D. J. Moll, Ph.D. Dissertation, California Institute of Technology, 1983.

81. D. R. Lide, *J. Chem. Phys.* **20**, 1761 (1952).

82. P. W. Fairchild, K. Shibuya, and E. K. C. Lee, *J. Chem. Phys.* **75**, 3407 (1981).

83. W. C. Price, *Phys. Rev.* **A-167**, 216 (1938).

84. C. F. Goodeve and A. W. C. Taylor, *Phys. Rev.* **A-154**, 181 (1936).

85. J. Romand, *Ann. de Phys.* **4**, 529 (1949).

86. J. M . White, Ph.D. Thesis, University of Illinois, Urbana (1966).

87. J. F. Ogilvie, *Trans. Far. Soc.* **67**, 2205 (1971).

88. R. S. Mulliken, *Phys. Rev.* **51**, 310 (1937).

89. R. S. Mulliken, *J. Chem. Phys.* **8**, 382 (1940).

90. S. G. Tilford, M. L. Ginter, and A. M. Bass, *J. Mol. Spectrosc.* **34**, 327 (1970).

91. M. L. Ginter, S. G. Tilford, and A. M. Bass, *J. Mol. Spectrosc.* **57**, 271 (1975).

92. D. S. Ginter, M. L. Ginter, and S. G. Tilford, *J. Mol. Spectrosc.* **92**, 40 (1982).

93. D. S. Ginter, M. L. Ginter, S. G. Tilford, and A. M. Bass, *J. Mol. Spectrosc.* **92**, 55 (1982).

94. J. D. Morrison, H. Hurzeler, M. G. Inghram, and H. E. Stanton, *J. Chem. Phys.* **33**, 821 (1961).

95. B. P. Tsai and T. Baer, *J. Chem. Phys.* **61**, 2047 (1974).

96. D. T. Terwilliger and A. L. Smith, *J. Chem. Phys.* **63**, 1008 (1975).

97. J. H. D. Eland and J. Berkowitz, *J. Chem. Phys.* **67**, 5034 (1977).

98. T. A. Carlson, P. Gerard, M. O. Krause, G. von Wald, J. W. Taylor, and F. Grimm, *J. Chem. Phys.* **84**, 4755 (1986).

99. D. W. Turner, C. Baker, A. D. Baker, and C. R. Brundle, *Molecular Photoelectron Spectroscopy*, (John Wiley & Sons, New York, 1970) p. 39.

100. M. G. White, S. H. Southworth, P. Kobrin, and D. A. Shirley, *J. Electron. Spectrosc. Rel. Phenom.* **19**, 115 (1980).

101. K. P. Huber and G. Herzberg, *Molecular Spectra and Molecular Structure: IV. Constants of Diatomic Molecules.*, (Van Nostrand Reinhold, New York, 1979) pp. 324–328.

102. M. L. Ginter, D. S. Ginter, and C. M. Brown, *Appl. Opt.* **19**, 4015 (1980).

103. The labeling of states in Ref. 102 differs from that used in previous papers by the same authors (Ref. 90–93) and from that adapted by Ref. 101. The labeling of states in Ref. 102 is followed in this chapter.

104. C. E. Moore, ed., *Atomic Energy Levels, National Bureau of Standards Circular 467*, (Washington, D. C. 1958).

105. R. N. Zare, *Mol. Photochem.* **4**, 1 (1972).

106. R. J. Donovan and D. Husain, *Trans. Far. Soc.* **62**, 1050 (1966).

107. R. D. Clear, S. J. Riley, and K. R. Wilson, *J. Chem. Phys.* **63**, 1340 (1975).

108. R. Schmiedl, H. Dugan, W. Meir, and K. H. Welge, *Z. Phys. A* **304**, 137 (1982).

109. K. Tsukiyama, B. Katz, and R. Bersohn, *J. Chem. Phys.* **84**, 1934 (1986).

110. K. Lorenz, H. Gg. Wagner, and R. Zellner, *Ber. Bunsenges. Phys. Chem.* **83**, 556 (1979).

111. R. Bersohn, personnal communication

112. R. C. Weast, editor, *CRC Handbook of Chemistry and Physics, 59th ed.*, (CRC Press, West Palm Beach, Florida, 1978).

113. W. C. Price, *J. Chem. Phys.* **4**, 147 (1936).

114. W. C. Price, J. P. Teegan, and A. D. Walsh, *Proc. Roy. Soc.* **A-201**, 600 (1950).

115. C. F. Goodeve and N. O. Stein, *Trans. Far. Soc.* **27**, 393 (1931).

116. K. Watanabe and A. S. Jursa, *J. Chem. Phys.* **41**, 1650 (1964).

117. L. B. Clark and W. T. Simpson, *J. Chem. Phys.* **43**, 3666 (1965).

118. S. D. Thompson, D. G. Carroll, F. Watson, M. O'Donnell, S. P. McGlynn, *J. Chem. Phys.* **45**, 1367 (1966).

119. A. R. Gallo and K. K. Innes, *J. Mol. Spectrosc.* **54**, 472 (1975).

120. H. Masuko, Y. Morioka, M. Nakamura, E. Ishiguro, and M. Sasanuma, *Can. J. Phys.* **57**, 745 (1979).

121. M. A. Baig, J. Hormes, J. P. Connerade, and S. P. McGlynn, *J. Phys.* **B-14**, L725 (1981).

122. R. N. Dixon, G. Duxbury, M. Horani, and J. Rostas, *Mol. Phys.* **22**, 977 (1971).

123. D. .C. Frost, A. Katrib, C. A.McDowell, and R. A. N. McLean, *Int. J. Mass Spectrom. Ion. Phys.* **7**, 485 (P1971).

124. A. W. Potts and W. C. Price, *Proc. Roy. Soc.* **326**, 181 (1972).

125. S. Durmaz, G. H. King, and R. J. Suffolk, *Chem. Phys. Lett.* **13**, 304 (1972).

126. L. Karlsson, L. Mattsson, R. Jadrny, T. Bergmark, and K. Siegbahn, *Phys. Scr.* **13**, 229 (1976).

127. S.-K. Shih, S. D. Peyerimhoff, and R. J. Buenken, *Chem. Phys.* **17**, 391 (1976).

128. M. F. Guest and W. R. Rodwell, *Mol. Phys.* **32**, 1075 (1976).

129. R. Roberge and D. R. Salahub, *J. Chem. Phys.* **70**, 1177 (1979).

130. G. Porter, *Disc. Far. Soc.* **9**, 60 (1950).

131. D. deB. Darwent, *Bond Dissociation Energies in Simple Molecules, NSRDS, NBS 31*, (US Government Printing Office, Washington, 1970).

132. W. G. Hawkins and P. L. Houston, *J. Chem. Phys.* **73**, 297 (1980).

133. W. G. Hawkins and P. L. Houston, *J. Chem. Phys.* **76**, 729 (1982).

134. G. N. A. Van Veen, K. A. Mohamed, T. Baller, and A. E. De Vries, *Chem. Phys.* **74**, 261 (1983).

FIGURE CAPTIONS

Figure 1 Potential energy curves for H_2 showing the $\tilde{X}$, $\tilde{B}$, and $\tilde{C}$ states and their vibrational energy levels.

Figure 2 Experimental absorption spectrum of room temperature H_2 taken with the Molectron dye laser system. This spectrum is the average of 7 complete data collection cycles as described in the text. The sample pressure was on the order of 4–6 torr.

Figure 3 Predicted absorption spectrum of room temperature H_2, calculated using Eq. 6.52. Theoretical values were used for all parameters, except for the laser linewidth which was assumed to be 1.87 cm^{-1} in the VUV.

Figure 4 Photoacoustic spectrum of H_2CO showing a portion of the $\tilde{A}\ ^1A_2 \leftarrow \tilde{X}\ ^1A_1$ electronic transition. The sample was approximately 0.1 torr H_2CO in 400–500 torr He. This spectrum was taken with the Molectron dye laser system. The locations of vibronic transitions seen in other spectra are shown above the spectrum.

Figure 5 Spectrum of the $2_0^1 4_0^3$ vibronic band of the $\tilde{A}\ ^1A_2 \leftarrow \tilde{X}\ ^1A_1$ electronic transition in H_2CO. The sample was approximately 0.1 torr H_2CO in 400–500 torr He. The top spectrum is a photoacoustic spectrum taken with the Molectron dye laser system, the middle spectrum is a photoacoustic spectrum taken with the Quanta Ray dye laser system, and the bottom spectrum is a theoretical spectrum calculated as described in the text. All three spectra have been scaled so that the tallest feature is 100.

Figure 6 Enlargement of Figure 5 to show the region near 30400 cm^{-1}. The two bands used for the H_2CO photodissociation experiments are labeled.

Figure 7 HI electron energy loss spectrum taken under near optical excitation conditions (50 eV incident energy, 10° detection angle). The location of

states seen in high resolution optical spectra[90-93] and in photoionization spectra[97] are labeled.

Figure 8 HI absorption spectrum taken with the Quanta Ray dye laser system. This spectrum is the average of 5 complete data collection cycles as described in the text. In order to reduce the effects of wall absorption, the scan direction was reversed for every other scan. The sample pressure was 10–20 torr of a 1.5% HI in He mixture.

Figure 9 H_2S electron energy loss spectrum taken under near optical excitation conditions (50 eV incident energy, 10° detection angle). The location of states seen in the optical spectrum[120] are labeled.

Figure 10 H_2S absorption spectrum taken with the Molectron dye laser system. This spectrum is the average of 3 complete data collection cycles as described in the text. The sample pressure was 100 torr of a 0.1% H_2S in He misture. The ⊙'s are the experimental points of Watanabe and Jursa[116] which have an estimated uncertainty of 10–15%.

FIGURE 1.

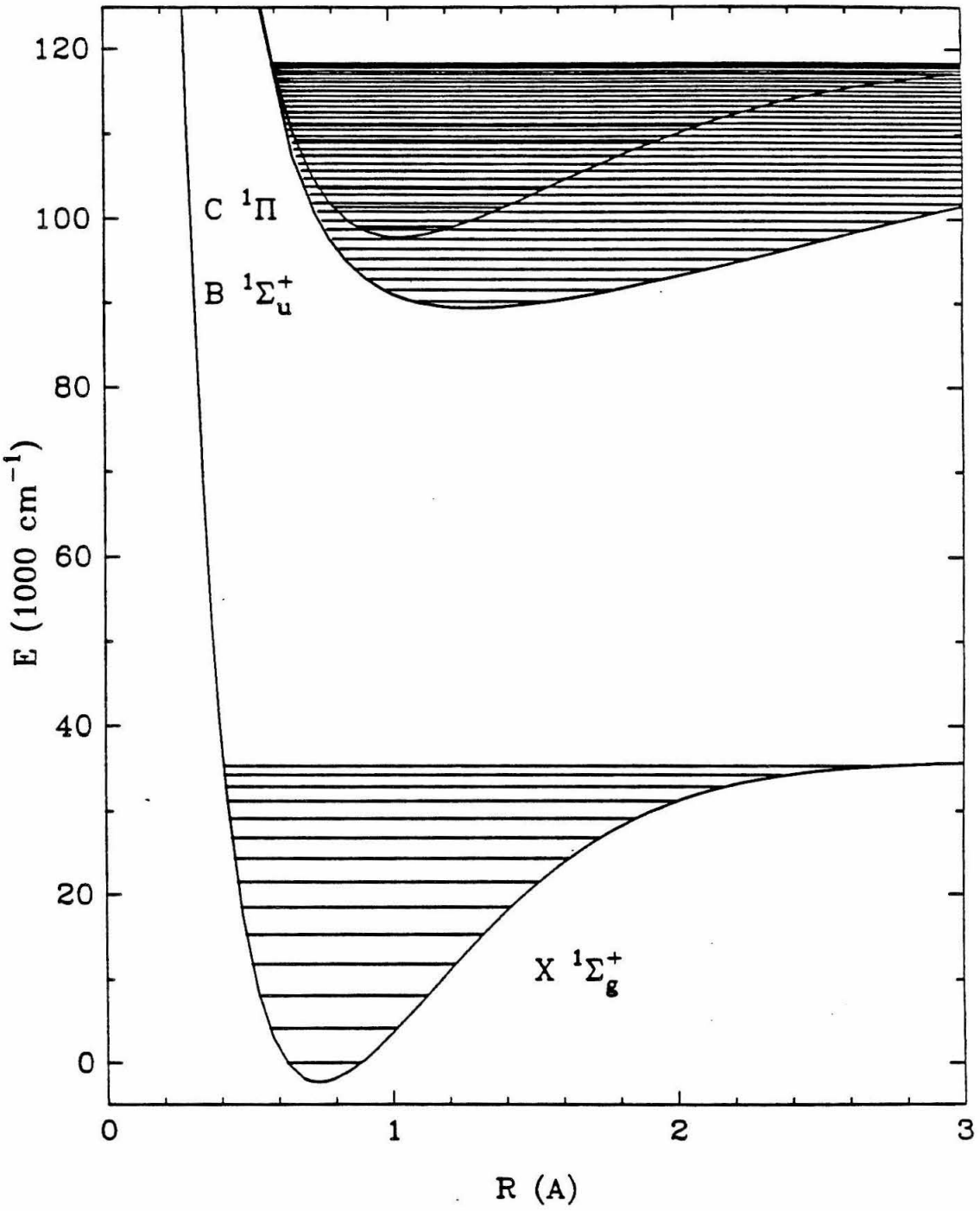

FIGURE 2.

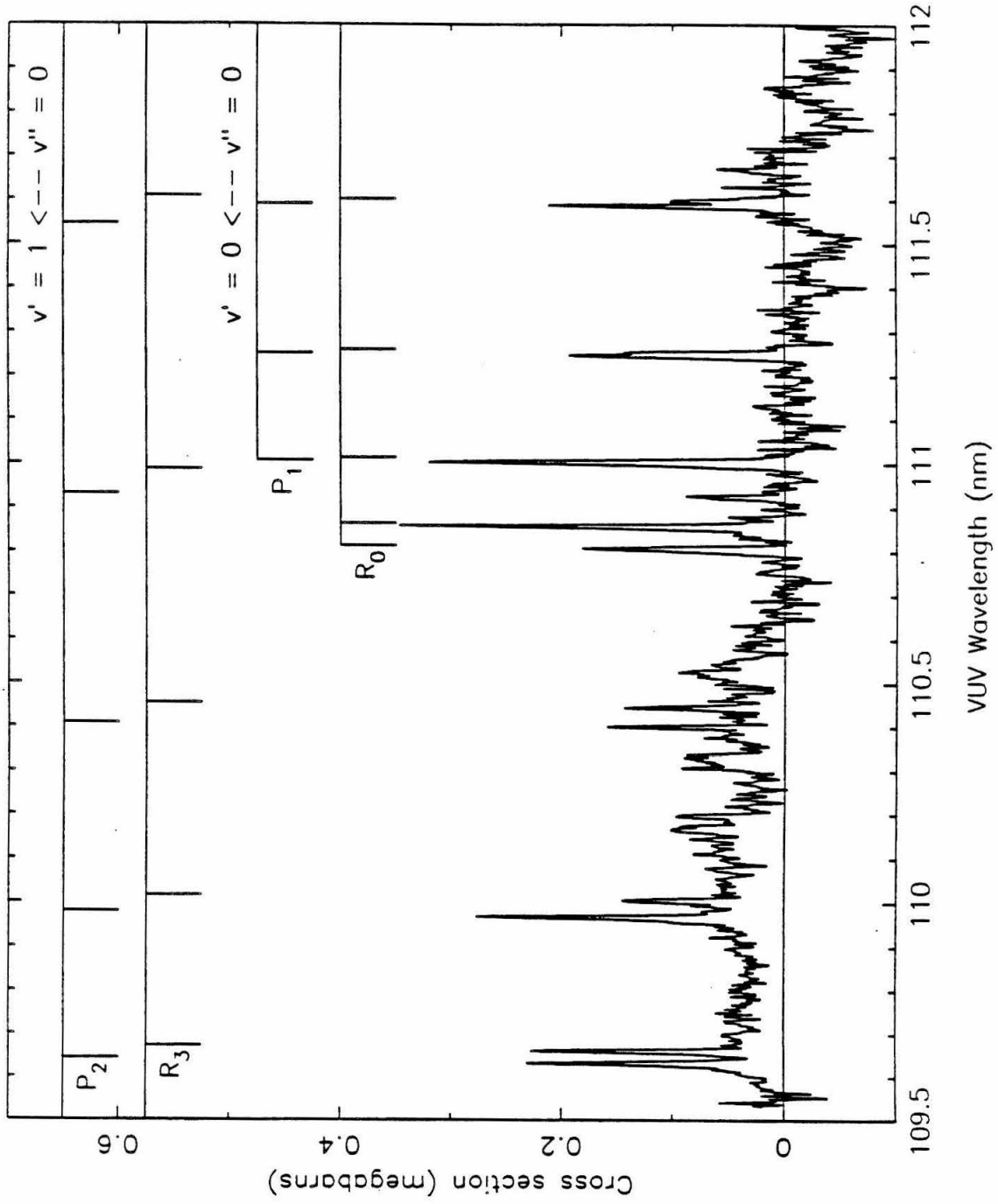
v' = 1 <-- v'' = 0
v' = 0 <-- v'' = 0
P2
R3
P1
R0
Cross section (megabarns)
0.6
0.4
0.2
0
109.5
110
110.5
111
111.5
112
VUV Wavelength (nm)

FIGURE 3.

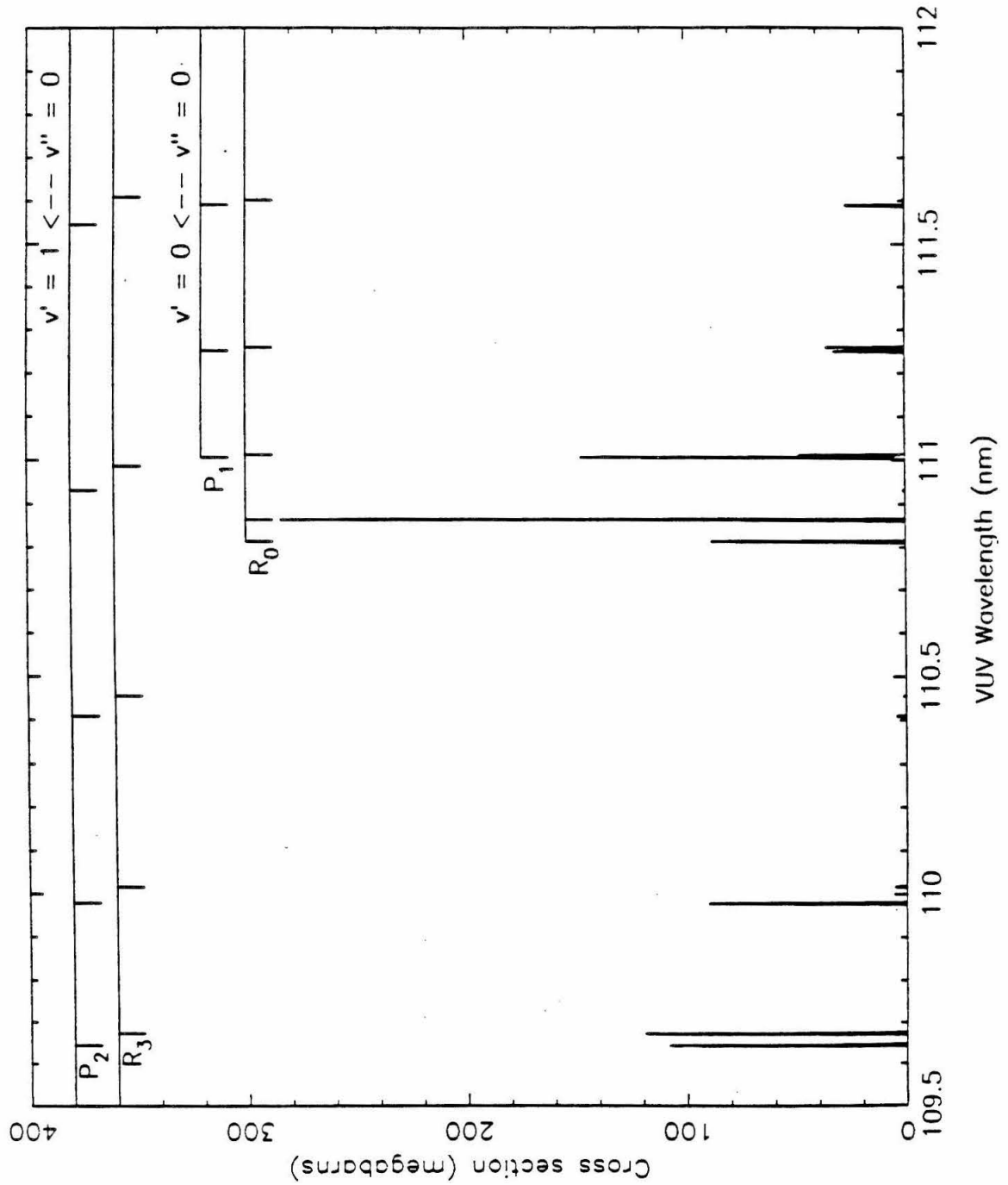
v' = 1 <-- v" = 0
v' = 0 <-- v" = 0
P2
R3
P1
R0
Cross section (megabarns)
0
100
200
300
400
109.5
110
110.5
111
111.5
112
VUV Wavelength (nm)

FIGURE 4.

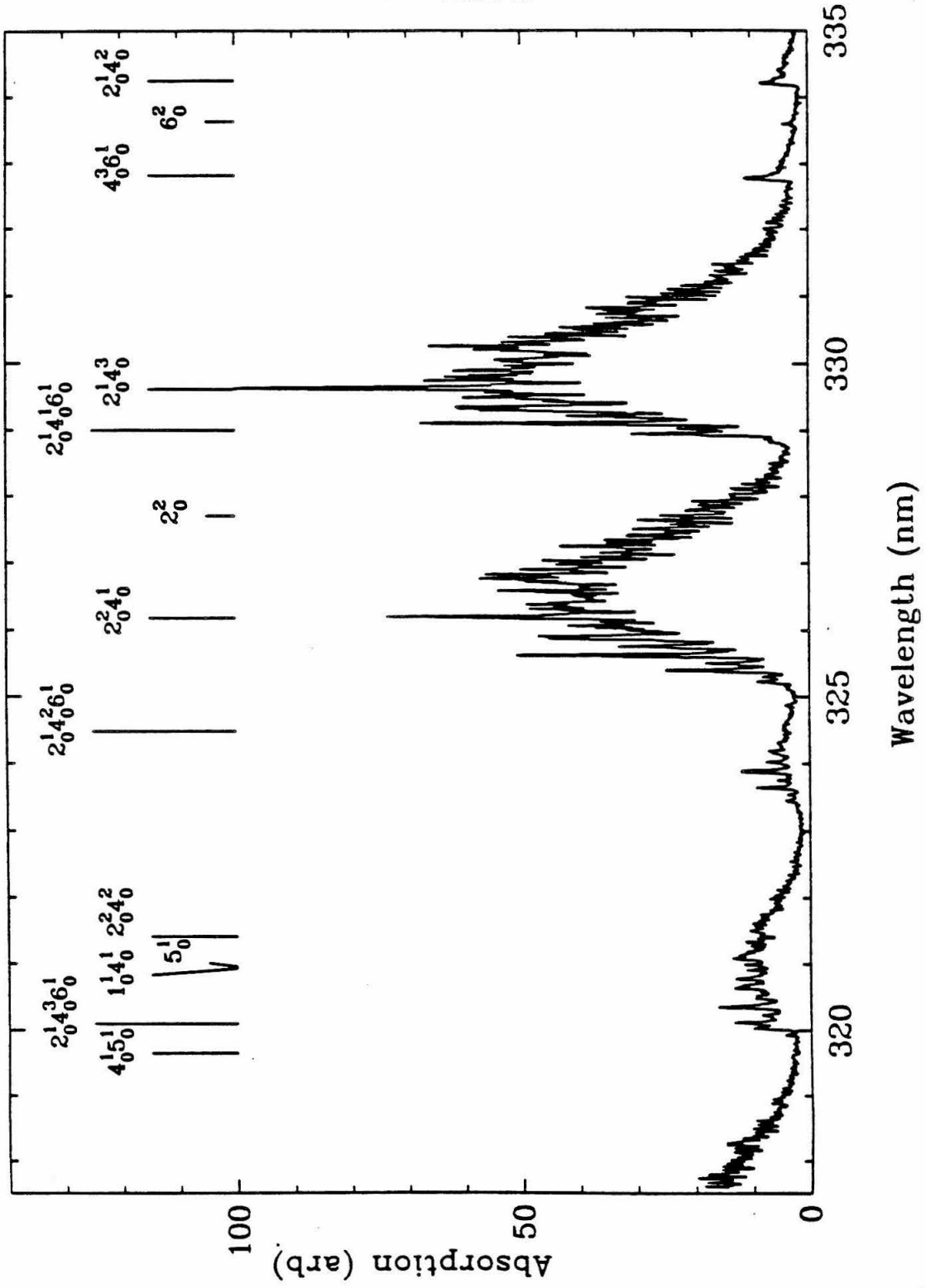
$4_0^1 5_0^1$
$2_0^1 4_0^3 6_0^1$
$1_0^1 4_0^1$
$2_0^2 4_0^2$
5_0^1
$2_0^1 4_0^2 6_0^1$
$2_0^2 4_0^1$
2_0^2
$2_0^1 4_0^1 6_0^1$
$2_0^1 4_0^3$
$4_0^3 6_0^1$
6_0^2
$2_0^1 4_0^2$
100
50
0
Absorption (arb)
320
325
330
335
Wavelength (nm)

FIGURE 5.

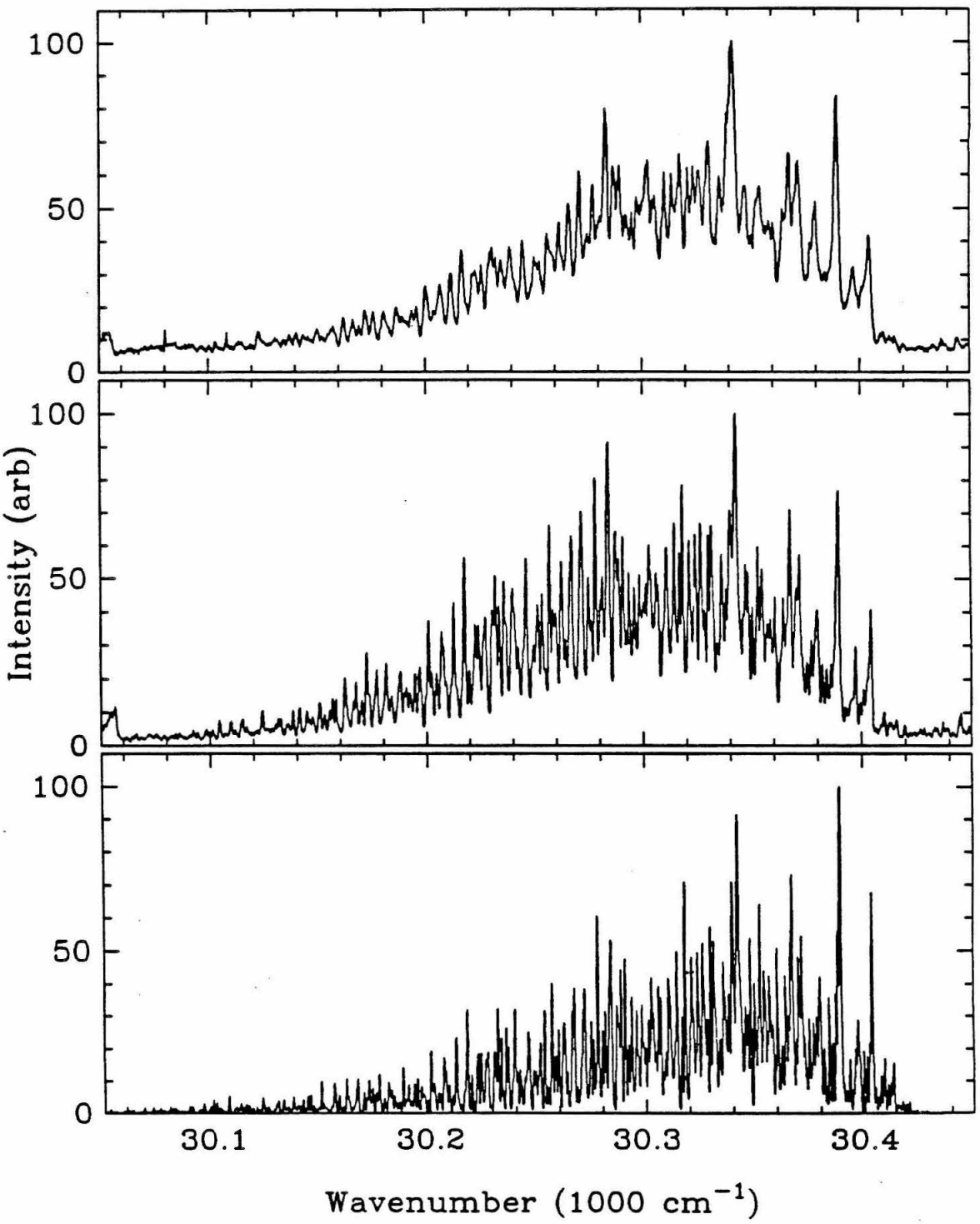
100
50
0
100
50
0
Intensity (arb)
100
50
0
30.1
30.2
30.3
30.4
Wavenumber (1000 cm^{-1})

FIGURE 6.

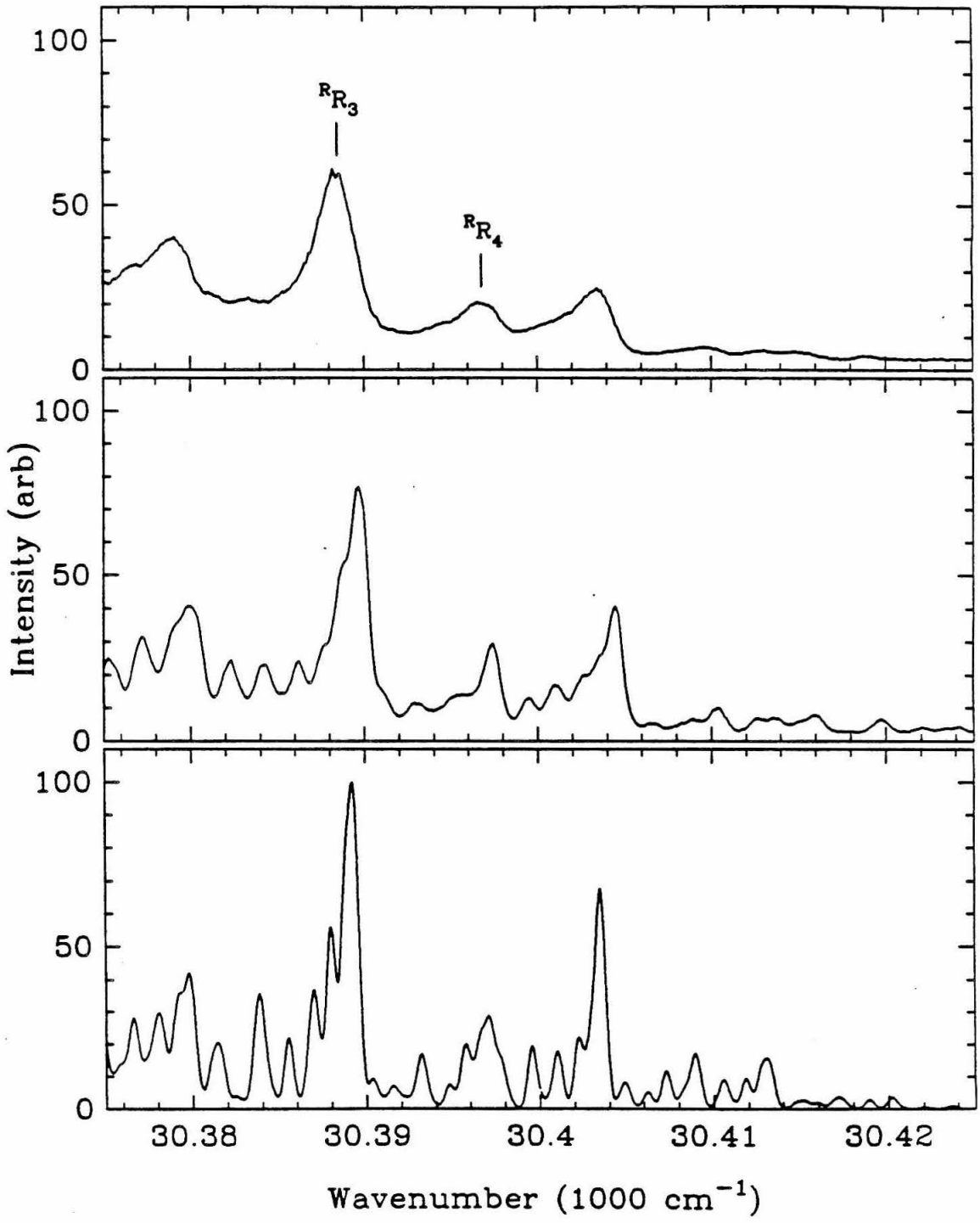
100
50
0
$^{R}R_3$
$^{R}R_4$
Intensity (arb)
30.38
30.39
30.4
30.41
30.42
Wavenumber (1000 cm^{-1})

FIGURE 7.

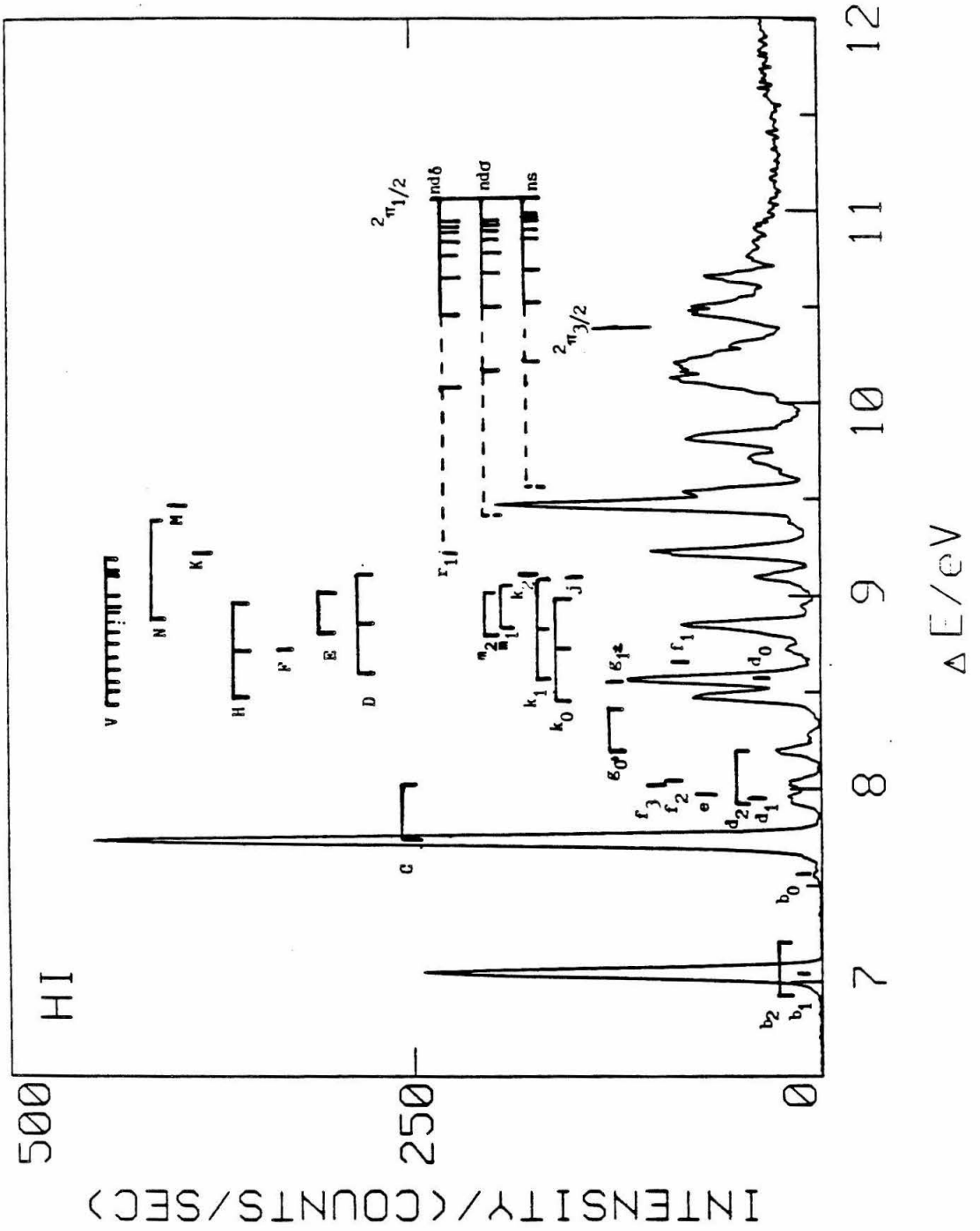
HI
INTENSITY/(COUNTS/SEC)
500
250
0
7
8
9
10
11
12
ΔE/eV
$^2\pi_{1/2}$
$^2\pi_{3/2}$
ndδ
ndσ
ns
V
N
M
K
H
F
E
D
C
r_{11}
m_2
m_1
k_2
k_1
k_0
j
$g_{1\pm}$
g_0
f_3
f_2
f_1
e
d_2
d_1
d_0
b_2
b_1
b_0

FIGURE 8.

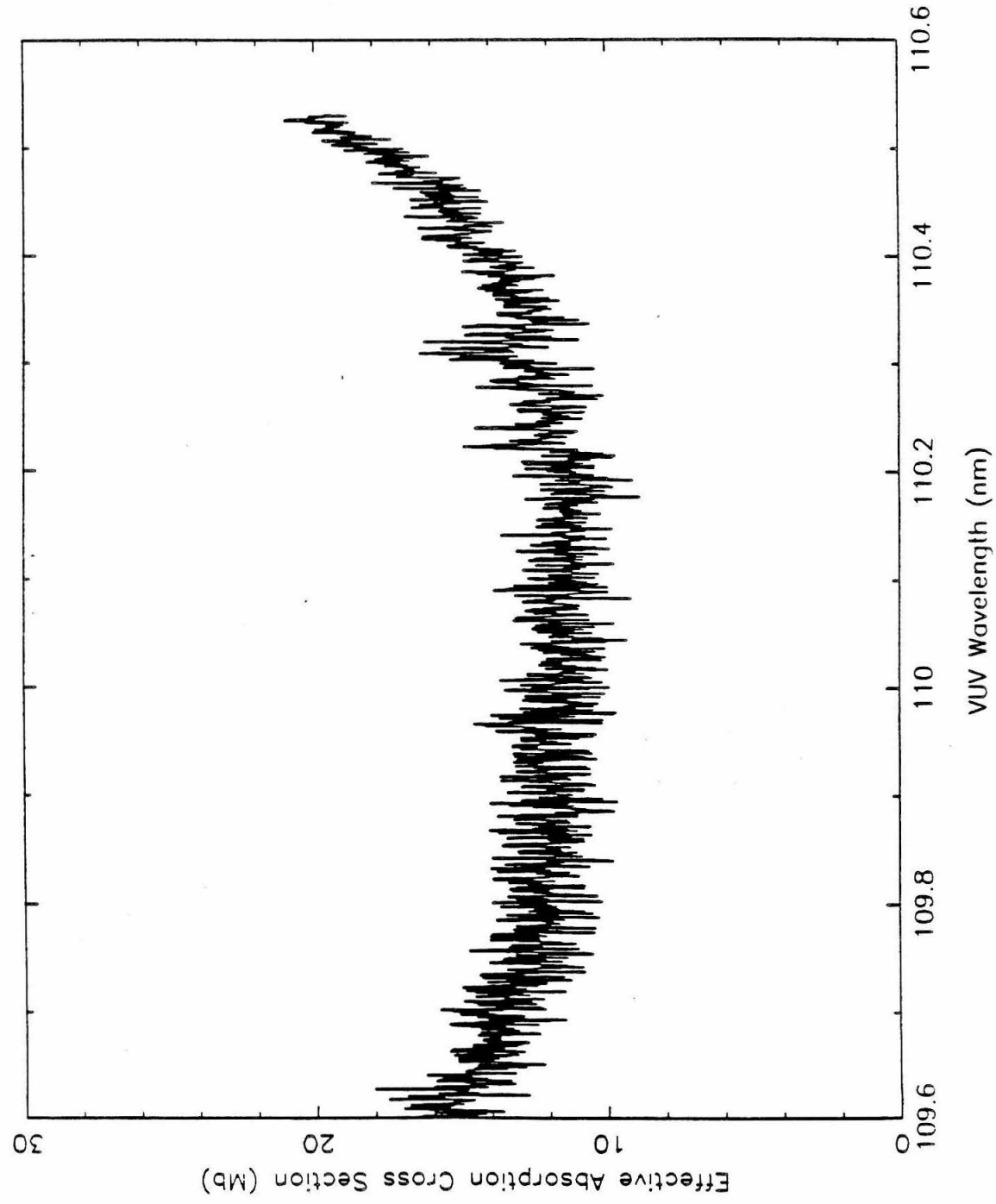
Effective Absorption Cross Section (Mb)
0
10
20
30
109.6
109.8
110
110.2
110.4
110.6
VUV Wavelength (nm)

FIGURE 9.

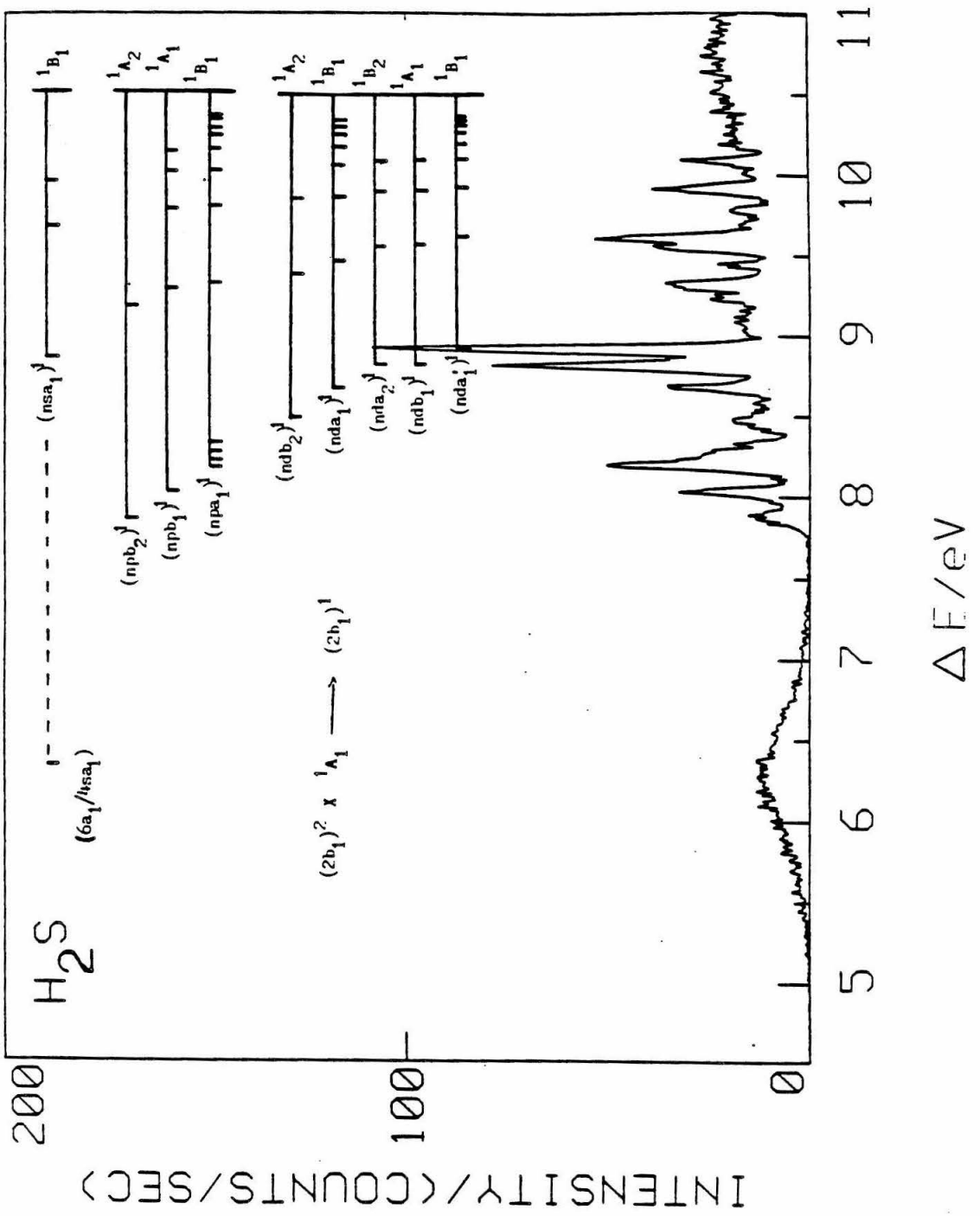
H2S
(6a1/4sa1)
(nsa1)1
(npb2)1
(npb1)1
(npa1)1
(ndb2)1
(nda1)1
(nda2)1
(ndb1)1
(nda'1)1
1B1
1A2
1A1
1B1
1A2
1B1
1B2
1A1
1B1
(2b1)2 x 1A1 ⟶ (2b1)1
INTENSITY/(COUNTS/SEC)
200
100
0
5
6
7
8
9
10
11
ΔE/eV

FIGURE 10.

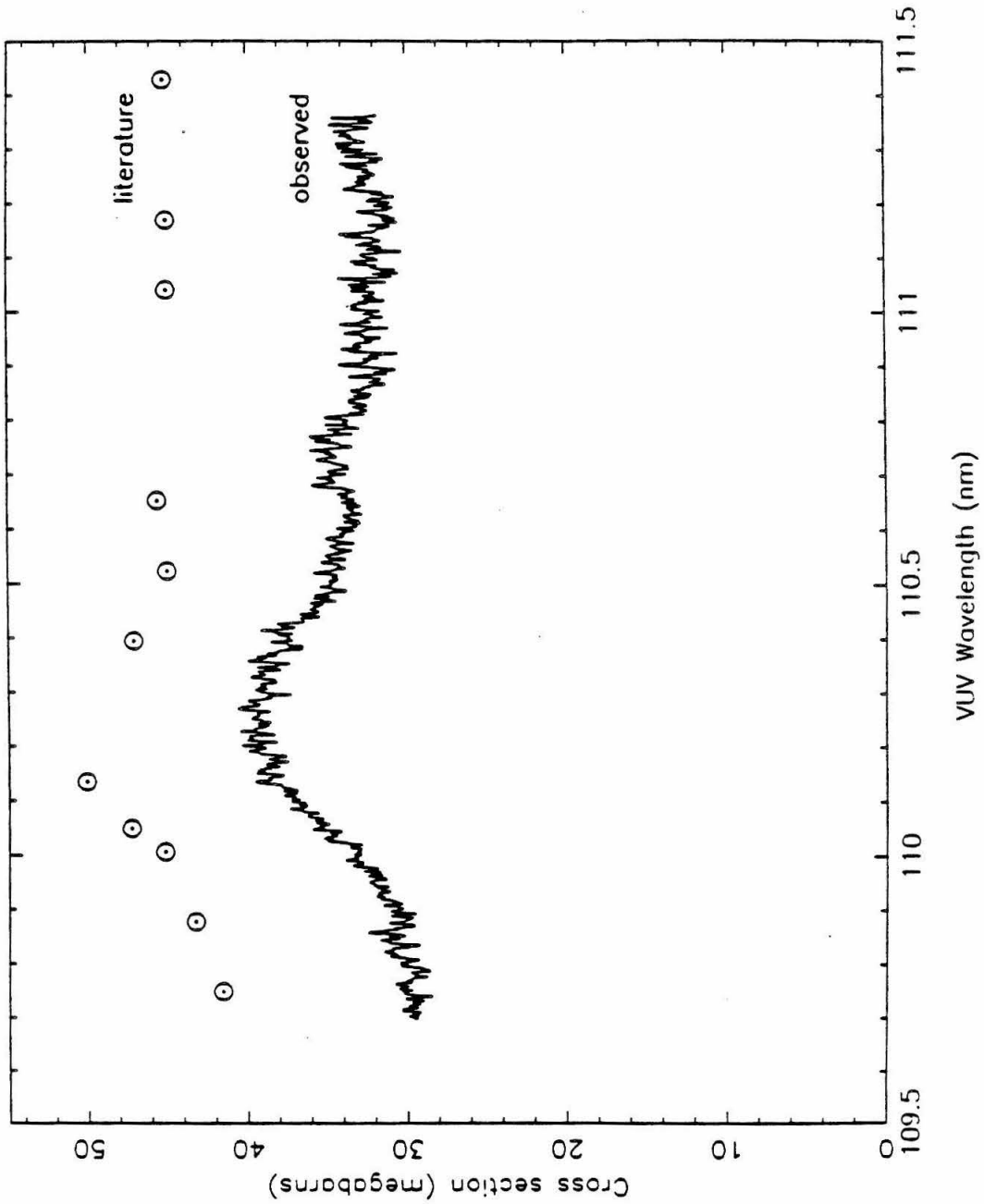
literature
observed
Cross section (megabarns)
0
10
20
30
40
50
109.5
110
110.5
111
111.5
VUV Wavelength (nm)

CHAPTER 6

DETECTION OF MOLECULAR HYDROGEN BY LASER INDUCED FLUORESCENCE

I. INTRODUCTION

In this chapter the detection of individual H_2 quantum states by the technique of Laser Induced Fluorescence (LIF) is discussed. This chapter is comprised of three parts. The first part is a discussion of LIF and includes the derivation of important formulas connecting the observed fluorescence signal to the intensity of the incident laser beam and the population of the initial quantum states. The second section describes LIF detection of H_2 by other researchers. The third section describes my own work on the detection of H_2 by LIF and includes results showing the great sensitivity and accuracy of this technique.

II. BACKGROUND

In this section the general LIF process is discussed. First, the Einstein A and B coefficients are developed in terms of the electric dipole matrix elements. Second, a general mechanism for LIF, including competing processes, is developed. Rough estimates of the various rate constants are used to eliminate unlikely reactions. Third, the rate equations derived from the mechanism are solved to give the total number of photons emitted by the sample. From this is derived a formula giving the total photomultiplier response in terms of the properties of the incident radiation, the properties of the molecule, the geometry of the apparatus, and the properties of the photomultiplier. Fourth, the lineshape function is derived.

A. Einstein A and B Coefficients

In the technique of laser induced fluorescence as applied to diatomic molecules,[1] a molecule in initial state $|\Sigma\Lambda pvJm\rangle$ is excited by a laser beam to an excited state $|\Sigma'\Lambda'p'v'J'm'\rangle$ which decays to a final state $|\Sigma''\Lambda''p''v''J''m''\rangle$ with the emission of a photon, which is detected by a photomultiplier or similar device. Σ characterizes the spin state of the molecule, Λ characterizes the electronic state, p gives the parity for $\Lambda \neq 0$ states, v is the vibrational quantum number, J is the total angular momentum quantum number, and m is the component of angular momentum around a laboratory fixed axis. The final state may or may not be identical to the initial state. The strength of the detected signal depends on several factors. Amongst these are the Einstein A and B coefficients, which connect the rate of photon-matter interactions to properties of the molecule and the states involved.

The strength of an electric dipole transition is often given in terms of an oscillator strength. The oscillator strength is the ratio of the probability of the transition to the probability of a classical vibrating electron making the same change in energy. The oscillator strength is proportional to the square of the

electric dipole matrix element connecting the two states. The oscillator strength of a electric dipole transition is defined by (by convention it is defined for absorption of radiation)[2,3]

$$f_{\Sigma\Lambda pvJm}^{\Sigma'\Lambda'p'v'J'm'} = \frac{32\pi^3\varepsilon_0 m_e \nu_0}{3he^2 g} \times \left|\langle \Sigma'\Lambda'p'v'J'm'|\vec{\mu}|\Sigma\Lambda pvJm\rangle\right|^2 \qquad (6.1)$$

in MKSA units. ε_0 is the permittivity of the vacuum ($C^2\,J^{-1}\,s^{-1}$), m_e is the mass of an electron (kg), h is Planck's constant (J s), e is the charge on the electron (C), ν_0 is the transition frequency (Hz) (defined by $h\nu_0 = \Delta E$), g is the degeneracy of the initial state, and $\vec{\mu}$ is the dipole operator (C m). Since this definition of the oscillator strength is for transitions between individual states, the degeneracy $g = 1$.

In the absence of a strong external field, the various states characterized by Σ and m are degenerate. As long as each of these states is equally populated, a modified oscillator strength for the energy level can be obtained by summing the squared dipole matrix elements over all possible Σ's and m's. This is the same as calculating the matrix element for the energy level and including the appropriate degeneracy. In this case the formula for the oscillator strength is[3]

$$f_{\Lambda pvJ}^{\Lambda'p'v'J'} = \frac{32\pi^3\varepsilon_0 m_e \nu_0}{3he^2} \times \frac{\left|\langle \Lambda'p'v'J'|\vec{\mu}|\Lambda pvJ\rangle\right|^2}{g} \qquad (6.2)$$

and the degeneracy becomes

$$g = (2S+1)(2J+1) \qquad (6.3)$$

where is S is the spin quantum number. It is also possible to perform the same summation over the parity levels, giving

$$f_{\Lambda vJ}^{\Lambda'v'J'} = \frac{32\pi^3\varepsilon_0 m_e \nu_0}{3he^2} \times \frac{\left|\langle \Lambda'v'J'|\vec{\mu}|\Lambda vJ\rangle\right|^2}{g} \qquad (6.4)$$

for the oscillator strength and

$$g = (2 - \delta_{0,\Lambda})(2S + 1)(2J + 1) \tag{6.5}$$

for the degeneracy, where $\delta_{0,\Lambda}$ is the Kronecker delta function.

It is often assumed that there is no interaction between the rotational degrees of freedom and the vibrational and electronic degrees of freedom.[3] Under this assumption, the matrix element can be separated into two components, a matrix element involving only the electronic and vibrational motion and a second matrix element involving just the angular momentum degrees of freedom denoted by $S_{\Lambda J}^{\Lambda' J'}$, giving

$$\left|\langle \Lambda' v' J' | \vec{\mu} | \Lambda v J \rangle\right|^2 = \left|\langle \Lambda' v' | \vec{\mu} | \Lambda v \rangle\right|^2 \times S_{\Lambda J}^{\Lambda' J'} \tag{6.6}$$

This separation was first performed by Hönl and London[4] in 1925. This rotational matrix element is often called the Hönl-London factor, the rotational line strength, or the rotational intensity factor. For any given particular electronic transition, $S_J^{J'}$ is a function of the total, electronic, and spin angular momentum of both states. Tables of the functional form of this factor are available.[5] These functions are often undetermined to within a constant factor; consequently, they should be normalized so that the sum of all factors from a given level is equal to the degeneracy of that level. (The uncertainty arises because untill recently there was no agreement on whether to include the $(2 - \delta_{\Lambda,\Lambda'})$ degeneracy in the Hönl-London factor normalization or in the electronic matrix element).[6]

In many cases a band oscillator strength is reported. This is the oscillator strength of a electronic and vibrational transition irrespective of rotation.

The rates of absorption, induced emission, and spontaneous emission can be given in terms of the Einstein A and B coefficients, which are defined in terms of

the oscillator strength and dipole matrix element by[7]

$$(B_{abs})^{\Sigma'\Lambda'p'v'J'm'}_{\Sigma\Lambda pvJm} = \frac{e^2 n}{4\varepsilon_0 m_e c} \times f^{\Sigma'\Lambda'p'v'J'm'}_{\Sigma''\Lambda''p''v''J''m''} \tag{6.7}$$

$$= \frac{8\pi^3 n\nu_0}{3hc} \times \frac{\left|\langle \Sigma'\Lambda'p'v'J'm'|\vec{\mu}|\Sigma\Lambda pvJm\rangle\right|^2}{g} \tag{6.8}$$

$$(B_{em})^{\Sigma'\Lambda'p'v'J'm'}_{\Sigma\Lambda pvJm} = \frac{e^2 n}{4\varepsilon_0 m_e c} \times \frac{g}{g'} \times f^{\Sigma'\Lambda'p'v'J'm'}_{\Sigma\Lambda pvJm} \tag{6.9}$$

$$= \frac{8\pi^3 n\nu_0}{3hc} \times \frac{\left|\langle \Sigma'\Lambda'p'v'J'm'|\vec{\mu}|\Sigma\Lambda pvJm\rangle\right|^2}{g'} \tag{6.10}$$

$$A^{\Sigma'\Lambda'p'v'J'm'}_{\Sigma\Lambda pvJm} = \frac{2\pi e^2 n^3 \nu_0^2}{\varepsilon_0 m_e c^3} \times \frac{g}{g'} \times f^{\Sigma'\Lambda'p'v'J'm'}_{\Sigma\Lambda pvJm} \tag{6.11}$$

$$= \frac{64\pi^4 n^3 \nu_0^3}{3hc^3} \times \frac{\left|\langle \Sigma'\Lambda'p'v'J'm'|\vec{\mu}|\Sigma\Lambda pvJm\rangle\right|^2}{g'} \tag{6.12}$$

where c is the velocity of light ($\mathrm{m\,s^{-1}}$) and n is the refractive index of the medium. The definition of the Einstein coefficient for a transition between levels of the molecule is self evident. These Einstein coefficients were defined in terms of the photon flux of the laser pulse $I(\nu_L)$, ($\mathrm{photon\,s^{-1}\,m^{-2}}$) and a lineshape function $g(\nu_L - \nu_0)$, normalized so that $\int_{-\infty}^{+\infty} g(\nu - \nu_0)\, d\nu = 1$. The lineshape function will be discussed in more detail later.

Consequently, the rates of absorption, stimulated emission, and spontaneous emsiion are given by

$$k_{abs} = B_{abs} I(\nu_L) g(\nu_L - \nu_0) \tag{6.13}$$

$$k_{stim.} = B_{em} I(\nu_L) g(\nu_L - \nu_0) \tag{6.14}$$

$$k_{spont.} = A \tag{6.15}$$

where the quantum numbers have been left off. Other formulas for the B coefficients exist; they differ from this definition in changing the definition of the light intensity, *i.e.*, energy density per unit frequency, energy flux, photon density per unit

frequency, etc. All these definitions give identical rate constants when properly used.

B. LIF Mechanism

The complete analysis of the general LIF detection scheme is quite complicated, due mainly to a nontrivial polarization dependence, even for an isotropic sample. Various authors don't even agree under which conditions can the polarization of the incident laser radiation be ignored. Kinsey[1] reported that if the detector is equally sensitive to all polarizations and if the angular momentum sublevels m are equally populated then the resulting signal is independent of the initial polarizations. Greene and Zare[8] reported that the signal will always have a dependence on the initial polarization if the system is cylindrically symmetric.

A photomultiplier should be insensitive to the polarization of the photon impinging on it.[9] The semitransparent cathodes used in end-on photomultipliers are formed by vacuum deposition onto the window. Thus, the atoms of the cathode will be randomly oriented and there will no polarization effect. If the window were inclined with respect to the direction of the impinging photon, there would be different Fresnel reflectivity at the front surface for the s and p polarizations; however, for near normal incidences, such as used in these experiments, the reflectivity is the same for both polarizations. Therefore, the assumption that all polarizations are detected equally seems to be quite valid.

The distribution of m sublevels is more difficult to analyze. One would expect that if the reagents were isotropic and the reaction was isotropic, then the products would be isotropic. These experiments are initiated by the photolysis of an appropriate molecule with a laser beam. Because the laser beam is polarized, there is a fixed reference axis and the reagents can no longer be considered isotropic. The $H + H_2$ experiment will be more sensitive to this anisotropy. The HI photodissociation is extremely rapid, so the fragments will "remember" the initial

polarization. Because of the electronic states involved, approximately two-third's of the absorption is a perpendicular transition leading to ground state I and hot H atoms, while one-third of the absorption is a parallel transition leading to excited state I and cooler H atoms.[10] Consequently, most of the H atoms leading to a reaction will be emitted in a plane perpendicular to the electric field vector, a definite anisotropy.

The anisotropy for the H_2CO photodissociation experiment is expected to be minimal. The average lifetime of H_2CO is on the order of 10 ns in the states considered.[10] Since the rotational constants in the ground state are $A = 281970.57$, $B = 38836.0455$, and $C = 34002.2034$ MHz, the corresponding classical rotational periods for the lowest energy level around each axis are on the order 1, 13, and 15 ps, respectively. These times are so much shorter than the lifetime of the excited state that that the molecules will totally randomize their orientation in space prior to the dissociation.

Because most of the work in this thesis was developmental in nature, it was decided not to pursue the polarization question further.

The overall LIF detection scheme can be represented by the following set of processes:

$$|\Lambda v J\rangle + h\nu_L \xrightarrow{k_1} |\Lambda' v' J'\rangle$$

$$|\Lambda' v' J'\rangle + h\nu_L \xrightarrow{k_2} |\Lambda v J\rangle + 2h\nu_L$$

$$|\Lambda' v' J'\rangle \xrightarrow{k_3} |\Lambda'' v'' J''\rangle + h\nu$$

$$|\Lambda v J\rangle \xrightarrow{k_4} \text{other}$$

$$|\Lambda' v' J'\rangle \xrightarrow{k_5} \text{other}$$

in which reaction 1 is the photon absorption process, reaction 2 is the competing stimulated emission process, reaction 3 is the spontaneous emission (fluorescence) process, while reactions 4 and 5 are any other competing process, *i.e.*, dissociation, ionization, collisional relaxation, radiative transitions to other states, etc.

When analyzing the above kinetic scheme, it is important to know the approximate magnitude of each rate constant. They can be estimated as follows. (In order to minimize congestion in the writing of the following section, the quantum numbers which distinguish the various A's, B's, and k's will be left off). The rate constant for absorption and for stimulated emission is just the product of the appropriate Einstein coefficient, the laser photon flux, and the linewidth function; specifically,

$$k_1 = B_{abs} I(\nu_L) g(\nu_L - \nu_0) \tag{6.16}$$

$$k_2 = B_{em} I(\nu_L) g(\nu_L - \nu_0) \tag{6.17}$$

where $I(\nu_L)$ is the photon flux at frequency ν_L of the laser pulse. For the purposes of estimation, it will be assumed that the VUV laser beam contains 10^8 photons in a 1 ns pulse with a radius of 1 mm, giving a photon flux of $\approx 3 \times 10^{22}$ photons s^{-1} m^{-2}. The Doppler linewidth of room temperature H_2 is on the order of 0.8 cm^{-1}, implying that $g \approx 4.2 \times 10^{-11}$ Hz^{-1} at its maximum (*vide infra*). As mentioned in the previous chapter during the discussion of H_2 spectroscopy, the band oscillator strength for the 0–0 band of the Lyman system is $f = 0.00175$. One therefore finds that for this band $k_1 = k_2 \approx 6 \times 10^3$ s^{-1} when rotation is ignored.

The rate constant for emission is simply the Einstein A coefficient; specifically,

$$(k_3)_i = A_i \tag{6.18}$$

if the fluorescence to only final state i is collected. However, if all of the fluorescence is collected, then

$$k_3 = \sum A_i \tag{6.19}$$

where the summation is over all possible final states. The A coefficient[11] for the 0–0 band of the Lyman system is 9×10^6 s^{-1} while the A coefficient for all possible

transitions from $v' = 0$ is 1.85×10^9 s^{-1}. It is seen that repopulation of the initial state by fluorescence is 3 orders of magnitude more likely than by stimulated emission. At the same time, the total emission rate is 200 times greater than the 0–0 emission rate. Two conclusions can be drawn from these figures: 1) that stimulated emission can be ignored, and 2) that repopulation of the initial state by any mechanism is not very likely.

The rates for reactions 4 and 5 are more difficult to estimate since many different processes are possible. The various processes can be broken into two categories, those involving a collision with another molecule and those that do not. The processes involving collisions will be examined first.

There are several outcomes from any collision. The rovibrational state within the ground electronic state could change, the rovibrational state within the excited electronic state could change, or the excited state could undergo collision induced dissociation. The first process would affect the number of molecules within a given initial quantum state, but would not really interfere with the LIF detection scheme. The second process would change the emission distribution from the excited electronic state, but if the total fluorescence from all possible states is being detected, there wouldn't be a major effect. On the other hand, if the molecule in the excited state dissociates as a result of a collision before it fluoresces, then the LIF signal would decrease.

As for all collisional processes, the important parameters are the relative velocity between the collision partners, the cross section for the process, and the number density of the second species. In the $H + H_2$ reaction the final H_2 laboratory translational energy is bounded by the laboratory translational energy of the incident H atom while for the H_2CO photodissociation reaction the H_2 laboratory translational energy is bounded by the energy of the incident photon (in order to provide an upper bound estimate, all of the available energy will be

given to the H_2 translational degrees of freedom). Therefore, the H_2 translational energy is bounded by 3.8 eV, the energy of the photons used in the H_2CO photodissociation experiments described in a later chapter, corresponding to a maximum laboratory velocity on the order of 1.9×10^4 m s^{-1}. Most experiments are performed at total pressures on the order of 0.5 torr, corresponding to a density of 1.6×10^{16} molecules cm^{-3}. It will be assumed that the collision cross section is bounded by 10^{-14} cm^2, *i.e.*, 100 Å^2. Then the pseudo first-order rate constant will be bounded by 4×10^8 s^{-1}, a result which is only 20 percent of the fluorescence rate constant. Collisions are thereby seen to be a minor competing process in a worst case scenario. Since the species involved actually are on the order of an Å or two in size, it is expected that the actual collision cross section will be less than 100 Å^2, and that the inelastic and collision induced dissociation cross sections will be even smaller. In addition, the actual laboratory velocities will be lower once the translational energy is correctly allocated to each fragment and internal degrees of freedom are excited. It is therefore concluded that competing processess brought about as the result of collisions are unimportant on the time scale of the LIF process, though they may be important during the time between the initiation of the reaction and the LIF detection of the product.

The second set of competing processes do not involve a collision with another species. These processes can be further subdivided into two categories: the multiphoton processes and those that are not. Specifically, the molecule in the excited electronic state could absorb a second photon, leading to ionization or dissociation, or the isolated molecule could undergo a radiationless transition either to another bound electronic state or to the dissociative continuum of the ground electronic state. The latter scenario will be investigated first.

The lowest two bound excited states[10] of H_2 are the $\tilde{B}\ ^1\Sigma_u^+$ and the $\tilde{C}\ ^1\Pi_u$ states, the two states involved in the LIF detection scheme. Therefore, the

only possible radiationless transitions would be to the dissociative continuum of the ground electronic state. Dalgarno and Stephens[12] calculated the fraction of molecules in each vibrational level of these two states which dissociate. They found that within the $\tilde{B}$ state this fraction was less than 0.2% for $v' = 0$ to 5 and then it sharply increases reaching 38.6% by $v' = 10$ and 55% by $v' = 15$, while for the $\tilde{C}$ state this fraction was less than 6% for $v' = 0$ to 9. Thus, dissociation need only be included for transitions to higher v's of the $\tilde{B}$ state.

The multiphoton processes are the most difficult to analyze. Because the laser beams are unfocussed and the resulting photon fluxes are relatively low, non-resonant multiphoton processes are expected to have a negligible probability. According to Birge,[13] a "typical" two photon absorptivity is on the order of 10^{-58} $m^4\,s\,molecule^{-1}\,photon^{-1}$. The flux of the VUV beam is on the order of 3×10^{22} photon $s^{-1}\,m^{-2}$. The flux of the UV beam which was used to generate and is collinear with the VUV beam is on the order of 5×10^{28} photon $s^{-1}\,m^{-2}$ (5 mJ at 330 nm, pulse-width of 4.2 ns and a radius of 3 mm). Consequently, the rate of multiphoton absorption is on the order of 1.5×10^{-7} photon s^{-1} and can safely be ignored.

Certain resonantly enhanced multiphoton processes are possible; specifically, molecules in certain vibrational levels of the $\tilde{B}$ and $\tilde{C}$ states are within a UV photon energy of the second dissociation limit of 118375.6 cm^{-1} and the H_2 ionization potential (IP) of 124417 cm^{-1}. The energetics of these multiphoton process are easily ascertained. The $\tilde{B}$ band is about 90000 cm^{-1} above the $\tilde{X}$ ground state, and it is reached by a single VUV photon. This VUV photon is produced by third harmonic generation using approximately 30000 cm^{-1} photons. The absorption of a UV photon by the $\tilde{B}$ state would produce a super-excited state with a total energy of approximately 120000 cm^{-1}, some 2000 cm^{-1} above the second dissociation limit and some 4000 cm^{-1} below the IP. If the H_2 molecule is in the $v = 1$ level, it has

a vibrational energy of 4161.14 cm^{-1}. Since the VUV tuning range is small, this molecule is excited with the same 90000 cm VUV photon to a total energy of 94000 cm, corresponding to $v' = 3$ of the $\tilde{B}$ state. Absorption of a UV photon brings the molecule to a super-excited state with 124000 cm of energy, above the dissociation limit and very close to the IP, and in fact the IP can be reached at the high energy, low wavelength, end of the typical scan ($\lambda_{VUV} \approx 109.65$ nm, 91200 cm^{-1}, 30400 cm^{-1} in the UV). If the molecule starts in the $v = 2$ level of the ground state, it has 8086.93 cm of vibrational energy. A similiar analysis shows that the intermediate energy of 98000 cm is near $v' = 6$ of the $\tilde{B}$ state and just below the $v = 0$ level of the $\tilde{C}$ state (which can be reached at the high energy end of the scan) and that absorption of a UV photon gives a state with an energy of 128000 cm, approximately 4000 cm^{-1} above the IP and in the energy range where the $v'' = 2$ level of the ionic ground state becomes accessible. Since the absorption of a second UV photon or a second VUV photon must be considered extremely unlikely, the only likely multiphoton process is the single UV photon absorption by the excited $\tilde{B}$ or $\tilde{C}$ state. Such absorption would lead to dissociation or ionization, and would consequently reduce the fluorescence signal from the LIF detection scheme.

In order to estimate the effect of these 2 photon processes on the LIF signal, one needs to know the absorption spectroscopy of the excited state. Because overall this is a two photon transition, the selection rules will be different and therefore different states will be populated as compared with single photon transitions from the ground electronic state. The most important difference is that for homonuclear diatomic molecules the single photon selection rule $g \leftrightarrow u$ becomes the two photon selection rule $g \leftrightarrow g$ and $u \leftrightarrow u$. Since the ground state is $\tilde{X}\ ^1\Sigma_g^+$, only g upper states are allowed following a two photon transition, instead of the usual u states.

Several of these excited g states have been observed in emission spectra.[14] The highest of these is the $\tilde{S}\ ^1\Delta$ state near 119893 cm^{-1}, approximately 27500 cm^{-1} above the $\tilde{B}$ state. This energy is less than the UV photon energy, consequently, the spectroscopy in the region of interest is not yet known. However, at this high an energy there are likely to be numerous Rydberg states converging to the ionization potential. The single photon VUV ionization spectrum is extremely complex at energies just above the IP, with numerous peaks due to autoionization. Berkowitz[15] provides a good discussion of this region of the spectrum. It is expected that at this high an energy the overall features of the spectrum will be similar for both the one and two photon absorptions, with the major differences being in the exact location of super-excited discrete states. As a point of reference, the single photon oscillator strengths from the ground state to that portion of the continuum between 124000 and 135000 cm^{-1}, the region with autoionization, is 0.077 for the ionization continuum, 0.083 for the quasi-discrete states, and 0.013 for the dissociative continuum. The oscillator strength for the discrete states below the IP and above the $\tilde{B}'$ and $\tilde{D}$ bands, at 111642 cm^{-1} and 11388.7 cm^{-1}, respectively, is essentially 0.0.

If these oscillator strengths from the ground state are representative of the oscillator strengths from the $\tilde{B}$ or $\tilde{C}$ states, then there is negligible absorption to super-excited states below the IP. This, along with the energetic data given earlier, implies that the competing multiphoton processes are important only when the LIF detection scheme is investigating vibrational levels at or above $v = 2$ in the ground electronic state.

Photoionization of H_2 by resonantly enhanced multiphoton ionization has been observed experimentally.[16] In these experiments a single VUV photon was used to excite the molecule to the $v' = 0$ and 3 levels of the $\tilde{B}$ state, followed by the absorption of a 266 nm photon to the ionization continuum. The ionization

cross section from a particular rovibrational level of the $\tilde{B}$ state varied from 2.3×10^{-19} cm^2 to 1.2×10^{-18} cm^2. Experiments in which the ionization wavelength was varied by ±0.5 nm showed that the ionization cross sections are not smooth, but show pronounced autoionizing resonances that vary with rotational level.

Theoretical calculations of the direct ionization process using 266.05 nm radiation gave ionization cross sections on the order of 1.2×10^{-17} cm^2 and 5×10^{-18} cm^2 from $v = 0$ and 3 of the $\tilde{B}$ state, respectively, results an order of magnitude larger than found experimentally. The theoreticians believe that the error lies with the experimentalists, specifically, effects due to pulse-to-pulse temporal jitter and uncertainty in the temporal and spatial distributions and overlap of the two laser beams.

The direct applicability of those results to the current experiments is unknown. They show that the ionization cross section from the $\tilde{B}$ state can be quite large; however, those experiments and calculations used a UV photon energy on the order of 37600 cm^{-1}, in which case the total energy and the electronic energy both exceed the IP. In the current experiments the UV photon energy varies from 29800 to 30400 cm^{-1}, some 7500 cm^{-1} less, in which case the total energy following a two photon absorption could exceed the IP (if $v = 2$ or greater in the ground state) but the electronic energy would be below the IP. Any absorption under these circumstances would be to states that autoionize or predissociate. It is known that the one photon oscillator strength to the second dissociative continuum is very weak.[15] Thus, it is expected that the absorption cross section will principally depend on the coupling between the low vibrational levels of the ion and the high vibrational levels of the discrete states, *i.e.*, on the Franck-Condon factors. Some preliminary calculations provided by H. Rudolph[18] show that the F-C factors are very poor for the transitions involved. For example, after a transition from $v = 1$ of $\tilde{X}$ to $v' = 4$ of $\tilde{B}$, the only accessible ionic state is $v'' = 0$ and the F-C

factor for this excited state to ion transition is 0.016, implying an approximate continuum cross section of $\approx 0.24 \times 10^{-18}$ cm^{-2}. From $v' = 7$ of the $\tilde{B}$ state only $v'' = 0, 1$ are accessible, and these F-C factors are 0.0004 and 0.007, implying that the cross section is even smaller. These estimates are for direct ionization and exclude autoionization, but they seem to show that direct ionization will not be very important. A more detailed analysis and calculation of these cross sections is beyond this dissertation.

The important question is will the absorption to these super-excited states from the $\tilde{B}$ and $\tilde{C}$ states effectively compete with the fluorescence? Two methods were derived to answer this question. The first method uses the theoretical cross section. Assuming that the total number of molecules in the excited state at some time is N, then the number of UV photons absorbed as given by Beer's law is

$$I_{abs} = I_{inc}\left(1 - \mathrm{e}^{-\sigma N l/V}\right) \tag{6.20}$$

where σ is the absorption cross section, l is the path length, and V is the volume (needed to convert the total number of particles to a density). Every absorbed photon will reduce the fluorescence signal, so the fractional drop in fluorescence will be

$$\frac{I_{abs}}{N} = \frac{I_{inc}}{N}\left(1 - \mathrm{e}^{-\frac{\sigma N}{\pi r^2}}\right) \approx \frac{I_{inc}\sigma}{\pi r^2} \tag{6.21}$$

where r is the radius of the region containing the excited state molecules. This result is independent of the number of excited state molecules. The initial number of UV photons is on the order of 8×10^{15} photons pulse^{-1}, assuming a 5 mJ pulse energy at 330 nm. However, many of these photons will not be usable to ionize the excited state molecules for two reasons. First, the divergence of the VUV beam as it leaves the Kr cell is one third the divergence of the UV beam.[19] Therefore, only 11% of the UV photons will interact with the region of the excited state molecules. Second, the UV beam has a larger temporal width than the VUV

beam, by a factor of $\sqrt{3}$; consequently, many UV photons will pass through the cell before the VUV photons first excite the hydrogen molecules or after the excited state has fluoresced. The UV pulse-width is approximately 4.2 ns and the VUV pulse-width is approximately 2.4 ns. Since the fluorescence lifetime is 0.5 ns (from $A = 1.8 \times 10^9$ s^{-1}), there are hydrogen molecules in the excited state for only 70% of the UV pulse-width (assuming square temporal pulses for convenience). It is estimated that the average cross section should not exceed than 10^{-17} cm^2. Not only is this approximately the theoretical cross section for 266 nm absorption by the $\tilde{B}$ state, it is also close to the experimental one photon cross section for absorption from the ground state. If one uses a VUV radius of 1 mm, one finds that approximately 20% of the excited state molecules will undergo further excitation and will not fluoresce in a worst case scenario. If the cross section is as small as the theory predicts, then less than 0.5% of the excited state molecules will ionize.

As a second approach, assume that the oscillator strength from the $\tilde{B}$ or $\tilde{C}$ states to the autoionzation regime is the same as from the ground state to the same region. The total oscillator strength is 0.173, the linewidth is 11000 cm^{-1}, the average UV photon flux is 2×10^{29} photon s^{-1} m^{-2}, implying that the average excitation rate calculated from Eq. 6.13 would be 2.8×10^8 s^{-1}, 15% of the fluorescence rate.

Both of these calculations, using different approaches, predict that the maximum excitation rate from the $\tilde{B}$ and $\tilde{C}$ states to the ionization regime will be on the order of 1/6'th the fluorescence rate If the theoretical Franck-Condon factors are even close to being correct, then the actual direct excitation rate to the ionization continuum from the $\tilde{B}$ state will be two orders of magnitude smaller and can be ignored.

In summary, estimates of the various rate constants that take part in the LIF detection scheme predict 1) that stimulated emission can be ignored, 2) the initial

state will not be repopulated in the timescale of the experiment, 3) collision induced changes in the initial state populations are not important on the timescale of the LIF process, but could be important if there is a long delay between the formation and detection of the H_2 fragments, 4) collisional effects on the excited state are negligible, 5) radiationless transitions to the dissociative continuum are important only for very high vibrational levels of the $\tilde{B}$ state, and 6) multiphoton absorption processes are expected to become important only when detecting the $v \geq 2$ levels of H_2.

C. LIF Signal Levels

With the information from the previous section, it is now possible to construct a realistic mechanism for the LIF detection scheme that will only include the important side reactions. From the earlier reaction scheme, only reactions 1, 3, and 5 need to be considered. Thus, the mechanism is

$$|\Lambda v J\rangle + h\nu_L \xrightarrow{k_1} |\Lambda' v' J'\rangle$$

$$|\Lambda' v' J'\rangle \xrightarrow{k_3} |\Lambda'' v'' J''\rangle + h\nu$$

$$|\Lambda' v' J'\rangle \xrightarrow{k_5} \text{other}$$

The differential equations controlling the kinetics will then be

$$\frac{dn_{|\Lambda v J\rangle}}{dt} = -k_1 \times n_{|\Lambda v J\rangle} \tag{6.22}$$

$$\frac{dn_{|\Lambda' v' J'\rangle}}{dt} = +k_1 \times n_{|\Lambda v J\rangle} - (k_3 + k_5) \times n_{|\Lambda' v' J'\rangle} \tag{6.23}$$

$$\frac{dn_{|\Lambda_i'' v_i'' J_i''\rangle}}{dt} = (k_3)_i \times n_{|\Lambda' v' J'\rangle} \tag{6.24}$$

for each final state. If one assumes that the laser pulse has a square temporal profile (so that k_1 is either 0 or a constant) and that the initial state population

density at time $t = 0$ (the beginning of the laser pulse) is given by the constant n_0, then the time evolution of the state population densities while the laser is on is

$$n_{|\Lambda v J\rangle}(t) = n_0 e^{-k_1 t} \tag{6.25}$$

$$n_{|\Lambda' v' J'\rangle}(t) = n_0 \frac{k_1}{k_3 + k_5 - k_1} \times \left(e^{-k_1 t} - e^{-(k_3+k_5)t}\right) \tag{6.26}$$

$$n_{|\Lambda_i'' v_i'' J_i''\rangle}(t) = n_0 \frac{k_1 (k_3)_i}{k_3 + k_5 - k_1} \times \left(\frac{1 - e^{-k_1 t}}{k_1} - \frac{1 - e^{-(k_3+k_5)t}}{k_3 + k_5}\right) \tag{6.27}$$

At time $t = \tau$ the laser pulse is over. There is no further excitation and the time evolution of the state population densities after the laser pulse is

$$n_{|\Lambda v J\rangle}(t) = n_0 e^{-k_1 \tau} \tag{6.28}$$

$$n_{|\Lambda' v' J'\rangle}(t) = n_0 \frac{k_1}{k_3 + k_5 - k_1} \times \left(e^{(k_3+k_5-k_1)\tau} - 1\right) \times e^{-(k_3+k_5)t} \tag{6.29}$$

$$\begin{aligned} n_{|\Lambda_i'' v_i'' J_i''\rangle}(t) = {} & n_0 \frac{(k_3)_i}{k_3 + k_5} \times \left(1 - e^{-k_1 \tau}\right) \\ & - n_0 \frac{k_1 (k_3)_i}{k_3 + k_5 - k_1} \times \left(e^{(k_3+k_5-k_1)\tau} - 1\right) \times e^{-(k_3+k_5)t} \end{aligned} \tag{6.30}$$

At time $t = \infty$, the population density in the final state is

$$n_{|\Lambda_i'' v_i'' J_i''\rangle}(\infty) = n_0 \frac{(k_3)_i}{k_3 + k_5} \times \left(1 - e^{-k_1 \tau}\right) \tag{6.31}$$

This is just the result one would have expected. The final population density of state i is just the product of the initial population density of the initial state, the fraction of the initial state molecules which absorb a photon and are excited to the excited state, and the fraction of the excited state molecules which end up in state i as opposed to other states.

As mentioned earlier, in the current experiments the laboratory velocity of the H_2 molecules is bounded by 1.9×10^4 m s^{-1}. The total fluorescence rate is on the order of $k_3 = 2 \times 10^9$ s^{-1}, which provides a lower bound to $k_3 + k_5$. Therefore, the maximum distance the H_2 molecules could travel is 10 μm per lifetime, less than

1% of the laser beam radius. The molecules in final state i therefore occupy the same volume as the initial state. The total number of molecules in final state i is given by

$$N_{|\Lambda_i'' v_i'' J_i'')}(\infty) = n_0 V \frac{(k_3)_i}{k_3 + k_5} \times \left(1 - e^{-k_1 \tau}\right) \tag{6.32}$$

where V is the volume probed by the VUV beam.

Since every transition to final state i results in the emission of a photon at frequency ν_i, the number of photons with frequency ν_i will be given by

$$N_{\nu_i} = n_0 V \frac{(k_3)_i}{k_3 + k_5} \times \left(1 - e^{-k_1 \tau}\right) \tag{6.33}$$

The number of photons that reach the photomultiplier is just the total number of photons times the fractional solid angle, $\Omega/4\pi$. If there is a filter before the photomultiplier, the number of photons reaching the photocathode will be reduced by the transmission efficiency of the filter, $T(\nu_i)$. The photons which reach the photocathode will cause the emissions of photoelectrons with efficiency $Q(\nu_i)$, the quantum efficiency of the cathode. Each electron will be amplified by G, the photomultiplier gain, giving a charge pulse of Ge. The overall signal from the photomultiplier will then be

$$\mathrm{SIG}(\nu_i) = \frac{\Omega}{4\pi} T(\nu_i) Q(\nu_i) G e n_0 V \frac{(k_3)_i}{k_3 + k_5} \times \left(1 - e^{-k_1 \tau}\right) \tag{6.34}$$

This formula contains two parts, one that is independent of the final state i and consequently the same for all i, and a second part that depends on i. This formula can be factored to explicitly show these parts, giving

$$\mathrm{SIG}(\nu_i) = \frac{\Omega G e n_0 V}{4\pi(k_3 + k_5)} \left(1 - e^{-k_1 \tau}\right) \times (k_3)_i T(\nu_i) Q(\nu_i) \tag{6.35}$$

The product $k_1\tau$ is on the order of 10^{-5}. Since this is much less than 1, the approximation $1 - e^{-x} \approx x$ can be made. One should remember that the signal is

a function of the excitation frequency, so the signal at frequency ν_i resulting from absorption of a frequency ν_L will be designated as $\mathrm{SIG}(\nu_i;\nu_L)$. If the appropriate definitions are included for k_1 and k_3, the final result is

$$\begin{aligned}
\mathrm{SIG}(\nu_i;\nu_L) =& \frac{\Omega G e n_0 V k_1 \tau}{4\pi(k_3+k_5)} \times (k_3)_i T(\nu_i) Q(\nu_i) \\
=& \frac{\Omega G e n_0 V B_{abs} I(\nu_L) g(\nu_L-\nu_0)\tau}{4\pi(k_3+k_5)} \times (k_3)_i T(\nu_i) Q(\nu_i) \\
=& \frac{\Omega G e n_0 (l\pi r^2) B_{abs} \frac{N_{\nu_L}}{\tau \pi r^2} g(\nu_L-\nu_0)\tau}{4\pi(k_3+k_5)} \times (k_3)_i T(\nu_i) Q(\nu_i) \\
=& \frac{\Omega G e n_0 l B_{abs} N_{\nu_L} g(\nu_L-\nu_0)}{4\pi(k_3+k_5)} \times (k_3)_i T(\nu_i) Q(\nu_i) \\
=& \frac{\Omega G e n_0 l B_{abs} N_{\nu_L} g(\nu_L-\nu_0)}{4\pi(A+k_5)} \times A_i T(\nu_i) Q(\nu_i)
\end{aligned} \tag{6.36}$$

where l is the length of the volume probed by the VUV laser and observed by the photomultiplier and N_{ν_L} is the number of incident VUV photons.

If the fluorescence is undispersed, then there will be a similar term for every emission line. The total signal is just the sum of the signals for each line, giving

$$\mathrm{SIG}(tot;\nu_L) = \frac{\Omega G e n_0 l B_{abs} N_{\nu_L} g(\nu_L-\nu_0)}{4\pi(A+k_5)} \times \sum_i \left(A_i T(\nu_i) Q(\nu_i)\right) \tag{6.37}$$

where the summation is over all possible final states. If all of the quantum numbers are inserted, the final result is

$$\begin{aligned}
\mathrm{SIG}(tot;\nu_L)^{\Lambda' v' J'}_{\Lambda v J} =& \frac{\Omega G e n_{|\Lambda v J\rangle} l (B_{abs})^{\Lambda' v' J'}_{\Lambda v J} N_{\nu_L} g(\nu_L-\nu_0)}{4\pi(A^{\Lambda' v' J'}+k_5)} \\
& \times \sum_i \left(A^{\Lambda' v' J'}_{\Lambda_i'' v_i'' J_i''} T(\nu_i) Q(\nu_i)\right)
\end{aligned} \tag{6.38}$$

If more than one transition is at the same excitation frequency, each transition will contribute a term as in the previous equation to the total.

The previous formula is the primary result of this section. The LIF signal depends on the following factors: 1) the states used in the LIF scheme, 2) the

Einstein coefficients connecting these states, 3) the frequency distribution of the fluorescence, the transmission of any filter, and the quantum efficiency of the photomultiplier, 4) the population density of initial the quantum state, 5) the number of VUV photons and the linewidth function, 6) the solid angle subtended by the photomultiplier, and 7) the gain of the photomultiplier. Because LIF is a linear process, the final signal 1) is independent of the temporal profile of the incident VUV beam, and 2) is independent of the spatial profile of the incident VUV beam.

This formula assumes optically thin conditions, *i.e.*, that the incident VUV laser beam is not attenuated by the time it reaches the detection region. If there is a strong absorption by H_2, there will be less incident radiation at the center frequencies then on the wings and the previous equation will not be accurate.

D. Lineshape Function

The lineshape function is an important part of Eq. 6.38. It determines the shape of the LIF signal: short and broad or tall and narrow. This can have a major effect on the ability to see any signal above background levels. Two different lineshape functions will be derived in this section, differing only in the form of the Doppler profile. In the first case it will be assumed that the molecules have a velocity distribution characterized by a Maxwell-Boltzmann distribution, in which case the Doppler profile is a Gaussian. In the second case it is assumed that the molecules have a velocity distribution characterized by a delta function, *i.e.*, the particles are monoenergetic. This case arises during a photodissociation when the energy released is much greater than the initial thermal energy. Both cases use a Gaussian for the laser linewidth.

The absorption cross section is related to the Einstein B coefficient through[7]

$$\sigma(\nu) = Bg(\nu - \nu_0) \tag{6.39}$$

where B is the Einstein B coefficient for absorption and $g(\nu - \nu_0)$ is the lineshape function of the absorbing species. This function is normalized such that $\int_{-\infty}^{+\infty} g(\nu - \nu_0)\, d\nu = 1$.

Under most circumstances, the lineshape is dominated by the Doppler broadening; therefore, the lineshape function is given by

$$g(\nu - \nu_0) = \frac{2}{\Delta\nu_D}\sqrt{\frac{\ln 2}{\pi}}e^{-x^2} \tag{6.40}$$

where the scaled frequency x is given by

$$x = \frac{2\sqrt{\ln 2}}{\Delta\nu_D}(\nu - \nu_0) \tag{6.41}$$

and the Doppler width (full-width at half-maximum) for a thermal velocity distribution is

$$\Delta\nu_D = \sqrt{\frac{8kT\ln 2}{m}}\frac{\nu_0}{c} \tag{6.42}$$

where k is Boltzmann's constant, T is the temperature, and m is the molecular mass.

The above definition of the lineshape is correct if the laser beam has an infinitesimal linewidth. In reality, the laser linewidth is finite and can be adequately described by a Gaussian lineshape with $I_\nu\, d\nu$, the photon flux with frequency between ν and $\nu + d\nu$, given by

$$I_\nu\, d\nu = I_0 e^{y^2}\, d\nu \tag{6.43}$$

where y is a scaled frequency given by

$$y = \frac{2\sqrt{\ln 2}}{\Delta\nu_L}(\nu - \nu_L) \tag{6.44}$$

with the ν_L the center of the laser line and $\Delta\nu_L$ the laser linewidth. The constant I_0 is chosen so that $\int_{-\infty}^{+\infty} I_\nu\, d\nu = I_{inc}$, the total incident flux. This means that

$$I_0 = \frac{2}{\Delta\nu_L}\sqrt{\frac{\ln 2}{\pi}}\, I_{inc} \tag{6.45}$$

The transmittance is the ratio of the transmitted light to the incident light. Combining the effects of the laser and Doppler linewidths following Bemand and Clyne,[20] one obtains

$$T = \frac{\int_{-\infty}^{+\infty} I_\nu e^{-\sigma(\nu)nl}\, d\nu}{\int_{-\infty}^{+\infty} I_\nu\, d\nu} \tag{6.46}$$

$$= \frac{\int_{-\infty}^{+\infty} I_\nu \left(\sum_{j=0}^{\infty} \frac{(-\sigma(\nu)nl)^j}{j!}\right) d\nu}{\int_{-\infty}^{+\infty} I_\nu\, d\nu} \tag{6.47}$$

$$= \sum_{j=0}^{\infty} \frac{\int_{-\infty}^{+\infty} I_\nu \frac{(-\sigma(\nu)nl)^j}{j!}\, d\nu}{\int_{-\infty}^{+\infty} I_\nu\, d\nu} \tag{6.48}$$

$$= \sum_{j=0}^{\infty} \frac{\left(-Bnl\frac{2}{\Delta\nu_D}\sqrt{\frac{\ln 2}{\pi}}\right)^j}{j!} \int_{-\infty}^{+\infty} e^{-y^2} e^{-jx^2}\, d\nu \tag{6.49}$$

$$= \sum_{j=0}^{\infty} \frac{\left(-Bnl2\sqrt{\ln 2/\pi}\, \exp\left[-4\ln 2\left(\frac{\nu_L-\nu_0}{\Delta\nu_D\sqrt{j\alpha^2+1}}\right)^2\right]\right)^j}{j!\Delta\nu_D\sqrt{j\alpha^2+1}} \tag{6.50}$$

where $\alpha = \Delta\nu_L/\Delta\nu_D$ is a dimensionless parameter relating the laser and Doppler linewidths. This last formula gives the reduction in transmittance in both the low and high absorption limits. The only error will occur at frequencies way off to the side of the center of the line where the Lorentzian profile of the natural linewidth dominates over the Gaussian profile of the Doppler broadening.

In the weak signal limit the transmittance is

$$T \approx 1 + \frac{-Bnl2\sqrt{\ln 2/\pi}\, \exp\left[-4\ln 2\left(\frac{\nu_L-\nu_0}{\Delta\nu_D\sqrt{\alpha^2+1}}\right)^2\right]}{\Delta\nu_D\sqrt{\alpha^2+1}} \tag{6.51}$$

Now,

$$\frac{dn}{dt} = \frac{dI_{trans}}{dl} = \frac{-BnI_{inc}2\sqrt{\ln 2/\pi}\, \exp\left[-4\ln 2\left(\frac{\nu_L-\nu_0}{\Delta\nu_D\sqrt{\alpha^2+1}}\right)^2\right]}{\Delta\nu_D\sqrt{\alpha^2+1}} \tag{6.52}$$

which shows by comparison with Eq. 6.16 that the lineshape function for thermally distributed particles including laser linewidth effects to first order is

$$g(\nu_L - \nu_0) = \frac{2}{\sqrt{\Delta\nu_L^2 + \Delta\nu_D^2}} \sqrt{\frac{\ln 2}{\pi}} \exp\left[-4 \ln 2 \left(\frac{\nu_L - \nu_0}{\sqrt{\Delta\nu_L^2 + \Delta\nu_D^2}}\right)^2\right] \tag{6.53}$$

which is a Gaussian with linewidth

$$\Delta\nu_{LD} = \sqrt{\Delta\nu_L^2 + \Delta\nu_D^2} \tag{6.54}$$

A much different lineshape is obtained if the molecules do not have a thermal velocity distribution. An example of this situation would be if the molecules are produced by photodissociation. If the energy released during the dissociation is significantly greater than thermal energies, the translational energy of the particles will be monoenergetic, in which case the velocity distribution can be represented by a delta function. This situation will be examined.

During a photodissociation, the fragments are not isotropically distributed. As shown by Zare,[21] the molecules will have an angular distribution of

$$P(\theta, \phi) = \frac{1}{4\pi}\left(1 + \frac{\beta}{2}\left(3\cos^2\theta - 1\right)\right) \tag{6.55}$$

where β is the asymmetry parameter, bounded by $-1 \leq \beta \leq +2$. For an isotropic distribution, $\beta = 0$. The value of β depends on several factors, including the angle between the dipole moment and the molecular axis, the angle by which the molecule rotates during the dissociation process, and the lifetime of the excited state. If we further assume that the molecules have a delta function velocity distribution, then the three dimensional velocity distribution in spherical coordinates is simply given by

$$P(v_r, \theta, \phi) = \frac{1}{4\pi}\frac{\delta(v - v_r)}{v_r^2}\left(1 + \frac{\beta}{2}\left(3\cos^2\theta - 1\right)\right) \tag{6.56}$$

and in cartesian coordinates by

$$P(v_x, v_y, v_z) = \frac{1}{4\pi} \frac{\delta\left(v - \sqrt{v_x^2 + v_y^2 + v_z^2}\right)}{v_x^2 + v_y^2 + v_z^2} \left(1 + \frac{\beta}{2}\left(\frac{3v_z^2}{v_x^2 + v_y^2 + v_z^2} - 1\right)\right) \quad (6.57)$$

where v is the velocity of the fragment, θ is measured from the z axis, and the incident radiation is incident along the x-axis (with polarization vector in the z axis if polarized).

If this probability distribution is integrated over all v_z and then v_y, the velocity distribution in the x direction becomes

$$P(v_x) = \begin{cases} \frac{1}{2v}\left(1 + \frac{\beta}{4} - \frac{3\beta}{4}\left(\frac{v_x}{v}\right)^2\right) & v_x^2 \leq v^2 \\ 0 & v_x^2 > v^2 \end{cases} \quad (6.58)$$

The Doppler shift of a particle moving with velocity v_x in the direction of a radiation source at frequency ν is[22]

$$\frac{\Delta\nu}{\nu} = \frac{v_x}{c} \quad (6.59)$$

If the definition of the Dopper shift is inserted into the distribution of v_x, one obtains the following Doppler profile for a monoenergetic particle:

$$g(\nu - \nu_0) = \begin{cases} \frac{1}{2\Delta\nu_{max}}\left(1 + \frac{\beta}{4} - \frac{3\beta}{4}\left(\frac{\nu - \nu_0}{\Delta\nu_{max}}\right)^2\right) & (\nu - \nu_0)^2 \leq (\Delta\nu_{max})^2 \\ 0 & (\nu - \nu_0)^2 > (\Delta\nu_{max})^2 \end{cases} \quad (6.60)$$

where $\Delta\nu_{max} = v\frac{\nu_0}{c}$ is the maximum Doppler shift which occurs when the molecule is heading directly towards or away from the incident photon. It is interesting to note that if $\beta = 0$, the monoenergetic particle lineshape function is a square distribution with the same probability for all accessible Doppler shifts, unlike the Gaussian distribution for thermal distributions which is sharply peaked.

The transmittance is found in a manner similar to above, giving

$$T = \frac{\int_{-\infty}^{+\infty} I_\nu e^{-Bnlg(\nu-\nu_0)}\, d\nu}{\int_{-\infty}^{+\infty} I_\nu\, d\nu} \tag{6.61}$$

$$= \frac{2}{\Delta\nu_L}\sqrt{\frac{\ln 2}{\pi}} \sum_{j=0}^{\infty} \frac{(-Bnl)^j}{j!} \int_{-\infty}^{+\infty} [g(\nu-\nu_0)]^j \exp\left[-4\ln 2\left(\frac{\nu-\nu_L}{\Delta\nu_L}\right)^2\right] d\nu \tag{6.62}$$

$$= 1 + \frac{2}{\Delta\nu_L}\sqrt{\frac{\ln 2}{\pi}} \sum_{j=1}^{\infty} \frac{\left(\frac{-Bnl}{2\Delta\nu_{max}}\right)^j}{j!}$$

$$\times \int_{\nu_0-\Delta\nu_{max}}^{\nu_0+\Delta\nu_{max}} \left[1 + \frac{\beta}{4} - \frac{3\beta}{4}\left(\frac{\nu-\nu_0}{\Delta\nu_{max}}\right)^2\right]^j \exp\left[-4\ln 2\left(\frac{\nu-\nu_L}{\Delta\nu_L}\right)^2\right] d\nu \tag{6.63}$$

Unfortunately, the general integral in Eq. 6.63 does not have a analytic solution, even for $j = 1$. However, in the case of an isotropic distribution, $\beta = 0$ and the integral can be solved exactly,[23] giving

$$T_{\beta=0} = 1 + \sum_{j=1}^{\infty} \frac{\left(\frac{-Bnl}{2\Delta\nu_{max}}\right)^j}{2j!} \left\{\Phi\left(\frac{2\sqrt{\ln 2}}{\Delta\nu_L}(\nu_0 - \nu_L + \Delta\nu_{max})\right)\right.$$

$$\left. - \Phi\left(\frac{2\sqrt{\ln 2}}{\Delta\nu_L}(\nu_0 - \nu_L - \Delta\nu_{max})\right)\right\} \tag{6.64}$$

$$\approx 1 - \frac{Bnl}{4\Delta\nu_{max}} \left\{\Phi\left(\frac{2\sqrt{\ln 2}}{\Delta\nu_L}(\nu_0 - \nu_L + \Delta\nu_{max})\right)\right.$$

$$\left. - \Phi\left(\frac{2\sqrt{\ln 2}}{\Delta\nu_L}(\nu_0 - \nu_L - \Delta\nu_{max})\right)\right\} \tag{6.65}$$

where $\Phi(x)$ is the error function. Consequently, following the same line of reasoning as used above, one finds that the lineshape function for isotropically distributed monoenergetic particles is

$$g(\nu_L - \nu_0) = \frac{\Phi\left(\frac{2\sqrt{\ln 2}}{\Delta\nu_L}(\nu_L - \nu_0 + \Delta\nu_{max})\right) - \Phi\left(\frac{2\sqrt{\ln 2}}{\Delta\nu_L}(\nu_L - \nu_0 - \Delta\nu_{max})\right)}{4\Delta\nu_{max}} \tag{6.66}$$

III. PREVIOUS WORK

The detection of H_2 by the technique of Laser Induced Fluorescence was first accomplished by Marinero *et al.*[24] in 1983. The XUV (extreme UV) radiation at wavelengths between 97.3 and 102.3 nm was generated by third harmonic generation in a pulsed argon source. Because of the wavelength, it was not possible to use a window to physically isolate the XUV generation region from the H_2 detection region. They estimated that their apparatus produced $\approx 7 \times 10^9$ photons pulse^{-1}. The fluorescence from H_2 was detected by a solar-blind photomultiplier with a KBr photocathode and a MgF_2 window.

Fluorescence excitation spectra were taken with H_2 pressures of 4×10^{-6} torr which equals 1.3×10^{11} molecules cm^{-3} at room temperature. Portions of 6 rovibrational bands were observed: $\tilde{B} \leftarrow \tilde{X}$, $v' = 7, 8, 9, 10$, $v = 0$; $\tilde{C} \leftarrow \tilde{X}$, $v' = 0$, 1, $v = 0$. The weakest lines observed corresponded to $J = 4$, which is present as only 0.38% of the total population. Therefore, they estimated their detection sensitivity to be on the order of 5×10^8 states cm^{-3} at a signal-to-noise ratio of 3. The linewidth of the H_2 lines in the fluorescence excitation spectrum was 1.9 cm^{-1}. Since the Doppler width of H_2 lines at room temperature in this wavelength region is 0.88 cm^{-1}, they estimated that their XUV source had a linewidth of ≈ 1.7 cm^{-1} using Eq. 6.54.

A second study on the detection of H_2 by LIF by Northrup *et al.*[25] was reported in 1984. The VUV radiation between 105.8 and 106.8 nm was generated using third harmonic generation in a static cell filled with Xe. Radiation at these wavelengths can be transmitted by LiF, so LiF windows were used to isolate the VUV generation region from the H_2 detection region. No attempt was made to measure the VUV photon intensity; instead, they estimated it was $\approx 10^9$ photons pulse^{-1} on the basis of a published conversion efficiency. The fluorescence from the H_2 was detected by a solar-blind photomultiplier with a CsI photocathode and a MgF_2 window.

They obtained LIF spectra of H_2, HD, and D_2 at various pressures. The weakest line observed was the P(7) line of the (5-0) band of D_2 at a sample pressure of 2×10^{-3} torr at a signal-to-noise ratio of 30:1. At this pressure the population of the $J = 7$ state is 3.3×10^{10} states cm^{-3}, implying that their detection sensitivity was 3.3×10^9 states cm^{-3} at a signal to noise ratio of 3:1. This result is a factor of 6.5 worse than the result of Marinero *et al.*Part of the difference is due to the different oscillator strengths for the transitions used. The (8-0) band of H_2 has a band oscillator strength of 0.02523 while the (5-0) band of D_2 has a band oscillator strength of 0.01168, a factor 2.16 smaller. The remaining differences in the sensitivities can be explained by the different VUV intensities.

Meier and coworkers have published two papers in which LIF detection of H_2 was used.[26,27] In the first of these[26] the thrust of the paper was on the ionization of the $\tilde{B}$ state by a 266 nm photon. A LIF spectrum was taken as a control to prove that the excitation of $\tilde{B}$ was as expected, so that any deviations in the observed ionization signals was due to changes in ionization efficiency. Using third harmonic generation in Kr at 110 nm or in Xe at 106 nm, they generated 8×10^8 or 5×10^9 VUV photons per pulse, respectively. In the second paper[27] the collisional relaxation of vibrationally excited H_2 and D_2 molecules in various gases was followed using LIF. In these experiments they were able to produce 1×10^{10} photons per pulse at 110 nm. In neither paper did they report their detection sensitivity.

IV. H_2 DETECTION BY LIF

In this section experiments on the specific quantum state detection of H_2 using the technique of Laser Induced Fluorescence are reported. First will be a short description of the apparatus. Second will be a short description of the experimental procedure and the data analysis procedures. Third will be the results: assignments, linewidth and resolution, detection sensitivity, and rotational state distributions. The results will emphasize the utility of H_2 detection by LIF, showing its great accuracy and sensitivity.

A. Apparatus and Reagents

Most of the apparatus is described in detail elsewhere in this dissertation. A diagram of the apparatus is shown in Fig. 1. 660 nm visible laser radiation is produced in a 20 Hz Nd:YAG pumped dye laser system manufactured by Quanta Ray, models DCR-2A and PDL-2 (described in Appendix 1). 330 nm UV laser radiation is produced by second harmonic generation in the Quanta Ray WEX-1c which is equipped with an auto-locking system to facilitate wavelength scans. VUV laser radiation at 110 nm is generated by third harmonic generation in a static gas cell filled with Kr.

The dye DCM is used in the dye laser. The oscillator and preamplifier dye concentration is $\approx 5 \times 10^{-4}$ M, while that of the final amplifier is $\approx 7 \times 10^{-5}$ M, close to the concentrations recommended by the manufacturer. However, the solvent is not pure methanol as they recommend, but an approximately 50:50 mixture of methanol and dimethyl sulphoxide (DMSO). This had the desired effect of increasing the wavelength of maximum efficiency to $\approx$ 650 nm from 640 nm. More importantly from the stand-point of these experiments, the long-wavelength cutoff was raised substantially; the cutoff is 685 nm, some 15 nm above the 670 nm obtainable when pure methanol is the solvent. The major disadvantages of the solvent mixture is that the dye lifetime is seriously degraded. Quanta Ray estimate

that the dye halflife with a 10 Hz laser is greater than 300 hr; in the solvent mixture noticeable degradation of performance (10% or so) occurs in a few hours. The amplifier dye solution is noticeably bleached at the end of a day's experiments if no stock dye solution is added.

The dye laser is configured with the 2.5 ns optical delay line, a transversely pumped preamplifier, and a longitudinally pumped amplifier. Typical output powers are 81 mJ/pulse at 660 nm when pumped with 350 mJ/pulse of the Nd:YAG second harmonic at 532 nm, a conversion efficiency of 23% at a wavelength off of the lasing maximum (the dye laser "typical" conversion efficiency for this dye is 21% at the lasing maximum, according to the manufacturer). The UV pulse energy at 330 nm is 8 mJ/pulse, a conversion efficiency of only 10% which compares poorly with the "typical" conversion efficiency of 18% reported by the manufacturer. The reason for the poor performance by the WEX is unknown.

The visible output is separated from the UV output with a Schott UG-11 filter instead of the Pellin-Broca prism normally used with the WEX. It is estimated that the Pellin-Broca prism introduces a dispersion of 2.2 mrad during a scan from 328.5 to 336 nm (109.5 to 112 nm in VUV). Since the distance from the WEX to the center of the cell is approximately 1.5 m, the UV beam shifts position by 3 mm. This shift in position is greater than the laser beam radius at that point of 2–2.5 mm.

The UV radiation is focused into the third harmonic generation cell using the 100 mm Suprasil "best form" lens described in Chapter 4.

The cell for these experiments is described in Chapter 4 and is shown in Fig 2. It consists of 3 stainless steel compartments separated from each other with 2 VUV grade LiF windows (1 mm by 1 in). The first compartment holds the Kr for the third harmonic generation process. The second compartment holds the sample

for spectroscopic studies. The third compartment is a NO ionization chamber for detecting VUV photons, as discussed in detail in Chapter 4.

The design of the sample compartment underwent several revisions, principally to increase the PMT solid angle, decrease the distance from the cell entrance window to the PMT axis, decrease the scattered light, and protect the PMT and VUV filter. The first design used 5 apertures along the cell axis to reduce scattered light. These Al apertures were coated with with flat black paint and had clear apertures of 0.5 to 0.6 in. The overall length of the compartment, window-to-window, was about 5.5 in, with the central axis of the photomultiplier 2 in from the entrance window. The PMT photocathode was approximately 3.25 in from the compartment axis, giving a collection efficiency of ≈ 0.0023. The second design had similar apertures along the axis, but 3 apertures were added along the side-arm to the PMT, the overall compartment length was reduced to 5.0 in, and the photocathode was moved to 2 in from the axis, giving a threefold improvement in the collection efficiency to ≈ 0.006.

The experiments described in this section use the third design. First, there is a major increase in the number of apertures, to 3 on the entrance side, 5 on the exit side, and 3 on the PMT side-arm. Second, the apertures are no longer planar, but instead are cones with an apex angle of 60°. The clear diameter is 0.20 in for the entrance side apertures, 0.30 in for the exit side apertures, and 0.625 in for the PMT apertures. The apertures and their holders are no longer painted black but are black anodized (the only paint remaining in the cell is on the stainless steel). A LiF window is added to isolate the reaction part of the central compartment from the side-arm containing the filter and PMT, both to protect the PMT window and the VUV filter and also to reduce the chance that the fluorescence would be absorbed before the PMT. This region between the side-arm window and the PMT is kept evacuated with a mechanical vacuum pump. The overall cell dimensions

are similar to those of the second design. Figure 3 shows a closeup of the design of the central compartment.

All of the experiments described in this chapter use the solar-blind photomultiplier, model G26E314LF by EMI, described in Appendix 2. This PMT has a CsI photocathode with a MgF_2 window and is sensitive to radiaton from the MgF_2 cutoff near 115 nm to approximately 180 nm. The PMT is operated at a voltage of +3000 V, which gives a nominal gain of $\approx 10^7$.

The PMT has only a slight sensitivity to UV radiation near 330 nm. It was decided that the reduction of this background would not compensate for the loss of signal if the VUV bandpass filter were used (described in more detail in the next chapter). Consequently, the filter was not used.

The electronics used for these experiments are shown on Figure 4. Each component is described in detail in Appendix 2. The photomultiplier response is considered to be the "SIGNAL." The charge output from the photomultiplier is converted to a voltage pulse using a current-to-voltage amplifier, model A2 from EMI, and a homebuilt integrating amplifier. The overall response is 7.09 ± 0.10 mV pC^{-1} (95% confidence interval, 68 points). The output from the charge amplifier passed through a homebuilt 10× amplifier (response was 7.12× due to bandwidth limitations) and then to a dual gated integrator. The output of the dual gated integrater was digitized and the data stored by the laboratory minicomputer.

The NO ionization compartment response is considered the "LASER INTENSITY." The charge output was integrated using a homebuilt integrating amplifier similar to the one used for the PMT. The response was 20.90 ± 0.33 mV pC^{-1}. The output from this amplifier is further amplified by a Molectron model 131 amplifier/shaper before being sent to a second dual gated integrator system, the output of which is also collected by the minicomputer.

The third harmonic generation compartment is filled with research purity (99.995%) Kr from Alpha Products. The experiments in this chapter used 700 torr of Kr. The ionization compartment is filled with approximately 8 torr of 10% NO/He gas mixture prepared as discussed in Chapter 4.

In the sensitivity experiments it is important that the concentration of the H_2 be known very accurately. Because of the extreme sensitivity of the LIF technique, H_2 pressures on the order of μtorr are needed, pressures which are difficult to measure accurately. It was decided to use a gas mixture instead of pure H_2. A cylinder of 100 ± 1 ppm H_2, balance ultra high purity He (99.999%), was purchased from MG Industries. This is a "Primary Standard" gas mixture and the analysis is guaranteed to $\pm 1\%$.

B. Experimental Procedure

The experimental procedure for the H_2 LIF spectra described in this chapter is straight forward. During initialization the laser performance is optimized, the NO ionization cell is filled with approximately 8 torr of the 10% NO/He mixture, the cell is placed on the laser table and aligned wih the laser beam, and the electronics and high voltage supplies are connected and turned on. Next the electronics and VUV cell are adjusted for correct performance: the monitor output from the "INTENSITY" gated integrator is observed while the correct Kr pressure and the cell alignment are checked, the amplifier gain is adjusted, and the gate position is adjusted. Then a slight amount of H_2 is introduced into the sample cell and the dye laser is tuned to a H_2 line for performance checks of the PMT, the gate positions for the gated integrator are adjusted, and after evacuation of the cell the final tweak of cell alignment is performed to minimize scattered background. Then the scan is taken: the computer is set up, the dye laser is set to the correct starting wavelength, the sample cell is filled, and data is collected. This last set of procedures is repeated for every scan, with the dye laser performance tweaked up

after every 2 or 3 hr. After every day the cell is disassembled and the LiF windows are cleaned.

The manufacturer of the dye laser recommends that all scans be in the same direction, preferably in the decreasing wavelength direction. This provides optimum reproducibility in laser performance, especially in the WEX which is extremely sensitive to asymmetry in the dye laser profile. However, for the spectra shown in this chapter, scans were taken in both direction and then averaged together in order to reduce any systematic drifts in sample pressure. Such drift is especially noticeable if the sample cell has recently contained one of the H_2 precursors such as HI or H_2CO. Even after several days evacuation on a vacuum line with an ionization gauge reading of 4×10^{-7} torr, there is sufficient material desorbing off of the cell walls to add at least 20 μtorr of H_2 to the sample, an amount close to the amount being used for the spectra.

The scans in this section were all taken under nearly identical conditions in one afternoon. The laboratory temperature was 21.5 C. The average pressure of the H_2/He mixture was 0.255 torr, giving a H_2 partial pressure of 25.5 μtorr. Each scan was 15 nm in the dye laser fundamental (672.00 $\leftrightarrow$ 657 nm) at a rate of 0.5 nm min^{-1}. Data was taken at a density of 333 pt nm^{-1}, the maximum possible with the current stepping motor on the dye laser. The RC time constant on each gated integrator was $RC = 3 \times 10^3 \times 10^{-10} = 3 \times 10^{-7}$ s, which gives an overall time constant 0.15 s (3 laser pulses) when Eq. A2.6 is used with a gatewidth of 0.1 μs and a laser repetition period of 0.05 s. Since data was collected every 0.36 s (7.2 laser pulses), the effective time constant is 0.42 pt.

Figure 5 shows a typical raw spectrum. The only data manipulation was to convert the digital signal levels to their real values using the known gain and sensitivity factors for the electronics. Figure 6 shows the same spectrum after normalization. This 2-step process involves first subtracting the baseline from each

channel, and second dividing the PMT signal by the NO ionization cell signal to normalize for VUV power fluctuations. All further spectra shown in this chapter are normalized spectra. The computer program WAVECAL then examines the spectrum for peaks and prints out the results. Further analysis depends on the objective and is discussed in the next section.

C. Results

1. Assignments

Figure 7 is an average of 6 scans taken during a single afternnon. The spectral features are easily assigned using literature positions.[28,29] Since the sample was room temperature H_2 only $v = 0$ of the $\tilde{X}$ ground state is populated, and all transitions originate from that level. The spectrum shows two overlapping bands, the (0-0) and the (1-0) bands. By convention, the quantum number of the upper state is always given first. Table 1 gives the assignments, literature and observed line positions in vacuum wavenumbers, and the devitions in position.

The mean deviation for the 14 observed lines is -1.72 ± 0.53 cm^{-1} (95% confidence level). This deviation is much worse than usual. The most recent wavelength calibration of the PDL-2 dye laser gave a mean deviation of 0.05 ± 0.06 cm^{-1} at 660 nm, corresponding to 0.30 ± 0.36 cm^{-1} at 110 nm. The dye laser step size of 0.069 cm^{-1} in the fundamental corresponds to 0.41 cm^{-1} at the 6th harmonic in the VUV. This means that the average line position is in error by four steps of the dye laser stepping motor. The reason for the poor wavelength accuracy is not known. There also appears to be a slight systematic drift in the deviations, with the $v' = 1$/high transition energy lines having smaller then average errors while the $v' = 0$/low transition energy lines have a deviation greater than average. The differences were not enough to cause a problem and were not pursued further.

2. Linewidth and Resolution

One important performance characteristic of the VUV laser source cannot be determined without taking a spectrum, the linewidth and the resolution. A H_2 LIF spectrum provides a convienent method to measure this important parameter.

Figure 8 is an enlargement of a portion of the H_2 LIF spectrum. The lines of the P(1), R(2) doublet near 90082 cm^{-1} are only separated by 4.7 cm^{-1} and are clearly resolved to baseline. The linewidth was calculated by fitting a Gaussian to the data of the R(0) and R(1) lines at 90242 and 90201 cm^{-1}. The observed linewidth was 4.91 ± 0.18 points which equals 2.01 ± 0.07 cm^{-1}. Since the room temperature Doppler width of H_2 at this wavelength is 0.78 cm^{-1}, Eq. 6.54 can be used to estimate a VUV linewidth of 1.85 ± 0.07 cm^{-1}.

This observed linewidth is slightly larger than expected. The dye laser fundamental has a specified linewidth of 0.20 cm^{-1} at 560 nm. The 6th harmonic should have a linewidth 6× larger, *i.e.*, 1.2 cm^{-1}, a result one-third less than the observed result. There are a couple of explanations for the discrepancy. First, if there were a wavelength reproducibility error in bidirectional data scans then the linewidth in an average scan would be larger than in a single scan. This error is probably bounded by the size of a single dye laser step, *i.e.*, 0.4 cm^{-1} in the VUV. Second, the dye laser linewidth at 660 nm could be significantly larger than the 0.2 cm^{-1} at 560 nm since the linewidth is a function of the wavelength.

There is one advantage to this large a linewidth. It gives the spectral features some width. If the VUV linewidth were actually 1.20 cm^{-1}, then the observed linewidth would be 1.4 cm^{-1} which is only 3.4 data points. Spectral lines that narrow would be extremely difficult to get accurate areas from.

3. Detection Sensitivity

One of the principal reasons for developing the LIF detection technique for H_2 is to make use of its great sensitivity. It is therefore important to determine the exact sensitivity.

Figure 9 is an enlargement of another portion of Fig. 7, showing one of the lines from the weakest observed state. The (1-0) R(5) line at 90534.8 cm^{-1} is clearly seen. The $J = 5$ state has a room temperature population of only 0.0963% of the total, corresponding to 3.12×10^{13} state cm^{-3} $torr^{-1}$. Since the H_2 partial pressure is 25.5 μtorr, the actual density of the $J = 5$ state is 7.96×10^8 state cm^{-3}. The noise level as determined over an interval of 1000 points centered on the (1-0) R(5) line gave an observed S/N ratio for that line of 3.9. This implies that that the detection sensitivity at a S/N ratio of 3 is

$$\cdot 6.0 \times 10^8 \text{ state cm}^{-3}.$$

The next state is $J = 6$, which has a (1-0) R(6) line at 90101.5 cm^{-1}. The $J = 6$ state has a population of only 0.014% of the total, corresponding to 4.74×10^{12} state cm^{-3} $torr^{-1}$. At the H_2 partial pressure used for Fig. 7, this state would have a density of 1.21×10^7 state cm^{-3} which is 2% of the detection limit for a S/N ratio of 3.

The current sensitivity is much greater than that obtained by the other principal non-ionization method for detecting individual H_2 quantum states, Coherent Anti-Stokes Raman Scattering (CARS),[30] and is comparable to that obtained by other researchers using LIF. Typical sensitivities using CARS are $\approx 10^{12}$ state cm^{-3}, some three and one-half orders of magnitude poorer than the current results. This detection limit is comparable to that obtained by Marinero *et al.*[24] and a factor of 6 better than that obtained by Northrup *et al.*[25] for the same S/N ratio of 3.

Since Marinero *et al.* provided more experimental details, the current results will be compared with their results in some detail. The band oscillator strength for the (8-0) band that they used is 0.02523, while that for the (1-0) band used in the current experiments is only 0.00579, a factor of 4 lower. In addition, they claimed that their XUV laser power was on the order of 7×10^9 photons pulse^{-1}, while for the current experiments the peak signal from the NO ionization cell was 20 pC pulse^{-1} corresponding to 2.3×10^8 photon pulse^{-1}, an factor of 30 less. In the current apparatus the PMT subtends a solid angle of 0.065 sr corresponding to a collection efficiency of 0.51%, while in their apparatus the PMT subtended a solid angle of 0.029 sr, a little less than one-half as much. In summary, the current experiments have the same senstivity using one-fourth the oscillator srength, one-thirtieth the number of photons, and twice the collection efficiency, suggesting that the current apparatus has an efficiency approximately 60 times that of Marinero *et al.* In addition, the current apparatus is much simpler since it uses static gas cells and LiF windows while they used flowing systems, pulsed Ar jets, and differential pumping.

The VUV laser beam has an approximate radius of 0.76 mm and the path length as seen by the PMT is 1.6 cm. Thus, the total volume probed by the VUV laser and seen by the PMT is on the order of 0.029 cm^3, implying that the absolute detection sensitivity is

$$1.8 \times 10^7 \text{ states}$$

4. Rotational Distributions

The great sensitivity of LIF is not useful if the method does not provide accurate rotational state distributions. Consequently, the spectrum shown in Fig. 7 was analyzed in order to determine the rotational state distribution.

The area of each spectral feature in Fig. 7 is found by numerical integration using the parabolic integration formula of Bevington.[31] Unlike Simpson's rule and

other integration formulas for equally spaced points, the Bevington formula gives every point in the central region of the integral an equal weight. The beginning and end of each integral is determined from examination of the first and second derivatives calculated using the 5-pt formulas in Abramowitz and Stegun. The standard deviation of the mean area of each spectral feature is found by applying the definition of the standard deviation of the mean to the areas of the spectral features in each of the individual spectra which were averaged together to give Fig. 7. Table 2 gives the mean area and standard deviation of the mean for each of the identified transitions.

Each transition in the spectrum has a different signal strength because of differing Einstein absorption coefficients, emission distribution patterns, and average PMT quantum yields. Because the area of the spectral feature is used and not the peak intensity, the linewidth factors (which are normalized to give an integral of 1) are unimportant. In addition, the spectra have already been normalized against the VUV laser intensity. With these factors in mind, equation 6.38 can be inverted giving

$$n_{|\Lambda v J\rangle} = \mathrm{AREA}_{\Lambda v J}^{\Lambda' v' J'} \times \frac{4\pi(A^{\Lambda' v' J'} + k_5)}{\Omega Gel(B_{abs})_{\Lambda v J}^{\Lambda' v' J'} \sum_i \left(A_{\Lambda'' v'' J''}^{\Lambda' v' J'} T(\nu_i) Q(\nu_i)\right)} \qquad (6.67)$$

for the initial population of state $|\Lambda v J\rangle$.

Many of the factors in Eq. 6.67 are the same for every observed spectral feature, and therefore can be ignored when determining relative populations. The magnitude of k_5 was discussed earlier in this chapter, the conclusion being that it is unimportant under the current experimental conditions. As mentioned earlier, the VUV bandpass filter was not needed for these experiments, so $T(\nu_i)$ can be ignored. The PMT quantum efficiency as a function of wavelength is assumed to follow the functional form discussed in Appendix 2 with a MgF_2 cutoff of 112.5 nm. The

Einstein A and B_{abs} coefficients are found by substituting published theoretical band oscillator strengths[11] and Hönl-London factors[3] into Eqs. 6.7 and 6.11.

Table 2 gives the population of each rotational level as determined from Eq. 6.67. In most cases, the populations of the same level as determined from different transitions are within two standard deviations of each other. There is, however, a trend for the populations determined from $v' = 1$ transitions to exceed those determined from $v' = 0$ transitions. This observation will be discussed later.

The population of each rotational level can be divided by the rotational degeneracy $(2J + 1)$ of each level to give the population of each rotational state. If the nuclear spin degeneracy of 3 for odd J is also included, then the rotational state populations shown in the right-hand column of Table 2 are obtained. These rotational state populations should be described by a Boltzmann distribution since the sample is at thermal equilibrium. Figure 10 is a semi-logarithmic plot of state population as a function of rotational energy. The points all fall close to a straight line. The rotational temperature found by an appropriately weighted linear-least squares fit to the logarithmic transformation of the populations as a function of rotational energy is 305.8 ± 3.0 K, only 3.8% above the laboratory temperature of 294.7 K. This is very good agreement; however, the deviation is 3.7 standard deviations, which is significant at the 95% confidence level. The χ^2 for the fit was 16.4 with 12 degrees of freedom. The critical value of[33] χ^2 at the 95% confidence level for 12 degrees of freedom is 21.0; consequently, there is no expectation that the model $(\ln(\mathrm{POP}) = a + bE)$ is in error.

V. DISCUSSION

The LIF technique for detecting individual quantum states of H_2 worked quite well. The detection sensitivity at a signal-to-noise ratio of 3 is 6.0×10^8 state cm^{-3} with a probed volume of 0.029 cm^3. This is more than sufficient sensitivity to detect H_2 produced during chemical reactions.

The LIF technique also seems to be accurate. The observed rotational temperature of 305.8 ± 3.0 K in a calibration spectrum compares favorably with the actual laboratory temperature of 294.7 K.

There are, however, a couple of points which need to be addressed. First, the state populations determined from $v' = 1$ transitions are larger than those determined from $v' = 0$ transitions. In three cases the same rotational transition, P(2), R(3), and P(3), was seen in both the (1–0) and (0–0) bands. The ratios of the population determined from the (1–0) transition to that from the (0–0) transition were 1.42 ± 0.42, 1.40 ± 0.40, and 1.64 ± 0.41 for the three rotational transitions, respectively, giving an average of 1.49 ± 0.24.

There are four possible explanations for the discrepancy. First, the portion of the (1–0) band that is used for the current experiments is in the wavelength interval 109.5–110.5 nm while the (0–0) band is in the interval 110.5–111.5 nm. This allows for the possibility of a wavelength dependent systematic error mimicking a transition dependent error. One possibility for such a systematic error is if the transmission of the LiF window located between the sample compartment and the NO ionization cell changes drastically over this wavelength interval. If the window transmission at 110 nm were to be less than at 111 nm, then the recorded VUV intensity would be low and the normalized signal would be artificially high. The nominal cutoff of a LiF window is 105 nm, so it would not be unexpected if the transmission were lower at 110 than at 111 nm. Heath and Sacher[34] measured the transmission characteristics of a LiF window from the manufacturer of the current

windows. Their window had a transmission of 53% at 112 nm and 49% at 110 nm, an 8% decrease. If the current window has transmission characteristics similar to their window, then a decrease in LiF transmission with wavelength would not be sufficient to explain the observed deviations. A second wavelength dependent error would involve the response of the NO ionization cell; however, as can be seen from Figure 10 of Chapter 4, the NO response should be flat in the wavelength region being used.

A second possible explanation for the observed discrepancy is if the detection sensitivities for emitted photons were not calculated correctly, *i.e.*, if the PMT quantum efficiency as a function of wavelength is inaccurate. The PMT response is a fairly smooth function except in the vicinity of the MgF_2 cutoff. Therefore, it is not expected that there could be a major error in the calculation, unless there is a large amount of emission right at the cutoff, in which case the value chosen for the cutoff becomes important. For the analysis in this chapter, a cutoff of 112.5 nm was chosen. The detection calculated sensitivity for photons emitted from $v' = 1$ relative to those emitted from $v' = 0$ is 0.855. If this ratio were assumed to be actually 1.00,then the $v' = 1$ relative populations are being overestimated by 15%, about one-third of the actual discrepancy. However, there is no reason to expect that the actual ratio of detection sensitivities would be 1.00. The photocathode is most sensitive to wavelengths in the range 120–140 nm. The intensity peak[11,29] of the $v' = 0$ emission distribution is 133 nm, while for $v' = 1$ the intensity peaks at 120 and 148 nm. In addition, only 2% of the $v' = 0$ emission is outside of the range 115–155 nm, while 15% of the $v' = 1$ emission is outside of the same range. In any case, it would not be possible for the $v' = 1$ sensitivity to exceed the $v' = 0$ sensitivity. Therefore, errors in the calculated PMT response could account for no more than one-third of the oberved discrepancy, and probably much less.

The third possibility is that the calculated B_{abs}'s are in error. It has been assumed that the dipole matrix element connecting the two states is separable in the rotational degrees of freedom and in the vibrational and electronic degrees of freedom, allowing the B_{abs} to be determined from knowlege of the band oscillator strength and the Hönl-London factor. The theoretical band oscillator strengths neglect centrifugal distortion and nonadiabatic effects arising from electron-rotation coupling due to the perturbations between the $\tilde{B}$ and $\tilde{C}$ states.[35,36] Consequently, in some cases the product of the calculated band oscillator strength and the Hönl-London factor can be in error by large amount. For the transitions discussed in this chapter, these perturbations are not expected to be very large since the $v' = 0$ and $v' = 1$ levels of $\tilde{B}$ are 10000 cm^{-1} away from the $\tilde{C}$ state. The "effective" Hönl-London factor was determined by Ford[35] for many transitions. For excitation from $v =$ of $\tilde{X}$ to low lying v''s of $\tilde{B}$, the correction is on the order of a few percent, increasing as J increases. For the P(2), R(3), and P(3) transitions, the calculated ratios of the "effective" Hönl-London factors for $v' = 1$ to $v' = 0$ transitions were 1.00, 1.01, and 1.00. Therefore, for the transitions being considered, neglect of centrifugal distortion and nonadiabatic effects would lead to small errors in the calculated rotational distribution, but could not explain the observed dependency on vibrational state.

The fourth possibility is that the theoretical band oscillator strengths are wrong for some other reason. The ratio of $v' = 1$ to $v' = 0$ oscillator strengths is 3.43, while the experimental ratio is 2.97 ± 0.34. If the experimental oscillator strengths were used in the analysis, then the discrepancy would be even worse.

None of these four explanations can account for the entire observed dependency on vibrational state. It is expected that some combination of all three would be needed. However, given that the overall rotational temperature is so close to correct, a more comprehensive study is not needed.

The second factor that needs to be addressed is the slightly high calculated rotational temperature. Even though the temperature is only high by 11 K, this deviation is 3.7 standard deviations, a statistically significant result. The reason for this deviation is unknown. One possibility is that the H_2 in the cell was not at thermal equilibrium with the laboratory, but was slightly warmer. The divider network for the PMT dissipates 4.2 W which is sufficient to warm the PMT housing slightly; however, the divider network is at least 20 cm from the region of the sample compartment being probed and it is not possible for the this small heat source to warm the sample sufficiently to explain the deviation in rotational temeperature. It is further believed that this error is not a result of using the theoretical Hönl-London factors and not the more accurate "effective" factors of Ford. For the transitions involved in the current studies, the average of the corrections for the R-branch and for the P-branch for the same J is 1.03, independent of J. Thus, while the population calculated from a single transition could be in error by up to $\pm 7\%$ depending on J, the population calculated from both a R and a P transition would only be in error by 3%, independent of J. This would not affect a calculation of the rotational temperature.

In any case, it needs to be stressed that the technique worked very well, providing more than sufficient sensitivity and accuracy to be used in the study of chemical reactions producing H_2.

TABLE 1. Assignment of H_2 LIF Spectrum[a]

ASSIGNMENT				LINE POSITION		DEVIATION
v'	v''	J'	J''	ν_{lit}	ν_{obs}	$\Delta\nu = \nu_{obs} - \nu_{lit}$
1	0	1	2	91204.42	91203.0	-1.4
1	0	4	3	91180.70	91179.3	-1.4
1	0	2	3	90926.79	90926.5	-0.3
1	0	5	4	90895.69	90895.1	-0.6
1	0	3	4	90572.97	90571.4	-1.6
1	0	6	5	90534.84	90533.7	-1.1
0	0	1	0	90242.35	90240.9	-1.5
0	0	2	1	90201.17	90199.4	-1.8
1	0	4	5	90145.89	90143.9	-2.0
0	0	0	1	90085.05	90083.0	-2.1
0	0	3	2	90080.32	90078.1	-2.2
0	0	1	2	89888.01	89885.1	-2.9
0	0	4	3	89880.88	89878.2	-2.7
0	0	2	3	89614.17	89611.7	-2.5

a. all positions in cm^{-1}.

TABLE 2. Rotational State Distribution H_2 LIF Spectrum

TRANSITION				PEAK AREA	LEVEL POPULATION	STATE POPULATION
v'	v''	J'	J''	(arb)	(arb)	(arb)
1	0	1	2	196.2 ±48.9	10.49 ±2.61	2.098 ±0.523
1	0	4	3	194.4 ±44.7	7.275 ±1.67	0.3465 ±0.0795
1	0	2	3	159.0 ±18.4	7.933 ±0.916	0.3778 ±0.0438
1	0	5	4	8.005± 0.823	0.3087 ±0.0317	0.03430±0.00350
1	0	3	4	5.726± 0.321	0.2755 ±0.0154	0.03063±0.00171
1	0	6	5	1.764± 0.351	0.06932±0.0138	0.00210±0.00042
1	0	4	5	1.800± 0.313	0.08467±0.0147	0.00257±0.00045
0	0	1	0	142.6 ±11.1	8.942 ±0.698	8.942 ±0.698
0	0	2	1	451.9 ±54.8	42.64 ±5.17	4.738 ±0.575
0	0	0	1	197.3 ±25.3	37.06 ±4.75	4.118 ±0.528
0	0	3	2	63.92 ± 8.65	6.732 ±0.911	1.347 ±0.183
0	0	1	2	47.16 ± 7.79	7.393 ±1.221	1.479 ±0.244
0	0	4	3	46.85 ± 8.09	5.214 ±0.900	0.2483 ±0.0429
0	0	2	3	32.97 ± 7.29	4.839 ±1.070	0.2304 ±0.0509

REFERENCES

1. J. L. Kinsey, *Ann. Rev. Phys. Chem.* **28**, 349 (1977).
2. I. N. Levine, *Molecular Spectroscopy*, (John Wiley, NY, 1975) p. 307.
3. A. Schadee, *J. Quant. Spectrosc. Radiat. Transfer* **7**, 169 (1967).
4. H. Hönl and F. London, *Z. Physik* **33**, 803 (1925).
5. A. Schadee, *Bull. Astr. Inst. Neth.* **17**, 311 (1964).
6. E. E. Whiting, A. Schadee, J. B. Tatum, J. T. Hougen, and R. W. Nichols, *J. Mol. Spectrosc.* **80**, 249 (1980).
7. A. Yariv, *Quantum Electronics, 2nd ed.*, (John Wiley, NY, 1975).
8. C. H. Greene and R. N. Zare, *J. Chem. Phys.* **78**, 6741 (1983).
9. W. Budde, *Optical Radiation Measurements, Volume 4: Physical Detectors of Optical Radiation*, (Academic Press, NY, 1983) p. 199.
10. See discussion in Chapter 5 of this dissertation.
11. A. C. Allison and A. Dalgarno, *Atom. Dat.* **1**, 289 (1970).
12. A. Dalgarno and T. .L Stephens, *Astrophys. J.* **160**, L107 (1970).
13. R. Birge, *Ultrasensitive Laser Spectroscopy, Chapter 2*, D. S. Kliger,ed. (Academic Press, NY, 1983).
14. K. P. Huber and G. Herzberg, *Molecular Spectra and Molecular Structure: IV. Constants of Diatomic Molecules*, (Van Nostrand Reinhold, NY, 1979).
15. J. Berkowitz, *Photoabsorption, Photoionization, and Photoelectron Spectroscopy*, (Academic Press, NY, 1979).
16. W. Meier, H. Rottke, H. Zacharias, and K. H. Welge, *J. Chem. Phys.* **83**, 4360 (1985).
17. H. Rudolph, D. L. Lynch, S. N. Dixit, and V. Mckoy, *J. Chem. Phys.* **84**, 6657 (1986).
18. H. Rudolph, personal communication.
19. See discussion in Chapter 3.

20. B. P. Bemand and M. A. A. Clyne, *Chem Soc. Far. Trans. II* **69**, 1643 (1973).

21. R. N. Zare, *Mol. Photochem.* **4**, 1 (1972).

22. W. Heitler, *Quantum Theory of Radiation, 3rd ed.*, (Dover, NY, 1984) p.187.

23. L. S. Gradshteyn and I. M. Ryzhik *Table of Integrals, Series, and Products, 4th ed.*, (Academic press, NY, 1980) p.306.

24. E. E. Marinero, C. T. Rettner, R. N. Zare, and A. H. Kung, *Chem. Phys. Lett.* **95**, 486 (1983).

25. F. J. Northrup, J. C. Polanyi, S. C. Wallace, and J. M. Williamson, *Chem. Phys. Lett.* **105**, 34 (1984).

26. W. Meier, H. Rottke, H. Zacharias, and K. H. Welge, *J. Chem. Phys.* **83**, 4360 (1985).

27. W. Meier, G. Ahlers, and H. Zacharias, *J. Chem. Phys.* **85**, 2599 (1986).

28. P. G. Wilkinson, *Can. J. Phys.* **46**, 1225 (1968).

29. I. Dabrowski, *Can. J. Phys.* **62**, 1639 (1984).

30. D. Debarre, M. Lefebure, M. Péalat, J.-P. E. Taran, D. J. Bamford, and C. B. Moore, *J. Chem. Phys.* **83**, 4476 (1985).

31. P. R. Bevington, *Data Reduction and Error Analysis for the Physical Sciences*, (McGraw-Hill, NY, 1969) p.271.

32. M. Abramowitz and I. E. Stegun,ed. *Handbook of Mathematical Functions*, (National Bureau of Standards, Washington,D.C., 1972) p.914.

33. F. J. Rohlf and R. R. Sokal, *Statistical Tables, 2nd ed.*, (W. H. Freeman, San Francisco, 1969).

34. D. F. Heath and P. A. Sacher, *Appl. Opt.* **5**, 937 (1966).

35. A. L. Ford, *J. Mol. Spectrosc.* **53**, 364 (1974).

36. H. Abgrall, F. Launay, E. Roueff, and J.-Y. Roncin, *J. Chem. Phys.* **87**, 2036 (1987).

FIGURE CAPTIONS

Figure 1. Scale drawing of the apparatus used to take the laser induced fluorescence spectra of this chapter.

Figure 2. Scale drawing of the cell used for the experiments in this chapter. The cell is constructed of stainless steel with black anodized aluminum apertures. Compartment 1 is the VUV generation compartment which is filled with Kr to a pressure of $\approx$ 700 torr. Compartment 2 is the sample compartment. Compartment 3 is an ionization chamber used to detect VUV radiation. It is normally filled 8 torr of a 10% NO/He mixture. The identity of the windows separating the compartments is shown below each window. There is an additional LiF window on the side arm of the "T" containing the PMT. The location of the 100 mm Suprasil focusing lens and the edge of the laser beam are shown.

Figure 3. Enlargement of Figure 2 showing details of the sample compartment, showing the location of apertures, the LiF windows, and the PMT.

Figure 4. Electronics for the experiments in this chapter. The operation of the equipment is described in Appendix 2. The solid lines represent analog signals, the $-\cdot-$ represent control lines carrying pulses and gates between components, and the $\cdots$ represent the digital data bus controlling the dye laser.

Figure 5. Raw LIF spectrum of H_2 as a function of laser wavelength. The top spectrum shows the output of the NO ionization cell, which is proportional to the number of VUV photons in each laser pulse. The dips in power near 329, 330, and 333 nm are discussed in Chapter 4. The bottom spectrum shows the signal from the photomultiplier. The sample pressure is 25.6 μtorr of H_2 in 0.256 torr of He.

Figure 6. Normalized LIF spectrum of H_2 as a function of dye laser UV wavelength. This is the same data as used for Fig. 5. The PMT signal has been divided by the NO ionization cell signal after the background was subtracted off. The extreme noise near 328.5 nm and the spike near 333.15 nm are the result of zero VUV power at those wavelengths.

Figure 7. Average of 6 normalized H_2 LIF spectra as a function of vacuum wavelength. The extreme noise near 109.5 nm and the spike near 111.08 nm are the result of zero VUV power at those wavelengths. All of the observed spectral features are assigned in Table 1.

Figure 8. Closeup of Fig. 7 showing the P(1) and R(2) lines of the 0–0 band of H_2 at 90085.05 and 90080.32 cm^{-1}, respectively. This spectrum clearly shows that these two lines are resolved to baseline. The observed linewidth is 2.01 cm^{-1}.

Figure 9. Closeup of Fig. 7 showing the P(3) and R(5) lines of the 1–0 band of H_2 at 90572.97 and 90534.84 cm^{-1}, respectively. The $J = 5$ state has a room temperature population of 3.12×10^{13} state cm^{-3} $torr^{-1}$. With a sample pressure of 25.5 μtorr, the detection sensitivity from this spectrum is better than 7.96×10^{8} state cm^{-3}

Figure 10. Semilogarithmic plot of the state populations in arbitrary units as a function of rotational energy. The line determined from a weighted least-squares fit has a slope corresponding to a rotational temperature of 305.8 ± 3.0 K.

FIGURE 1.

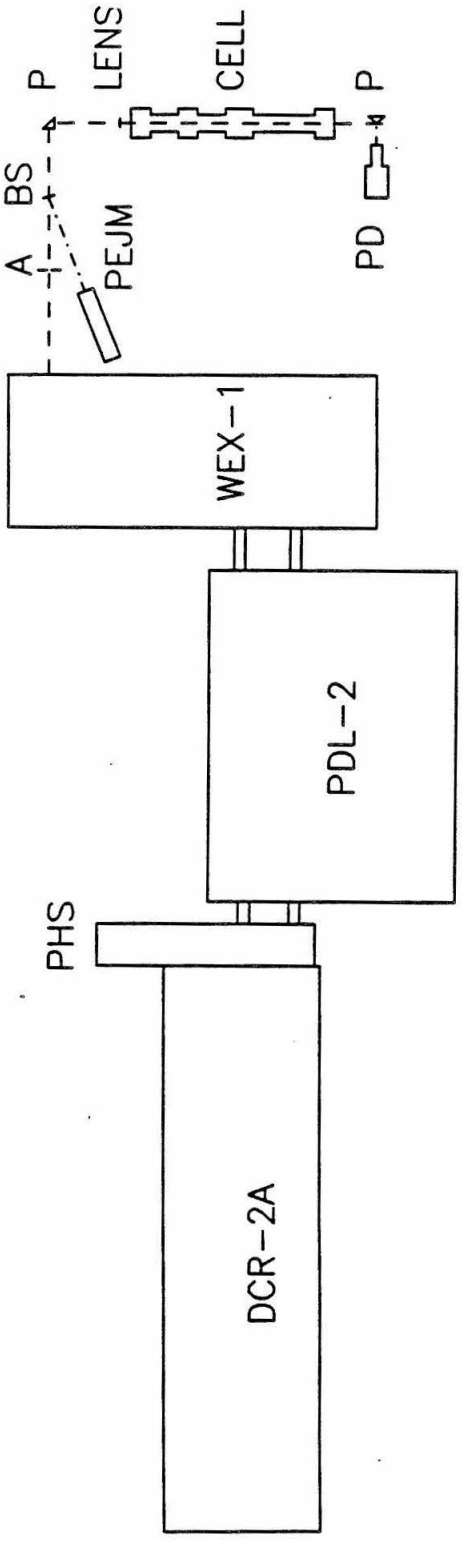

FIGURE 2.

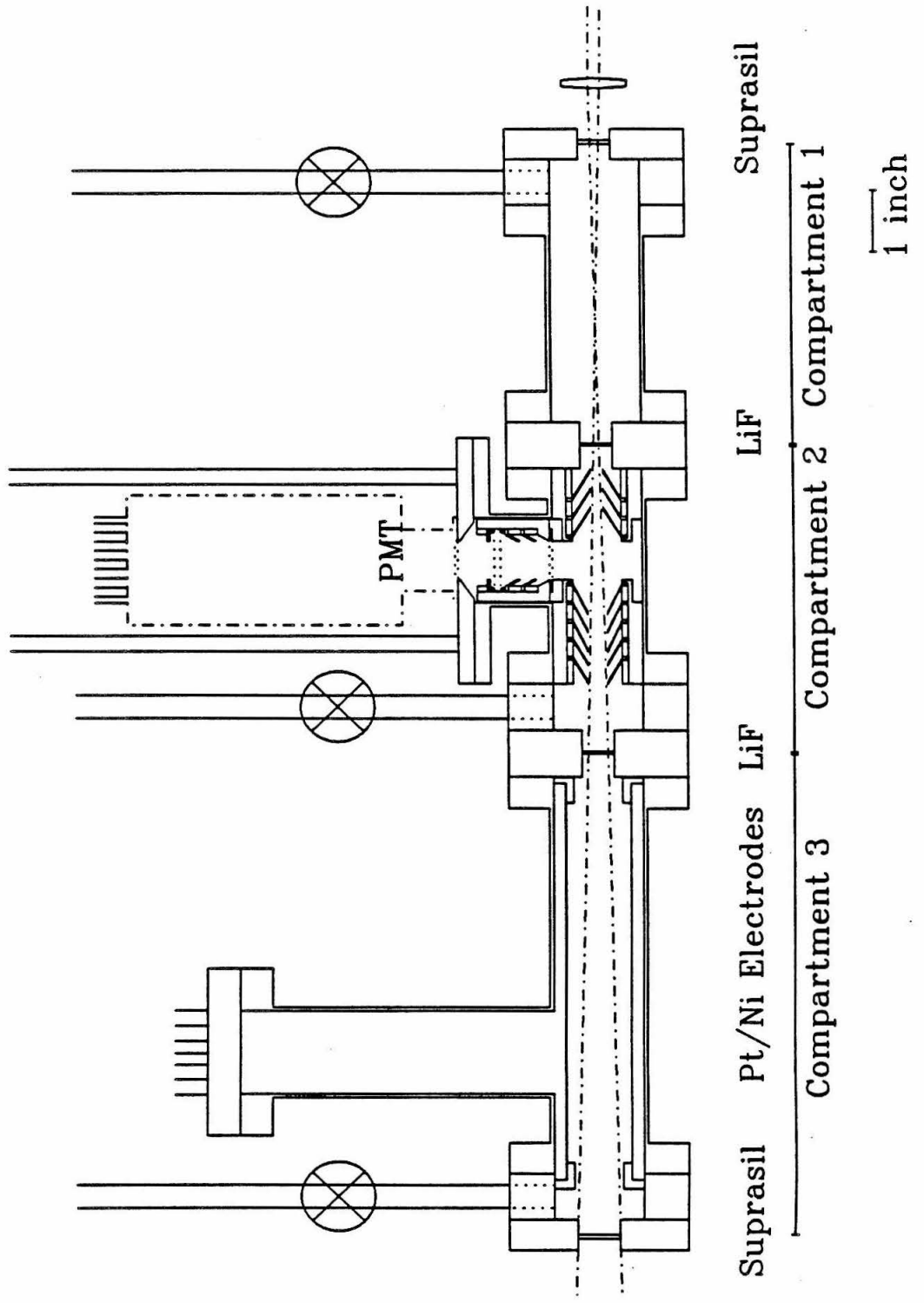
PMT
Suprasil
LiF
Compartment 1
Compartment 2
Pt/Ni Electrodes
LiF
Compartment 3
Suprasil
1 inch

FIGURE 3.

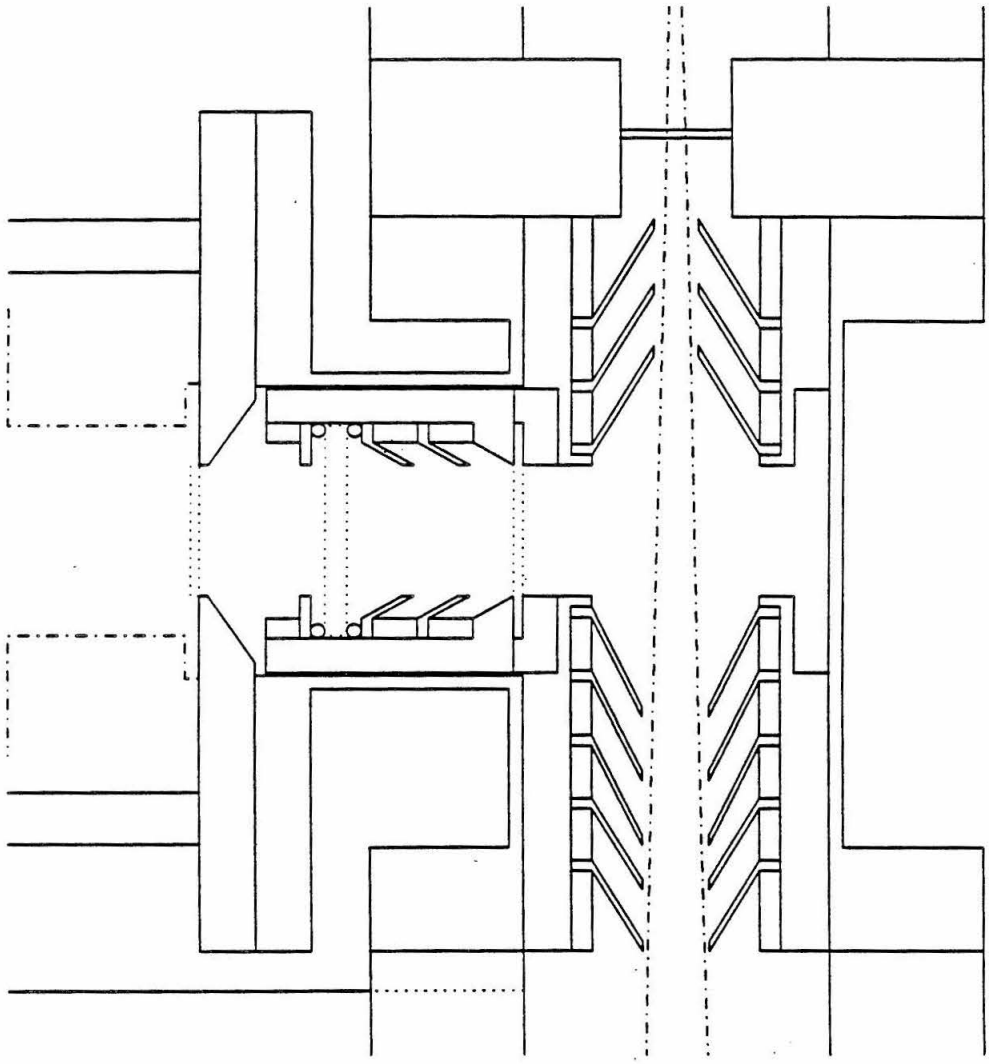

FIGURE 4.

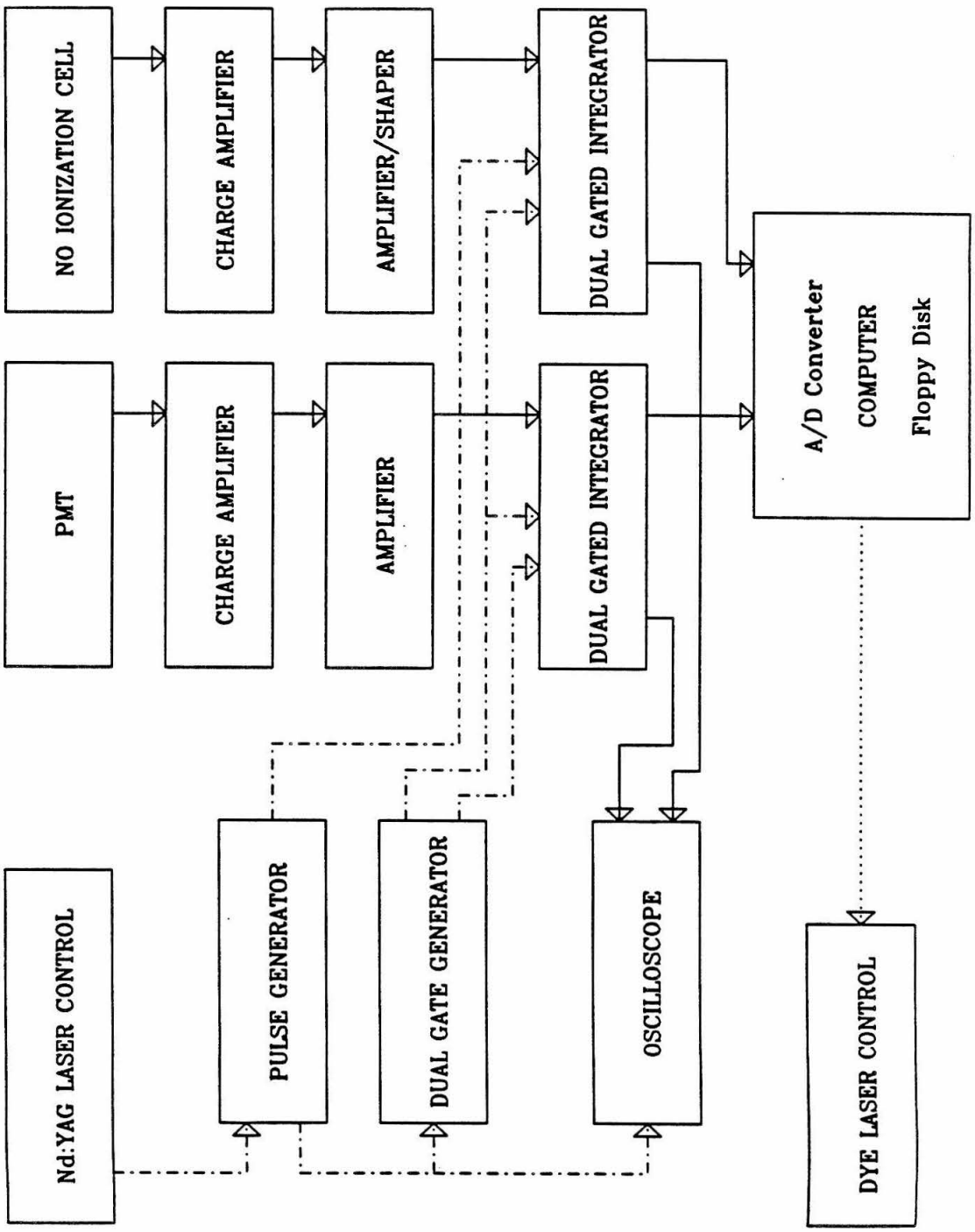
NO IONIZATION CELL
CHARGE AMPLIFIER
AMPLIFIER/SHAPER
DUAL GATED INTEGRATOR
PMT
CHARGE AMPLIFIER
AMPLIFIER
DUAL GATED INTEGRATOR
A/D Converter
COMPUTER
Floppy Disk
Nd:YAG LASER CONTROL
PULSE GENERATOR
DUAL GATE GENERATOR
OSCILLOSCOPE
DYE LASER CONTROL

FIGURE 5.

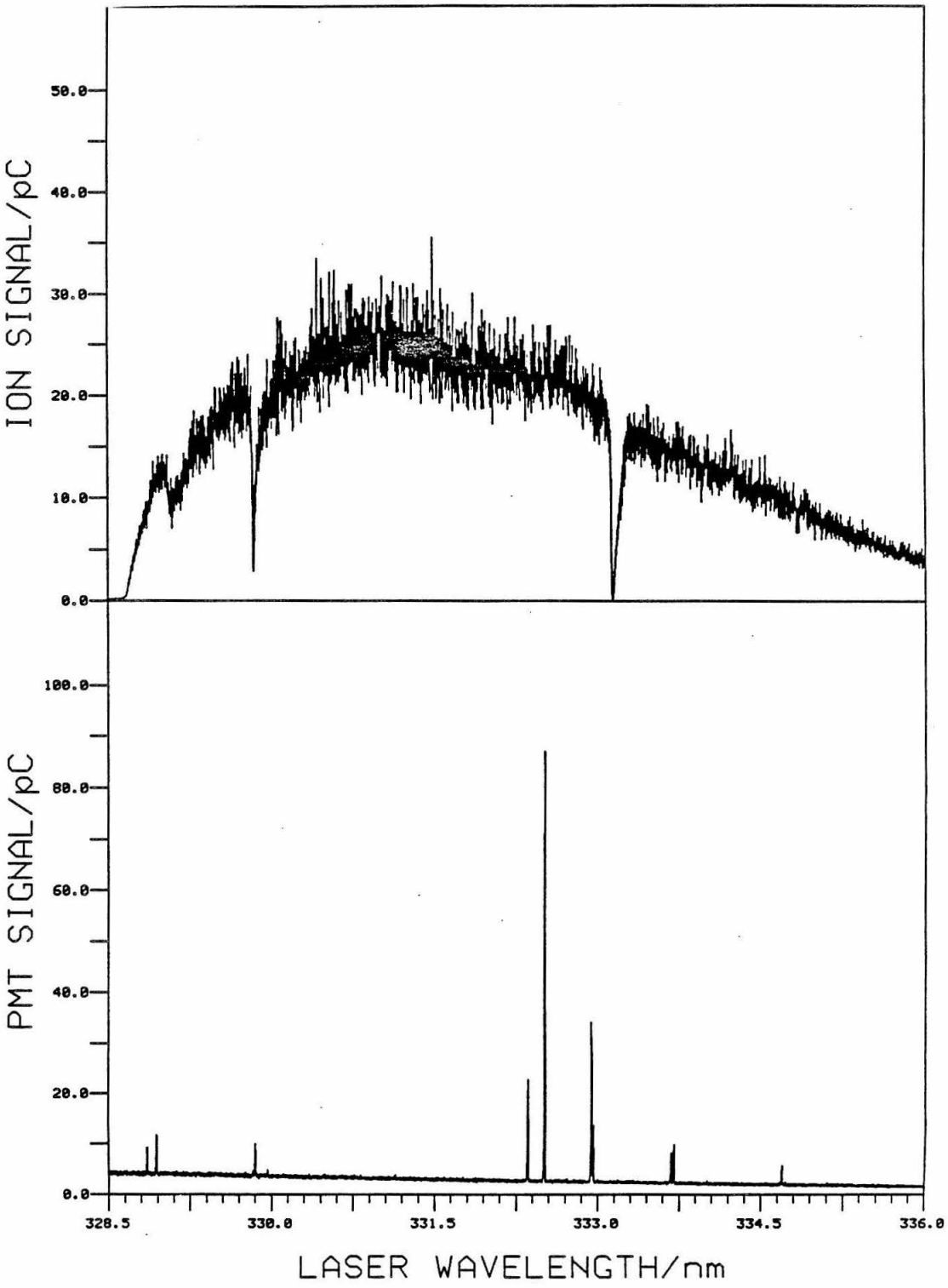
ION SIGNAL/pC
50.0
40.0
30.0
20.0
10.0
0.0
PMT SIGNAL/pC
100.0
80.0
60.0
40.0
20.0
0.0
328.5
330.0
331.5
333.0
334.5
336.0
LASER WAVELENGTH/nm

FIGURE 6.

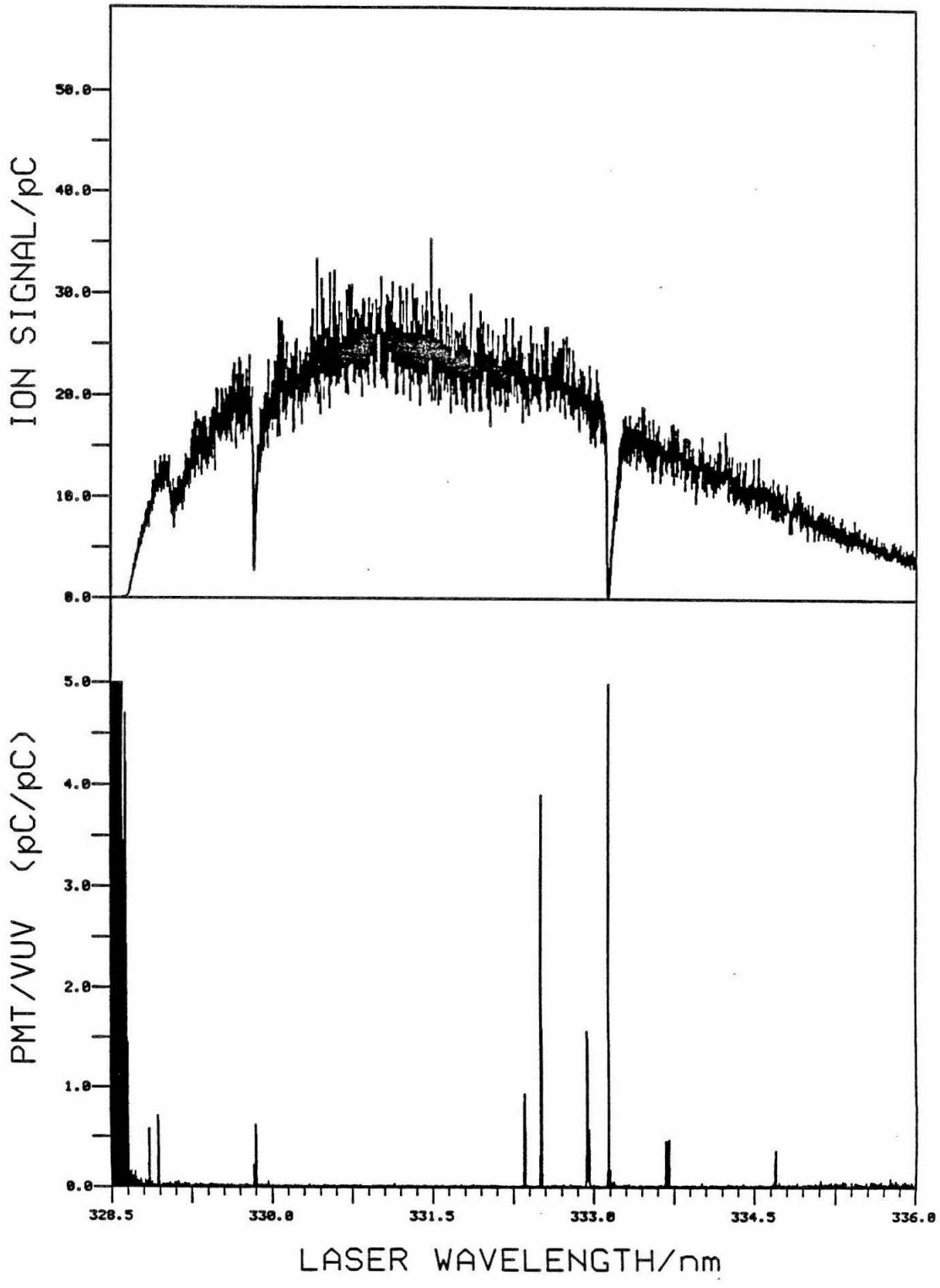
ION SIGNAL/pC
50.0
40.0
30.0
20.0
10.0
0.0
PMT/VUV (pC/pC)
5.0
4.0
3.0
2.0
1.0
0.0
328.5
330.0
331.5
333.0
334.5
336.0
LASER WAVELENGTH/nm

FIGURE 7.

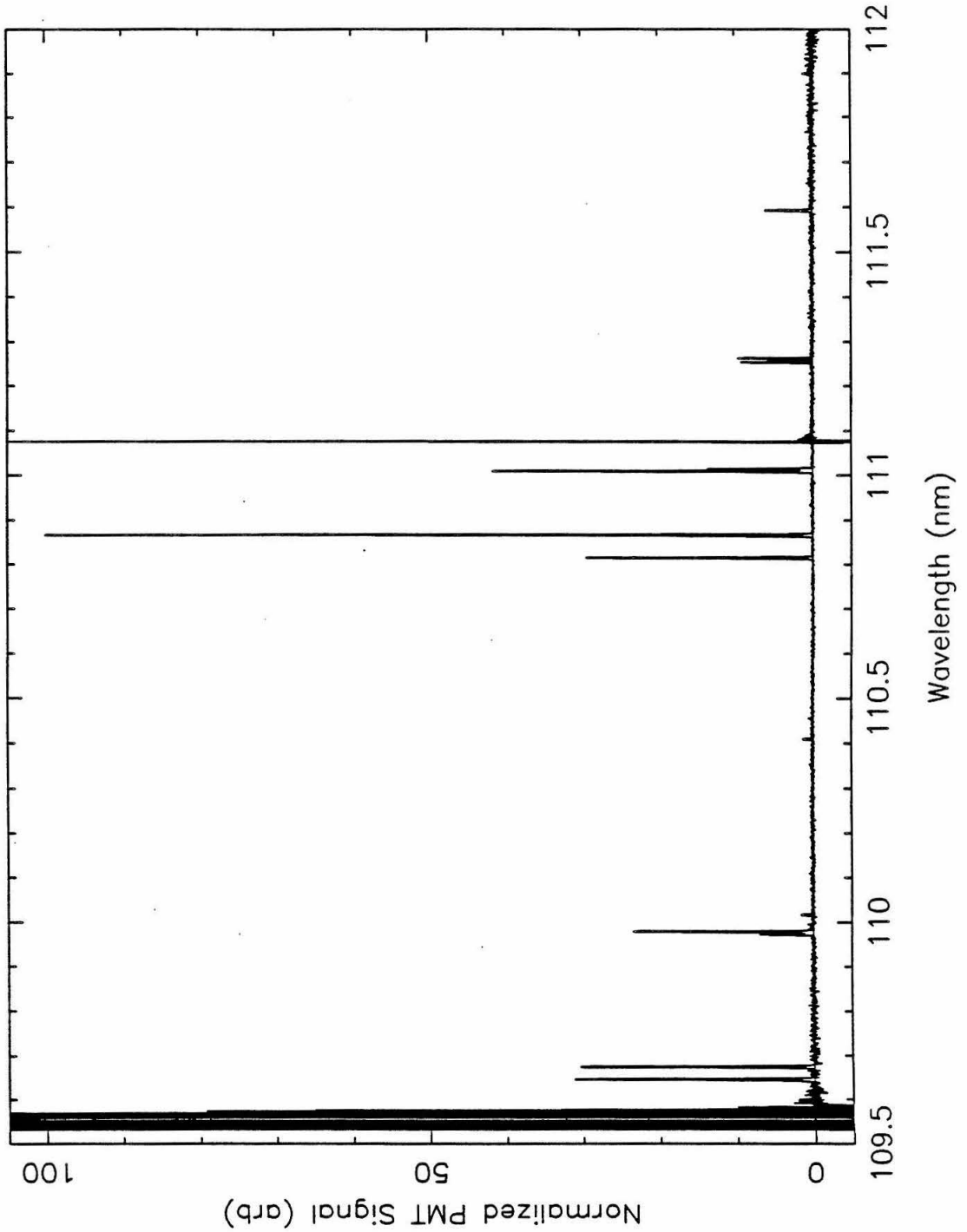
Normalized PMT Signal (arb)
0
50
100
109.5
110
110.5
111
111.5
112
Wavelength (nm)

FIGURE 8.

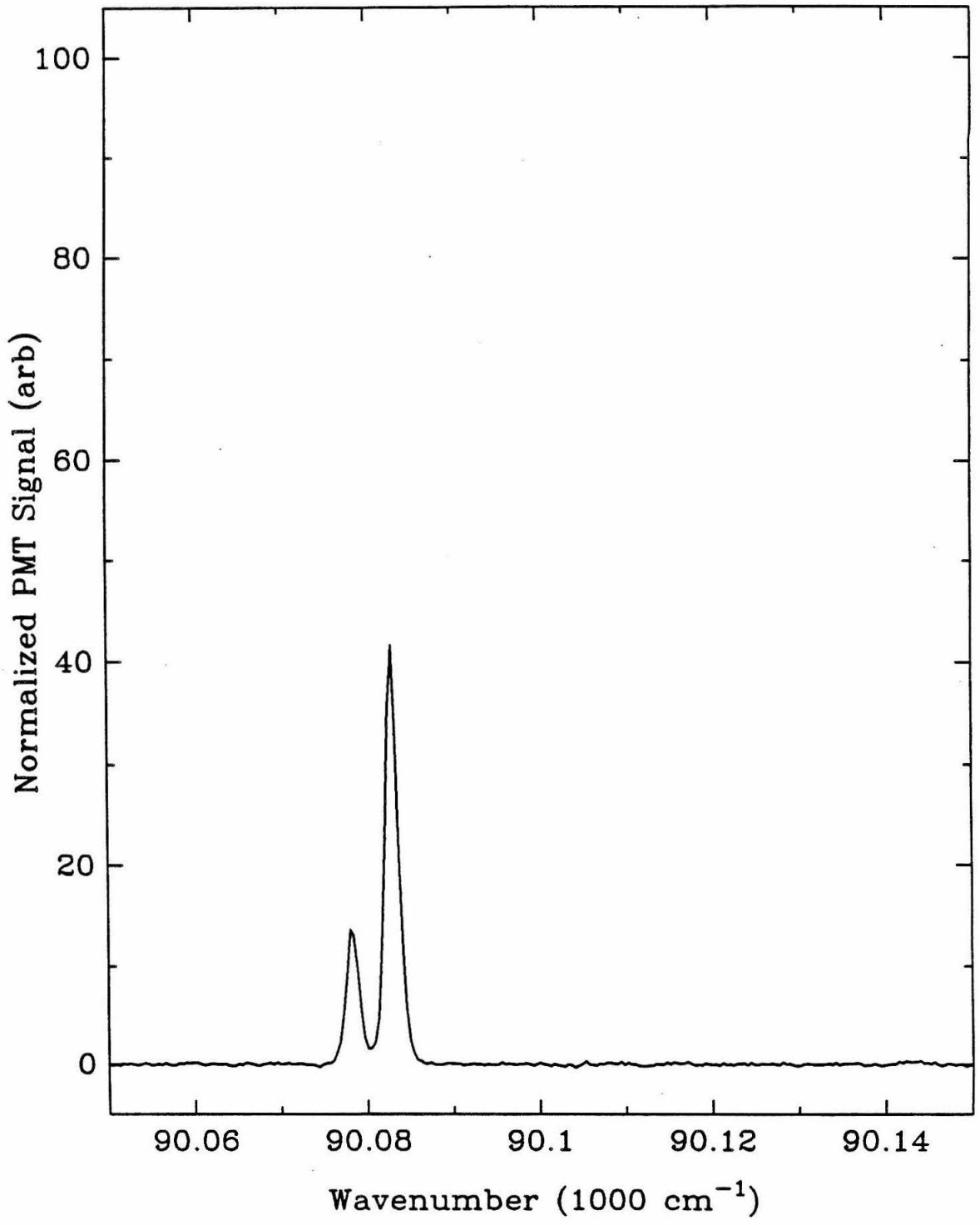
100
80
60
40
20
0
Normalized PMT Signal (arb)
90.06
90.08
90.1
90.12
90.14
Wavenumber (1000 cm^{-1})

FIGURE 9.

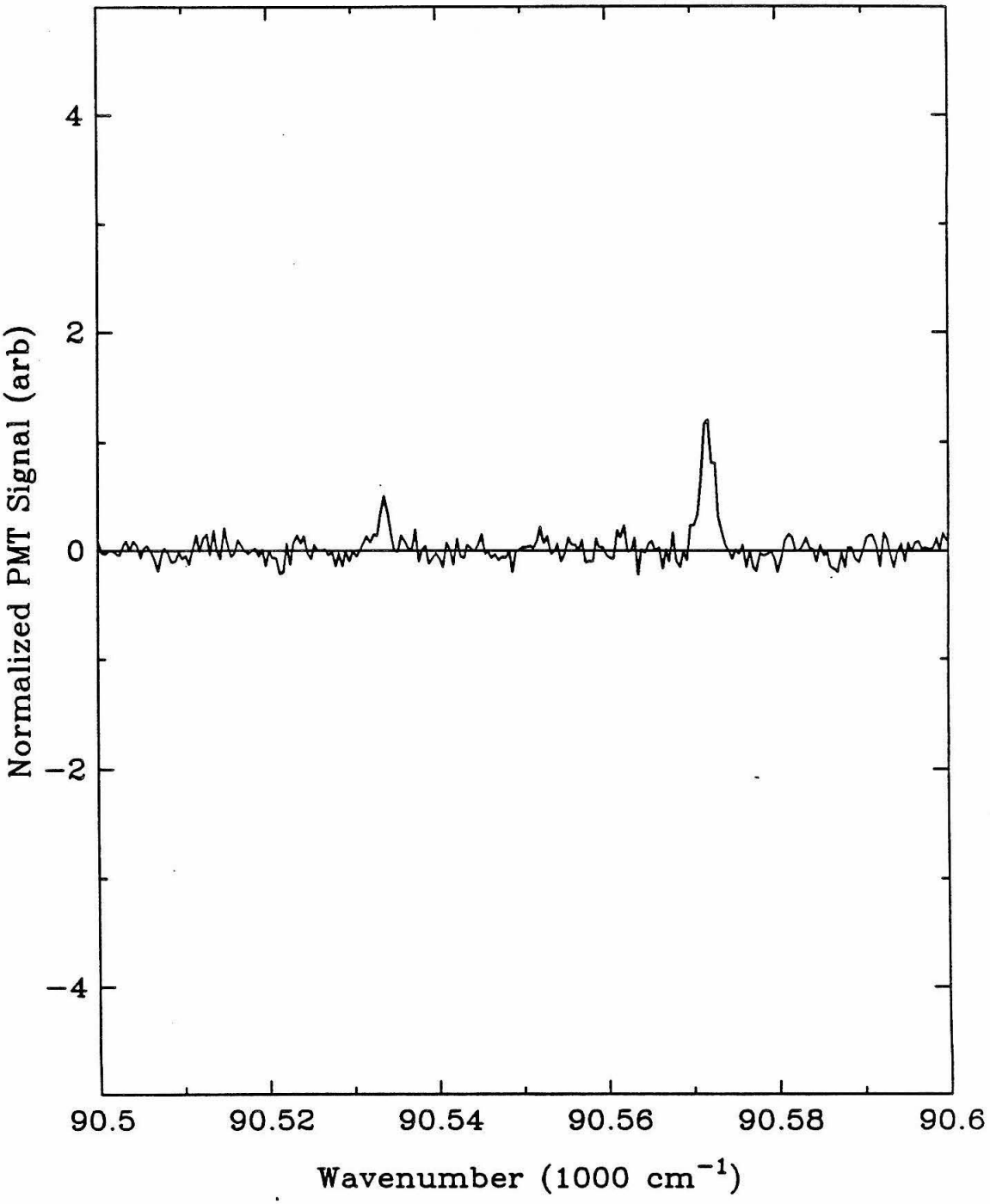
4
2
0
−2
−4
Normalized PMT Signal (arb)
90.5
90.52
90.54
90.56
90.58
90.6
Wavenumber (1000 cm^{-1})

FIGURE 10.

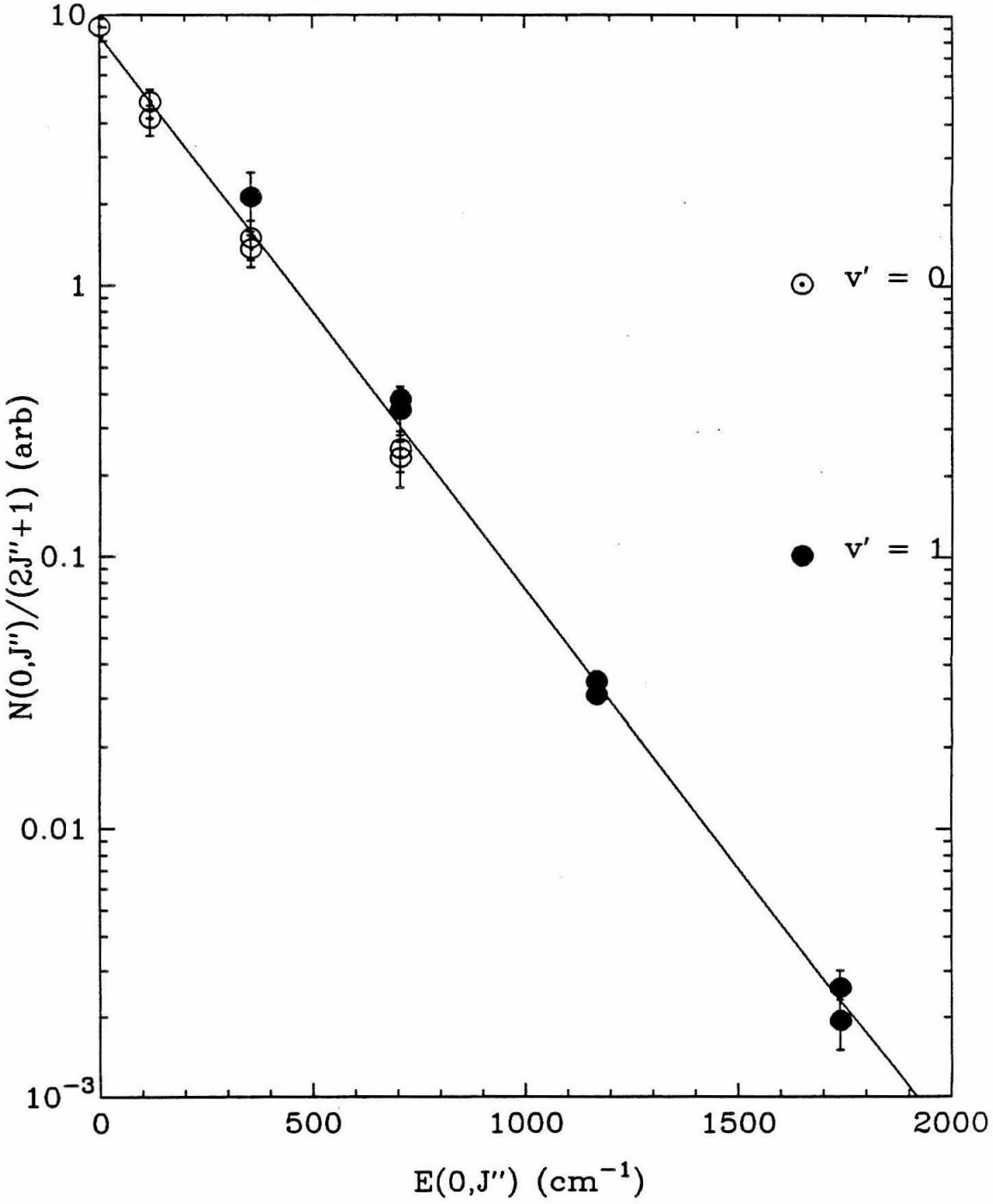

CHAPTER 7

FORMALDEHYDE PHOTODISSOCIATION EXPERIMENTS

I. INTRODUCTION

In this chapter the formaldehyde photodissociation experiments are discussed. The first section describes details of the experiments, specifically, the apparatus, the photodissociation wavelength, the time delay between the lasers, the sample handling procedures, and the experimental procedure. The second section describes the data analysis procedures that were followed. The third section presents the results of these experiments, including H_2 velocity and rotational distributions. These results are then compared with previous work in the field.

II. EXPERIMENTAL DETAILS

A. Apparatus

A scale drawing of the experimental apparatus is shown in Figure 1. In summary, the UV output of the Molectron dye laser system (described in Appendix 1) is used to initiate the H_2CO photodissociation reaction while the UV output of the Quanta Ray dye laser system (described in Appendix 1) is used to generate tunable VUV laser radiation which is used to detect nascent H_2 by LIF.

The Quanta Ray dye laser is configured in the exact same manner as for the H_2 LIF experiments described in the previous chapter. The Molectron dye laser is configured with a transversely pumped preamplifier and a longitudinally pumped amplifier. This laser also used the dye DCM in Methanol/DMSO. Typical output powers are 64.6 mJ pulse^{-1} at 658 nm when pumped with 300 mJ pulse^{-1} of the Nd:YAG second harmonic at 532 nm, a conversion efficiency of 21.5%. The UV pulse energy at 329 nm is 7.36 mJ pulse^{-1}, a conversion efficiency of only 11.4%.

The Molectron DL-18 dye laser operates at a fixed wavelength, the second harmonic of which corresponds to the peak of the desired H_2CO transition. The UV output radiation is separated from the visible incident radiation by a Pellin-Broca prism. The prism is oriented such that reflective losses were minimized for the UV radiation. This radiation then enters the reaction cell through the NO ionization compartment, passes through the sample compartment containing H_2CO, and then exits the cell through the Kr VUV generation compartment. Burn pattterns show that the beam diameter in the center of the sample compartment is 3.0 mm.

The Quanta Ray PDL-2A dye laser operates at tunable wavelengths, the second harmonics of which are then converted to VUV radiation by third harmonic generation. The UV radiation is separated from the visible radiation by a Schott

UG-11 glass filter. This ultraviolet-transmitting, visible blocking filter has a specified minimum transmission at 334 nm of 84%. After passing through a right angle prism, the UV radiation is focused into the Kr VUV generation compartment by a 100 mm Suprasil lens. The resulting VUV radiation and the remaining UV radiation pass through the sample compartment and enter the NO ionization compartment where the VUV radiation is detected by the ionization of the NO (see Chapter 4). Burn patterns show that that the UV beam diameter in the center of the sample compartment is approximately 4.5 mm. The VUV beam is expected to have one third the diameter of the UV beam; consequently, the VUV beam diameter is expected to be $\approx$ 1.5 mm, one-half of the photolysis laser beam diameter.

The two laser beams are collinear and counterpropagating. The alignment is such that the UV radiation from each laser system reaches the amplifier dye cell of the other dye laser. However, the presence of a 100 mm lens in the system means that both laser beams are divergent and large (greater than 30 mm in diameter) when then they get into the other system.

The electronics used for these experiments are shown in Figure 2. Each component is described in Appendix 2. The Laser Timing Controller is used to control the two Nd:YAG lasers, triggering both the flashlamps and the Q-switches at the correct repetition rate and at the correct time. Jitter between the two laser pulses was less than 1 ns. The data collection electronics are the same as used for the H_2 LIF experiments of the previous chapter.

The data in this chapter were all taken with the gated integrator on the PMT channel operating in the "auto-subtract" mode. In this mode the order of the gates to the gated integrator are toggled after every pulse from the Quanta Ray laser; consequently, the signal present when only one laser fires is subtracted from

the signal present when both lasers fire, greatly reducing the effects of background signals.

The sample cell is the same one used for the H_2 LIF experiments in the previous chapter and is thoroughly described there. The PMT is also the same. The PMT response to scattered 330 nm radiation is sufficiently small that there was no need for any additional filtering.

B. Photodissociation Wavelength

It was decided to photolyze H_2CO on the ${}^rR_3$ and ${}^rR_4$ bandheads of the $2_0^1 4_0^3$ vibronic band of the ${}^1A_2 \leftarrow {}^1A_1$ electronic transition. This vibronic band has 2 additional quanta in ν_4 compared with the $2_0^1 4_0^1$ vibronic band used for the other product state distribution experiments.[1-3] Both states have the exact same vibronic symmetry. The additional vibronic energy in the current experiments allows the radical dissociation process to compete with the molecular dissociation process (see Chapter 2). The rotational lines were chosen because they were reasonably intense and well resolved. In addition, these two subbands have more angular momentum and include both even and odd K_a'''s whereas the previous work only used states with $K_a'' = 1$.

The Molectron DL-18 dye laser diffraction grating counter is calibrated by taking optogalvanic spectra of a Ur/Ne hollow cathode lamp.[4] The final grating error was -0.10 ± 0.12 counter units, which is equivalent to $0.0025 \pm 0.0.0030$ nm or 0.06 ± 0.07 cm^{-1}. For the ${}^rR_3$ experiments, the dye laser diffraction grating counter was 26318.5 ± 0.2 counter units, giving $\lambda = 657.963 \pm 0.005$ nm and $\nu_{vac} = 30388.5 \pm 0.1$ cm^{-1}. For the ${}^rR_4$ experiments, the dye laser diffraction grating counter was 26311.4 ± 0.2 counter units, giving $\lambda = 657.785 \pm 0.005$ nm and $\nu_{vac} = 30396.7 \pm 0.1$ cm^{-1}.

Tables 1 and 2 show all known H_2CO transitions within ± 2 cm^{-1} of the ${}^rR_3$ or ${}^rR_4$ photolysis energies, respectively.[5,6] Because perturbations often exceed 2 cm^{-1},

these lists include only experimentally observed transitions. From analysis of the information in Table 1, one finds that 87.6% of the absorption intensity within 2 cm^{-1} of the photolysis energy is a result of $^rR_3$ transitions, 9.2% of the intensity is a result of odd $K_a'' \neq 3$ transitions, and only 3.1% of the intensity is a result of even K_a'' transitions. A similar analysis of the Table 2 data shows that only 73.7% of the absorption intensity is the result of $^rR_4$ transitions, 3.1% is the result of even $K_a'' \neq 4$ transitions, and 23.2% of the intensity is the result of odd K_a'' transitions. The ratio of the $^rR_4$ absorption intensity to the $^rR_3$ absorption intensity is 22.9%. This implies that the signal from the $^rR_4$ experiment will be one-fourth of that from the $^rR_3$ experiment.

C. Time Delay

In order to measure the time delay between the two laser beams, the apex of a right angle prism can be inserted into the edge of both laser beams, sending a small fraction of the light onto a HP 5082-4220 photodiode. When reversed biased with −18 V, this diode has a specified risetime less than 1 ns. The output of the photodiode is observed on a Tektronix 2465 300 MHz oscilloscope with a 1.2 ns risetime. During an actual experimental scan, the prism is lowered out of the laser beam path.

The relative time delay between the two laser pulses is adjusted using the *Q-Switch Timing* potentiometer on the Laser Timing Controller (see description in Appendix 2).

The average time delay $\Delta t = t_{\text{probe}} - t_{\text{pump}}$ at the photodiode is 20.8 ns for the experiments in this section. The photodiode is 10 cm from the apex of the prism, and the apex of the prism is 35 cm from the center of the PMT on the NO ionization compartment side. Consequently, the pump laser beam arrives at the photodiode 25 cm/c = 0.83 ns before it reaches the PMT, while the probe

laser beam arrives 45 cm/c = 1.50 ns after it passes the PMT. Therefore, the total correction is 2.3 ns and the actual time delay at the PMT is 18.5 ns.

D. Sample

The H_2CO for these experiments was prepared by the thermal depolymerization of paraformaldehyde from J. T. Baker. Several grams were placed in an evacuated 1 l glass bulb which was heated to 80 C overnight. This material was used without further purification to fill the sample compartment just before each scan.

In order to maintain H_2CO partial pressure during the scans as it was being consumed, a glass vial containing a small amount of paraformaldehyde was placed in a stainless steel side arm off the side of the sample compartment. This side arm was wrapped with heating tape and was warmed to approximately 45–50 C.

At the end of positive direction scans the VUV intensity was measured before and after the sample was pumped off. This allows for an estimation of the H_2CO partial pressure using Beer's law, the absorbance, the cell path length of 12 cm, and the H_2CO absorption cross section of 15.2 Mb at 110 nm.[7]

Experiments were tried with initial H_2CO pressures of 0.2–0.4 torr. Most of the spectra reported in this chapter were taken at an initial pressure of 0.3 ± 0.01 torr. Final pressures were usually in the range of 0.6–0.7 torr, representing the buildup in pressure due to the evolution of H_2CO from the side arm and the decomposition of H_2CO by the UV laser beams. The final H_2CO partial pressurres as calculated from the absorbance were usually 0.3 ± 0.03 torr.

E. Experimental Procedure

The experimental procedure for these experiments is straightforward. The performance of both dye lasers is optimized and the timing is adjusted with the LASER TIMING CONTROLLER. The alignment of the UV laser beams is adjusted until the counterpropagating collinear beams are centered on each other

to a tolerance of 0.25 mm as seen by a burn pattern taken at the PMT location. The NO ionization cell is filled with approximately 8 mtorr of the 10% NO/He mixture. At this time the cell is placed on the laser table and aligned with respect to both laser beams. Next the the Kr cell is filled with the correct Kr pressure. The electronics are adjusted for correct performance and the gates for the gated integrators are set for the correct time delay relative to the SYNC from the LASER TIMING CONTROLLER. While this is going on, the paraformaldehyde sample in the glass vial is introduced into the side arm and warmed up. All is now ready for the taking of data. The computer is set up, the Quanta Ray dye laser is set to the correct starting wavelength, the sample compartment is filled with H_2CO, the scan is started and the computer collects the data. This last set of procedures is repeated for every scan, with the dye laser performance tweaked up after every 4 scans. At the end of the day the sample cell is disassembled and the LiF windows are cleaned.

Data was collected under similar circumstances as for the previously described H_2 LIF experiments; the only change involves using the "auto subtract" mode for the gated integrator on the PMT signal channel. Each scan is 15 nm in the dye laser fundamental (672 $\leftrightarrow$ 657 nm) at a rate of 0.5 nm min^{-1}. Data is taken at a density of 333 pt nm^{-1}, the maximum possible for the Quanta Ray dye laser. The gated integrator time constant is 0.3 s.

III. DATA ANALYSIS PROCEDURES

Because of the extremely poor signal-to-noise ratio of the raw data, numerous spectra were taken for signal averaging purposes. This section describes the data analysis procedures that were followed for both photolysis wavelengths.

The signals from both the PMT and the NO ionization cell contained appreciable background components. This background arises from several sources. The ionization cell generally has a small response at wavelengths where no VUV is present due to the photoelectric effect and multiphoton ionization. The PMT signal has two sources of background. First, the output of the gated integrator has a slight positive bias voltage. This way, any small negative going noise peaks would not be clipped by the A/D converter on the computer which can only measure positive voltages. Second, the PMT has a slight response to the incident UV radiation from both lasers.

The background in the NO ionization cell signal is assumed to be wavelength independent. The average signal level for the 50 points nearest the 657 nm (109.5 nm in the VUV) end of the scan is subtracted from all the data.

The background in the PMT signal is not assumed to wavelength independent. Instead, a fifth-order polynomial is fit to the data. Points whose deviation from the fit are significant are excluded from a new fit. This process is repeated until convergence is obtained and the number of points remaining is constant. The last fit is then subtracted from the data set. This process always gave fits which were visually correct.

After both channels had been corrected for background, the PMT signal was normalized by dividing it by the NO ionization chamber signal. Figure 3 is a typical "raw" spectrum while Figure 4 shows the same scan after normalization.

The numerous spectra taken for each photolysis wavelength did not always have identical response levels. This is a result of several factors. First, the computer

system did not allow for the simultaneous collection of the UV photolysis pulse energy; consequently, changes in the performance of this Molectron dye laser could not be corrected for. Second, the transparency of the various windows varies with time as photodecomposition products accumulate on the surfaces. Third, the signal level depends not on the geometrical overlap of the two laser beams, but on the overlap of their intensity distributions. Neither laser beam was perfectly uniform, so signal levels were higher when the "hot spots" of the two beams coincided. Fourth, slight changes in H_2CO partial pressure have major effects on the normalized signal. As the pressure increases, the transmittted VUV intensity decreases, and the normalized signal increases, irrespective of the effect of the pressure change on the absolute signal level.

For these reasons, it was decided to scale each spectrum before averaging. The areas of 10 prominent spectral features were obtained for every spectrum using the previously described program WAVECAL. Each spectrum was then multiplied by the appropriate scale factor so that the summed area of these 10 spectral features would be independent of spectrum.

At this point, the spectra were averaged together to provide the final spectrum for that photolysis wavelength. At the same time, the standard deviation of the mean was obtained for each point of the spectrum. Figure 5 shows the final averaged spectrum and the averaged VUV intensity while Figure 6 shows the final spectrum and the standard deviation of the mean for the ${}^rR_3$ photolysis experiment. Figures 7 and 8 show the same data for the ${}^rR_4$ photolysis experiments.

The results of both photolysis wavelengths are shown together in Figure 9 to facilitate comparisons between them. The final ${}^rR_3$ spectrum is the average of 22 scans. The final ${}^rR_4$ spectrum is the average of 38 scans. Because the absorption intensity for this latter band is only one-quarter of the former band, approximately 350 spectra would have been needed to get the same signal-to-noise ratio.

Figures 10:a–t are an enlargement of Figure 9. Each spectrum covers only 100 cm^{-1}. The short vertical bars are $\pm$ one standard deviation of the mean for each point of the spectrum. Along the top of the top spectrum are the positions of all known transitions[8] ($\approx$ 224) in H_2 with ground state rotational and vibrational quantum numbers bounded by 13 and 4, respectively. These line positions were not determined using a set of rotational constants, but were calculated from the known energy levels. These 224 lines include 18 vibronic bands of the $\tilde{B} \leftarrow \tilde{X}$ and 4 vibronic bands of the $\tilde{C} \leftarrow \tilde{X}$ electronic transitions.

The positions and area of all observed peaks were determined in the usual manner using the previously described program WAVECAL. Two methods were used to determine the error limits for each peak. Method one involves using the standard propagation-of-errors formulas[9] with the standard deviations of the mean for each point in the peak. Method two involves calculating the area for each spectrum over the region in which the average spectrum has a peak, and then determining the standard deviations of these areas. The latter method was eventually chosen since it more accurately reflects the uncertainty in the area of a given peak.

This procedure found 112 peaks in the ${}^{r}R_3$ spectra and 111 peaks in the ${}^{r}R_4$ spectra. These peaks were then assigned using the known transition energies.

Once the areas and identities of each spectral feature is known, it is possible to determine the population of each initial state by using Eq. 6.67. The detection sensitivity coefficient of that equation was evaluated for every possible transition. In order to use a consistent set of input parameters, the Einstein A and B coefficients were calculated with the theoretical band oscillator strength[10] and the appropriate Hönl-London factor.[11] While this method ignores centrifugal distortion and the perturbations, more detailed calculations have been performed for only 6

of the necessary transitions.[12,13] It was further assumed, as was the case in the previous chapter, that the short wavelength cutoff of the PMT is 112.5 nm.

However, a straightforward implementation of Eq. 6.67 is not possible because of the many overlapping transitions. Instead, a least-squares method is needed to determine the best fit. Conceptually, every peak area is assumed to be a linear combination of the populations of each state, with the coefficients being the detection sensitivity of that state at that peak position. In matrix formalism,

$$\mathbf{S} \times \mathbf{P} = \mathbf{A} \tag{7.1}$$

where $\mathbf{A}$ is a $m \times 1$ column vector containing the experimentally determined peak areas, $\mathbf{S}$ is a $m \times n$ matrix containing the calculated sensitivities, and $\mathbf{P}$ is a $n \times 1$ column vector containing the desired populations.

If $\mathbf{S}$ were a square matrix, then Eq. 7.1 could be solved by any one of a number of standard algorithms. However, in this case $\mathbf{S}$ is decidely non-square, with many more rows than columns (since there are more transitions than states). This problem, however, can be solved using a singular value decomposition (SVD) algorithm.[14] In the SVD algorithm, any $m \times n, n \leq m$ matrix can be broken down into the product of a $m \times n$ column-orthogonal matrix $\mathbf{U}$, an $n \times n$ diagonal matrix $\mathbf{W}$ with positive or zero elements, and the transpose of an $n \times n$ orthogonal matrix $\mathbf{V}$, *i.e.*,

$$\mathbf{S} = \mathbf{U} \cdot \mathbf{W} \cdot \mathbf{V}^{\mathbf{t}} \tag{7.2}$$

This decomposition can be made for any matrix. Since $\mathbf{U}^{\mathbf{t}} \cdot \mathbf{U} = \mathbf{I}$, $\mathbf{W}^{-1} \cdot \mathbf{W} = \mathbf{I}$, and $\mathbf{V}^{\mathbf{t}} \cdot \mathbf{V} = \mathbf{V} \cdot \mathbf{V}^{\mathbf{t}} = \mathbf{I}$ where $\mathbf{I}$ is the identity matrix and the elements of $\mathbf{W}^{-1}$ are just the reciprocal of the elements of $\mathbf{W}$ (if the diagonal element of $\mathbf{W} = 0$, the diagonal element of $\mathbf{W}^{-1} = 0$), the left-hand side of both sides of Eq. 7.1 can be multiplied by the appropriate matrices, yielding

$$\mathbf{P} = \mathbf{V} \cdot \mathbf{W}^{-1} \cdot \mathbf{U}^{\mathbf{t}} \cdot \mathbf{A} \tag{7.3}$$

as the desired solution. When $m \geq n$, this solution is the "best" solution in the least-squares sense.[14]

Before the SVD algorithm for determining the population was implemented, several additional peaks with an area of 0 were added to the total. These additional peaks were for spectral features that were not seen. As an example, in the ${}^rR_3$ experiment, the peak at $\approx$ 89804 cm^{-1} could be the result of the (8–2) R(7), (10-3) P(2), or (4–0) P(11) lines at 89804.8, 89806.7, and 89808.2 cm^{-1}, respectively. However, the (10–3) R(2) line at 89937.6 cm^{-1} occurs in a featureless region of the spectrum. Therefore, a peak of area 0 with that assignment is included in the fit. In addition, several peaks were removed from the fit. These were shoulders on the tails of the extremely strong signal from background H_2 or noise spikes at the end of the scans and at the Xe absorption line of 90032 cm^{-1}. Rotational states in the ground vibrational level with $J \leq 5$ were ignored since the background from the residual H_2 saturated the PMT response.

The SVD analysis of the ${}^rR_3$ spectrum started with 174 transitions from 41 states in 112 spectral features, while the analysis of the ${}^rR_4$ spectrum started with 171 transitions from 47 states in 111 spectral features. In each case, the state whose population was most insignificant, *i.e.*, one in which the standard deviation of the population exceeded the population by the greatest margin, was removed from the fit. In addition, any unassigned peaks were removed from the fit. This process was repeated until all of the remaining states had statistically significant populations.

The final populations and standard deviations are shown in Table 3. Each set of results was independently normalized so that the total population in $v = 1, J =$ odd or $v = 1, J =$ even was 100 for the ${}^rR_3$ and ${}^rR_4$ experiments, respectively. At the end, the former data set contained 102 transitions from 22 states in 66 spectral features while the latter data set contained 116 transitions from 27 states in 75 spectral features.

The overall quality of the fits were not very good, with final χ^2's of 254 and 209. The critical values of χ^2 at the 95% confidence level are 60.481 and 65.171 for 44 and 48 degrees of freedom, respectively.

IV. RESULTS AND DISCUSSION

This experiment has investigated the photodissociation of the $2_0^1 4_0^3$ vibronic band of the $^1A_2 \leftarrow {}^1A_1$ electronic transition of H_2CO under essentially collision free conditions. The product H_2 was detected by laser induced fluorescence. In this section the results of this experiments are presented and discussed.

The time delay between the photolysis and the probe laser beams was 18.5 ns. The lifetime of the $2^1 4^3$ state is on the order of 10–15 ns,[15] limiting the H_2 to only 10 ns in which to undergo any collisional relaxation. The product translational energy is bounded by the total energy available for the products, 3.79 eV, which means that the relative velocity is bounded by 1.97×10^4 m s^{-1}. This total energy is just the sum of the UV photolysis photon energy and the endothermicity of the reaction (see chapter 2). Using the usual formulas for the partitioning of energy between two products while conserving linear momentum, the H_2 fragment's translational energy and velocity are bounded by 3.53 eV and 1.85×10^4 m s^{-1}, respectively. The average pressure of the sample cell was on the order of 0.5 torr, giving a number density of collision partners of 3.0×10^{16} cm^{-3}. The collision cross section between H_2 and H_2CO is estimated to be bounded by 3.1×10^{-15} cm^2 (determined from the known geometry of each species[17,18] and adding a van de Waals radius[19] to each atom). The collision frequency is on the order of 2×10^8 s^{-1}, giving a mean time between collisions of 5 ns. Thus, in the 10 ns after the H_2CO dissociation and before the H_2 detection, the H_2 fragment can undergo no more than 2 collisions. This is an upper bound since upper bounds of the estimated cross section and the velocity were used. In addition, the actual sample is only 0.3 torr of H_2CO, the remainder being the much smaller H_2 and CO residuals from previous laser pulses. Consequently, the number of collisions that the H_2 actually undergoes before detection is expected to be on the order of 1.

The previous experiment on the H_2 distributions from H_2CO photodissociation were deliberately in the multi-collision regime. Debarre *et al.*[3] used CARS to detect the product H_2. Because of their much poorer sensitivity ($\approx 10^{12}$ state cm^{-3}), they used 9 mbar of He and a delay of 150 ns in order to translationally cool the H_2.

When examining the large scale Figure 10a–t, one of the first things that is noticed is the extreme breadth of each spectral line. For example, the (3-1) R(3) line at 89552.9 cm^{-1} has a FWHM of 8.66 cm^{-1}, significantly greater than the room temperature Doppler width of 0.78 cm^{-1}. For comparison purposes, Fig. 8 of Chapter 6 (which is plotted to the same scale) has a Doppler width of 2.01 cm^{-1}, mostly due to the 1.85 cm^{-1} laser linewidth. If the observed broad linewidth were the result of thermal motion, then the $v = 1, J = 3$ state with a deconvoluted Doppler width of 8.46 cm^{-1} has a thermal translational temperature of 34800 K, corresponding to an average translational energy of 4.50 eV (36300 cm^{-1}). However, it is not expected that the linewidth of the H_2 fragments would be described by a Gaussian, but rather by the more complicated Eq. 6.66 for isotropically distributed monoenergetic particles. Solving that equation for $\Delta\nu_{max}$, one finds that $\Delta\nu_{max} \approx 4.33$ $cm^{-1}$and that $v_{max} \approx 14500$ $m\,s^{-1}$, corresponding to a translational energy of 2.18 eV.

The total energy available for product degrees of freedom is approximately 3.79 eV (30600 cm^{-1}) which is determined by 30400 cm^{-1} from the photolysis laser plus 200 cm^{-1} from the endothermicity of the reaction. The translational energy of the $v = 1$, $J = 3$ state of H_2 is 2.18 eV from the Doppler width of the (3–1) R(3) transition. Conservation of linear momentum requires that the CO fragment have a velocity of 1000 $m\,s^{-1}$, an energy of 0.16 eV, giving a total of 2.34 eV of product translational energy, 62% of the total available. The H_2 fragment has 4800 $cm^{-1}$of internal excitation, 16% of the total, leaving 8200 cm^{-1}, 22% of that available, for CO internal excitation.

This is the first case in which the distribution of energy has been determined for a single rotational level. The previous work of Moore and coworkers[1-3] showed that the average partition of energy when H_2CO is dissociated using the $2_0^1 4_0^1$ vibronic band near 29500 cm^{-1} is 65% into product translation, 20% into H_2 internal degrees of freedom, and 12% into CO degrees of freedom. Their results are close to the current results. Because of the crudeness in the estimation of the translational energy, the differences are not expected to be significant.

Figure 11 shows the rotational distributions for the $v = 1$ vibrational level. The top figure shows the *ortho*-H_2 rotational distribution from the ${}^rR_3$ photolysis, while the bottom figure shows the *para*-H_2 rotational distribution from the ${}^rR_4$ photolysis. Qualitatively, the two distributions appear to be similar, peaking at $J = 3$ and $J = 4$, respectively.

Figure 12 shows a Boltzmann plot of the data in Fig. 11. In this plot some differences between the results of the two experiments become obvious. It is seen that the Boltzmann distribution from the ${}^rR_4$ experiment has a shallower slope, implying that the "rotational temperature" is higher. These observations are borne out by an appropriately weighted linear least-squares fit of the logarithm of the population divided by its degeneracy as a function of rotational energy. The *ortho*-H_2 rotational distribution is described by a rotational temperature of 1950 ± 130 K. The χ^2 for the fit is 5.375. The *para*-H_2 rotational distribution is described by a rotational temperature of 4390 ± 880 K. The χ^2 for this fit was 2.863. The critical value of χ^2 for three degrees of freedom is 7.815. Consequently, the model that the rotational distribution is described by a Boltzmann distribution is adequate.

Also shown on these figures are previous results. Debarre *et al.*[3] measured the H_2 distribution using CARS following excitation near 29500 cm^{-1}. Their distribution for the odd J levels is similar to the current results, agreeing to within 1 standard deviation for all but $J = 3$. The principal difference is that the current

distribution peaks at $J = 3$ while their distribution peaks at $J = 5$. The similarity between the two distributions is evident on the Boltzmann distribution plot, where the two sets of experimental results are almost superimposable, except for $J = 3$. They did not measure the *para*-H_2 rotational distribution.

Schinke calculated the product rotational distributions using a simple model of the system derived from the infinite order sudden (IOS) photodissociation amplitude of a triatomic molecule. The ingredients in the model are the potential energy in the exit channel and the geometry of the transition state. He calculated both the H_2 and CO distributions. His results for CO and *ortho*-H_2 are in reasonably good agreement with the experimental results of Bamford *et al.* and Debarre *et al.* His results for *ortho*-H_2 are also shown on Figures 11 and 12.

The principal disagreement with the experiments is that he predicts much less $J = 0$ population than seen by Debarre *et al.* Schinke pointed out that it wasn't known whether the discrepancy was due to an error in the model or a result of collisional relaxation in the experiments. Since he was principally interested in the qualitative trends and in its dynamical interpretation, he did not adjust his model in an attempt to obtain a better fit with the experiment.

The agreement between the current experiment and the Debarre *et al.* experiment suggests that the error does not lie with the experiment but instead lies with the theoretical model.

Schinke[20] also predicted the *para*-H_2 distribution. Instead of looking similar to the *ortho*-H_2 distribution, he predicted that the distribution would peak at $J = 0$, reach a minimum at $J = 6$, and then reach a second maximum at $J = 10$. This is not close to what was observed in the current experiments, as can be easily seen in Figures 11 and 12. The reason for this major discrepancy is unknown. The current experiments used a different rovibronic band with approximately 900 cm^{-1} of additional energy but with the same overall symmetry. However, the agreement

with the *ortho*-H_2 distribution would tend to rule this change in rovibronic band as an explanation for the discrepancy. It is suprising that a model that accurately predicts the CO and the *ortho*-H_2 rotational distributions does such a poor job with the *para*-H_2 rotational distribution.

Analysis of the rotational distributions for the other vibrational levels is hampered by the extremely poor quality of the data as evidenced by the extremely large χ^2' for the least squares fits to the two sets of data. Qualitatively, the *para*-H_2 rotational distributions all peak at $J = 4$, while those *ortho*-H_2 rotational distributions which are smooth peak at $J = 3$. The prediction by Schinke was disproven for every vibrational level seen.

Since the CARS experiments of Debarre *et al.* had little difficulty (beyond poor sensitivity), it is concluded that the problem lies with the LIF detection scheme. The difficulties will be discussed in more detail in Chapter 9. The principal problem is that for these higher ground state vibrational levels the intermediate state in the LIF detection scheme is not just the $\tilde{B}$ but also the $\tilde{C}$ excited electronic states. This causes problems in that there are strong perturbations of the position of some rotational levels and intensities of some transitions. The method used to calculate the Einstein B coefficient, using the band oscillator strength and the Hönl-London factors, ignores these perturbations.

In summary, several conclusions about the H_2CO photodissociation reaction can be drawn from the current experiments. First, the *ortho*-H_2 rotational distribution from the photolysis of the ${}^rR_3$ $2_0^1 4_0^3$ band used for the current experiment with LIF detection agrees within experimental error with that from the photolysis of the ${}^rQ_1$ $2_0^1 4_0^1$ band used for the previous experiment with CARS detection. This agreement suggest that the *ortho*-H_2 rotational distribution is insensitive to slight changes in the total energy of the system. Second, the *para*-H_2 rotational distribution from the photolysis of the ${}^rR_4$ $2_0^1 4_0^3$ band agrees qualitatively

with the *ortho*-H_2 distribution, thougth the *para*-distribution does seem to be slightly "hotter." This agreement between the *ortho*- and *para*-H_2 distributions is counter to the prediction by Schinke, who predicted that the *para*-H_2 distribution would be bi-modal with peaks at $J = 0$ and $J = 10$ and a minimum at $J = 6$. Thus, the last words of Schinke's paper "*Without awaiting experimental results for para*-H_2 *or — even more interestingly — the distribution for HD we conclude that the dynamics of* H_2CO *fragmentation concerning the rotational state distributions of both molecular fragments is understood,* " (italics added) are incorrect, and more work on this reaction is needed.

TABLE 1. Formaldehyde Transitions Near 30388.5 cm^{-1}

Assignment	ν_{vac}	Intensity
${}^rQ_6(8)$	30390.37	0.58
${}^rQ_7(10)$	30390.25	1.20
${}^rR_3(6)$	30389.49	12.86
${}^rQ_5(6)$	30389.34	1.64
${}^rR_3(5)$	30389.34	13.20
${}^rR_3(7)$	30389.34	12.42
${}^rR_5(16)$	30389.19	3.40
${}^rR_3(8)$	30388.92	11.86
${}^rR_3(4)$	30388.79	13.46
${}^rR_4(13)$	30388.67	2.24
${}^rR_3(9)$	30388.13	11.20
${}^rR_3(3)$	30387.94	13.74
${}^rQ_6(9)$	30387.57	0.74
${}^rQ_5(7)$	30387.07	2.84
${}^rR_3(10)$	30386.97	10.42
${}^rQ_7(11)$	30386.75	1.36

TABLE 2. Formaldehyde Transitions Near 30396.7 cm^{-1}

Assignment	ν_{vac}	Intensity
${}^rR_6(15)$	30397.49	0.96
${}^rR_5(13)$	30396.98	5.26
${}^rR_7(17)$	30396.80	1.34
${}^rQ_7(8)$	30397.30	0.56
${}^rR_4(5)$	30396.98	4.10
${}^rR_4(6)$	30396.98	3.92
${}^rR_4(7)$	30396.80	3.74
${}^rR_4(4)$	30396.55	4.18
${}^rR_4(8)$	30396.21	3.52
${}^rR_4(9)$	30395.33	3.28

TABLE 3. Results of H_2CO Photodecomposition Experiment

STATE		$2_0^1 4_0^3$ ${}^rR_3$ SUBBAND		$2_0^1 4_0^3$ ${}^rR_4$ SUBBAND	
v	J	n	Population	n	Population
0	7	3	18.29 ±9.61		
0	9	2	3.924 ±0.555		
0	11	3	2.247 ±0.656		
1	1	4	18.10 ±4.14	3	3.865 ±1.215
1	3	4	36.45 ±7.55	4	20.62 ±2.720
1	5	3	25.18 ±4.99	3	3.768 ±1.067
1	7	3	16.47 ±2.20	3	3.651 ±0.866
1	9	2	3.793 ±0.653		
2	1	6	9.496 ±1.248	6	3.175 ±1.041
2	3	6	7.481 ±1.525	6	3.969 ±0.747
2	5	7	3.581 ±0.949	7	0.7704±0.1800
2	7	7	12.62 ±1.226	7	2.116 ±0.514
3	1	6	2.981 ±0.522		
3	3	6	3.233 ±1.466	6	2.181 ±0.252
3	5	6	0.8744±0.2406	6	1.629 ±0.687
3	7	3	0.5289±0.5396	3	1.827 ±0.845
4	1	5	0.1203±0.2972		
4	3	7	1.019 ±0.187		
4	5	6	1.205 ±0.260		
0	6			3	4.702 ±1.589
0	8			2	0.7301±1.591
1	0			2	3.363 ±0.622
1	2	4	0.6567±0.1075	4	20.53 ±3.26
1	4	2	1.174 ±0.1637	3	30.61 ±7.03
1	6			4	28.28 ±5.05
1	8			4	17.21 ±4.09
2	0			3	3.244 ±0.864
2	2			6	1.735 ±0.459
2	4	7	1.112 ±0.3992	7	4.599 ±1.241
2	6			5	1.253 ±0.375
2	8			2	4.216 ±0.842
3	0			3	0.1777±0.1967
3	2			6	0.9647±0.1294
3	4			4	1.232 ±0.962
3	6			4	0.2853±0.0822

REFERENCES

1. P. Ho, D. J. Bamford, R. J. Buss, Y. T. Lee, and C. B. Moore, *J. Chem. Phys.* **76**, 3630 (1982).
2. D. J. Bamford, S. V. Filseth, M. F. Foltz, J. W. Hepburn, and C. B. Moore, *J. Chem. Phys.* **82**, 3032 (1985).
3. D. Debarre, M. Levebvre, M. Péalat, J.-P. E. Taran, D. J. Bamford, and C. B. Moore, *J. Chem. Phys.* **83**, 4476 (1985).
4. R. A. Keller, R. Engleman, Jr., and B. A. Palmer, *Appl. Opt.* **19**, 836 (1980).
5. V. Sethuraman, V. A. Job, and K. K. Innes, *J. Mol. Spectrosc.* **33**, 189 (1970).
6. C. M. L. Kerrm D. C. Moule, and D. A. Ramsay, *Can. J. Phys.* **61**, 6 (1983).
7. M. Suto, X. Wang, and L. C. Lee, *J. Chem. Phys.* **85**, 4228 (1986).
8. I. Dabrowski, *Can. J. Phys.* **62**, 1639 (1984).
9. P. R. Bevington, *Data Reduction and Error Analysis for The Physical Sciences*, (McGraw-Hill, NY, 1969).
10. A. C. Allison and A. Dalgarno, *Atom. Dat.* **1**, 289 (1970).
11. A. Schadee, *Bull. Astr. Inst. Neth.* **17**, 311 (1964).
12. A. L. Ford, *J. Mol. Spectrosc.* **56**, 251 (1975).
13. H. Abgrall, F. LAunay, E. Roueff, and J.-Y. Roncin, *J. Chem. Phys.* **87**, 2036 (1987).
14. W. H. Press, B. P. Flannerym, S. A. Teukolsky, and W. T. Vetterling, *Numerical Recipes: The Art of Scientific Computing*, (Cambridge University Press, NY, 1986).
15. E. C. Apel and E. K. C. Lee, *J. Phys. Chem.* **89**, 1391 (1985).
16. D. J. Clouthier and D. A. Ramsay, *Ann. Rev. Phys. Chem.* **34**, 31 (1983).
17. R. D. Levine and R. B. Bernstein, *Molecular Reaction Dynamics*, (Oxfor University Press, NY, 1974)

18. K. P. Huber and G. Herzberg, *Molecular Spectra and Molecular Structure: IV. Constants of Diatomic Molecules*, (Van Nostrand Reinhold, NY, 1979).

19. L. Pauling, *Nature of the Chemical Bond, 3rd. ed*, (Cornell University Press, Ithaca, NY, 1960) pp. 257–264.

20. R. Schinke, *J. Chem. Phys.* **84**, 1487 (1986).

FIGURE CAPTIONS

Figure 1. Scale drawing of the layout for the two laser experiments described in this chapter. The Molectron MY-34 Nd:YAG laser and DL-18 dye laser is the photolysis or pump laser system. The Quanta Ray DCR-2A Nd:YAG laser, PDL-2 dye laser, and WEX-1 wavelength extension unit form the probe laser system. Abbreviations used in the figure include: A— Aperture, BS— Beam Splitter, P— Prism, PD— Photodiode, PEJM— Pyroelectric Joule Meter.

Figure 2. Electronics for two laser experiments. The PMT is the SIGNAL channel and the NO ionization cell is the LASER INTENSITY channel. The LASER TIMING CONTROLLER controls both dye lasers, triggering them at the correct repetition rate with less that 1 ns jitter. It also toggles the order of gates to the dual gated integrator when data is collected in the "auto subtract" mode. The solid lines represent analog signal lines, the $\cdot - \cdot -$ lines represent the control lines and the $\cdots$ represent the digital data bus connecting the computer to the dye laser.

Figure 3. Typical "raw" H_2 LIF spectrum taken during a H_2CO photodissociation experiment as a function of probe laser UV wavelength. The H_2CO pressure was initially 0.300 torr, the photolysis wavelength was 328.98 nm, and the time delay was 20.4 ns. The gated integrator on the SIGNAL channel was in "auto subtract" mode.

Figure 4. Same data as in Figure 3 after the backgroound was removed and the PMT signal normalized by dividing it by the NO ionization cell signal. The large noise spikes near 328.5 nm arise from the loss of VUV power near 109.5 nm.

Figure 5. Final H_2 LIF spectrum showing the results following photolysis of the ${}^rR_3$ subband of the $2_0^1 4_0^3$ vibronic band in formaldehyde. The top panel is

the average transmitted VUV intensity as detected by the NO ionization cell. The absorption lines are due to H_2, Xe, XeKr, Kr_2, and H_2O. The bottom panel is the average normalized PMT signal. The data in both panels are scaled so that the tallest real feature was 100. 22 spectra were averaged together to generate this spectrum.

Figure 6. Same as Fig. 5 only this time the top panel shows the standard deviation of the mean for each data point. The arbitrary units are the same for both panels.

Figure 7. Same as Fig. 5 showing the results following photolysis of the ${}^rR_3$ subband of the $2_0^1 4_0^3$ vibronic band of formaldehyde. This spectrum is the average of 38 spectra.

Figure 8. Same as Fig. 7 only this time the top panel shows the standard deviation of the mean for each data point.

Figure 9. Final H_2 LIF spectrum showing the results from the H_2CO dissociation experiments. The top panel is the results from the ${}^rR_3$ experiments, the bottom panel is the results from the ${}^rR_4$ experiments.

Figure 10. A twenty page enlargement of Fig. 9 showing the H_2 LIF spectrum following the photodissociation of H_2CO. The top panel is the results from the ${}^rR_3$ experiments, the bottom panel is the results from the the ${}^rR_4$ experiments. Each page covers only 100 cm^{-1} of the VUV scan. The short vertical bars at each data point on each spectrum represent ± 1 standard deviation of the mean. Across the top are the location and assignments of all known H_2 transitions with ground electronic state quantum numbers $v \leq 4$, $J \leq 13$. Those transitions with short lines are in the $\tilde{B} \leftarrow \tilde{X}$ Lyman band system, those transitions with the longer lines are in the $\tilde{C} \leftarrow \tilde{X}$ Werner band system. The notation is ${}^{v'}_{v}(\Delta J)_J$ where the unprimed quantum numbers are in the ground electronic state.

Figure 11. Rotational distribution of H_2 product in $v = 1$ from H_2CO photodissociation as a function of rotational quantum numbers. The top panel is for *ortho*-H_2 from odd K_a states, the bottom panel is for *para*-H_2 from even K_a states. The $\bigcirc$ are the current experimental results from the ${}^rR_3$ and ${}^rR_4$ experiments, respectively. The $\oplus$ represent the experimental results of Debarre *et al.* The $\diamond$ is the theoretical results of Schinke. Each data set was normalized so that the total population was 100.

Figure 12. Semi-logarithmic plot of rotational level population divided by $(2J + 1)$ as a function of rotaional energy. The data and labels are the same as for Fig. 11.

FIGURE 1.

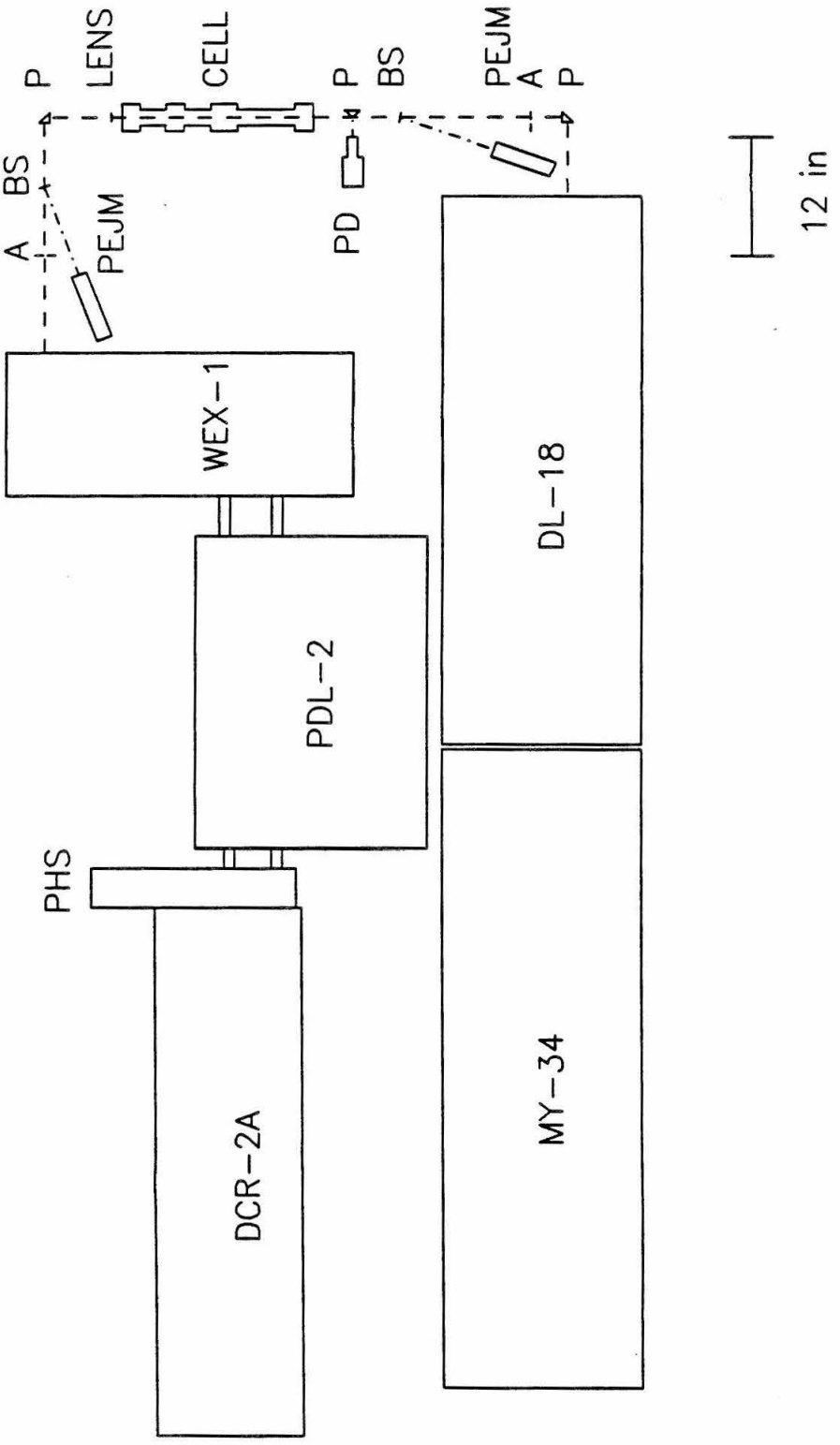
P
LENS
CELL
P
BS
PEJM
A
P
A
BS
PEJM
PD
12 in
WEX-1
DL-18
PDL-2
PHS
DCR-2A
MY-34

FIGURE 2.

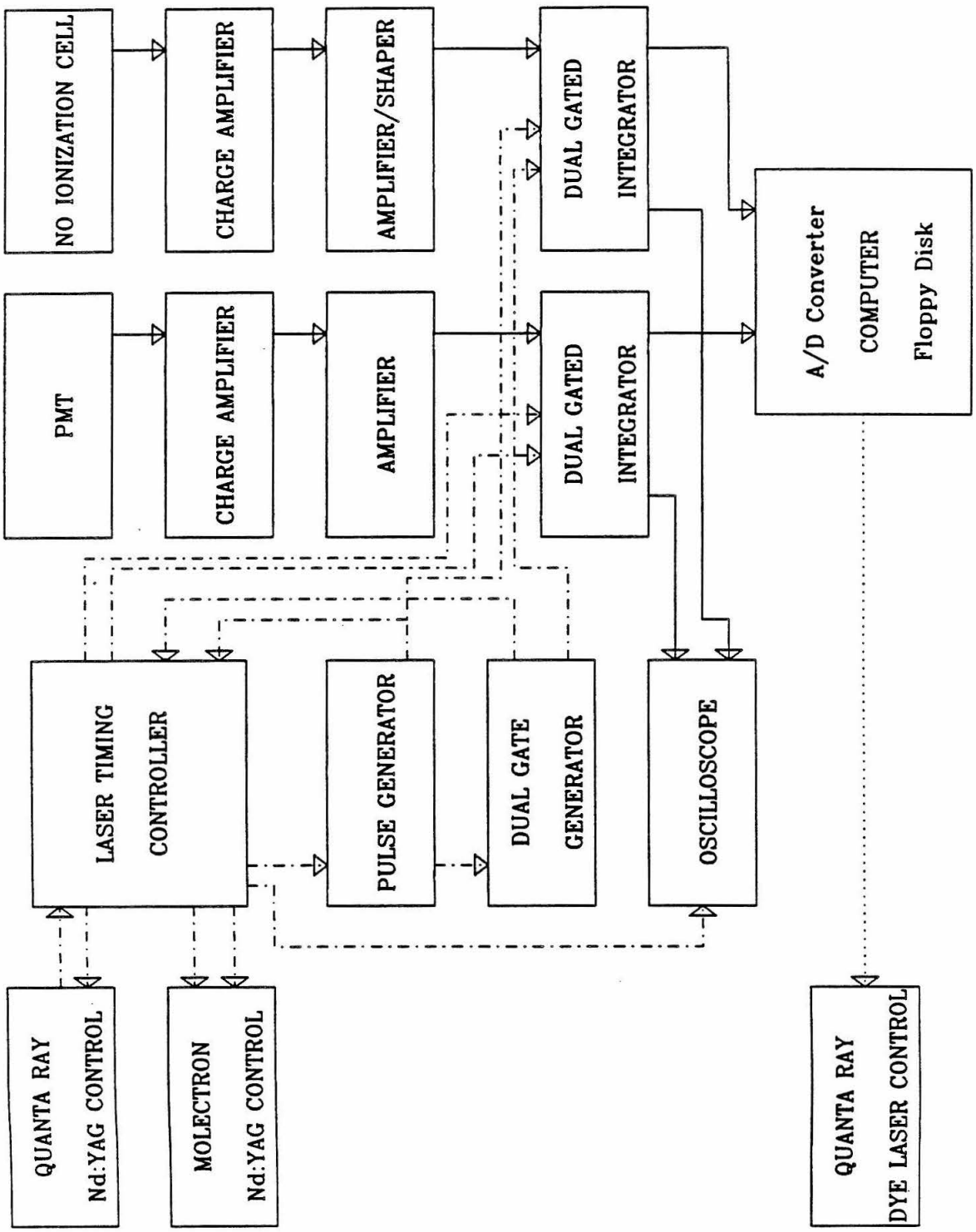
NO IONIZATION CELL
CHARGE AMPLIFIER
AMPLIFIER/SHAPER
DUAL GATED INTEGRATOR
PMT
CHARGE AMPLIFIER
AMPLIFIER
DUAL GATED INTEGRATOR
A/D Converter
COMPUTER
Floppy Disk
LASER TIMING CONTROLLER
PULSE GENERATOR
DUAL GATE GENERATOR
OSCILLOSCOPE
QUANTA RAY Nd:YAG CONTROL
MOLECTRON Nd:YAG CONTROL
QUANTA RAY DYE LASER CONTROL

FIGURE 3.

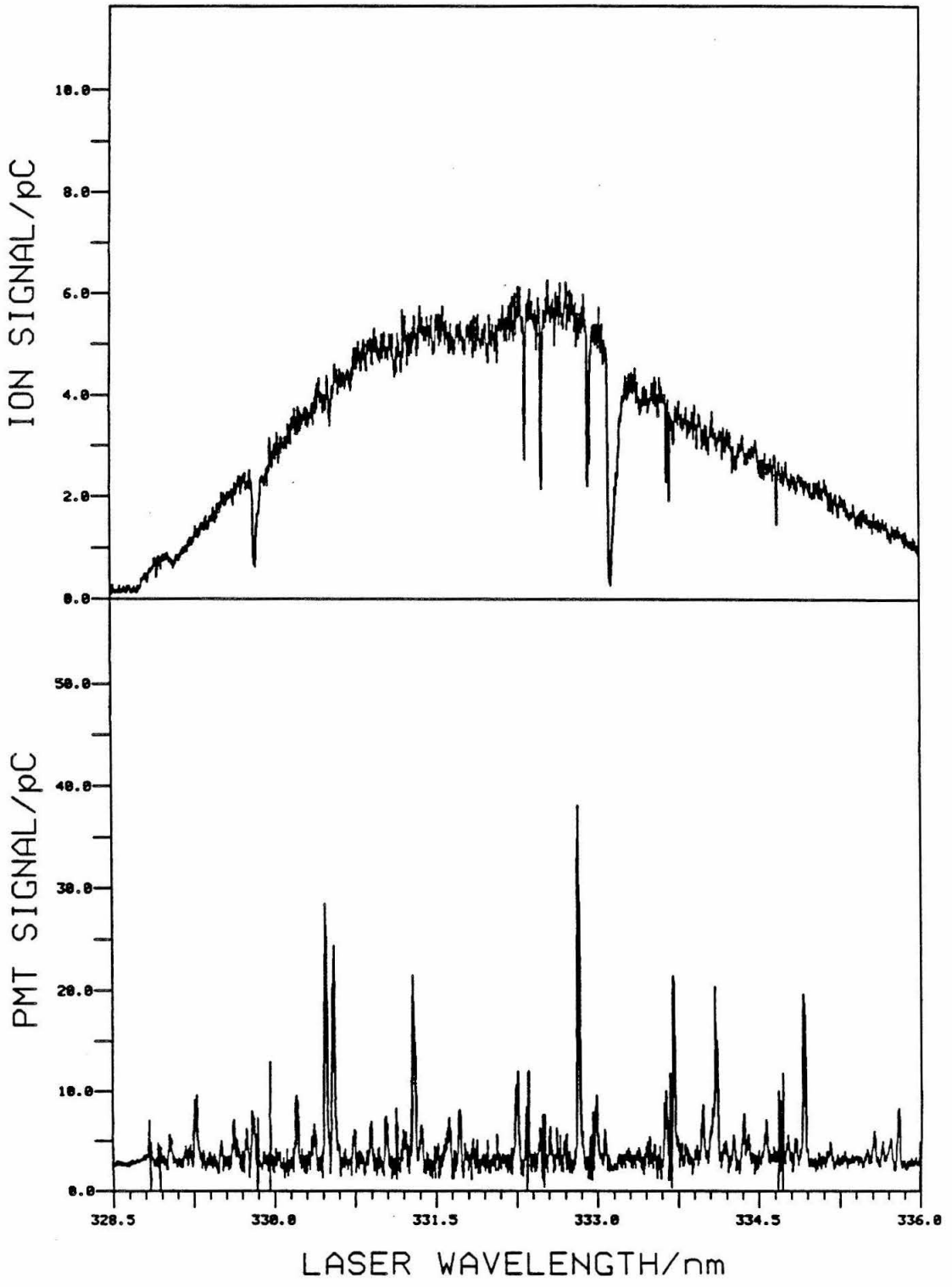
ION SIGNAL/pC
10.0
8.0
6.0
4.0
2.0
0.0
PMT SIGNAL/pC
50.0
40.0
30.0
20.0
10.0
0.0
328.5
330.0
331.5
333.0
334.5
336.0
LASER WAVELENGTH/nm

FIGURE 4.

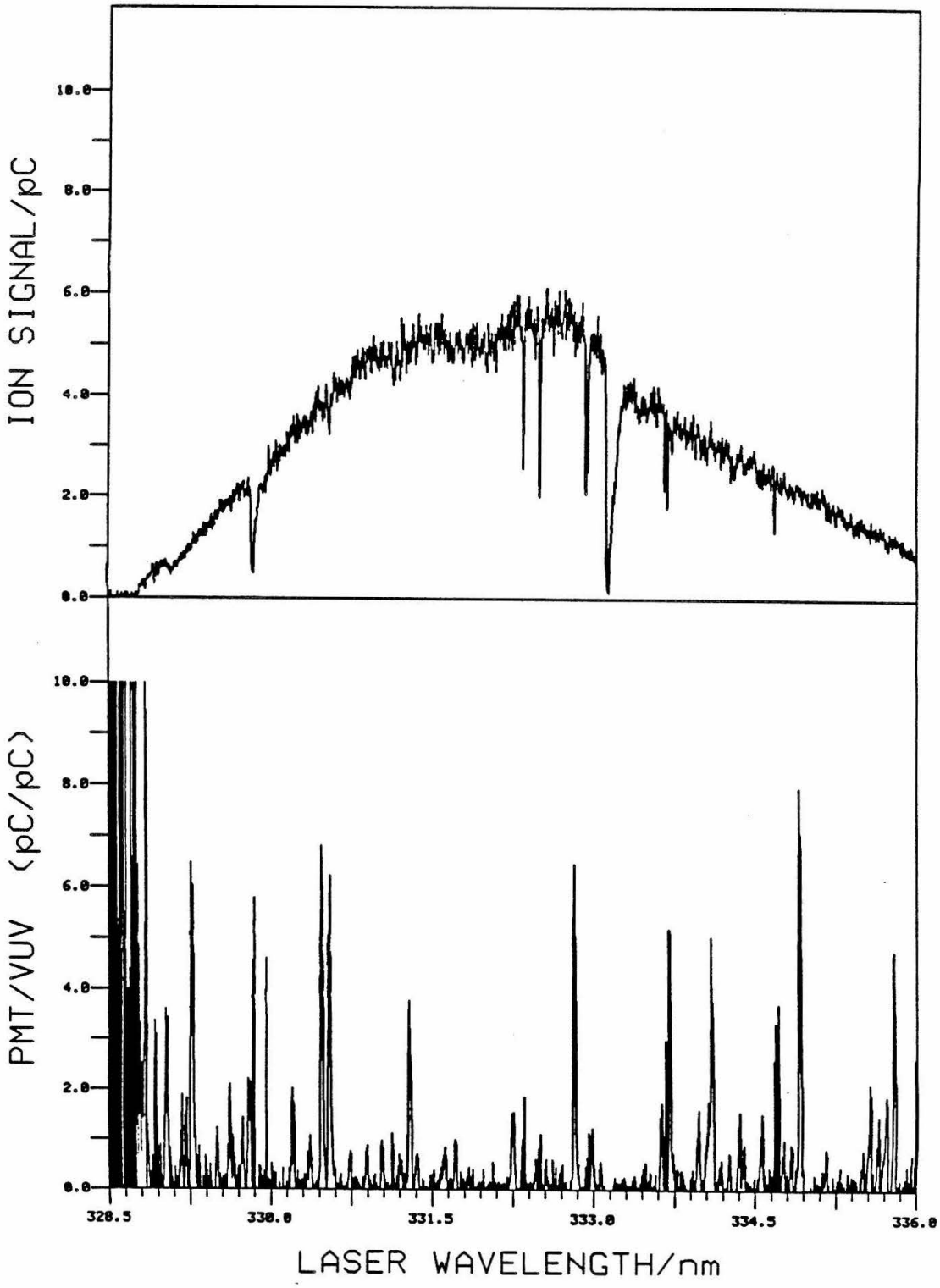
ION SIGNAL/pC
10.0
8.0
6.0
4.0
2.0
0.0
PMT/VUV (pC/pC)
10.0
8.0
6.0
4.0
2.0
0.0
328.5
330.0
331.5
333.0
334.5
336.0
LASER WAVELENGTH/nm

FIGURE 5.

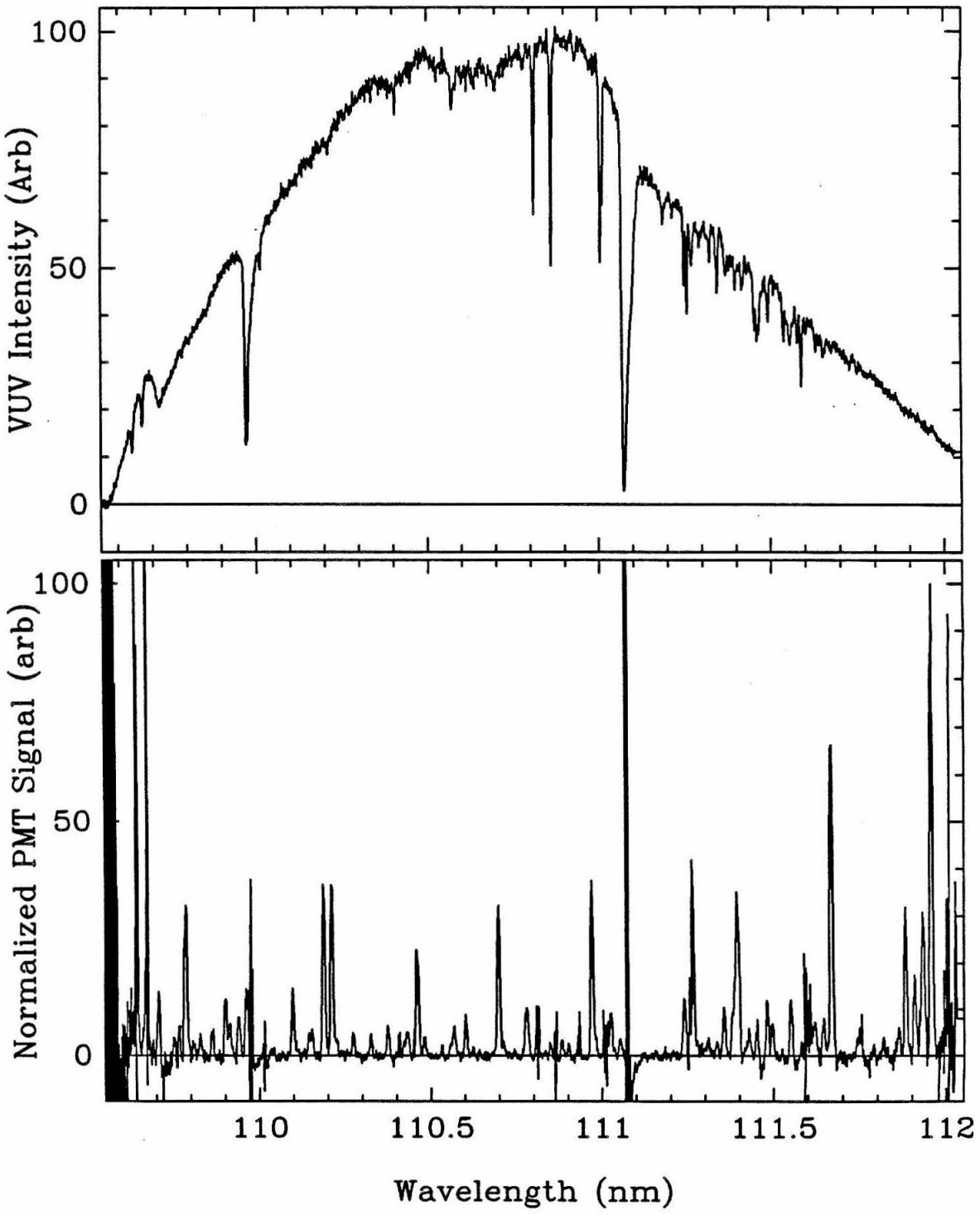
100
50
0
VUV Intensity (Arb)
100
50
0
Normalized PMT Signal (arb)
110
110.5
111
111.5
112
Wavelength (nm)

FIGURE 6.

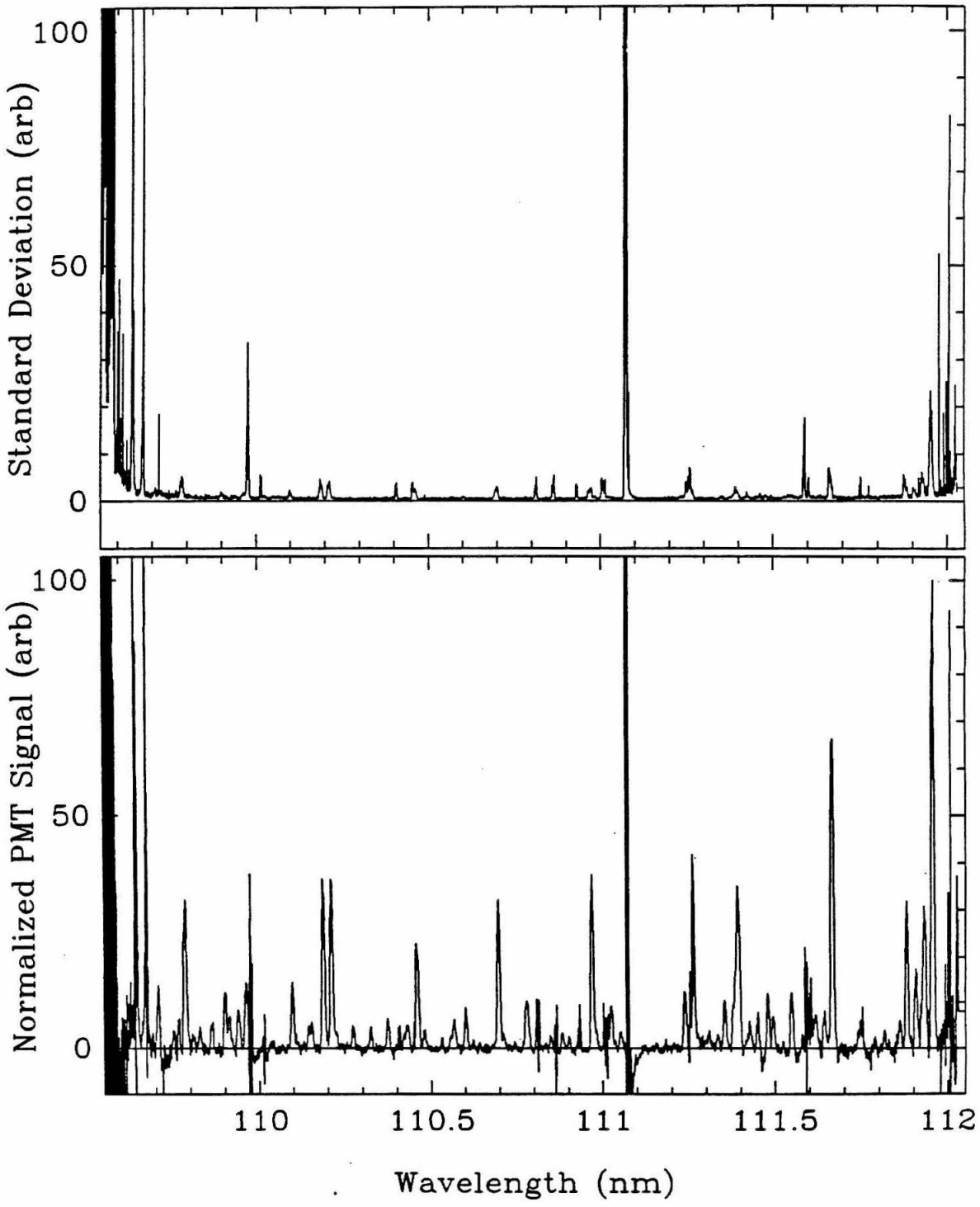
100
50
0
Standard Deviation (arb)
100
50
0
Normalized PMT Signal (arb)
110
110.5
111
111.5
112
Wavelength (nm)

FIGURE 7.

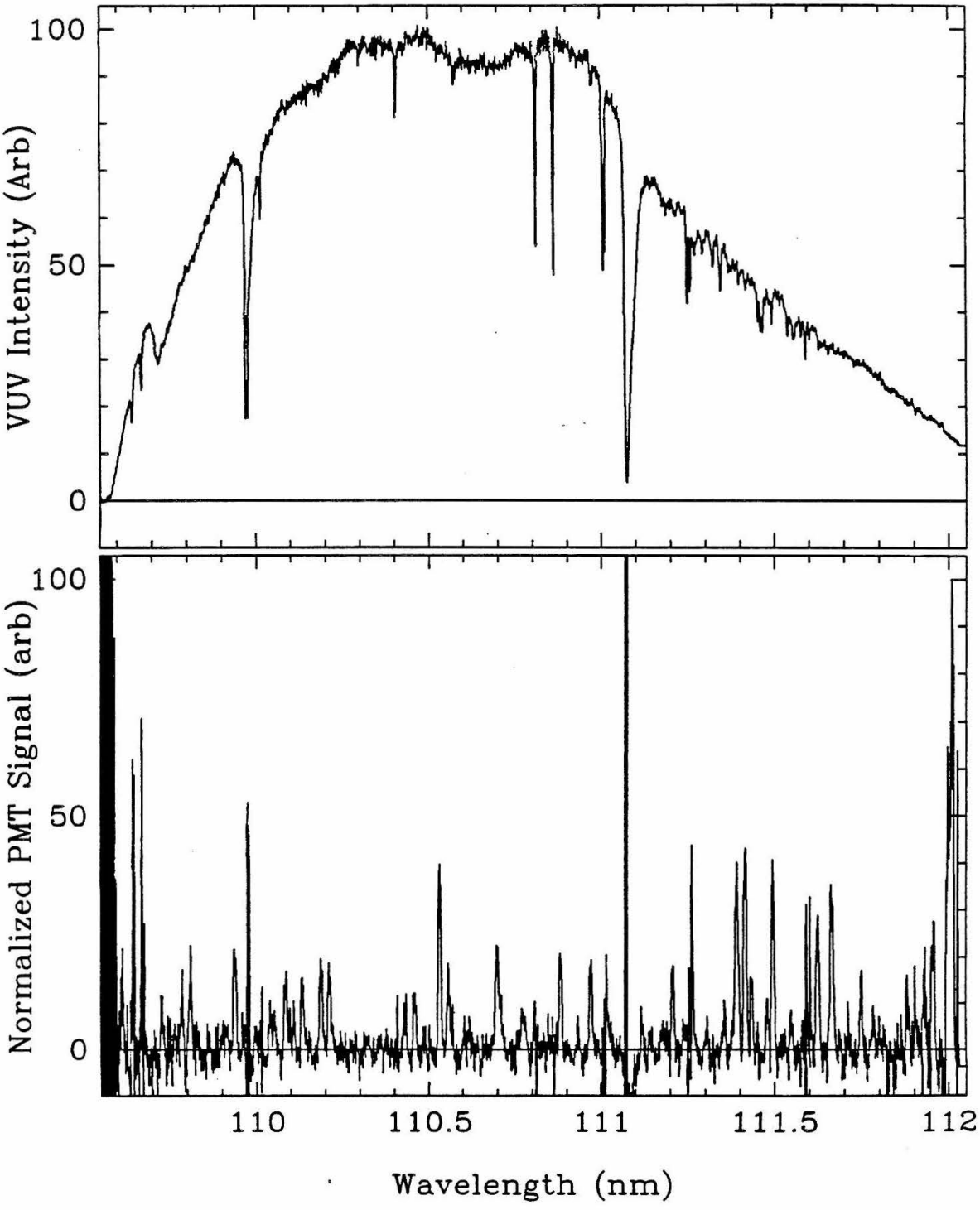
100
50
0
VUV Intensity (Arb)
100
50
0
Normalized PMT Signal (arb)
110
110.5
111
111.5
112
Wavelength (nm)

FIGURE 8.

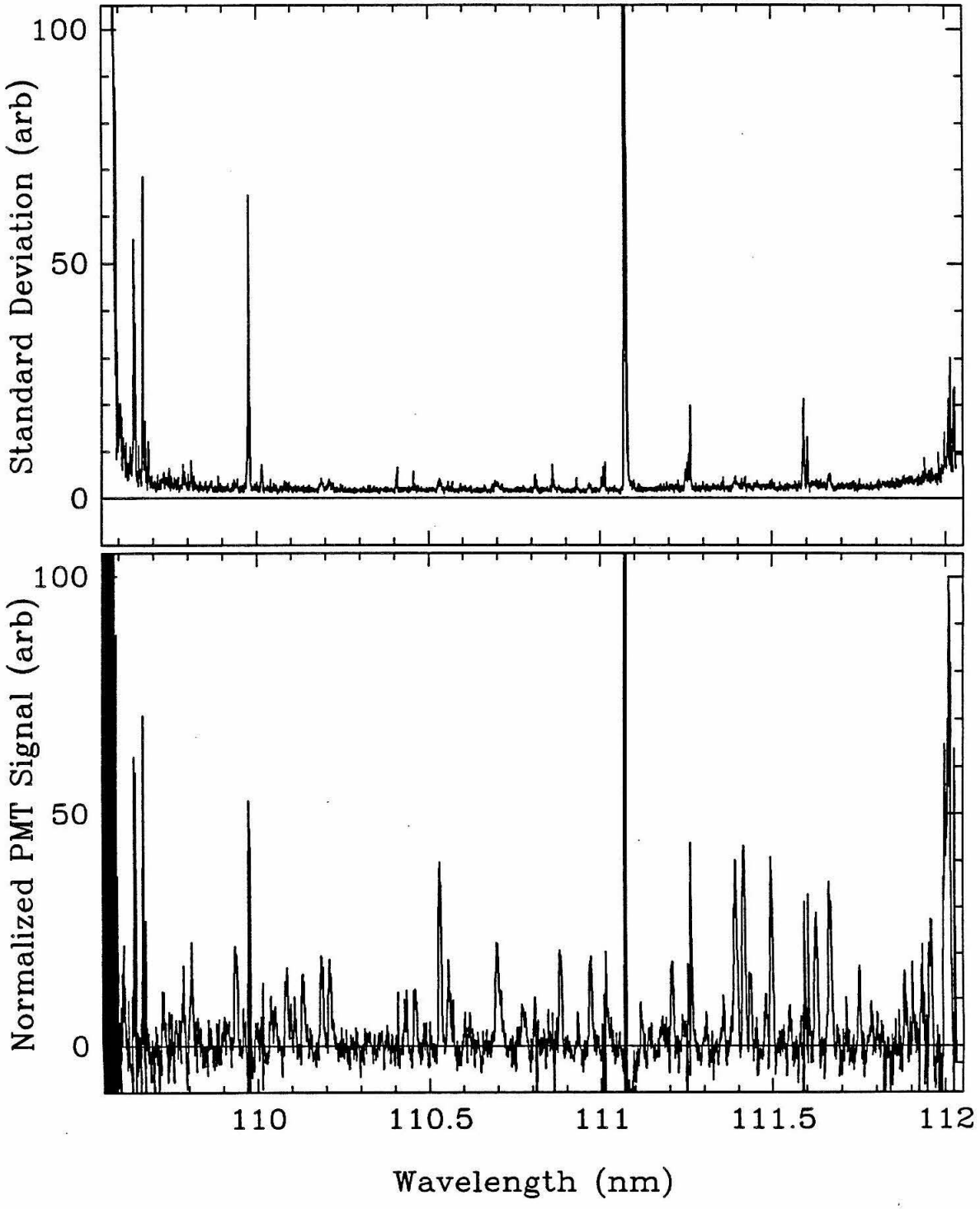
100
50
0
Standard Deviation (arb)
100
50
0
Normalized PMT Signal (arb)
110
110.5
111
111.5
112
Wavelength (nm)

FIGURE 9.

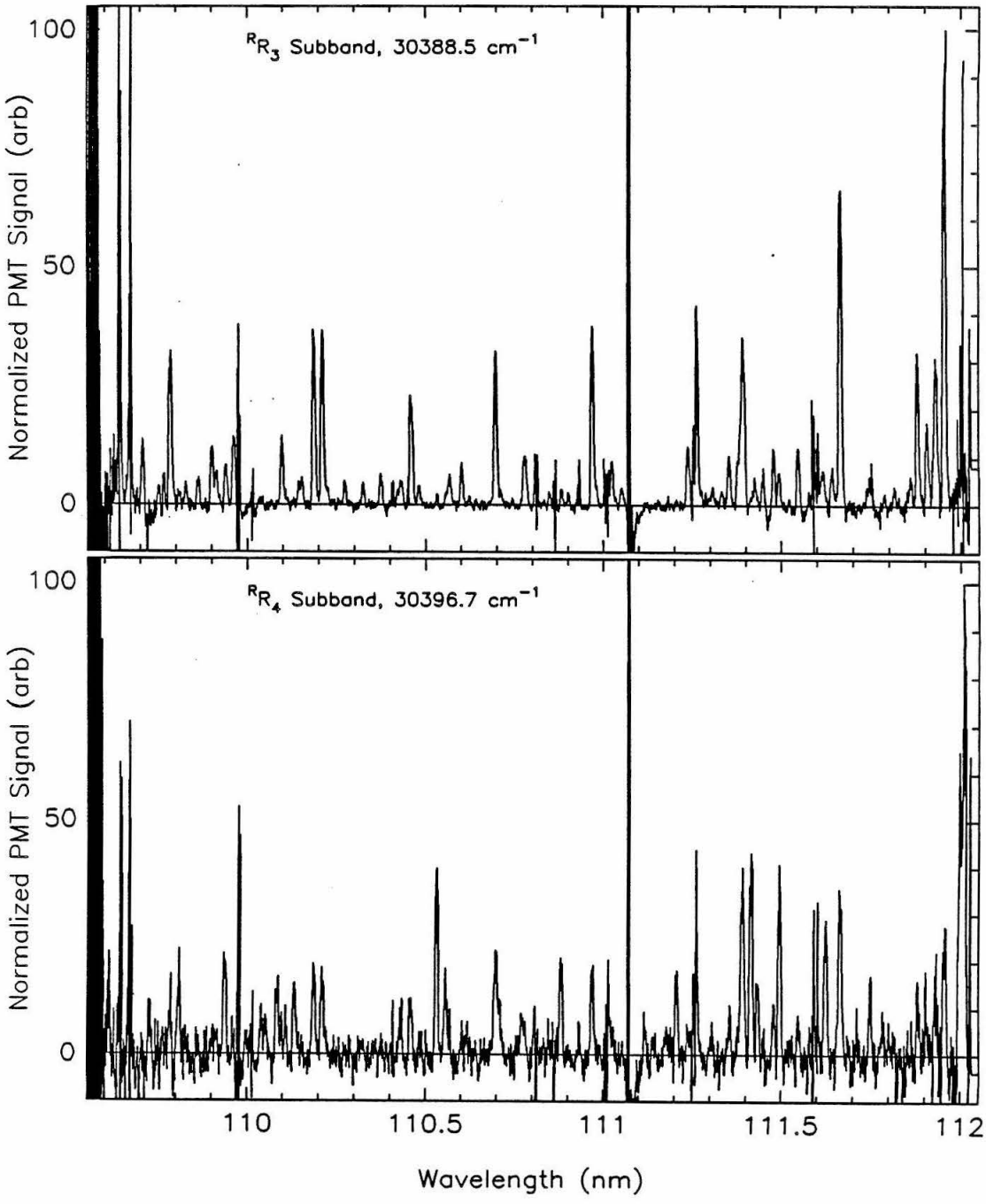
100
50
0
Normalized PMT Signal (arb)
$^{R}R_{3}$ Subband, 30388.5 cm^{-1}
100
50
0
Normalized PMT Signal (arb)
$^{R}R_{4}$ Subband, 30396.7 cm^{-1}
110
110.5
111
111.5
112
Wavelength (nm)

FIGURE 10: a.

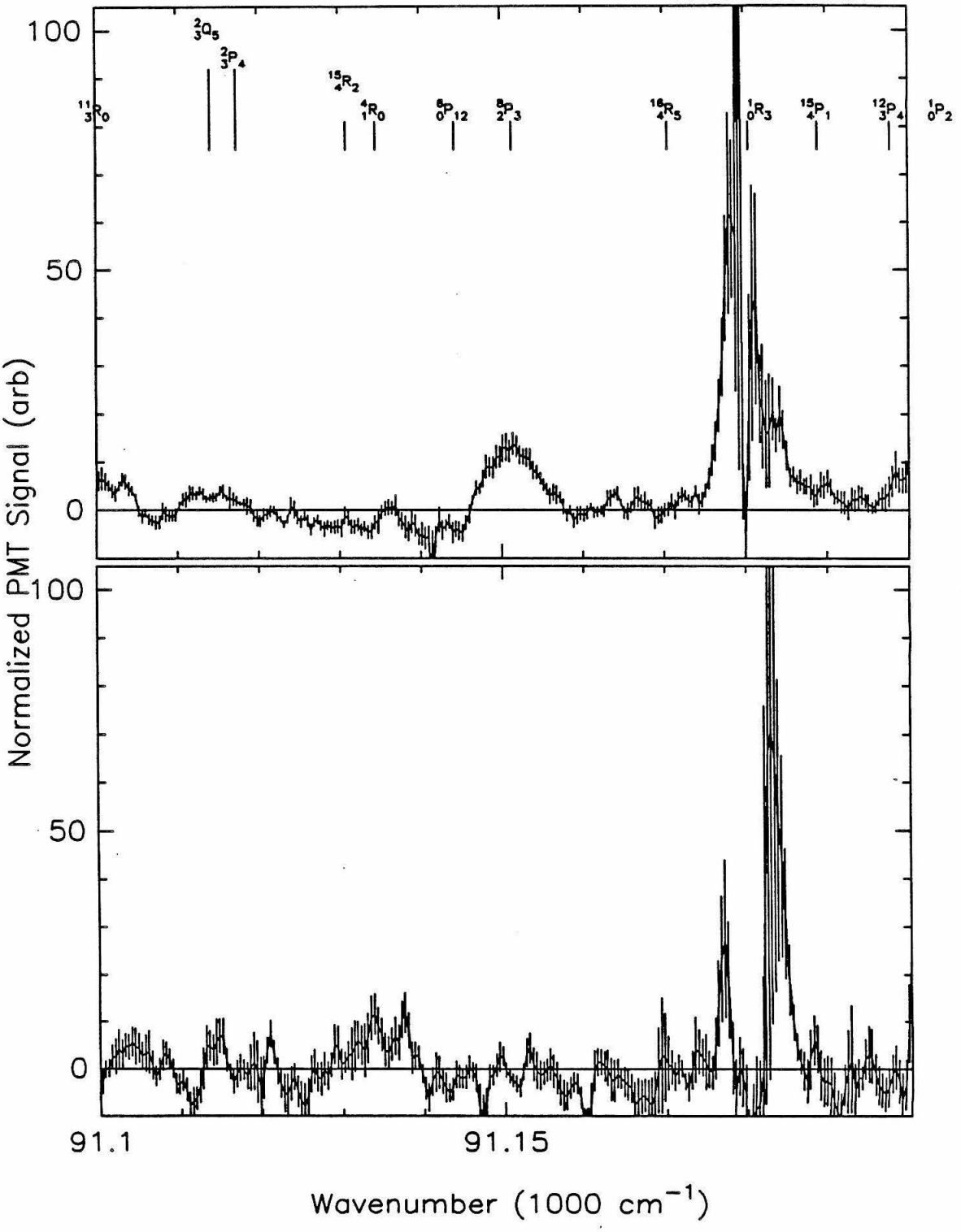
100
50
0
100
50
0
Normalized PMT Signal (arb)
91.1
91.15
Wavenumber (1000 cm^{-1})
$^{2}_{3}Q_{5}$
$^{2}_{3}P_{4}$
$^{15}_{4}R_{2}$
$^{11}_{3}R_{0}$
$^{4}_{1}R_{0}$
$^{6}_{0}P_{12}$
$^{8}_{2}P_{3}$
$^{16}_{4}R_{5}$
$^{1}_{0}R_{3}$
$^{15}_{4}P_{1}$
$^{12}_{3}P_{4}$
$^{1}_{0}P_{2}$

FIGURE 10: b.

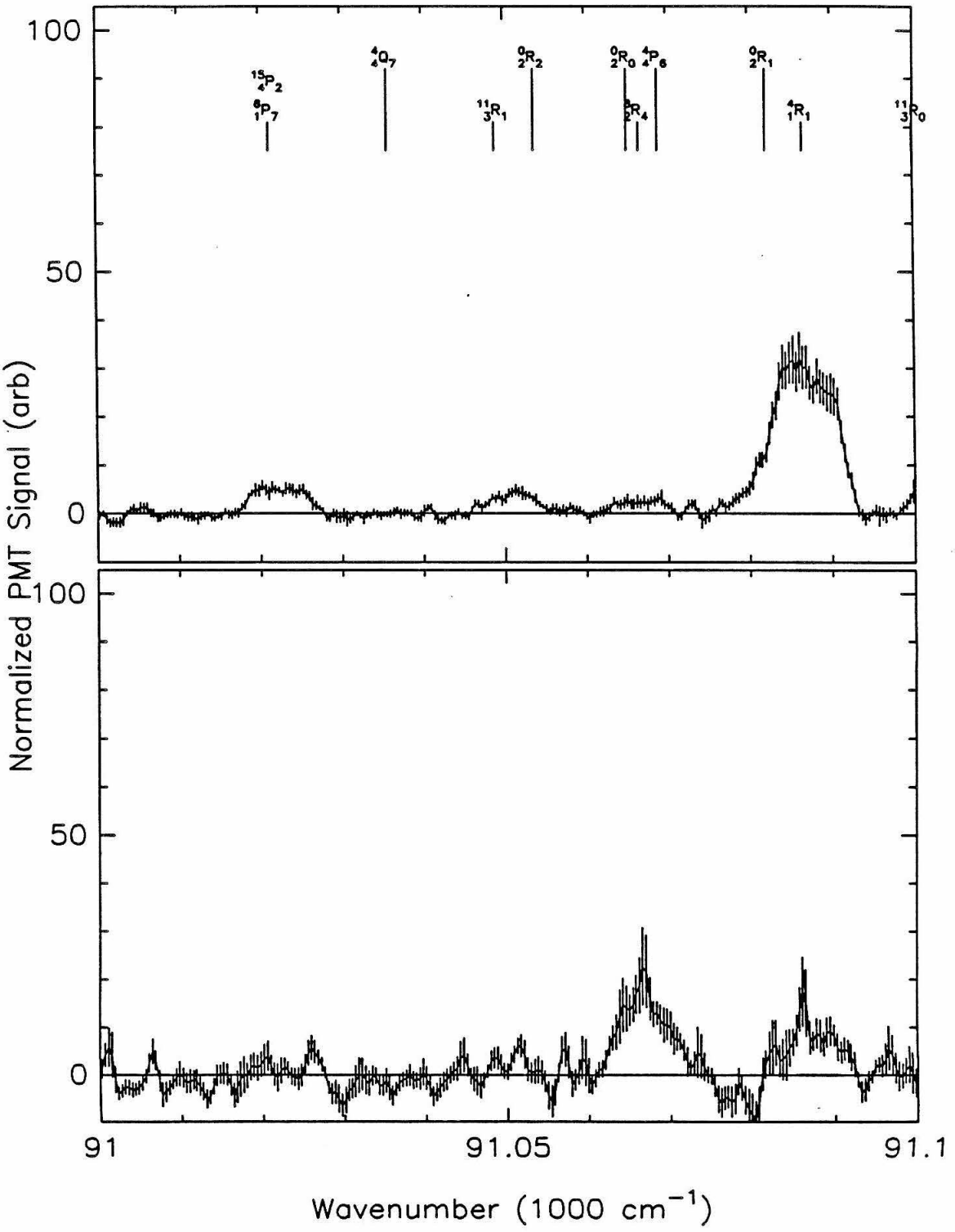
100
50
0
100
50
0
Normalized PMT Signal (arb)
$^{15}_{4}P_2$
$^{6}_{1}P_7$
$^{4}_{4}Q_7$
$^{11}_{3}R_1$
$^{0}_{2}R_2$
$^{0}_{2}R_0$
$^{6}_{2}R_4$
$^{4}_{4}P_6$
$^{0}_{2}R_1$
$^{4}_{1}R_1$
$^{11}_{3}R_0$
91
91.05
91.1
Wavenumber (1000 cm^{-1})

FIGURE 10: c.

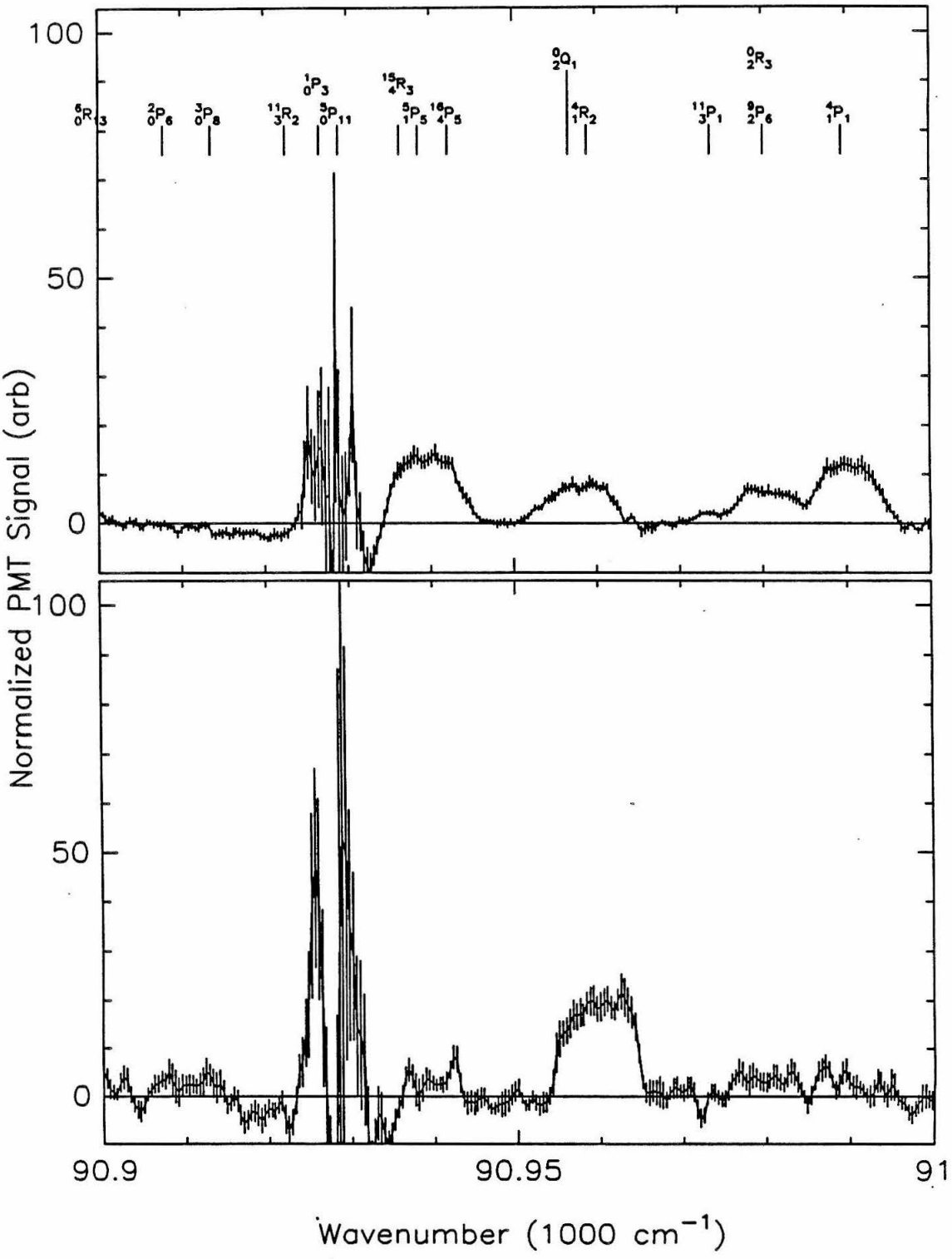
100
50
0
Normalized PMT Signal (arb)
$^{6}_{0}R_{3}$
$^{2}_{0}P_{6}$
$^{3}_{0}P_{8}$
$^{11}_{3}R_{2}$
$^{1}_{0}P_{3}$
$^{5}_{0}P_{11}$
$^{15}_{4}R_{3}$
$^{5}_{1}P_{5}$
$^{16}_{4}P_{5}$
$^{0}_{2}Q_{1}$
$^{4}_{1}R_{2}$
$^{11}_{3}P_{1}$
$^{0}_{2}R_{3}$
$^{9}_{2}P_{6}$
$^{4}_{1}P_{1}$
100
50
0
90.9
90.95
91
Wavenumber (1000 cm^{-1})

FIGURE 10: d.

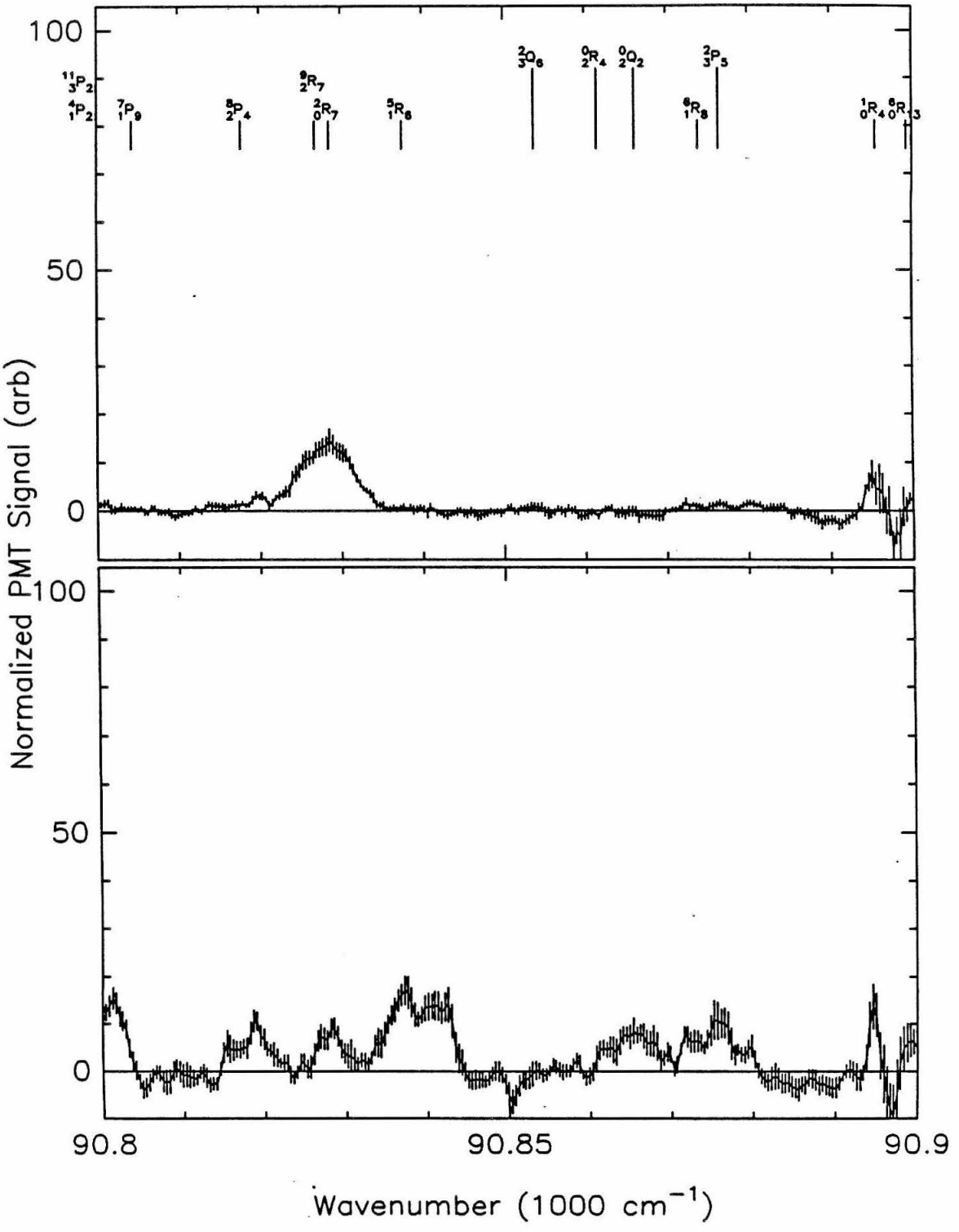
100
50
0
100
50
0
Normalized PMT Signal (arb)
$^{11}_{3}P_2$
$^{4}_{1}P_2$
$^{7}_{1}P_9$
$^{8}_{2}P_4$
$^{9}_{2}R_7$
$^{2}_{0}R_7$
$^{5}_{1}R_6$
$^{2}_{3}Q_6$
$^{0}_{2}R_4$
$^{0}_{2}Q_2$
$^{2}_{3}P_5$
$^{6}_{1}R_8$
$^{1}_{0}R_4$
$^{6}_{0}R_{13}$
90.8
90.85
90.9
Wavenumber (1000 cm^{-1})

FIGURE 10: e.

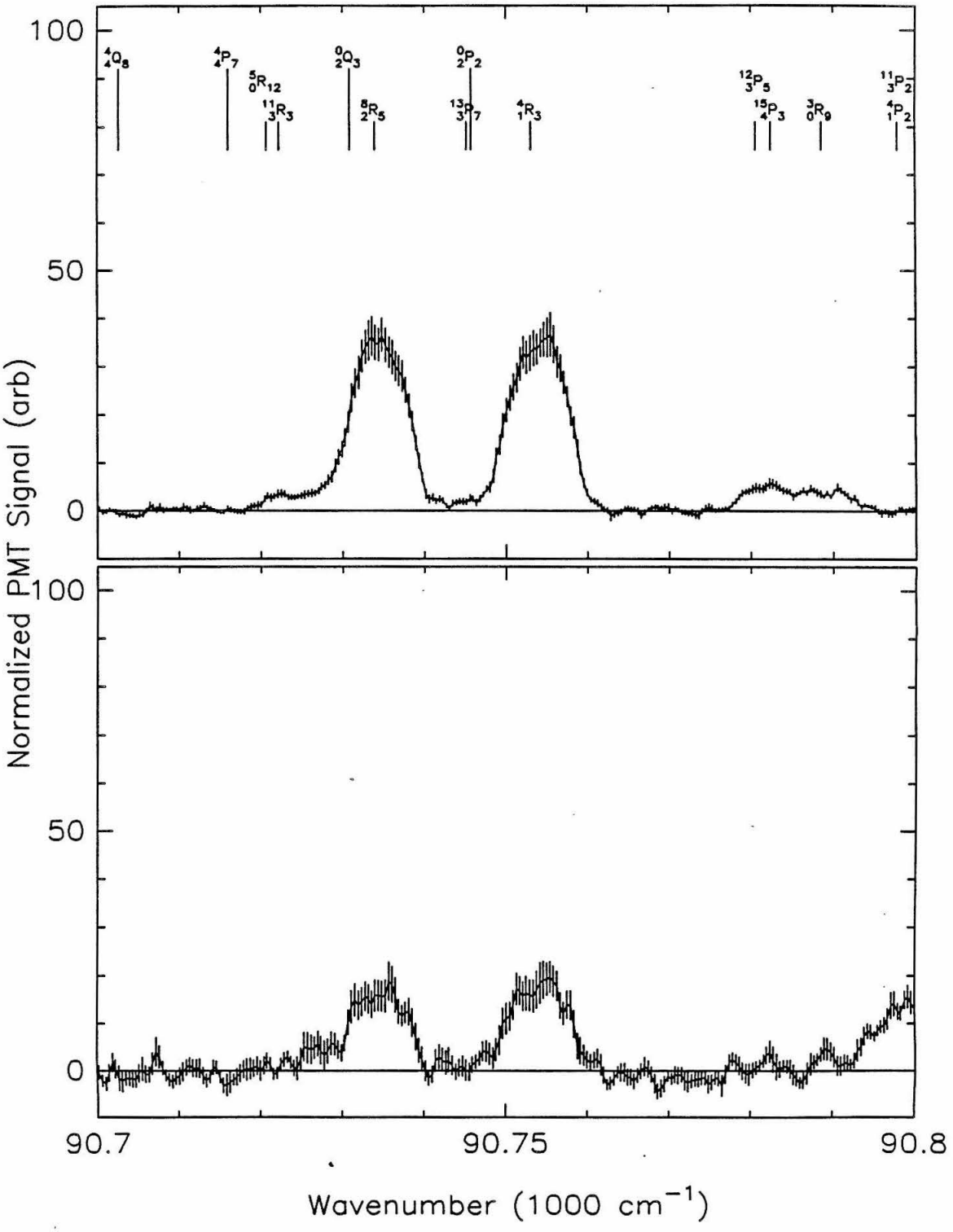
100
50
0
100
50
0
Normalized PMT Signal (arb)
$^{4}_{4}Q_{8}$
$^{4}_{4}P_{7}$
$^{5}_{0}R_{12}$
$^{11}_{3}R_{3}$
$^{0}_{2}Q_{3}$
$^{8}_{2}R_{5}$
$^{0}_{2}P_{2}$
$^{13}_{3}P_{7}$
$^{4}_{1}R_{3}$
$^{12}_{3}P_{5}$
$^{15}_{4}P_{3}$
$^{3}_{0}R_{9}$
$^{11}_{3}P_{2}$
$^{4}_{1}P_{2}$
90.7
90.75
90.8
Wavenumber (1000 cm^{-1})

FIGURE 10: f.

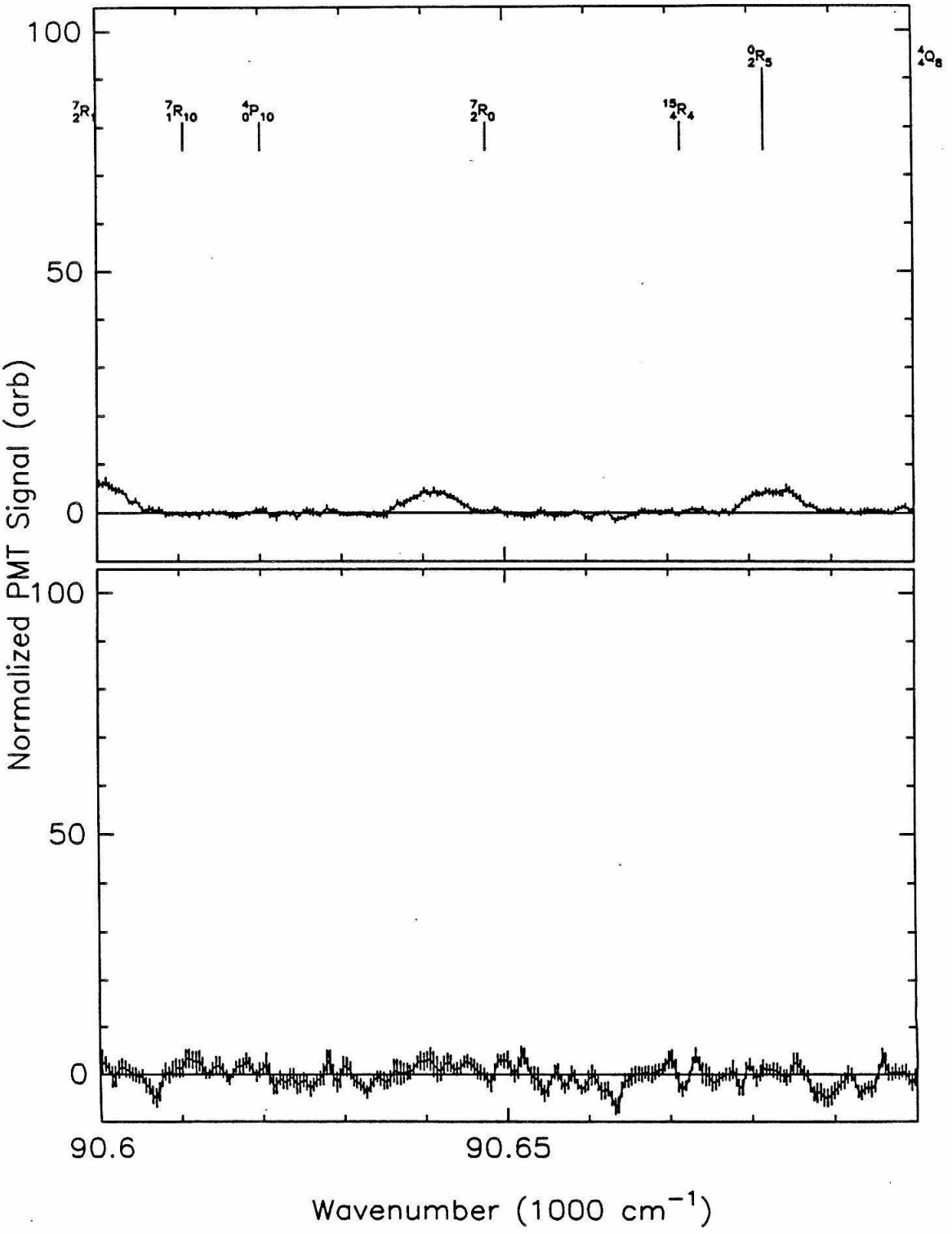
100
50
0
100
50
0
$^{7}_{2}R_{1}$
$^{7}_{1}R_{10}$
$^{4}_{0}P_{10}$
$^{7}_{2}R_{0}$
$^{15}_{4}R_{4}$
$^{0}_{2}R_{5}$
$^{4}_{4}Q_{8}$
Normalized PMT Signal (arb)
90.6
90.65
Wavenumber (1000 cm^{-1})

FIGURE 10: g.

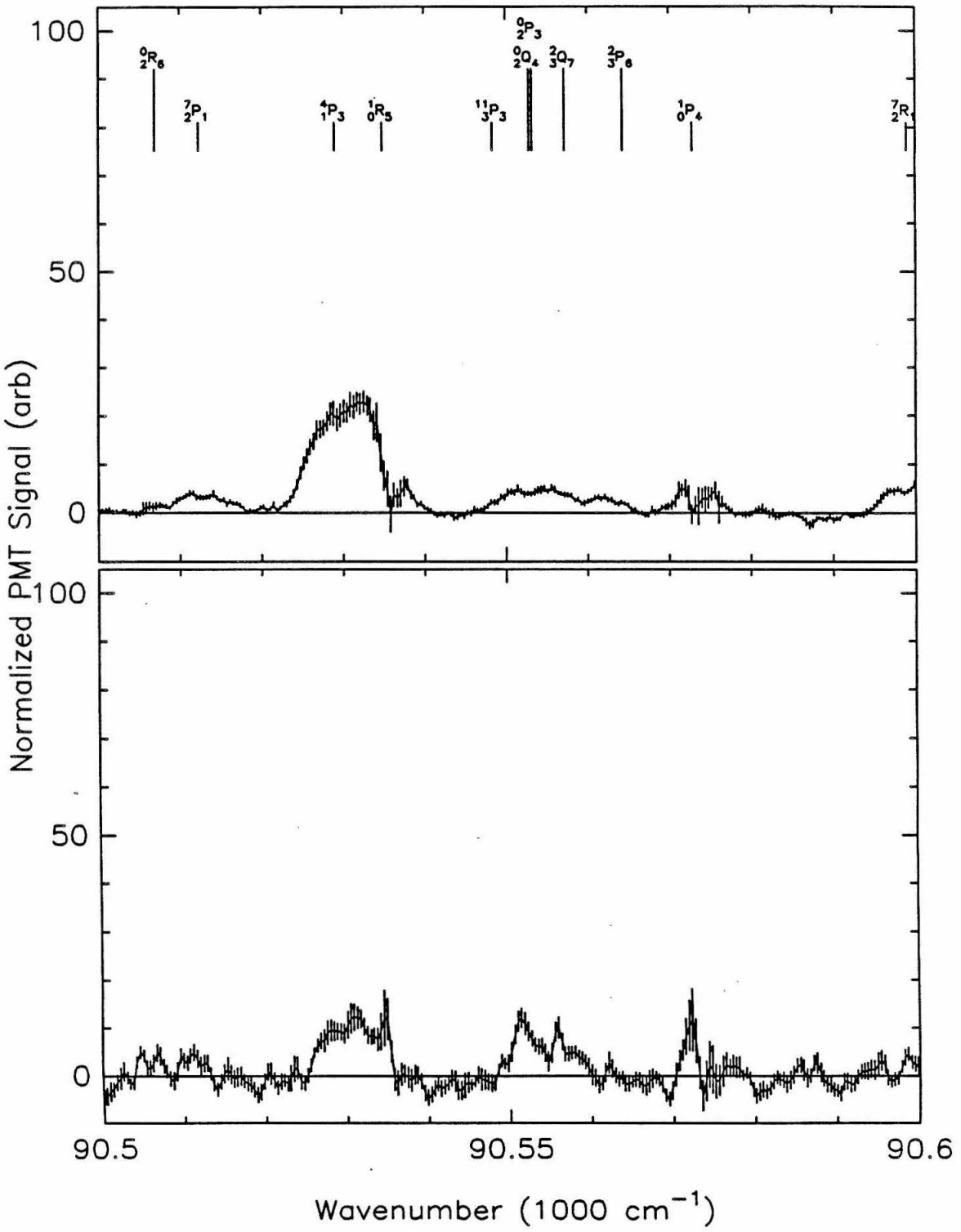
100
50
0
100
50
0
Normalized PMT Signal (arb)
$^{0}_{2}R_{6}$
$^{2}_{2}P_{1}$
$^{4}_{1}P_{3}$
$^{1}_{0}R_{5}$
$^{11}_{3}P_{3}$
$^{0}_{2}P_{3}$
$^{0}_{2}Q_{4}$
$^{2}_{3}Q_{7}$
$^{2}_{3}P_{6}$
$^{1}_{0}P_{4}$
$^{7}_{2}R_{4}$
90.5
90.55
90.6
Wavenumber (1000 cm^{-1})

FIGURE 10: h.

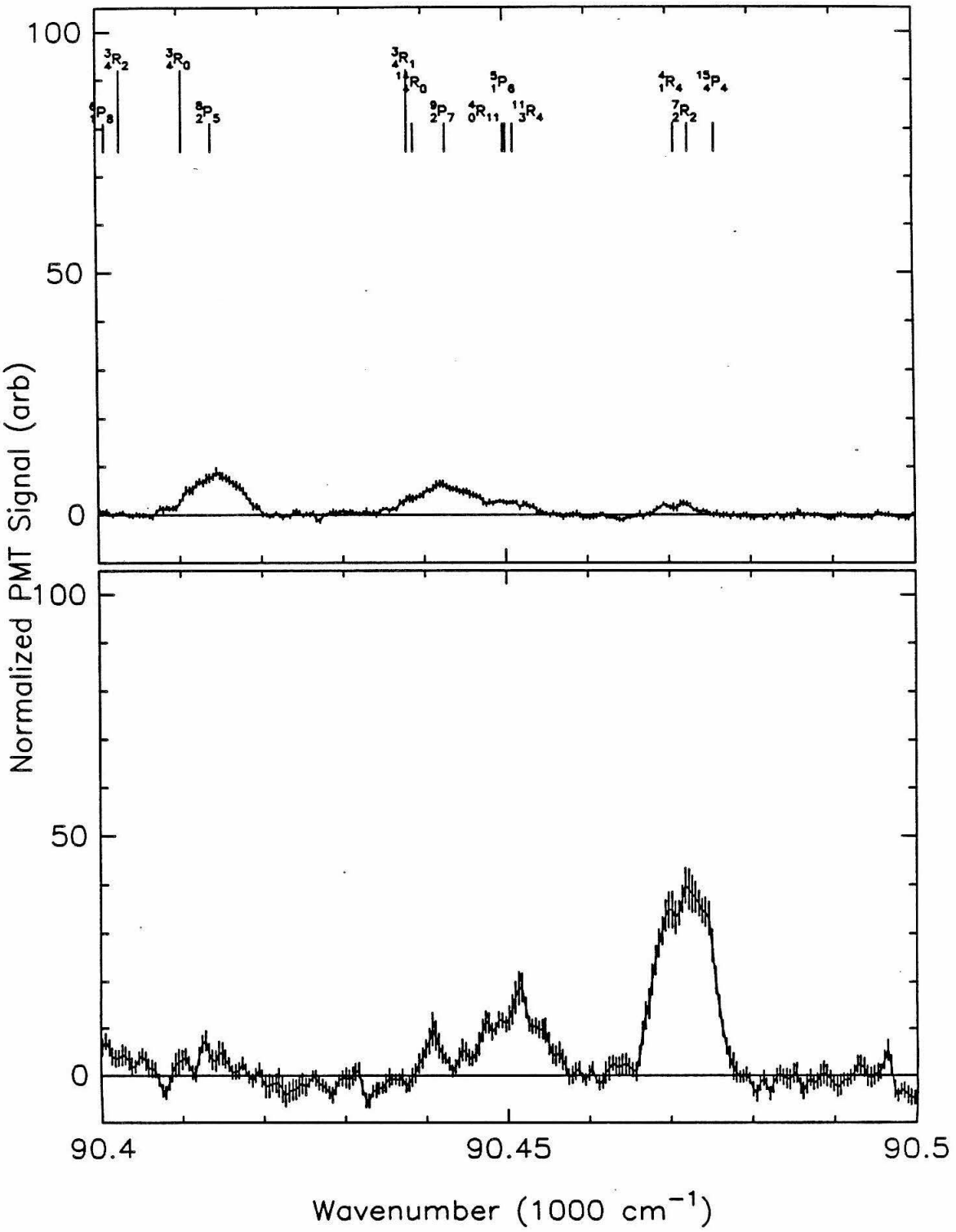
100
50
0
100
50
0
Normalized PMT Signal (arb)
90.4
90.45
90.5
Wavenumber (1000 cm^{-1})

FIGURE 10: i.

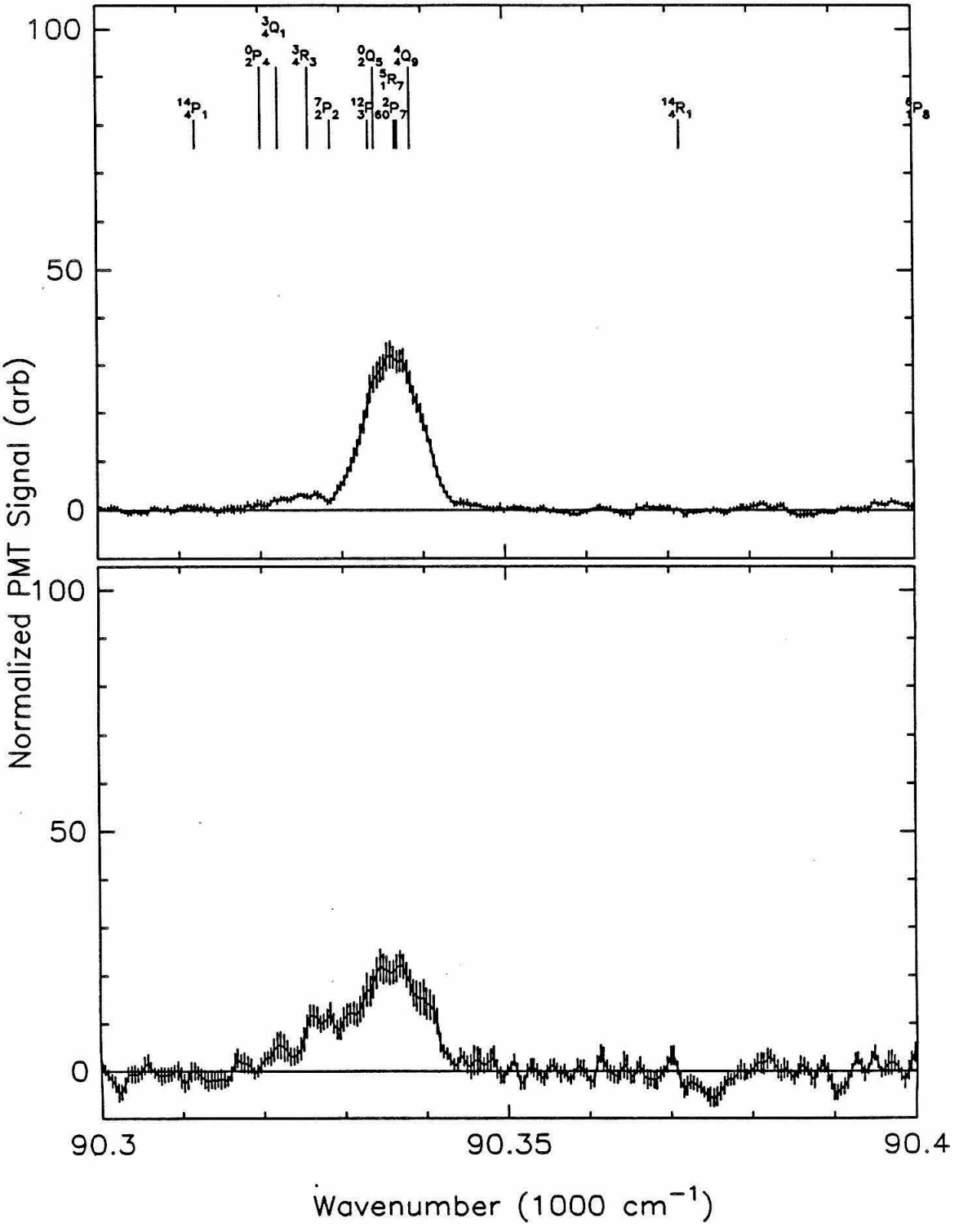
100
50
0
100
50
0
Normalized PMT Signal (arb)
$^{14}_{4}P_1$
$^{3}_{4}Q_1$
$^{0}_{2}P_4$
$^{3}_{4}R_3$
$^{7}_{2}P_2$
$^{12}_{3}P_6$
$^{0}_{2}Q_5$
$^{5}_{1}R_7$
$^{2}_{0}P_7$
$^{4}_{4}Q_9$
$^{14}_{4}R_1$
90.3
90.35
90.4
Wavenumber (1000 cm^{-1})

FIGURE 10: j.

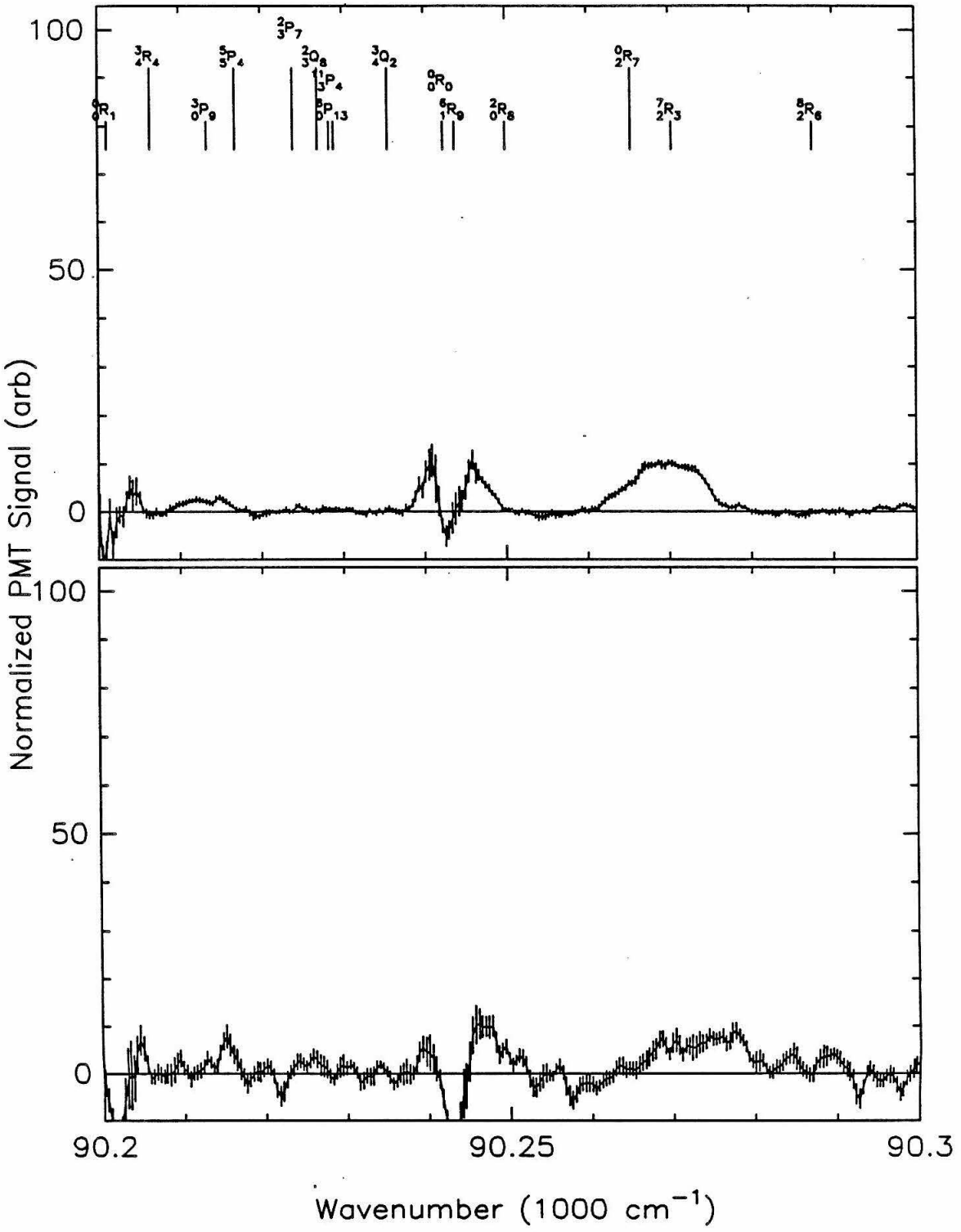
100
50
0
100
50
0
Normalized PMT Signal (arb)
90.2
90.25
90.3
Wavenumber (1000 cm^{-1})
$^{2}_{3}P_{7}$
$^{3}_{2}R_{4}$
$^{5}_{5}P_{4}$
$^{2}_{3}Q_{8}$
$^{1}_{3}P_{4}$
$^{3}_{4}Q_{2}$
$^{0}_{0}R_{0}$
$^{0}_{2}R_{7}$
$^{6}_{0}R_{1}$
$^{3}_{0}P_{9}$
$^{8}_{0}P_{13}$
$^{6}_{1}R_{9}$
$^{2}_{0}R_{8}$
$^{7}_{2}R_{3}$
$^{8}_{2}R_{6}$

FIGURE 10: k.

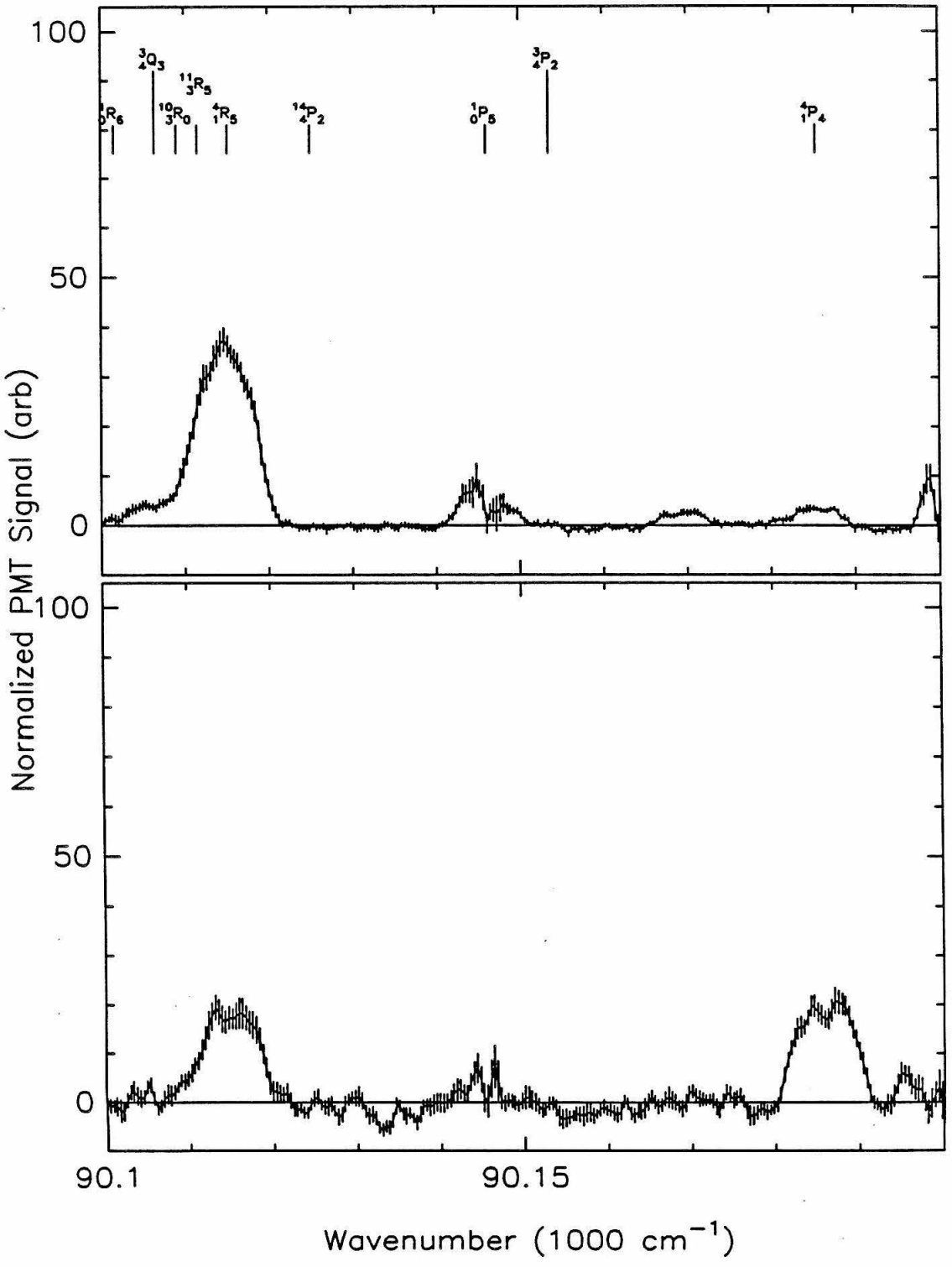
100
50
0
100
50
0
Normalized PMT Signal (arb)
$^{1}_{0}R_{6}$
$^{3}_{4}Q_{3}$
$^{11}_{3}R_{5}$
$^{10}_{3}R_{0}$
$^{4}_{1}R_{5}$
$^{14}_{4}P_{2}$
$^{1}_{0}P_{5}$
$^{3}_{4}P_{2}$
$^{4}_{1}P_{4}$
90.1
90.15
Wavenumber (1000 cm^{-1})

FIGURE 10: l.

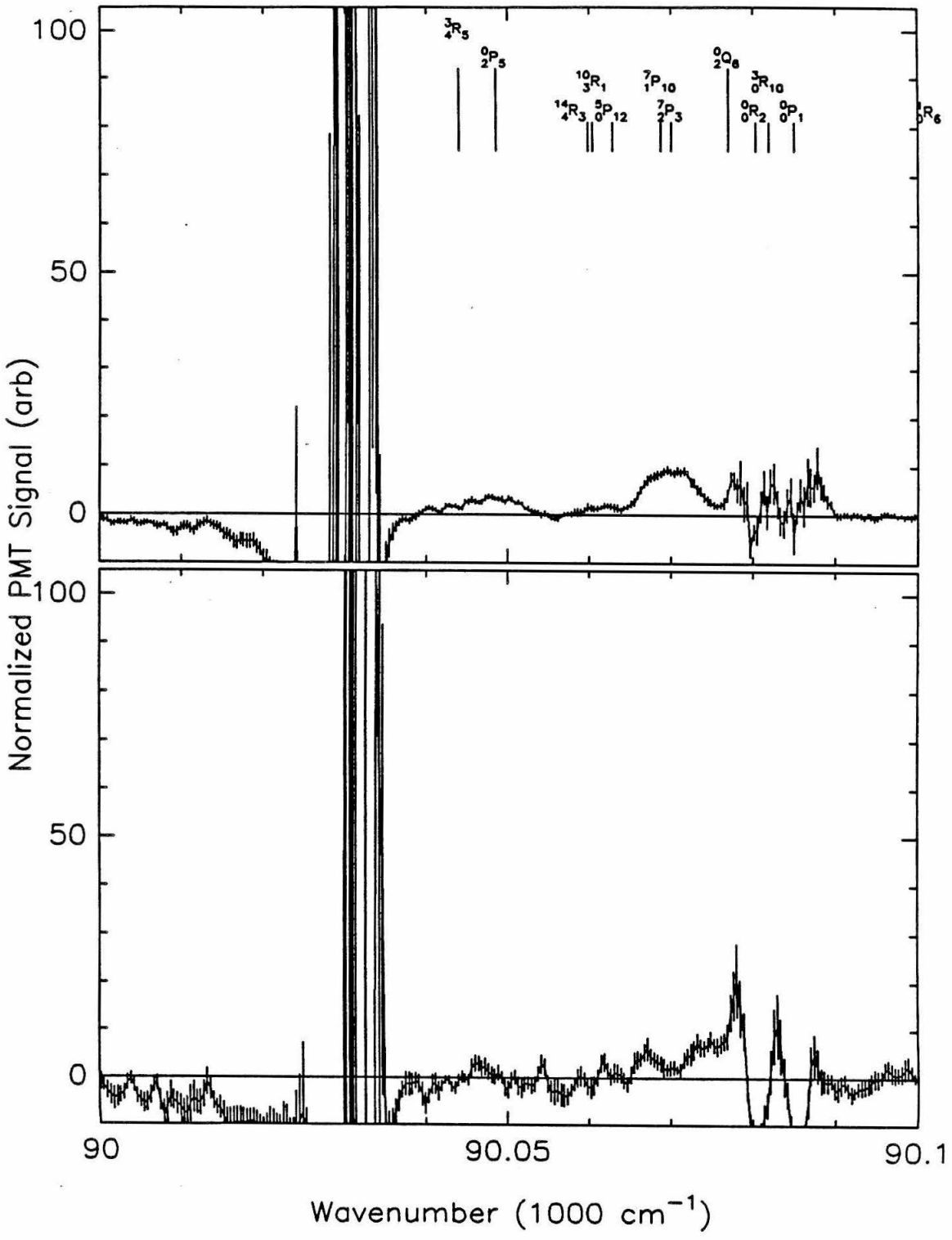
100
50
0
100
50
0
Normalized PMT Signal (arb)
90
90.05
90.1
Wavenumber (1000 cm^{-1})
$^{3}_{4}R_5$
$^{0}_{2}P_5$
$^{10}_{3}R_1$
$^{14}_{4}R_3$
$^{5}_{0}P_{12}$
$^{7}_{1}P_{10}$
$^{7}_{2}P_3$
$^{0}_{2}Q_6$
$^{3}_{0}R_{10}$
$^{0}_{0}R_2$
$^{0}_{0}P_1$

FIGURE 10: m.

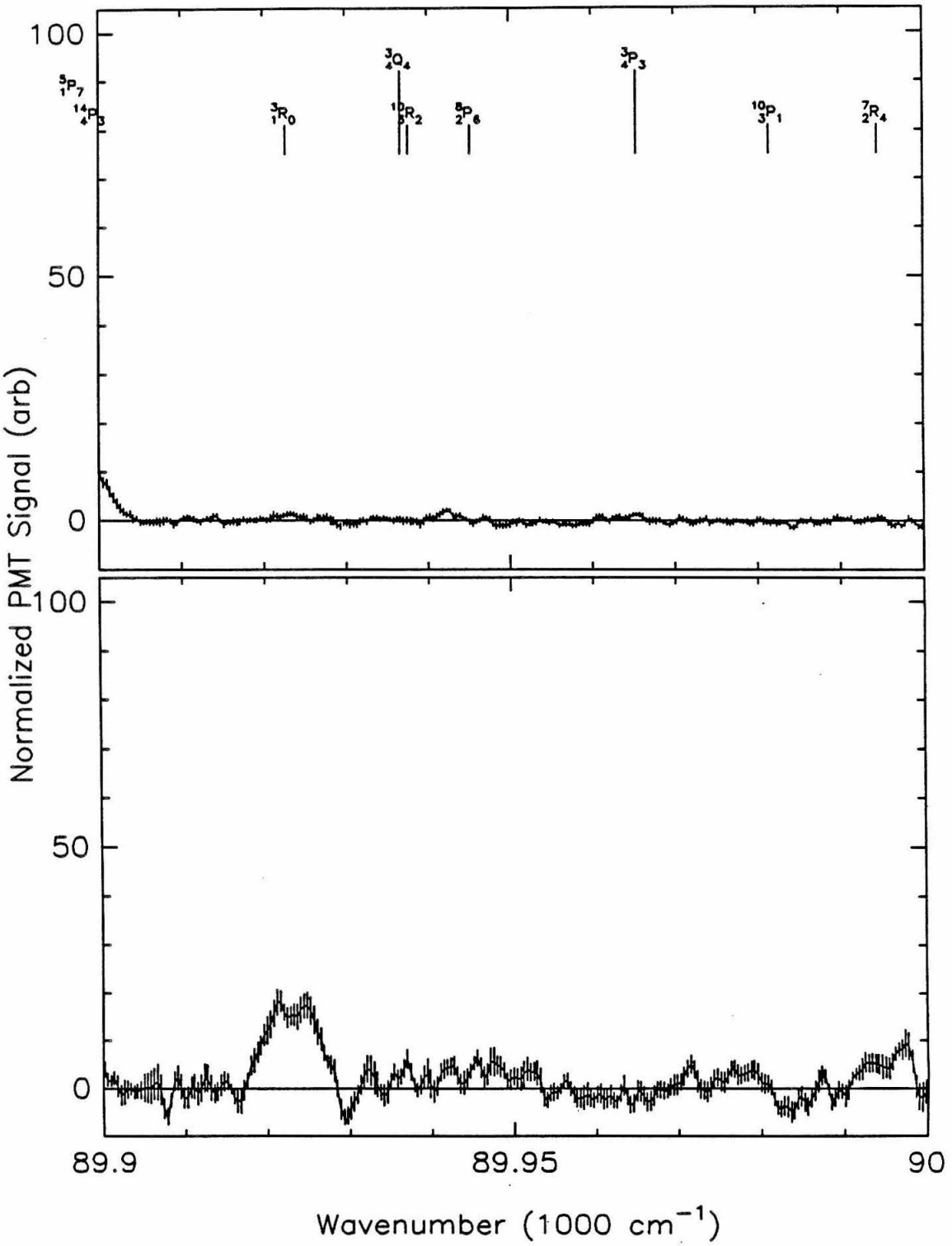
100
50
0
100
50
0
Normalized PMT Signal (arb)
$^{5}_{1}P_{7}$
$^{14}_{4}P_{3}$
$^{3}_{1}R_{0}$
$^{3}_{2}O_{4}$
$^{10}_{5}R_{2}$
$^{8}_{2}P_{6}$
$^{3}_{4}P_{3}$
$^{10}_{3}P_{1}$
$^{7}_{2}R_{4}$
89.9
89.95
90
Wavenumber (1000 cm^{-1})

FIGURE 10: n.

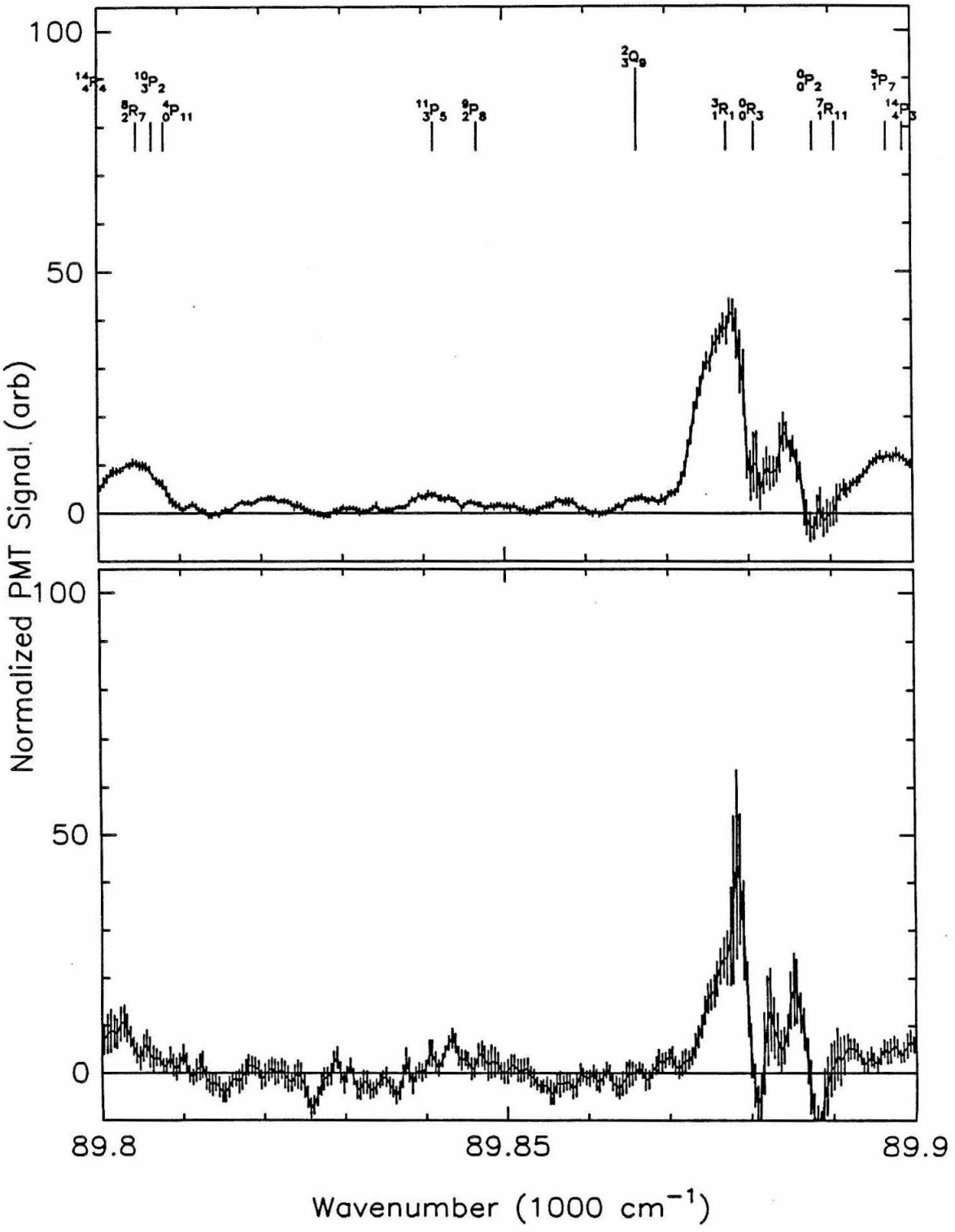
100
50
0
Normalized PMT Signal (arb)
$^{14}_{4}P_{4}$
$^{10}_{3}P_{2}$
$^{8}_{2}R_{7}$
$^{4}_{0}P_{11}$
$^{11}_{3}P_{5}$
$^{9}_{2}P_{8}$
$^{2}_{3}Q_{9}$
$^{3}_{1}R_{1}$
$^{0}_{0}R_{3}$
$^{0}_{0}P_{2}$
$^{7}_{1}R_{11}$
$^{5}_{1}P_{7}$
$^{14}_{4}P_{5}$
100
50
0
89.8
89.85
89.9
Wavenumber (1000 cm^{-1})

FIGURE 10: o.

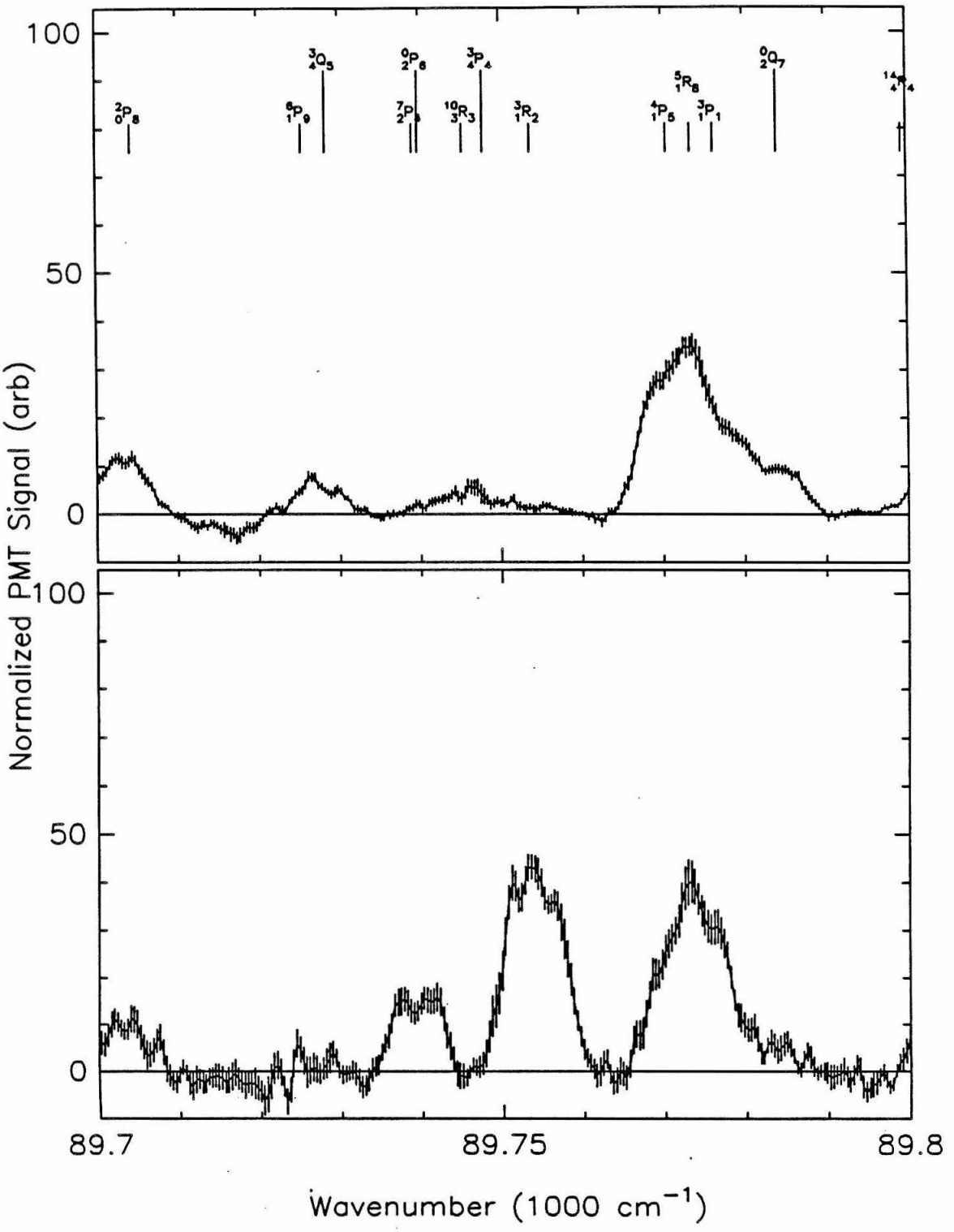
100
50
0
100
50
0
Normalized PMT Signal (arb)
$^{2}_{0}P_{8}$
$^{6}_{1}P_{9}$
$^{3}_{4}Q_{5}$
$^{0}_{2}P_{6}$
$^{7}_{2}P_{7}$
$^{10}_{3}R_{3}$
$^{3}_{4}P_{4}$
$^{3}_{1}R_{2}$
$^{4}_{1}P_{5}$
$^{5}_{1}R_{8}$
$^{3}_{1}P_{1}$
$^{0}_{2}Q_{7}$
$^{14}_{4}R_{4}$
89.7
89.75
89.8
Wavenumber (1000 cm^{-1})

FIGURE 10: p.

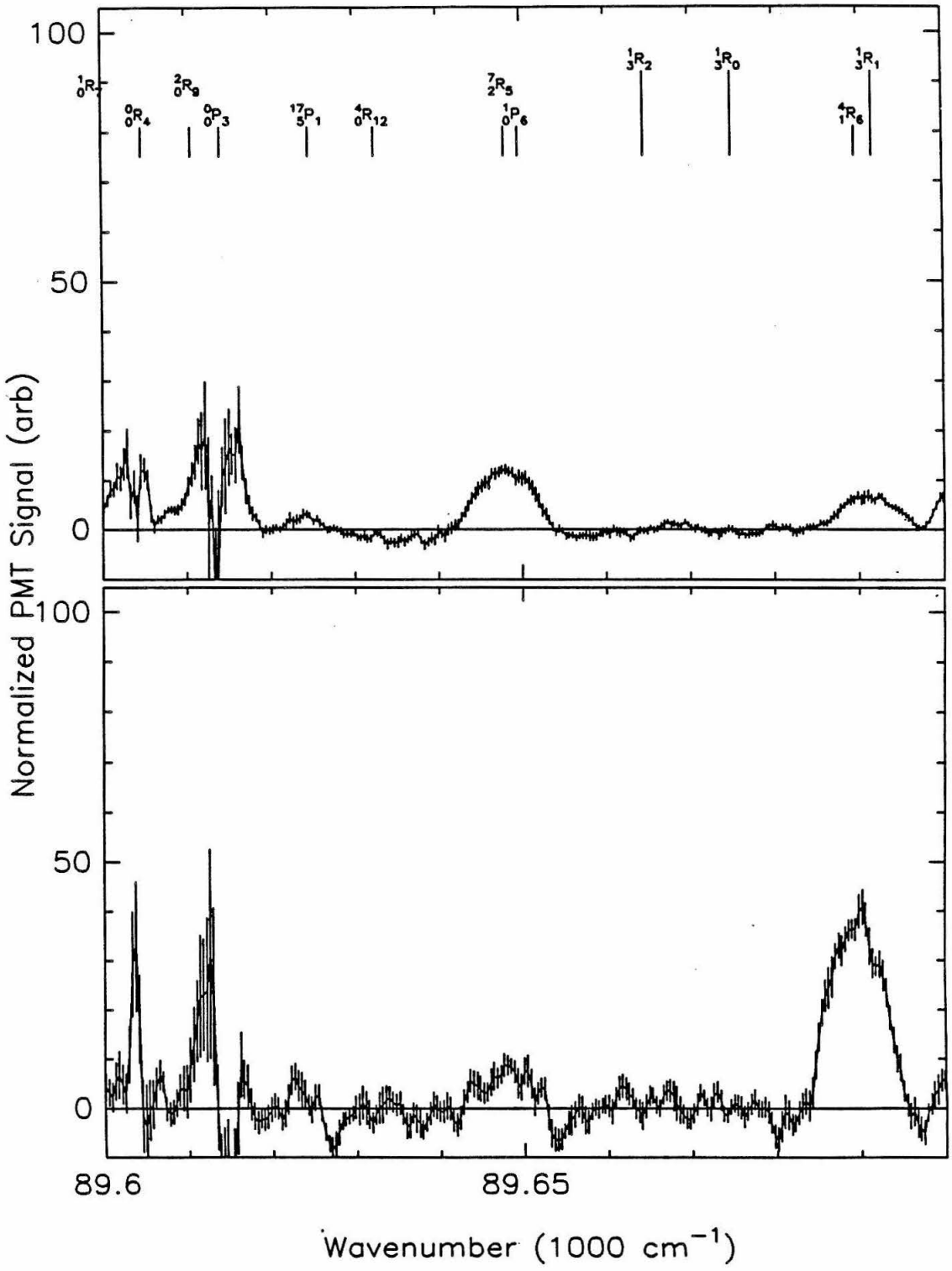
100
50
0
100
50
0
Normalized PMT Signal (arb)
$^{1}_{0}R_{7}$
$^{0}_{0}R_{4}$
$^{2}_{0}R_{9}$
$^{0}_{0}P_{3}$
$^{17}_{5}P_{1}$
$^{4}_{0}R_{12}$
$^{7}_{2}R_{5}$
$^{1}_{0}P_{6}$
$^{1}_{3}R_{2}$
$^{1}_{3}R_{0}$
$^{4}_{1}R_{6}$
$^{1}_{3}R_{1}$
89.6
89.65
Wavenumber (1000 cm^{-1})

FIGURE 10: q.

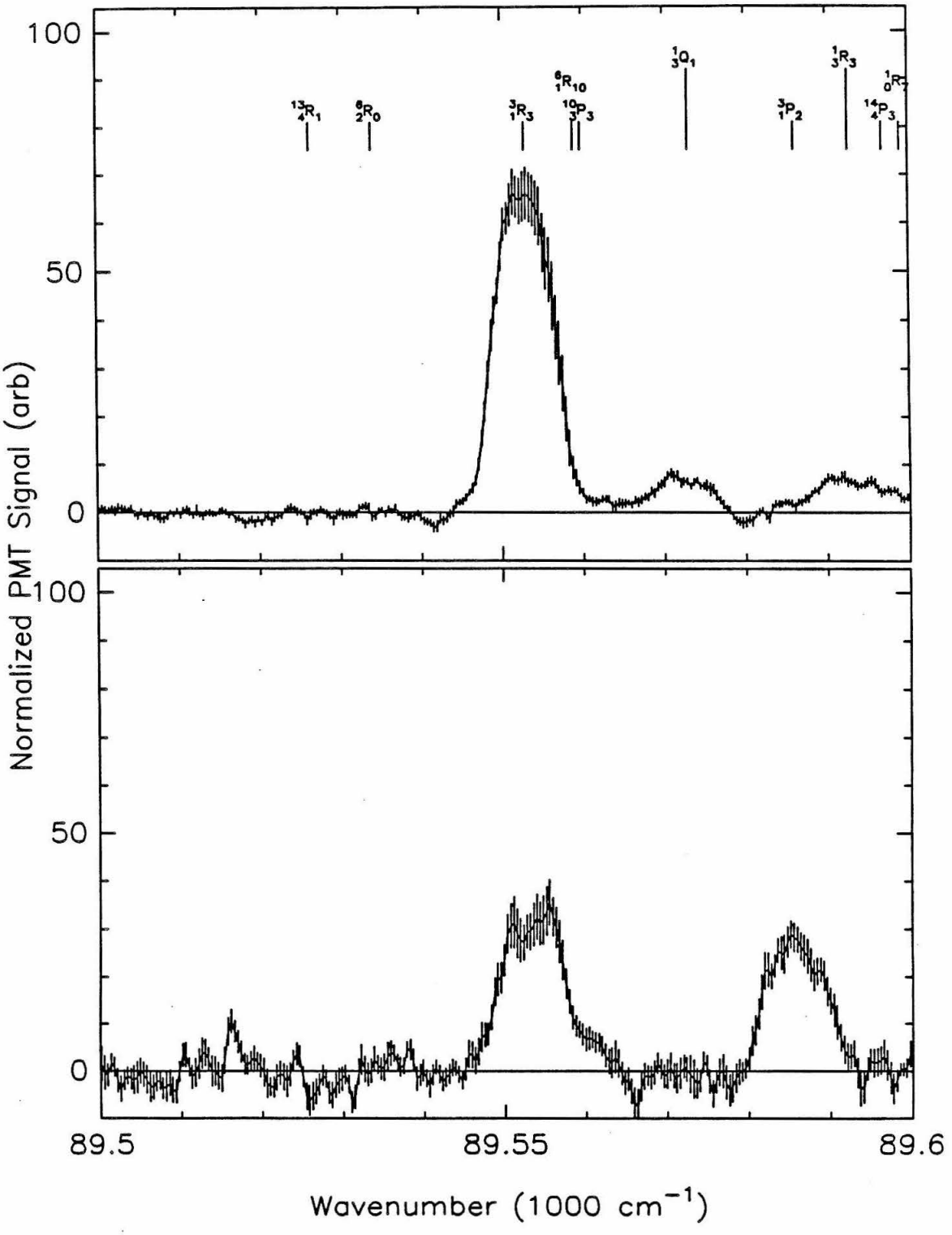
100
50
0
100
50
0
Normalized PMT Signal (arb)
$^{13}_{4}R_1$
$^{6}_{2}R_0$
$^{3}_{1}R_3$
$^{6}_{1}R_{10}$
$^{10}_{3}P_3$
$^{1}_{3}Q_1$
$^{3}_{1}P_2$
$^{1}_{3}R_3$
$^{14}_{4}P_3$
89.5
89.55
89.6
Wavenumber (1000 cm^{-1})

FIGURE 10: r.

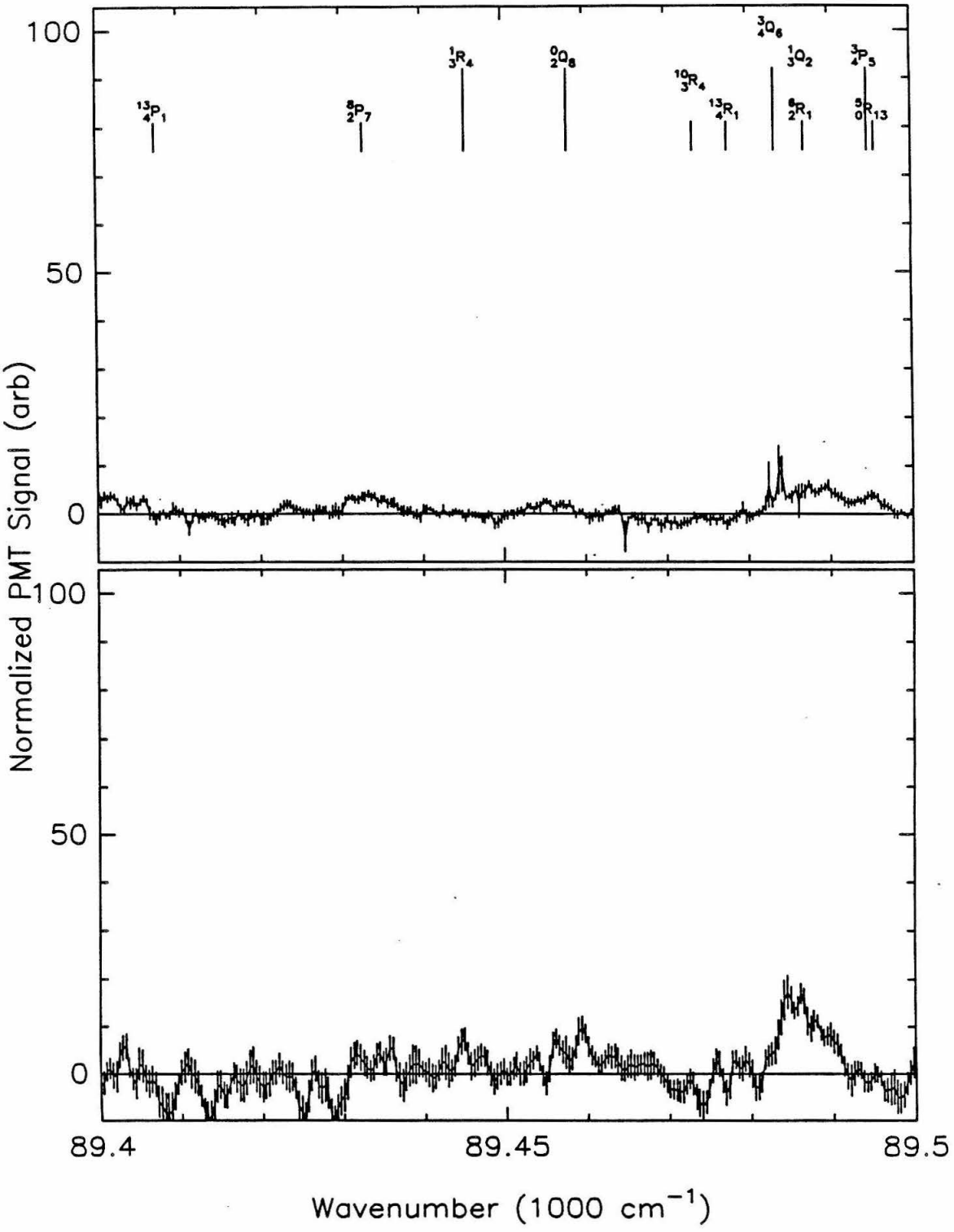
100
50
0
100
50
0
Normalized PMT Signal (arb)
$^{13}_{4}P_1$
$^{8}_{2}P_7$
$^{1}_{3}R_4$
$^{0}_{2}Q_8$
$^{10}_{3}R_4$
$^{13}_{4}R_1$
$^{3}_{4}Q_6$
$^{1}_{3}Q_2$
$^{8}_{2}R_1$
$^{3}_{4}P_5$
$^{5}_{0}R_{13}$
89.4
89.45
89.5
Wavenumber (1000 cm^{-1})

FIGURE 10: s.

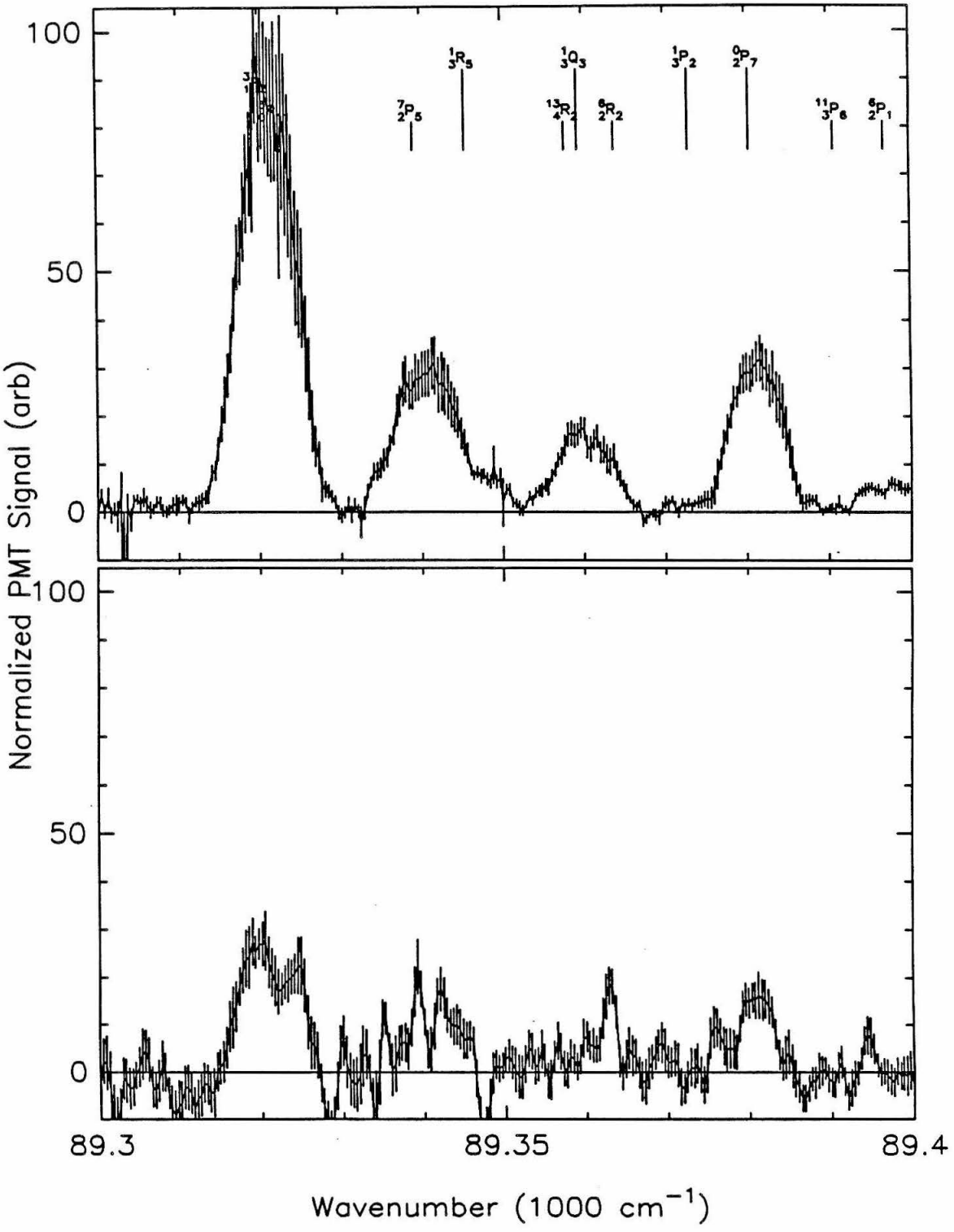
100
50
0
Normalized PMT Signal (arb)
100
50
0
89.3
89.35
89.4
Wavenumber (1000 cm^{-1})

FIGURE 10: t.

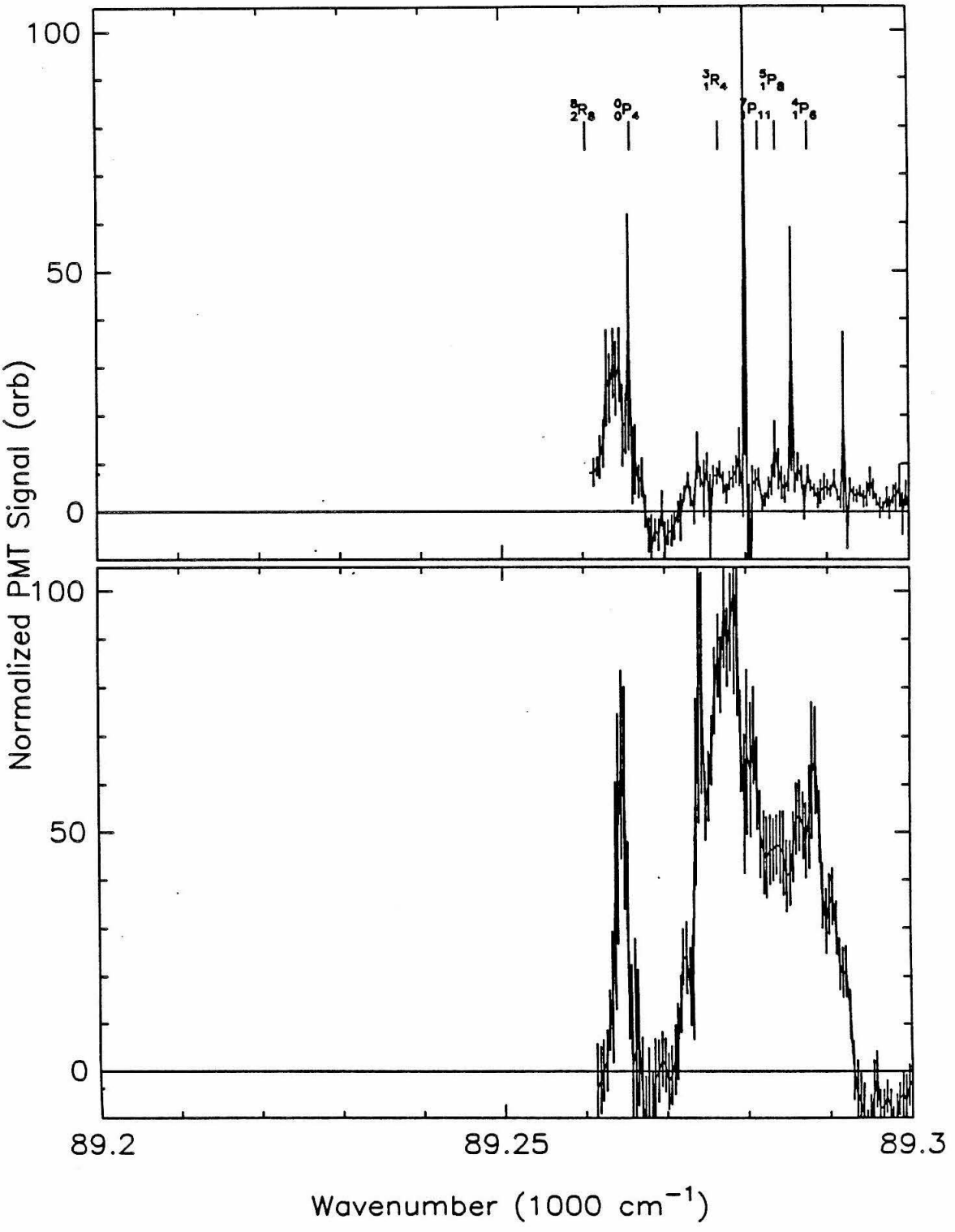
100
50
0
100
50
0
Normalized PMT Signal (arb)
$^{8}_{2}R_{8}$
$^{0}_{0}P_{4}$
$^{3}_{1}R_{4}$
$^{7}_{1}P_{11}$
$^{5}_{1}P_{8}$
$^{4}_{1}P_{6}$
89.2
89.25
89.3
Wavenumber (1000 cm^{-1})

FIGURE 11.

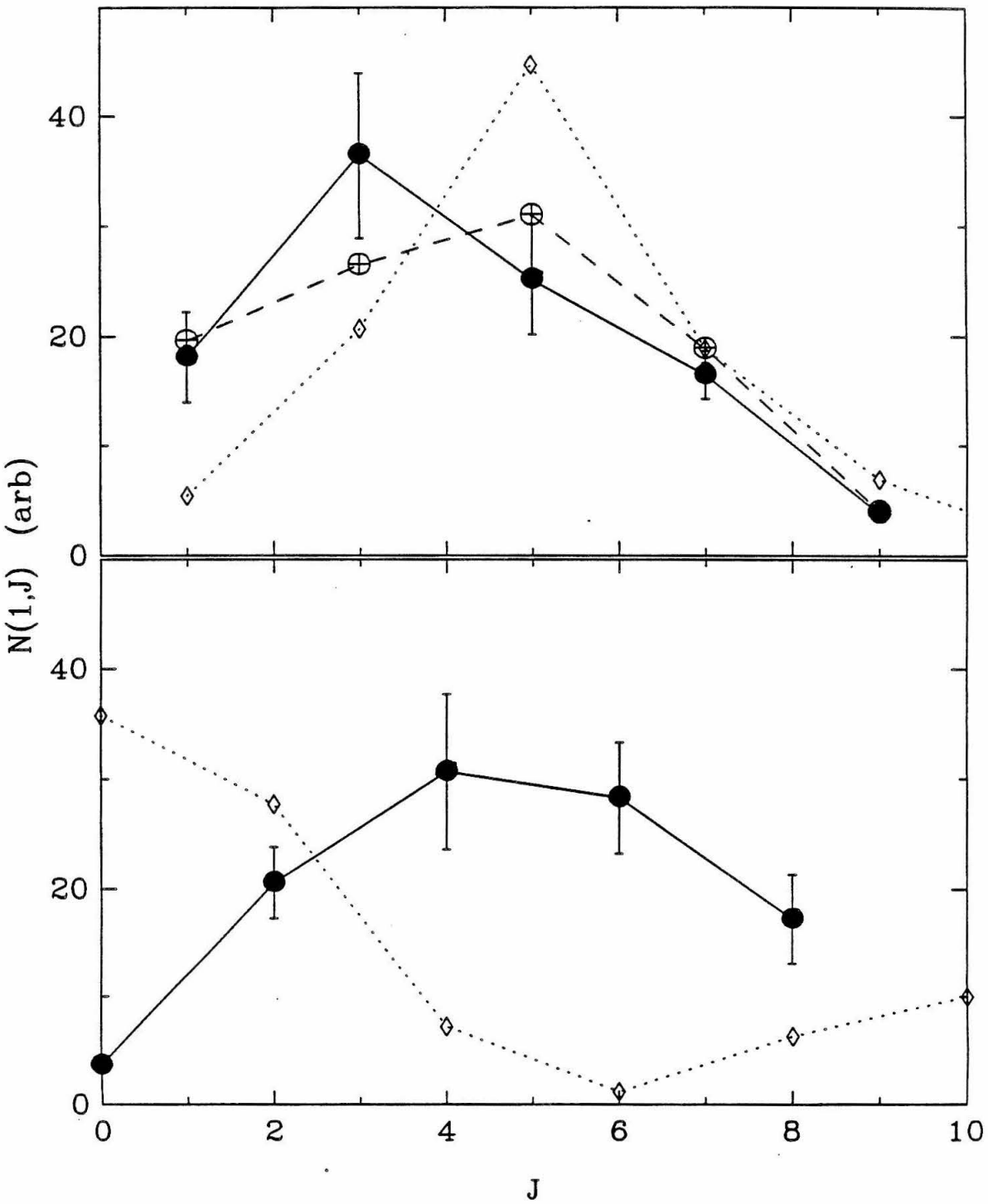

FIGURE 12.

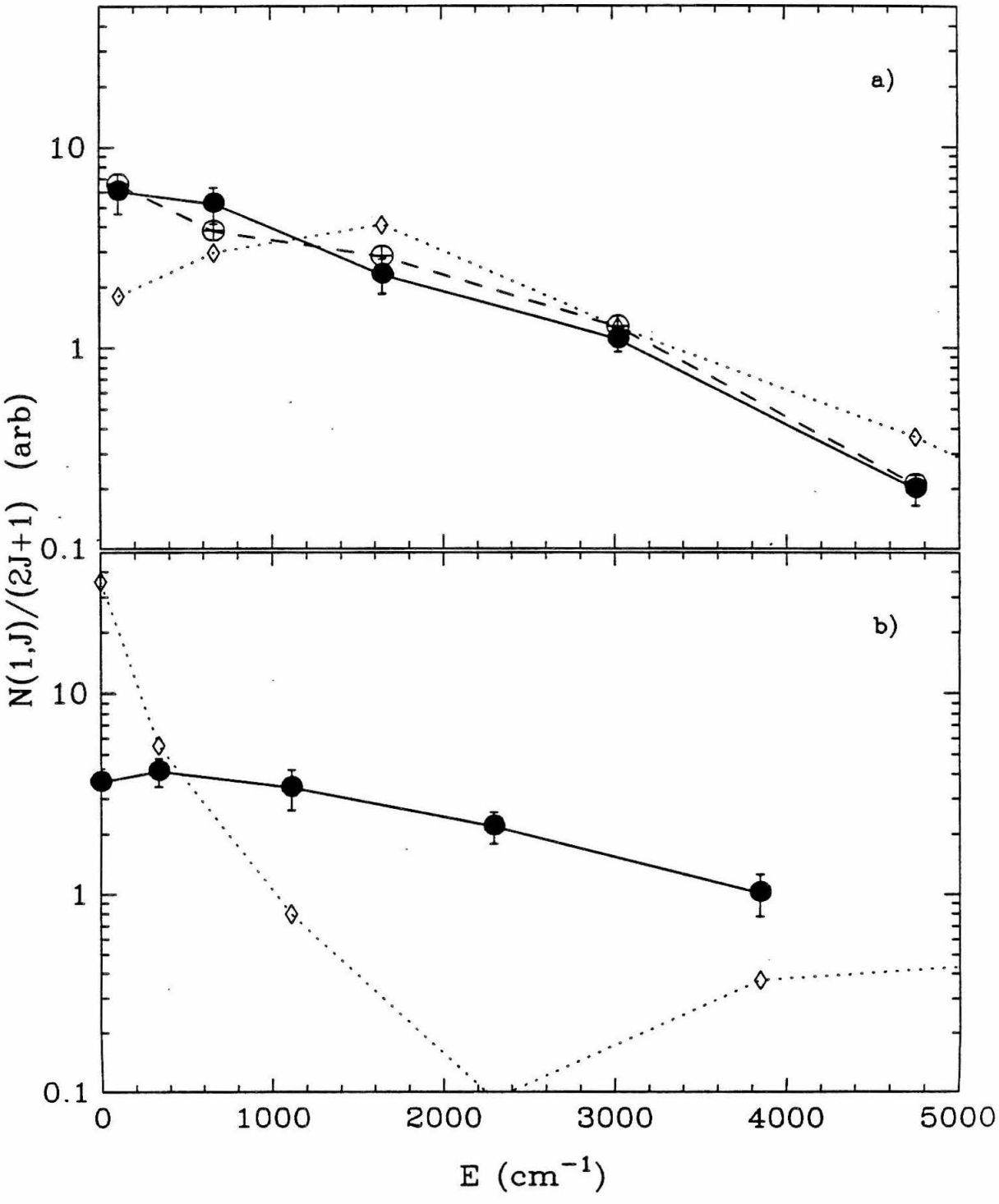

CHAPTER 8

HYDROGEN EXCHANGE REACTION EXPERIMENTS

I. INTRODUCTION

In this chapter the status of the hydrogen exchange reaction experiments is reported. This experiment has not yet been successful. The first section describes the minor differences in the experimental apparatus and procedure for this experiment compared with what was used for the H_2CO photodissociation experiment described in the previous chapter. The second section presents typical results, while the third section discusses the problems to date and the attempts to rectify them.

II. EXPERIMENTAL DETAILS

A. Apparatus

The apparatus used for the hydrogen exchange reaction is essentially identical to that used for the H_2CO photodissociation reaction, with only a few modifications.

The Quanta Ray laser system (DCR-2A, PDL-2, and WEX) is configured in the exact same configuration as for the H_2 LIF experiments and the H_2CO photodissociation reaction described in the previous two chapters. The Molectron laser system (MY-34 and DL-18) is configured with only the longitudinally pumped amplifier. This dye laser operates with the dye Rhodamine 590 tetrafluoroborate in methanol. Typical output powers are 67.3 mJ pulse^{-1} at 560 nm when pumped with 253 mJ pulse^{-1} of the Nd:YAG second harmonic at 532 nm, a conversion efficiency of 26.5%. The UV pulse energy at 280 nm is 15.5 mJ pulse^{-1}, a conversion efficiency of 23.1%.

The optical alignment of the lasers and the three compartment cell is identical to that used before. The electronics are used in the exact same manner as before.

The one major change was the addition of a VUV bandpass filter just before the solar blind photomultiplier. The quantum efficiency of the CsI photocathode rises by at least two orders of magnitude when going from 330 nm, the wavelength of the photolysis laser in the H_2CO experiments and the UV used to generate the VUV laser radiation, and 280 nm, the approximate wavelength for the photolysis laser in the experiments in this chapter. A VUV interference filter was purchased from Acton Research Corporation. The original filter, serial number 120-3-25A, had a peak transmission of 19% at 142.5 nm and a FWHM bandwidth of 29 nm. This filter was destroyed after an overnight exposure to air, apparently from a reaction of absorbed HI with atmospheric water. The replacement filter, # 130-9-8A, has a peak transmission of 16.8% at 141.5 nm and a FWHM bandwidth of 23.5 nm.

This filter is protected when not in use by storage in a vacuum dessicator. The current version of the LIF cell has a LiF window between the filter and the sample region. While this extra window reduces sensitivity to some degree, it protects the filter and the window of the PMT. The region between the LiF window and the PMT is kept evacuated by a mechanical pump.

In order to reduce the presence of I_2 in the sample cell, a stainless steel cold finger was added to the sample cell. This is kept cool using a dry ice and acetone slush whenever HI is present in the cell.

B. Photodissociation Wavelengths

The exact wavelength of the photolysis laser is not as critical for this experiment as it was for the H_2CO experiment. In that experiment, the desired photolysis wavelength had to coincide with a rotational band of the molecule. In the current experiment, the excited state is the dissociative continuum of HI, and therefore, an error of a few wavenumbers in position would have a minuscule effect.

The choice of photolysis wavelength has several effects on the experiment. First, the absorption cross section is a function of wavelength. Second, the dissociation channel, and therefore the dissociation energy, depends on the wavelength. Third, the energy of the translationally hot H atoms also depends on the photolysis wavelength. Fourth, the sensitivity of the PMT to scattered laser radiation is a function of wavelength.

In the wavelength region reachable with the doubled output of a dye laser operating on Rhodamine 590, the HI absorption cross section approximately doubles for every 10 nm decrease in photolysis wavelength.[1] In HI photolysis, two dissociation channels are possible: one gives ground state I atoms while the other yields electronically excited I atoms (see discussion in chapter 4). The excited

state channel begins to become important around 280 nm. The average laboratory energy of the recoiling H atom is given by[1]

$$\langle E_{\mathrm{H}} \rangle = \frac{m_{\mathrm{I}}}{m_{\mathrm{HI}}} \left(\frac{hc}{\lambda} - D_0^0 + kT \right) + \frac{m_{\mathrm{H}}}{m_{\mathrm{HI}}} \frac{3}{2} kT$$

which includes the contributions from the initial translational and rotational motion of the HI. The H atom will have an average laboratory translational energy of 1.237 and 1.389 eV following photolysis at 290 and 280 nm, respectively. Several different wavelengths within this region were tried in an attempt to get this experiment to work.

C. Time Delay

The time delay between the two lasers was measured and adjusted in the same manner as for the H_2CO experiment. Time delays from 10 ns to 100 ns were used in an attempt to get this experiment to work.

D. Sample

The HI for these experiments was purchased from Matheson. The material from the gas cylinder is purified before use by a vacuum distillation. Several liquid nitrogen freeze-pump-thaw cycles are used to eliminate any noncondensibles (usually H_2). In one case, more than 80% of the gas from the cylinder was noncondensible in liquid nitrogen. The HI was then distilled while still under vacuum from a glass bulb immersed in dry ice/acetone to a glass bulb immersed in liquid nitrogen. With careful technique, it was possible to obtain snow white HI without the slightest tinge of yellow to it. The purified HI is stored in a black painted glass bulb in a dewar filled with dry ice until needed.

The mixture of HI/H_2 for reactions was usually prepared at least 24 hr before use. The HI concentration was usually on the order of 2–5% in H_2. The H_2 was research purity (99.9999%) from Alpha Products and was used without further

purification. The gas mixture was stored in a blackened glass bulb in a regrigerator until use.

E. Experimental Procedure

The experimental procedure for the hydrogen exchange reaction experiments is the same as for the H_2CO photodissociation experiment with only two minor changes. First, the sample cell is filled with approximately 10 torr of pure HI and then evacuated just before the first HI/H_2 sample is introduced. This tends to saturate the walls of the cell with HI and reduces the consumption of HI by the cell during a scan. Second, much shorter scans were taken, usually only 6 nm in the visible. The scan rate stayed the same at 0.5 $nm\,min^{-1}$

III. DISCUSSION

The hydrogen exchange reaction has been attempted numerous times to date with no success. Figure 1 shows the results from the most recent experiment. The strong saturated lines are from the H_2 reagent which have a signal too strong for the "auto subtract" on the gated integrator to handle. There are no lines present which can be assigned to a vibrationally excited product molecule.

At the moment there are no clear explanations as to why this experiment hasn't worked. It is obvious that the culprit is not the LIF detection scheme since it was possible to detect H_2 from H_2CO photodissociation, as was shown in the previous chapter. The HI absorption cross section[1] at these wavelengths is on the order of 0.1 Mb, while the H_2CO absorption cross section[2] at the peak of the $2_0^1 4_0^3$ vibronic band is only 0.02 Mb, and is obviously much less at the weak $^rR_4$ line. This means that there are at least 5 times as many initial H atoms in the exchange reaction as there were initial H_2 molecules in the H_2CO photodissociation reaction.

Of course, these H atoms are not detectable until they undergo a reactive collision to form a H_2 molecule in a vibrationally excited state. The reactive cross section[3] for the hydrogen exchange reaction is on the order of 0.5–1.0 Å^2. When photolyzed with 280 nm laser radiation, the H atom will have an average laboratory translational energy of 1.389 eV, and will have an average relative velocity with a H_2 target of 0.939 eV, *i.e.*, the relative velocity is 1.65×10^4 m s^{-1}. The H_2 reagent is usually present at a pressure on the order of 5 torr. Therefore, the average time between reactive collisions is on the order of 40 ns. Time delays as long as 100 ns were used. Thus, most of the H atoms present should have reacted in the time between the photolysis and the probe laser. Since there 5 times as many H atoms as H_2 molecules in the H_2CO experiment, one would expect 5 times as much signal for this experiment. Yet nothing at all has been seen.

The VUV bandpass filter will reduce the detection sensitivity by at least a factor of 6 because the maximum transmission is 16%. The actual reduction expected for the (3–1) band is a factor of 13 because the emission distribution does not overlap the filter transmission peak. Even including the filter transmission, however, does not reduce the expected signal from the hydrogen exchange reaction to less than one-third of the observed signal from the H_2CO experiment. Even if other correction factors are included (differences in Doppler width and the reduction in the number of accessible states), the fact remains that the signal from the hydrogen exchange reaction is expected to be at least an order of magnitude above the detection sensitivity seen in the H_2CO experiment.

Current attempts to solve this dilemma are focusing on the HI partial pressure. Earlier experiments showed that HI would absorb onto the cell walls at an alarming rate, with half-lives as short as 1 min. Passivation of the cell walls with large quantities of HI and a change in the surface of the apertures within the cell seem to have helped; in the most recent test the HI pressure decreased by less than a factor of two in an hour. A new cell is currently under design to allow for flowing the reagents through the cell.

REFERENCES

1. J. M. White, Ph.D. Thesis, University of Illinios, Urbana, 1966.
2. S. J. Strickler and R. J. Barnhart, *J. Phys. Chem.* **86**, 448 (1982).
3. See Chapter 2.

FIGURE CAPTIONS

Figure 1. Recent H_2 LIF spectrum taken during a hydrogen exchange reaction experiment. The H_2 pressure was 5 torr, the HI pressure was 0.1 torr, and the time between the 280 nm photolysis pulse and the VUV probe pulse was 30 ns. This spectrum is the average of 6 scans. The top panel is the standard deviation of the mean, the bottom panel is the average of the data. The observed spectral features all belong to low-lying rotational levels of ground vibrational level H_2.

FIGURE 1.

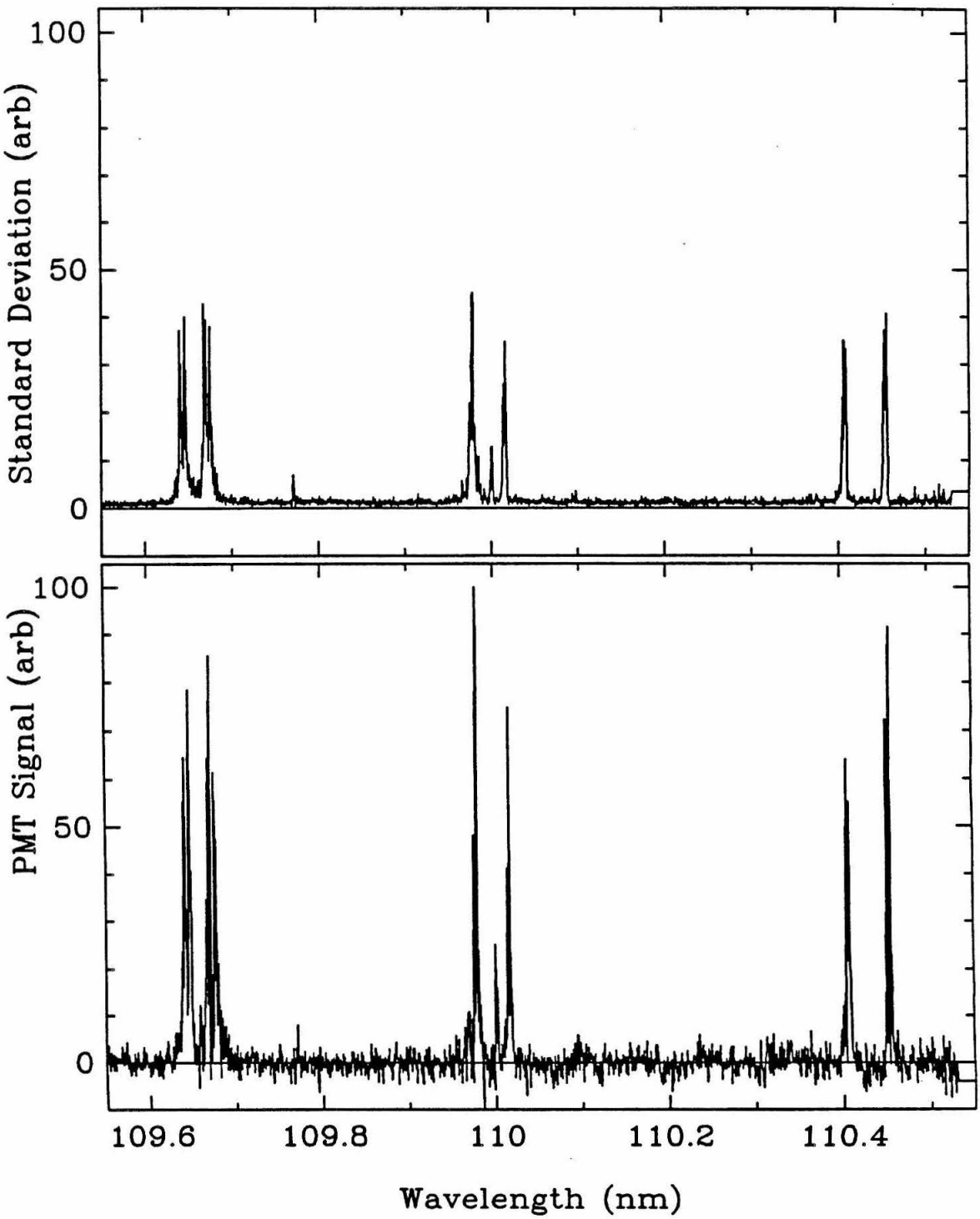
100
50
0
Standard Deviation (arb)
100
50
0
PMT Signal (arb)
109.6
109.8
110
110.2
110.4
Wavelength (nm)

CHAPTER 9.

CONCLUSION

The technique of laser induced fluorescence has been applied to the detection of individual quantum states of H_2 produced during chemical reactions. The technique shows great sensitivity and accuracy. The detection limit at a signal-to-noise ratio of 3 is 6.0×10^8 state cm^{-3} in a probed volume of approximately 0.029 cm^3. This sensitivity is comparable to that obtained by other researchers studying LIF of H_2.[1,2] However, whereas Marinero *et al.* worked at wavelengths below the LiF cutoff of 105 nm and therefore used a windowless system employing pulsed jets for the nonlinear medium and differential pumping to isolate the various compartments, the current experiments were conducted at wavelengths above the LiF cutoff. Consequently, the apparatus for these experiments consists of static gas cells separated by LiF windows.

The technique is also very accurate. A room temperature spectrum of H_2 had a rotational temperature of 305.8 ± 3.0 K.

The first reaction studied was the H_2CO photodissociation reaction. In this system, the H_2CO absorbs a photon and is excited to the first excited singlet state. This state then internally converts to high lying vibrational levels of the ground electronic state, from which it dissociates to form either H_2 + CO or H + HCO. The initial nuclear spin states of the H_2CO are conserved in the product H_2. Consequently, odd K_a states of H_2CO produce odd J states of H_2. Previous research has determined the distribution of energy into rotational and vibrational degrees of freedom of both the H_2 and CO fragments and the translational degrees of freedom, but only for odd K_a states.[3] There has been no measurement of the H_2 rotational distribution following dissociation from even K_a states. The H_2 distribution was determined by CARS.[4] Because their sensitivity was only 10^{12} state cm^{-3}, it was not possible to obtain results in a collision free regime. In fact, He was added to the system to translationally cool the molecules. They found that the product *ortho*-H_2 was greatly excited in the vibrational degrees of

freedom (peaks at $v = 1$) with only moderate amounts of rotational excitation (peaks at $J = 5$). Recently, a theoretical model[5] of the dissociation predicted that *para*-H_2 would have a significantly different distribution from *ortho*-H_2, specifically, that *para*-H_2 would have a bimodal rotational distribution with peaks at $J = 0$ and $J = 10$ and a minimum at $J = 6$.

LIF was used to detect the H_2 produced after excitation of the ${}^rR_3$ and ${}^rR_4$ bandheads of the $2_0^1 4_0^3$ transition in H_2CO. These experiments were performed in essentially the collision free regime; a worst case scenario suggest that there could be up to 2 collisions between the time the H_2 is produced and the time it is detected. The *ortho*-H_2 rotational distribution was very similar to that seen in the CARS experiment, peaking at $J = 3$. The *para*-H_2 rotational distribution was very close to the *ortho*-H_2 rotational distribution, peaking at $J = 4$. This result is almost the exact opposite of what had been predicted theoretically. The vibrational distribution was more difficult to obtain quantitatively but several rotational lines of $v = 4$ were observed. In addition, the H_2 lines were extremely broad, with Doppler widths exceeding 8.5 cm^{-1}. This is a result of the large amount of energy, approximately 2.18 eV representing 62% of the available energy, that is carried away as product translation.

The second reaction studied was the hydrogen exchange reaction. This experiment has been unsuccessful to date, with no evidence of vibrationally excited H_2.

The LIF detection scheme has several advantages over other techniques used to detect individual quantum states of H_2. The detection sensitivity is 3 orders of magnitude better than can be obtained with CARS and is comparable to an order of magnitude better than that obtained with REMPI.[6] It is a simpler technique in that only a single laser source is needed. The greater sensitivity allows LIF to study reactions in collision free regimes whereas CARS often requires collisional relaxation

of the nascent translational distribution, which could alter the nascent rotational distribution. Another advantage arises from all of the overlapping rotational and vibrational structure in H_2: most states are seen in several transitions, with a few seen as often as 7 times. This allows for greater confidence in the results.

However, the LIF detection of individual H_2 quantum states does have several disadvantages. These became apparent during analysis of the $v = 2$ and higher vibrational levels that were populated during the H_2CO photodissociation experiment. For these levels, the internal energy is such that the $\tilde{C}$ state, as well as the $\tilde{B}$ state, can be reached by a single photon. This region of the spectrum is complicated because of perturbations between these two electronic states, which alter the position and intensities of transitions to and from these states. In this region, simple models of transition strength based on a band oscillator strength and Hönl-London factors is no longer valid. Instead, more detailed methods are needed to explicitly handle the perturbations. To date, only a few of the numerous transition strengths have been calculated at this higher level of theory.[7] Reliance on this simple model, in order to be internally consistent, can lead to transition strengths which are significantly in error, leading to erroneous populations.

Another difficulty associated with the perturbations is that the spectrum becomes difficult to assign. Within the $\tilde{B}$ state, for low v's rotational energies are known as high as $J = 30$; however, for many of the higher vibrational levels ($v > 9$) the rotational energies are known for only a few states, often just 5 to 6. Because of the limitations in excitation energy, excitation from moderate J's of $v \geq 2$ are in many cases to states of unknown energy. For example, Fig. 10 of Chapter 7 contains some 224 known transitions; however, a calculation using the rotational constants derived in Chapter 5 predicts more than 370 transitions in the same region. Because of the perturbations, these extrapolated transition energies

cannot be trusted. Consequently, the LIF spectrum contains many unassigned lines.

Many of these difficulties are not with the LIF technique *per se*, but instead lie in the lack of spectroscopic knowledge about H_2, the simplest of all molecules. With improved knowledge of H_2 spectroscopy in the regions of interest, LIF detection of H_2 can become a powerful tool in the study of many simple chemical reactions.

REFERENCES

1. E. .E Marinero, C. T. Rettner, R. N. Zare, and A. H. Kung, *Chem. Phys. Lett.* **95**, 486 (1983).
2. F. J. Northrup, J. C. Polanyi, S. C. Wallace, and J. M. Williamson, *Chem. Phys. Lett.* **105**, 34 (1984).
3. See discussion in Chapter 2.
4. D. Debarre, M. Levebvre, M. Péalat, J.-P. E. Taran, D. J Bamford, and C. B. Moore, *J. Chem. Phys.* **83**, 4476 (1985).
5. R. Schinke, *J. Chem. Phys.* **894**, 1487 (1986).
6. H. Rottke and K. H. Welge, *Chem. Phys. Lett.* **99**, 456 (1983).
7. H. Abgrall, F. Launay, E. Roueff, and J.-Y. Roncin, *J. Chem. Phys.* **87**, 2036 (1987).

APPENDIX 1.

LASER SYSTEMS

I. INTRODUCTION

This appendix describes the optical and electrical characteristics of the laser systems used for the research described in this dissertation. Two Nd:YAG pumped dye laser systems were used: the first, manufactured by Molectron,[1] consists of a MY-34 Nd:YAG laser and a DL-18 dye laser; the second, manufactured by Quanta Ray,[2] consists of a DCR-2A Nd:YAG laser, a PDL-2 dye laser, and a WEX-1c wavelength extension unit. The specifications of each laser system are shown in Table 1.

II. MOLECTRON DYE LASER SYSTEM

A. MY-34 Nd:YAG Laser

A schematic of the Molectron MY-34 Nd:YAG laser is shown in Fig. 1. A Nd:YAG laser (Nd^{3+} impurity in a yttrium aluminum garnet $Y_3Al_5O_{12}$) produces laser radiation at 1064.1 nm. The Molectron MY-34 laser uses an unstable resonator cavity with polarization coupled output followed by an amplifier. This design produces an output beam that is near diffraction limited in the near and far field (< 1 and > 10 m) with a quasi Gaussian spatial intensity profile. The Nd:YAG fundamental at 1064.1 nm is frequency doubled to 532 nm using a type II KD*P (potassium di-deuterium phosphate, KD_2PO_4) crystal in a temperature controlled oven. This frequency conversion method produces horizontally polarized radiation. The crystal is rotated around a vertical axis to provide optimum phase-matching. If desired, an additional KD*P crystal can be used to generate the Nd:YAG third harmonic at 355 nm. This crystal is rotated around a horizontal axis to provide phase-matching and the output polarization is vertical. The crystal needed to generate the fourth harmonic at 266 nm was not purchased for this laser. A series of dichroic beamsplitters and reflectors allows for the separation of the harmonics from the fundamental and each other. A $\lambda/2$ plate is used to rotate the polarization of the 532 nm beam to vertical.

This laser operates at an optimum repetition rate of 10 Hz. When originally installed in April 1980 this laser had an output pulse energy of 360 mJ at 532 nm. The oscillator and amplifier rods of this laser have been replaced several times since then. The current pulse energy at 532 nm is 290 mJ/pulse. This laser oscillates over several axial modes, causing the temporal profile to consist of several pulses separated by 7 ns, the cavity round trip transit time. The relative importance of the various pulses varies continuously with the flashlamp energy. The extreme cases are either a single dominant pulse or two equally strong pulses.

This laser uses a cylindrical-ring-electrode KD*P Pockels cell for Q-switching. A Pockels cell is a voltage dependent polarization rotator. At an appropriate voltage, it acts as a $\lambda/4$ plate, lasing action is inhibited, and energy is stored within the cavity. If the voltage is suddenly brought to 0, the Pockels cell no longer prevents lasing and the stored energy is emitted in a short, intense pulse. In the timing sequence for each pulse, the Pockels cell high voltage supply is triggered first so that the voltage corresponding to $\lambda/4$ retardation is achieved before there is any gain in the oscillator. The flashlamps are fired approximately 400 μsec later. The Q-switch is triggered approximately 165 μsec later, with the laser pulse following 100 nsec later.

B. DL-18 Dye Laser

A schematic of the Molectron DL-18 dye laser is shown in Fig. 2. This dye laser is pumped by the second or third harmonics of a Nd:YAG laser. All the work in this dissertation used the second harmonic. The incident pump laser beam is vertically polarized. A dielectric partial reflector diverts approximately 10% of the incident energy into a dye cell contained within the oscillator cavity. The oscillator cavity is of the standard Hänsch design, consisting of a diffraction grating, a 40× achromatic prism beam expander, a 1/2 wave plate, a dye cell, and an output mirror. The output from the oscillator passes through an optional preamplifier, an optional beam expanding telescope, and then the amplifier. A 30% dielectric partial reflector is used to transversely pump the preamplifier, if it is being used. The remaining incident radiation is used to pump the amplifier stage which can be either longitudinally or transversely pumped. The exact configuration of the dye laser depends on the wavelength desired, the dye chosen, and on considerations involving pulse energy, beam quality, and amplified spontaneous emission (ASE).

The normal configuration of this dye laser is to use the beam expanding telescope and a longitudinally pumped amplifier. In this configuration the specified

dye laser efficiency at 560 nm using Rhodamine 590 Perchlorate (R590 or R6G) is 30%. Recent measurements show an efficiency of 28%.

C. Dye Laser Control

The Intel[3] SBC 80/20 microcomputer which collects the data also scans the dye laser wavelength. The hardware and original software are described in the dissertation of R. Rianda.[4] The hardware will be described briefly in Appendix II.

The software is written in 8080 assembly language. The original software by R. Rianda as modified by D. J. Moll[5] has been rewritten to eliminate some errors, reduce the chance of accidental data loss, provide a more structured program, and include documentation. The original executable file is LSCM0 while the current executable file is LSCM3. The current source code is LSCMS.

The stepping motor on the DL-18 dye laser has a step size of 0.025 counter units. (The counter reading divided by the grating order gives the wavelength in Å). Its controller (Molectron 245) requires only 2 bits of information: a "direction" bit and a pulse for each step to take. During scans the computer system generates a continuous stream of pulses of appropriate frequency in hardware and transmits it to the controller. After an appropriate number of pulses has been transmitted, the hardware generates an interrupt which causes the computer to collect data, plot the data on an X-Y plotter, update the console display, and update the doubling crystal position. Software and hardware limitations prevent data acquisition more often than after every fourth step, *i.e.*, 0.100 counter units. When generating laser radiation near 660 nm the dye laser is operated in fourth order, consequently, the minimum interval between points is 0.025 nm, a density of 400 pts/nm. The linewidth of this laser is specified to be ≈ 0.30 cm^{-1}, so there is a maximum of 5.2 pts/linewidth when operating in this wavelength region.

D. UV Generation

Wavelengths in the ultraviolet are produced by either doubling the dye laser fundamental or by mixing the dye laser fundamental with the Nd:YAG fundamental or harmonics. This is accomplished using seven temperature stabilized crystals to cover the range 420–217 nm: 3 KDP crystals (potassium di-hydrogen phosphate, KH_2PO_4, a KD*P crystal, and 3 KPB (potassium pentaborate, $K_2B_{10}O_{16}$ crystals. These crystals are mounted within the DL-18 dye laser after the final amplifier. The appropriate crystal depends on the wavelength and conversion process chosen. More complete information is provided in the product literature.

The crystals are rotated around either a horizontal (KPB) or vertical axis (KDP and KD*P in order to maintain phase-matching. During wavelength scans the micro-computer which collects data adjusts the phase-matching angle. The system used was modified by D. J. Moll from that originally provided by Molectron, and the details of operation can be found in his thesis. In summary, a reference tuning curve is obtained by manually determining the correct angle for various dye laser wavelengths. The BASIC computer program XTAL (which I have modified) performs a polynomial least squares fit of the crystal angle as a function of dye laser counter and stores the coefficients in memory. During a wavelength scan the computer recalculates the crystal position after each data point is taken and sends this new position to the dye laser. The crystal servo-mechanism then rotates the crystal to the new position.

The UV output can be separated from the dye laser fundamental by either a UV transmitting/visible blocking filter or by a dispersive prism system. Most of the work using the Molectron laser system described in this dissertation used filters, usually a Corning 7-54, a Schott UG-11, or a Schott UG-5.

III. QUANTA RAY LASER SYSTEM

A. DCR-2A Nd:YAG Laser

A schematic of the Quanta Ray DCR-2A Nd:YAG laser is shown in Fig. 3. This laser uses an unstable resonator cavity with diffraction coupled output followed by an amplifier. This design produces an output beam with a "donut" spatial intensity in both the near and far fields. The second harmonic at 532 nm is produced by frequency doubling in a type II KD*P crystal contained within a temperture controlled oven. This crystal is rotated around a vertical axis to provide optimum phase-matching. Additional crystals are used to generate the third and fourth harmonics, if desired. These crystals are rotated around a horizontal axis to provide optimum phase-matching. The various harmonics are separated using a prism separation system, PHS, consisting of a Pellin-Broca prism, a Porro prism, and 2 right angle pickoff prisms. Losses through the PHS are on the order of 15%. The PHS also includes a $\lambda/2$ plate to rotate the polarization of the 532 nm beam to vertical.

This laser operates at an optimum repetition rate of 20 Hz. When installed in November 1986 the output pulse energy after the PHS was approximately 290 mJ. Because of severe birefringence within the Nd:YAG rods, the spatial intensity profile was not a clean "donut," but instead appeared as a "daisy." This degradation of beam quality greatly degraded performance of the harmonic generators, the PDL-2 dye laser, and the WEX. The recently released Quanta RAY model DCR-3A Nd:YAG laser incorporated several optical and electrical design changes. Among these was a second polarizer assembly which suppresses the birefringence. This second polarizer was retro-fitted to our laser approximately 4 months after its initial installation. The intensity profile was greatly improved, as was the performance of the PDL-2 and WEX. Currently, the output pulse energy at 532 nm after the PHS is 360 mJ.

This laser also uses a Pockels cell for Q-switching. For this laser system the Q-switch high voltage supply is turned on approximately 3 msec before the flashlamps are fired. Approximately 215 μsec later, the Q-switch is triggered, with the laser pulse following 50 nsec later.

B. PDL-2A Dye Laser

A schematic of the Quanta Ray PDL-2 dye laser is shown in Fig. 4. This dye laser is pumped by the second or third harmonic of a Nd:YAG laser. All the work in this dissertation used the second harmonic. The incident pump laser beam is vertically polarized. A beamsplitter diverts approximately 10% of the incident energy into a flowing dye cell located within the oscillator cavity. This cavity is also of the Hänsch design. The oscillator output passes through an optional preamplifier, a beam expanding telescope, and then the final amplifier. If the preamplifier is used a second beamsplitter is used to transversely pump it. The remaining radiation is used to pump the amplifier stage which can be either transversely or longitudinally pumped. An extra delay of 2.7 nsec between when the oscillator and the amplifiers are pumped can be introduced by the optional optical delay line consisting of 2 Porro prisms. This delay reduces the amount of ASE produced, especially when the preamplifier is used.

The normal configuration of this dye laser is to use only the longitudinally pumped final amplifier. In this configuration, the specified dye laser efficiency at 560 nm using Rhodamine 590 Tetrafluoroborate 28%, while the observed efficiency is 29%.

C. Dye Laser Control

The SBC 80/20 microcomputer which collects data also scans the dye laser wavelength. The same hardware is used as for the Molectron DL-18; however, the hardware is used in a much different manner and the software is greatly changed. Consequently, it is not possible to scan both dye lasers at the same time.

The Software is written in 8080 assembly language. The current source code is LSCQS and the current executable file is LSCQ1.

The stepping motor on the PDL-2 dye laser has a step size of 0.12 counter units. Its controller (Quanta Ray MCI) requires 12 bits of information: "direction" bit, two "motor address" bits, a "new data ready" bit, and an 8 bit word giving the number of steps to take. Unlike the Molectron system which steps continuously, the Quanta Ray system jumps immediately to the next wavelength and then waits. During scans, the circuitry which generated the pulse stream for the Molectron system instead is used as a timer. After an appropriate time interval, the hardware generates an interrupt which causes the computer to collect data, plot the data on the X-Y plotter, update the console display, calculate the number of steps to the next wavelength, and sends the number of steps to the controller. There is no software or computer hardware limitation as to the number of steps between data points, but since only an integer number of steps can be taken, the minimum useful interval is one step. Therefore, when operating near 660 nm the minimum interval between data points is 0.0030 nm, a density of 333.3 pts/nm. The linewidth of this laser is specified to be ≈ 0.20 cm^{-1}, so there is a maximum of 2.9 pts/linewidth when operating in this wavelength region.

D. WEX-1 Wavelength Extension Unit

Laser radiation at wavelengths outside of that covered by the dye laser is provided by the Quanta Ray model WEX-1 wavelength extension unit. The complete ultraviolet WEX-1 unit can cover the wavelength interval 217–432 nm using three frequency conversion techniques: doubled dye, dye + Nd:YAG fundamental, and double dye + Nd:YAG fundamental. This is accomplished by using 7 KD*P crystals: 4 crystals in one module for the first two processes and 3 crystals in a second module for the latter process. The appropriate crystal depends

on the wavelength and conversion process chosen. More complete information is provided in the product literature.

The crystals in the first module are rotated around a vertical axis, while those in the second module are rotated around a horizontal axis, to maintain phase-matching. In both modules the correct phase-matching angle is maintained automatically. A small portion of the output from each crystal module is fed to a pair of photodiodes. If the phase-matching is correct then each photodiode will receive equal levels of UV radiation; however, if the phase-matching angle is incorrect then the output will "walk" to one side or the other of the desired direction, the photodiodes will receive unequal levels of UV radiation, and a servo-mechanism will rotate the crystal back to the correct position. The success of this technique requires a very good beam quality, but when correctly aligned, scan rates of several nm/min are possible.

The various wavelengths are normally separated using a Pellin-Broca prism. The prism is oriented in a manner to minimize reflective losses for the desired wavelength. For example, the doubled dye output is polarized horizontally, hence the prism lies on its side with all optical faces in a vertical plane. In this configuration the prism faces are at approximately Brewster's angle with respect to the UV laser radiation and reflective losses are minimized. The prism is very efficient at separating the visible and the UV laser beams; however, it does have one major drawback. The dispersive power of the prism causes the output beam to shift position and direction during scans in wavelength. This problem is worse the further one works from the WEX and the longer the scan. In some cases the shift in position was unacceptable, and the Pellin-Broca prism was replaced with a right-angle prism and a filter.

TABLE 1. Dye Laser System Specifications

LASER	PARAMETER	SPECIFICATION			UNITS
	Manufacturer	Molectron	Quanta-Ray		
Nd:YAG					
	Model	MY-34	DCR-2A	DCR-3A	
	Repetition Rate	10	20	20	Hz
	Pulse Energy @ 532 nm	250	250	300	mJ/pulse
	Pulse Duration	15	8	8	nsec
	Beam Diameter	8	6	6	mm
	Beam Divergence	0.6	0.5	0.5	mrad
	Bandwidth	0.5	1.0	1.0	cm^{-1}
DYE					
	Model	DL-18	PDL-2		
	Efficiency @ 560 nm	30	28		%
	Stability (p-p)		8		%
	Pulse Duration	4	6		nsec
	Beam Diameter	8	6		mm
	Beam Divergence	0.6	0.5		mrad
	Bandwidth	0.25	0.20		cm^{-1}
UV					
	Model		WEX-1		
	Efficiency @ 280 nm		23		%
	Bandwidth		0.40		cm^{-1}

a) All specifications are taken from the manufacturers' literature.

b) Dye laser is configured with transversely pumped oscillator, a beam expanding telescope, and a longitudinally pumped amplifier. The dye solution is Rhodamine 590 in methanol.

REFERENCES

1. Molectron Corp., now part of Laser Photonics Corp., Orlando, FL.
2. Quanta Ray Corp., now part of Spectra Physics Corp., Mountain View, CA.
3. Intel Corp., Santa Clara, CA.
4. R. Rianda, Ph.D. Thesis, California Institute of Technology, Pasadena, CA, 1982.
5. D. J. Moll, Ph.D. Thesis, California Institute of Technology, Pasadena, CA, 1983.
6. Corning Glass Works, Corning, NY.
7. Schott Glass Technologies, Duryea, PA.

FIGURE CAPTIONS

Figure 1. Optical schematic of the Molectron MY-34 pulsed Nd:YAG laser. This configuration is used to generate 532 nm radiation for pumping a dye laser.

Figure 2. Optical schematic of the Molectron DL-18 dye laser. This configuration is used to generate 660 nm radiation using the dye DCM. The following symbols are used: A– shutter, B– partially reflective dichroic beamsplitters, C– totally reflective dichroic mirror, D– cylindrical lenses, E– dye cells, F– prism beam expander, G– grating, H– output coupling mirror, J, 1/2 wave plate, K– beam expanding telescope, L– amplifier dye cell, M– turning prism, O– second harmonic crystal, and P– output aperture.

Figure 3. Optical schematic of the Quanta Ray DCR-2A pulsed Nd:YAG laser. This configuration is used to generate 532 nm radiation for pumping a dye laser.

Figure 4. Optical schematic of the Quanta Ray PDL-2 dye laser. This configuration is used to generate 660 nm radiation using the dye DCM.

FIGURE 1.

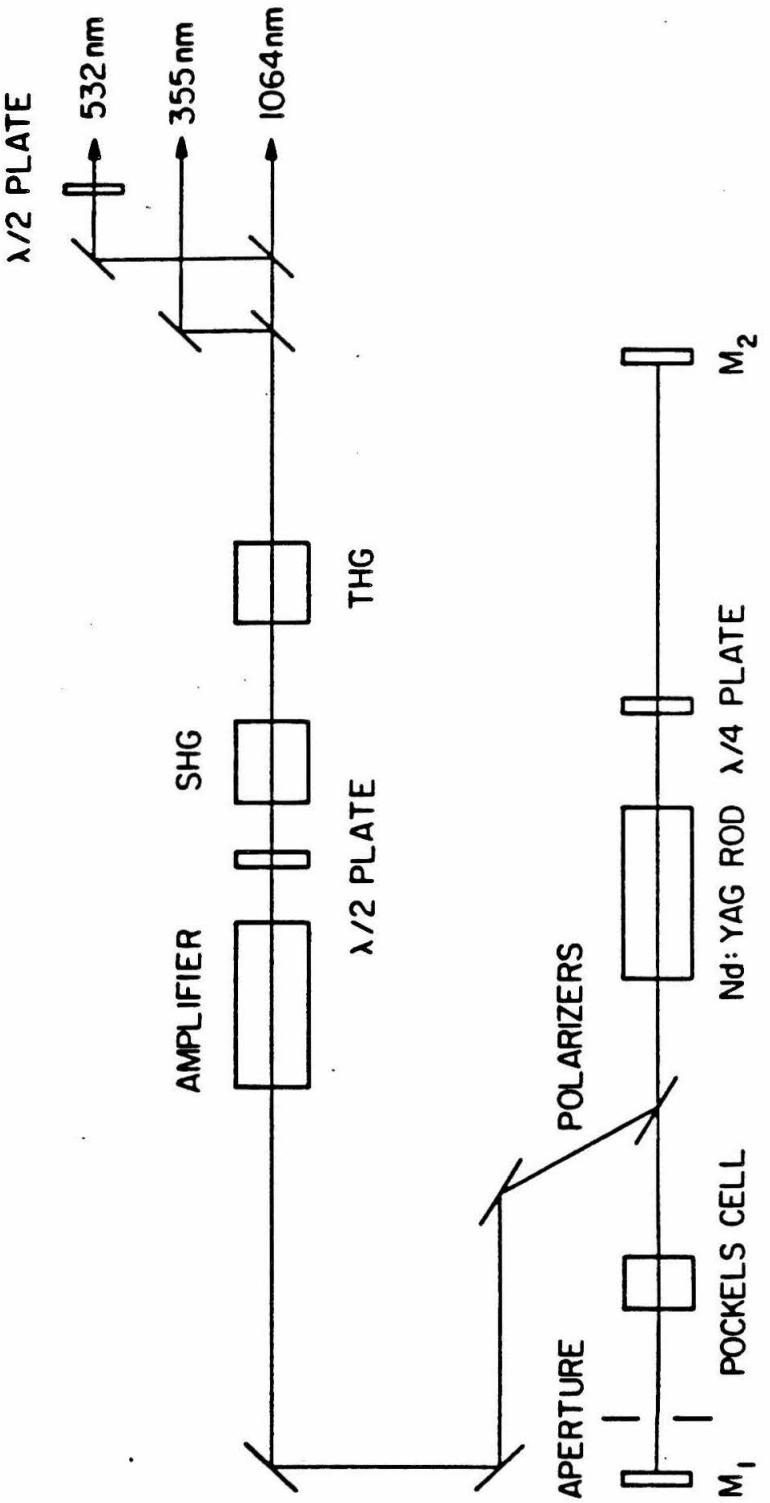
λ/2 PLATE
532nm
355nm
1064nm
AMPLIFIER
SHG
λ/2 PLATE
THG
POLARIZERS
APERTURE
POCKELS CELL
Nd:YAG ROD
λ/4 PLATE
M1
M2

FIGURE 2.

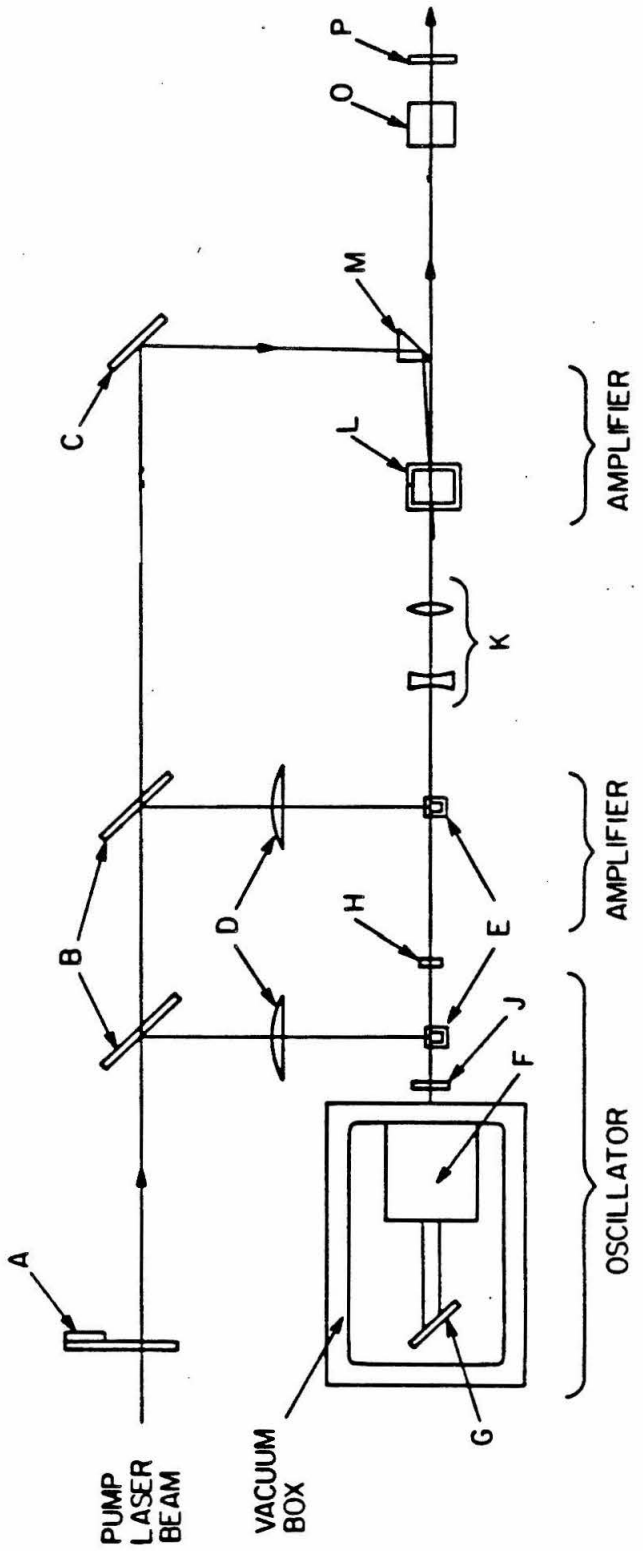
P
O
M
C
L
AMPLIFIER
K
AMPLIFIER
B
D
H
E
J
F
OSCILLATOR
A
G
VACUUM BOX
PUMP LASER BEAM

FIGURE 3.

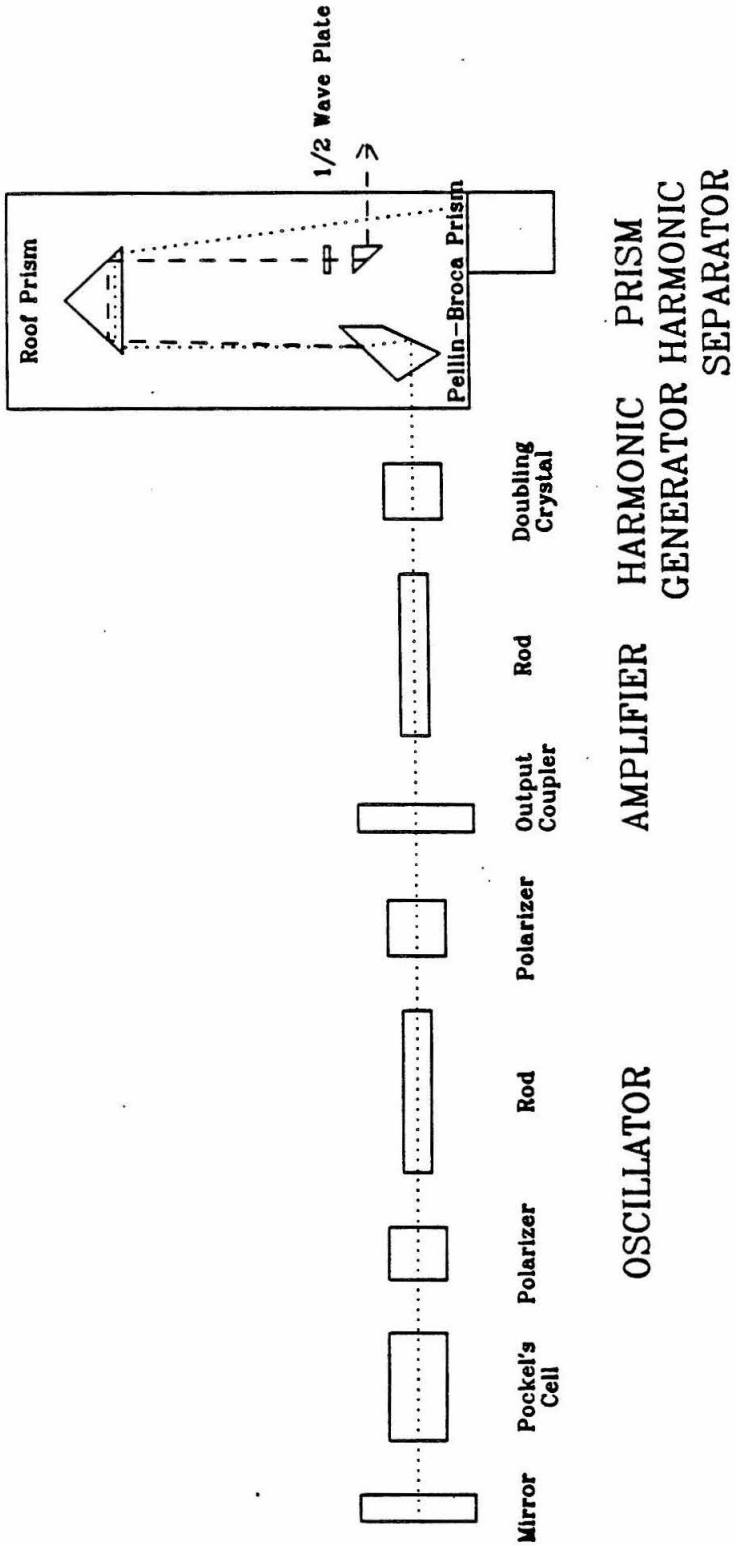
1/2 Wave Plate
Roof Prism
Pellin-Broca Prism
Doubling Crystal
Rod
Output Coupler
Polarizer
Rod
Polarizer
Pockel's Cell
Mirror
OSCILLATOR
AMPLIFIER
HARMONIC GENERATOR
PRISM HARMONIC SEPARATOR

FIGURE 4.

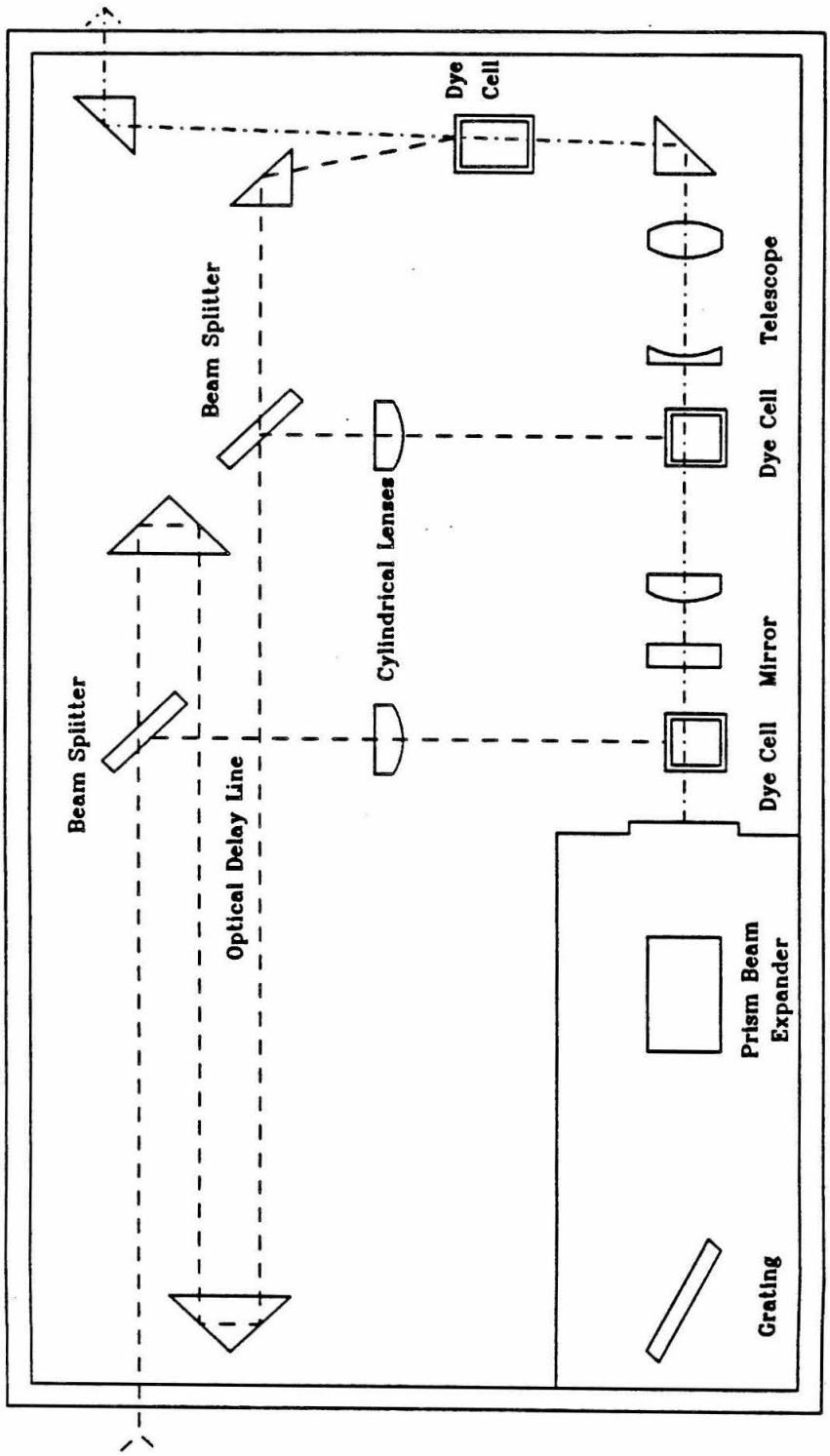
Dye Cell
Beam Splitter
Cylindrical Lenses
Beam Splitter
Optical Delay Line
Dye Cell
Mirror
Dye Cell
Telescope
Prism Beam Expander
Grating
OSCILLATOR
PREAMPLIFIER
AMPLIFIER

APPENDIX 2

ELECTRONICS

I. INTRODUCTION

This appendix contains a detailed description of the electronic equipment used for the experiments described in this dissertation. The first section is concerned with commercially available equipment and provides an overview of their operation along with a description of any changes that were made. Included in this category are the electronics for the photomultiplier and the Molectron Laser Spectroscopy Detection System. The second section is concerned with homebuilt equipment which has not yet been described in detail. A complete description, including schematics, is given for each device in this section. These devices include the Nd:YAG laser timing controller and several charge sensitive preamplifiers. The third section describes the SBC 80/20 microcomputer which is used to control the dye lasers and collect the data.

II. COMMERCIALLY AVAILABLE ELECTRONICS

A. Photomultiplier

A G26E314LF photomultiplier (PMT) from Thorn EMI Gencom[1] is used to collect the fluorescence from H_2. Purchased along with this PMT were a high-voltage power supply, a divider network, and a current-to-voltage preamplifier.

The G26E314LF solar-blind photomultiplier is equipped with a MgF_2 window and a CsI photocathode. This window-cathode combination has a nominal spectral range of 110–220 nm; consequently, the PMT is insensitive to UV and visible radiation. The measured quantum efficiencies for the PMT used for the experiments in this dissertation, serial number 109205, are 0.10, 0.11, 0.01, and 10^{-10} at 122, 140, 180, and 420 nm, respectively. The photoelectrons are amplified by 14 BeCu linear focused dynodes. This design gives very fast risetimes and good linearity at high peak currents. For example, the specified risetime and pulsewidth are 2.2 and 3.4 ns, respectively, while it is estimated that peak anode currents of 100 mA will cause a gain nonlinearity of less than 5% with a well designed divider network.

The model 3000R power supply is used to supply the high voltage necessary for the PMT. The output voltage is adjustable from 0 to 3000 V with 1 V precision. The specified maximum peak-to-peak ripple is 15 mV. The maximum output current is 5 mA.

A resistive divider network is used to provide the necessary inter-dynode voltages for the PMT. The original divider network consisted of 15 $\frac{1}{2}$ W resistors in series with a total resistance of 1.079 MΩ and three decoupling capacitors. At an operating voltage of 3000 V, the resistors are dissipating a total of 8.3 W, well above the rated 7.5 W. After several resistors had burned out, it was decided to rebuild the network. Figure 1 is a schematic of the new network, which has a total resistance of 2.168 MΩ. Consequently, the power dissipation at 3000 V is only

4.2 W, well within the rating of the network. In addition, the redesigned network has one additional capacitor.

Because the photocathode is in close proximity to metal surfaces at ground potential, it was decided to hold the cathode at ground and the anode at positive high voltage.

Connected to the PMT anode through a 2 nF 6 kV capacitor is a model A2 high speed photomultipier preamplifier which is mounted within the PMT housing adjacent to the divider network. The current from the anode is terminated into 51 Ωand the resulting voltage is amplified by a factor of 10 by a LeCroy VV1000B hybrid circuit. The amplifier has a risetime of 2.5 ns and can source -4 V into one or two devices with 51 Ωinput impedances. The overall effect of the amplifier is to provide a voltage pulse proportional to the anode current pulse with a gain of 0.510 V/mA.

It is important to know if the PMT, divider network, and preamplifier have sufficient dynamic range. Assume that N photons per laser pulse reach the photomultiplier with a Gaussian temporal profile characterized by a FWHM pulsewidth of $\tau_{h\nu}$. The instantaneous photon flux is then given by

$$I_{h\nu}(t) = \frac{N}{\tau_{h\nu}} \times \sqrt{\frac{4\ln 2}{\pi}} \times e^{-4\ln 2\left(\frac{t}{\tau_{h\nu}}\right)^2} \qquad (A2.1)$$

If the photomultiplier temporal response is also Gaussian, then the anode instantaneous current is given by

$$I_e(t) = \frac{NGqe}{\tau} \times \sqrt{\frac{4\ln 2}{\pi}} \times e^{-4\ln 2\left(\frac{t-t_t}{\tau}\right)^2} \qquad (A2.2)$$

where G is the photomultiplier gain, q is the photomultiplier quantum efficiency, e is the charge on an electron, τ is the output pulsewidth given by $\tau = \sqrt{\tau_{h\nu}^2 + \tau_{PMT}^2}$,

and t_t is the transit delay. The statistical nature of the photoemission process has been ignored. The total charge produced by the PMT during the pulse is then

$$Q = NGqe \qquad (A2.3)$$

In order to maintain gain linearity during the light pulse, the fractional change in voltage between the dynodes should be kept very small. This is accomplished with the aid of capacitors on the divider network. A change of charge ΔQ across a capacitor with a capacitance C biased with V volts leads to fractional voltage change of

$$\frac{\Delta V}{V} = \frac{\Delta Q}{CV} \qquad (A2.4)$$

The total number of VUV photons incident on the sample is on the order of 2×10^8 photons/pulse. It is assumed that 0.1% of the photons will be absorbed and then isotropically reemitted as fluorescence. The PMT cathode subtends a solid angle of $5 \times 10^{-3} \times 4\pi$; consequently, there will be 1000 photons/pulse incident to the PMT. The VUV laser pulsewidth is nominally 2.4 nsec. The photomultiplier is usually operated at a cathode to anode bias of +3000 V, leading to a gain of $\approx 10^7$. With a peak quantum efficiency of 0.10 and a pulsewidth of 3.4 ns, the peak anode current is 40 mA, approximately one-third of the maximum peak current for linear operation. The total charge produced is 160 pC. The decoupling capacitor which supplies this charge has a capacitance of 10 nF and is biased by approximately 345 V; thus, the fractional voltage change between the last two dynodes is 5×10^{-5}, an insignificant amount. It is therefore expected that the photomultiplier response will be linear for incident fluxes up to 3000 photons/pulse.

The 2 nF coupling capacitor and the 51 Ωload resistor on the input to the preamplifier act as an RC high-pass filter[2] with a 3 dB cutoff frequency of 3 MHz, well below the signal frequency components. A 40 mA peak current from the anode would produce 2 V across the resistor, a value well above the maximum

for linear operation of 0.5 V. (In fact, the signal input is clamped by a pair of diodes to be 0.0 ± 0.6 V). As a result, the peak anode current must be less than 10 mA for linear operation of the preamplifier. In the absence of pulse distortions which stretch out the PMT output pulse, such peak currents are reached for fluxes of 250 photons/pulse at the cathode. Consequently, the preamplifier is the limiting component to signal linearity and dynamic range, with the limit occurring under normal operating conditions for fluxes on the order of 250 photons/pulse at the PMT cathode. The total charge produced under these circumstances is 40 pC/pulse.

It is necessary to have some idea of the PMT quantum efficiency for wavelengths other than those given on the PMT test ticket. It was decided that a reasonable functional form is

$$q(\lambda) = \begin{cases} 0 & \lambda < \lambda_w \\ a \times (1 - e^{-b(\lambda - \lambda_w)}) \times (1 - e^{-c(\lambda_c - \lambda)}) & \lambda_w \leq \lambda \leq \lambda_c \\ 0 & \lambda_c < \lambda \end{cases} \qquad (A2.5)$$

in which λ_w represents the low wavelength transmission limit of the window and λ_c represents the high wavelenth cutoff of the photocathode. While the exact $q(\lambda)$ is unknown, the above formula does have the correct qualitative behaviour; q is 0 when the window is not transparent, then at wavelengths above the cutoff the transmission increases to nearly unity, while the photocathode quantum efficiency decreases from its maximum value as the cathode's cutoff is approached, with negligible quantum efficiency above a certain wavelength. This equation requires 5 parameters; unfortunately, the quantum efficiency has only been measured at 3 wavelengths. If the measured quantum efficiencies are fit to a quadratic in λ, the resulting polynomial has roots at 86.73 and 187.33 nm. It was therefore decided to fix $\lambda_c = 187.33$ nm. This wavelength is not very critical since there is no H_2 fluorescence above approximately 160 nm.[3]

The location of λ_w was much more difficult to determine. MgF_2 has a short wavelength cutoff in the vicinity of 110 nm, depending on the thickness, purity and manufacturing history of the window. For example, various manufacturers[1,4] of solar-blind photomultipliers using this window material report cutoffs of 110 or 115 nm, Harshaw,[5] the leading manufacturer, reports 110 nm, while Heath and Sacher[6] reported a cutoff of 113 nm. The exact wavelength is critical since several H_2 emission lines are in this spectral region.[3] It was decided to determine fits for λ_w = 110.0, 112.5, and 115.0 nm. The results are as follows: a = 0.14756, 0.143068, 0.143076, b = 0.19336, 0.24880, 0.24610, and c = 0.03011, 0.03110, 0.03109, respectively, when wavelengths are given in nm.

B. Molectron Laser Spectroscopy Detection System

The Molectron Laser Spectroscopy Detection System (LSDS) converts the rapidly varying signal from the experiments (μsec timescale) into a slowly varying signal (tens of msec timescale) which can be collected by the computer. The LSDS is built around a gated integrator, also known as a "boxcar" integrator. The LSDS consists of 5 components within a single NIM-bin power supply: a model 122 dual gate generator, two model 131 amplifier/shapers, and two model 112 differential gated integrators. This equipment allows two channels of data to be collected, a signal channel and a laser intensity channel.

The model 122 dual gate generator is used to generate the two gates for the model 112 differential gated integrator. This device is triggered by either the positive or negative going edge of a TTL compatible pulse. The input impedance is 1 kΩ. The first gate is delayed with respect to the trigger by 100 nsec to 150 msec. At the minimum, the second gate is delayed with respect to the first gate by the gate width, with a maximum delay of 150 msec. The same circuit is used to generate both gates, so they always have the same width (30 nsec to 150 msec) and it is impossible for the gates to overlap.

The model 131 amplifier/shaper is used as the final amplifier. It is a three stage amplifier consisting of a differentiator and two integrators. The gain of the amplifier varies from 0.3 to 1000. The bandpass of the amplifier is adjustable: the low pass cutoff varies from 160 Hz to 160 kHz or the differentiator can be bypassed to provide operation at DC, while the high pass cutoff varies from 1.6 kHz to 1.6 MHz. The input impedance is selectable from 50 Ω, 100 Ω, or 100 MΩ. The output impedance is 0.1 Ω; however, since the maximum output current is only 10 mA, the load impedance should exceed 1 kΩ to insure proper operation.

The model 112 differential gated integrator consists of a pair of RC integrators, each of which is active only during an externally supplied gate. Gate 1 is normally adjusted to measure the signal pulse while gate 2 is normally adjusted to measure the signal baseline. The output is the differential response between the outputs of the gate 1 integrator and the gate 2 integrator, *i.e.*, the net signal level. The signal input impedance is 50 Ω, 100 kΩ, or 100MΩ. The gate input impedance is 1 kΩ while the minimum gate width is 30 nsec. The output impedance is 100 Ω; however, since the maximum output current is 10 mA, the load impedance should exceed 1 kΩ to insure proper operation.

The response of the gated integrator depends on three factors: 1) the integrator time constant, $\tau = RC$; 2) the signal pulse width, τ_S; and 3), the duty factor, $\delta = t_g/T$, where t_g is the gate width and T is the gate repetition period. If $\tau \ll \tau_S$ then each integrator will follow the pulse shape while the gate is on and will hold the signal amplitude when the gate turns off, *i.e.*, each integrator will act as a sample-and-hold amplifier. If $\tau \gg \tau_S$ then each integrator will integrate the signal during the gate window, the response being attenuated severely by the factor τ_s/τ for a single pulse. If a fixed number of pulses is applied during any measurement period then the output will be a summation of the individual pulse integrals as long as the output remains less than 10% of the input. After each measurement period

the integration capacitor must be discharged. If the capacitor is not discharged and the output becomes a significant fraction of the input or if $\tau \approx \tau_S$ then a weighted average results. In effect the integrator "forgets" previous pulses in favor of more recent pulses with an effective time constant of

$$\tau_{\text{eff}} = \frac{\tau}{\delta}. \qquad (A2.6)$$

This last mode is the one normally used.

In normal operation two gated integrators are used, one for the signal channel and the second for the laser intensity channel. Each integrator requires two gates, yet the dual gate generator can only provide two of the needed four gates. The number of needed gates can be reduced to three if the same gate is used as the baseline gate for both integrators. The necessary third gate is provided by an E-H model 139B pulse generator.[7] This device is a more versatile pulse generator than the model 122 dual gate generator, but it only produces a single pulse. The output impedance of this device is 50 Ω. There are two modes of operation which have been used: 1) the model 122 dual gate generator provides the signal gate to one integrator and both baseline gates while the model 139B pulse generator provides the second signal gate; or 2) the model 122 provides a signal gate to each integrator while the model 139 provides the baseline gates. The former mode is used to get identical gatewidths for the signal and baseline gates for one channel, while the latter mode is used to get a baseline gate before the first signal gate (the model 139 pulse generator has a significantly shorter insertion delay).

Normally, the SYNC pulse from the laser is used to trigger the E-H model 139B pulse generator, and a trigger SYNC output from this device is then used to trigger the model 122 dual gate generator. If the laser SYNC pulse is used to trigger both devices independently, there is some jitter in the relative time delay caused by fluctuations in the laser SYNC pulse and the different sensitivities of the trigger

inputs. By connecting the two pulse generators together in the manner described, there is much less jitter.

When using very short gates, < 0.5 μs, there was often trouble because of impedance mismatching. The gates are produced with a 50 Ω source impedance, 50 Ω coaxial cable is used to connect the gate generators to the integrators, but the gate inputs on the integrators are only terminated with 1 kΩ. The impedance mismatch problem was reduced by placing 91 Ω termination resistors on the gate inputs to the gated integrators. This termination reduced the amplitude of the reflected wave by a factor of three. It was not possible to use 50 Ω resistors because the baseline gates on both integrators are often connected together and neither gate generator could source sufficient current into two 50 Ω resistors in parallel.

III. HOMEBUILT ELECTRONICS

A. NO Ionization Cell Charge Preamplifier

The VUV photon intensity is measured using a NO ionization cell, as described in Chapter 4. The output from this cell is a quantity of charge which is directly proportional to the total number of VUV photons incident on the cell. A preamplifier was built to convert this charge pulse to a long lived voltage pulse which could be used by the relatively slow electronics of the LSDS.

The schematic of this preamplifier is shown in Figure 2. It is based on a LeCroy TRA1000 monolithic charge/current pulse preamplifier[8] with external feedback components. When a capacitor C_F is used for the feedback element, the preamplifier integrates the charge pulse, giving a final output voltage

$$V_{out} = \frac{Q_{in}}{C_F} \qquad (A2.7)$$

The circuit is based on case 10, a low charge to voltage amplifier, in the manufacturer's technical data manual with only a few modifications. These modifications are as follows: 1) a 47 V battery was attached between the input and ground through a 10 MΩ resistor and a DPDT switch (to change bias polarity) to provide the bias for the Pt plates in the ionization cell, 2) the feedback components were a 47 pF capacitor (nominal gain of 21.3 mV/pC) and a 5 MΩ resistor, (nominal decay time of 10 μs) and 3) the inverted and noninverted outputs were connected through a DPDT switch to either the output or a 50 Ω resistor to ground (to change output polarity). Since the maximum output voltage is only 1 V into 50 Ω, the maximum input signal that can be handled without saturation is approximately 47 pC.

The entire circuit is built on a copper plated peg board. A Weller mini-drill was used to remove thin bands of copper, leaving behind thin strips of copper as the electrical connections between components; consequently, there are no wires on

the board. The copper plating not used for connections is maintained at ground potential; thus, the circuit is effectively built on a ground plane.

The circuit requires ±12 V supplies. Originally, these were supplied by the NIM bin holding the LSDS; however, there were strong glitches at twice the line frequency. The high voltage power supply used for the PMT also provides ±15 V outputs, which were reduced to 12.000 ± .001 V using LM337 and LM317 voltage regulators. These voltage supplies had much less noise. The supply voltages were further filtered by a pair of capacitors and an inductor inside the preamplifier

The preamplifier is calibrated using a E-H Model 139B Pulse Generator and an oscilliscope. A pulse of known voltage and width is passed through a 51 Ω resistor in order to generate a known current pulse. The product of the current and the pulse width gives the total incident charge, which was compared with the voltage of the preamplifier output displayed on the oscilloscope. Calibration with pulses as short as 4 ns showed that the sensitivity was 20.90 ± 0.33 mV/pC and 22.90 ± 0.31 mV/pC for the inverted and noninverted outputs, respectively (95% confidence levels, 33 points). These results are close to the design sensitivity of 21.3 mV/pC.

B. PMT Filter and Charge Amplifier

The output signal from the PMT housing is a voltage pulse proportional to the current from the PMT anode. This voltage pulse has a pulsewidth less than 10 ns; consequently, this pulse is much too fast to be used by the LSDS. In addition, a signal proportional to the total charge, not the instantaneous current, is desired. A charge to voltage preamplifier, similar to that used for the ionization cell, is used to perform the necessary current integration.

The schematic of this preamplifier is shown in Figure 3. It is very similar to the one used for the ionization cell, except that a 510 pF feedback capacitor (1.96 mV/pC) is used and there is obviously no need for a bias battery. Added

to the input were a 51 Ω resistor to ground (to provide termination) and a 510 Ω resistor in series (to convert voltage to current). The overall effect of the A2 preamplifier and the homebuilt preamplifier is a voltage pulse with a maximum proportional to the total charge at the PMT anode. The overall gain should be 10 mV/pC. The circuit is designed for output voltages on the order of ± 1 V; consequently, the circuit is designed for a maximum of 100 pC.

Early experiments with this integrator showed tremendous amounts of ripple, > 2 V. The ripple was traced to a several mV ripple in the PMT high voltage power supply at the switching frequency of 26 kHz. This ripple passes from the high voltage lead attached to the anode through the 2 nF coupling capacitor to the A2 preamplifier and then to the homebuilt amplifier, where it is integrated. Attempts to reduce the ripple at the source by adding two capacitors and an inductor in a π configuration were unsuccessful.

A conventional active high pass filters was not able to handle the 5 nsec long pulses without severe attenuation and pulse distortion. A passive 7 pole Butterworth filter consisting of 4 inductors and 3 capacitors in a π configuration was built following the design in a standard text on electronics.[2] This filter is shown on the schematic for the preamplifier. The nominal component values were within 4% of that needed for a 7 pole filter with 50 Ω source and load resistive impedances and a 3 dB cut frequency of 87.5 kHz ($\omega = 550$ kHz). For a perfect filter the attenuation at 26 kHz would be 2×10^{-4} (-74 dB). Using a sine-wave generator as a signal source, the 3dB cut frequency was approximately 110 kHz. The 26 Hz ripple was attenuated approximately 1000-fold.

Unfortunately, the filter/integrator combination did not work as well as designed. The output pulse was not a rapid rise to the maximum followed by an approximately 10 μs decay, but instead is a sinusoid with exponentially decaying amplitude that is clipped for very negative excursions. This waveform results from

an interaction between the filter and the integrator, as shown by the fact that both work fine when they are isolated from each other. Fortunately, the voltage maximum of the first peak is still proportional to the incident charge, with a sensitivity of 7.09 ± 0.10 mV/pC (95% confidence limits, 68 points). Any non-linearity in response was less than 10% over a factor of 333 change in input charge. The maximum signal from the integrator of 1 V corresponds to a PMT output of approximately 140 pC.

Because the A2/filter/integrator combination does perform its primary goal of providing a voltage signal which is proportional to the charge produced at the PMT anode with minimal noise, it was decided to use this configuration for all the experiments in theis dissertation. However, this is probably a primary area for further improvments in the apparatus used for the experiments.

C. Laser Timing Controller

One of the important parts of any multi-laser experiments is the accurate generation of the timing sequences. The correct sequence of pulses needed to fire a Nd:YAG laser might extend over 3 or 4 ms, yet the jitter between the laser outputs should be less than 1 ns. The situation is exacerbated when, as is the case in our laboratory, the lasers are by different manufacturers, with different timing and interfacing requirements, and even different design repetition rates.

The Quanta Ray system is designed to operate at 20 Hz while the Molectron system is designed to operate at 10 Hz. It is possible to operate both lasers at any frequency between 10 and 20 Hz, with a sacrifice in beam quality and pulse energy. Instead, both lasers are operated at their design repetition rate, with the Molectron laser firing on alternate Quanta Ray pulses. The electronics needed to do this are contained in a custom built laser timing controller.

The overall timing sequence is initiated by the Quanta Ray Nd:YAG laser's OSC SYNC output. This pulse (3.3 V into 1 kΩ, duration approximately 3 ms)

is generated at the very beginning of the internal firing sequence. At the end of the pulse the flashlamps are fired. The delay gives the Q-switch time to reach a stable high voltage prior to the lamp discharge. After a time interval of approximately 210 μs, the Q-switch is triggered, with the laser pulse being emitted shortly thereafter. The external Q-switch trigger requires 3 to 10 V into 50 Ω, a pulsewidth less than 1 μs, and risetime on the order of 15 ns. Since it is not possible to externally turn on the Q-switch high voltage supply, all timing must be made relative to the OSC SYNC output.

The Molectron Nd:YAG laser external timing sequence begins with a lamp trigger pulse (5 to 12 V, 50 Ω, pulsewidth between 100 μs and 50 ms). On the receipt of this pulse the Q-switch is brought to its high voltage state. After a delay of $\approx$ 600 μs the flashlamps are fired. After a time delay of approximately 160 μs the Q-switch is triggered, with the laser pulse being emitted shortly thereafter. The external Q-switch trigger requires 5 to 12 V into 50 Ω, a pulsewidth between 1 μs and 50 ms, with a risetime less than 15 ns.

A schematic of the timing controller is shown if Fig. 4. It consists of 4 pairs of monostable multivibrators (a fifth pair was installed to control the Quanta Ray laser flashlamp, but its output is not needed). Monostable multivibrator pair 1 (U1) is triggered by the rising edge of the Quanta Ray OSC SYNC and generates a 100 μs pulse delayed approximately 2.4 ms. The duration of the time delay is adjustable using the front panel 10-turn potentiometer, *LAMP DELAY*. This pulse becomes the lamp trigger pulse for the Molectron laser, M-LAMP.

The output of the first pair of monostable multivibrators is used to trigger the second pair of monostable multivibrators (U3), generating an approximately 780 μs long pulse. The duration of this pulse is adjustable by the front panel 10-turn potentiometer, *Q-SWITCH DELAY*. This pulse length is the time after M-LAMP that the Q-switches should be fired. Consequently, the output from this

monostable multivibrator produces the SYNC output pulse and the input to the third and fourth pairs of monostable multivibrators.

The output, M-QS of the third pair of monostable multivibrators (U4) is used to trigger the Molectron Q-switch. The pulse duration is 1.2 μs and the time delay is adjustable from 50 to 250 ns by a front panel potentiometer, *Q-SWITCH TIMING*. The output, QR-QS, of the fourth pair of monostable multivibrators (U5) is used to trigger the Quanta Ray Q-switch. A pulse of 1.2 μs duration is generated after a fixed time delay of 100 ns. This allows the relative time delay between the two laser pulses to vary from having the Molectron laser pulse 50 ns after to 150 ns before the Quanta Ray laser pulse. Because the longest timing interval involving only a single laser is on the order of 100 ns, it is expected that the jitter between the two laser pulses would be very small.

Original implementations of the laser timing controller had excessive pulse-to-pulse jitter in the long timing delays. This problem was traced to transients from the integrated circuits on the +5 V supply, affecting the *RC* timing components. This problem was greatly reduced by using three separate power supplies for the circuit: the first for just the *RC* timing components, a second for the integrated circuits, and a third for the output drivers. The final design had jitter in the long delays of less than a microsecond, with the jitter in the laser pulses being less than 1 ns.

In order to operate the Molectron laser at half the repetition rate of the Quanta Ray laser, the OSC SYNC pulse was also connected to a J-K flip-flop acting as a toggle. The output from this toggle was "anded" with the pulses being sent out to the Molectron laser, inhibiting this laser for alternate Quanta Ray pulses.

The correct operation of the front panel potentiometers is easily understood and is summarized in Table 4. *Q-SWITCH TIMING* is a fine adjust of the relative timing between the two laser pulses. *Q-SWITCH DELAY* adjusts the time between

the M-LAMP pulse and the lasers firing. *LAMP DELAY* adjusts the time delay between the original OSC SYNC pulse from the Quanta Ray laser and M-LAMP. In normal operation, *Q-SWITCH DELAY* is adjusted for maximum power from the Molectron laser. Then, *LAMP DELAY* is adjusted for maximum power from the Quanta Ray laser. (This adjustment changes rapidly during laser warmup). Finally, *Q-SWITCH TIMING* is adjusted for the correct relative time interval between the two laser pulses. This potentiometer should have no effect on the power output from either laser.

The Molectron laser system normally provides the photolysis laser pulse while the Quanta Ray system provides the probe laser pulse. If the signal produced when only the probe laser fires could be subtracted from the signal produced when both the photolysis and probe lasers fire, any background effects due to the probe pulse are cancelled out, leaving just the net signal. Such a subtraction can be carried out using a dual gated integrator if the gates are appropriately manipulated.

The necessary gate manipulations are performed by a second section of the laser timing controller. The J-K flip-flop which toggles the Molectron laser trigger pulses also toggles four 2-to-1 multiplexers. The multiplexers work in pairs. A pair of gate generators are connected to the inputs of two multiplexers, while the outputs from these multiplexers are connected to the gate inputs on one of the dual gated integrators. Depending on the state of the toggle, either gate generator is connected to either gate input, the order toggling on each Quanta Ray pulse sequence. Suppose when both lasers are to fire gate A is adjusted to occur when no signal is present and is connected to the negative gate input of the integrator while gate B is adjusted to occur when the signal is present and is connected to the positive gate input of the integrator. The resulting output would be the two-laser signal minus the baseline. On the next laser pulse only one laser fires and the connections between gate generators and gated integrator are toggled, A to

positive gate input and B to negative gate input, so the resulting output is the baseline minus the single laser signal. The output after many laser pulses would just be the average of the two laser signal minus the single laser signal, as desired. By using the same toggle control on the lasers and on the gates, it is impossible for the gates to get out of synchronization with the lasers, unlike the situation with the circuit developed by D. Moll and described in his dissertation.[9]

IV. COMPUTER SYSTEMS

Digital data acquisition and dye laser control capabilities are provided by an Intel SBC 80/20 single board computer system,[10] originally purchased in 1977. This system consists of an Intel SBC 80/20 single board computer, an Intel SBC 116 combination memory and I/O expansion board, and Intel SBC 310 high speed mathematics board, an Analog Devices RTI-1200 analog-to-digital and digital-to-analog conversion board,[11] an iCOM FD3712 dual 8" floppy disk drive and controller board,[12] and a memory expansion and interface board designed by R. Rianda.[13] The hardware is described in great detail in his thesis, so this section is just a summary of its operation.

The heart of the SBC 80/20 is an Intel 8080A microprocessor. This computer has an 8 bit data word and a 16 bit address bus. The maximum addressable memory space is 64K words. More than one-third of the address space is reserved for hardware or PROM, with 42K of RAM extending from 3800 to DFFF (addresses are given in hexadecimal, all other numbers are decimal). Unfortunately, the utility routines written by R. Rianda assume that the high speed math board will use memory from 7FF0 to 7FFF, smack in the middle of the usable RAM. In principle it would be possible to remove all the PROM's, disassemble all the utility subroutines, change the addresses, reassemble the programs and replace them on PROM's; however, the absence of detailed source codes for the subroutines makes this a risky procedure. The software for operating the dye lasers uses all the RAM up to 4D90; consequently, the largest single data array that can fit is 12895 8 bit words, or 6448 16 bit words. This corresponds to the data from a 16 nm scan at a density of 400 pts/nm, which is more than sufficient for most work. (The data from the signal channel is stored below 7FF0, the laser intensity data is stored above 8000). The coefficients used to determine the doubling crystal position for the Molectron DL-18 are stored at BF00-BFFF, also in the center of RAM memory.

However, this position places no new restrictions on memory allocation, so no attempt has been made to move it.

The heart of the hardware for controlling the dye lasers is a pair of Intel 8253 programmable interval timers located on the memory expansion and interface board built by R. Rianda. Each 8253 contains three independent 16 bit counters, so the six counters are labeled C0C0, C0C1, C0C2, C1C0, C1C1, and C1C2. The following is a description of how these counters are used for wavelength scans using the Molectron laser system. C0C0 is configured as a square wave generator. The clock input is 1.26 MHz. When the counter is programmed with a count of 15, the output is an 84 KHz square wave. This square wave is the clock input to C0C1 which is configured as a rate generator. It is programmed with $12600/R/G$ where R is the desired scan rate in nm/min and G is the dye laser grating order. After every $12600/R/G$ pulses from C0C0, C0C1 sends a single pulse to C0C2, C1C0, and the Molectron DL245 dye laser grating scan controller. As mentioned earlier, the dye laser moves one step (.025 counter units) for each pulse. C0C2 is used as a counter and is programmed with the number of pulses per 0.01 nm, which nominally is $4G$. After the terminal count an INTERRUPT 4 is generated, which tells the software that 0.01 nm has been scanned. The software will collect data, update the doubling crystal position, update displays giving the current position on the monitor, and plot the new data point on an X-Y plotter. C1C0 is also used as a counter and keeps track of the total number of pulses sent to the stepping motor. This information is used by several subroutines to determine the current dye laser wavelength. If this counter overflows, an INTERRUPT 3 is generated which changes the base dye laser counter position from which the current counter position is determined and then C1C0 is reset. C1C1 and C1C2 are unused. It is possible to take data at point densities greater than 0.01 nm/pt by inputting values of G and R to the computer that are different from physical reality. When

using this method, one must make sure to adjust the scan length appropriately. As an example, a 15 nm scan taken at a rate of 1 nm/min in 4th order at a point density of 0.0025 nm/pt can be obtained by inputting a 60 nm scan taken at a rate of 4 nm/min in 1st order to the computer.

Communication between the computer and the doubling crystal controller is through an Intel 8251 programmable interface on the R. Rianda built expansion board. More information on this system is contained in the thesis of D. Moll.[9] The only modification was to extend the order of the polynomial fit (crstal counter as a function of grating counter) to 9th order. The BASIC program to determine these coefficients is XTAL.

In some experiments the dye laser wavelength is held constant while data is taken as a function of time. In this case the counters are programmed so that an INTERRUPT 4 is generated every 0.01 min. The software inhibits changes in doubling crystal position during time scans; however, it is not possible to inhibit the sending of pulses to the stepping motor controller. *Therefore, during time scans the operator must manually disengage the Molectron DL245 Grating Scan Controller, either by turning its control knob off of the external input position, or by disconnecting the cable.*

The counters are used slightly differently when the Quanta Ray laser system is used. In this case C0C0 is a rate generator converting 1.26 MHz to 84 KHz and C0C1 is a rate generator converting 84 KHz to 1 Khz. This 1 KHz pulse train is counted by C0C2, which is acting as a timer with ms accurracy. After every $1000/R/D$ pulses, where R is the rate in nm/min. and D is the point density in pts/nm, an INTERRUPT 4 is generated, signifying to the software that it is time to collect data and move the dye laser. Communication from the computer to the MCI-1 dye laser controller uses an Intel 8251 programmable peripheral interface on the SBC-116 expansion board. Once again it is not possible to prevent the pulses

from being sent to the Molectron scan controller. *Therefore, the operator must manually disengage the Molectron scan controller or disconnect the cable whenever the Quanta Ray dye laser is used.* However, it is not necessary to disconnect the cable to the Quanta Ray dye laser when the Molectron dye laser is used.

After a scan is completed the data is written to a 8" floppy disk for permanent storage. This section of the software was greatly modified to reduce the risk of accidental data loss, and even includes a recovery routine if there is a disk drive error. The data is stored as $4N + 2$ bytes of data, where N is the number of data points. The storage format is a single 2 byte binary number giving N, followed by $2N$ bytes containing the signal channel binary data, followed by another $2N$ bytes containing the laser intensity channel binary data. All data is stored in normal 8080 format (low byte then high byte).

The programs to run the computer and collect data are all written in 8080 assembly language. The Molectron source code is LSCMS while that for the Quanta Ray system is LSCQS, the executable files are LSCM3 and LSCQ0.

Further data analysis takes place on the divisional VAX 11/780 computer. The data is transferred from floppy disk to the computer using the public program FLOPPY. The resulting file is an unformatted binary file usually given the extension .FDS. The program CONVERT takes the .FDS file and generates a formatted FORTRAN file usually given the extension .VXD. In addition, CONVERT places a header on the .VXD file which contains the following information about the scan: file name, date, label, signal channel amplifier settings, integrator gate time, intensity channel settings, the dye laser initial and final grating counter positions, the grating order, and some codes describing the type of scan (wavelength or time) and which detector/amplifier combination was used. When the storage allocation on the VAX is exhausted, the .VXD files are transferred to magnetic tape.

All data analysis uses the .VXD files. Programs have been written to plot the data (LASERPLOT), manipulate the data within a single spectrum (CRVMANIP1), add, subtract, or divide one spectrum by another (CRVADD, CRVDIFF, CRVABS and their variants), and search a spectrum for peaks (WAVECAL). Descriptions of these and all the other programs can be found in the listings.

TABLE 1. Ionization Cell Charge Preamplifier Components

Component	Value		Notes
U1	TRA1000		preamplifier
Q1	2N5486		n-JFET
Q2	MPS6519		npn
R1	100	Ω	
R2	1	kΩ	
R3	300	Ω	
R4	51	Ω	1 W
R5	5.1	MΩ	
R6	430	Ω	
R7	10	MΩ	
C1	15-60	pF	trim
C2	6.8	μF	electrolytic
C3	15-60	pF	trim
C4	680	nF	tantalum
C5	100	nF	disc
C6	51	pF	silver mica
C7	680	nF	tantalum
B1	47	V	
S1	DPDT		
S2	DPDT		

TABLE 2. PMT Charge Preamplifier Components

Component	Value	Notes
U1	TRA1000	preamplifier
Q1	2N5486	n-JFET
Q2	MPS6519	npn
R1	100 Ω	
R2	1 kΩ	
R3	300 Ω	
R4	51 Ω	1 W
R5	5.1 MΩ	
R6	430 Ω	
R7	499 Ω	1%
R8	49.9 Ω	1%
C1	15-60 pF	trim
C2	6.8 μF	electrolytic
C3	15-60 pF	trim
C4	680 nF	tantalum
C5	10 nF	disc
C6	100 pF	silver mica
C7	680 nF	tantalum
C8	30 nF	silver mica (10 + 10 + 10)
C9	18 nf	silver mica (10 + 4.7 + 3.3)
C10	30 nf	silver mica (10 + 10 + 10)
L1	200 μH	(100 + 100)
L2	52 μH	(47 + 4.7)
L3	52 μH	(47 + 4.7)
L4	200 μH	(100 + 100)
S1	DPDT	

TABLE 3. Laser Timing Controller Components

Component	Value	Notes
U1	74LS221	Dual Monostable Multivibrator
U2	74LS221	Dual Monostable Multivibrator
U3	74LS221	Dual Monostable Multivibrator
U4	74LS221	Dual Monostable Multivibrator
U5	74LS221	Dual Monostable Multivibrator
U6	74LS107	Dual J-K Flip-Flop
U7	74128	Quad 50Ω Line Driver
U8	74128	Quad 50Ω Line Driver
U9	74128	Quad 50Ω Line Driver
U10	74LS158	Quad 2 to 1 Data Multiplexer
U11	7404	Hex Inverter
U12	7437	Quad NAND

TABLE 4. Laser Timing Sequence

Potentiometer Adjustment	Time	Cont. Output	Laser Action
−(LAMP DELAY + QS DELAY)	−3 ms		QR OSC SYNC
−(QS DELAY)	−760 μs	M-LAMP	
	−210 μs		QR lamps fire
	−160 μs		M lamps fire
	0	SYNC	
+(QS TIMING)	80 ns	M-QS	
	100 ns	QR-QS	
	180 ns		M lases
	200 ns		QR lases

1. QR = Quanta Ray DCR-2A Nd:YAG laser, M = Molectron MY-34 Nd:YAG laser, QS = Q-switch.
2. The timings are only approximate and are relative to the SYNC output of the laser timing controller. The lasing times include the propagation delays from the controller to the laser and the delays within each laser.

REFERENCES

1. THORN EMI Gencom, Inc., 23 Madison Road, Fairfield, NJ 07006.
2. P. Horowitz and W. Hill, *The Art of Electronics*, (Cambridge University Press, NY, 1980).
3. I. Dabrowski, *Can. J. Phys.* **62**, 1639 (1984).
4. EMR Photoelectric, Box 44, Princeton, NJ 08542.
5. Harshaw/Filtrol Partnership, 30100 Chagrin Blvd., Cleveland, OH 44124.
6. D. F. Heath and P. A. Sacher, *Appl. Opt.* **5**, 937 (1966).
7. E-H International, Inc., 7303 Edgewater Drive, Oakland, CA 94621.
8. LeCroy Research Research Systems, Inc., 700 South Main Street, Spring Valley, NY, 10977.
9. D. J. Moll, Ph.D. Thesis, California Institute of Technology, 1983.
10. Intel, Inc., 3065 Bowers Ave., Santa Clara, CA 95051
11. Analog Devices, Route One Industrial Park, Norwood, MA 02062.
12. iCOM Microperipherals, Pertec Computer Corp., 21111 Erwin St., Woodland Hills, CA 91367.
13. R. Rianda, Ph.D. Thesis, California Institute of Technology, 1982.

FIGURE CAPTIONS

Figure 1. Schematic of the voltage divider network for the solar blind photomultiplier. A2 is the preamplifier from EMI. All resistances are in kΩ, all capacitances are in nf. The number in parentheses is the pin number on the socket.

Figure 2. Schematic of the charge-to-voltage preamplifier used with the NO ionization cell. All component values are given in Table 1. The supply voltages are ±12 V.

Figure 3. Schematic of the charge-to-voltage preamplifier used with the photomultiplier/A2 preamplifier combination. The passive 100 kHz high frequency filter consists of the four inductors and three capacitors on the left-hand side of the figure; everything else is the preamplifier. All component values are given in Table 2. The supply voltages are ±12 V.

Figure 4. Schematic of the laser timing controller. There are three separate 5 V supplies for this circuit: one for the *RC* timing components, a second for the integrated circuits, and the third for the output drivers.

FIGURE 1.

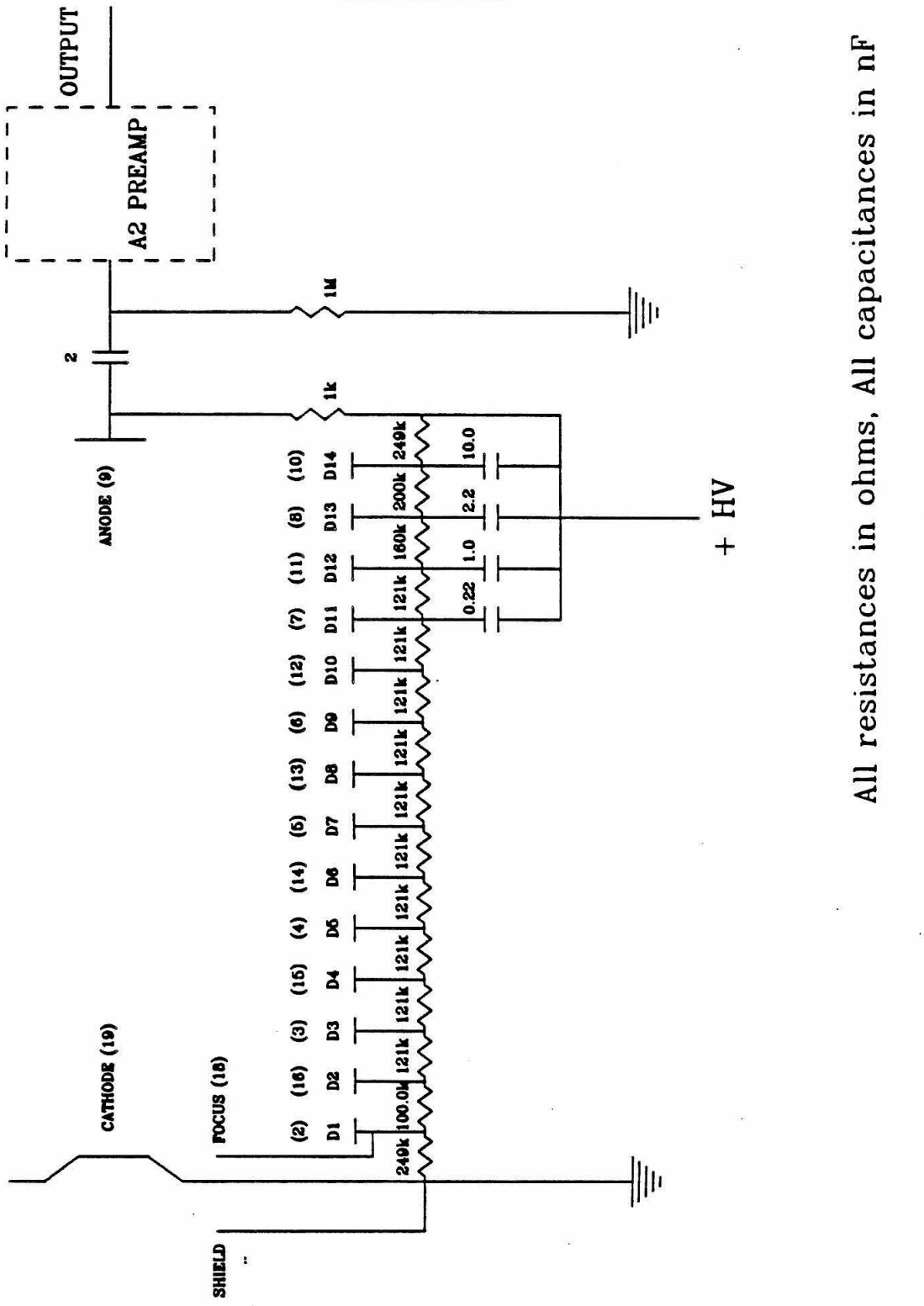

All resistances in ohms, All capacitances in nF

FIGURE 2.

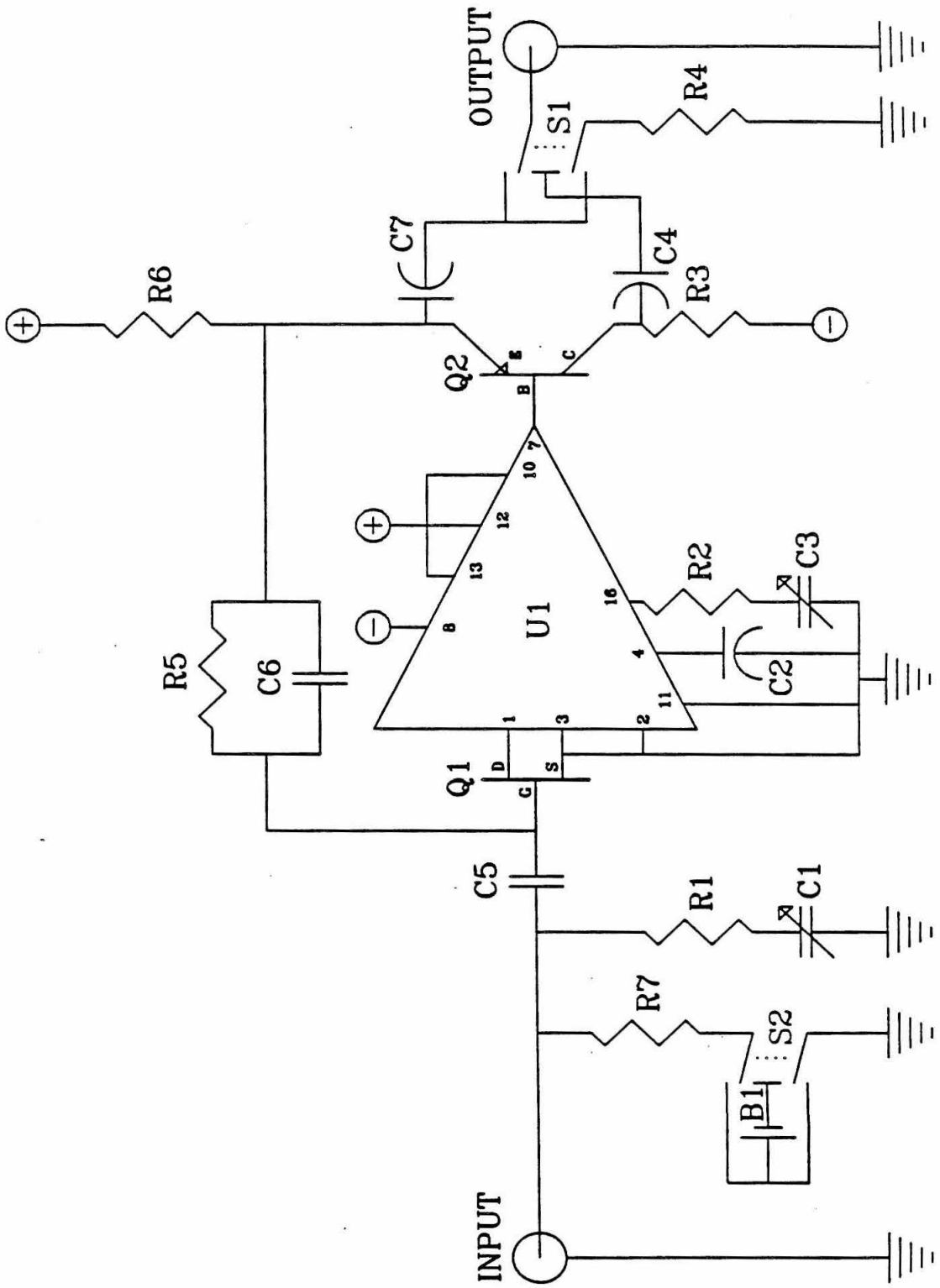
OUTPUT
S1
R4
C7
C4
R3
R6
Q2
U1
R2
C3
C2
R5
C6
Q1
C5
R1
C1
R7
S2
B1
INPUT

FIGURE 3.

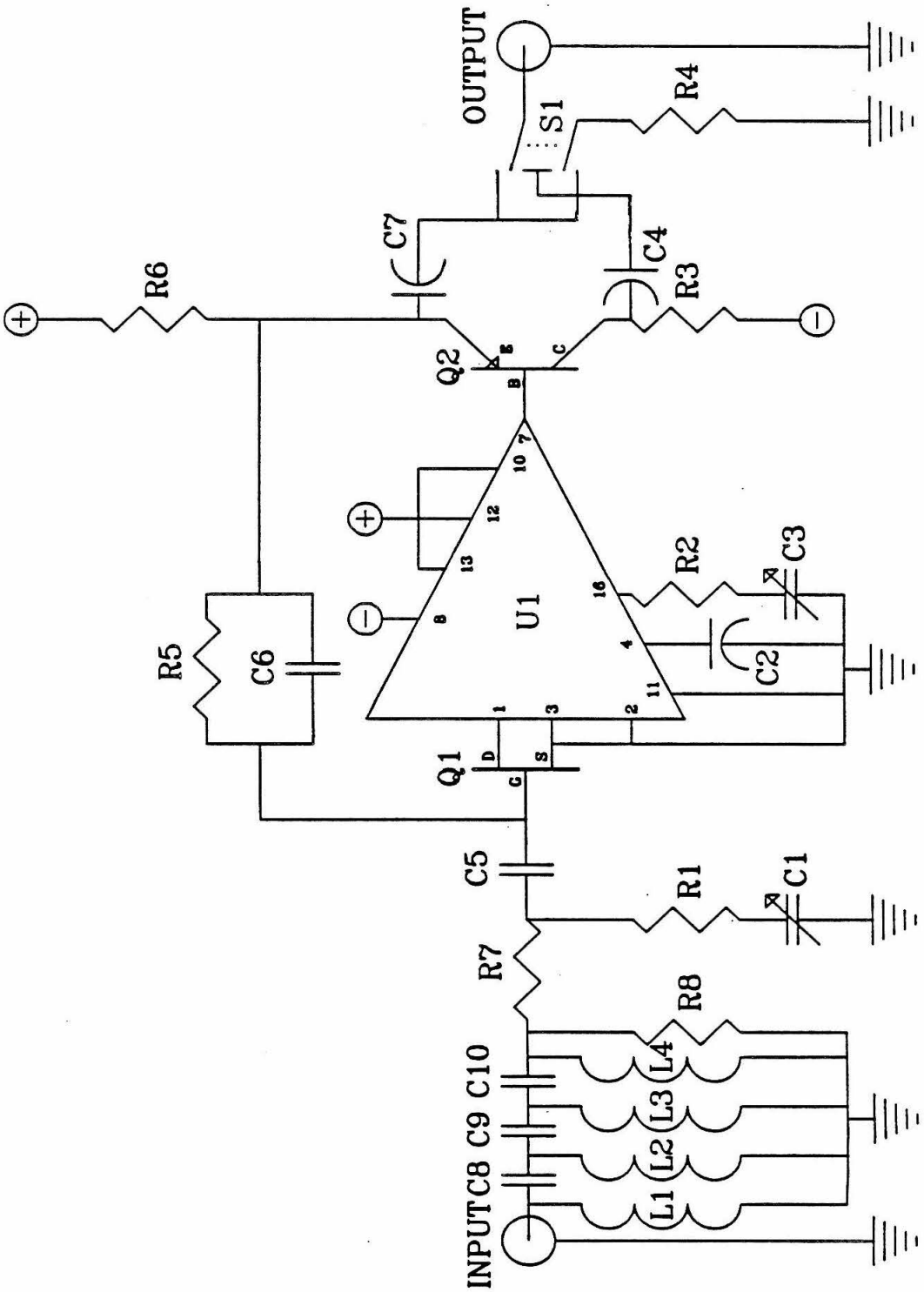
OUTPUT
S1
R4
C7
C4
R6
R3
Q2
U1
R2
C3
R5
C6
C2
Q1
C5
R1
C1
R7
R8
INPUT
C8
C9
C10
L1
L2
L3
L4

FIGURE 4.

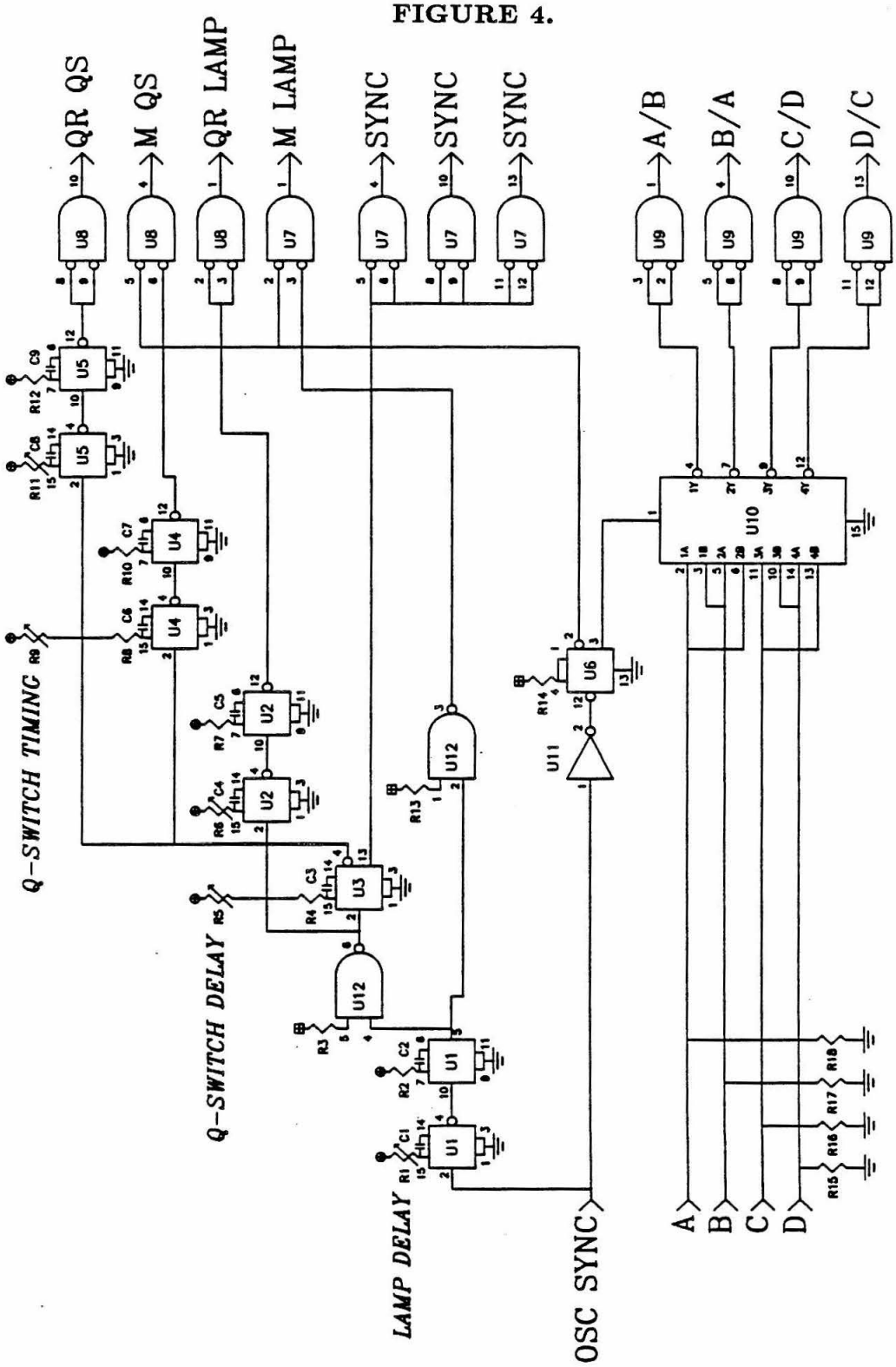
QR QS
M QS
QR LAMP
M LAMP
SYNC
SYNC
SYNC
A/B
B/A
C/D
D/C
Q-SWITCH TIMING
Q-SWITCH DELAY
LAMP DELAY
OSC SYNC
A
B
C
D
U10